OAK RIDGE NATIONAL LABORATORY LIBRARIES

3 4456 0578490 6

ORNL-5540

ornl

OAK RIDGE NATIONAL LABORATORY

UNION CARBIDE

High-Temperature Structural Design Program Semiannual Progress Report for Period Ending December 31, 1978

J. M. Corum
C. E. Pugh

OAK RIDGE NATIONAL LABORATORY
CENTRAL RESEARCH LIBRARY
CIRCULATION SECTION
4500N ROOM 175
LIBRARY LOAN COPY
DO NOT TRANSFER TO ANOTHER PERSON
If you wish someone else to see this report, send in name with report and the library will arrange a loan.

[redacted]

OPERATED BY
UNION CARBIDE CORPORATION
FOR THE UNITED STATES
DEPARTMENT OF ENERGY

Printed in the United States of America. Available from
the Department of Energy
Technical Information Center
P.O. Box 62, Oak Ridge, Tennessee 37830
Printed Copy: A11 Microfiche A01

This report was prepared as an account of work sponsored by an agency of the United States Government. Neither the United States nor any agency thereof, nor any of their employees, makes any warranty, express or implied, or assumes any legal liability or responsibility for any third party's use or the results of such use of any information, apparatus, product or process disclosed in this report, or represents that its use by such third party would not infringe privately owned rights.

ORNL-5540
Dist. Category UC-79,
-79h, -79k

Contract No. W-7405-eng-26

Engineering Technology Division

HIGH-TEMPERATURE STRUCTURAL DESIGN PROGRAM SEMIANNUAL PROGRESS REPORT FOR PERIOD ENDING DECEMBER 31, 1978

J. M. Corum, Program Manager
C. E. Pugh, Assistant Program Manager

Date Published: October 1979

Prepared by the
OAK RIDGE NATIONAL LABORATORY
Oak Ridge, Tennessee 37830
operated by
UNION CARBIDE CORPORATION
for the
DEPARTMENT OF ENERGY

Previous Reports in This Series

Report No.	Period Covered
ORNL/TM-3736	August–December 1971
ORNL/TM-3845	January–March 1972
ORNL/TM-3917	April–June 1972
ORNL/TM-4058	July–September 1972
ORNL/TM-4089	October 1972–March 1973
ORNL/TM-4356	April–June 1973
ORNL-4947	July–December 1973
ORNL-4977	January–March 1974
ORNL-5005	April–June 1974
ORNL-5048	July–December 1974
ORNL-5087	January–June 1975
ORNL-5136	July–December 1975
ORNL-5235	January–June 1976
ORNL-5281	July–December 1976
ORNL-5339	January–June 1977
ORNL-5374	July–December 1977
ORNL-5433	January–June 1978

CONTENTS

Page

PREFACE vii

SUMMARY AND STATUS ix

1. CONSTITUTIVE EQUATION DEVELOPMENT 1

1.1 Recommendation of Modifications to Constitutive Equations in RDT Standard F9-5T 2

1.1.1 Background to equation modifications 2
1.1.2 Recommended modifications to constitutive equations 5
1.1.3 Illustrative analyses 7

1.2 Development of Refined Constitutive Laws 16

1.2.1 Basic model development 16
1.2.2 Exploratory experiments contributing to a data base for the ORNL unified equations 22
1.2.3 Numerical integration studies 26

1.3 Uniaxial Exploratory Testing 29

1.3.1 Testing of type 304 stainless steel 29
1.3.2 Representation of uniaxial creep data for type 304 stainless steel (heat 9T2796) at 538°C (1000°F) 33
1.3.3 Testing of type 316 stainless steel 36
1.3.4 Testing of 2 1/4 Cr–1 Mo steel 37
1.3.5 Deformation studies of 308 CRE weldments 43

1.4 Multiaxial Exploratory Testing 47

1.4.1 Multiaxial creep tests 47
1.4.2 Multiaxial plasticity experiments at room and elevated temperatures 51

1.5 Development of Methods for Measuring Biaxial Strains at Elevated Temperatures 78

References 84

2. INELASTIC STRUCTURAL TESTS AND ANALYSES 87

2.1 Development and Evaluation of Computer Codes and Analysis Methods 87

2.1.1 Development of the HEX module of PLANS (PLANS/HEX) 87
2.1.2 CREEP-PLAST II, dissemination 88

2.2 Beam and Plate Tests 88

2.2.1 Type 316 stainless steel beam B16 89
2.2.2 2 1/4 Cr–1 Mo steel beam B17 92

Page

2.2.3 Type 304 stainless steel beam with type 308 stainless steel weld-beam B18 (WB-1) 97
2.2.4 2 1/4 Cr–1 Mo steel circular plate test CP8 105
2.2.5 Type 316 stainless steel circular plate test CP9 ... 105

2.3 Analysis of the Capped Cylindrical Shell Test CC2 108

2.4 Nozzle-to-Sphere Tests and Analyses 117

2.4.1 High-temperature deformation phase of test of NS-2 117
2.4.2 Test plan for failure phase of NS-2 120

2.5 High-Temperature Strain Gage Development and Verification 127

2.6 International Piping Benchmark Problem Effort 128

References 131

3. DESIGN CRITERIA AND RULES FOR TIME-DEPENDENT DEFORMATION AND FAILURE 133

3.1 Creep-Rupture Failure Under Uniaxial and Multiaxial Conditions 134

3.1.1 Constant-load uniaxial tests 134
3.1.2 Constant-load multiaxial tests 134
3.1.3 Uniaxial step-load tests 142

3.2 Investigation of Cumulative Creep-Rupture Damage Under Variable Load and Temperature (VLT) Conditions 145

3.2.1 Uniaxial VLT tests 145
3.2.2 Multiaxial VLT tests 148

3.3 Effect of Biaxiality in Creep-Fatigue at Elevated Temperature 149

3.4 Failure Under Cyclic, Relaxing Residual Stresses: Restrained-Cylinder Tests 160

3.4.1 Base metal tests 161
3.4.2 Weldment tests 166

3.5 Failure Studies and Notched-Bar Rupture Tests on Type 304 Stainless Steel 167

3.5.1 Failure studies on type 304 stainless steel 167
3.5.2 Notch-bar rupture tests on type 304 stainless steel 168

3.6 Analysis of a Notched-Bar Specimen 169

3.7 Assessment of Multiaxial Fatigue Criteria for Type 304 Stainless Steel 170

Page

3.8 Sensitivity Study of Current Design Rules to Heat-to-Heat Material Property Variations 184

3.8.1 Compilation and analysis of applicable data 184
3.8.2 Inelastic ratchetting analyses 206

3.9 Fatigue and Creep-Rupture Curves for Use in Projecting Failure in ORNL Laboratory Structural Tests 206

3.9.1 Fatigue curve for annealed type 304 stainless steel (heat 9T2796) at 593°C (1100°F) 207
3.9.2 Uniaxial and biaxial 593°C (1100°F) creep-rupture curves for annealed type 304 stainless steel (heat 9T2796) 210

3.10 Development of Matrix of Tests for Evaluation of Creep-Fatigue Methods 217

References 219

4. SIMPLIFIED DESIGN METHODS 223

4.1 Analyses of Axisymmetric Cylindrical Shells 224

4.1.1 One-dimensional infinite cylinders 225
4.1.2 Two-dimensional circular cylindrical shell analyses 227

4.2 Detailed Inelastic Analysis of Nozzle-to-Spherical-Shell Attachment 229

4.3 Improved Elastic Ratchetting and Creep-Fatigue Damage Evaluation Procedures 234

4.4 Examination of Simplified Inelastic Analysis Procedures ... 238

4.4.1 Summary of CRBRP-IHX primary inlet nozzle inelastic analysis results 239

4.5 Analytical Investigation of the Applicability of the Isochronous Method for Predicting Deformations in Simple Beam and Plate Structures 247

References 249

5. THERMAL RATCHETTING TESTS 251

5.1 Analysis of the Weldment Region of Specimen TTT-3 251

5.2 Type 316 Stainless Steel Seamless to Seam-Welded Pipe Specimen TTT-4 255

5.3 Test TT-6 of a Type 304 Stainless Steel Pipe to Creep-Fatigue Failure 255

References 256

Page

6. STRUCTURAL DESIGN METHODS FOR WELDMENTS 257

6.1 Plate-Weldment Tests 257

6.1.1 Room-temperature tests 257
6.1.2 Elevated-temperature tests 268

6.2 Residual Stress Effects 271

6.2.1 Simulation of residual stress in a thermal ratchetting problem 272
6.2.2 Measurement of residual stresses by the hole-drilling technique 273
6.2.3 Analysis of plate-weldment deformation field in the presence of residual stresses 279

6.3 Uniaxial Tests of Type 308 Stainless Steel Weld Metal 284

6.4 Notch Effects in Uniaxial Tension Specimens 285

6.5 Development of High-Temperature Moire Technology 288

References 289

PREFACE

This report summarizes progress in the ORNL High-Temperature Structural Design Program for July through December 1978. The technical activities of the program are comprehensively reported under six major headings, or subtasks, which correspond to the subtasks of the current 189a OH048 document:

A. Constitutive Equations for Inelastic Design Analysis
B. Inelastic Structural Tests and Analyses
C. Design Criteria and Rules for Time-Dependent Deformation and Failure
D. Simplified Design Methods
E. Thermal Ratchetting Tests
F. Structural Design Methods for Weldments

The Summary and Status, which precedes the text, gives a short synopsis of the progress and the status of each subtask and includes brief discussions of pertinent program management and liaison activities. It provides the reader an opportunity to survey the contents of the report prior to reading the technical sections.

The purposes of the program are to develop verified high-temperature structural design methods and criteria applicable to liquid-metal fast breeder reactor (LMFBR) and other reactor system components that operate at temperatures in the creep range and to assist in making the technology available to component designers in the form of design analysis tools, guidelines, codes, and standards. The program makes extensive use of subcontractors and consultants and is closely related to, and coordinated with, three other high-temperature structural design programs sponsored by the Department of Energy/Division of Reactor Research and Technology (DOE/RRT). Two of these programs at Westinghouse Advanced Reactors Division (WARD) relate to validation and application of high-temperature design methods; the third, at Rockwell Energy Systems Group/Atomics International (ESG/AI), relates to high-temperature structural design methods for piping. These four High-Temperature Structural Design Program Elements — development (ORNL), validation (WARD), application (WARD), and

piping (AI) — are described in the *Long-Range Plan for High-Temperature Structural Design*, ORNL-5369 (December 1977).

The ORNL program was initiated in 1969, when it was recognized that the existing structural design methods and criteria, which were developed for light-water reactors, did not provide an adequate basis for the design of LMFBRs. From the beginning, it was felt that the development of an adequate high-temperature structural design technology would require a knowledge and understanding of essential features of inelastic material behavior and that the ability to predict inelastic structural behavior resulting from time-varying thermal and mechanical loadings should be an essential ingredient of that technology. The initial development effort was thus divided into two significant parts:

- Development and evaluation of analysis methods for predicting inelastic structural behavior;
- Development and evaluation of design rules and criteria to preclude structural failures.

Two additional parts — the development and evaluation of simplified methods and the development of design methods for weldments — make up the current program, as shown diagrammatically below.

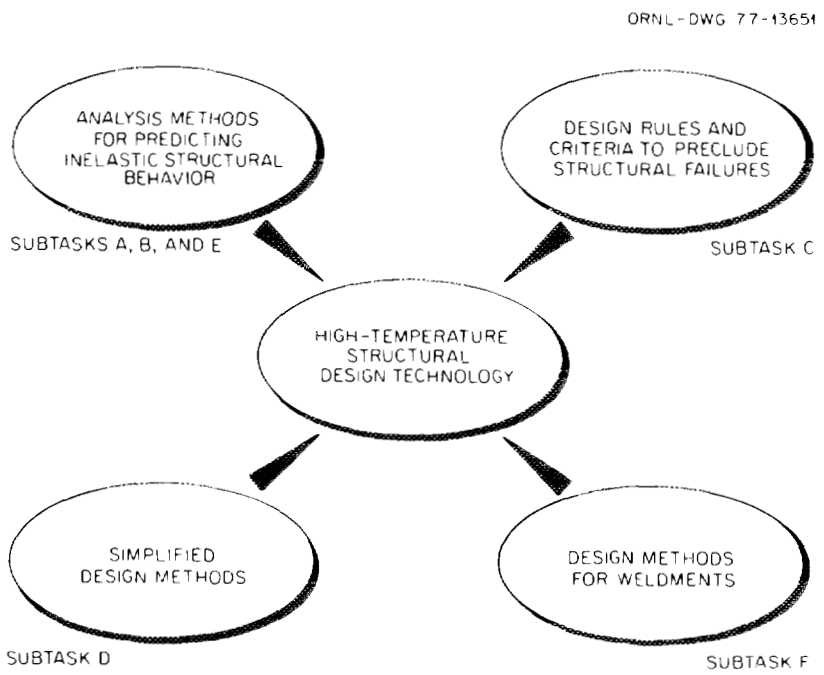

Two objectives are being served by the program. In addition to the development of the required technology as an end product, interim needs for structural design guidance, methods, and criteria are being met on a continuing basis. In the initial phases of the program, existing knowledge and data concerning material behavior, existing constitutive theories and structural analysis methods, and existing design rules and criteria were exploited to meet design requirements and to help establish bases for identification and pursuit of program activities aligned with the twofold objective. Thus, the activities established for the near term naturally lead toward those for the long term.

Our goal is a technology developed on theoretically consistent and experimentally verified rational bases. The benefits of such a technology will include (1) improved component reliability and confidence levels, (2) more economical and defensible design procedures, and (3) an improved technological basis for licensing.

SUMMARY AND STATUS

Significant activities and accomplishments of the ORNL High-Temperature Structural Design (HTSD) Program during this report period include (1) preparation of revisions to the constitutive equation guidelines now in RDT Standard F9-5T for types 304 and 316 stainless steels and 2 1/4 Cr–1 Mo steel and submittal of a revised version of Chapter 4 (Inelastic Analysis Methods) to the RDT Standard F9-4 Task Force for approval; (2) completion of high-temperature yield surface tests on type 316 stainless steel showing that initial yielding is approximated by the von Mises criterion and that movement of the yield surface is "kinematic" in nature, as described in the revised guidelines; (3) completion of the deformation phase of the first high-temperature nozzle-to-sphere test and favorable comparison of the pressure test results with inelastic analysis predictions; and (4) completion, at O'Donnell and Associates, of an extension of the O'Donnell-Porowski procedure to provide creep ratchetting bounds in the plastic ratchetting regime where the method could not previously be used.

Program staff members participated in the following committee meetings:

1. American Society of Mechanical Engineers (ASME) Code groups: Task Force on Strain Limits and Creep Fatigue (Sept. 12, Oct. 31); Working Group on Creep Analysis (Sept. 12, Oct. 31); Working Group on Creep Fatigue (Sept. 12, Oct. 31); Subgroup on Elevated-Temperature Design (Sept. 13, Nov. 1).
2. Pressure Vessel Research Committee: Subcommittee on Elevated-Temperature Design (Oct. 2); Subcommittee on Plastic-Fatigue Strength (Oct. 3).

Staff members also participated in or attended the following special meetings:

1. Meeting of RRT Task Force on Thermal Striping (July 27);
2. Clinch River Breeder Reactor Project (CRBRP) Quality Assurance Audit on the ratchetting test for CRBRP 316 stainless steel hot-leg crossover piping (test TTT-4) (Aug. 7);

3. Third Meeting of the RRT Working Group on High-Temperature Structural Design (Aug. 8);
4. Fourth Meeting of the RRT Subgroup on High-Temperature Structural Design Program Coordination (Aug. 9);
5. Meeting at DOE/RRT on transition joint testing (Aug. 17);
6. Special Information Meeting on High-Temperature Structural Design Applications Experience, held at DOE (Sept. 14-15); ORNL was the organizer;
7. Meeting of American Nuclear Society (ANS)-54 Committee on LMFBR Design Standards (Sept. 20);
8. Seminar given to the CRBRP/Project Office (PO) Engineering Staff (Oak Ridge) entitled "Summary and Status of HTSD Technology Activities" (Sept. 22);
9. Breeder reactor information exchange meeting between ORNL Breeder Reactor Program (BRP) technology managers and WARD personnel (Oct. 17-18);
10. Meeting at DOE/RRT to discuss the status and plans for the basic specimen and tubular testing subtasks of the WARD HTSD—Validation program (Oct. 27);
11. Symposium on Future Trends in Computerized Structural Analysis and Synthesis, held in Washington, D.C. (Oct. 30—Nov. 1);
12. American Society of Metals (ASM) Triple Engineering Shows and Conferences, held in Philadelphia, Pennsylvania (Nov. 8);
13. American Society for Testing and Materials (ASTM) Meeting held in Houston, Texas (Nov. 13-16); presentation was made at the workshop sponsored by the Metal Properties Council entitled "Parameter Extrapolation of High-Temperature Data for Use in Materials Specifications";
14. Nuclear Regulatory Commission Elevated-Temperature Primary System Integrity Review Meeting, held at Sandia Laboratories, Albuquerque, New Mexico (Nov. 14-15);
15. Meeting at ORNL between ORNL and WARD personnel to discuss FY-1979 plans for the tubular testing subtask of the HTSD—Validation program at WARD (Nov. 16);

16. Meeting at National Aeronautics and Space Administration (NASA)-Lewis Research Center, Cleveland, Ohio, to help develop a matrix of tests that could aid in the determination of which of the various candidate creep-fatigue correlation methods should be used as the basis for elevated-temperature design (Nov. 21);
17. United States/United Kingdom Atomic Energy Authority (US/UKAEA) Specialists Meeting on Mechanical Properties, held in Oak Ridge, Tennessee (Dec. 4-6);
18. Technical discussions on high-temperature strain gages with Energy Technology Engineering Center (ETEC) and Ailtech personnel (Dec. 5-7);
19. Visit to Cornell University to discuss work on constitutive equations (Dec. 6);
20. 99th ASME Winter Annual Meeting (Dec. 12-15); while there, R. W. Swindeman chaired meeting of the Nuclear Systems Materials Handbook (NSMH) Working Group C.1 and Pressure Vessel and Piping Division Subcommittee MF-4;
21. Meeting of Computer Technology Committee of ASME Pressure Vessel and Piping Division (Dec. 12).

Technical coordination meetings were held with S. Y. Zamrik, Pennsylvania State University (Sept. 11-15, Sept. 27) to discuss subcontract activities and to assess accuracy of temperature and strain measurements; Joliet Metallurgical Laboratories (Oct. 10) to review the status of the creep-rupture damage subcontract; F. A. Leckie, University of Illinois (Dec. 12) to negotiate a potential subcontract.

Technical exchange meetings were held with T. J. Walker, Nuclear Regulatory Commission (Aug. 3); J. A. Williams, Central Electricity Generating Board (CEGB), Marchwood (Sept. 11); K. G. Eickhoff, F. I. Buckley, and D. C. Smith, UKAEA, Risley Nuclear Laboratories (Sept. 21); T. Takahasi, PNC, S. Nomoto, JOYO, S. Abe, MONJU, M. Hori, O-arai, and Y. Mimoto, O-arai (Japan) (Nov. 16); Brian Tomkins, UKAEA-Springfield, G. D. Branch, CEGB, Robert Boler, Nuclear Power Company (NPC), and G. J. Lloyd, UKAEA-Risley (Dec. 7).

Publications during this report period are as follows:

1. R. W. Swindeman, *Isochronous Relaxation Curves for Type 304 Stainless Steel After Monotonic and Cyclic Strain*, ORNL/TM-6380 (July 1978).

2. Staff, High-Temperature Structural Design Program, "Request for Approval-In-Principal for a Pipe Thermal Ratchetting Test to Failure at the Energy Technology Engineering Center," June 1978. Attachment to letter, P. Patriarca (ORNL) to Director (RRT), July 19, 1978.

3. ORNL, WARD, and AI, *High-Temperature Structural Design — 1977 Summary and Status Report*, ORNL-5419 (July 1978).

4. C. C. Schultz and W. E. Leyda, *Creep Failure Under Uniaxial and Multiaxial Stress Conditions*, ORNL/Sub-3654-4 (August 1978).

5. W. K. Sartory et al., *Thermal Ratchetting Test of Type 316 Stainless Steel Seamless to Seam-Welded Pipe: Specimen TTT-4*, ORNL-5430 (September 1978).

6. J. E. Stoneking, *Preliminary Investigation of Numerical Solution Algorithms for the Unified Plasticity-Creep Equations*, unpublished internal document, ORNL/CF-78/290 (Sept. 8, 1978).

7. Staff, High-Temperature Structural Design Program, "Modifications to Constitutive Equations for Types 304 and 316 Stainless Steel and 2 1/4 Cr—1 Mo Steel," Sept. 11, 1978. Attachment to letter, J. M. Corum (ORNL) to Members, RDT Standard F9-4 Task Force, Oct. 4, 1978.

8. D. N. Robinson, *A Unified Creep-Plasticity Model for Structural Metals at High Temperature*, ORNL/TM-5969 (October 1978).

9. J. S. Porowski and W. J. O'Donnell, *More Efficient Creep Ratchetting Bounds*, ORNL/Sub-7322-1, O'Donnell and Associates (October 1978).

10. D. N. Robinson, *A Nonlinear Plasticity Model for Structural Alloys at Elevated Temperature*, ORNL/TM-6582 (November 1978).

11. J. M. Corum and C. E. Pugh, *High-Temperature Structural Design Program Semiannual Progress Report for Period Ending June 30, 1978*, ORNL-5433.

12. R. W. Swindeman and C. E. Pugh, *The Influence of Cyclic Loadings on Creep Behavior of Austenitic Stainless Steels*, ORNL-5429 (December 1978).

13. Summary Report, *Special Information Meeting on High-Temperature Structural Design Applications Experience, Germantown, Maryland, Sept. 14-15, 1978*, ORNL/BRP-78-4 (December 1978).

14. J. M. Corum and A. W. Dalcher, "Materials Data Requirements for the High-Temperature Structural Design of 2 1/4 Cr—1 Mo Steel Components," pp. 69-73 in *Ferritic Steels for Fast Reactor Steam Generators*, vol. 1, British Nuclear Energy Society, London, 1978.

Activities and progress in each program subtask area are summarized below.

1. Constitutive Equations for Inelastic Design Analysis (Subtask A)

The objective of this subtask is to develop and verify mathematical descriptions (constitutive equations) of the inelastic behavior of breeder reactor structural metals through combined theoretical and experimental investigations. Activities during this report period included recommendation of a revision to the equations now in RDT Standard F9-5T, further development of unified constitutive equations, and exploratory uniaxial and multiaxial material behavior testing.

The assessment of the constitutive equations now in RDT Standard F9-4T that was undertaken during the last report period was completed, and specific revisions were recommended. A letter was sent in October to the RDT Standard F9-4 Task Force requesting their review and approval of the modifications. The modifications provide for a stronger influence of creep strains on subsequent plastic yield and flow and lead to an enhanced stability of stress-strain responses to cyclic loadings that involve periods of relaxation. The modifications are recommended for the three alloys now in, or approved for inclusion in, F9-5T (304 stainless steel, 316 stainless steel, and 2 1/4 Cr-1 Mo steel), and they were made after several alternative approaches were examined analytically and compared with experimental data. A complete statement of the modified equations is given in this report, along with some representative comparisons between predictions and experimental data. Predictions based on the modified equations are also contrasted with those based on the equations now in F9-5T.

A report was published on the development of the ORNL unified constitutive theory. A complete mathematical statement of the model for isothermal conditions is provided, along with the results of calculations made with a variety of combinations of the material parameters. The objective was to demonstrate the capability of the model to qualitatively represent important features of material behavior. More recently, values

for parameters in the model have been established to characterize existing data for a heat of 2 1/4 Cr–1 Mo steel at 566°C (1050°F). The mathematical statement of the model is outlined in this report, along with the parameter values determined from this study. Some favorable comparisons are presented between predictions and data for several tensile and creep tests.

Two parallel efforts have been under way to study whether special and, therefore, possibly inefficient numerical procedures are required to implement the unified constitutive equations into finite-element programs. The first is being conducted under subcontract with The University of Tennessee, and the second is being carried out within ORNL. Both use the unified equations and parameter values given herein. Under the first effort, a special-purpose code has been developed that utilizes an explicit Euler algorithm for time integration for axisymmetric geometries. The ORNL work has implemented the equations into the PLACRE code. Several simple problems have been successfully analyzed, as well as a trial problem involving the complex thermal transient histogram of our earlier pipe thermal ratchetting test TTT-1. A standard time integration routine available in the ORNL software library was used, and no apparent numerical difficulties have been encountered in these analyses. In performing the TTT-1 analysis, only material properties for 2 1/4 Cr–Mo steel were available, making it inappropriate to compare predictions with the experimental results from the 304 stainless steel specimen actually used in the TTT-1 experiment. However, the results appear qualitatively reasonable.

Efforts were made this period to summarize major aspects of the considerable uniaxial testing that has been completed to date for types 304 and 316 stainless steel and for 2 1/4 Cr–1 Mo steel. In the case of 304 stainless steel, two reports were prepared covering data from the ORNL reference heat. The first is on development of a Frost-Ashby–type deformation map and contour maps of several creep parameters in stress and temperature spaces. The second summarizes ORNL work and literature information on cyclic creep. Additionally, to support analysis of capped cylinder structural test specimens, an equation was developed to represent available creep data for the reference heat of 304 stainless steel at 538°C (1000°F).

Summary reports were also prepared on the exploratory testing that has been completed for the reference heat of 316 stainless steel and for 2 1/4 Cr–1 Mo steel. Most of the testing was performed at 593°C (1100°F) for the 316 stainless steel, and many of the behavioral features were similar to those for 304 stainless steel. Although testing on 2 1/4 Cr–1 Mo steel has been complicated by the lack of a comprehensive reference heat of material and by a variety of heat treatments, discussions of the general behavioral characteristics included in the summary report are abstracted herein.

The last review performed during this period concerns the available uniaxial data for type 308 stainless steel controlled-residual-element (CRE) weldments. This was a less extensive review and concentrated on tensile and creep data. The conclusion is that only a small amount of data exists that is useful to constitutive equation assessment efforts. We plan to conduct further exploratory tests to support such assessments, but the rate of test performance will be necessarily modest.

A torsional creep test of a type 304 stainless steel specimen was continued in the multiaxial test lab. In addition to examining the creep response under various levels of torsional loadings, the recovery of creep strains was examined for interspersed periods of load removal. The torsional recovery response was found to be consistent with our earlier observations made from tensile creep tests which showed limited recovery of creep strains that depend on the prior stress level.

A series of exploratory yield surface experiments were conducted on types 304 and 316 stainless steel at temperatures in the range 21 to 593°C (70 to 1100°F), with the primary aim of investigating the biaxial yield behavior at elevated temperatures. Before the study could begin, strain measurement methods had to be developed with sufficient resolution to determine yield surfaces defined by small offset strain (10 $\mu\varepsilon$). The method developed used Ailtech weldable-resistance strain gages oriented to form rectangular strain gage rosettes. Initial yield surfaces were generated for type 304 stainless steel at room temperature and 232°C (450°F). Failure of two strain gages prevented testing this specimen at high temperatures.

The experiment conducted on type 316 stainless steel was more successful, and initial yield surfaces were obtained at temperatures in the range 21 to 593°C (70 to 1100°F). In addition, a yield surface was determined subsequent to creep deformation at 593°C (1100°F). The important conclusions are that the von Mises yield criterion approximates the initial yield behavior over the temperature range investigated and that hardening behavior due to prior creep is "kinematic" in nature, as assumed in the equation modifications mentioned earlier.

Work continued on the development of our multiaxial extensometer for use in high-temperature experiments. A series of preliminary evaluation experiments were conducted to investigate the extensometer's capabilities in measuring torsional and diametral strains. They showed that the method of measurement is practicable if noise levels are kept to a minimum by using filters and that superimposed axial strains have negligible effects on torsional measurements. Components for the laser interferometric axial-strain-measuring portion of the system were received and assembled for evaluation. If further evaluations turn out as anticipated, the instrument will be available for use during the next report period.

2. Inelastic Structural Tests and Analysis (Subtask B)

The objectives of this subtask are to develop, evaluate, and improve computer-based techniques for solving inelastic structural problems and to provide structural test data for evaluating analysis procedures, constitutive equations, failure criteria, and computer codes. In addition to analysis efforts, work during this period included beam and plate tests, a high-temperature nozzle-to-sphere test, coordination of an international piping benchmark problem effort, and a high-temperature strain gage evaluation effort.

During this report period, the subcontract with Grumman Aerospace Corporation was continued, the development work on the three-dimensional HEX moduli of the PLANS computer program was completed, and a final report was begun, along with a revised user's manual for the program.

The CREEP-PLAST II computer program, a special-purpose finite-element code for the anaysis of two-dimensional, elastic-plastic-creep structures, has been transferred to the National Energy Software Center for public dissemination.

For the 316 stainless steel solid beam test (B16), which was completed in June 1978, the experimental data have been reduced, and preliminary graphical displays of the test results were completed.

The 2 1/4 Cr–1 Mo solid beam test (B17) was completed during this period. The test was run at 538°C (1000°F) and consisted of three phases: the first was compsed of 1-1/2 precreep cycles (load controlled) followed by a creep period of 2.1 hr and then by a 3/4-cycle load reversal to the nominal negative load; the second consisted of 22 cycles under prescribed, center deflections and was run for about 718 hr; and the third consisted of 7 cycles under prescribed center loads and was run for about 1175 hr. The experimental data were reduced, and graphical displays of the test results were made.

The first 304 stainless steel–welded solid beam (B18) (WB-1) was fabricated using a 308 stainless steel weld. The beam was instrumented, and a histogram for the first phase of testing was developed.

The 316 stainless steel circular plate test (CP9) was completed during this period. The test consisted of 12 cycles with 1- to 2-week hold periods, with the test lasting for 20 weeks.

The analysis of the capped cylindrical shell test (CC2) was completed. The inelastic structural analysis of the test gave fair agreement with the strain gage measurements during phase 1 (deformation test) of the loading and during the initial pressurization of phase 2 (failure test). Analysis of phase 2 could not be completed because of the small deformation limitations of the structural analysis program. Creep damage evaluations that were completed for phase 1 were quite conservative. They predicted failure in about 880 additional hours under the mild conditions of phase 1, whereas the specimen actually withstood over 1200 hr of additional testing under the much more severe loading of phase 2.

The first high-temperature inelastic test of a nozzle-to-sphere model (NS-2) was completed during this period. The test was run at 593°C (1100°F)

and consisted of two phases: the first involved only pressure loading and the second involved only a moment loading. Each phase of the test was run for approximately eight weeks. The pressure-only phase of the test was analyzed, and the predictions of inelastic strains in the junction region agreed reasonably well with the experimental values.

3. Design Criteria and Rules for Time-Dependent Deformation and Failure (Subtask C)

The objective of this subtask is the development and evaluation of design criteria aimed at precluding time-dependent failure through excessive deformation, cracking, or rupture. Current emphasis is on time-dependent damage accumulation under uniaxial and multiaxial fatigue and creep conditions.

During this report period, progress was made in the following areas:

1. concluded uniaxial/multiaxial creep rupture study at Babcock & Wilcox;
2. initiated exploratory variable load and temperature uniaxial and multiaxial creep-rupture damage tests;
3. calibrated biaxial creep-fatigue equipment and corrected previously reported data generated at Pennsylvania State University. Six additional data points were generated;
4. assessed multiaxial fatigue criteria on the basis of corrected Pennsylvania State University data on 304 stainless steel (heat 9T2796) at 538°C (1000°F);
5. initiated thermal-cycling, creep-rupture failure tests of a "restrained cylinder";
6. continued ongoing failure tests of 304 stainless steel notched bars and initiated a supporting inelastic analysis;
7. completed phase 1 (data compilation and modeling) of a "sensitivity study of current design rules to heat-to-heat material property variations;.
8. compiled existing 304 stainless steel data (heat 9T2796) and generated a set of reference fatigue and creep-rupture curves for use in design of in-house experiments;
9. began a matrix of tests designed to provide maximum separation between the various candidate time-dependent fatigue failure criteria.

The last test in a study conducted by Babcock & Wilcox of the creep-rupture behavior of 304 stainless steel at 593°C (1100°F) was completed when the tubular specimen (BWTR-5) failed after 21,840 hr at a biaxial effective stress of 119.4 MPa (17.32 ksi). This study included 11 constant-load multiaxial tests with failure times up to 21,840 hr, 19 constant-load uniaxial tests with failure times up to 44,296 hr, and 13 step-load uniaxial tests with failure times up to 13,258 hr. Final results for each of these test series are summarized in this report. A more comprehensive final report was issued by Babcock & Wilcox.

Two new exploratory variable-load and variable-temperature creep-rupture test series, one uniaxial and one multiaxial, were initiated during this period on annealed 304 stainless steel (heat 9T2796). Uniaxial tests are being done under subcontract by the Joliet Metallurgical Laboratory. The first 17 baseline tests have been initiated and have accumulated an average of approximately 800 test hours each. One multiaxial test (tubular specimen, internal pressure loading) was completed at ORNL. Additional test specimens are in preparation.

As a cooperative effort between Pennsylvania State University and ORNL, thermal gradient, thermal fluctuation, and high-temperature axial strain calibration tests were conducted on the Pennsylvania State University biaxial creep-fatigue testing equipment. Results of these calibrations indicated that some axial strain ranges have been previously reported as one-half the actual range. A tabulation of corrected data is provided in this report. These tests also indicated a need for improvements in the thermal distribution within the specimen. Efforts are under way to provide these improvements. Six new creep-fatigue tests were completed — two with symmetric holds, one with negative hold, and three without holds. Multiaxial fatigue criteria were reassessed during this period using the entire set of correlated Pennsylvania State University data.

Two cyclic thermal loading tests of restrained 304 stainless steel tabular specimens were initiated during this report period. These tests are designed to explore creep-rupture failure under relaxing residual stresses that are thermally induced. The specimen provides a homogeneous,

uniaxial stress state. Specimens are cycled through a temperature range, with peak temperature being 649°C (1200°F). No failures have been experienced to date.

An updated study of our creep-rupture data for 304 stainless steel reference heat 9T2796 was begun as part of an effort to develop Ashby-type fracture maps. The validity of the Monkman-Grant correlation between rupture life and creep rate was also examined. For temperatures above 650°C (1200°F), temperature dependencies of the secondary creep rate and rupture life were found to be similar, at least for test times <46 days. At lower temperatures, the dependencies were found to be different, primarily because of change in strain rate behavior.

Two previously reported notched-bar tests at 482 and 593°C (900 and 1100°F) are continuing. An inelastic analysis of a circular notched bar with fully reversed cyclic loading has been initiated.

The first phase of a "sensivity study of current design rules to heat-to-heat material property variations" was completed. Available property data from a number of heats of 304 stainless steel were compiled, statistically evaluated, and placed in a format suitable for incorporation into appropriate inelastic analyses. The statistically reduced data are summarized in this report.

A set of reference fatigue and creep-rupture curves were generated for the reference heat of type 304 stainless steel at 593°C (1100°F). These curves will be used in the program as a common basis for estimating the failure conditions for laboratory structural tests.

In cooperation with the ASME Boiler and Pressure Vessel Code, Task Force on Strain Limits and Creep Fatigue, efforts were undertaken to generate a matrix of tests to aid in assessing various candidate time-dependent fatigue criteria. The matrix is being selected on the basis of generating unique loading histories, which will provide maximum separation between the predictions of the various damage theories. The most promising short-term tests identified to date include those with a creep or relaxation hold period at some intermediate stress (within the cyclic stress-strain loop) during loading or reloading.

4. Simplified Design Methods (Subtask D)

The objective of this subtask is to verify and extend the range of applicability of existing simplified design methods and to develop and verify additional, less conservative methods that minimize the cost and time of analysis.

A series of detailed inelastic analyses of type 304 stainless steel cylindrical shells was continued for use in evaluating the applicability of simplified methods to more realistic stresses and lower temperatures than were covered in the phase 1 studies. All of the analyses were completed. However, postprocessing and assessment of the results will be done in the next report period.

The five-cycle inelastic axisymmetric analysis of a nozzle-to-spherical-shell attachment was completed. Postprocessing and assessment of the results will continue into the next report period.

O'Donnell and Associates obtained bounds on creep ratchetting for load histograms which include several cycles into the plastic ratchetting regimes where it was not previously possible to design using the O'Donnell-Porowski method. The method, which makes use of a new concept of partial relaxation of the elastic core stress, was presented in a topical report.

Foster-Wheeler Energy Corporation is working to (1) investigate the applicability of special-purpose, efficient computer codes in the assessment of inelastic structural response of actual components and (2) recommend guidelines for the use of simplified methods in engineering analysis. The simplified analyses are being performed for the CRBRP intermediate heat exchanger primary inlet nozzle and Z-forging. Detailed inelastic analyses on these two components were done to verify the design and are available for comparison with the results of the simplified analysis. Results are reported for the primary inlet nozzle. A simplified inelastic analysis using a one-dimensional generalized plane strain model can be used to evaluate, with reasonable accuracy, the creep and fatigue damage and peak inelastic strain accumulation at a critical section in an axisymmetric structural model. Unfortunately, the simplified inelastic analysis was not always conservative with respect to the detailed inelastic analysis results.

An analytical investigation of the applicability of the isochronous method was completed using two ORNL benchmark tests — one beam and one plate. The method underpredicted the measured maximum deflections by 21% in the case of the beam and by 28% in the case of the plate. Compared with detailed inelastic analysis, the isochronous method underpredicted the maximum deflections by 17% in the case of the beam and by 32% in the case of the plate.

A simplified inelastic piping analysis computer code named PACE was obtained from the UKAEA and used to analyze the Battelle-Columbus elbow inelastic test. Results for the PACE analysis were compared with analyses done with (1) another simplified inelastic piping analysis computer code named PIRAX2, (2) results from the general-purpose finite-element computer code MARC, and (3) the experimental data.

5. Thermal Ratchetting Tests (Subtask E)

The objective of this subtask is to provide carefully obtained ratchetting test data and creep-fatigue failure data under ratchetting conditions for evaluating basic design analysis methods and failure criteria and for verification and qualification of inelastic analysis computer codes by benchmark problem calculations. Four pipe ratchetting tests have been completed; a fifth and sixth test have been planned and are awaiting approval to proceed.

The first two tests, TTT-1 and TTT-2, were on type 304 stainless steel specimens. The final report was published earlier (ORNL-5386), and there was no activity on these tests during the present period.

The third test, TTT-3, was on a section of 2 1/4 Cr—1 Mo steel pipe welded with Inconel 82 filler metal to a section of type 316 stainless steel pipe. This test was in response to CRBRP Data Requirement Specification (DRS) 51.06. The final report (ORNL-5330) on the experimental results and one-dimensional analyses was published in an earlier period. A two-dimensional analysis of the weldment region of the specimen has now been completed, and the report on the analysis is awaiting final approval before being edited.

The fourth test, TTT-4, was also in response to CRBRP DRS 51.06; the specimen consisted of a section of seamless type 316 stainless steel pipe welded to a section of seam-welded type 316 stainless steel pipe. The final report on the test was published in September (ORNL-5430).

Test TTT-5 will consist of a section of type 304 stainless steel pipe welded (with 16-8-2 filler metal) to a section of Alloy 800 pipe which, in turn, will be welded (with Inconel 82) to a section of 2 1/4 Cr–1 Mo steel pipe. A circumferential notch will be machined in the center of the 2 1/4 Cr–1 Mo steel section to induce creep-fatigue failure of the specimen in a reasonable testing period. We are awaiting approval to proceed with facility modification for performance of this test and have taken no action during the present report period.

The TTT-6 test specimen is an unnotched type 304 stainless steel pipe that will be designed at ORNL but tested to creep-fatigue failure at ETEC. During this period, we prepared and sent to the Director, RRT, a report for Approval-In-Principle for this test and evaluated a test modification proposed by ETEC.

6. Structural Design Methods for Weldments (Subtask F)

The objective of this subtask is to develop and evaluate design methods for high-temperature structural components containing weldments. This is to be accomplished by experimental and analytical investigations into the high-temperature deformation and failure behavior of weldments. These investigations will be used to identify and evaluate approximate methods of predicting the stress and deformation fields in weldment regions and to develop appropriate failure criteria.

We have completed a series of three room-temperature plate-weldment tests. The purpose of those tests was to gain an increased understanding of the deformation field in the neighborhood of a weldment and to see whether or not finite-element analyses based on a two-property zone approach, considering only the base and weld metal and ignoring the heat-affected zone, could adequately predict the deformtion field. The specimens for the test series were long plates of type 304 stainless steel, 7.6 cm (3 in.) in width, which contained a type 308 stainless steel weld

located on the transverse centerline of the specimen. Two of the specimens were annealed after welding, while one was left in the as-deposited condition. The finite-element analyses could reasonably predict the measured deformation field in the annealed specimens, but a considerable discrepancy existed between analysis and experiment in the area of the heat-affected zone in the as-deposited specimen.

High-temperature testing is also under way on a plate-weldment specimen similar to those used in the room-temperature series mentioned above. Here, however, the weldment is located on the longitudinal centerline of the specimen. Thus far, ~600 hr of creep data have been accumulated at 593°C (1100°F).

In conjunction with the plate-weldment tests, we have been investigating the effects of welding residual stresses on the deformation behavior of welded components. A preliminary analytical investigation was carried out for a pipe wall thermal ratchetting situation with the inclusion of an assumed residual stress field. The results of the investigation indicated that the effects of the residual stresses became negligible after about ten thermal cycles. We have also been making residual stress measurements on plate-weldment specimens similar to those used in the room-temperature tests, but consideration of these has not led to improved agreement between analysis and experiment.

We are continuing our program of uniaxial testing on type 308 stainless steel weld metal with Battelle-Columbus Laboratories. The purpose of this series of tests is to enable us to develop and refine constitutive equations for this material. During this report period, the test program was extended to include an additional six cyclic stress-strain tests, five constant-load creep tests, and three composite cyclic-creep tests in which periods of creep are interspersed with periods of constant-strain-rate cycling. The data from these tests have now been received and are being analyzed.

In preparation for possible notch testing of welded specimens, a literature survey has been completed on the effects of notches on the failure of uniaxial tension specimens at elevated temperatures. The survey indicated that notch strengthening or weakening is not to be

thought of as an intrinsic material property. Instead, it is a complex phenomenon depending on such factors as notch geometry, specimen size, load level, and prior heat treatment.

We are continuing our efforts to develop the moire technique of strain measurement into a usable tool at high temperatures. At present, the principal aim is to develop a moire grid that will withstand lengthy periods of elevated-temperature service. We have been assisted here by a consultant, Professor Gary Cloud of Michigan State University. Professor Cloud has developed several techniques for forming high-temperature grids which are superior to previous methods and show great promise for future use.

1. CONSTITUTIVE EQUATION DEVELOPMENT

C. E. Pugh

The objective of this subtask is to derive and verify mathematical descriptions (constitutive equations) of the inelastic behavior of breeder reactor structural metals through combined theoretical and experimental investigations. Experimental activities include exploratory testing of uniaxial and biaxial specimens from reference heats of the materials involved. Constitutive models are assessed through detailed comparisons between predictions and data, and the applicability of the equations to predict the response of structural members is examined further in the structural test and analysis subtask reported in Chapter 2. Guidelines on constitutive equations for use in design analyses are formulated as a result of these efforts.

Interim equations have been identified for types 304 and 316 stainless steel and 2 1/4 Cr–1 Mo steel. As additional test data, advances in model development, and application experience are obtained, revisions or replacement equations have been and will continue to be made available on a continuing basis. Whereas equations for elastic-plastic and creep strains are presently formulated as additive quantities, a long-range goal is the development of a unified theory covering both short- and long-time behaviors.

Efforts to develop an adequate high-temperature, biaxial-strain extensometer are also included in this subtask. In addition, uniaxial tests performed to characterize various product forms of reference heats of materials are reported with this subtask. Finally, this chapter reports on the periodic assessments that are made of the mechanical properties data needed to support implementation of the recommended constitutive equations in design application.

1.1 Recommendation of Modifications to Constitutive Equations in RDT Standard F9-5T

C. E. Pugh J. A. Clinard
R. W. Swindeman

(Last reported in ORNL-5433, pp. 1-42)

1.1.1 Background to equation modifications

Our last progress report[1] discussed a reevaluation that was under way of the constitutive equations now in RDT Standard F9-5T (see Refs. 2-4). The study was emphasizing improved representation of the effects that creep (or relaxation) strains have on subsequent plastic yielding and flow. In particular, one shortcoming of the existing equations being addressed is that when relaxation hold periods are imposed at peak strain points in fixed-strain-range cycling, stress-strain loops predicted on the basis of existing F9-5T equations sequentially move so that unrealistic mean stresses can develop with continued cycling. That study was completed during the present report period, and modifications to the equations were recommended[5] to the RDT Standard F9-4 Task Force for their review and approval. While initial attention in this study was given to 2 1/4 Cr-1 Mo steel, we recognize that the same predictive features and questions are also present in the equations for types 304 and 316 stainless steel. Accordingly, Ref. 5 recommends the same type of equation modification for all three alloys.

Two attachments were prepared and provided to the Task Force for their convenience in reviewing the proposed modification. The first was a brief background write-up which described shortcomings of the existing equations, the proposed modifications and their bases, and several comparative calculations showing predictions made with and without the proposed modification. The second attachment was a complete copy of Chapter 4 of F9-5T with the modifications indicated by either a "C" (change) or "N" (new addition) in the margins. The following paragraphs and Sects. 1.1.2 and 1.1.3 summarize the first attachment. These modifications have been approved and will be included in the revision to F9-5T that is presently in preparation.

The initiation of this study was discussed extensively in our last progress report,[1] where we outlined several candidate modifications that had been examined at that time and compared analytical predictions with observed characteristics of material behavior. However, most of the candidate modifications examined focused on the idea that available data from tests involving fixed-strain-range cycling with relaxation hold periods can be better represented if incremental translations ($d\alpha_{ij}$) of the yield surface in stress space are allowed to depend on plastic-strain increments and on creep-strain increments. The various approaches incorporated such a dependence on creep strains in different ways. These include:

1. allowing the yield surface to translate with *total* creep strains in the exact manner as with plastic strains, that is,

$$d\alpha_{ij} = C\left(d\varepsilon^P_{ij} + d\varepsilon^C_{ij}\right) - \frac{d\kappa}{2\kappa}\left(\sigma'_{ij} - \alpha_{ij}\right) \; ; \tag{1.1}$$

2. allowing the yield surface to translate with *transient* creep strains in the same manner as with plastic strains, that is,

$$d\alpha_{ij} = C\left(d\varepsilon^P_{ij} + d\varepsilon^t_{ij}\right) - \frac{d\kappa}{2\kappa}\left(\sigma'_{ij} - \alpha_{ij}\right) \; ; \tag{1.2}$$

3. allowing the yield surface to translate with total creep-strain increments at a rate that is dependent on the instantaneous value of accumulated creep-strain hardening, that is,

$$d\alpha_{ij} = C\, d\varepsilon^P_{ij} + C(\xi)\, d\varepsilon^C_{ij} - \frac{d\kappa}{2\kappa}\left(\sigma'_{ij} - \alpha_{ij}\right) \; , \tag{1.3}$$

where $\xi = \varepsilon^P_{max} + \bar{\varepsilon}^H$ is the sum of the maximum expected plastic strain and the current value of creep-strain hardening;

4. allowing the yield surface to translate with total creep strain in the same manner as with plastic strain but with a limit placed on the amount of translation that can occur with creep (or relaxation) strains, that is,

$$d\alpha_{ij} = C\, d\varepsilon^P_{ij} + H d\varepsilon^C_{ij} - \frac{d\kappa}{2\kappa}\left(\sigma'_{ij} - \alpha_{ij}\right) \; , \tag{1.4}$$

where $H = C$ if $\alpha_{ij} \leq$ limit and $H = 0$ if $\alpha_{ij} >$ limit.

Consideration was also given to accommodating desired characteristics through modifications of only the plasticity model and not through creep-plasticity interactions, for example, resetting α_{ij} to zero on stress reversals. However, a comprehensive model of this type was not established. It was also recognized in this study that promising developments (e.g., see Sect. 1.2) are under way for equations that treat total inelastic strains in unified ways (i.e., they do not separate plastic and creep strains into distinct entities). However, these evolving models cannot be recommended for use in general design work at this time. They have to be assessed further in relation to their overall predictive capabilities, their adaptability in computational methods, and their requirements for material properties data.

The recommendation made[5] for inclusion in F9-5T falls within category (4) listed above, and it was made after each of those candidate modifications was examined in light of experimental data from several types of tests. The tests examined include (1) fixed-strain-range cycling with relaxation hold periods and no mean strain, (2) fixed-strain-range cycling with relaxation hold periods and tensile mean strains, (3) tensile tests after different amounts of creep straining, and (4) interspersed fixed-strain-range cycling and load-controlled creep periods. Three major behavioral features that factored heavily into the recommended modification are listed here. First, predicted stress-strain loops for fixed-strain-range cycling with no mean strain and with relaxation hold periods at either (or both) extremities of the cycles are stable (cycle to cycle), and no significant mean stress develops. Second, for this same type of cycling but with a mean strain, the initial mean stress can change by a limited amount in a direction away from the hold position (i.e., tensile relaxation hold periods can cause an initially tensile mean stress to change to a modest compressive mean stress). Third, the shift in the yield value with load-controlled creep strains must be limited and not allowed to continue indefinitely with the accumulation of large creep strains. These features contributed to selection of the specific recommendation stated in the next section. A topical report will be prepared during the next report period covering these developments.

1.1.2 Recommended modifications to constitutive equations

The recommendation made is of the type listed as category (4) above, in which motion of the yield surface due to creep (or relaxation) strains is limited to a maximum amount. Briefly, the recommendation leaves the equations for creep in Refs. 2 and 3 unchanged. The plasticity model also remains the same, except that creep strains are now allowed to affect the kinematic movement of the yield surface according to

$$d\alpha_{ij} = C\, d\varepsilon^{P}_{ij} + H\, d\varepsilon^{C}_{ij} - \frac{d\kappa}{2\kappa}\left(\sigma'_{ij} - \alpha_{ij}\right) , \tag{1.5}$$

where the first and last terms on the right are as before[3] and where

$$H = C \text{ if } \bar{\alpha} = \left(\frac{3}{2}\alpha_{ij}\,\alpha_{ij}\right)^{1/2} \leq A\sqrt{3\kappa} ,$$

$$H = 0 \text{ if } \bar{\alpha} > A\sqrt{3\kappa} .$$

In Eq. (1.6), C is the plastic-hardening coefficient that appears in Eq. (1.5), $\bar{\alpha}$ is the current effective value of the translation tensor α_{ij} which measures the distance from the origin of deviatoric stress space to the center of the yield surface, and $\sqrt{3\kappa} = \sigma_y$ is the current yield stress in use at any instant in an analysis. A is a coefficient that may be temperature, history, and material dependent; the basis on which to quantify it is presently incomplete. However, examinations such as those described in the next section of this report suggest that $A = 0.3$ is a reasonable approximation for 2 1/4 Cr–1 Mo steel at 538°C (1000°F). This temperature is, of course, in the range of fast breeder reactor (FBR) applications for this alloy. Although complete determinations of the coefficient A would undoubtedly indicate the dependencies cited above, until further evaluations are made, use of this constant value ($A = 0.3$) has been recommended for all three materials at FBR design temperatures in the creep regime.

The intent of the $A\sqrt{3\kappa}$ limit is to allow relaxation to occur and yet maintain stability of stress-strain loops in the vicinity of mean stress-free states. There, creep strains are to affect α_{ij} the same as if the same amount of plastic strain occurred. However, under load-controlled creep, the shift in the yield surface due to creep is not allowed to

exceed this limit. The limit actually allows recovery of the initial mean stress generated for situations with cycling about large mean strains.

The overall plasticity model is now stated below when the von Mises representation of the yield surface is used. The yield surface is expressed as

$$f = 1/2\ (\sigma'_{ij} - \alpha_{ij})(\sigma'_{ij} - \alpha_{ij}) - \kappa = 0\ , \tag{1.7}$$

where the yield surface (f) is located in deviatoric stress space (σ'_{ij}) by α_{ij} and its size is measured by κ. Location of the surface is expressed by the evolution of α_{ij} (kinematic hardening contribution) according to Eq. (1.5), and the change in its size is expressed by variations in κ (isotropic hardening contribution). The κ model in Refs. 2 and 3 remains unchanged; that is, κ is allowed to depend on the plastic strain ε^P_{ij}, the creep strain ε^C_{ij}, and temperature according to a number of options within the following framework:

$$d\kappa\ (\varepsilon^P_{ij},\ \varepsilon^C_{ij},\ T) = g_{ij}\ d\varepsilon^P_{ij} + h_{ij}\ d\varepsilon^C_{ij} + \frac{\partial\kappa}{\partial T}\ dT\ . \tag{1.8}$$

The flow equation for $d\varepsilon^P_{ij}$ is based on the normality postulate

$$d\varepsilon^P_{ij} = \lambda\ \frac{\partial f}{\partial \sigma_{ij}}\ , \tag{1.9}$$

and λ is evaluated through use of the consistency condition that $df = 0$ in going from one plastic state to another:

$$df = (\sigma'_{ij} - \alpha_{ij})\ d\sigma_{ij} - (\sigma'_{ij} - \alpha_{ij})\left(C\ d\varepsilon^P_{ij} + H\ d\varepsilon^C_{ij}\right) + \frac{\partial f}{\partial \kappa}\ d\kappa\ . \tag{1.10}$$

Plastic states exist only when $f = 0$, elastic states exist when $f < 0$. and no meaning is attached to $f > 0$. Combining these statements gives the loading conditions, flow equations, and kinematic hardening equations. In writing these, use is made of the term

$$d\Sigma = (\sigma'_{k\ell} - \alpha_{k\ell})(d\sigma_{k\ell} - H\ d\varepsilon^C_{k\ell}) - \frac{\partial\kappa}{\partial T}\ dT\ . \tag{1.11}$$

•<u>Elastic loading</u> (unloading) occurs when

$$f < 0 \text{ or } f = 0 \text{ and } d\Sigma < 0\ , \tag{1.12}$$

$$d\varepsilon^P_{ij} = 0 \ , \tag{1.13}$$

and

$$d\alpha_{ij} = H \ d\varepsilon^C_{ij} \ . \tag{1.14}$$

•Neutral loading gives rise to no plastic strains during a change in stress which remains on the surface;

$$f = 0 \text{ and } d\Sigma = 0 \ , \tag{1.15}$$

$$d\varepsilon^P_{ij} = 0 \ , \tag{1.16}$$

and

$$d\alpha_{ij} = H \ d\varepsilon^C_{ij} \ . \tag{1.17}$$

•Plastic loading occurs when

$$f = 0 \text{ and } d\Sigma < 0 \ , \tag{1.18}$$

$$d\varepsilon^P_{ij} = \frac{d\Sigma}{2C\kappa} (\sigma'_{ij} - \alpha_{ij}) \ , \tag{1.19}$$

and

$$d\alpha_{ij} = C \ d\varepsilon^P_{ij} + H \ d\varepsilon^C_{ij} - \frac{d\kappa}{2\kappa} (\sigma'_{ij} - \alpha_{ij}) \ . \tag{1.20}$$

Note that the creep strains appear in both the plastic flow equations [Eq. (1.19)] and the loading conditions through $d\Sigma$. Also, the influences of creep (or relaxation) that occur during hold periods are important to the overall model statement. Therefore, the influence of creep strains ($d\alpha_{ij} = H \ d\varepsilon^C_{ij}$) is present in the equations for elastic and neutral loadings [Eqs. (1.14) and (1.17)] as well as for plastic loading [Eq. (1.20)].

1.1.3 Illustrative analyses

As a part of these activities, analytical predictions of stress-strain responses were completed for several loading situations to illustrate predictive features of the constitutive equations. The predictions have been compared with those of other equations and with experimental data. Some

comparisons are shown below of predictions based on three models: (1) current[2,3] RDT F9-5T equations, (2) the equations* suggested by Rockwell International/Energy Systems Group (RI/ESG) in Ref. 6, and (3) the modified equations we recommended.[5] The same material properties were used in each of the three sets of predictions. Three different loading situations are shown below in order to discuss characteristics of these three models. Specific data are also shown for two of the cases.

The first case involves cyclic uniaxial loading of a specimen between strain limits ($\pm\varepsilon_{max} = \pm 0.25\%$) where there is no mean strain. At the compressive extremity of each cycle, the total strain is held constant for 0.1 hr and the stress allowed to relax. The predictions for this case are based on material properties from the *Nuclear Systems Materials Handbook* for 2 1/4 Cr–1 Mo steel at 538°C (1000°F). Figures 1.1 through 1.3 show the first 50 cycles predicted by the three sets of equations. Figure 1.1 illustrates the continued drift in the stress-strain loops that is predicted by the current F9-5T equations for this type of cycle, even with this relatively brief hold period. This drift would hypothetically continue with repeated cycling until the peak compressive stress approached zero. The predicted shift per cycle, of course, would initially be greater if the hold periods were longer. Figures 1.2 and 1.3 illustrate that both the method discussed in Ref. 6 and the one we recommended result in stable stress-strain loops throughout this cyclic loading. This stability is in keeping with experimental observations; for example, Ref. 6 included a test under these particular conditions in its Table I and noted that, at one-half of the cyclic life of the specimen, the ratio of peak tensile stress σ_T to peak compressive stress σ_C was seen to be $\sigma_T/\sigma_C = 1.08$ from experimental data. The predictions shown in Fig. 1.2 have $\sigma_T/\sigma_C = 1.0$, while those in Fig. 1.3 have $\sigma_T/\sigma_C = 1.03$.

The second type of loading considered here also involves uniaxial cycling between fixed strain limits with relaxation hold periods. Here,

---

*This suggestion was discussed in Ref. 1 and is of category (1) listed above in Sect. 1.1.1. The approach is actually the same as that recommended, except there is no limit placed on the amount of shift in the yield surface that can occur with continued creep straining.

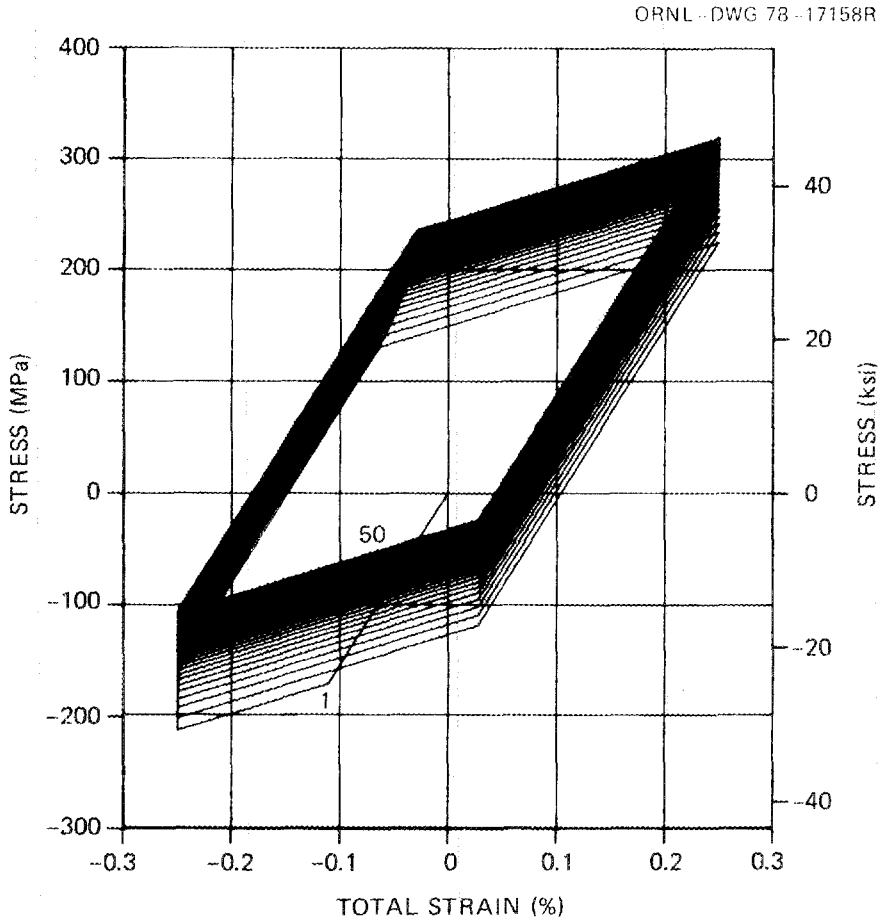

Fig. 1.1. Stress-strain loops for fixed-strain-range cycling predicted on basis of current[3] RDT Standard F9-5T constitutive equations; 2 1/4 Cr–1 Mo steel at 538°C (1000°F), 0.1-hr compressive relaxation hold.

however, the cycling is assumed to occur about a mean strain. The particular case presented here has a mean strain of 0.2% and a strain range of 0.4%. A longer hold time (24 hr) is taken to occur at the tensile extremity of each cycle, and the temperature is again taken to be 538°C (1000°F). Properties used in the analyses of this problem were taken from heat 3P5601 (air melted) of 2 1/4 Cr–1 Mo steel and are given in Ref. 1. Figures 1.4 through 1.6 show the three sets of stress-strain predictions for ten cycles of this type of loading. Figure 1.4 illustrates that the present F9-5T equations again predict loops that drift away from the end of the cycle where the hold period occurs. Predictions based on the suggestion made in Ref. 6 are shown in Fig. 1.5, and stable hysteresis loops

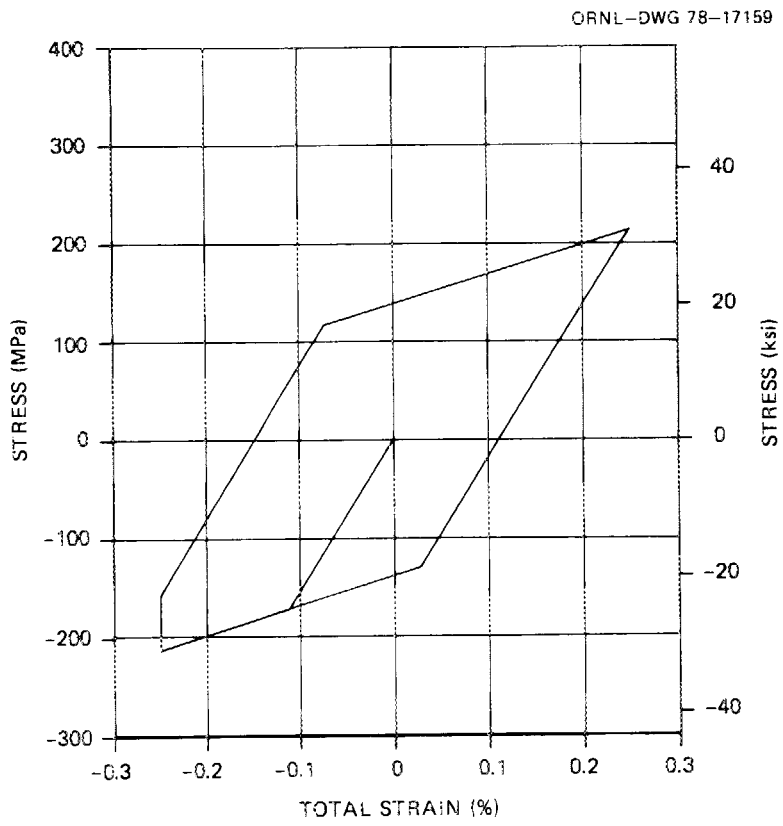

Fig. 1.2. Stress-strain loops predicted on basis of constitutive equations modification suggested in Ref. 6. Loading conditions are the same as in Fig. 1.1.

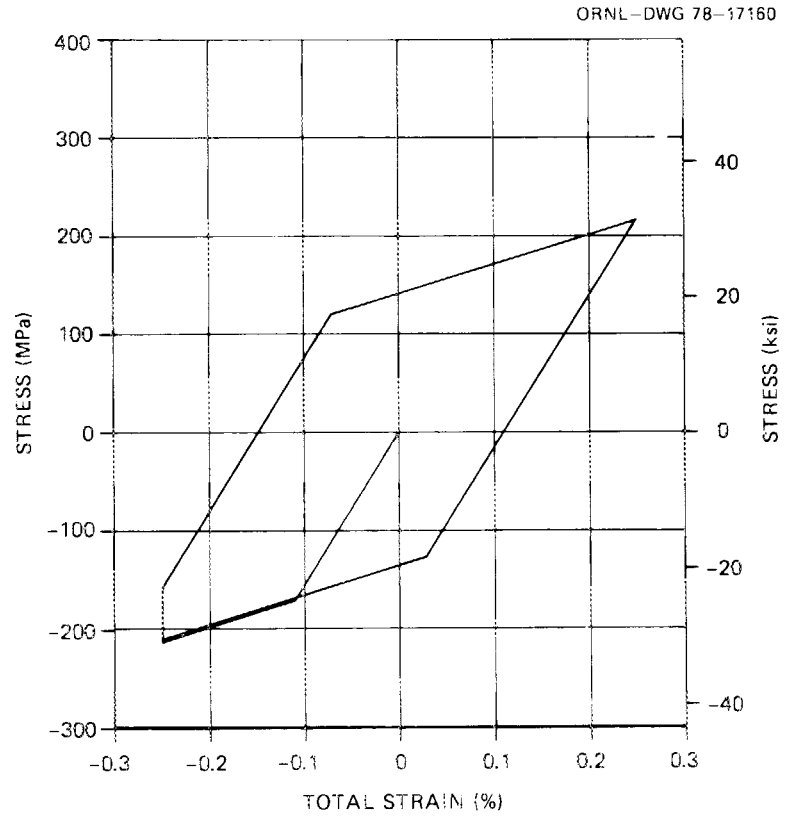

Fig. 1.3. Stress-strain loops predicted on basis of the constitutive equation modifications recommended in Ref. 5. Loading conditions are the same as in Figs. 1.1 and 1.2.

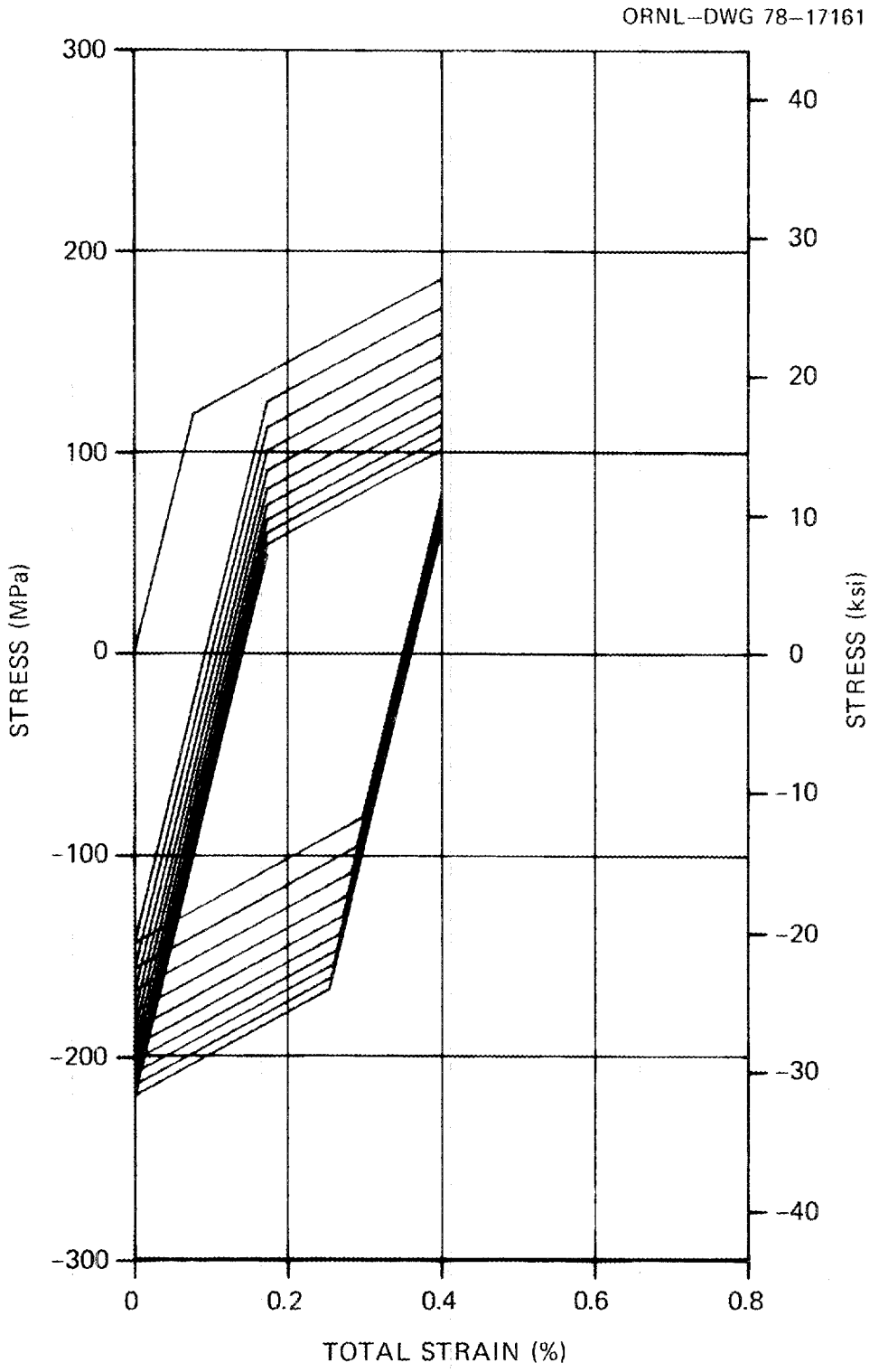

Fig. 1.4. Stress-strain loops predicted on basis of current[3] RDT Standard F9-5T constitutive equations for fixed-strain-range cycling with a mean strain and a tensile relaxation hold period of 24 hr; 2 1/4 Cr–1 Mo steel at 538°C (1000°F).

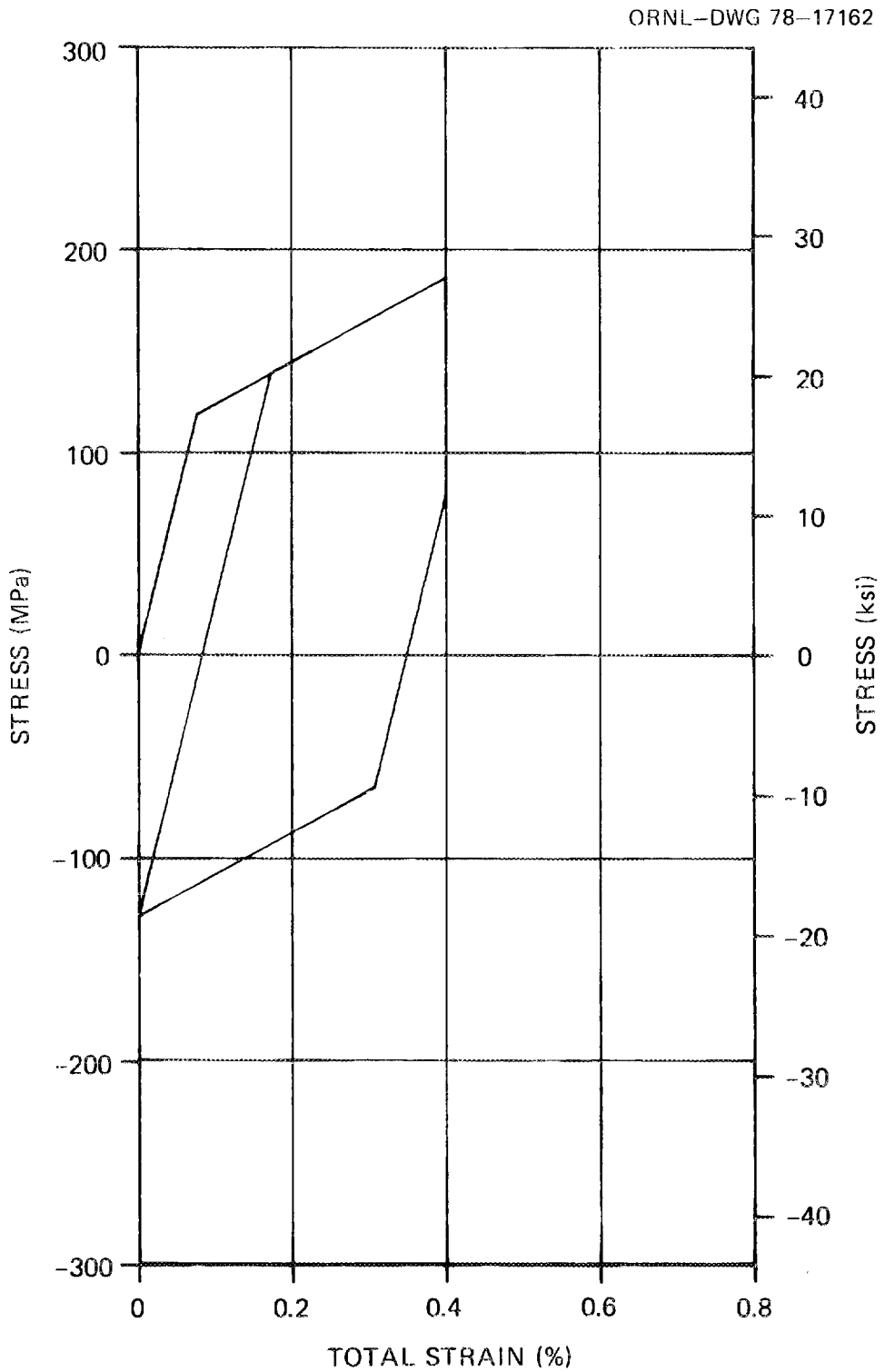

Fig. 1.5. Stress-strain loops predicted on basis of constitutive equations suggested in Ref. 6. Loading conditions are the same as in Fig. 1.4.

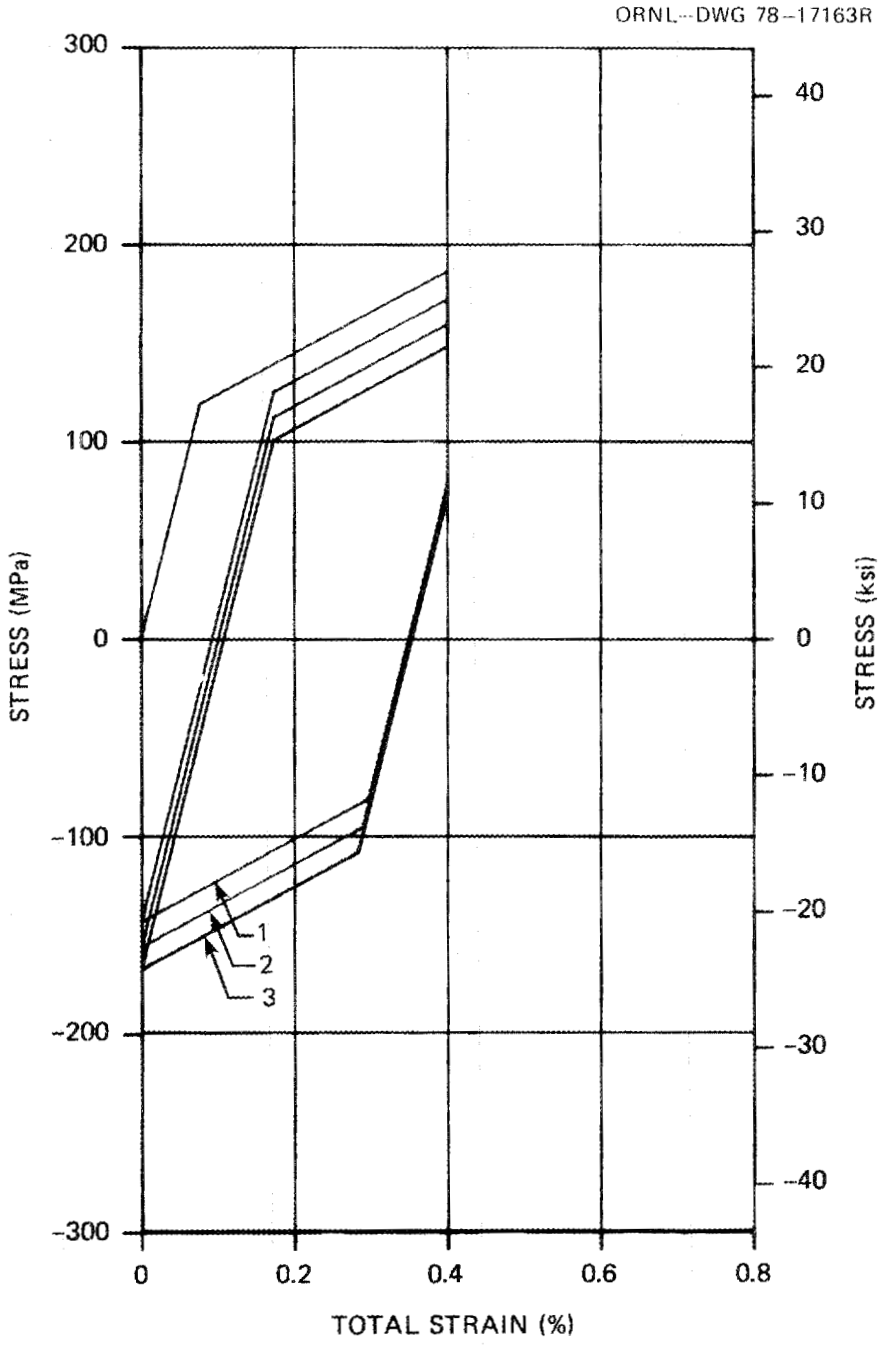

Fig. 1.6. Stress-strain loops predicted on basis of constitutive equation modifications recommended in Ref. 5. Loading conditions are the same as in Figs. 1.4 and 1.5.

are predicted for all cycles. These loops maintain the initial tensile mean stress [about 28.3 MPa (4.14 ksi)]. Loops predicted by the recommended procedures (shown in Fig. 1.6) show a modest (but limited) drift of the loops in the compressive direction. The initial mean *tensile* stress is lost, a stable loop is established after about four cycles, and the stable loop has a mean *compressive* stress of about 10 MPa (1.5 ksi). An experiment with precisely this loading and using a specimen from heat 3P5601 was performed, and stress-strain results are shown in Fig. 1.7.

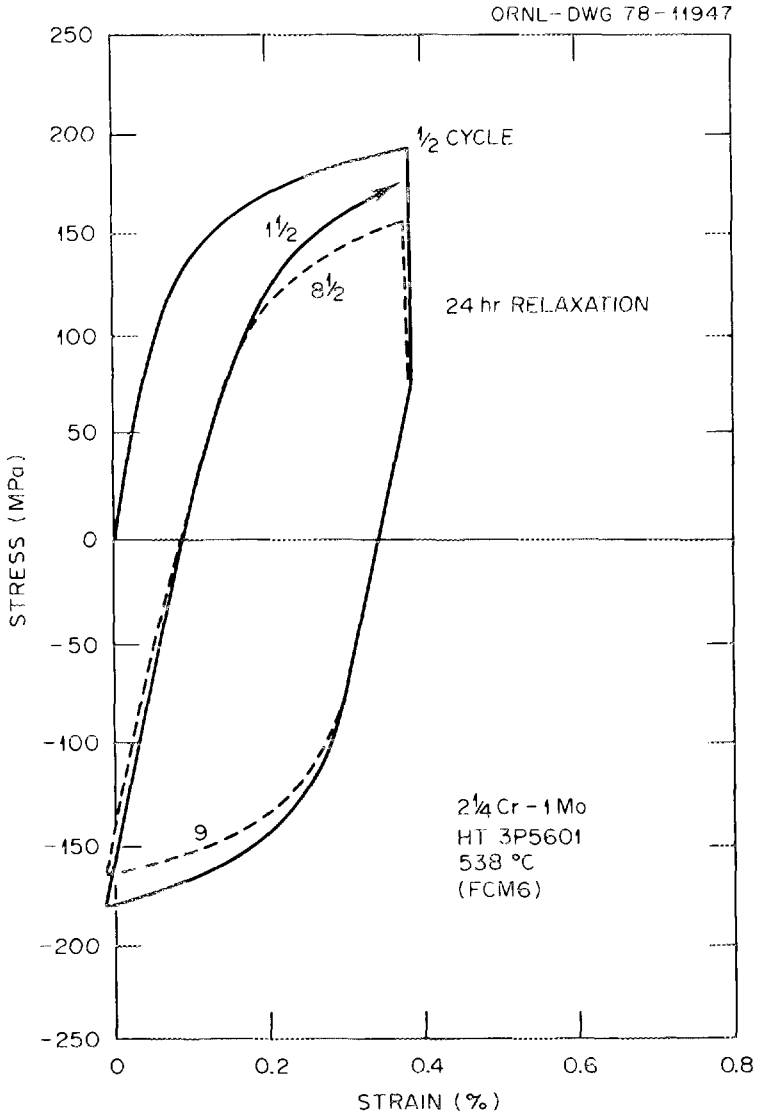

Fig. 1.7. Measured stress-strain loops for 2 1/4 Cr–1 Mo steel (heat 3P5601) for the loading conditions considered in Figs. 1.4 through 1.6.

Note that the initial mean stress indeed was not maintained, and the measured loop drifted for a few cycles until a stable loop was established with a mean *compressive* stress of 9.5 MPa (1.5 ksi). These results are in good agreement with the predictions of the recommended procedures, and, actually, these data played a role in the specific recommendations that $A = 0.3$ in Eq. (1.6).

The last loading situation to be discussed here involves single loadings through a fixed stress range after successive periods of creep have occurred. In particular, consider the load histogram shown in Fig. 1.8, to which the specimen used in Fig. 1.7 was subsequently exposed. Four cycles were performed between stress limits of ±150 MPa (21.7 ksi): the first immediately after the ten fixed-strain-range cycles shown in Fig. 1.7, the second after a 0.5-hr period of creep, the third after a 19-hr

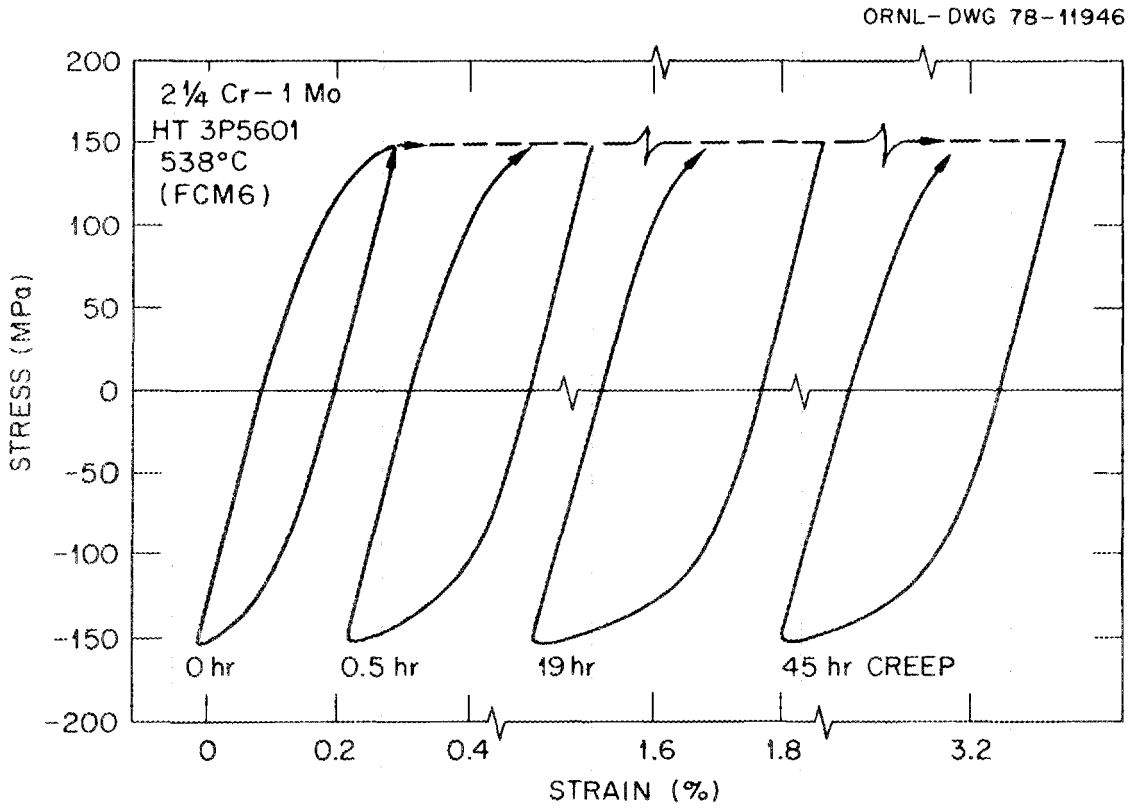

Fig. 1.8. Measured stress-strain responses for cycling between fixed stress limits [±150 MPa (±21.7 ksi)] after periods of creep; 2 1/4 Cr–1 Mo steel (heat 3P5601).

period of creep, and the fourth after a 45-hr period of creep. All periods of creep were at a stress of 150 MPa. The stress-strain (elastic-plastic plus creep-strain) responses predicted by the three sets of equations are shown in Figs. 1.9 through 1.11. General characteristics of the stress-strain loops are captured both by the current F9-5T equations (see Fig. 1.9) and by the equations we recommend (see Fig. 1.11). On comparing Fig. 1.8 with Figs. 1.9 and 1.11, one sees that the quantitative prediction of the loop widths is slightly better for the recommended revised equations than for the current F9-5T equations. However, on comparing Figs. 1.8 and 1.10, one sees that the characteristics of these data are not captured well by the modified equations suggested in Ref. 6. The Ref. 6 suggestion allows creep strains, however large, to continue to shift the yield surface as though they were plastic strains. Data such as those shown in Fig. 1.8 illustrate the need for a bound on this type of shift. We selected Eq. (1.6) for the bound.

1.2 Development of Refined Constitutive Laws

D. N. Robinson

(Last reported in ORNL-5433, pp. 42-47)

1.2.1 Basic model development

A report entitled *A Unified Creep-Plasticity Model for Structural Metals at High Temperature*[7] was published during this report period. The report outlines the development of the ORNL unified constitutive theory, presents a complete mathematical statement of the model for isothermal conditions, and contains numerous calculations conducted under a variety of combinations of the model parameters. The objective of the parameter study was to demonstrate the capability of the unified model to represent *qualitatively* most of the important phenomenological features observed in reactor system alloys at high temperature. Certain of the results of that study have been reported in previous progress reports (e.g., Ref. 8).

Since the writing of Ref. 7, an effort has been made to establish the unified model parameters to characterize *quantitatively* a limited set of experimental data representing 2 1/4 Cr—1 Mo steel (heat 20017) at 566°C

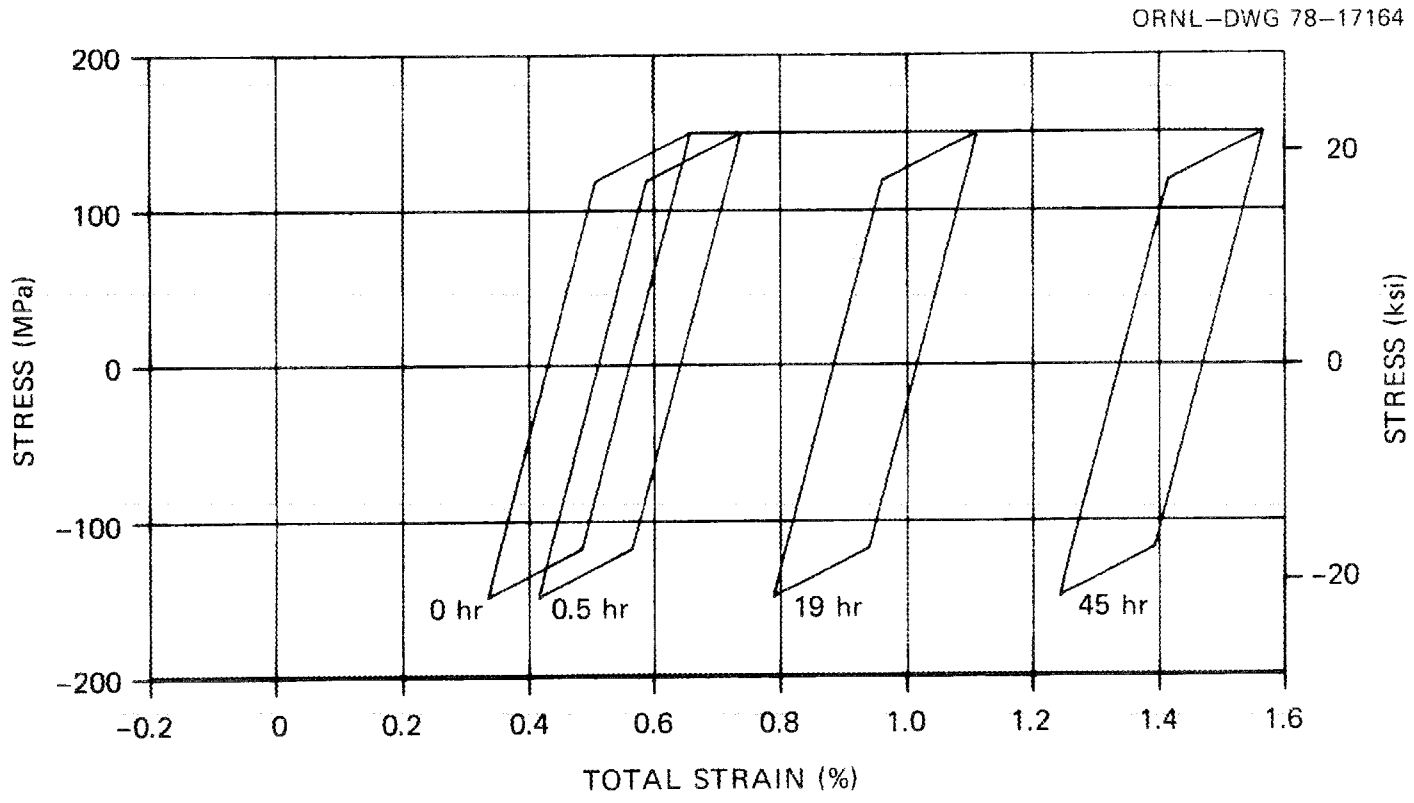

Fig. 1.9. Stress-strain loops predicted on basis of current[3] RDT Standard F9-5T constitutive equations for the test conditions of Fig. 1.8.

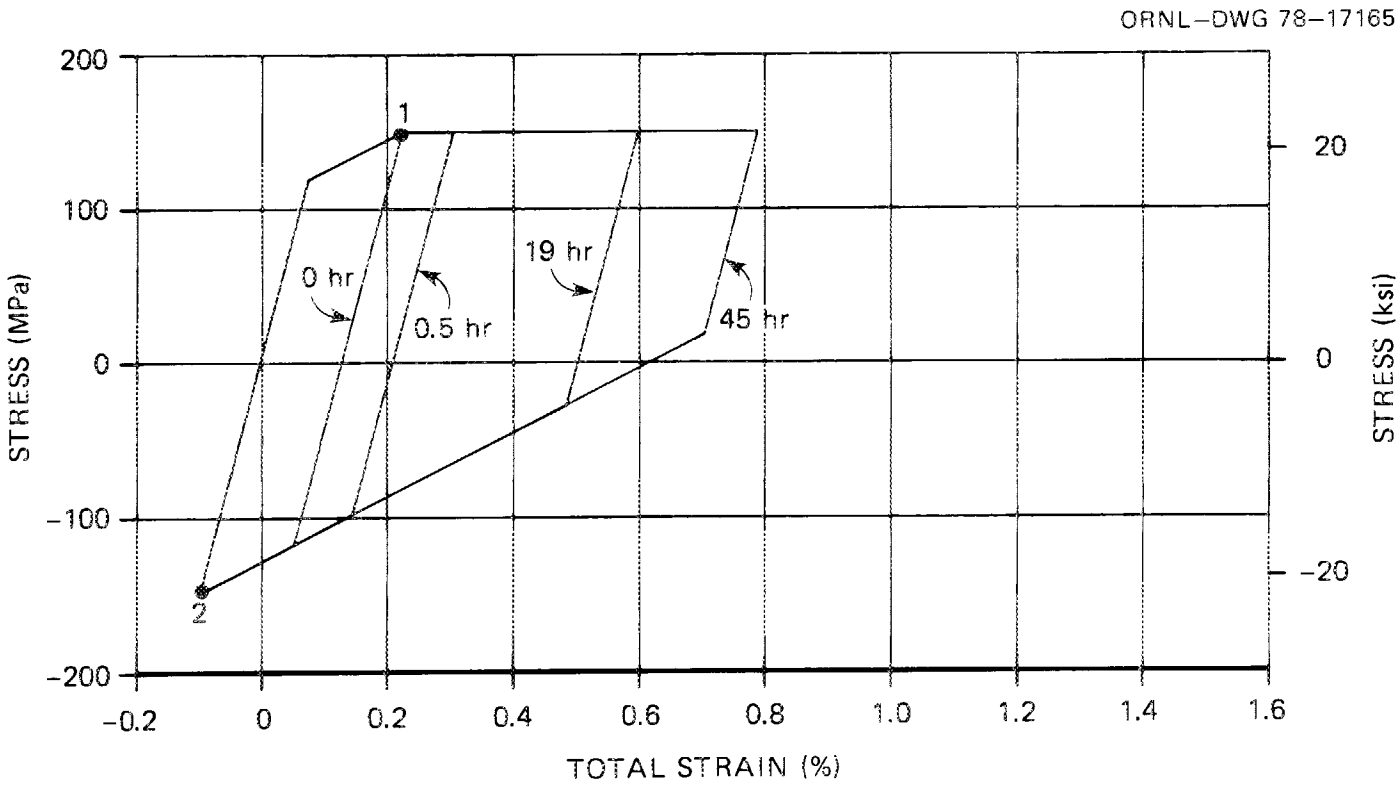

Fig. 1.10. Stress-strain loops predicted on basis of constitutive equations suggested in Ref. 6 for test conditions of Figs. 1.8 and 1.9. All creep periods begin at point 1, and each load reversal culminates at point 2.

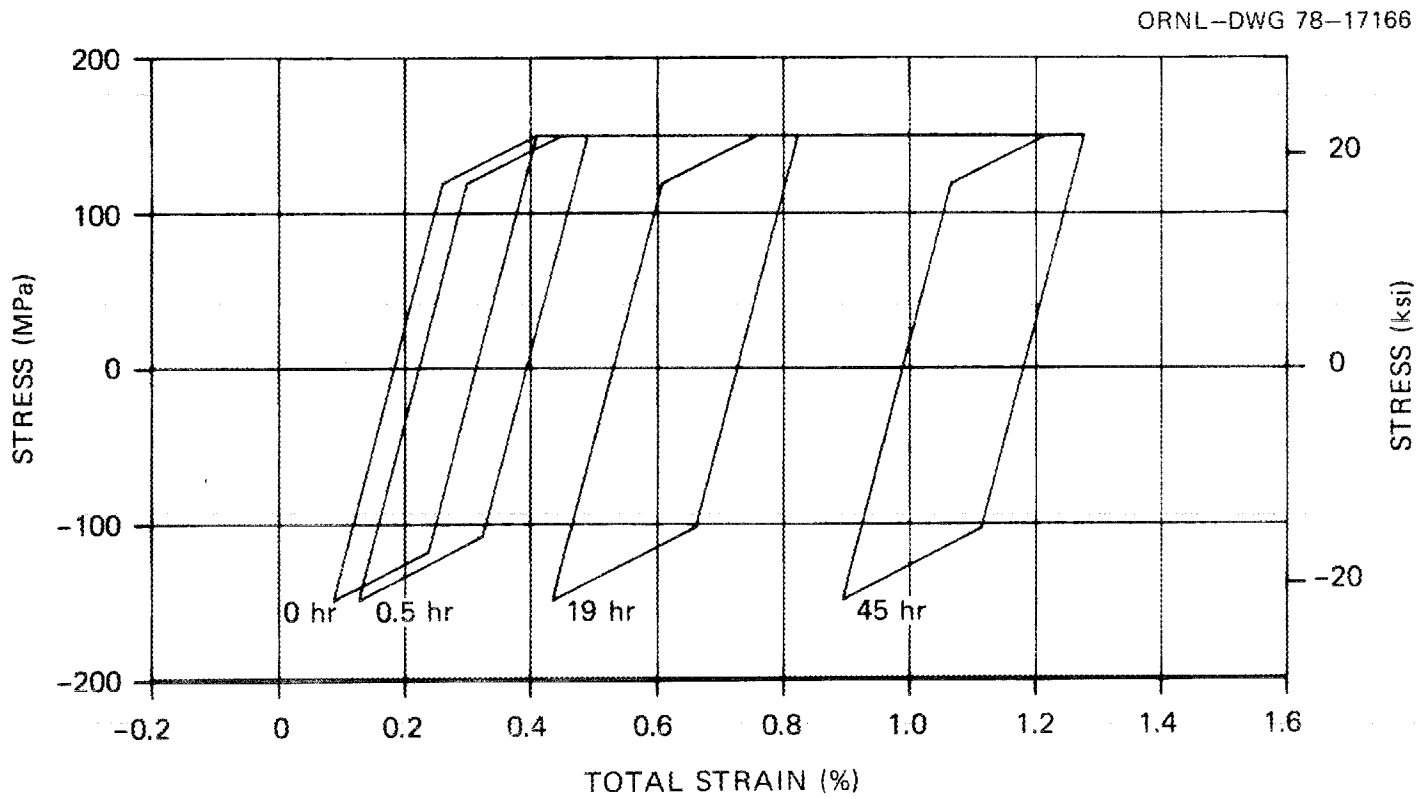

Fig. 1.11. Stress-strain loops predicted on basis of constitutive equation modifications recommended in Ref. 5. Test conditions are the same as in Figs. 1.8 through 1.10.

(1050°F). A resulting set of parameters is currently being used in structural analyses* to ensure that the model gives reasonable predictions of behavior under inhomogeneous and multiaxial stress states. Results of these structural analyses will be compared with test results.

For completeness, a statement of the (isothermal) unified constitutive equations is given here, together with a listing of the specific parameter values determined for heat 20017 of 2 1/4 Cr–1 Mo steel at 566°C (1050°F). The constitutive model is:

$$2\mu\dot{\varepsilon}_{ij} = \begin{cases} F^{(n-1)/2}\,\Sigma_{ij}\ ; & F > 0 \text{ and } S_{ij}\Sigma_{ij} > 0 \\ 0\ ; & \begin{cases} F \le 0 \\ \text{or} \\ F > 0 \text{ and } S_{ij}\Sigma_{ij} \le 0 \end{cases} \end{cases} \tag{1.21}$$

$$\dot{\alpha}_{ij} = \begin{cases} \dfrac{2\mu H}{G^{(\beta/2)}}\,\dot{\varepsilon}_{ij} - \left[RG^{(m-\beta-1)/2}\right]\alpha_{ij}\ ; & G > G_o \text{ and } S_{ij}\alpha_{ij} > 0 \\ \dfrac{2\mu H}{G_o^{(\beta/2)}}\,\dot{\varepsilon}_{ij} - \left[RG_o^{(m-\beta-1)/2}\right]\alpha_{ij}\ ; & G \le G_o \text{ or } S_{ij}\alpha_{ij} \le 0\ , \end{cases} \tag{1.22}$$

where

$$F = (J_2/\kappa^2) - 1 \qquad G = J_2/\kappa^2$$

$$J_2 = \frac{1}{2}\,\Sigma_{ij}\Sigma_{ij} \qquad J_2 = \frac{1}{2}\,\alpha_{ij}\alpha_{ij}$$

$$\Sigma_{ij} = S_{ij} - \alpha_{ij}$$

$$S_{ij} = \sigma_{ij} - \frac{1}{3}\,\sigma_{\kappa\kappa}\delta_{ij}\ .$$

Here, $\dot{\varepsilon}_{ij}$ is the inelastic strain rate, σ_{ij} is the applied stress, S_{ij} is the deviatoric stress, and α_{ij} is a state variable related to the internal

*The unified equations, together with these parameters, have been implemented in the ORNL finite-element computer code PLACRE, as well as in a special-purpose code being developed under subcontract at The University of Tennessee (see Sect. 1.2.3).

dislocation structure. The parameters are:

$$\begin{aligned} \eta &= 6.25 \\ m &= 4.50 \\ \beta &= 1 \\ \mu &= 10.61 \times 10^{7}\ \text{MPa}\cdot\text{hr}\ (1.539 \times 10^{7}\ \text{ksi}\cdot\text{hr}) \\ R &= 2.25 \times 10^{-5}\ \text{hr}^{-1} \\ H &= 3.0 \times 10^{-4}\ \text{hr}^{-1} \\ \kappa &= 6.895\ \text{MPa}\ (1.0\ \text{ksi}) \\ G_o &= 1 \times 10^{-6} \end{aligned} \quad . \tag{1.23}$$

Figures 1.12 and 1.13 are included to demonstrate that the above values provide a reasonably accurate representation of the stated heat

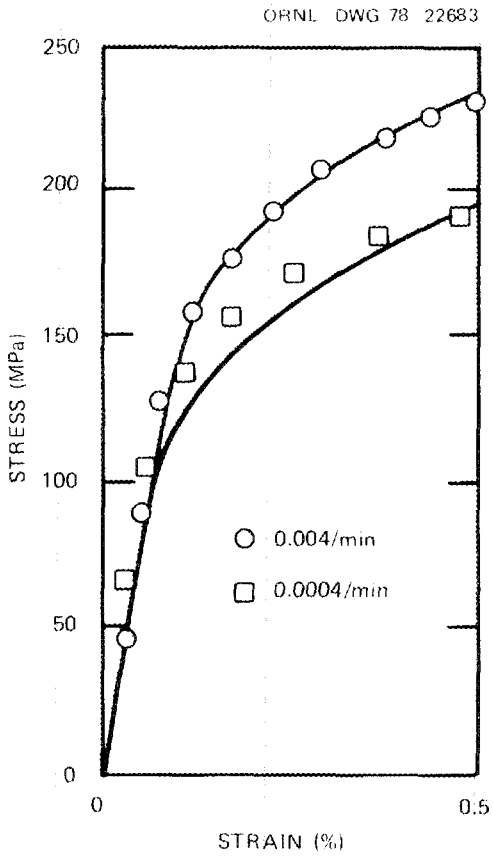

Fig. 1.12. Comparison of calculated response (solid lines) and experimental data taken under constant-strain-rate extensions of 0.004 and 0.0004/min. Experimental data are from 2 1/4 Cr–1 Mo steel (heat 20017) at 566°C (1050°F) and are taken from Ref. 9.

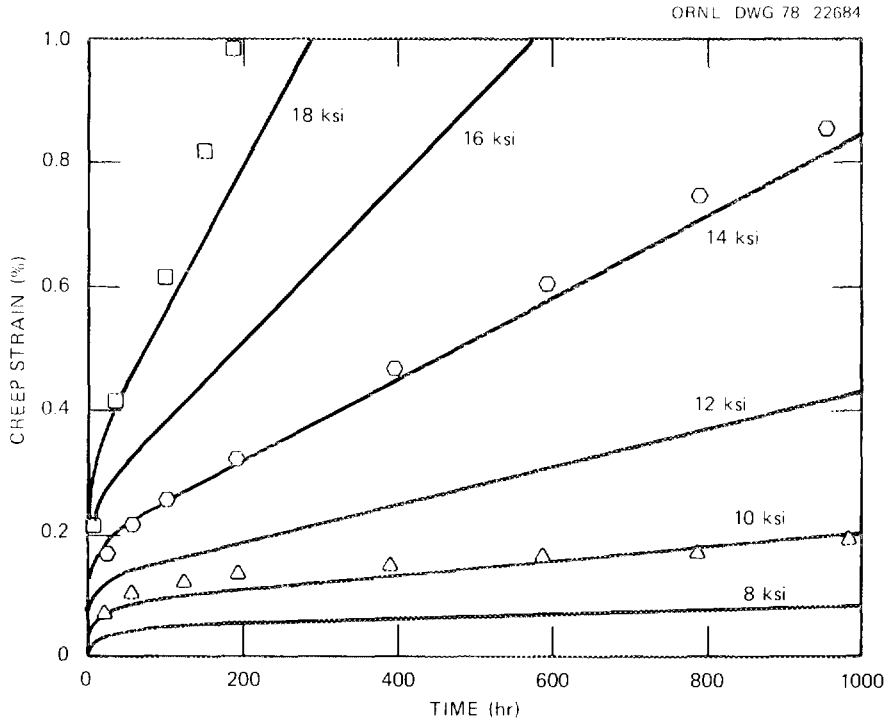

Fig. 1.13. Comparison of calculated creep response (solid lines) and experimental data. Calculated curves correspond to constant stress levels of 55, 69, 83, 97, 110, and 124 MPa (8, 10, 12, 14, 16, and 18 ksi). Experimental data (△ = 10 ksi, ○ = 15 ksi, □ = 18 ksi) are from 2 1/4 Cr–1 Mo steel (heat 20017) at 566°C (1050°F) and are taken from Ref. 9.

of this alloy, in terms of both strain-rate sensitive plasticity and transient and secondary creep. These figures compare model calculations with previously published uniaxial experimental data.

1.2.2 Exploratory experiments contributing to a data base for the ORNL unified equations

Material parameters for the ORNL unified constitutive law were specified in Sect. 1.2.1 representing a data set of 2 1/4 Cr–1 Mo steel (heat 20017) at 566°C (1050°F). These parameters were obtained by comparing calculations of uniaxial response with existing data (i.e., creep tests, relaxation tests, and monotonic and cyclic constant-strain-rate tests) and adjusting the parameters to give satisfactory agreement. Guidance for

adjusting the parameters was provided by the extensive parameter sensitivity study reported in Ref. 7. Thus, an "optimum" set of values was obtained basically through trial and error.

Ultimately, it will be necessary to define a complete data base for the unified model, together with a systematic procedure for determining the parameters exclusively from that data set. As pointed out in Ref. 7, the data base currently used in conjunction with the RDT Standard F9-5T procedures is a necessary, but not a sufficient, base on which to determine the complete set of material parameters of the unified model. Here, we outline briefly a set of exploratory tests not included in the current data base, which can be used to establish certain of the parameters in the model. These tests and others will be described in more detail in a forthcoming topical report.

The test sequence is illustrated by the preliminary test data shown in Figs. 1.14 and 1.15. These data were obtained from 2 1/4 Cr–1 Mo steel at 538°C (1000°F). Figure 1.14 shows a stress-strain hysteresis loop that was obtained by testing over a strain range of ±0.2% and a strain rate of ∿0.004/min. The loop represents a relatively stable stress-strain response produced after several cycles.

Stress relaxation was measured from each of the points indicated on the unloading segment of the hysteresis loop in Fig. 1.14; that is, the total strain was held constant for 0.1 hr at each of the indicated points and the stress-time response recorded; these responses are shown in Fig. 1.15. Cycling was resumed between each hold period to once again obtain essentially the same stable stress-strain loop.

Figure 1.15 shows that stress relaxation from the higher stress levels is "classical" in the sense that the (negative) relaxation rate is initially high and diminishes thereafter. For example, for starting stress levels of 138 MPa (20 ksi) or less, the initial stress rate is zero or, in some cases, slightly positive (a stress increase with time).* If the time scale in Fig. 1.15 were expanded, we would see that the stress

---

*At the low stresses where the initial stress relaxation rate is positive, the stress-rate magnitude is quite small and apparently saturates at some maximum value as the stress is further lowered.

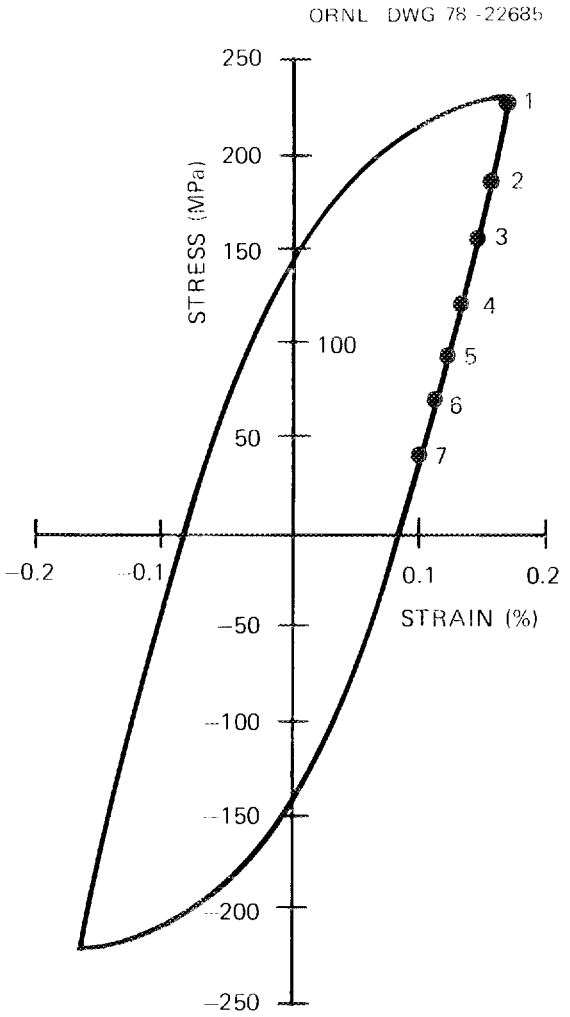

Fig. 1.14. Stable stress-strain hysteresis loop for 2 1/4 Cr–1 Mo steel at 538°C (1000°F). Points indicate where stress relaxation tests were conducted (1.0 ksi = 6.895 MPa).

does, in all cases, eventually relax. The greater the unloading prior to relaxation the longer the hesitation period before stress relaxation commences.*

Because the stress-strain response shown in Fig. 1.14 is essentially stable, we may assume that, in repeated cycles, the path in *state space*

*This hesitation phenomenon is believed to be the same as that which occurs in creep under abrupt stress reductions. The slight increase in stress before leveling off and then finally decreasing is believed to be of the same origin as the anelastic strain recovery observed under stress reductions in creep tests.

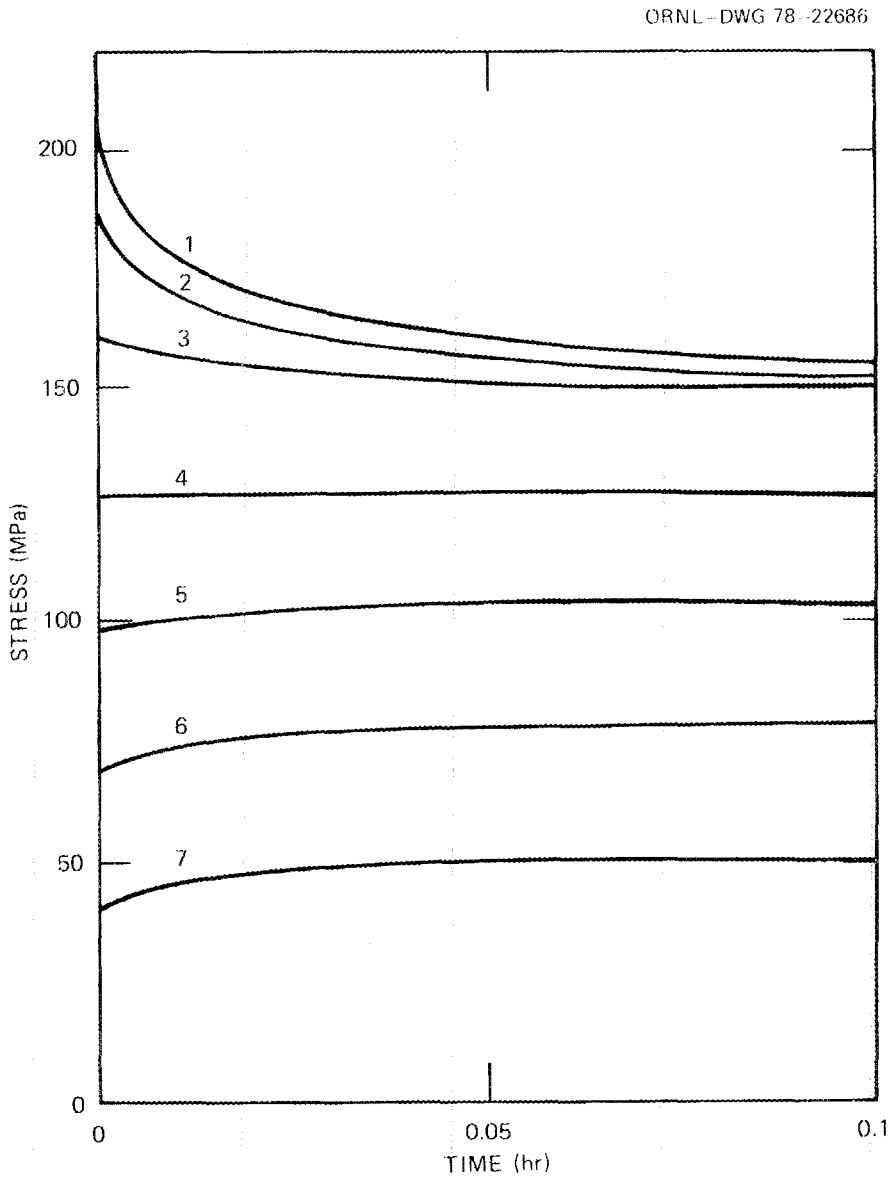

Fig. 1.15. Stress-time relaxation responses corresponding to points indicated in Fig. 1.14 (1.0 ksi = 6.895 MPa).

is likewise stable. Further, we can justifiably assume that the inelastic state of the material does not change significantly on abrupt unloading. Thus, at each of the indicated points in Fig. 1.14 from which the relaxation responses were measured, the material was in essentially the same state.

According to the model of Ref. 7, the stress σ, corresponding to a given state α, at which the inelastic strain rate (and thus the stress

relaxation rate) just vanishes on reducing the stress, is given by

$$\sigma = \alpha - \kappa ,$$

in which κ represents the *threshold* stress below which no inelastic strain rate occurs in the undeformed state of the material.* Conversely, if the stress is known at which the relaxation rate just vanishes, the material may be said to be in the inelastic state:

$$\alpha = \sigma - \kappa ,$$

assuming, of course, that κ is known from an independent test.

If, in a test such as that depicted in Figs. 1.14 and 1.15, we determine the value of $\sigma - \kappa$ at which the initial stress relaxation rate becomes zero on reducing the stress, then we know the inelastic state α of the material corresponding to each of the points indicated in Fig. 1.14. Thus, we know the *inelastic state*, the *stress*, and the *inelastic strain rate*† associated with each point in Fig. 1.14.

Many tests in which the cycling is performed over different strain rates and strain ranges, producing different inelastic states, allow us to know the inelastic strain rate corresponding to a range of state points (σ, α) for which $\sigma - \alpha > \kappa$. This is, of course, precisely what is necessary to quantitatively fix the parameters in the flow law appearing in the equations of Ref. 7 and Sect. 1.2.1. Several tests described above are now being conducted on 2 1/4 Cr–1 Mo steel at 538°C (1000°F).

1.2.3 Numerical integration studies (Last reported in ORNL-5433, p. 46)

A major consideration in the implementation of constitutive laws such as those stated in Sect. 1.2.1 and Ref. 7 is whether they require special and, therefore, possibly inefficient numerical procedures for their integration. If this is so, their incorporation into large-scale finite-element programs could lead to excessive costs in performing inelastic analysis.

---

*The measurement of κ is to be made independently by performing ordinary creep tests to determine the stress level below which one can *practically* consider no creep to occur.

†This is known for those points where $\sigma - \alpha > \kappa$ because we know the initial stress rate from the relaxation tests.

Two parallel efforts are now proceeding which are concerned with potential numerical problems involved in conducting structural analyses with the unified equations in finite-element codes. The first is performed under subcontract with The University of Tennessee* and the second within ORNL. In each case, the ORNL unified constitutive equations stated in Sect. 1.2.1 are being implemented, together with the specific parameters given in that section. These parameters are based on representations of data from 2 1/4 Cr–1 Mo steel (heat 20017) at 566°C (1050°F).

In The University of Tennessee study, a special-purpose finite-element code has been developed which is capable of solving axisymmetric structural problems. An implicit Euler algorithm for the time integration is being used in that study. The plan is to investigate several thick-walled cylinder problems involving various internal pressure histories and initial conditions, both to assess the numerical difficulties involved and to ensure that the unified constitutive model provides physically realistic predictions of response in such problems. To date, only uniaxial calculations have been carried out. These compare favorably with calculations reported in Ref. 7.

The ORNL study included the implementation of the unified constitutive equations into the PLACRE finite-element computer code. This was accomplished (by W. K. Sartory) using no special integration schemes beyond those available in the ORNL computer software library. Several trial structural problems have been run successfully, ranging from uniaxial loading to the complex biaxial-stress histogram corresponding to the thermal transient test TTT-1 (see Ref. 10).

Figures 1.16 through 1.19 give the results of the thick-walled cylinder (pipe) analysis using the TTT-1 thermal and pressure histogram. The hoop stress-strain responses at the inner and outer surfaces are shown in Figs. 1.16 and 1.17, respectively, and the hoop and axial (ratchetting) strains at the outer surface are shown in Figs. 1.18 and 1.19, respectively. These calculated results are not intended for comparison with the TTT-1 experimental results because the material constants used are

---

*The principal investigators in this study are Professors J. E. Stoneking and A. J. Baker.

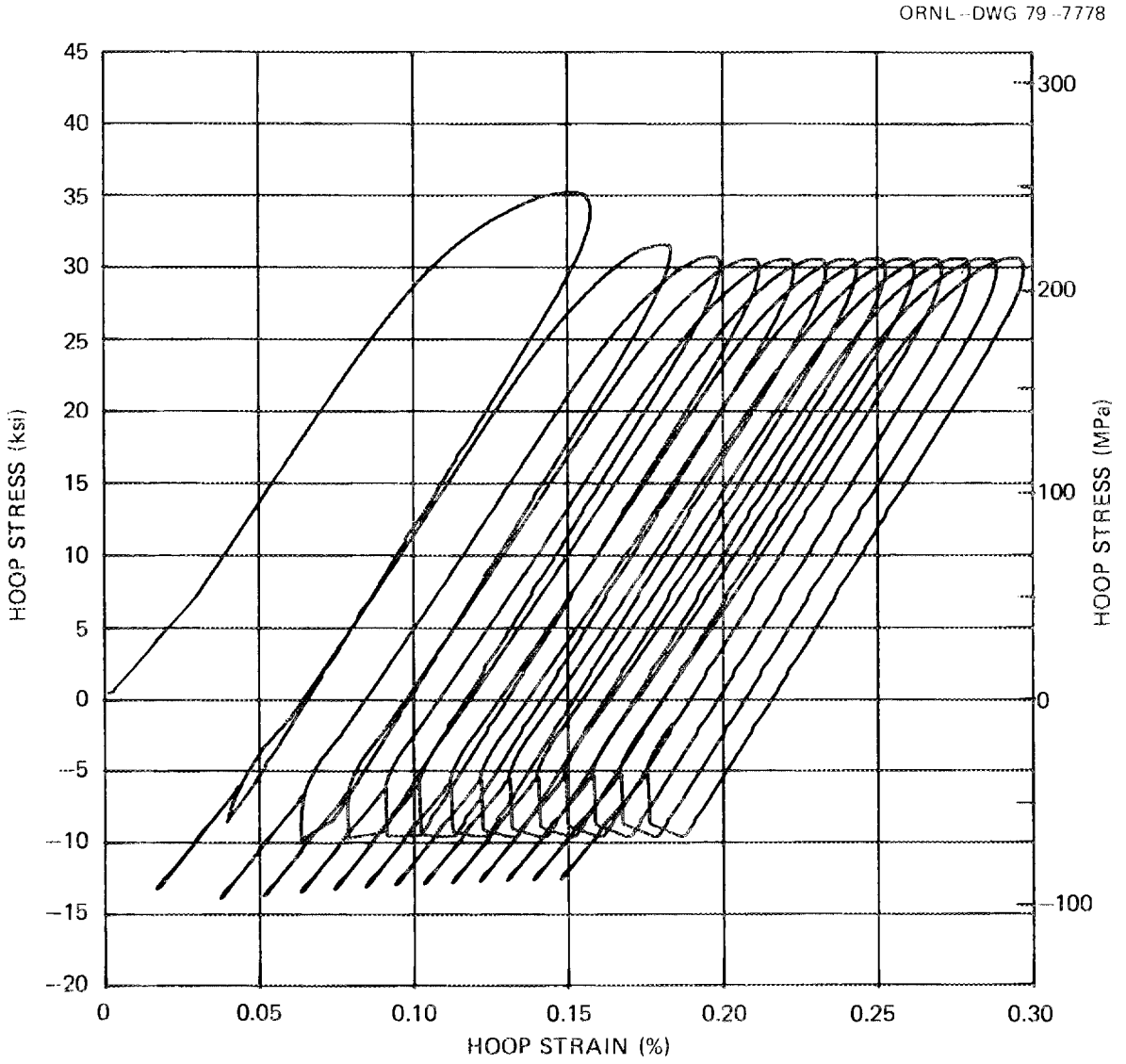

Fig. 1.16. Hoop stress-strain response at inner surface of cylinder using TTT-1 histogram and material parameters specified in Sect. 1.2.1.

representative of 2 1/4 Cr—1 Mo steel and not type 304 stainless steel, as used in the experiment. Furthermore, no temperature dependence of the material parameters was included in the analysis. It is encouraging that the results of this complex structural analysis do appear qualitatively reasonable and that they were obtained with no serious numerical difficulties.

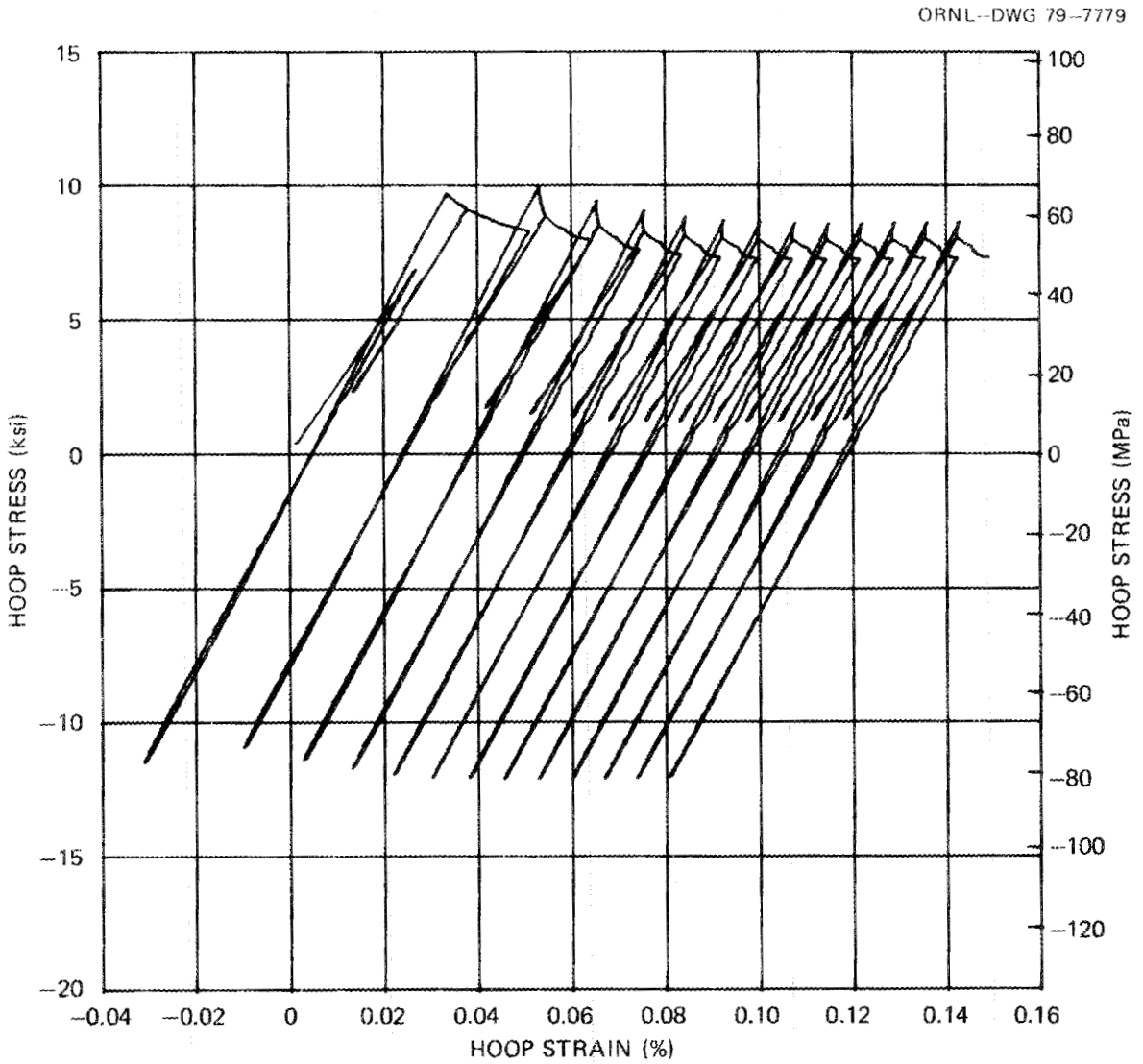

Fig. 1.17. Hoop stress-strain response at outer surface of cylinder using TTT-1 histogram and material parameters specified in Sect. 1.2.1.

1.3 Uniaxial Exploratory Testing

R. W. Swindeman

(Last reported in ORNL-5433, pp. 65-69)

1.3.1 Testing of type 304 stainless steel

During this report period, an updated analysis was completed of the creep data from the reference heat (9T2796) of type 304 stainless steel.

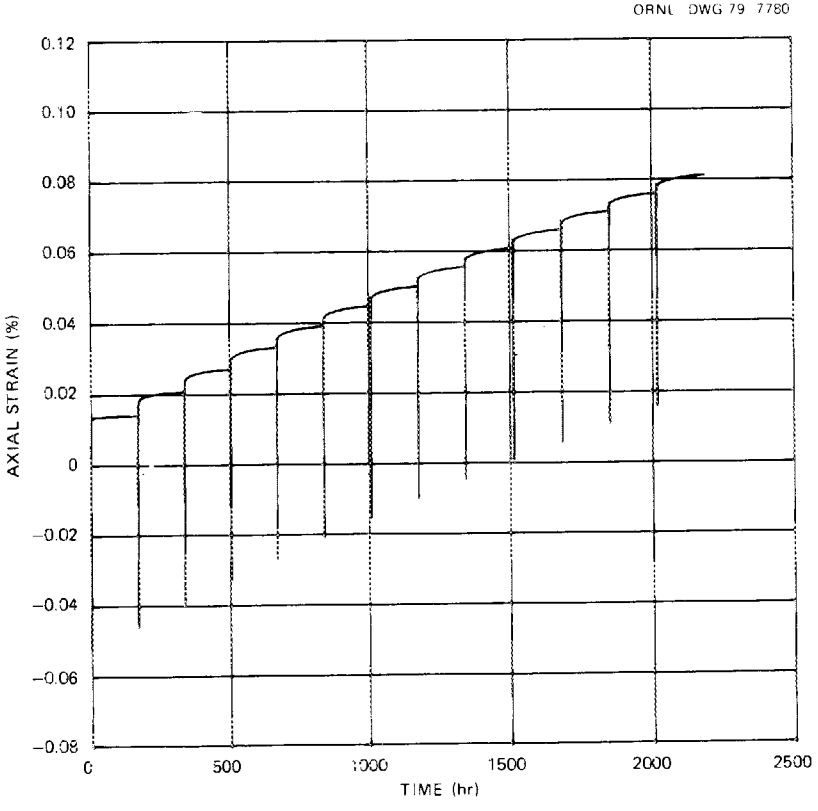

Fig. 1.18. Axial strain vs time at outer surface of a cylinder which was analyzed for 13 cycles of a TTT-1—type loading.

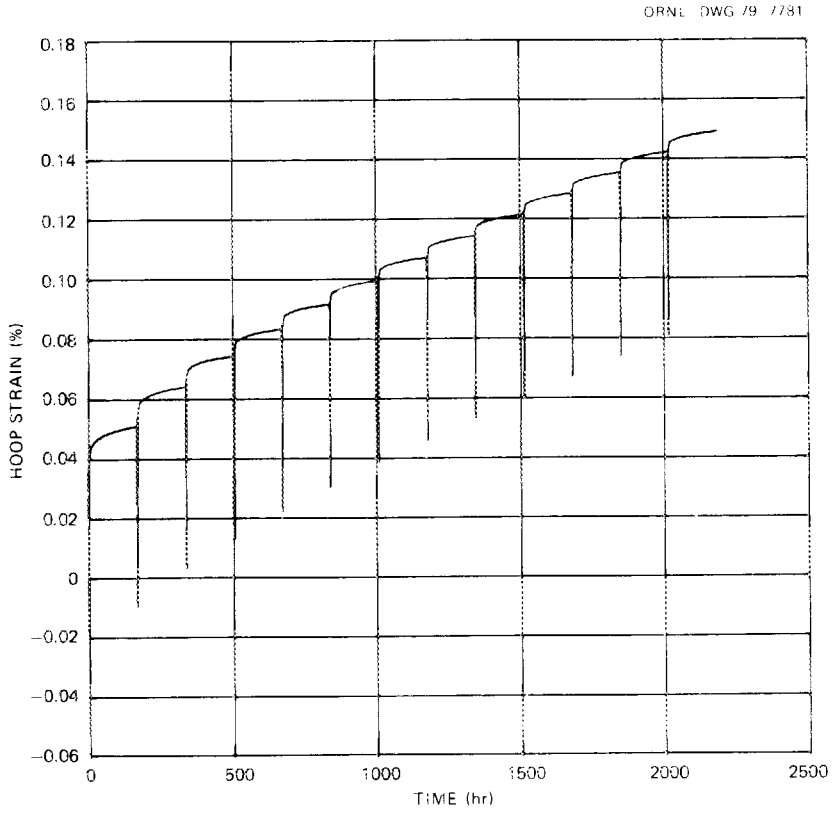

Fig. 1.19. Hoop strain vs time at outer surface of a cylinder which was analyzed for 13 cycles of a TTT-1—type thermal transient loading.

A careful study of the secondary creep rate was performed using the combined data sets on 25-mm (1-in.) plate,[11] 51-mm (2-in.) plate,[12,13] and 16-mm (3/8-in.) bar.[14,15] A final version of the Frost-Ashby deformation map[16] was developed, along with contour maps for several of the parameters that enter into the description of creep, including the stress exponent, thermal activation energy, transient strain asymptote, and associated transient rate constant. This information was put into a report,[17] which is now in the publication process. The following conclusions were drawn.

1. Evaluation of the stress and temperature dependencies of the parameters describing deformation in type 304 stainless steel indicate that at least four regions of different behavior exist in the temperature range 425 to 800°C (800 to 1500°F).
2. In the very low-stress region where Frost and Ashby predict diffusional creep, some experimental evidence exists to support their model.
3. In the high-temperature region [above 650°C (1200°F)] where Frost and Ashby predict dislocation creep, the experimental evidence also supports their model.
4. In the high-stress, low-temperature region where Frost and Ashby predict dislocation glide, experimental data do not support the assumed stress and temperature dependencies. If glide is the dominant mechanism, then new deformation models must be employed.
5. A region exists not far from where the dislocation glide, dislocation creep, and diffusional creep fields meet, where very high stress and temperature dependencies for creep are observed. This region is produced by the dynamic precipitation of M_2C_6 carbides, which stabilize a fine dislocation network and prevent subgrain formation.

Experimental work has been directed toward understanding creep behavior of type 304 stainless steel under cyclic and reversed stresses. A report was prepared that included a literature review and summary of ORNL work on cyclic creep at 593°C (1100°F).[18] We reached the following conclusions as a result of this study.

1. For temperatures ranging from 300 to 600°C (600 to 1100°F), the stress corresponding to gross plastic flow has an athermal character.

2. Above a critical stress, recovery processes influence the gross plastic flow stress. When the maximum stress under cyclic creep conditions exceeds this critical stress and the maximum stress to minimum stress ratio is near zero, the gross flow stress can recover during the period of the cycle at the minimum stress. This leads to recurrent yielding and also to an acceleration of the creep rate.
3. For some combinations of stress, temperature, frequency, and stress ratio, the creep rate in cyclic creep tests can be suppressed relative to the static creep rate. A more complete understanding of the relation between anelasticity and creep is needed before this phenomenon can be fully explained.
4. The reappearance of primary creep due to thermal recovery at low stress is not significant for temperatures to 600°C (1100°F) at stress levels in the range 100 to 140 MPa (15 to 20 ksi). The cyclic creep response here agrees reasonably well with predictions based on strain hardening.
5. For reversal creep conditions, the creep in any cycle is usually equal to or less than the creep in uncycled material over the same time period.
6. Transient strains during reversal creep are not solely a manifestation of anelasticity because the strain levels (1) can exceed the elastic component, (2) are not linearly related to stress, and (3) do not recover at zero stress. Reversal creep appears to involve dislocation remobilization and dynamic recovery mechanisms.
7. Interpretation of reversal creep data is complicated by uncertainty about the equivalence of tension and compression creep behavior. Existing data suggest that austenitic steels are about 10% stronger in compression than tension.
8. Relaxation data from cyclic relaxation tests are comparable to monotonic data from uncycled material for temperatures to 600°C (1100°F). After several cycles, the very short-time cyclic relaxation rates are often higher than predicted from a strain-hardening theory based on total accumulated creep strain, but relaxation rates approach creep rates at longer times.

9. The heat-to-heat variation in the creep strength of austenitic stainless steels is not manifested in cyclic relaxation for short hold times. This suggests that the time-dependent behavior is dominated by the influence of plasticity and anelasticity.
10. Short-time relaxation tests from various points on a stabilized stress-strain hysteresis loop suggest that anelasticity is a very important component of the deformation process.
11. In creep-plasticity interspersion tests, the short-time creep response is highly sensitive to the plastic-strain history. Reversed plastic strains produce some of the same short-time creep response as reversed creep strains.
12. Although small cyclic plastic strains can either accelerate or suppress the short-time transient strain rate, the long-term trend of the creep curve is not greatly affected by cyclic or monotonic plasticity.
13. Thermal cycling with temperature changes in the range ±27°C (±49°F) and low frequencies (10.8 Hz) produces creep that is dominated by the deformation at the maximum temperature.

In this report period, we have examined the impact of cyclic stresses on both creep and rupture at 538°C (1000°F). The results from one of several tests are plotted in Fig. 1.20. The test started under constant stress and then switched to cyclic stress after ∿500 hr. Thereafter, we alternated in 500-hr time blocks between constant stress and cyclic stress. A cyclic stress wave was selected that had no significant hold period at the minimum stress. More than 90% of the time in the test was spent at the maximum stress. We observed that the creep rate was reduced during the cycling periods and that the life was nearly doubled. This implies one of two things: (1) strain accumulation is more important than time accumulation in determining creep rupture, or (2) significant recovery of creep damage is possible under cyclic conditions.

1.3.2 Representation of uniaxial creep data for type 304 stainless steel (heat 9T2796) at 538°C (1000°F)

In support of the analysis of capped cylinder specimen CC-2 (see Sect. 2.3), a representation was prepared of available uniaxial creep

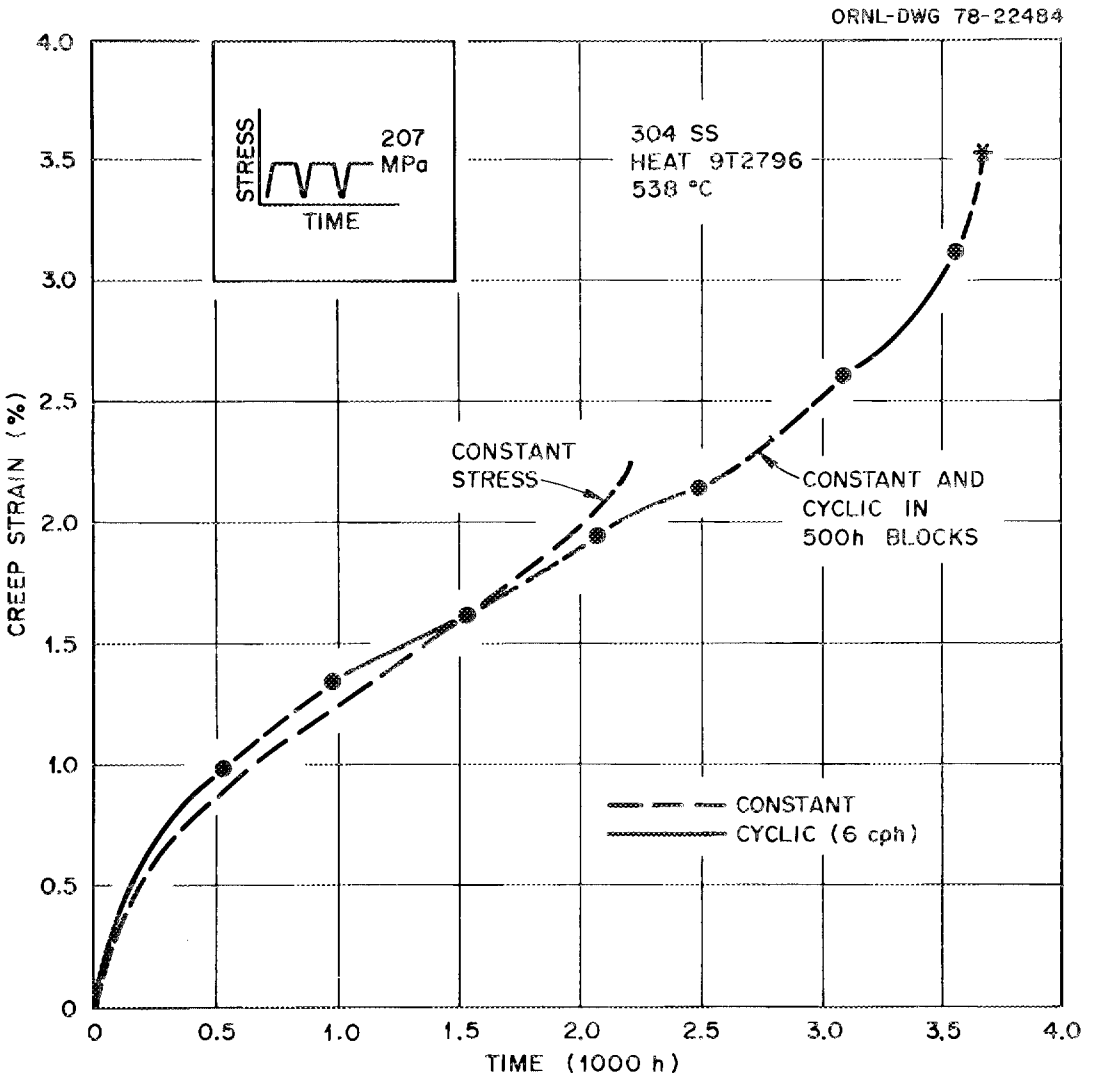

Fig. 1.20. Effect of cyclic stress on creep of type 304 stainless steel at 538°C (1000°F).

data for the reference heat (9T2796) of type 304 stainless steel at 538°C (1000°F). Available data consisted of (1) six relatively short-time tests on specimens from 25-mm (1-in.) plate and at stresses in the range 121 to 207 MPa (17.5 to 30 ksi) and (2) nine long-time tests on specimens from 51-mm (2-in.) plate at stresses in the range of 55 to 138 MPa (8 to 20 ksi). The creep strain ε_c was divided into three components:

$$\varepsilon_c = \varepsilon_{trans} + \varepsilon_{disc} + \varepsilon_{diff} , \tag{1.24}$$

where

ε_c = creep strain,

ε_{trans} = transient creep strain,

ε_{disc} = steady-state dislocation creep strain,

ε_{diff} = steady-state diffusional creep strain.

At 538°C (1000°F), we found that at any time t the diffusional creep strain was

$$\dot{\varepsilon}_{diff} = \varepsilon_{diff} t \ , \tag{1.25}$$

where the diffusional creep rate ε_{diff} is given by

$$\dot{\varepsilon}_{diff} = \begin{cases} 2.48 \times 10^{-7}\ \sigma \text{ (when } \sigma \text{ is in ksi)} \\ 3.6 \times 10^{-8}\ \sigma \text{ (when } \sigma \text{ is in MPa)} \end{cases} ,$$

where $\dot{\varepsilon}$ is in percent per hour and σ is true stress. The dislocation creep strain was found to be

$$\varepsilon_{disc} = \dot{\varepsilon}_s t \ , \tag{1.26}$$

where the secondary creep rate is given by

$$\dot{\varepsilon}_s = \begin{cases} (\sigma/63)^{10} \text{ (when } \sigma \text{ is in ksi)} \\ (\sigma/434)^{10} \text{ (when } \sigma \text{ is in MPa)} \end{cases} .$$

Representation of the transient creep component was examined in terms of two relationships:

$$\varepsilon_{trans} = \varepsilon_t [1 - \exp\ (-rt)]^{\alpha} \ , \tag{1.27}$$

and

$$\varepsilon_{trans} = \frac{cpt}{(1 + pt)} \ .$$

In Eq. (1.27), if $\alpha = 1$, r is defined by the inverse of the time for the ratio $\varepsilon_{trans}/\varepsilon_t$ to be 0.632, and ε_t is the transient creep strain asymptote. The parameter α is available to provide more short-time curvature to the

exponential function. For example, α could be selected as 0.5. In this instance, the r value would be $\sim$0.5 of the r value when $\alpha = 1$. The stress dependence of ε_t was found to be

$$\varepsilon_t = \begin{cases} 6.25 \times 10^{-4}\ \sigma^2 \text{ (when } \sigma \text{ is in ksi)} \\ 1.31 \times 10^{-5}\ \sigma^2 \text{ (when } \sigma \text{ is in MPa)} \end{cases} .$$

and r to be related to stress by:

$$r = \begin{cases} 3.265 \times 10^{-6}\ \sigma^2 \text{ (when } \sigma \text{ is in ksi)} \\ 6.868 \times 10^{-8}\ \sigma^2 \text{ (when } \sigma \text{ is in MPa)} \end{cases} .$$

Here, ε_t is in percent and r is in $(h)^{-1}$.

The single rational polynomial form provides a finite initial creep rate, and the primary creep-hardening value can also be solved explicitly. The parameter c is equivalent to the parameter ε_t in the exponential form, while the parameter p is given by $1.72r$.

1.3.3 Testing of type 316 stainless steel

All of our planned tests on the reference heat (8092297) of type 316 stainless steel were completed, and a summary report was prepared[19] during this period. Testing was primarily at 593°C (1100°F) and included tensile strain-cycling, creep, and relaxation tests. A few variable-temperature tensile tests and variable-stress creep tests were also performed.

Most behavioral features of type 316 stainless steel were similar to those displayed by type 304 stainless steel. Both exhibited plastic deformations that were essentially "athermal" over a range of temperatures and strain rates. Both displayed a tendency toward strain hardening under variable-stress creep testing. Both exhibited an increase in plastic-flow stress due to thermal aging and a decrease in creep strength due to aging. Other conclusions drawn from this study on type 316 stainless steel are as follows.

1. The true stress vs true strain tensile flow curve for reannealed specimens above the 0.2% yield strength can be separated into three hardening stages on the basis of the behavior of the strain-hardening coefficient (θ).

2. At low stresses, θ is relatively constant. At intermediate stresses, θ decreases with increasing stresses. At high stresses, θ tends toward zero, and steady-state deformation develops where the flow stress σ_∞ is constant.
3. The steady-state flow stress in the tensile test is the same as the true stress in the creep test when the strain rates are the same. The uniform strain (at ultimate) in the tensile test and the total inelastic strain at the onset of tertiary creep in creep tests are nearly the same.
4. The creep curves to 10,000 hr can be characteristically described by three parameters: the secondary creep rate $\dot{\varepsilon}_s$, the transient creep strain asymptote ε_t, and the transient creep rate constant r. The transient rate constant can be related to the other parameters.
5. Under variable-load conditions, the creep and tensile responses are dominated by strain hardening (as opposed to thermal recovery) for stresses up to 200 MPa (29 ksi). Above 200 MPa, dynamic and thermal recovery become increasingly important.
6. The relaxation strength for multiple loading situations increases with accumulated creep strain and plastic strain. Except for a transient period at the start of relaxation tests, most of the log ε_r vs log σ curves obtained from relaxation tests can be superimposed onto a master curve by simple translations. Generally, the log ε_r vs log σ curves exhibited a region in which the ε_r had the same slope as the secondary creep rate curve log ε_r vs log σ. The stress exponent was near 8.
7. Strain cycling at room temperature produced the maximum stress range before 100 cycles were completed. After 100 cycles, softening was observed.
8. High-temperature strain cycling revealed that most of the hardening was produced after ten cycles. The hardening rate increased with increasing temperature in the range 316 to 593°C (600 to 1100°F).

1.3.4 Testing of 2 1/4 Cr–1 Mo steel

The lack of a "reference" heat of 2 1/4 Cr–1 Mo steel has made it difficult to perform a proper exploratory testing program on this material.

The problem is compounded by a variety of heat treatments. Our earlier studies involved relaxation and creep-plasticity tests on heat 20017; when the supply of this material was exhausted, we started tests on heat 3P5601. This work was temporarily suspended to do some testing on the Metals Properties Council (MPC) heat of material for TTT-3. We then returned to more testing on heat 3P5601 to get data to support revisions of constitutive equations. Tests on heat 3P5601 included tensile, creep, creep-plasticity, and relaxation tests at 538°C (1000°F). Data were processed and summarized this report period in a report[20] that draws the following conclusions.

1. The yield strength of heat 3P5601 is not sensitive to strain rate in the range 6.7×10^{-6} to 6.7×10^{-4}/sec. This is consistent with similar observations for other heats of 2 1/4 Cr–1 Mo steel.
2. The ultimate tensile strength at 538°C (1000°F) decreases with strain rate below 10^{-4}/sec and merges with stress vs strain-rate data derived from constant-stress creep tests. This is typical of other heats.
3. Tensile elongation increases with decreasing strain rate but then decreases at rates typical of constant-stress creep tests.
4. Sigmoidal creep occurs at 538°C (1000°F) in the stress range 103 to 155 MPa (15 to 22.5 ksi). The behavior is identical to the "nonclassical" creep phenomenon observed in heat 20017 in the same range of stress and temperature. The sigmoidal character is generally limited to creep strains below 0.5%.
5. Some aspects of the creep response for varying stresses are not quantitatively predicted by constant-stress creep data when the strain-hardening rule is invoked. Generally, the observed creep rates are lower than expected immediately after stress reductions and higher than expected immediately after stress increases.
6. The initial relaxation strain rates are generally higher than predicted from the strain-hardening rule, but, for times around 100 hr, the relaxation strain rates at low stresses are generally lower than predicted. The flow stress recovers significantly during relaxation

and needs careful attention when further creep-plasticity interaction models are formulated.

We are now testing a VAR heat of material (heat 56448) in the post-weld heat-treated conditions (PWHT). Tests planned on heat 56448 are summarized in Table 1.1 and include tensile, strain-cycling, relaxation, creep, and yet-to-be-defined creep-plasticity experiments. Preliminary data showing results of a few tensile, creep, and relaxation tests are provided in Figs. 1.21 through 1.23. These tests reveal that the PWHT produces a material that is fairly stable and follows a well-ordered flow stress vs strain-rate response. This means that unified constitutive equations of the type currently under development should work reasonably well for this material because dynamic strain aging and strain-induced metallurgical instabilities are not special considerations here.

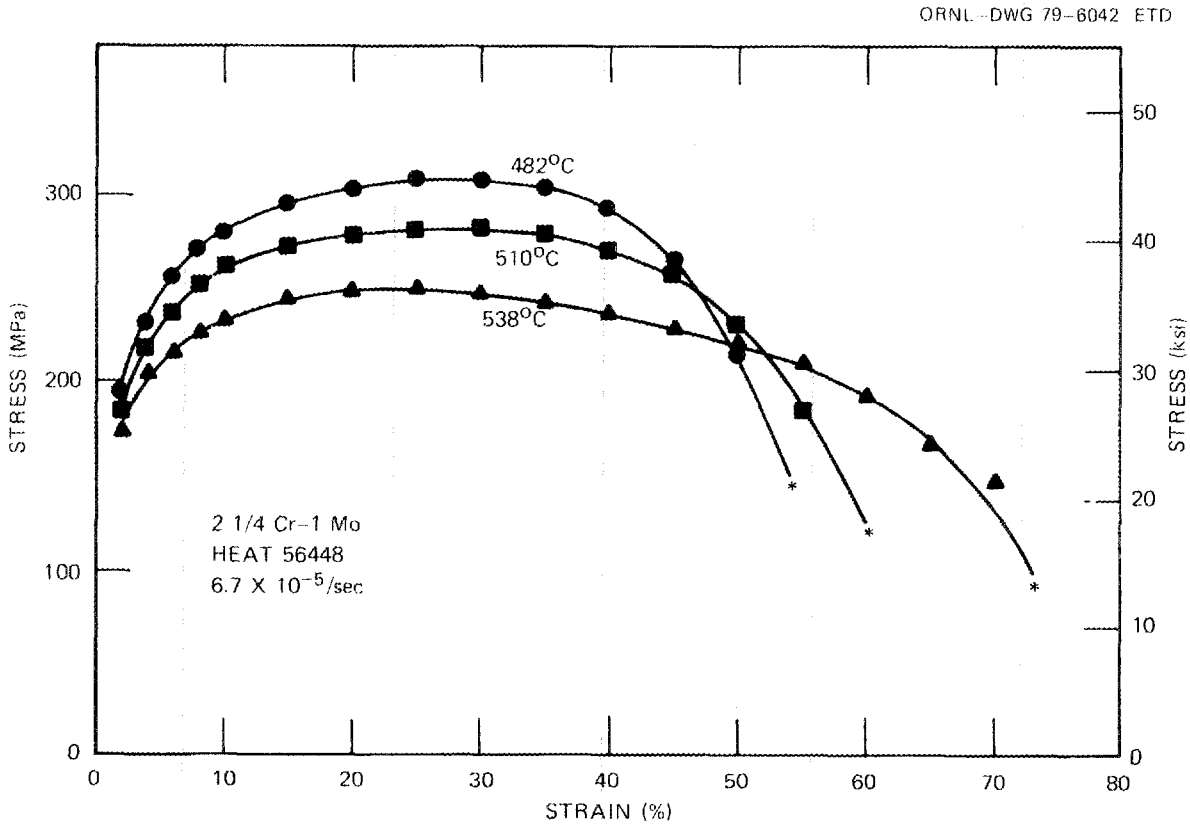

Fig. 1.21. Engineering stress vs strain current at three temperatures for VAR 2 1/4 Cr–1 Mo steel, heat 56448 PWHT.

Table 1.1. Exploratory tests on 2 1/4 Cr–1 Mo steel VAR heat 56448 (annealed + 40 hr PWHT)

Tests	Temperature [°C (°F)]	Strain rate (sec^{-1})	Starting stress [MPa (ksi)]	Stress	Status	Strain range (%)
Tensile	482 (900)	6.7×10^{-5}				
	510 (950)	6.7×10^{-5}			Completed	
	538 (1000)	6.7×10^{-4}			Completed	
	538 (1000)	6.7×10^{-5}				
	538 (1000)	6.7×10^{-6}			Completed	
	538 (1000)	6.7×10^{-7}				
	566 (1050)	6.7×10^{-5}				
Strain cycling (some tests with relaxation holds ≤1 hr)	482 (900)	6.7×10^{-5}				0.4
	510 (950)	6.7×10^{-5}				0.4
	538 (1000)	6.7×10^{-4}				0.6
	538 (1000)	6.7×10^{-4}				0.4
	538 (1000)	6.7×10^{-5}				0.3
	538 (1000)	6.7×10^{-5}				0.6
	538 (1000)	6.7×10^{-5}				0.4
	538 (1000)	6.7×10^{-5}				0.3
	538 (1000)	6.7×10^{-5}				0.6
	538 (1000)	6.7×10^{-5}				0.4
	538 (1000)	6.7×10^{-5}				0.4
	566 (1050)	6.7×10^{-5}				0.4
Strain cycling with relaxation holds (10 hr or more)	482 (900)	6.7×10^{-5}				0.4
	510 (950)	6.7×10^{-5}				0.4
	538 (1000)	6.7×10^{-5}				0.6
	538 (1000)	6.7×10^{-5}				0.4
	538 (1000)	6.7×10^{-5}				0.3
	566 (1050)	6.7×10^{-5}				0.4
Multiple-load uniaxial relaxation (100 hr or more)	482 (900)		140 (20.3)		Three runs complete	
	510 (950)		140 (20.3)		Three runs complete	
	538 (1000)		100 (14.5)			
	538 (1000)		140 (20.3)			
	538 (1000)		200 (29.0)			
	566 (1050)		140 (20.3)			
Constant stress creep (100 hr or more)	482 (900)			125 (18.1)	In progress	
	510 (950)			125 (18.1)	In progress	
	538 (1000)			140 (20.3)		
	538 (1000)			125 (18.1)		
	538 (1000)			100 (14.5)		
	538 (1000)			85 (12.3)		
	538 (1000)			70 (10.0)		
	538 (1000)			50 (7.3)		
	566 (1050)			125 (18.1)		

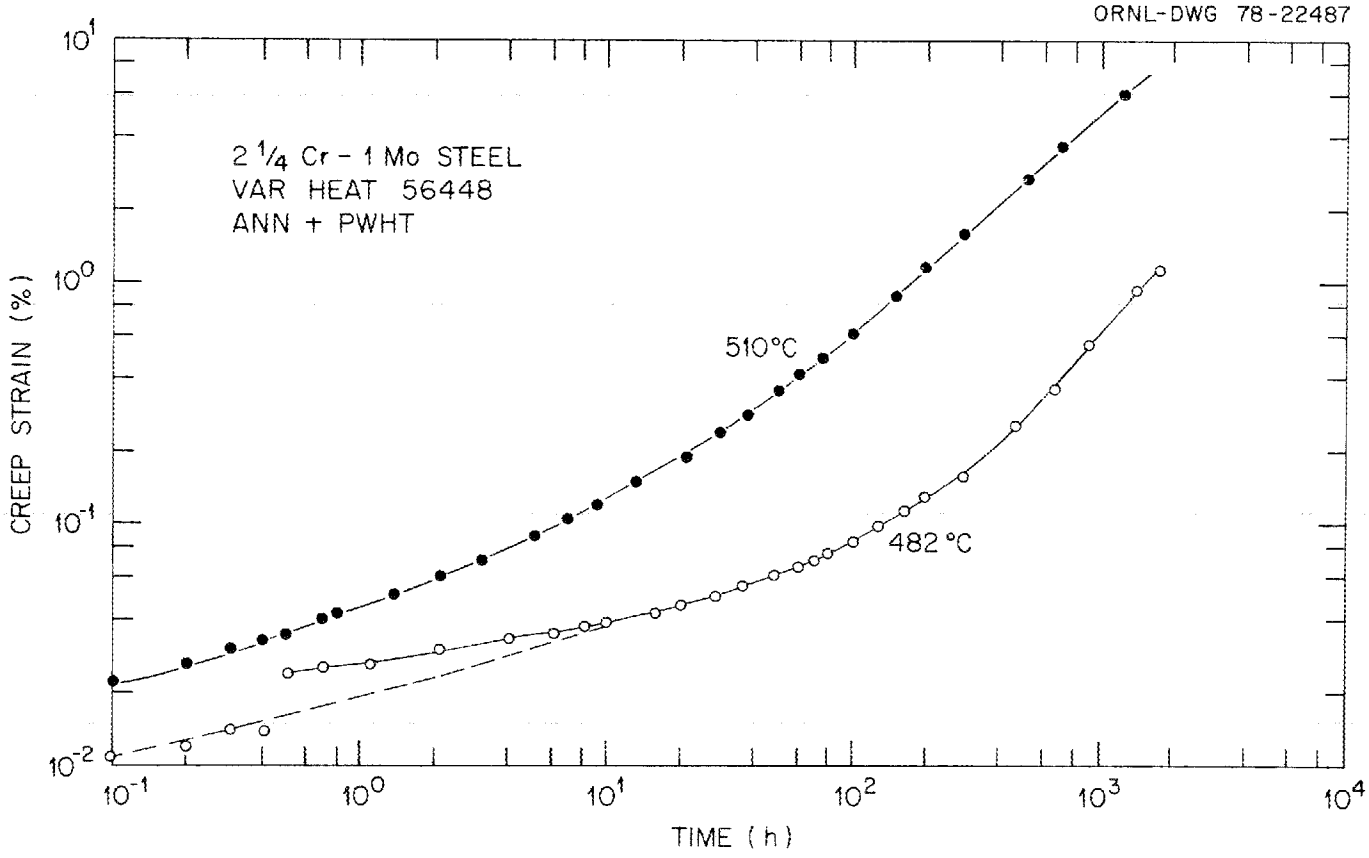

Fig. 1.22. Creep curves for VAR 2 1/4 Cr–1 Mo steel (PWHT) at 125 MPa (17.8 ksi).

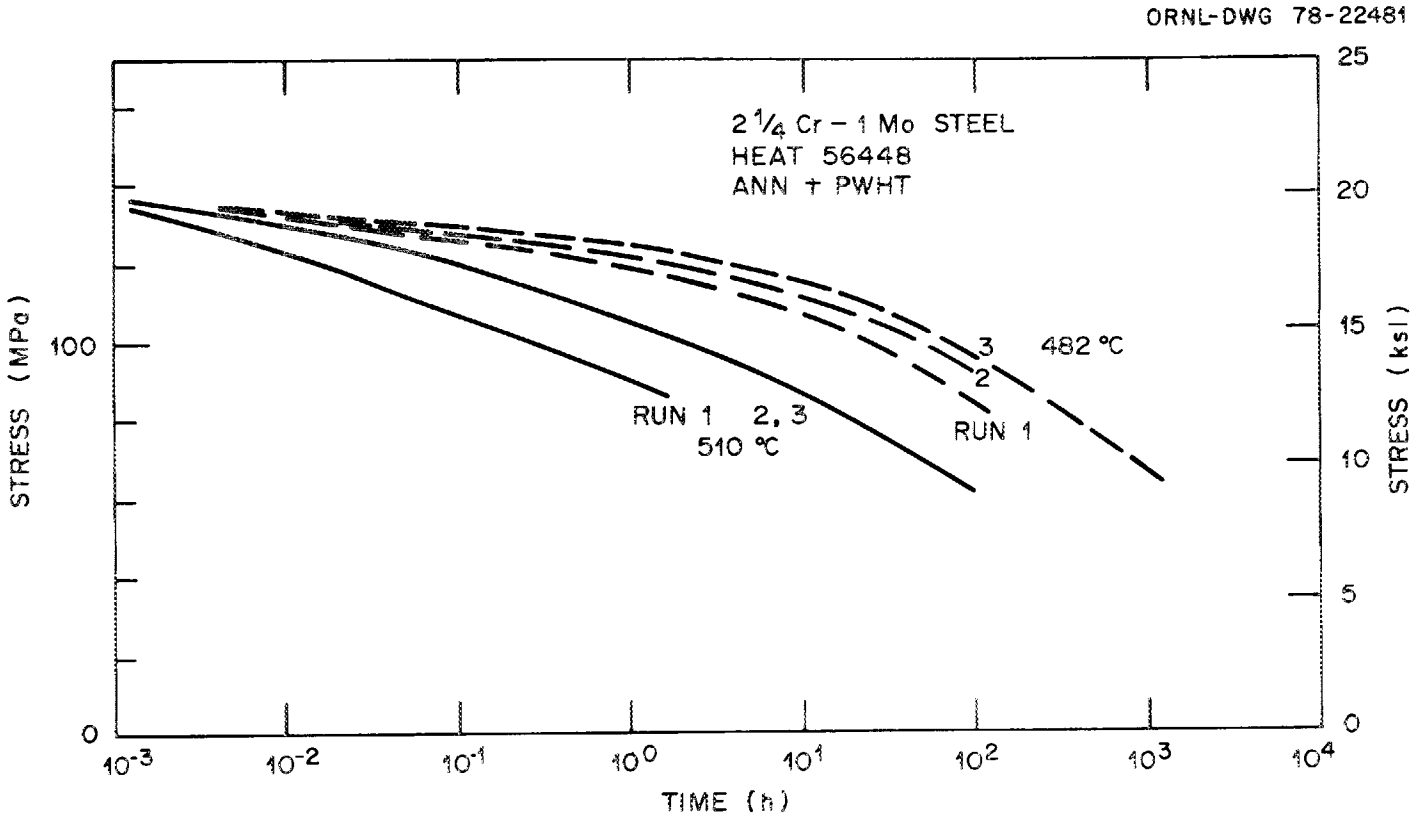

Fig. 1.23. Relaxation curves for VAR 2 1/4 Cr–1 Mo steel (PWHT) at 482 and 510°C (900 and 950°F). Runs 2 and 3 follow run 1 by reloading to the same maximum stress as employed at the beginning of run 1.

1.3.5 Deformation studies of 308 CRE weldments

The status of information on 308 controlled-residual-element (CRE) weldments was reviewed. This review included work at ORNL, Hanford Engineering Development Laboratory (HEDL), Idaho National Engineering Laboratory (INEL), and Argonne National Laboratory (ANL). Major emphasis was placed on gathering useful tensile and creep data rather than stress-rupture, fatigue, and crack growth information. Somewhat arbitrarily, we defined useful creep information as data for temperatures in the range 427 to 649°C (800 to 1200°F) and for stresses covered by the code isochronous stress-strain curves at 1% strain. On the basis of this definition, we found about 18 creep tests of interest. Of nine tests at 593°C (1100°F), several were on samples prepared by ORNL for the Westinghouse Advanced Reactors Division (WARD) program on weldments.[21] Although these welds were not typical of welds produced by current welding practices, some long-time creep data and availability of untested specimens made this material attractive for more studies. Log creep-strain vs log time plots for longitudinal weld metal are provided in Fig. 1.24. These data were produced by King et al.[22] We see that the curves tend to be flat at short times. This implies extremely high initial creep rates. The curves are steep at long times, which implies substantial tertiary creep periods. The creep data were well behaved, and we attempted modeling the behavior by a fairly simple modified exponential creep equation:

$$e_c = e_t[1 - \exp(-rt)]^{\alpha} + \dot{e}_s t \ , \tag{1.28}$$

where

e_c = creep strain,
e_t = transient strain asymptote,
r = transient strain rate parameter,
$\dot{e}_s$ = minimum creep rate,
α = constant, which was selected to be 1/2.

The e_t values varied, more or less, with a power of stress (see Fig. 1.25), while the $\dot{e}_s$ values seemed to vary exponentially with stress (see Fig. 1.26). We chose to let r be a function of e_t and $\dot{e}_s$ according to the

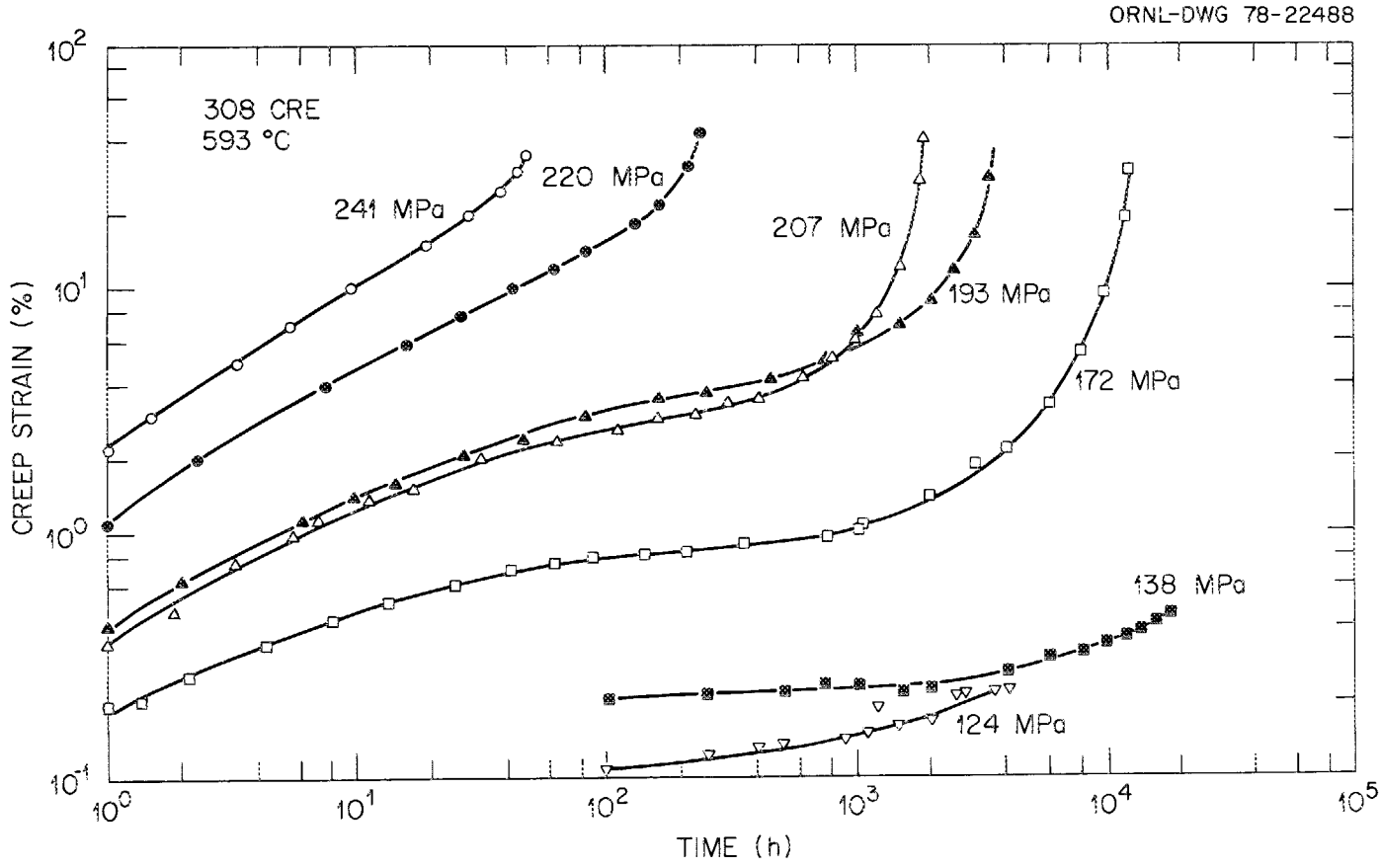

Fig. 1.24. Creep curves for type 308 CRE weld metal at 593°C (1100°F) longitudinal direction.

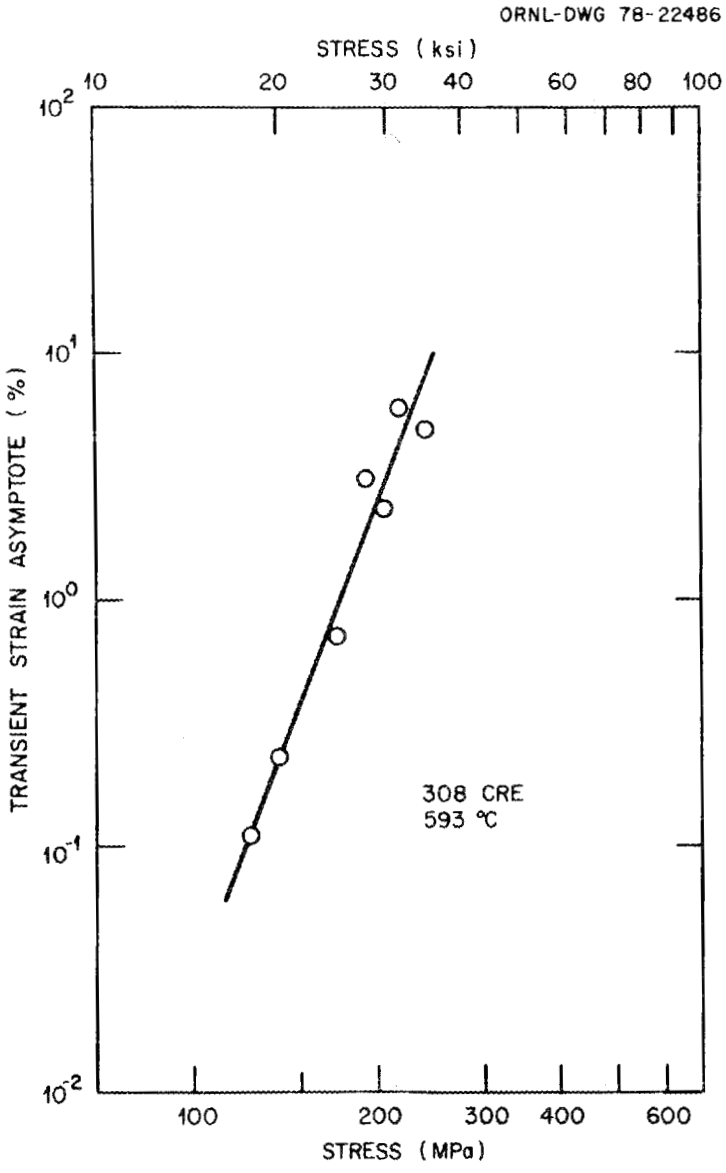

Fig. 1.25. Transient strain asymptote vs stress for type 308 CRE weld metal at 593°C (1100°F).

relation

$$e_t^r = be_s^\beta \ , \tag{1.29}$$

where b and β are parameters determined from the data plotted in Fig. 1.27. The creep law defined by Eqs. (1.28) and (1.29) will be used for further studies of weldment behavior under varying stresses.

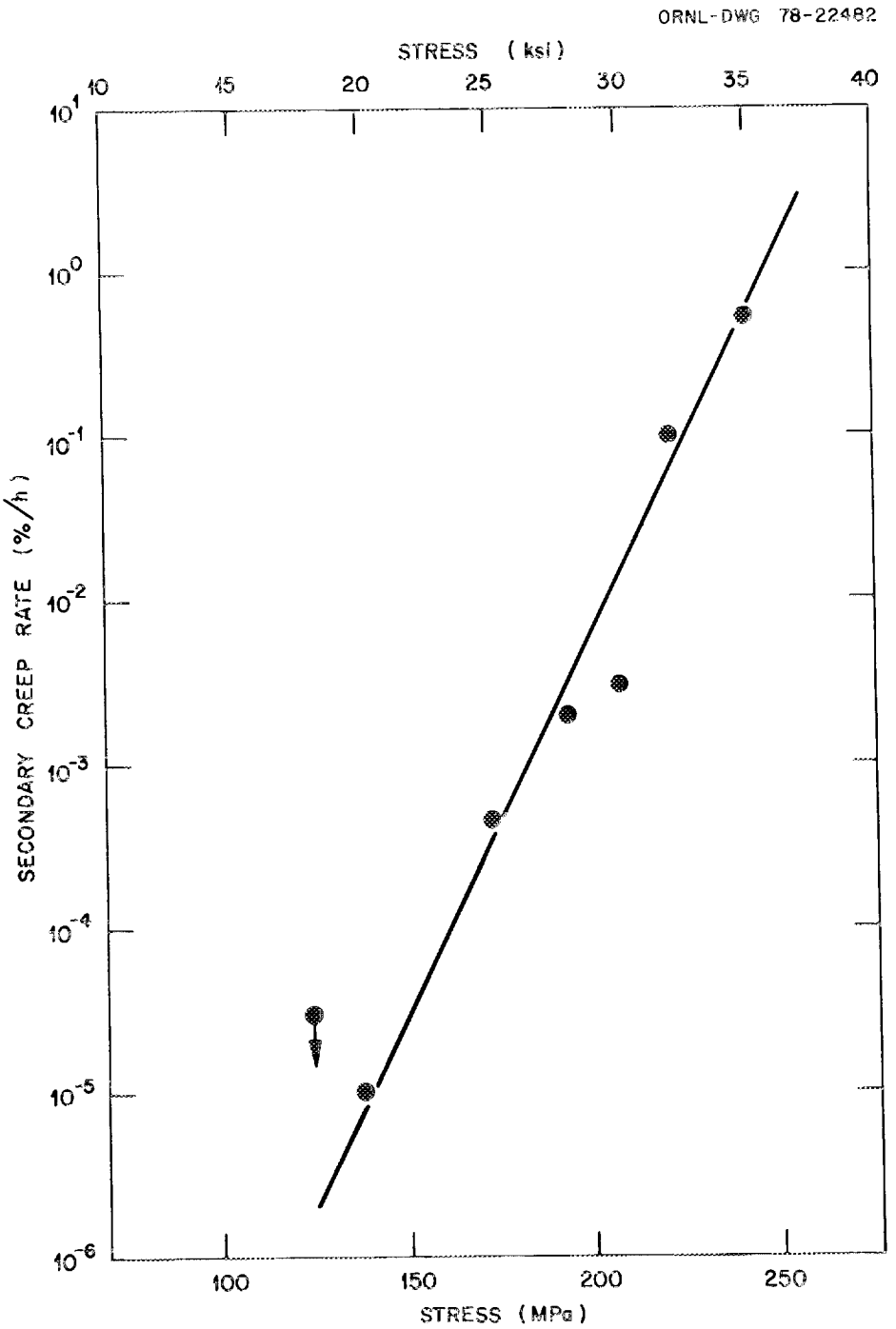

Fig. 1.26. Secondary creep rate vs stress for type 308 CRE weld metal at 593°C (1100°F).

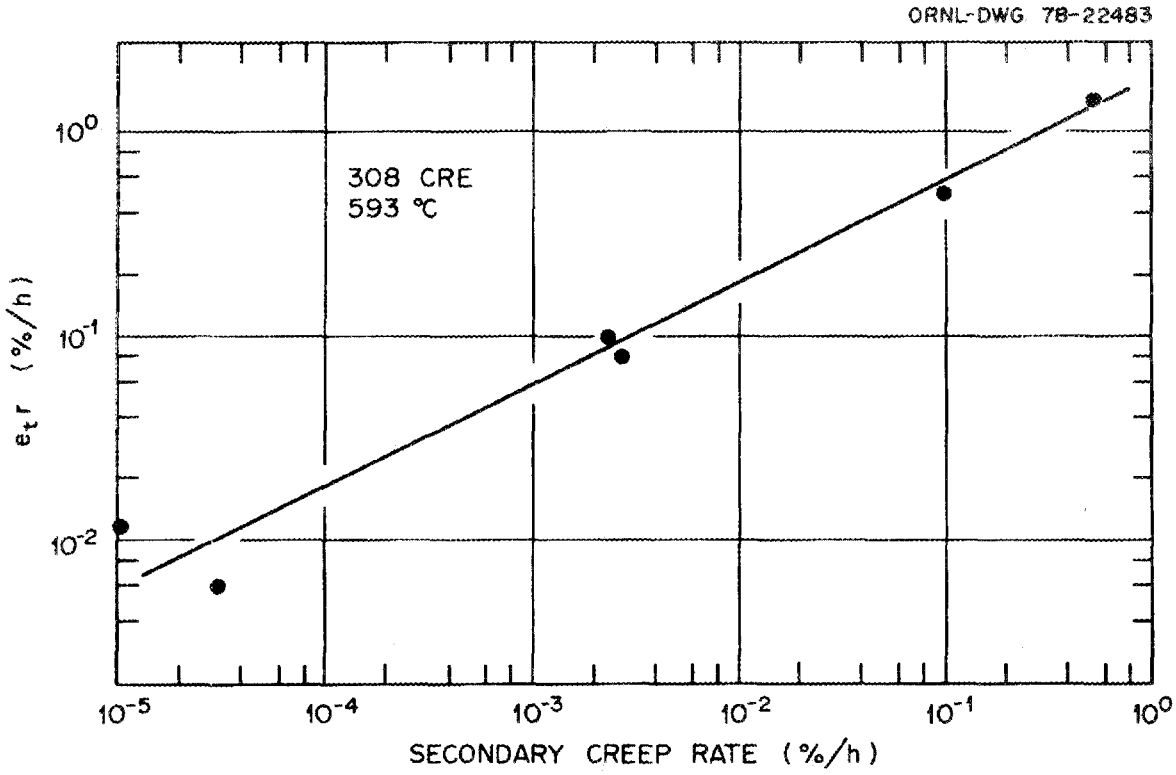

Fig. 1.27. Correlation between $\varepsilon_t r$ and secondary creep rate for type 308 CRE weld metal at 593°C (1100°F).

1.4 Multiaxial Exploratory Testing

J. R. Ellis

(Last reported in ORNL-5433, pp. 69-87)

1.4.1 Multiaxial creep tests

Test C4009, investigating creep and recovery phenomena in type 304 stainless steel at 593°C (1100°F) under purely torsional loading, was continued for four weeks into the current report period. Details of the start-up of this test were given in our last progress report,[23] along with the data generated during the first seven weeks of the experiment. The data generated during this report period are described below.

Test conditions investigated during the four additional weeks, designated loading stages (8) through (11), are summarized in Table 1.2. The main difference between these conditions and those used in earlier stages

Table 1.2. Summary of the loading history during the final stages of test C4009, type 304 stainless steel

Loading stage	Time of particular loading stage (hr)		Torsional stress [MPa (ksi)]	Objective of loading stage
	Start	Finish		
8	1159.3	1327.7	55.11 (7.99)	Establish baseline creep data at an increased torsional stress level
9	1327.7	1494.1	5.01 (0.73)	Investigate torsional strain recovery at a low stress level
10	1494.1	1659.5	55.11 (7.99)	Repeatability check
11	1695.5	1823.67	5.01 (0.73)	Repeatability check

is the higher stress level — 55.11 MPa (7.99 ksi) as opposed to 45.76 MPa (6.64 ksi). Creep curves determined during loading stages (8) and (10) are shown in Figs. 1.28 and 1.29. Comparison of these curves with earlier data[23] show, as expected, that increasing the torsional stress by 9.4 MPa (1.35 ksi) to 55.11 MPa (7.99 ksi) caused significant increases in the creep strains occurring during the one-week hold periods. The creep curves for loading stages (8) and (10) are compared with each other in Fig. 1.30. As was the case for earlier loading, the ends of the two curves are relatively well matched in terms of both total strain and strain rate. Figures 1.31 and 1.32 show that slight, but measurable, strain recovery occurred during the one-week periods at low stresses. Present data on shear-strain recovery are compared in Fig. 1.33 with data determined earlier in this test and also with uniaxial recovery data reported for this material in Ref. 24. Keeping in mind the small strains involved, the present data are in reasonably good agreement with the uniaxial data.

As in the earlier stages of the experiment, the calibration of the transducer/shim assembly used for strain measurement was checked at the beginning and end of each recovery period; the results are shown in Table 1.3. Procedures used in this work were identical to those described previously in Ref. 23. Table 1.3 indicates that the values obtained show no

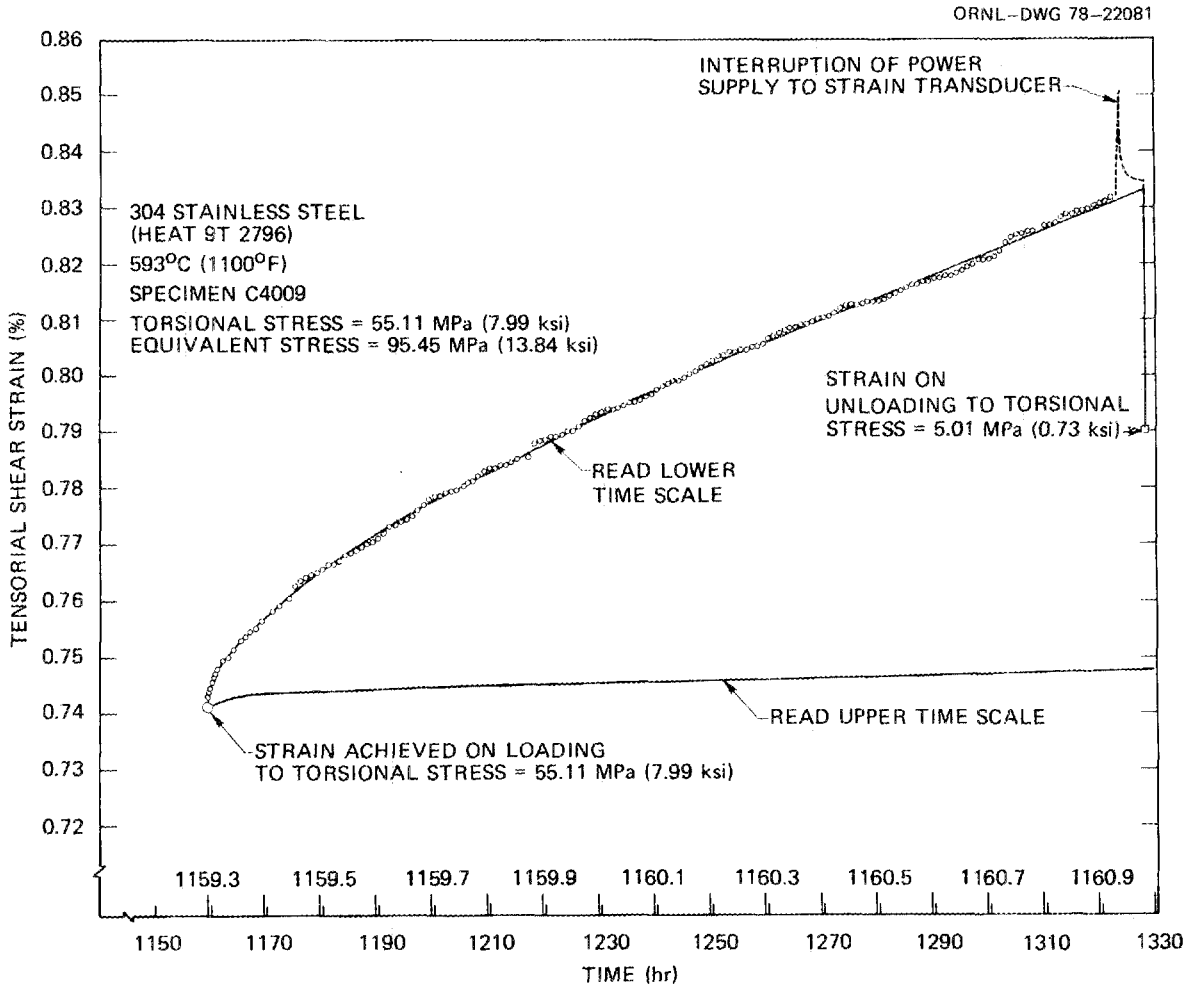

Fig. 1.28. Total tensorial shear strain vs time for torsional creep test C 4009; stage (8) loading.

well-defined trend and that they fall within 2% of the average value, 0.496%/V, assumed to hold for the entire test. This small deviation was taken to mean that the transducer/shim assembly was functioning properly during the latter stages of the experiment.

This temporarily concludes the biaxial creep/recovery experiments for type 304 stainless steel. The plan is to shift the emphasis of our next biaxial creep testing to 2 1/4 Cr–1 Mo steel; the next tests will be under pure torsional loadings at 538°C (1000°F). The studies on 2 1/4 Cr–1 Mo steel are to contribute to further validation of the equations now in RDT F9-5T and to support development of unified constitutive equations with an emphasis on multiaxial aspects.

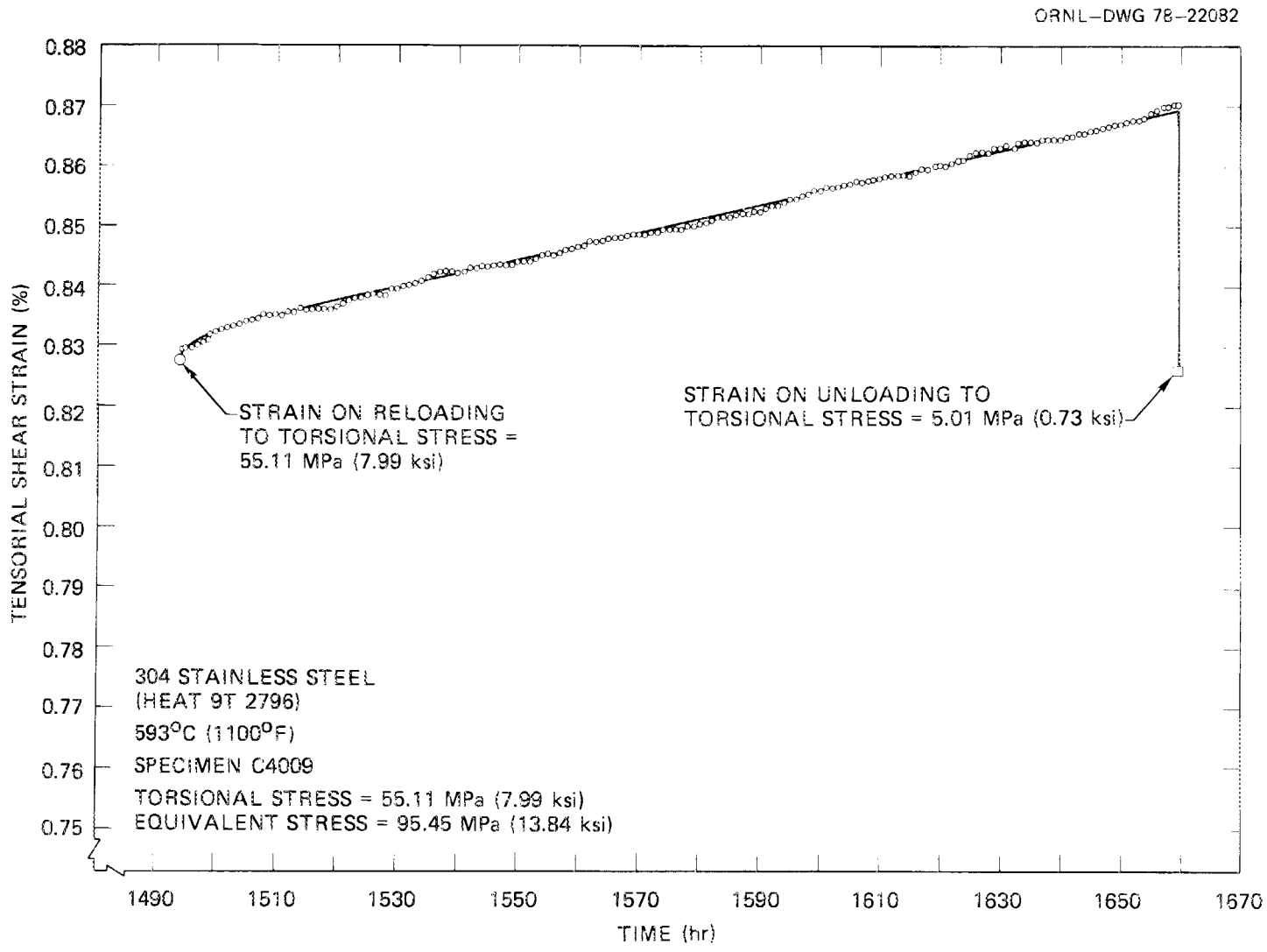

Fig. 1.29. Total tensorial shear strain vs time for torsional creep test C 4009; stage (10) loading.

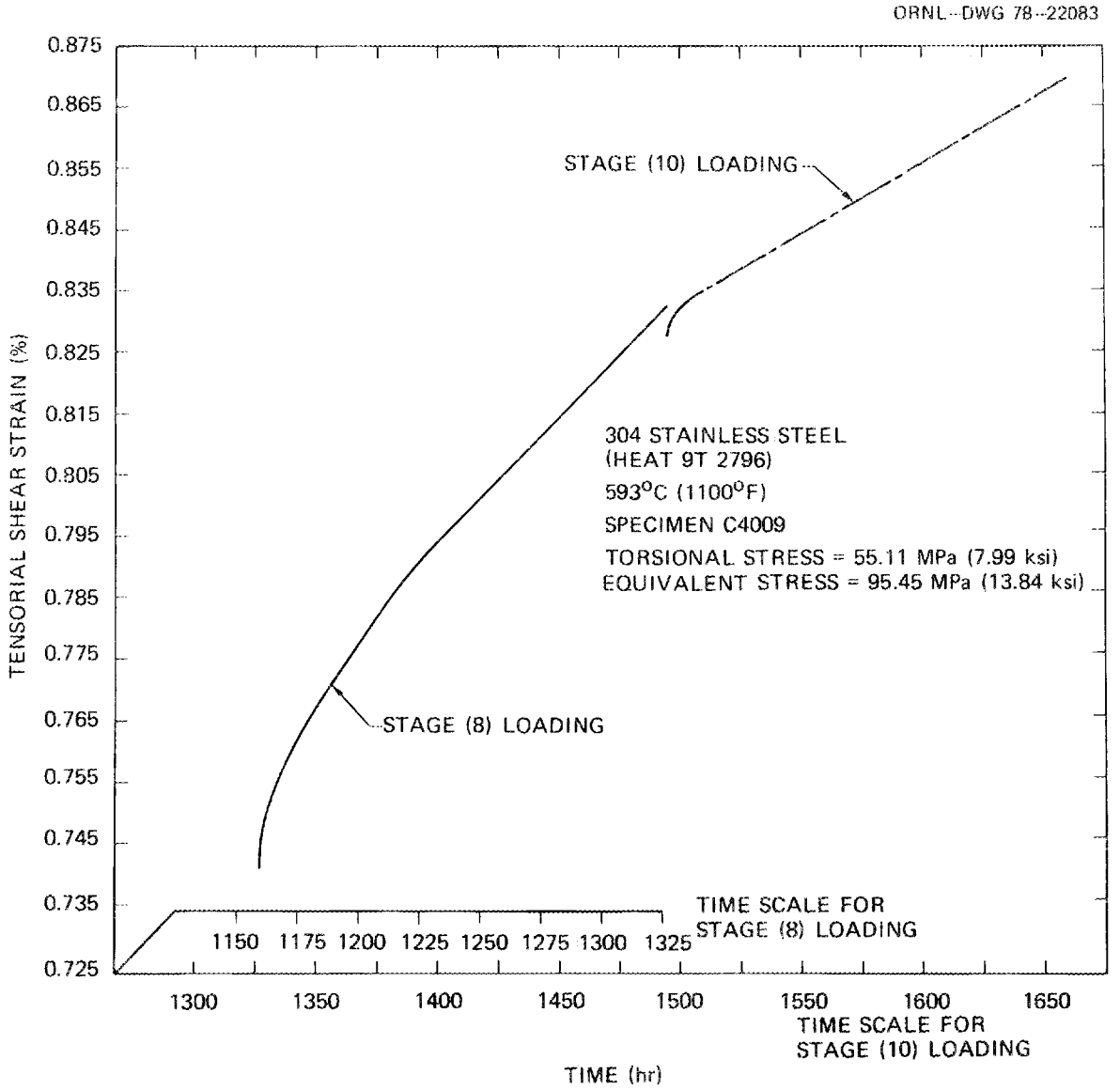

Fig. 1.30. Comparison of creep curves determined during loading stages (8) and (10); torsional stress = 55.11 MPa (7.99 ksi).

1.4.2 Multiaxial plasticity experiments at room and elevated temperatures

Two exploratory tests were conducted in the multiaxial stress-state laboratory to investigate the biaxial yield behavior of types 304 and 316 stainless steel at temperatures in the range 21 to 593°C (70 to 1100°F), including some interaction between creep and plasticity. The first of these experiments was conducted on type 304 stainless steel and the second

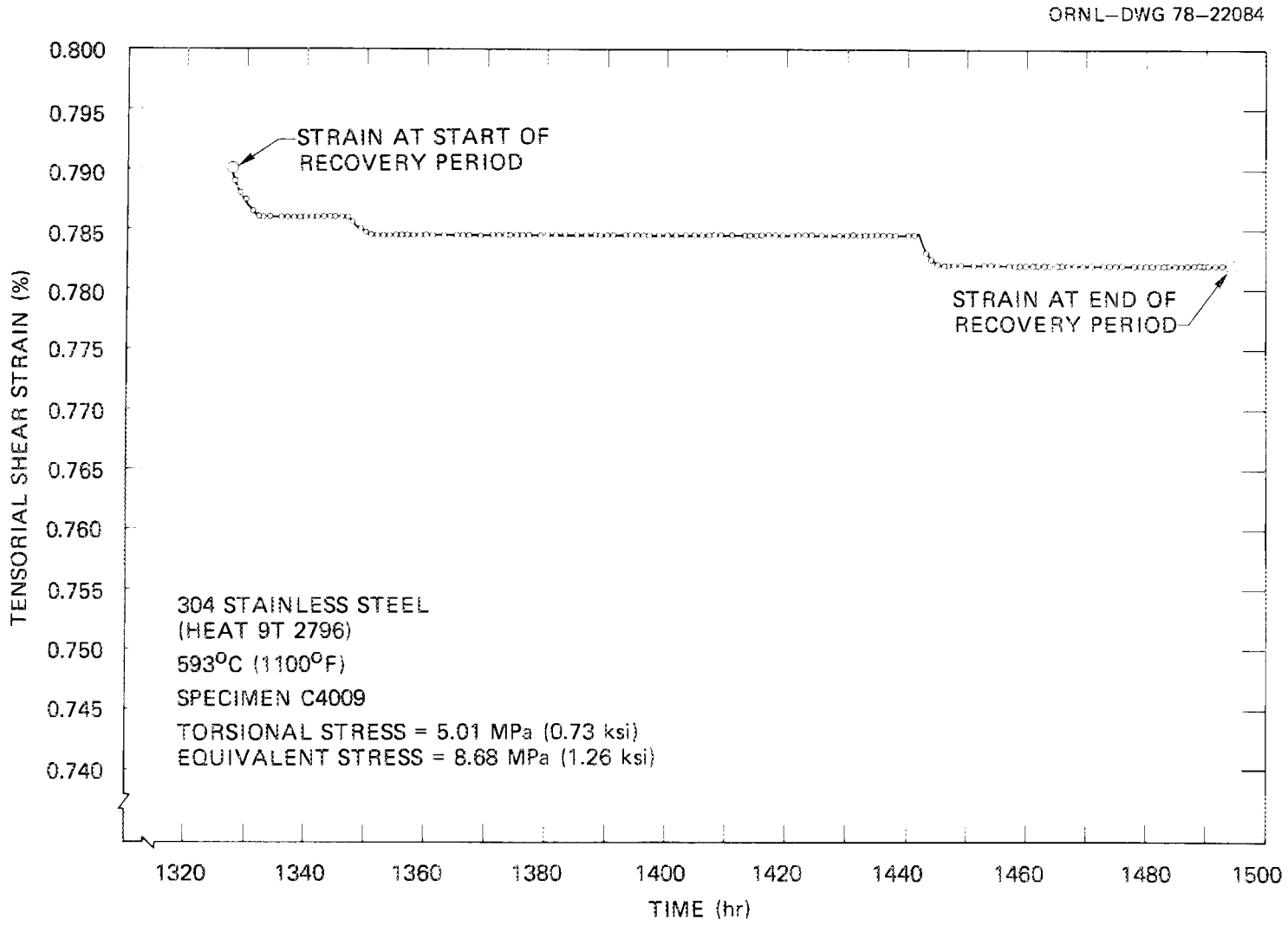

Fig. 1.31. Total tensorial shear strain vs time for torsional creep test C 4009; stage (9) loading.

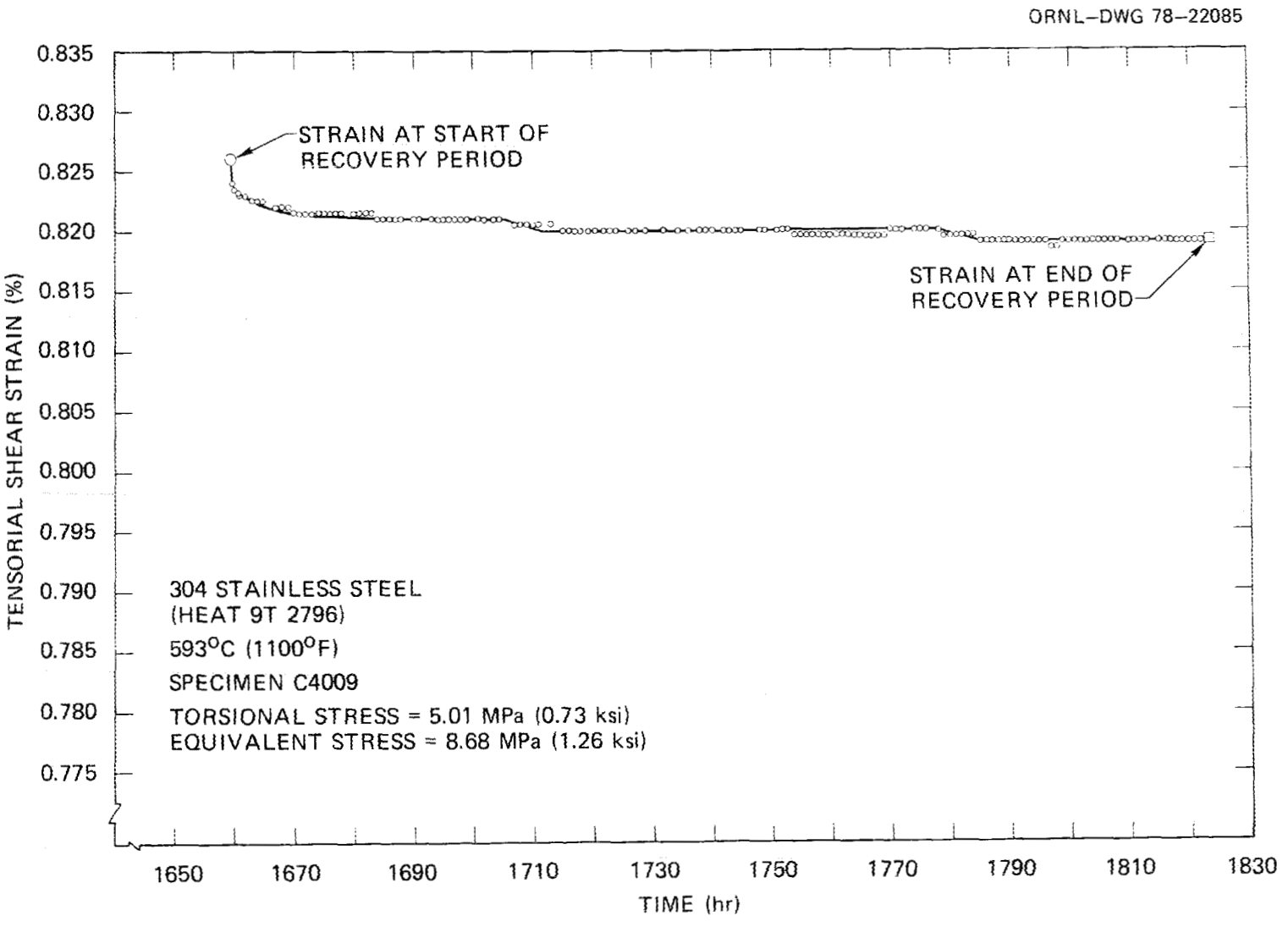

Fig. 1.32. Total tensorial shear strain vs time for torsional creep test C 4009; stage (11) loading.

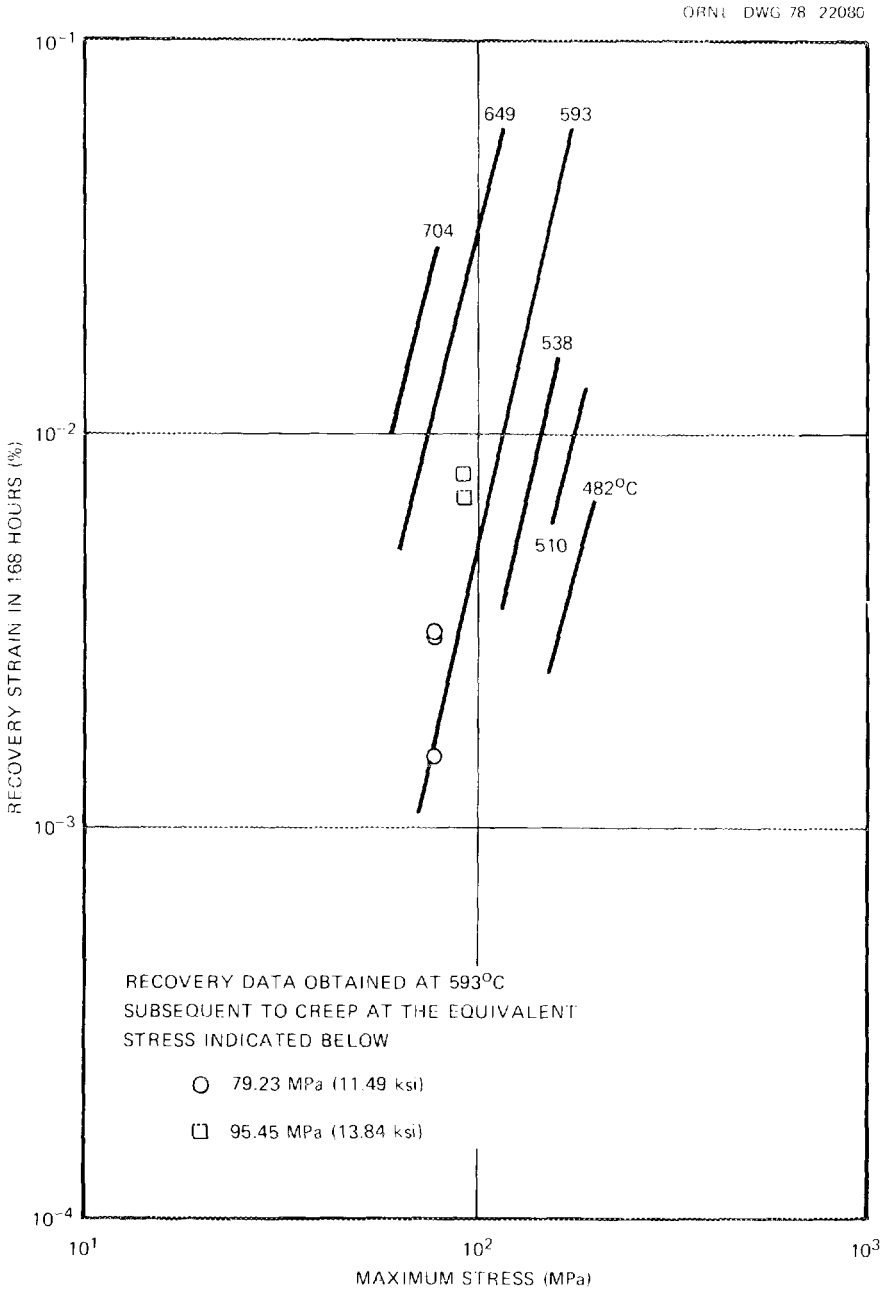

Fig. 1.33. Comparison of tensorial shear strains recovered under low torsional stresses in test C 4009 with earlier data determined under uniaxial loading (Ref. 24). Solid lines represent uniaxial results, and points represent torsional test results.

Table 1.3. Summary of transducer sensitivities determined during the final stages of test C4009

Stage when sensitivity determination was made	Method of determination	Transducer sensitivity (%/V)
Between stages (7) and (8)	Specimen loaded incrementally within the elastic range and corresponding strain increments determined	0.502
Between stages (8) and (9)	Specimen unloaded in single step and corresponding strain determined	0.491
Between stages (9) and (10)	Specimen loaded incrementally within the elastic range and corresponding strain increments determined	0.487
Between stages (10) and (11)	Specimen unloaded in single step and corresponding strain determined	0.491
Conclusion of experiment	Specimen loaded incrementally within the elastic range and corresponding strain increments determined	0.495

on type 316 stainless steel. Prior to these experiments, strain measurement methods had to be developed with sufficient resolution to allow definition of small offset yield surfaces at elevated temperatures. Details are given in the following paragraphs of the instrumentation techniques developed and also of the data generated for the two materials.

1.4.2.1 Specimen instrumentation. The strain gages selected for these experiments were weldable-resistance type manufactured by Ailtech. Since the experiments were to be conducted under isothermal conditions, it was not judged necessary to attempt precise temperature compensation using the dummy elements of these gages. Rather, we planned to use the active elements of suitably oriented gages to form rectangular strain gage rosettes.

Two of the four Ailtech gages that were mounted on 45° helix angles are shown in Fig. 1.34. These four gages were connected in a full bridge circuit and used for torsional strain measurement. The setup for axial-strain measurement consisted of two gages positioned along the specimen axis and two dummy gages positioned at 90° to the specimen axis. These four gages were connected in a half-bridge circuit, with the dymmy gages being used to give some degree of temperature compensation. Prior to attachment, gages were selected from a batch of 25 (all with nominally the same gage factor) so that the bridge circuits could be formed using relatively well-matched gages. This selection was made on the basis of gage resistance measurements made at the test temperature of most interest, 593°C (1100°F).

Also shown in Fig. 1.34 is one of four foil strain gage rosettes which were bonded at diametrically opposed locations on the specimen's midsection. The primary function of these gages was to allow the performance of the Ailtech gages to be evaluated at room temperature and at intermediate temperatures before proceeding to the high temperatures.

A total of seven intrinsic thermocouples were also attached to the specimens. Six of them were positioned as diametrically opposed pairs, one pair being positioned at the specimen's midsection and the other two at locations equidistant above and below the midsection. The seventh thermocouple was used for temperature control and was positioned on the specimen's midsection.

ORNL PHOTO 6889–78A

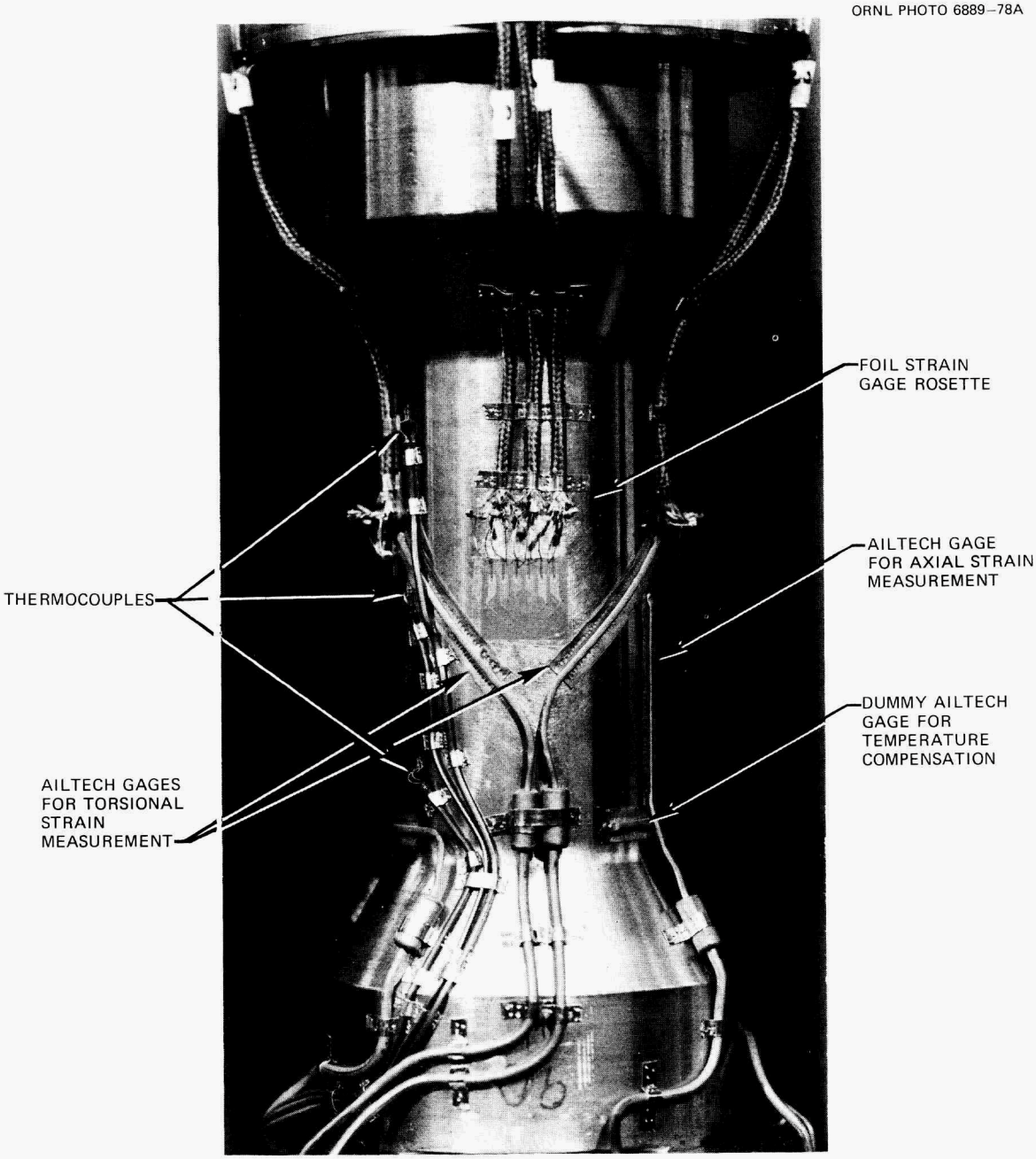

Fig. 1.34. Instrumented specimen for biaxial test 10-5 for room- and elevated-temperature experiments.

1.4.2.2 Strain gage calibration procedures. Because of the non-standard nature of the application, it was decided to avoid use of nominal gage factors during calibration of the Ailtech strain gage circuits. The preferred approach was to force these gages to agree with foil gages

in calibration experiments conducted within the elastic range of the material. Procedures used in this work are described in the following.

As a first step, the foil strain gage circuits were set up using standard shunt calibration procedures so that 10 V was equivalent to 300 $\mu\varepsilon$ on their smallest range and 30,000 $\mu\varepsilon$ on their largest range. A series of preliminary experiments showed that similar resolutions could not be achieved with the Ailtech gages used in conjunction with standard Endevco signal conditioning. This difficulty was resolved by incorporating the amplifiers of a TR-10 analog computer into the Ailtech circuits to simply increase their outputs until the required resolution was obtained. To obtain a precise calibration of the Ailtech gages, the specimens were first subjected to a predetermined axial load within the elastic range of the material and the corresponding output from the foil gages was determined. Adjustments were then made to the Endevco signal conditioner associated with axial-strain measurement until the output from the Ailtech gage circuit was the same as that from the foil gage circuit. The same approach was used in setting up the Ailtech gage circuit for torsional strain measurement. In this case, a predetermined torsional load was used to obtain a reference torsional elastic strain.

Finally, a series of experiments using axial loads only, torsional loads only, and combined tension-torsion loads were conducted to investigate the performance of the Ailtech strain gage rosettes under these three types of loading. Of particular interest was whether or not the torsional strain measurements were affected by axial loading and vice versa. As can be seen in Table 1.4, the Ailtech rosettes performed as well as the foil rosettes in these experiments.

1.4.2.3 Yield surface data for type 304 stainless steel. The first yield surface determined from specimen 10-5 was to establish baseline data using proven experimental techniques at room temperature. Here, foil strain gages provided the strain input for computer control, and the experimental procedures were identical to those described previously in Ref. 25. This initial yield surface is shown in Fig. 1.35 and has the same basic features as those determined earlier for this material.[25] The near-circular form indicates that the von Mises yield criterion provides

Table 1.4. Comparison of data obtained from Ailtech and foil strain gages subjected to uniaxial and biaxial loading during test 10-5

Axial loading only					Torsional loading only					Combined tension-torsion loading					
Axial load (V)[a]	Strain from axial gages (με)		Strain from torsional gages (με)		Torsional load (V)[b]	Strain from axial gages (με)		Strain from torsional gages (με)		Axial load (V)[a]	Torsional load (V)[b]	Strain from axial gages (με)		Strain from torsional gages (με)	
	Ailtech	Foil	Ailtech	Foil		Ailtech	Foil	Ailtech	Foil			Ailtech	Foil	Ailtech	Foil
0	0	0	0	0	0	0	0	0	0	0	0	0	0	0	0
0.25	27	26	1	−1	0.25	−1	1	23	23	0.25	0.25	26	26	25	23
0.50	53	53	1	−1	0.50	−2	1	46	47	0.50	0.50	52	53	48	44
0.75	80	79	2	−2	0.75	−4	1	69	69	0.75	0.75	76	69	70	67
1.00	105	104	2	−3	1.00	−4	1	92	92	1.00	1.00	102	106	93	89
0.75	79	79	1	−2	0.75	−3	1	69	69	0.75	0.75	76	79	70	68
0.50	53	52	1	−2	0.50	−2	1	46	46	0.50	0.50	51	53	47	46
0.25	26	26	0	−1	0.25	0	1	23	23	0.25	0.25	26	27	23	23
0	0	0	0	0	0	0	0	0	0	0	0	0	0	0	0
−0.25	−25	−26	0	1	−0.25	0	−1	−23	−23	−0.25	−0.25	−24	−26	−24	−23
−0.50	−53	−53	−1	2	−0.50	2	−1	−46	−46	−0.50	−0.50	−50	−53	−47	−45
−0.75	−80	−78	−2	2	−0.75	4	−1	−69	−69	−0.75	−0.75	−74	−78	−70	−68
−1.00	−104	−105	−2	3	−1.00	5	−1	−93	−92	−1.00	−1.00	−100	−105	−94	−90
−0.75	−79	−79	−1	2	−0.75	4	−1	−70	−69	−0.75	−0.75	−77	−80	−71	−68
−0.50	−54	−53	−1	1	−0.50	3	−1	−47	−47	−0.50	−0.50	−50	−53	−48	−47
−0.25	−28	−27	0	0	−0.25	2	0	−23	−24	−0.25	−0.25	−25	−27	−24	−24
0	0	0	0	0	0	0	0	0	0	0	0	0	0	0	0

[a] 1.0 V = 11.99 MPa (1.74 ksi).

[b] 1.0 V = 14.31 MPa (2.08 ksi).

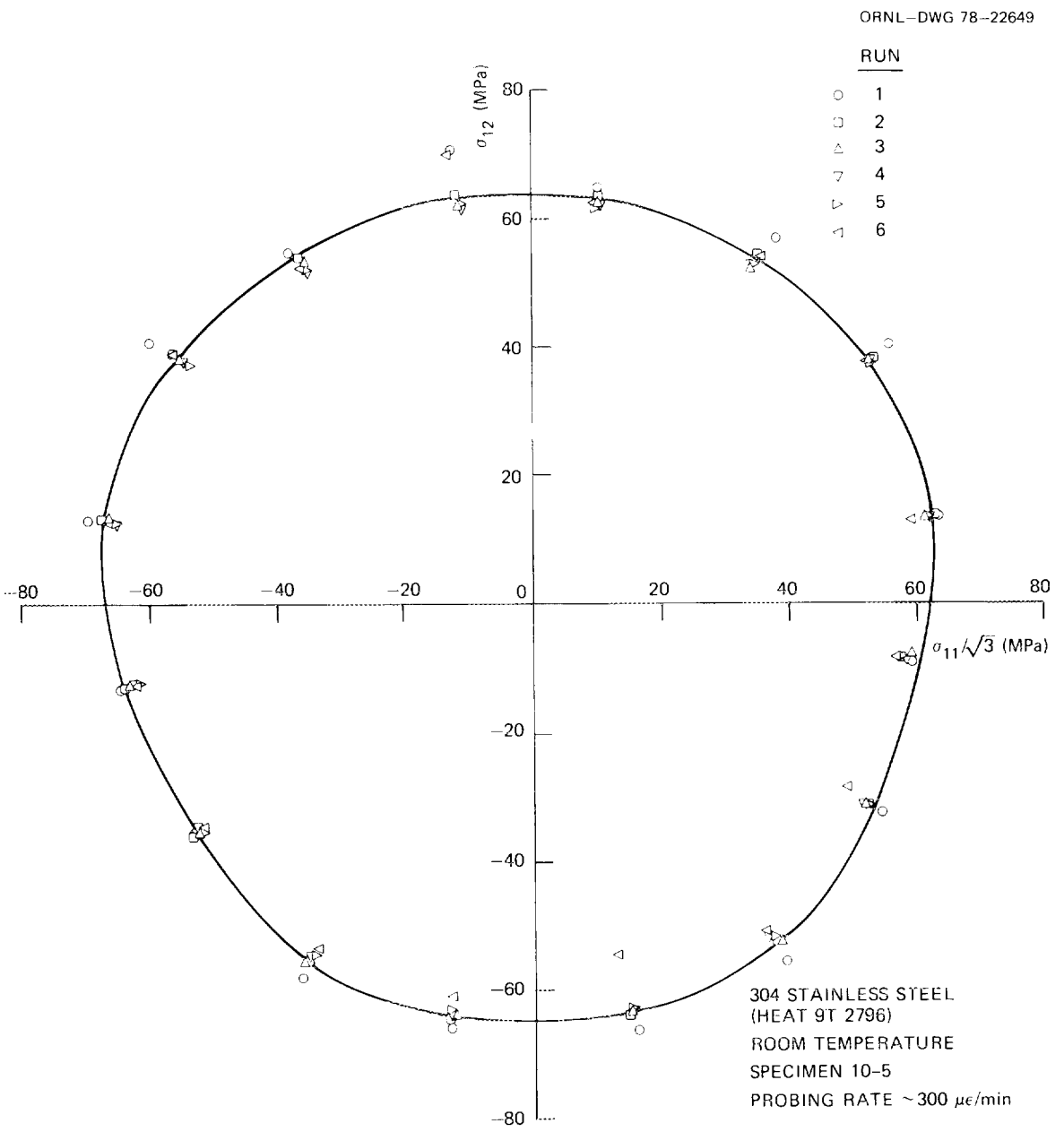

Fig. 1.35. Initial yield surface determined for type 304 stainless steel at room temperature using foil strain gages.

a reasonable approximation of the measurements. The average radius of the measured surface is about 63.4 MPa (9.2 ksi), and this is in reasonable agreement with the earlier[25] values which averaged about 59.3 MPa (8.6 ksi).

In the second step of these experiments, an initial yield surface was determined using Ailtech strain gages for computer control. That yield surface is shown in Fig. 1.36 and is compared to the one generated using foil strain gages in Fig. 1.37. Probes in this second experiment fell short of those in the experiment using foil gages, most noticeably in loading directions involving negative axial loading and negative torsional

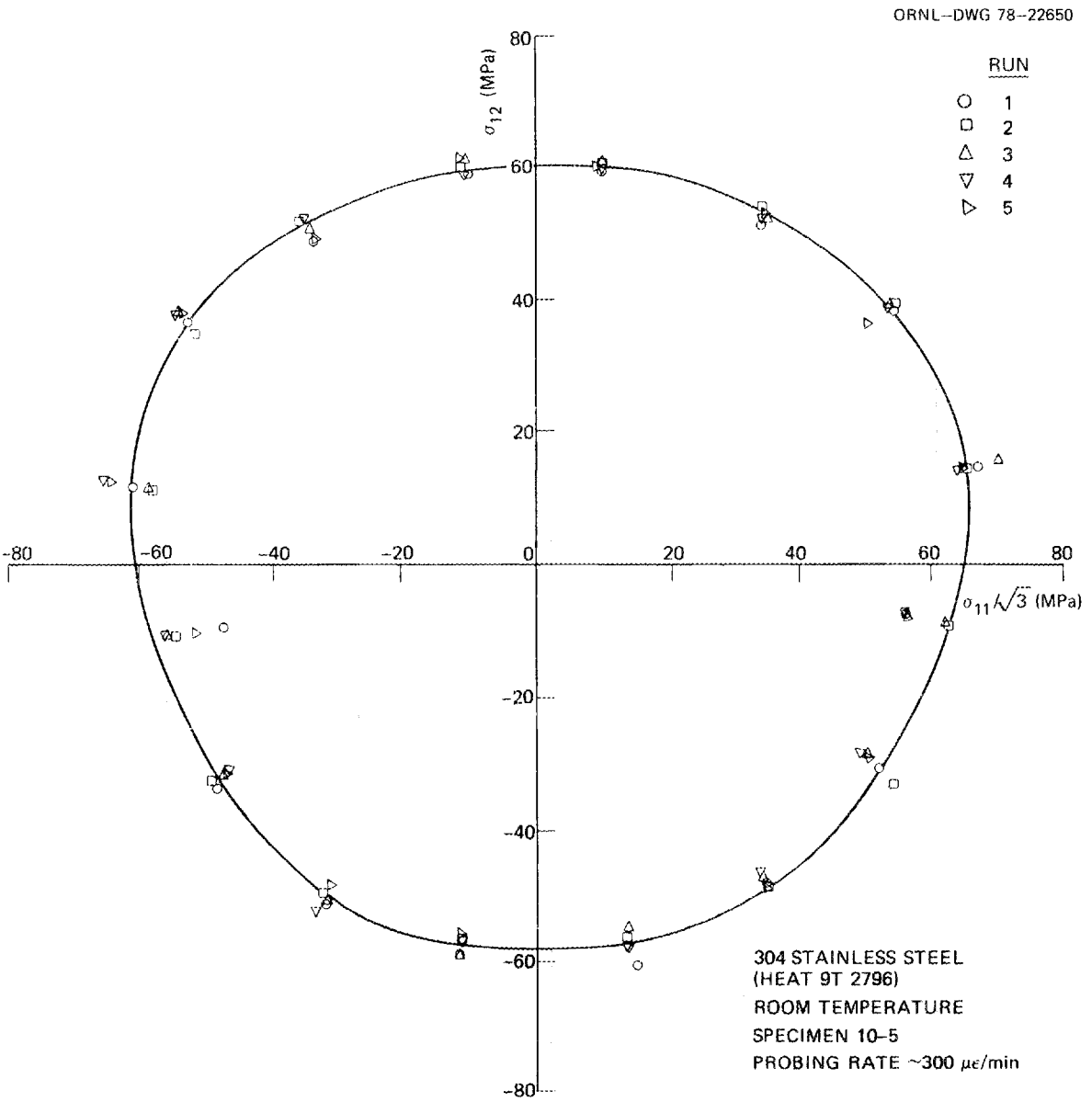

Fig. 1.36. Initial yield surface determined for type 304 stainless steel at room temperature using Ailtech strain gages.

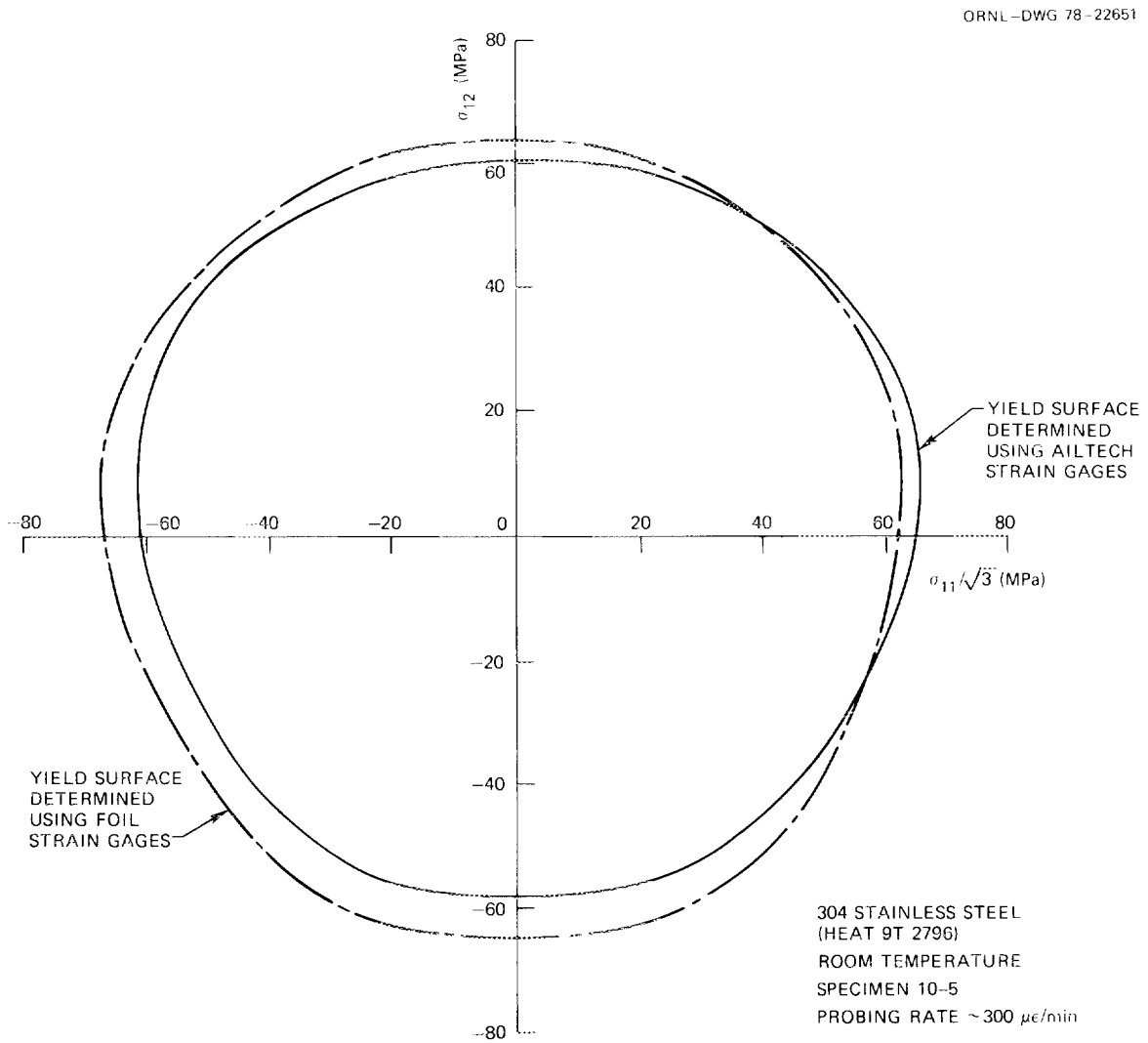

Fig. 1.37. Comparison of initial yield surfaces determined for type 304 stainless steel at room temperature using foil and Ailtech strain gages.

loading. Interestingly, the average radius for the yield surface generated using Ailtech gages [60.7 MPa (8.8 ksi)] is in close agreement with the data in Ref. 25. The relatively good agreement noted above was taken to mean that using Ailtech gages for yield determinations is possible, at least at room temperature. However, because questions still remained regarding their performance at elevated temperatures, we decided to conduct a similar evaluation at an intermediate temperature [232°C (450°F)] before proceeding to the test temperature of most interest, 593°C (1100°F).

Specimen heating was achieved using a single-zone, quartz-element radiant furnace. The six thermocouples described earlier were used to obtain an optimum temperature profile in the specimen's gage length. This involved experimentation with different amounts of thermal insulation on the gage length and also adjustment of the position of the furnace relative to the specimen. With the specimen's midsection at the nominal test temperature, 232°C (450°F), the best temperature profile that could be obtained involved a drop of about 5°C (9°F) at stations 25.4 mm (1 in.) above and below the midsection.

The general approach adopted at 232°C (450°F) was identical to that used in the room temperature experiments. After recalibration of the Ailtech strain gages, an initial yield surface was determined in a series of repeated experiments using the foil strain gages. A second series of yield surface determinations was then made using the Ailtech strain gages. The results of these experiments are shown in Figs. 1.38 and 1.39, and the two yield loci are compared in Fig. 1.40. Again, the von Mises yield criterion provides a reasonable approximation of initial yield behavior, and, again, the Ailtech yield surface falls within that determined using foil gages. The average radii for the two yield surfaces were about 37.2 MPa (5.4 ksi) and 35.2 MPa (5.1 ksi). Both these values are significantly less than the value obtained by interpolating the earlier data of Ref. 26, where the radius of the initial yield surface was determined to be about 44.1 MPa (6.4 ksi) at the temperature under consideration. The conclusion reached as a result of this second series of evaluation experiments was that the Ailtech strain gage setup appeared suitable for yield surface studies at elevated temperatures.

Prior to continuing the experiment at higher temperatures, the foil gages and their associated lead wires were removed from the specimen. On resuming the test and heating to 593°C (1100°F), it was found that two of the four Ailtech gages mounted on 45° helix angles had failed during heatup. Rather than replacing the defective gages, we decided to terminate this test and to instrument a second type 304 stainless steel specimen for a repeat experiment that will emphasize data generation at 593°C (1100°F).

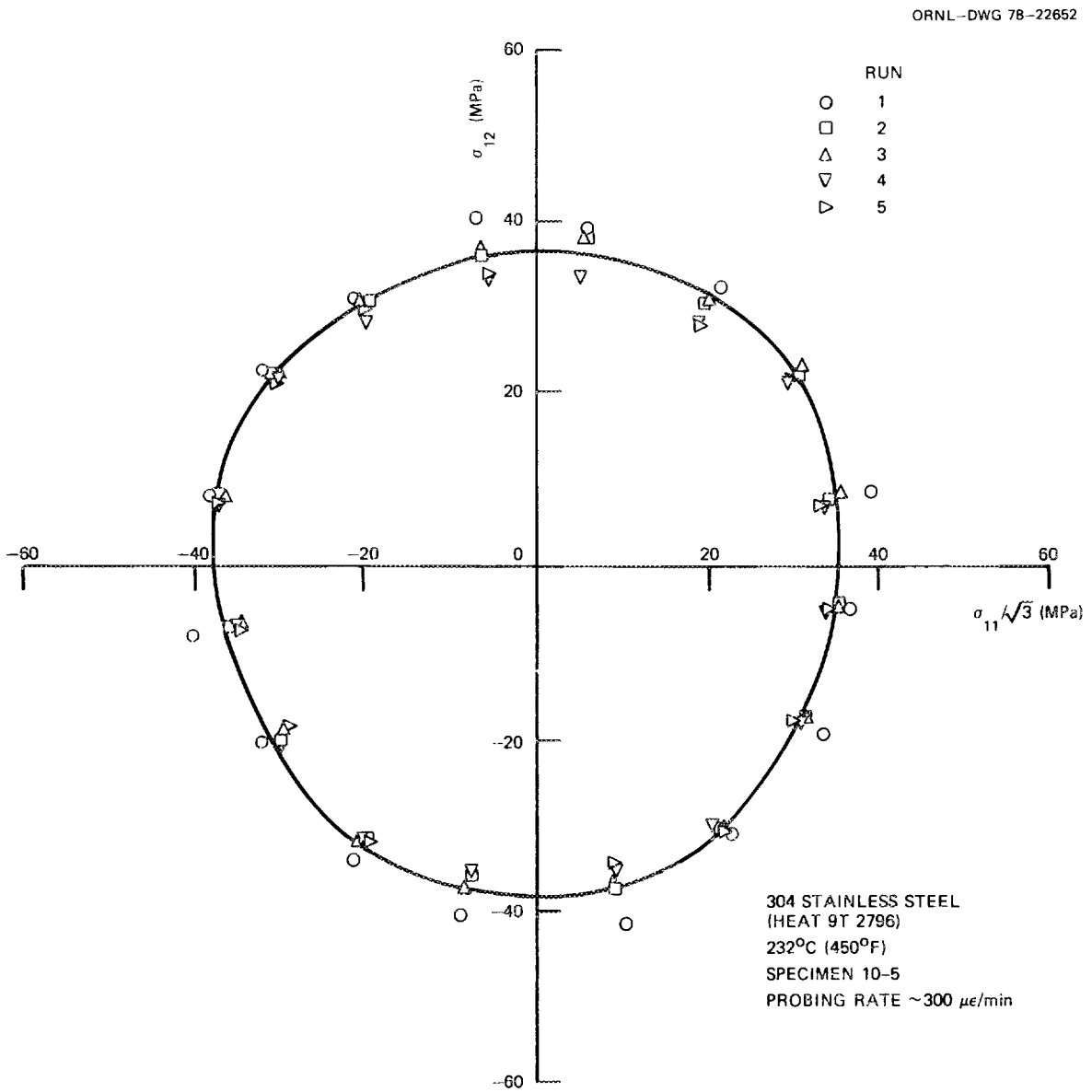

Fig. 1.38. Initial yield surface determined for type 304 stainless steel at 232°C (450°F) using foil strain gages.

1.4.2.4 Yield surface data for type 316 stainless steel. The first experiments conducted on type 316 stainless steel were to provide baseline data for this material at room temperature and also to check the operation of the installed Ailtech strain gages. Initial yield surfaces were determined using foil strain gages (see Fig. 1.41) and Ailtech gages (see Fig. 1.42). Figure 1.43 shows that the two yield surfaces are

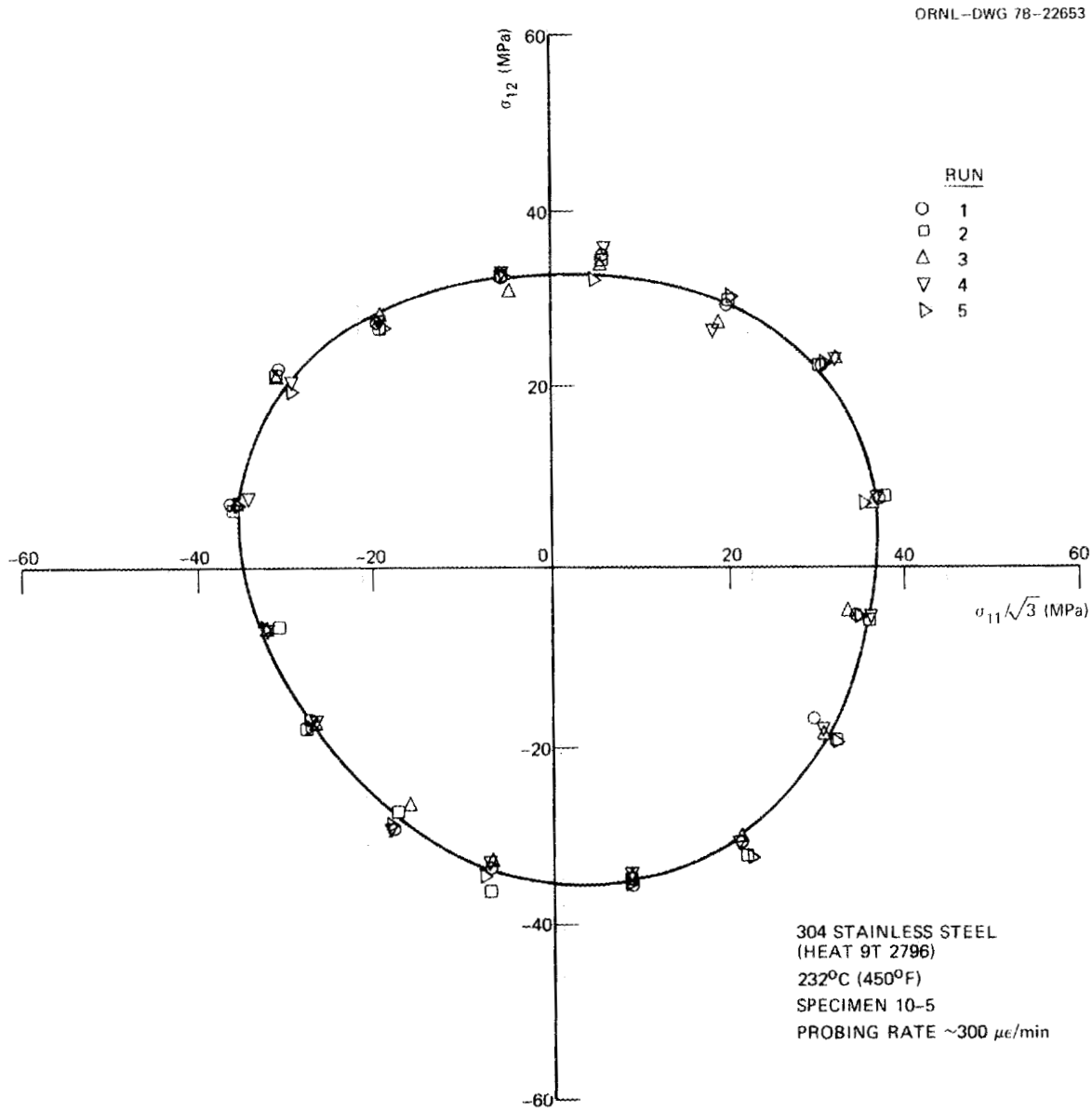

Fig. 1.39. Initial yield surface determined for type 304 stainless steel at 232°C (450°F) using Ailtech strain gages.

approximately circular and have an average radius of about 89.6 MPa (13.0 ksi). This value compared closely with the average radii [86.2 MPa (12.5 ksi)] determined in earlier experiments.[27] The good overall agreement between the two yield surfaces was taken to mean that the Ailtech gages were functioning properly.

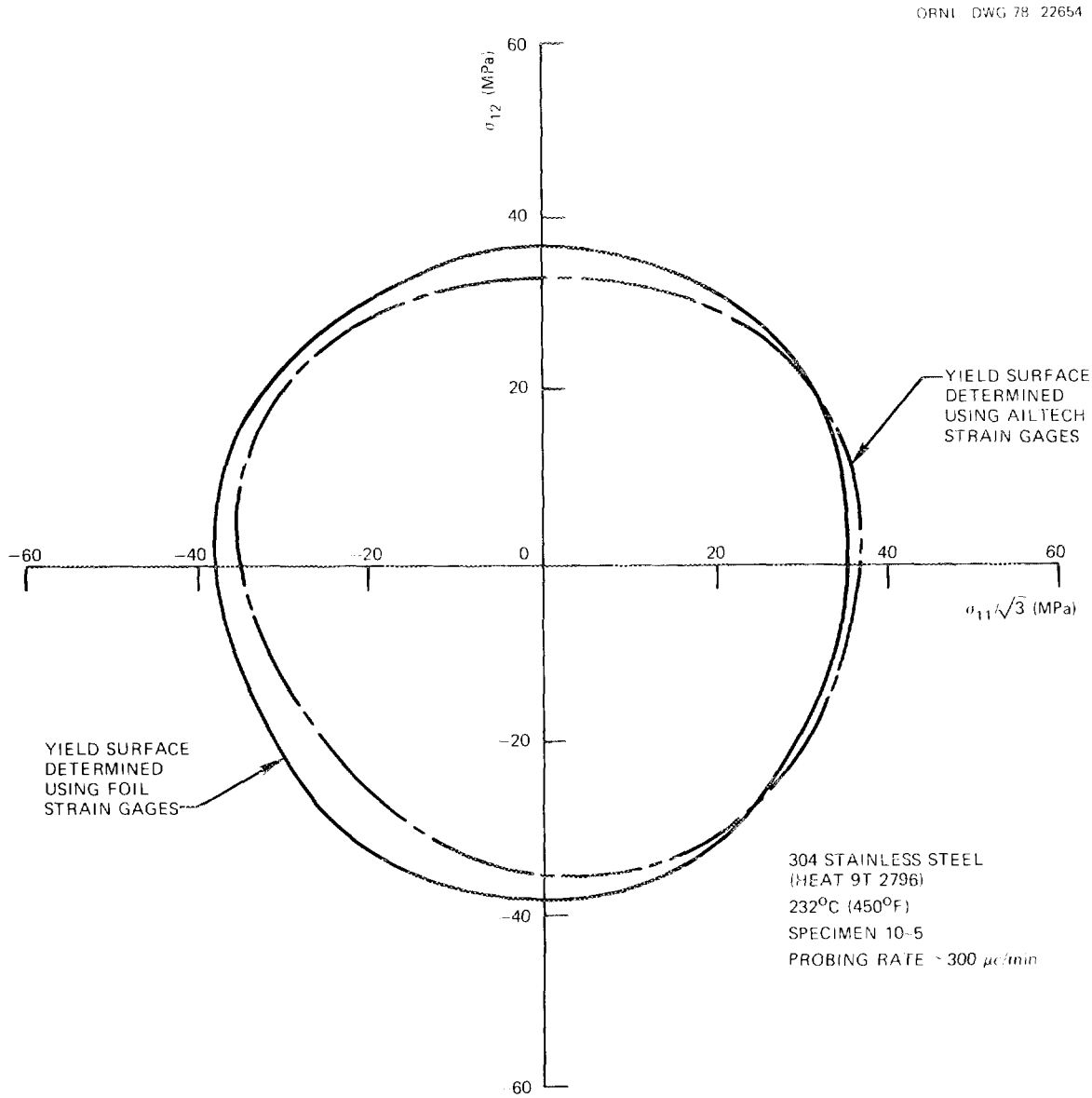

Fig. 1.40. Comparison of initial yield surfaces determined for type 304 stainless steel at 232°C (450°F) using foil and Ailtech strain gages.

The specimen was next heated to 232°C (450°F), and the Ailtech gages were calibrated by loading the specimen to a predetermined value in the elastic range and forcing the Ailtech gages to read the same as the foil gages. The yield surfaces subsequently determined using foil and Ailtech strain gages are shown in Figs. 1.44 and 1.45, respectively, and both yield loci are shown for comparison in Fig. 1.46. The radii of these yield surfaces are 70% of the radius at room temperature. One feature of

ORNL-DWG 78-22655

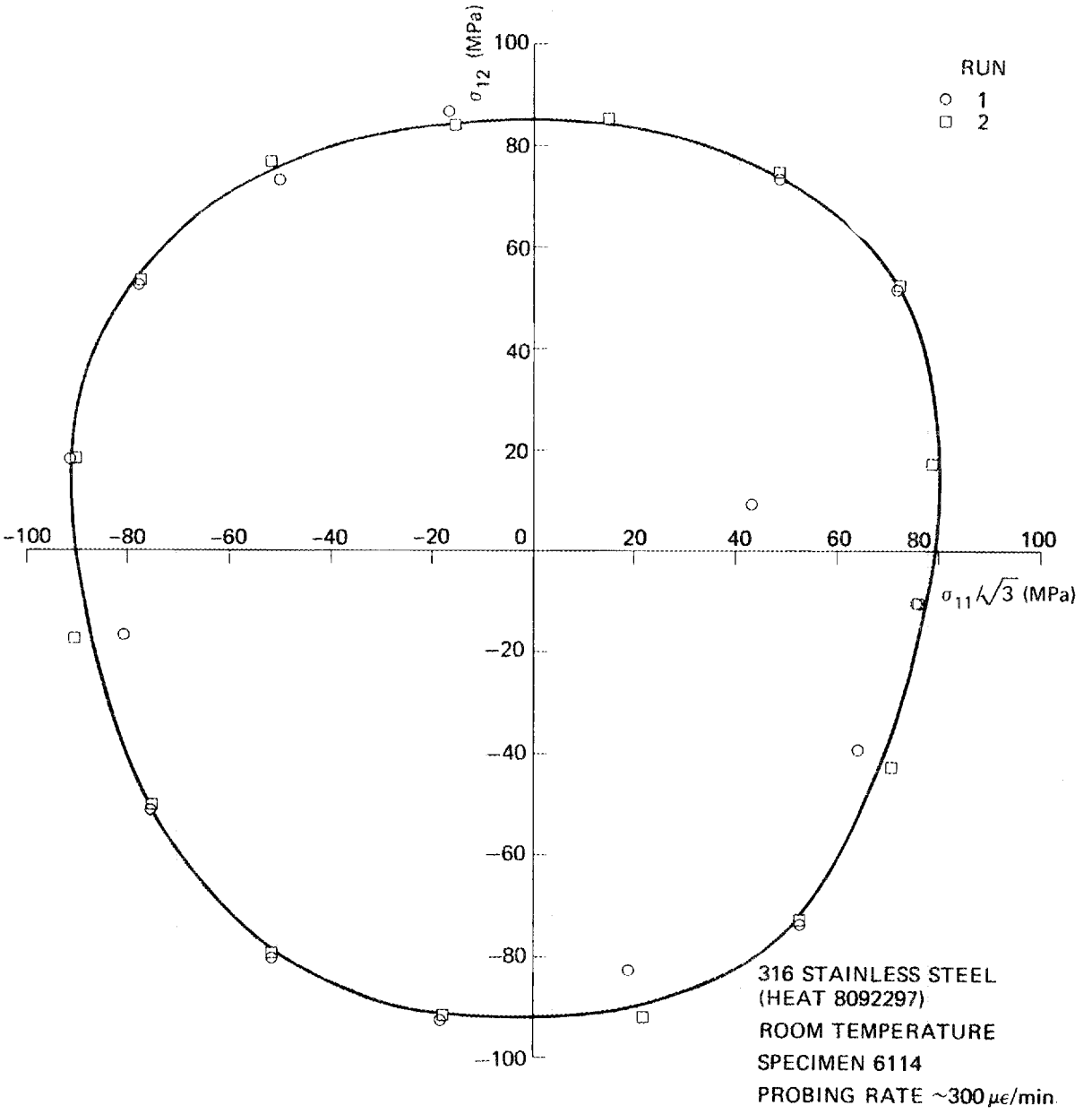

Fig. 1.41. Initial yield surface determined for type 316 stainless steel at room temperature using foil strain gages.

ORNL-DWG 78-22656

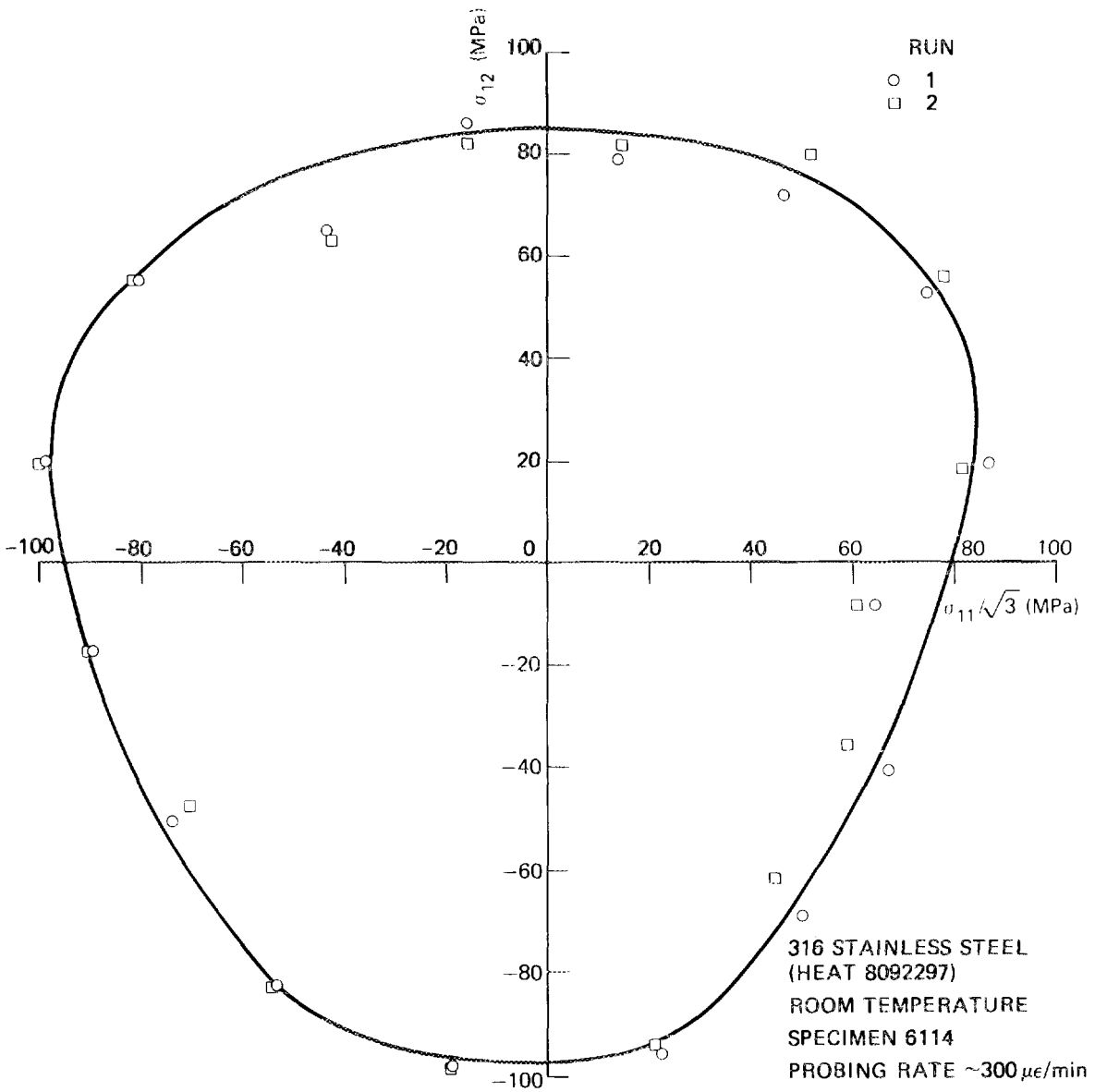

Fig. 1.42. Initial yield surface determined for type 316 stainless steel at room temperature using Ailtech strain gages.

the data shown in Fig. 1.45 is that probes involving small negative torsional loadings fall consistently short of the average curve. Later, this was found to be caused by noise generated by one of the Ailtech gages being used for torsional strain measurement. Another difficulty identified in Fig. 1.45 was that a system control problem caused the specimen

ORNL-DWG 78-22657

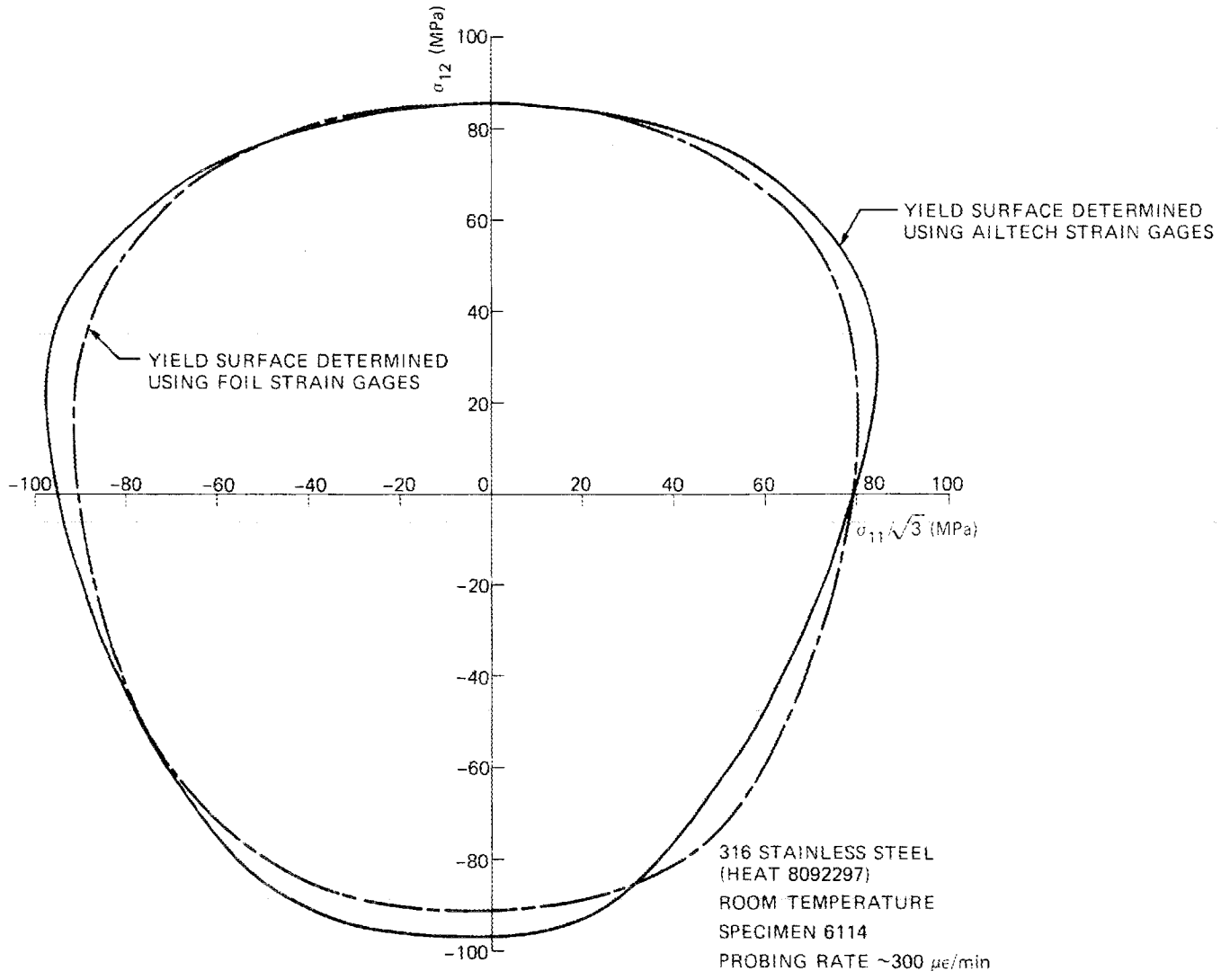

Fig. 1.43. Comparison of initial yield surfaces determined for type 316 stainless at room temperature using foil and Ailtech strain gages.

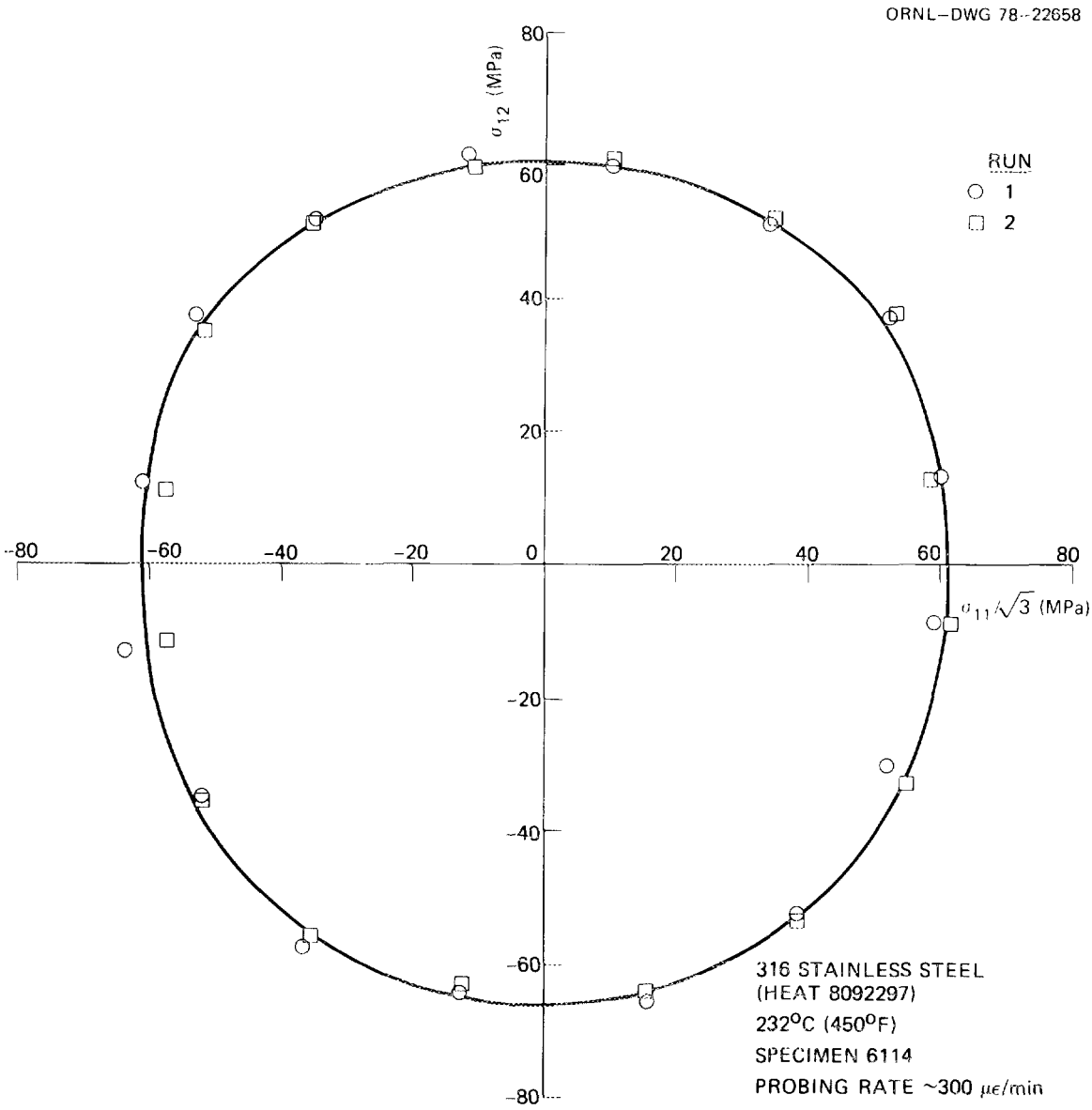

Fig. 1.44. Initial yield surface determined for type 316 stainless steel at 232°C (450°F) using foil strain gages.

to be overloaded during the experiments using Ailtech gages. On unloading the specimen, the residual strain in the axial sense was found to be 0.14% while that in the torsional sense was 0.017%. To eliminate these residual strains, the specimen was subjected to a sequence of loading to return it to a state of zero stress and zero strain. Two further yield surfaces were then determined using foil strain gages to establish the effect of the overload. The data generated are compared in Fig. 1.47

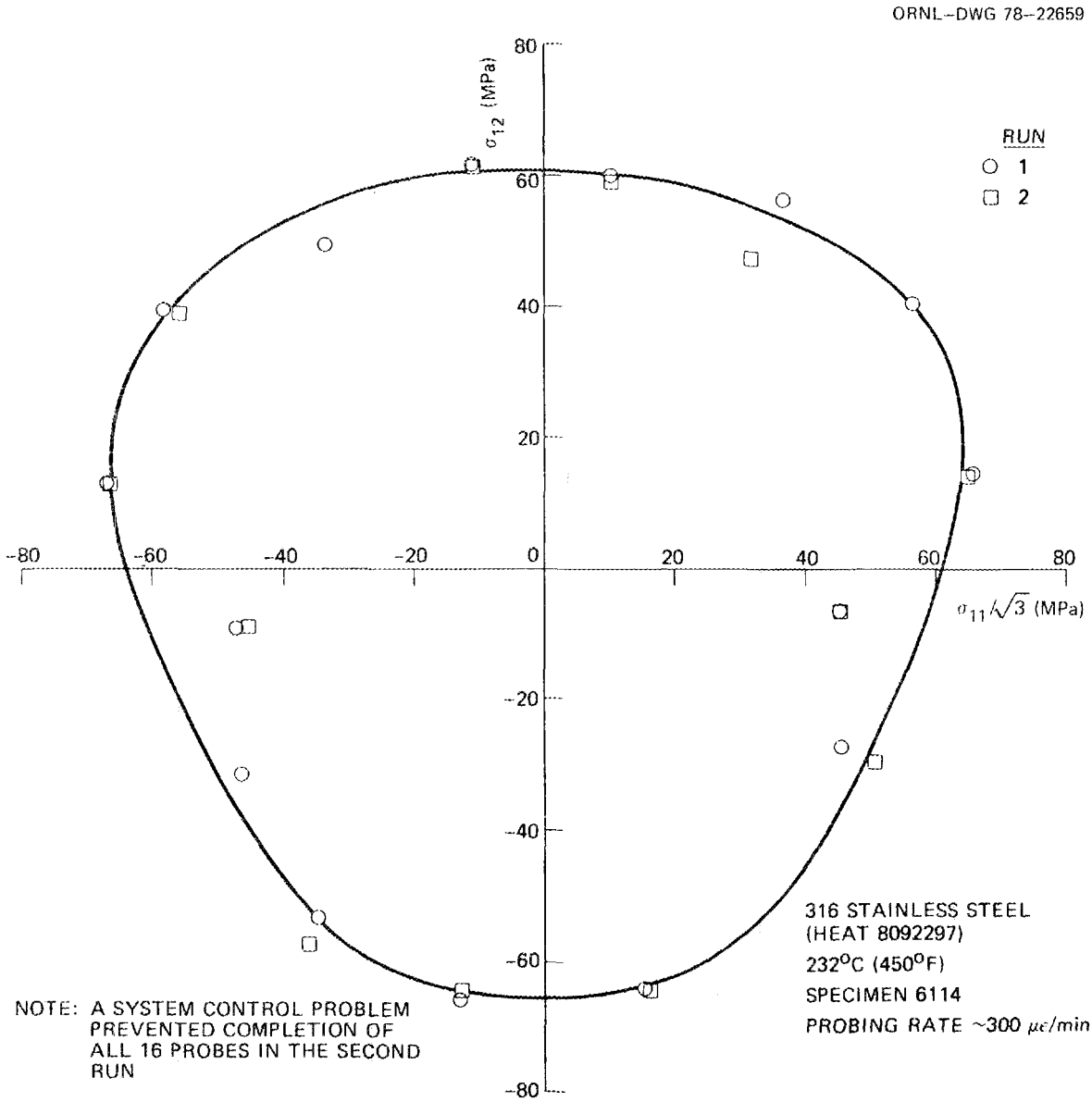

Fig. 1.45. Initial yield surface determined for type 316 stainless steel at 232°C (450°F) using Ailtech strain gages.

with the average yield surface determined using foil gages prior to the overload. As anticipated from the relative magnitudes of the residual strain values, the data fell short of the average curve most markedly in probe directions nearest the abscissa. That the data were approximately symmetrical about the origin of loading indicated that the attempt to return the specimen to a state of zero strain had been successful.

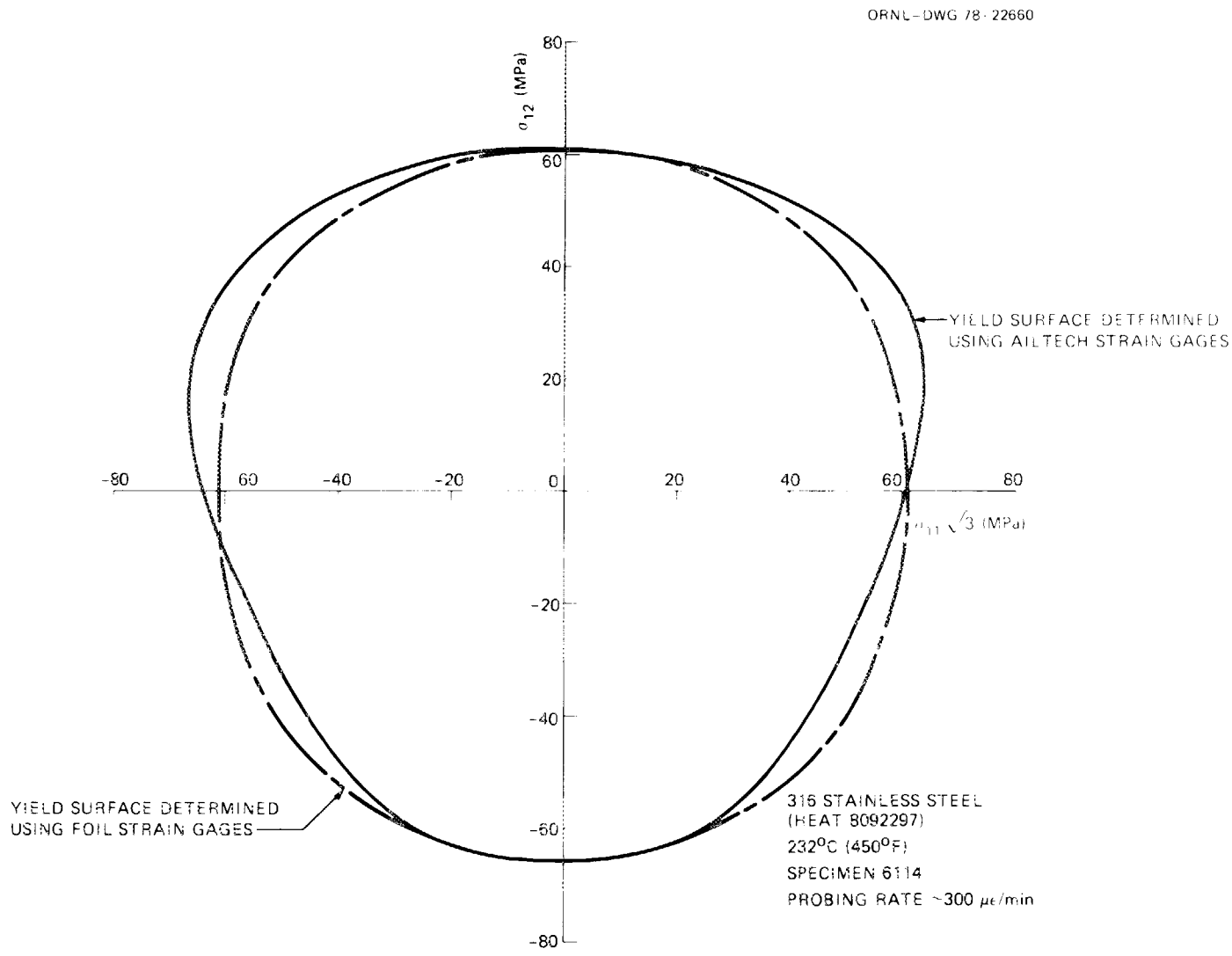

Fig. 1.46. Comparison of initial yield surfaces determined for type 316 stainless steel at 232°C (450°F) using foil and Ailtech strain gages.

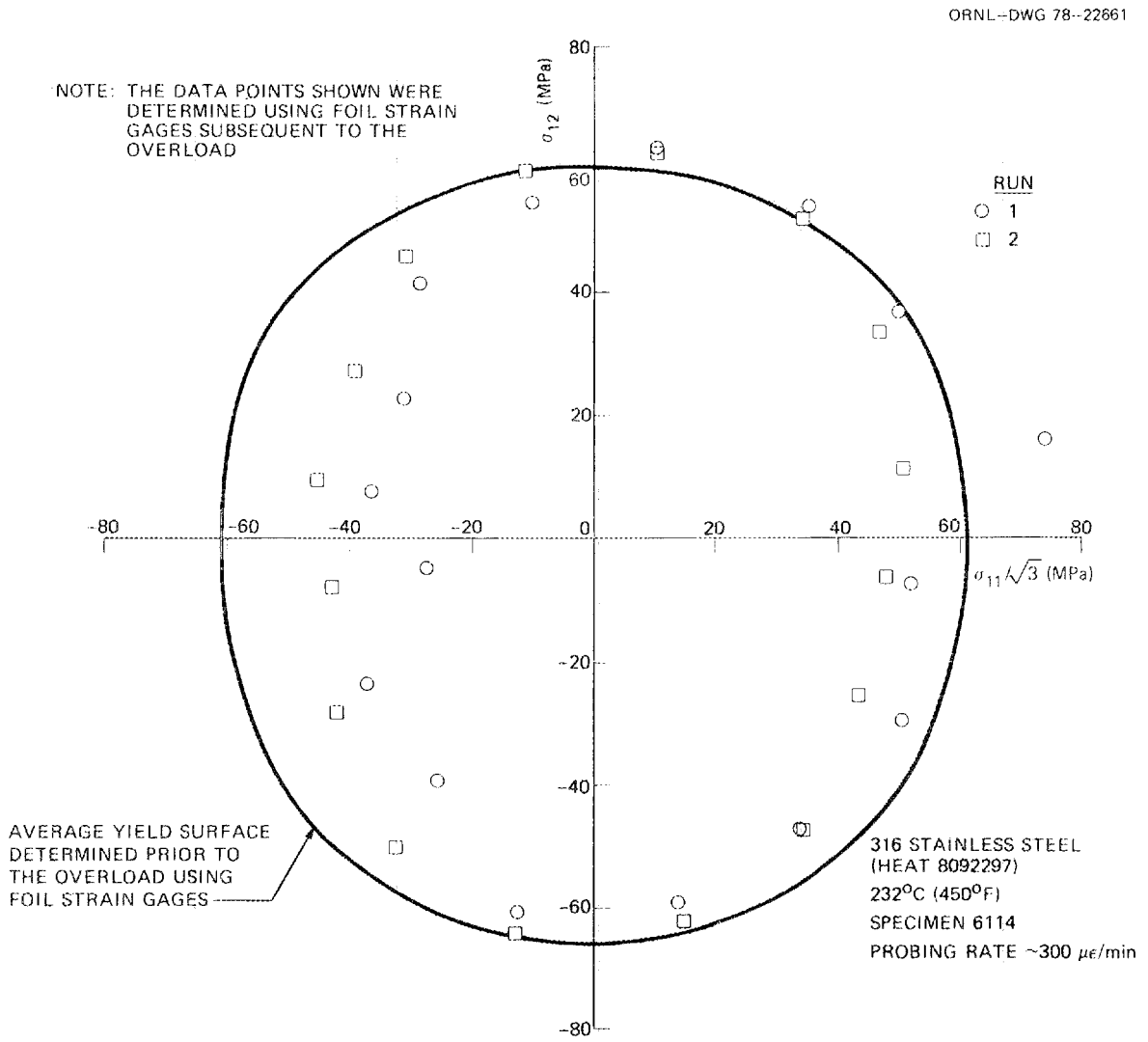

Fig. 1.47. Effect of accidental overload on the initial yield behavior of type 316 stainless steel at 232°C (450°F).

Before continuing the experiment at higher temperatures, the foil strain gages and their lead wires were removed. The specimen was then heated to 454°C (850°F). Prior to determining any further yield surfaces, the Ailtech strain gages had to be recalibrated at this temperature. First, the specimen was loaded to predetermined levels within the elastic range of the material. Handbook values of the elastic modulus and shear modulus were used to calculate the corresponding strain values and, assuming 3000 με was equivalent to 10 V, calculating corresponding voltages

was possible. The final step was to adjust the gain of the Endevco signal conditioning until the required voltages were obtained.

Results of the yield surface determination subsequently undertaken at 454°C (850°F) are shown in Fig. 1.48. The average radius is about 57.1 MPa (8.3 ksi), a factor of 0.6 of the room temperature value. The trend noted earlier for data from probes with small negative components of

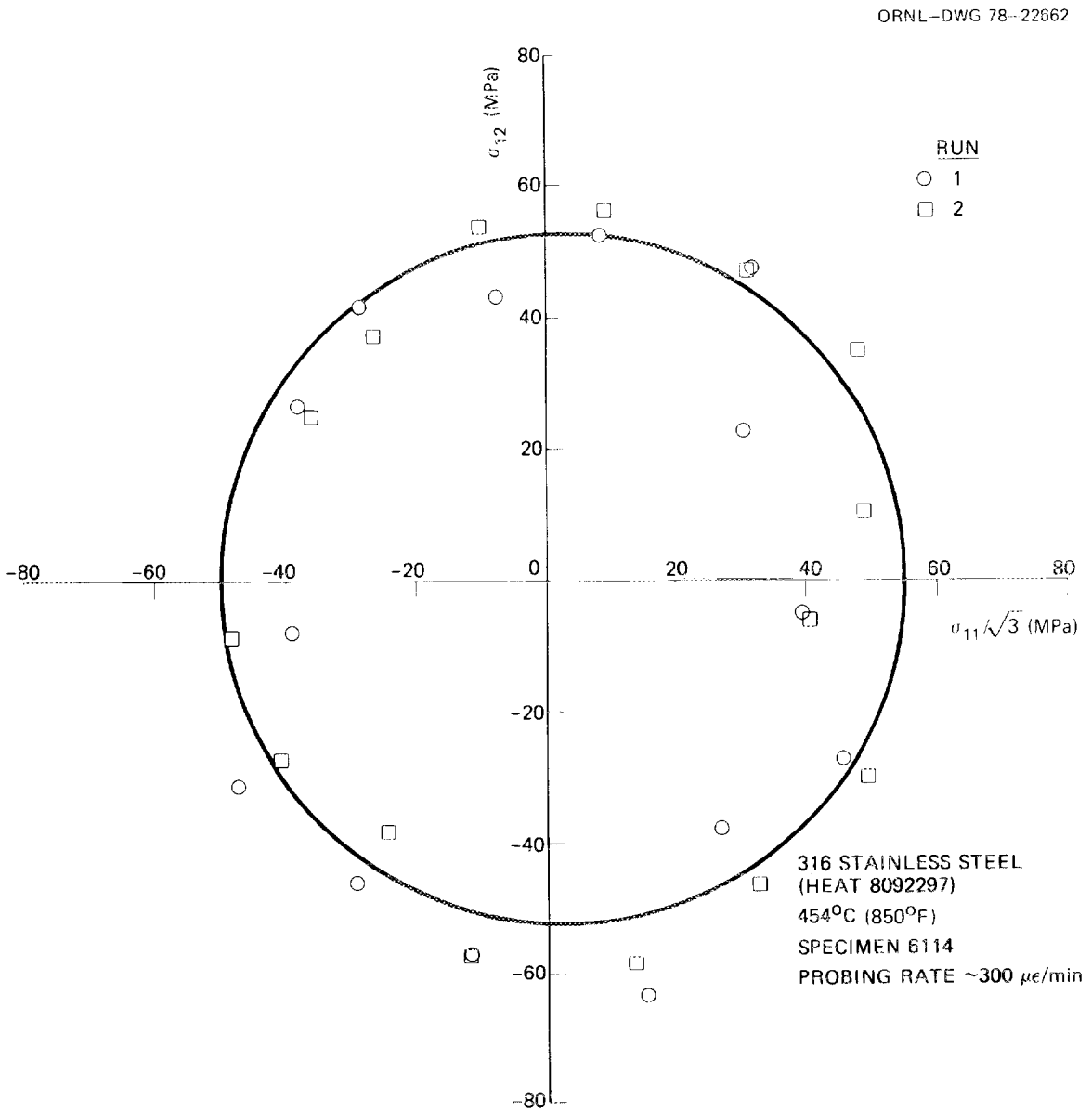

Fig. 1.48. Initial yield surface determined for type 316 stainless steel at 454°C (850°F).

torsional loading to fall short of average behavior can also be observed in Fig. 1.48. Another characteristic of the data is the significant increase in scatter between values obtained in runs 1 and 2. This problem was investigated at some length in the next stage of the experiment, as described below.

On increasing the test temperature to 593°C (1100°F), the noise levels on the torsional strain signals increased to the point that accurate calibration was impossible. The output of each torsional gage was monitored independently, and we established that a single gage was largely responsible for the noise problem. This gage and its opposite number were eliminated from the strain gage setup by reducing the full-bridge circuit to a half-bridge circuit. Although solving the immediate problem, this modification reduces the accuracy of the torsional strain measurements by eliminating compensation for bending. Another check performed at this time concerned drift in the strain measurements. With the specimen in an unloaded condition, both axial and torsional strains were monitored over a 66-hr period. During the last 10 hr of this period, the drift rate in both axial and torsional measurements was determined to be about 1 $\mu\varepsilon$/hr. Drift rates of this order were not viewed as a problem because it was known that complete yield surfaces could be defined in less than 30 min.

Procedures used in calibrating the Ailtech strain gages at 593°C (1100°F) involved loading within the elastic range and using handbook values of Young's modulus and shear modulus, as described previously. The initial yield surface subsequently determined at this temperature is shown in Fig. 1.49. Its average radius was determined to be 48.3 MPa (7.0 ksi), about half the size of the yield surface determined at room temperature. Even with the elimination of the noisy torsional gage, the data suffer considerable scatter.

The final stage of the experiment was aimed at determining the effect of creep deformation on subsequent yield behavior. Because the performance of Ailtech gages had previously been shown to be questionable at strains greater than 1%, relatively low-stress values would be used to keep strains below this level. The specimen was prestressed along the radial loading path ($\sqrt{3}\,\sigma_{12} = \sigma_{11}$) to the point $\sigma_{12} = \sigma_{11}/\sqrt{3} = 41.4$ MPa

ORNL-DWG 78-22663

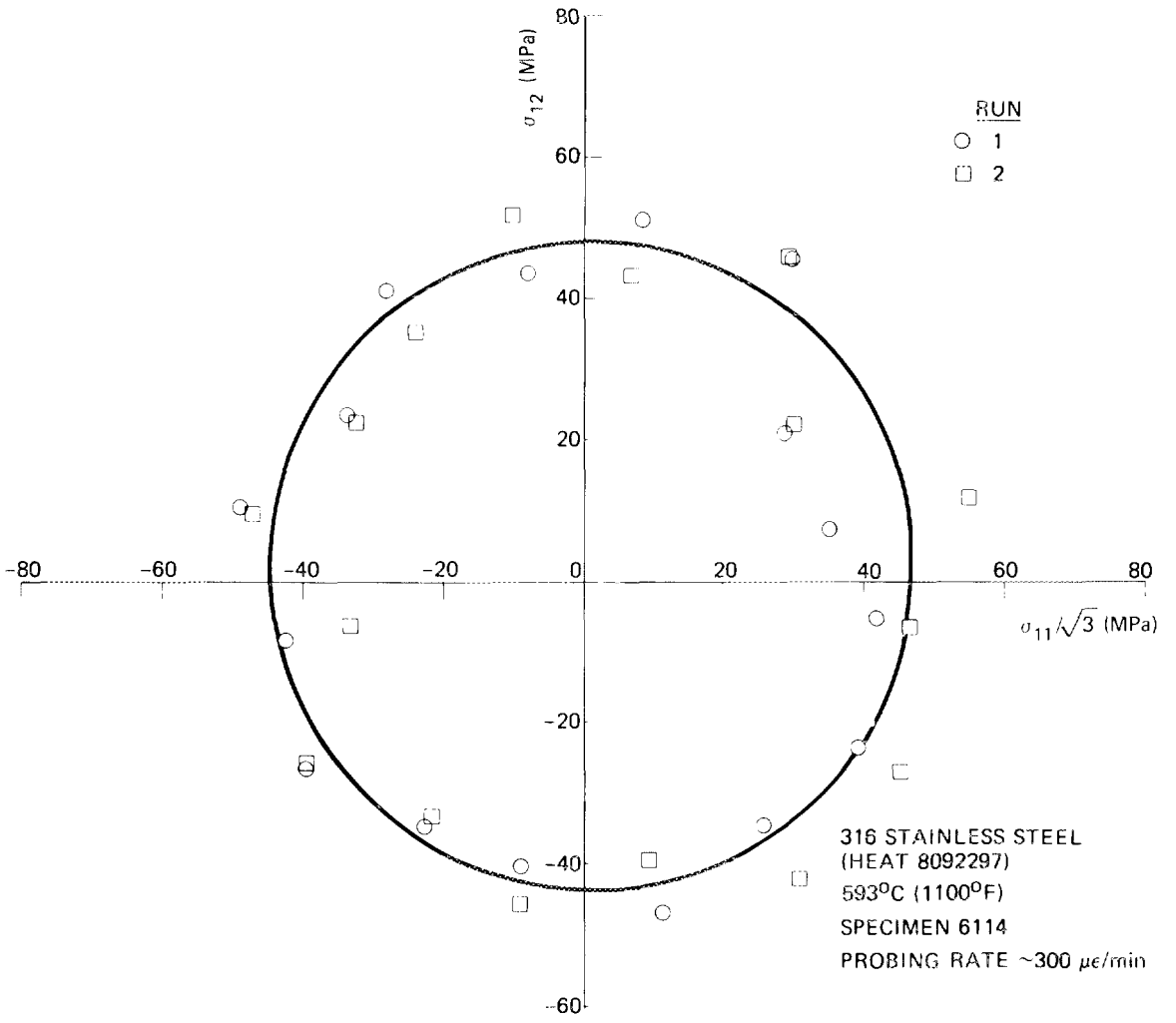

Fig. 1.49. Initial yield surface determined for type 316 stainless steel at 593°C (1100°F).

(6.0 ksi) in tension-torsion stress space and held at this point for 84 min. The specimen was then unloaded to the estimated center of the new yield surface, $\sigma_{12} = \sigma_{11}/\sqrt{3}$ = 13.8 MPa (2.0 ksi), and a yield surface determination made. The results are shown in Fig. 1.50.

During the hold period, little useful multiaxial creep data were obtained because the computer software necessary for rapid data acquisition was not available at the time of the experiment. Thus, the high strain rates during the initial stages of creep were not quantified with any degree of certainty. At the end of the 84-min hold period, the

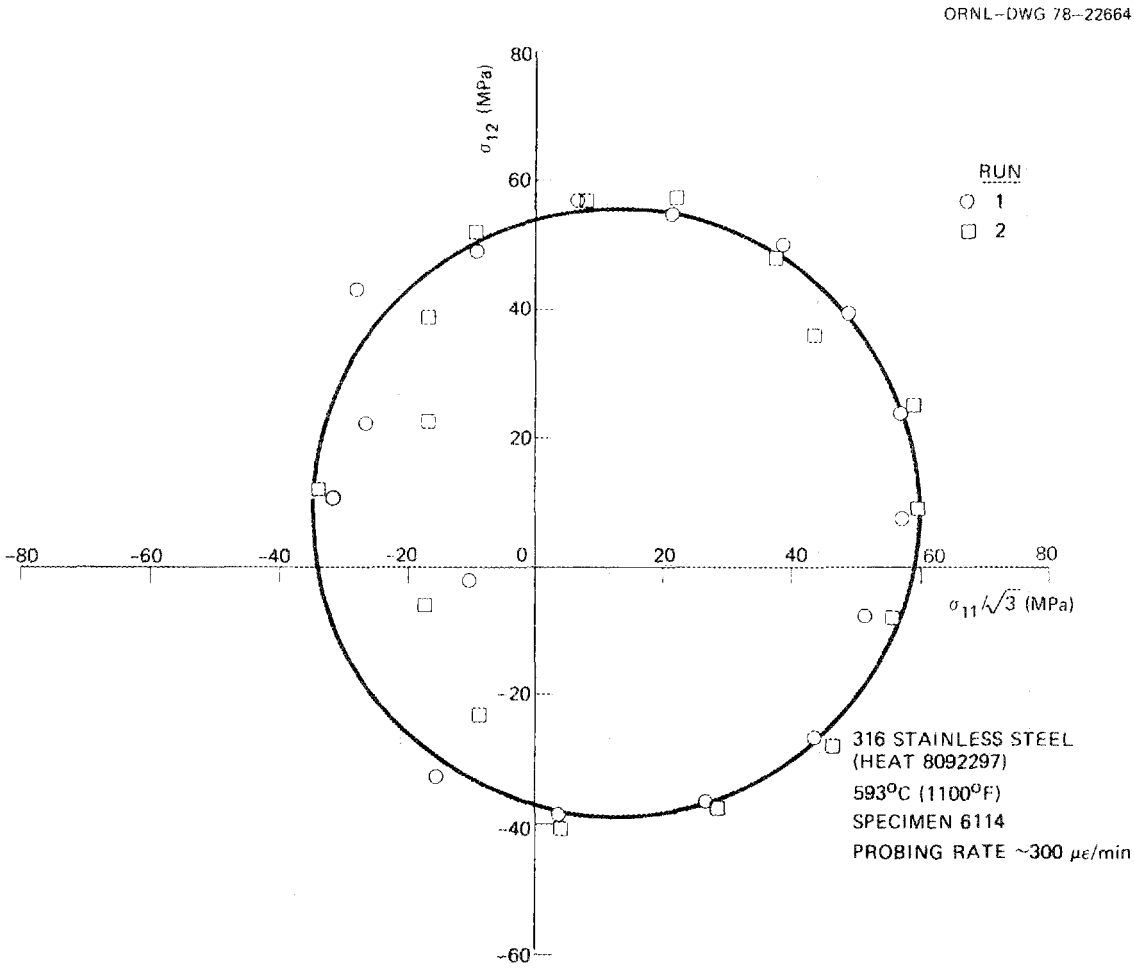

Fig. 1.50. Subsequent yield surface determined for type 316 stainless steel at 593°C (1100°F) after preloading to $\sigma_{12} = \sigma_{11}/\sqrt{3} = 41.4$ MPa (6.0 ksi) and holding for 1.4 hr.

inelastic strain accumulated in both the axial and torsional senses was about 0.02%. Figure 1.50 shows that even these relatively small inelastic strains caused a significant shift of the center of the yield surface away from the origin of loading. The prestress and associated period of creep appeared to have little, if any, effect on the size of the subsequent yield surface, its radius being about 48.3 MPa (7.0 ksi). Whether or not the yield surface was deformed by the prestress is difficult to determine with certainty because of the scatter in the data.

The experiment plan called for increasing the level of prestress in small increments and for definition of subsequent yield surfaces when creep rates had dropped to acceptable values. During attempts to introduce

more significant levels of inelastic strain into the specimen, the two Ailtech gages used for axial-strain measurement failed in quick succession, causing the test to be terminated.

1.4.2.5 Conclusions. The following conclusions were reached regarding the instrumentation techniques used in this experiment.

1. Ailtech strain gages can be used to form strain gage rosettes, which, in turn, can be used to determine small-offset-yield surfaces under tension-torsion loading.
2. Yield surfaces determined using Ailtech strain gages at room and intermediate temperatures show some evidence of distortion, the most likely cause of which is noise.
3. At temperatures above 232°C (450°F), the Ailtech strain gages proved unreliable, with almost half the installed gages failing at various stages of the experiment.

The following conclusions were drawn regarding the yield behavior of types 304 and 316 stainless steel at room, intermediate, and elevated temperatures.

1. The von Mises yield criterion provides a reasonable approximation of initial yield behavior over the temperature range 21 to 593°C (70 to 1100°F).
2. The hardening behavior of type 316 stainless steel subsequent to one radial creep deformation is "kinematic" in nature. This observation is in keeping with the constitutive equation modification discussed in Sect. 1.1 of this report.

1.5 Development of Methods for Measuring Biaxial Strains at Elevated Temperatures

J. R. Ellis

(Last reported in ORNL-5433, pp. 87-92)

During the current report period, a series of preliminary evaluation experiments was conducted on our multiaxial strain extensometer. These experiments were aimed at investigating the instrument's capabilities in measuring torsional and diametral strains and also finalizing the design

of the filter/amplifiers necessary to achieve the required resolution. More recently, the various optical and electronic components of the laser interferometer system (to be used for axial strain measurement) were received from the manufacturer and assembled for evaluation on the multiaxial calibration fixture. Details of this work are given below.

As described in detail in Ref. 28, torsional strain measurements made using the multiaxial extensometer involve the summation of output from two pairs of rotary variable differential transformers (RVDTs). The first experiment was aimed at determining whether or not these outputs could be summed using a simple summing junction without the RVDTs interacting to produce an excessively noisy output signal. The approach adopted in answering this question was to mount a single sensor and its associated RVDTs on the multiaxial calibration fixture and to subject it to simulated strains. The fixture's rotary table was used to investigate angular rotations over a ±200 arc-min range at 20 arc-min intervals. Output from the two RVDTs was measured independently at each setting. These outputs were summed mathematically, with the results shown in Table 1.5. The angular range was investigated again, this time with the combined outputs from the RVDTs being obtained directly from a summing junction; the results are also given in Table 1.5. Comparison of the two sets of summed data and measurement of noise levels made during the experiments show that the method of torsional strain measurement under consideration is practicable, provided noise levels are kept to a minimum using filters.

The second experiment evaluating the torsional-strain measurement system investigated possible cross-coupling effects during simulated tension-torsion loading. An angular range of ±60 arc-min was investigated using the calibration fixture, and readings of the summed output from the RVDTs were taken at 10 arc-min intervals. After establishing baseline data for zero axial displacement, the experiment was repeated to investigate superimposed axial displacements in the range of ±1.27 mm (±0.050 in.) at 0.254-mm (0.010-in.) intervals. Typical results are shown in Table 1.6; in this case, the data are for negative angular rotations and positive axial displacements. Note that the effect of these superimposed axial displacements is negligible. This was taken to mean that

Table 1.5. Preliminary evaluations of the torsional strain measurement system; comparison of mathematical and direct summations of outputs from two RVDTs

Angular rotation (arc-min)	Experiment 1			Experiment 2
	Output from RVDT 1 (V)	Output from RVDT 2 (V)	Mathematical sum of outputs from RVDTs 1 and 2 (V)	Direct sum of outputs from RVDTs 1 and 2 (V)
200	0.986	1.649	2.635	2.636
180	0.904	1.427	2.331	2.331
160	0.826	1.239	2.065	2.066
140	0.753	1.082	1.835	1.837
120	0.654	0.888	1.542	1.543
100	0.552	0.709	1.261	1.263
80	0.441	0.536	0.977	0.977
60	0.328	0.379	0.707	0.709
40	0.223	0.247	0.470	0.472
20	0.127	0.138	0.265	0.266
0	0	0	0	0
−20	−0.134	−0.128	−0.262	−0.263
−40	−0.285	−0.255	−0.540	−0.540
−60	−0.437	−0.369	−0.806	−0.805
−80	−0.583	−0.470	−1.053	−1.052
−100	−0.704	−0.544	−1.248	−1.243
−120	−0.883	−0.646	−1.529	−1.525
−140	−1.068	−0.740	−1.808	−1.803
−160	−1.275	−0.833	−2.108	−2.103
−180	−1.486	−0.917	−2.403	−2.394
−200	−1.687	−0.987	−2.674	−2.666

Table 1.6. Effect of superimposing axial displacements on the summed outputs from RVDTs 1 and 2 during simulated specimen rotations in the range 0 to −60 arc-min

Angular rotation (arc-min)	Summed output voltage from RVDTs 1 and 2 for particular axial displacements											
	0 mm (0 in.)		0.254 mm (0.010 in.)		0.508 mm (0.020 in.)		0.762 mm (0.030 in.)		1.016 mm (0.040 in.)		1.270 mm (0.050 in.)	
	Run 1	Run 2	Run 1	Run 2	Run 1	Run 2	Run 1	Run 2	Run 1	Run 2	Run 1	Run 2
0	0	0	0.003	0.001	0.003	0	−0.001	0.001	0	0	−0.002	−0.001
−10	1.493	1.498	1.498	1.496	1.501	1.496	1.486	1.490	1.499	1.498	1.504	1.493
−20	2.953	2.947	2.952	2.945	2.950	2.951	2.930	2.932	2.948	2.953	2.950	2.953
−30	4.495	4.487	4.502	4.483	4.502	4.494	4.502	4.495	4.505	4.515	4.497	4.499
−40	6.044	6.038	6.032	6.031	6.038	6.043	6.035	6.029	6.055	6.058	6.038	6.033
−50	7.545	7.535	7.543	7.527	7.533	7.535	7.511	7.527	7.538	7.528	7.541	7.522
−60	8.995	8.995	9.011	8.998	8.999	8.992	8.996	8.995	8.993	8.988	8.998	8.996

the instrument successfully decouples torsional strain measurements from axial straining.

Regarding the resolution of the torsional strain measurement system, we decided to aim for the value found adequate in yield surface experiments conducted using foil strain gage rosettes. In these experiments, the full-bridge circuit and associated signal conditioning are set up so that a tensorial shear strain of 3000 $\mu\varepsilon$ is equivalent to 10 V. Assuming a 25.4-mm (1.0-in.) gage length and a specimen outside diameter of 38.76 mm (1.526 in.), the angular rotation corresponding to this shear strain was calculated to be about 30 arc-min. Using "bread-boarded" filter/amplifiers, attempts were made to set up the extensometer so that 30 arc-min was equivalent to 10 V. This proved to be a relatively easy matter, and finalizing design of the filter/amplifiers for torsional strain measurement was possible.

Subjecting the system for diametral-strain measurements to preliminary evaluation experiments was not judged necessary because the same basic approach has been used successfully for the past ten years in high-temperature, low-cycle fatigue experiments. However, it was necessary to examine the question of resolution and to develop the necessary filter/amplifiers. Again, a value was selected based on experience gained in yield surface studies conducted using foil strain gages. Here, the half-bridge circuit and signal conditioning is set up so that an axial strain of 3000 $\mu\varepsilon$ is equivalent to 10 V. Assuming elastic straining and a specimen outside diameter of 38.76 mm (1.526 in.), the change in diameter corresponding to an axial strain of 3000 $\mu\varepsilon$ was calculated to be 0.038 mm (0.015 in.). It was possible to set up the diametral system so that 0.038 mm (0.015 in.) was equivalent to 10 V using the filter/amplifier already developed for torsional strain measurements. Therefore, in the interest of simplicity, we decided to also use this filter/amplifier for diametral strain measurements.

As noted previously, toward the end of the present report period, the optical and electronic components of a laser interferometric system were received from the manufacturer. This system will be used for axial-strain measurement; the components were assembled using the specially designed fixtures shown in Fig. 1.51. The various components were mounted

ORNL PHOTO 6842–79R

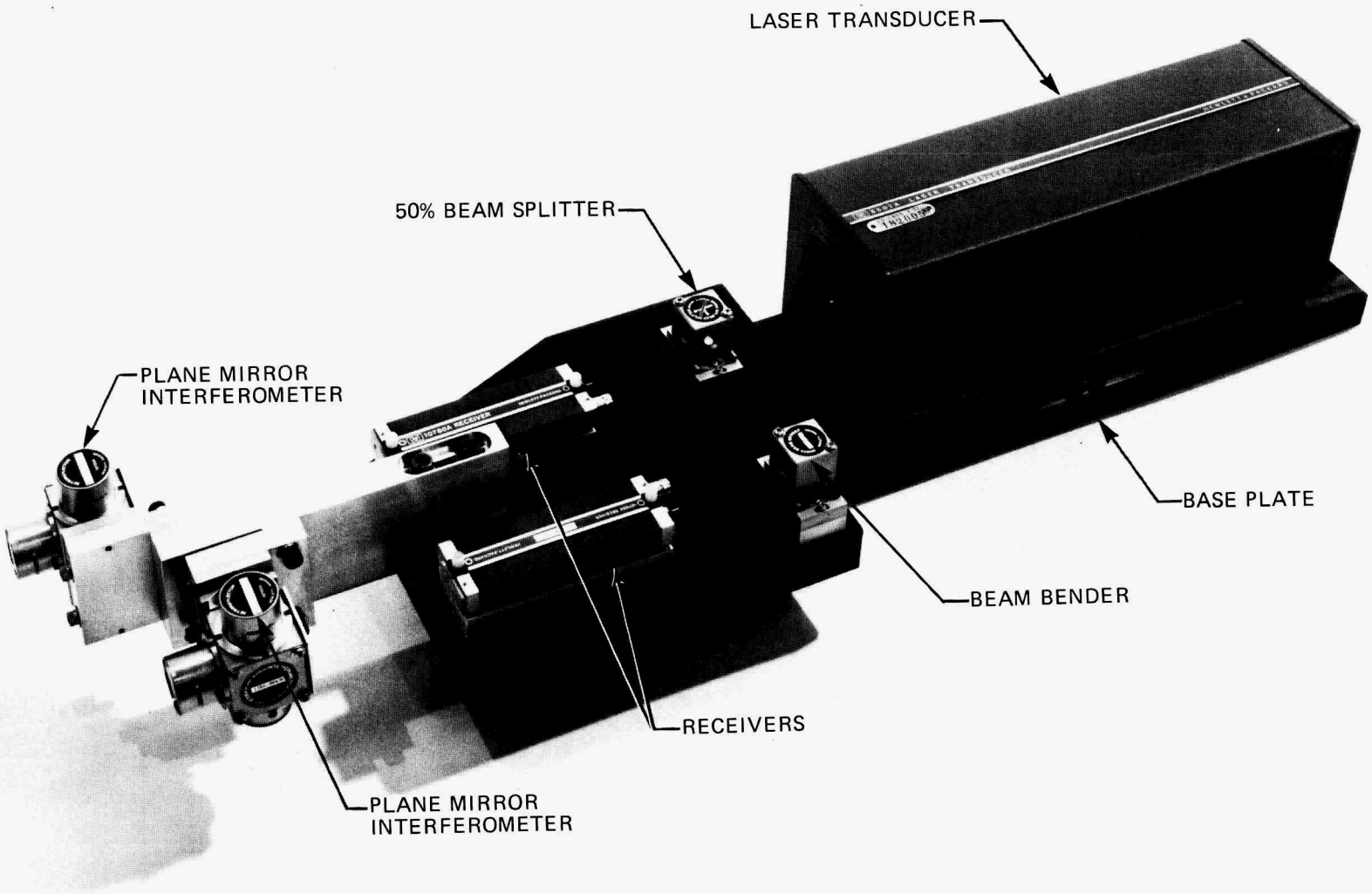

Fig. 1.51. Details of the laser transducer system used for axial strain measurement.

on a single base plate. Using this approach, the system can be treated as a single unit and positioned as required on either the calibration fixture or the electro-hydraulic test system. Another feature of the fixturing shown in Fig. 1.51 is the intermediate blocks, which are positioned between the various components and the base plate. The function of these blocks is to facilitate angular and linear adjustment during initial alignment of the laser system.

Currently, the multiaxial extensometer is being subjected to final evaluation. This work is aimed at further investigating the performance characteristics in such areas as stability, resolution, range, and cross-coupling effects. Provided no serious difficulties arise in this work, the instrument will probably be available for planned deformation and damage studies during the second quarter of FY 1979.

References

1. C. E. Pugh et al., "Assessment of Constitutive Equations in RDT Standard F9-5T for 2 1/4 Cr–1 Mo Steel," *High-Temperature Structural Design Program Prog. Rep. June 30, 1978*, ORNL-5433, pp. 1-42.

2. Energy Research and Development Administration, *Guidelines and Procedures for Design of Nuclear System Components at Elevated Temperatures*, RDT Standard F9-5T (September 1974).

3. Letter, J. M. Corum (ORNL) to RDT Standard F9-4 Task Force, "Updated Inelastic Analysis Guidelines for RDT Standard F9-5T" (April 21, 1977).

4. C. E. Pugh, "Updated Guidelines for Constitutive Equations for RDT Standard F9-5T," *High-Temperature Structural Design Program Prog. Rep. June 30, 1977*, ORNL-5339, pp. 1-5.

5. Letter, J. M. Corum (ORNL) to RDT Standard F9-4 Task Force, "Proposed Modification to RDT Standard F9-5T Inelastic Analysis Guidelines" (Oct. 4, 1978).

6. Letter, R. I. Jetter (Rockwell International/Energy Systems Group) to A. L. Snow (Chairman, RDT Standard F9-4 Task Force), "Addition of Creep Hardening to Hardening Rules in RDT F9-5T," Letter No. 78AT-1537 (Feb. 13, 1978).

7. D. N. Robinson, *A Unified Creep-Plasticity Model for Structural Metals at High Temperatures*, ORNL/TM-5969 (October 1978).

8. D. N. Robinson, "Development of Refined Constitutive Laws," *High-Temperature Structural Design Program Prog. Rep. June 30, 1978*, ORNL-5433, pp. 42-47.

9. C. E. Pugh et al., *Background Information for Interim Methods of Inelastic Analysis for High-Temperature Reactor Components of 2 1/4 Cr–1 Mo Steel*, ORNL/TM-5226 (May 1976).

10. J. M. Corum et al., *Thermal Ratchetting Tests of Type 304 Stainless Steel Pipe: Specimens TTT-1 and TTT-2*, ORNL-5386 (June 1978).

11. R. W. Swindeman, "Exploratory Studies in Support of Structural Design Methods," *Mechanical Properties Test Data for Structural Materials Quarterly Prog. Rep. Oct. 31, 1974*, ORNL-5103, pp. 241-60.

12. H. E. McCoy, Jr., *Interim Report of Tensile and Creep Data for Type 304 Stainless Steel Plate (Reference Heat 9T2796, 2-in. Thick)*, ORNL/TM-4627 (October 1974).

13. V. K. Sikka, *Long-Term Creep Tests after 30,000-h on Reference Heat (9T2796) of Type 304 Stainless Steel – Interim Report*, ORNL/TM-6269 (August 1978).

14. R. W. Swindeman, "Creep Testing," *High-Temperature Structural Design Methods for LMFBR Components Quarterly Prog. Rep. March 1972*, ORNL/TM-3845, pp. 87-97.

15. W. E. Leyda and C. C. Schultz, *Variability in Creep and Rupture Test Results in a Single Heat of Type 304 Stainless Steel*, Babcock & Wilcox Company, ORNL/Sub-3654-3 (September 1975).

16. H. J. Frost and M. F. Ashby, "Deformation-Mechanism Maps for Pure Iron, Two Austenitic Stainless Steels, and a Low Alloy Ferritic Steel," pp. 27-65 in *Fundamental Aspects of Structural Alloy Design*, R. K. Jaffee and B. A. Wilcox, eds., Plenum Press, 1977.

17. R. W. Swindeman, *Contour Maps for Parameters Describing the Temperature-Stress Strain Rate Behavior of Type 304 Stainless Steel (Heat 9T2796)*, ORNL-5473 (February 1979).

18. R. W. Swindeman and C. E. Pugh, *The Influence of Cyclic Loadings on Creep Behavior of Austenitic Stainless Steels*, ORNL-5429 (December 1978).

19. R. W. Swindeman, *Mechanical Behavior of Type 316 Stainless Steel Heat 8092297 25-mm Plate at 593°C*, ORNL-5553 (in preparation).

20. R. W. Swindeman and R. L. Klueh, *Constant-and-Variable Stress Creep Tests on 2 1/4 Cr–1 Mo Steel at 538°C*, ORNL/TM-6590 (March 1979).

21. M. J. Manjoine, *Basic Creep-Rupture Testing at 1100°F (593°C) of Type 304 Stainless Steel for Uniaxially Loaded Specimens with Stress and Strain Gradients*, WARD-HT-3045-26 (June 1977).

22. R. T. King et al., "Characterization Tests of Type 308 CRE Stainless Steel Welds in Type 304 Reference Heat Base Metal," *Mechanical Properties Test Data for Structural Materials Quarterly Prog. Rep. Oct. 31, 1975*, ORNL-5107, pp. 112-26.

23. J. R. Ellis, "Multiaxial Exploratory Testing," *High-Temperature Structural Design Program Prog. Rep. June 30, 1978*, ORNL-5433, pp. 69-87.

24. R. W. Swindeman, "Uniaxial Exploratory Tests," *High-Temperature Structural Design Program Prog. Rep. Dec. 31, 1977*, ORNL-5374, pp. 17-18.

25. J. R. Ellis, "Multiaxial Elastic-Plastic Behavior: Evaluation of the New Computer Control System," *High-Temperature Structural Design Program Prog. Rep. June 30, 1976*, ORNL-5235, pp. 25-49.

26. K. C. Liu and W. L. Greenstreet, "Experimental Studies to Examine Elastic-Plastic Behavior of Metal Alloys Used in Nuclear Structures," pp. 35-56 in *Constitutive Equations in Viscoplasticity: Computational and Engineering Aspects*, ASME Publication AMD, vol. 20 (December 1976).

27. J. R. Ellis, "Multiaxial Tests of Type 316 Stainless Steel," *High-Temperature Structural Design Program Prog. Rep. June 30, 1977*, ORNL-5339, pp. 36-54.

28. J. R. Ellis, "Conceptual Design Study for a High-Temperature Tension-Torsion Extensometer," *High-Temperature Structural Design Program Prog. Rep. Dec. 31, 1976*, ORNL-5281, pp. 88-99.

2. INELASTIC STRUCTURAL TESTS AND ANALYSES

R. C. Gwaltney

The primary objective of this subtask, which is closely related to the subtasks reported in Chapters 1 and 3, is to develop, evaluate, and improve computer-based techniques for solving inelastic design problems and to provide structural test data for evaluating analysis procedures, constitutive equations, failure criteria, and computer codes. Specifically, subordinate objectives are

1. to develop and evaluate structural analysis methods and associated computer codes for conducting inelastic analyses and damage evaluations;
2. to utilize these codes in the evaluation and improvement of constitutive theories and failure criteria; and
3. to provide benchmark problem data for computer code verification and qualification.

The status of the efforts under this subtask for development and evaluation of computer codes; tests of beams and plates, cylindrical shells with flat heads, and nozzle-to-spherical shells; participation in an international piping benchmark problem effort; and high-temperature strain gage development and verification is described in the following sections.

2.1 Development and Evaluation of Computer Codes and Analysis Methods

2.1.1 Development of the HEX module of PLANS (PLANS/HEX)

(J. A. Clinard, A. Levy, Grumman Aerospace Corporation)
(Last reported in ORNL-5433, pp. 97-102)

Oak Ridge National Laboratory has been adapting the PLANS/HEX computer program to inelastic analyses through subcontract to Grumman Aerospace Corporation, Bethpage, New York, to expand our analysis capabilities to include three-dimensional elastic-plastic-creep problems. Assemblage of these capabilities is a necessary complement of our testing efforts for complex structural geometries such as the high-temperature nozzle-to-sphere test, NS-2. The software will be used to aid in planning tests and to provide problem solutions necessary for assessment/validation of

analysis methods. We selected the PLANS/HEX program for our purposes because of its advanced state of development, its compatibility with our IBM computer system, and its public domain status (the code will be transferred to the National Energy Software Center for public dissemination).

During this report period, Grumman development work was completed and documented in a final report (drafted but not yet published). A revised user's manual was also drafted and will soon be transferred to ORNL, along with an updated source-tape of PLANS/HEX. Also, demonstration problems were solved at Grumman which validated the program for creep calculations.

We plan to subcontract with Grumman to use PLANS/HEX to analyze the deformation phase of test NS-2 (see Sect. 2.4 for further information concerning this test) as follow-on work. This work will be completed by November 1979.

2.1.2 CREEP-PLAST II, dissemination (J. A. Clinard)
(Last reported in ORNL-5433, p. 105)

Late in the last report period, the user's manual for the CREEP-PLAST II computer program, a special-purpose finite-element code for analysis of two-dimensional elastic-plastic-creep structures, was published.[1] Following this publication, the program was transferred during this period to the National Energy Software Center (NESC, formerly known as Argonne Code Center) for public dissemination. At NESC, the code met preliminary check-outs; it is now scheduled for release in early CY 1979. The code has been assigned the official NESC number, R810.

Any requests for CREEP-PLAST II should be addressed to National Energy Software Center, Argonne National Laboratory, 9700 South Cass Avenue, Argonne, IL 60439.

2.2 Beam and Plate Tests

J. A. Clinard R. L. Battiste
M. Richardson

Analysis and tests of beam and plate specimens are used in our activities to confirm the validity of inelastic analysis methods (embracing

constitutive equations, numerical techniques, and computer codes) for each material. The set of simple structural tests for type 316 stainless steel is composed of slotted beam B15 (SB-3), circular plates CP7 and CP9 (see Sect. 2.2.5), and solid beam B16. On completion of the test group and the required associated structural analyses, assessments will be assembled into a final report dealing with methods for both types 304 and 316 stainless steel. Progress toward this final goal and preliminary assessments are presented on a continuing basis in these semiannual reports.

Paralleling activities for the austenitic stainless steels, we have conducted several simple structural tests for 2 1/4 Cr–1 Mo steel. The set is presently composed of slotted beams B12a (SB-1) and B12b (SB-2), circular plate CP8 (see Sect. 2.2.4), and solid beams B13, B14, and B17. During this report period, we conducted beam test B17, which is discussed below in Sect. 2.2.2.

2.2.1 Type 316 stainless steel beam B16 (Last reported in ORNL-5433, pp. 108-117)

Test B16 was completed in June 1978, and the bulk of progress reporting appeared in our last progress report. During the present period, data reduction and preliminary graphical display of test results were completed. These results will be included in forthcoming topical reports. The intent of these efforts is to completely and concisely document the test for use in benchmark analyses.

Efforts to complete elastic-plastic-creep analyses of this test are to be carried out in upcoming report periods, and further quantitative experimental-analytical assessments await completion of these analysis activities. However, some of the test results are discussed below. Figure 2.1 gives the test histogram for B16 and shows that the load-controlled conditions involved a series of 12 one-week hold periods after short-term load excursions. The creep response of the beam is expressed in terms of center deflection vs time in Fig. 2.2 and in terms of strains from the west Boeing-HITEC strain gage [located at the bottom surface of the beam at 50.8 mm (2 in.) west of its center] vs time in Fig. 2.3. Further creep-response information is given in Table 2.1, which gives

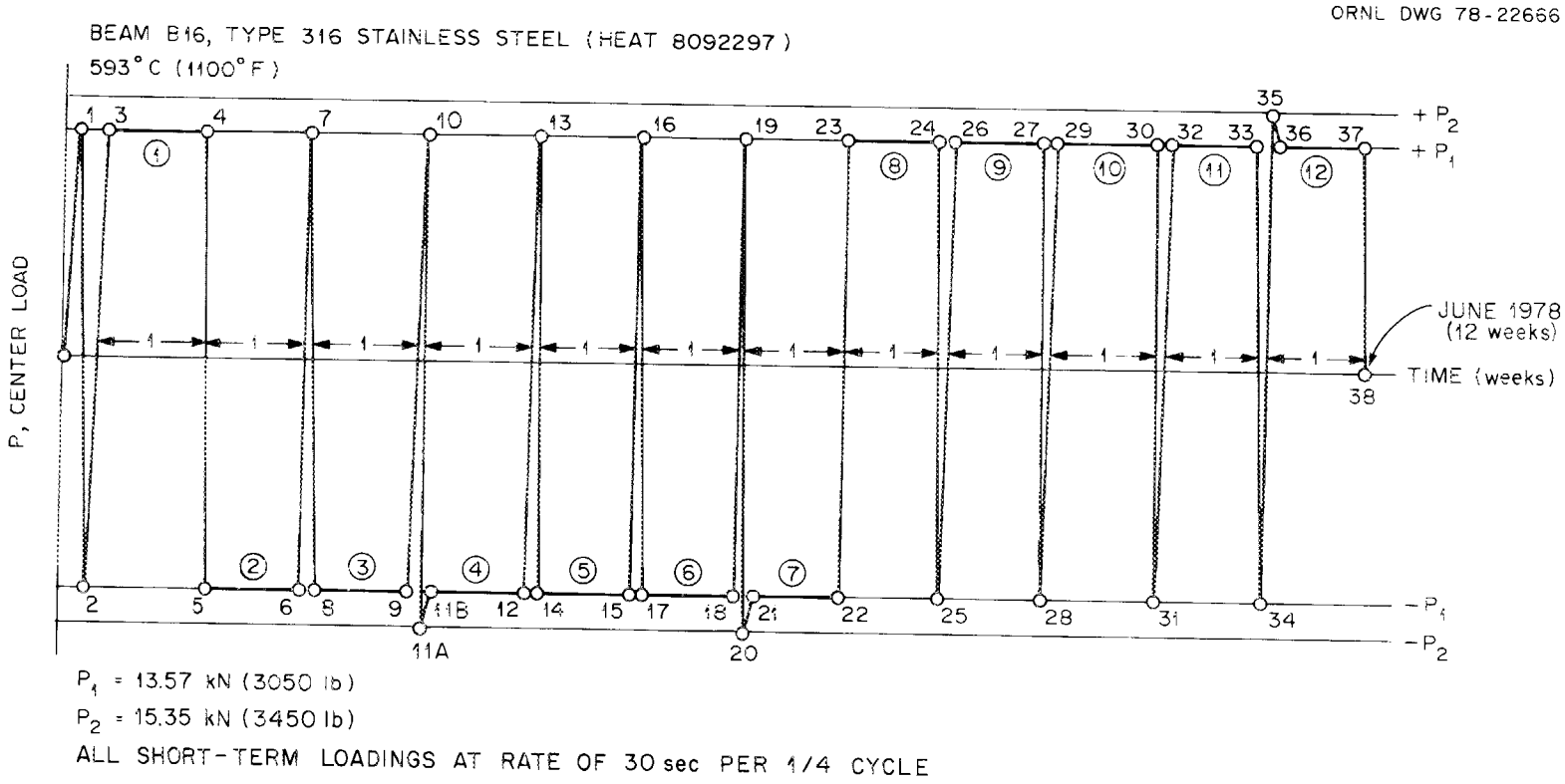

Fig. 2.1. Test histogram for beam B16, type 316 stainless steel solid beam tested at 593°C (1100°F). Numbered points (38) identify discrete testing sequences referred to in subsequent figures. Circled numbers are reference numbers for the 12 hold periods and are also referred to in later figures.

ORNL-DWG 78-22667

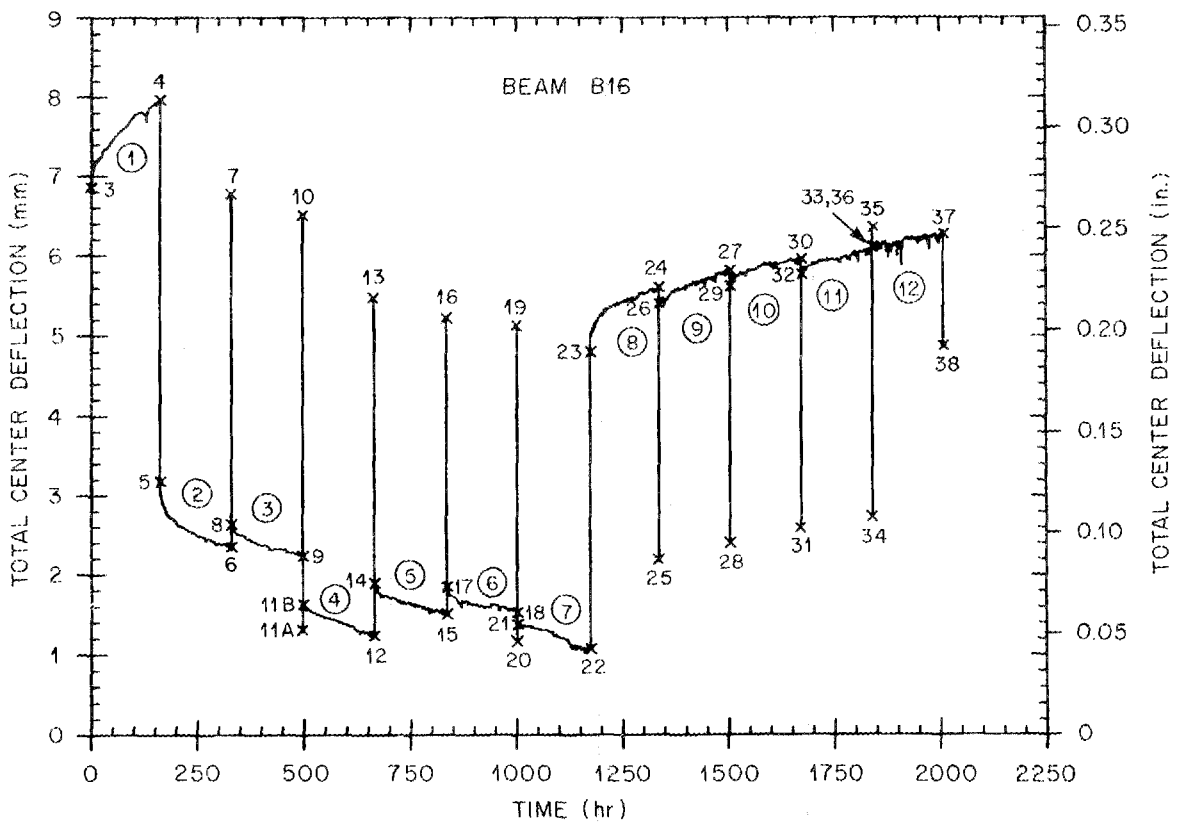

Fig. 2.2. Total center deflection vs time as measured by DCDT at the center of beam B16. Numbered points refer to Fig. 2.1.

normalized magnitudes of the creep-deflection and creep-strain responses during each of the 12 hold periods. A consistency appears between the deflection response and the strain response.

A few additional points may be noted from Table 2.1. First, periods 1, 2, and 8 produced the most creep. Qualitatively, this is consistent with characteristics of the analysis methods now in RDT Standard F9-5T because those rules predict these periods to be initiated at the virgin state of zero creep hardening. Periods 3 through 7 and 9 through 12 were each preceded by a short-time load reversal that included significant reversed plastic strains but little reversed creep strains.

The revival of transient creep (though it is unmistakably present) was little and short-lived in these periods. The RDT F9-5T analysis

ORNL-DWG 78-22668

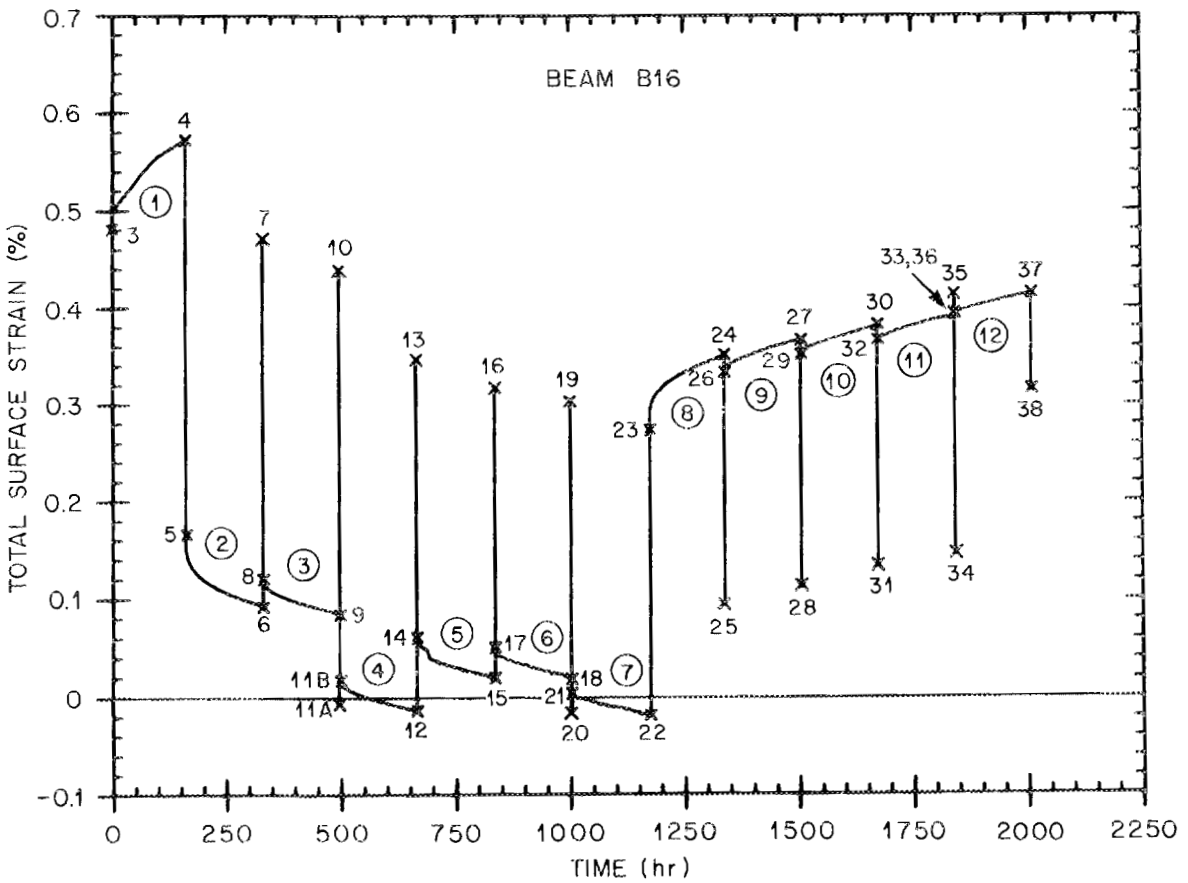

Fig. 2.3. Measured total surface strain vs time response 50.8 mm (2 in.) from center of beam test B16 (measured by West Boeing-type strain gage). Numbered points refer to Fig. 2.1.

methods predict nearly continuous growth rate in creep hardening during each of these two sequences (3 through 7 and 9 through 12) and thus little, if any, discontinuity in creep-rate-time response for either sequence. Although these observations differ in detail, the significance of the differences is not considered critical.

2.2.2 2 1/4 Cr–1 Mo steel beam B17 (Last reported in ORNL-5433, pp. 117-119)

Beam test B17 of 2 1/4 Cr–1 Mo steel was initiated in July and ended in September after about 1895 hr (11.3 weeks). Isothermal temperature conditions of 538°C (1000°F) were maintained throughout the period. The

Table 2.1. Normalized creep deflection and creep strain responses for the 12 hold periods in beam test B16 of type 316 stainless steel at 593°C (1100°F)

Period[a]	Normalized center deflection[b] ($D = \delta/1.11 \times 100$)	Normalized strain[c] ($\varepsilon = 6/0.091$)
1	100	100
2	76	81
3	36	41
4[d]	36	34
5	35	46
6	29	36
7[d]	28	25
8	73	85
9	37	37
10	30	34
11	30	34
12	15	22

[a]Periods are identified in the load histogram, Fig. 2.1.
[b]A value of 100 equals a deflection of 1.11 mm (0.437 in.).
[c]A value of 100 equals a strain of 0.0910%.
[d]Period preceded by an overload.

specimen was machined from heat 3P5601 of 2 1/4 Cr–1 Mo steel, and it was a standard solid beam in terms of its size, heat treatment, specimen instrumentation, and test procedures. However, it varied from beams B13 and B14 in two aspects: the loading histogram was more complex, leading to voluminous data (26,700 scans of the 24 transducers were collected and reduced to engineering units), and additional instrumentation here included a pair of Boeing-type capacitive strain gages (which appeared to function properly throughout the test).

The test had three phases whose loading histograms are shown in Figs. 2.4 through 2.6. Phase 1 was composed of 1-1/2 precreep cycles

ORNL-DWG 78-22669

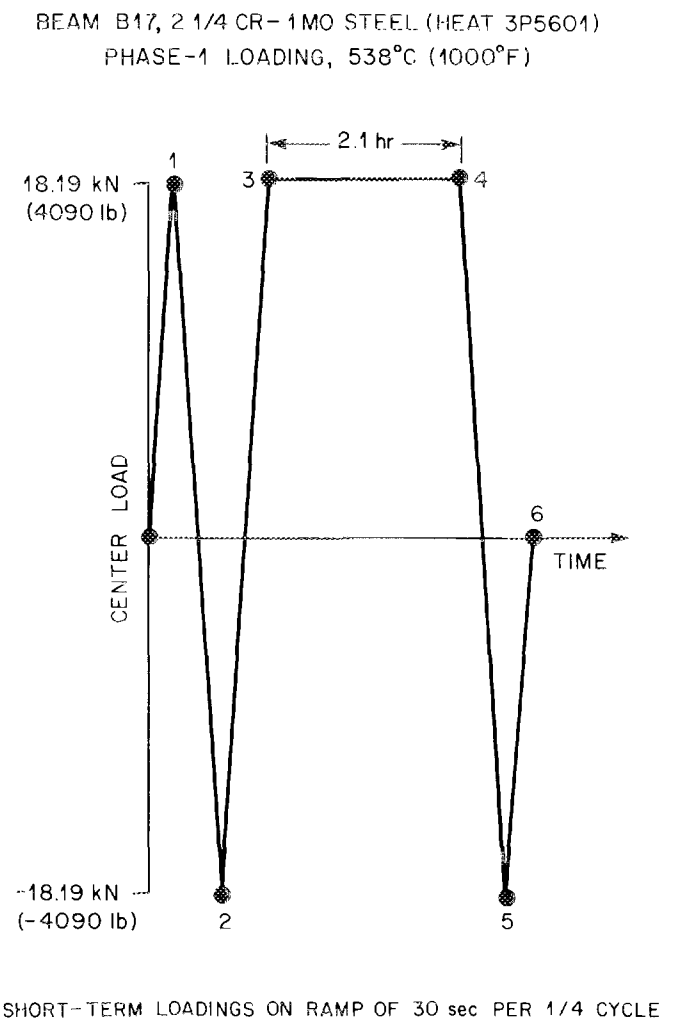

Fig. 2.4. Histogram for phase 1 testing of beam B17, 2 1/4 Cr–1 Mo steel solid beam tested at 538°C (1000°F). Six numbered points are used to identify testing sequences and are referred to in a subsequent figure.

(load-controlled) followed by a creep period of 2.1 hr and then by a 3/4-cycle load reversal to the nominal negative load. Phase 2 of the test consisted of 22 cycles under prescribed center deflection and was run for about 718 hr. Each phase 2 cycle contained a relaxation-type hold period of from one to three days. Phase 3 of the test consisted of seven cycles under prescribed center load and was run for about 1175 hr. Each phase 3 cycle contained a one-week hold period.

ORNL-DWG 78-22670

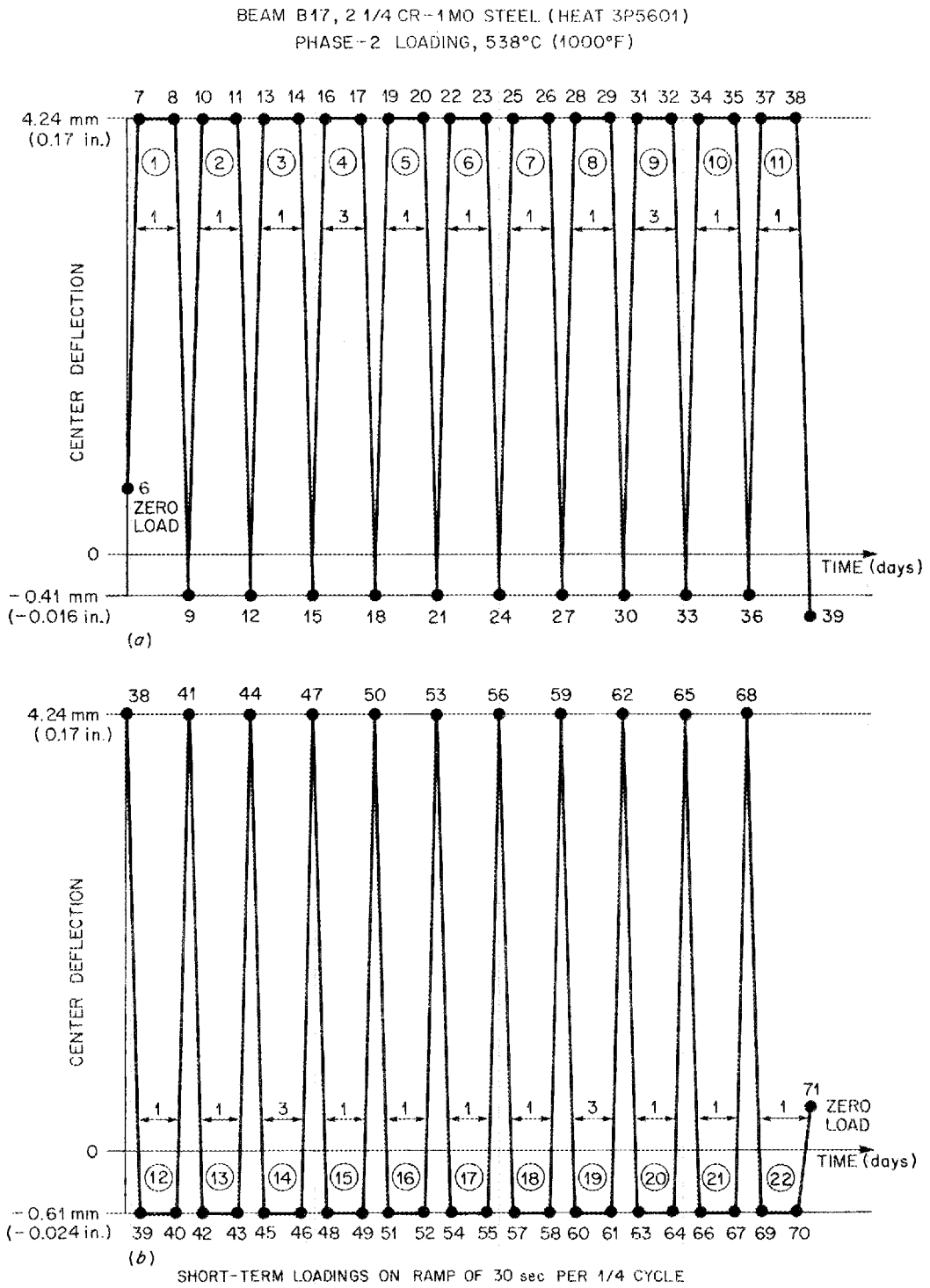

Fig. 2.5. Histogram for phase 2 testing of beam B17. Numbered points (6 through 71) are used to identify testing sequences. Circled numbers (1 through 22) are reference numbers for the hold periods at constant center deflection. Both sets of numbers are referred to in subsequent figures. (*a*) Cycles 1 through 11; (*b*) Cycles 12 through 22.

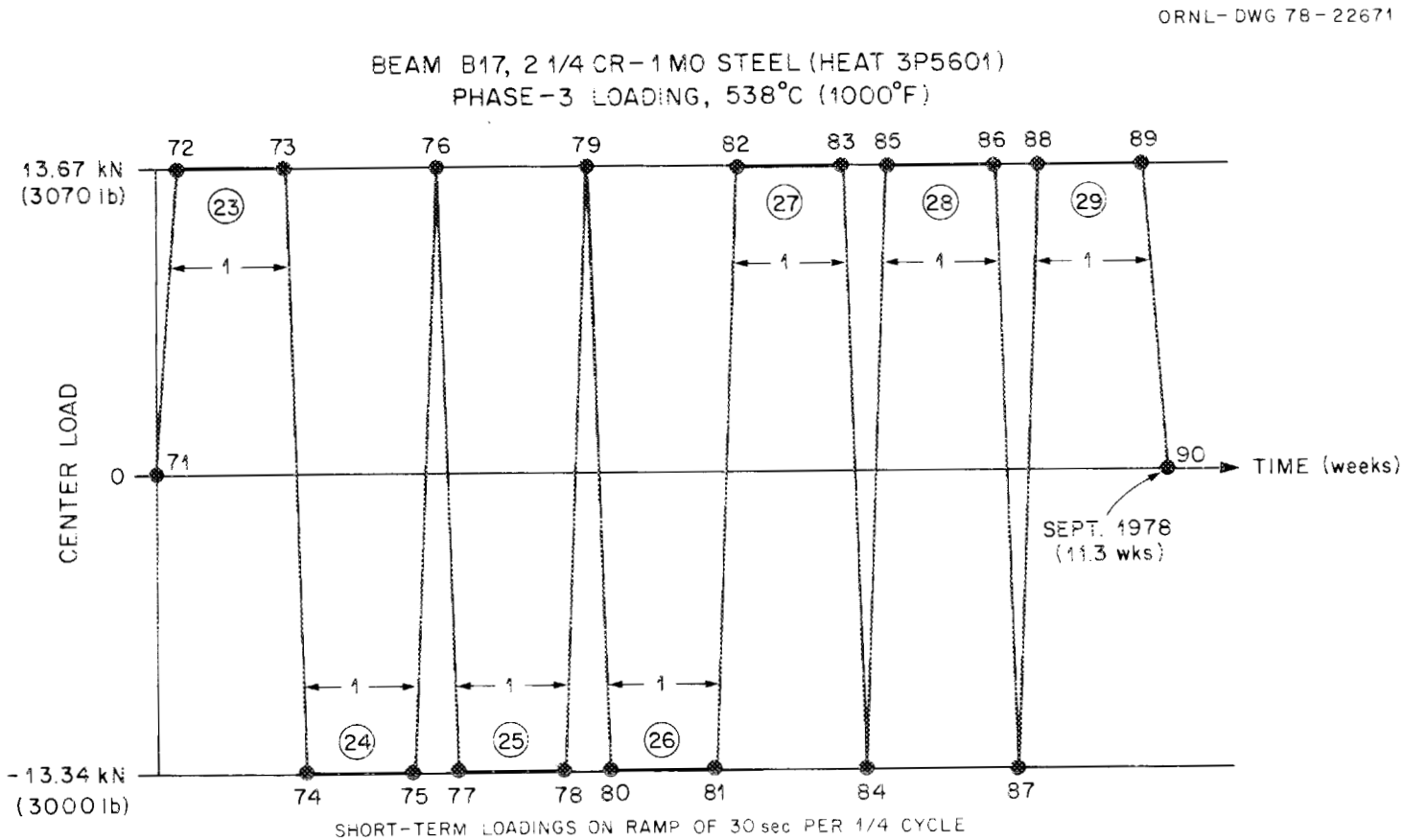

Fig. 2.6. Histogram for phase 3 testing of beam B17. Numbered points (71 through 90) and circled numbers (23 through 29) provide reference points used in a later figure.

Data reduction and preliminary graphical display of results were performed during this period. Some sample plots are included here. Figure 2.7 shows the center deflection vs load response for phase 1. Figures 2.8 and 2.9 compare some phase 2 cycles with each other in terms of the center deflection vs load. Figure 2.10 compares strain vs time data from the two strain gages for all of phase 3.

Significant comments on these test results cannot be made at this time because of the limited effort directed thus far toward studying the vast amount of data. We feel that much will be concluded from this test in future studies and that it will be an important confirmatory structural test for 2 1/4 Cr–1 Mo. This test also appears to be, overall, the most successful ever conducted in our beam and plate facilities in terms of measurement success.

2.2.3 Type 304 stainless steel beam with type 308 stainless steel weld-beam B18 (WB-1) (Last reported in ORNL-5433, pp. 119-120)

This work supplements the activities to develop structural design methods for weldments as reported in Chapter 6. (See Chapter 6 for overall philosophy and purpose of these activities.) Plans include the testing of a series of welded-beam specimens fabricated from type 304 stainless steel with a 308 stainless steel weld (of a double-U geometry) at the center of the beam to produce half symmetry (see Fig. 2.11).

The welded-beam specimens resemble the solid-type beams that we tested previously in our beam facility. Both are nominally 50.8 mm high, 25.4 mm wide, and 0.66 m long (2 × 1 × 26 in.). Although the solid-type beams are simply supported and centrally loaded, the welded beams will be loaded in four-point bending. The 308 stainless steel weld will be located in the central, pure-moment portion. A loading fixture has been prepared and is illustrated in Fig. 2.12. The pure-moment portion is 20.3 cm (8 in.) wide; the outside supports span 0.61 m (24 in.) so that an effective moment arm of 20.3 cm (8 in.) results. The load (or deflection) is applied through the central load arm and is distributed to the two load points (on the top of the beam for downward force and on the bottom for upward force) by the loading fixture. The test can be conducted

ORNL-DWG 78-22672

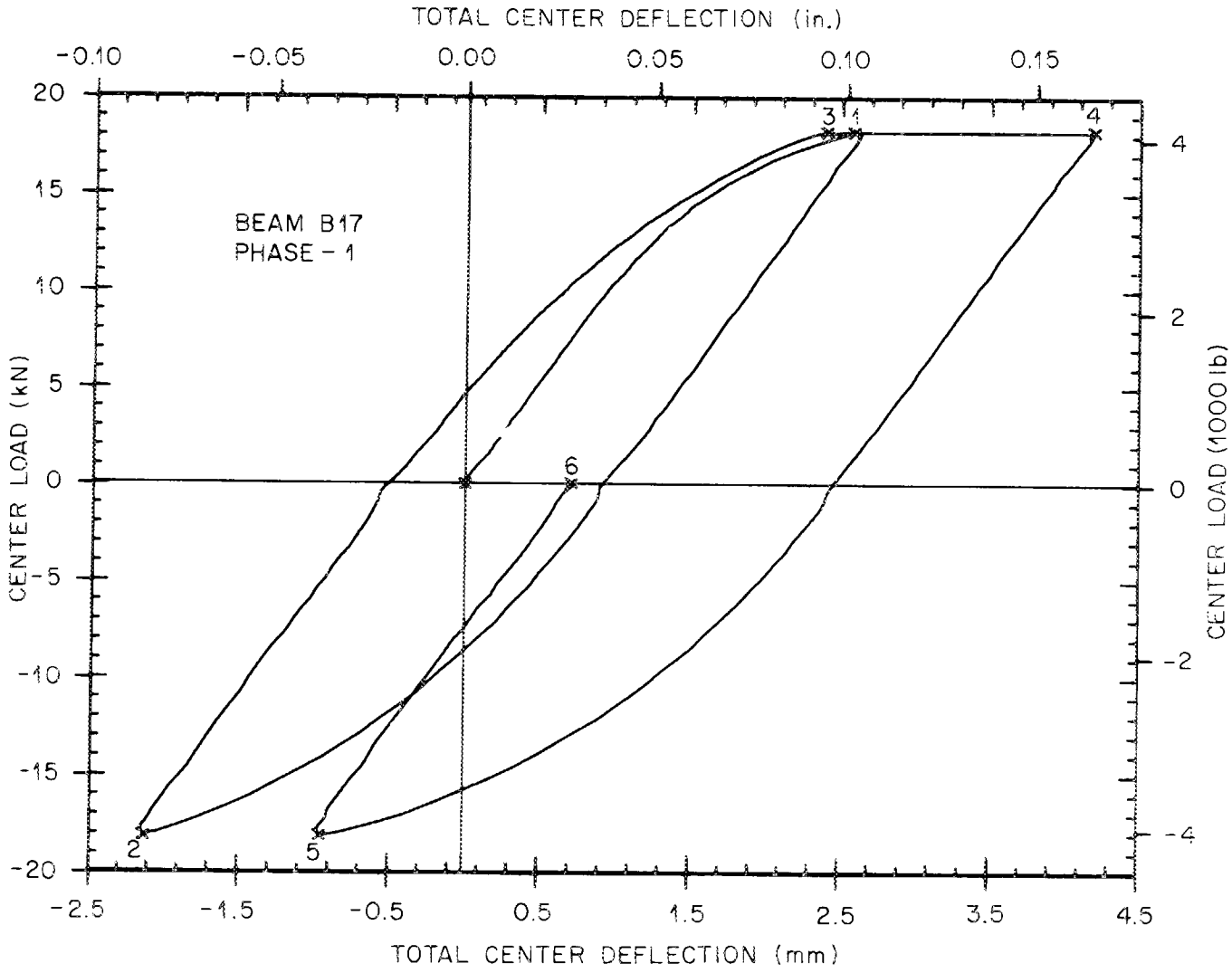

Fig. 2.7. Total center deflection vs center load for phase 1 testing of beam B17. Numbered points refer to Fig. 2.4.

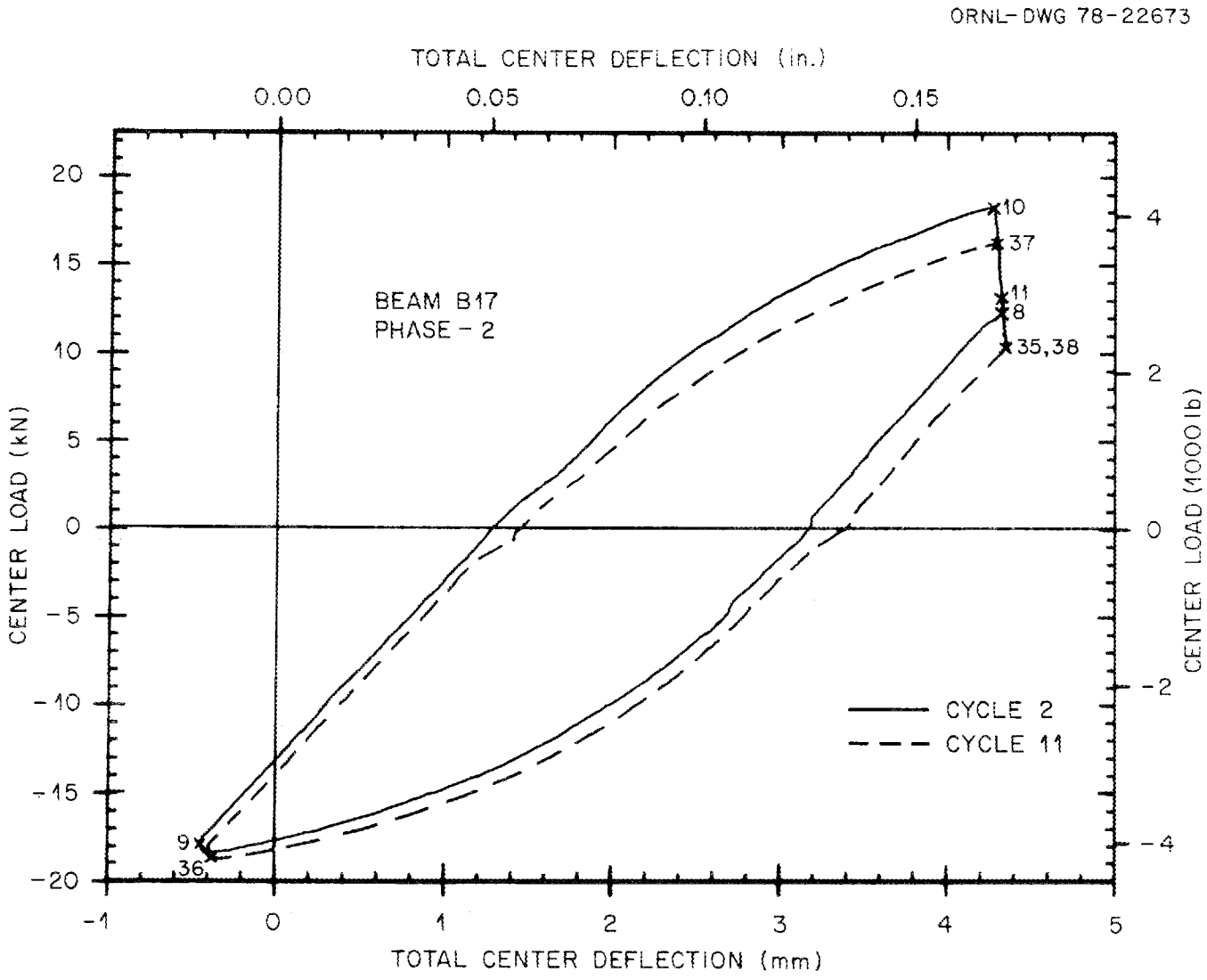

Fig. 2.8. Total center deflection vs center load for cycles 2 and 11 of phase 2 testing of beam B17. Numbered points refer to Fig. 2.5.

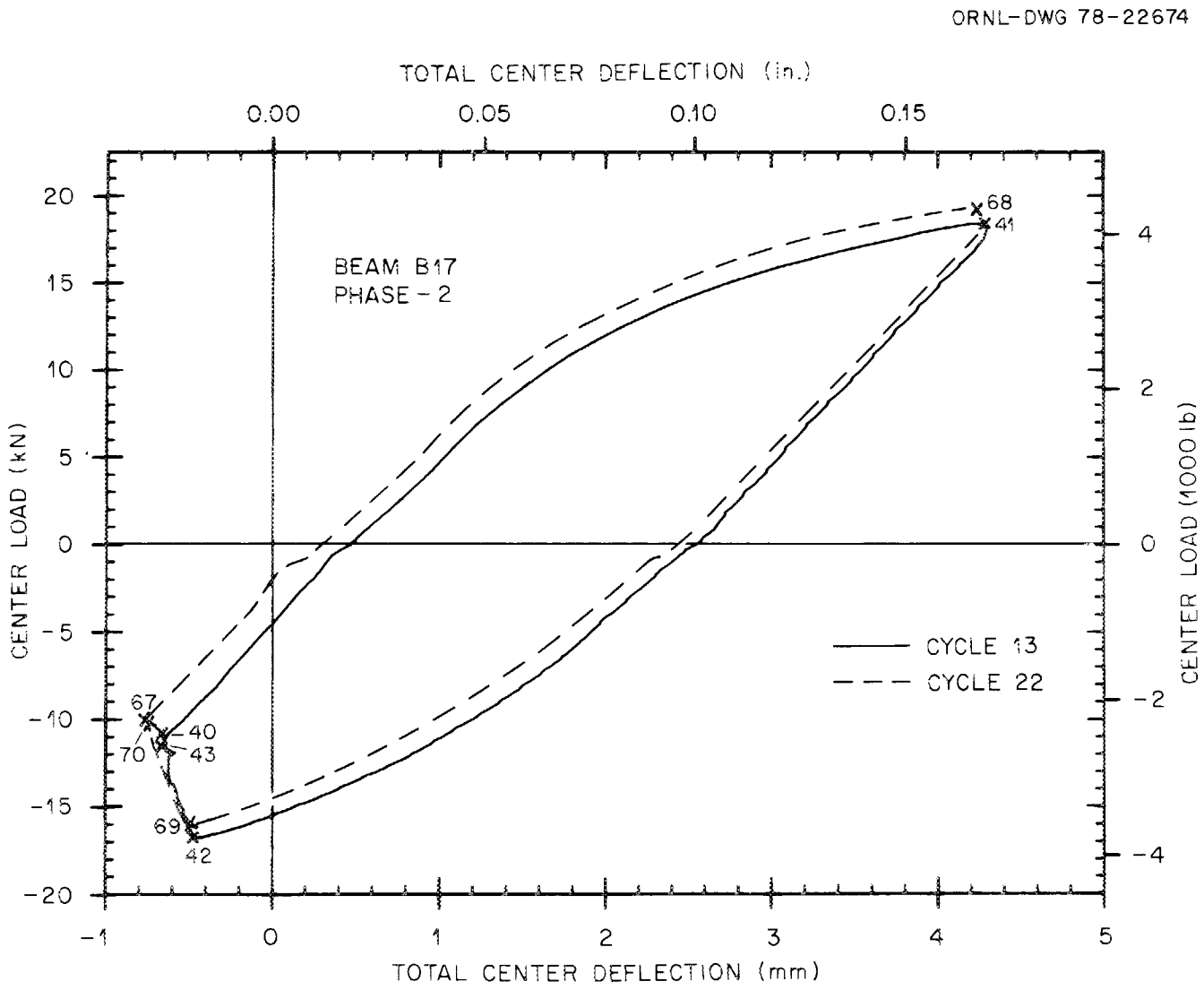

Fig. 2.9. Total center deflection vs center load for cycles 13 and 22 of phase 2 testing of beam B17. Numbered points refer to Fig. 2.5.

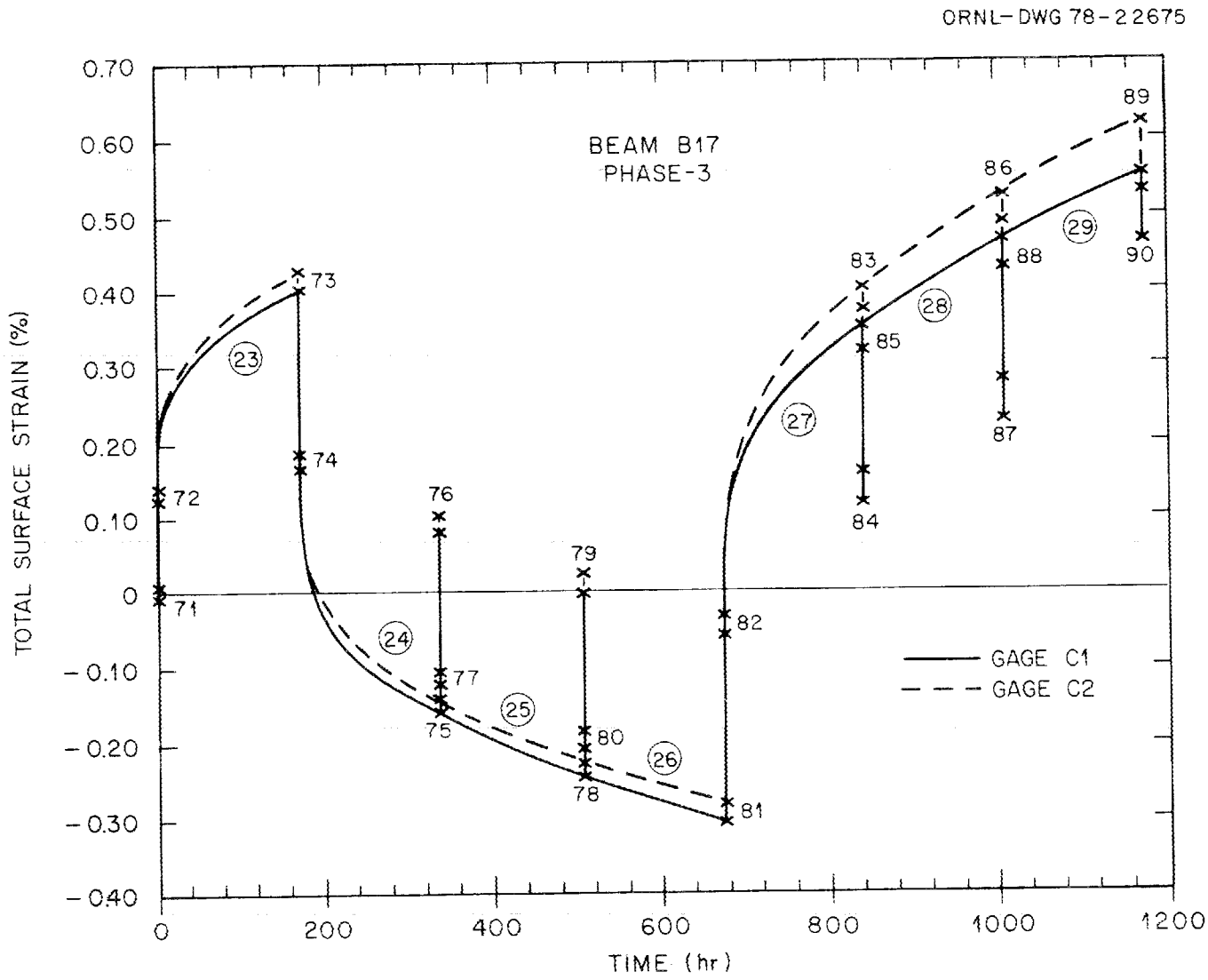

Fig. 2.10. Comparison of strain vs time responses measured by the two Boeing-type strain gages during phase 3 of test beam B17. Numbered points refer to Fig. 2.6.

ORNL-DWG 78-12797

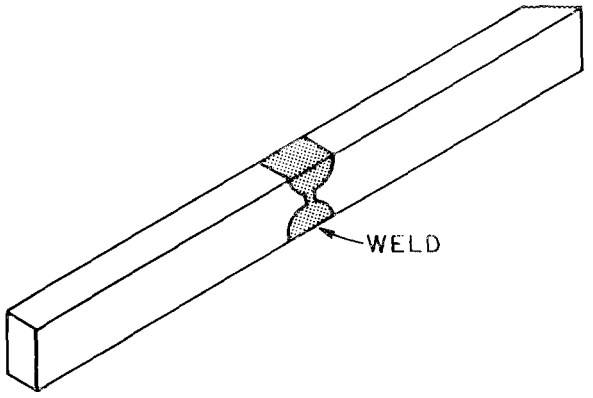

Fig. 2.11. Schematic of the 304/308 stainless steel welded-beam specimen showing double-U weld. Geometry lends itself to half-symmetry modeling.

under load control (equivalent to moment control) or under deflection control (not equivalent to curvature control).

The first welded-beam specimen, B18 (WB-1), has been instrumented and is essentially ready for testing. A photograph of the instrumented specimen in the loading fixture is included (Fig. 2.13). The five quartz rods shown are equally spaced at 50.8-mm (2-in.) intervals across the pure-moment portion of the beam, and they lead to standard dial gages, which, in turn, are connected to direct-current differential transformers (DCDTs). The dial gages and DCDTs (not pictured in Fig. 2.13) make up the displacement-measuring devices. The photograph also shows housings for four Boeing-HITEC capacitive strain gages. One of these strain gages is located on both the top and bottom on a transverse line running down the middle of the double-U weld; two other gages are located top left and bottom right at a 50.8-mm (2-in.) distance from the symmetry line. All four Boeing-HITEC gages have a 6.4-mm (1/4-in.) gage length. A fifth gage, a CERL-Planer capacitive gage has a 19-mm (3/4-in.) gage length and has been installed at the top right position (not shown in the photograph).

Preliminary structural analyses of the 304/308 welded beam were conducted using CREEP-PLAST II.[1] A spatially crude discretization (only 28 three-mode, triangular finite elements were employed to model the weld) was used in this preliminary exercise. Elastic-plastic-creep constitutive

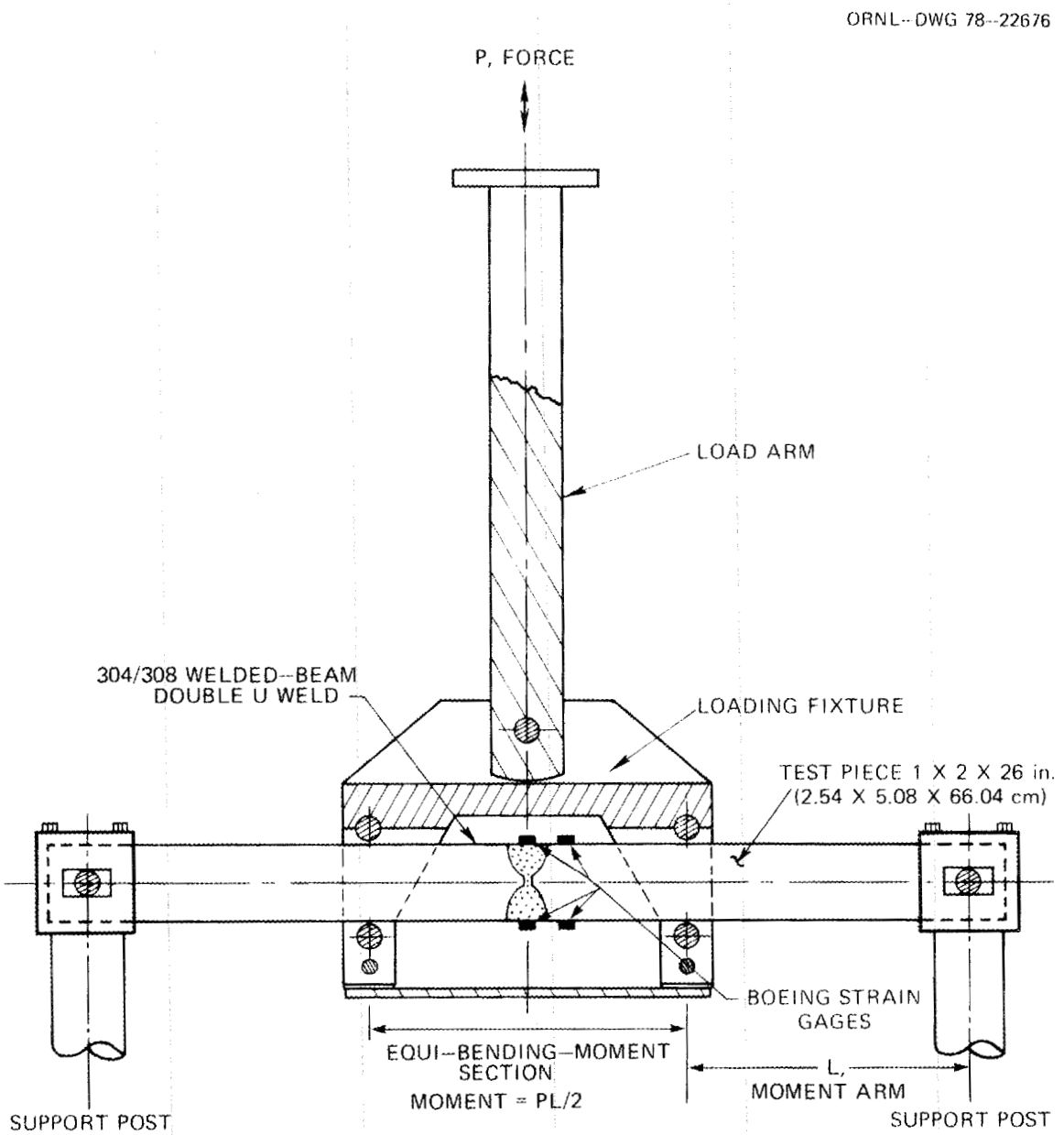

Fig. 2.12. Schematic of the loading fixture for the welded-beam tests. Weldment region is placed in a state of controlled bending moment.

equations like those in RDT Standard F9-5T were employed for both the weld and parent materials. Different constants for the two materials were employed; these differentiated the 304 stainless steel elements from the 308 stainless steel elements. Material anisotropy and the residual stresses caused by the weld process were ignored (as well as unknown) for

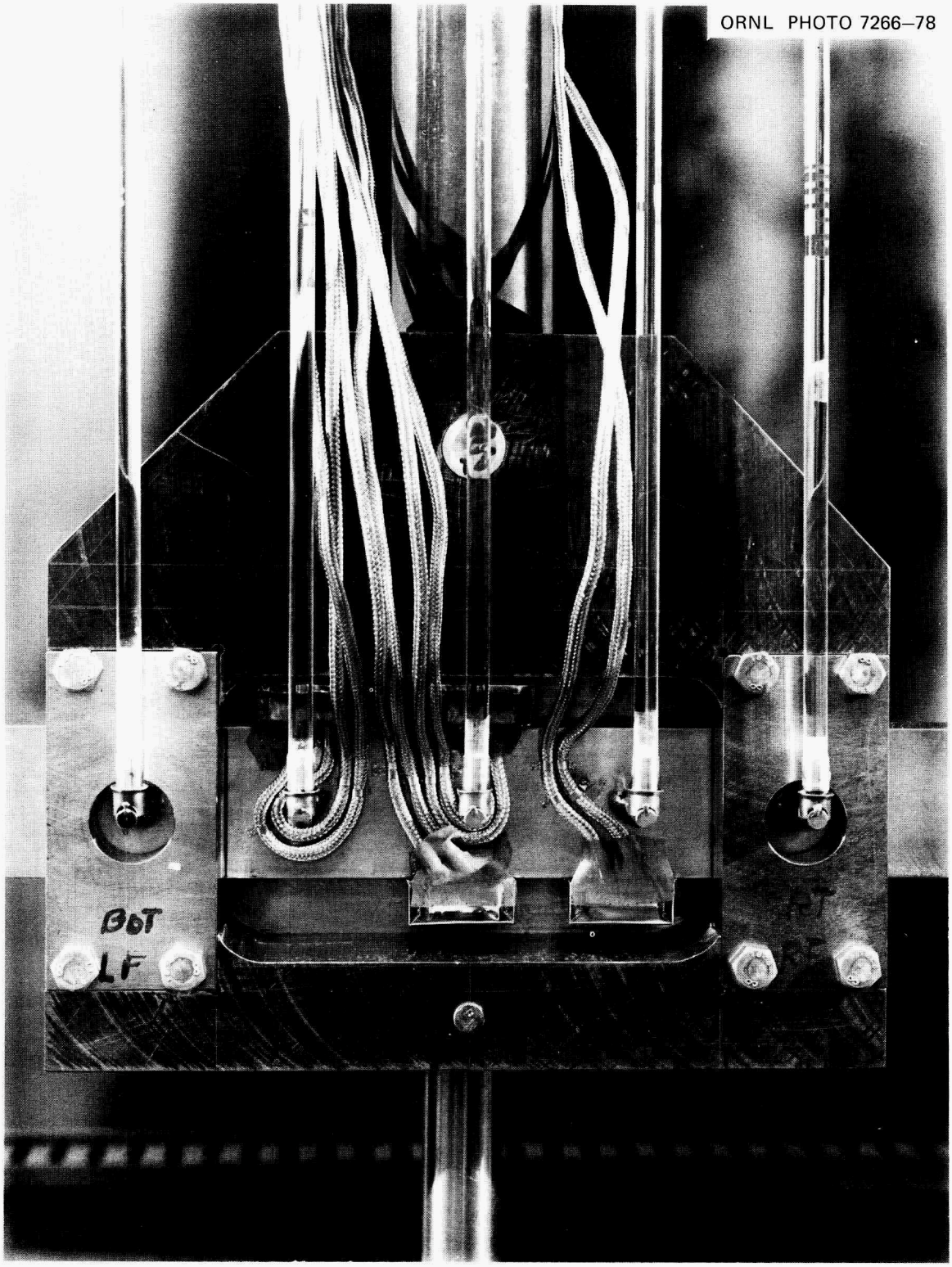

Fig. 2.13. Photograph of the instrumented welded-beam specimen, B18 (WB-1), in the loading fixture. Phase 1 testing is to be conducted at 593°C (1100°F) under conditions of moment control.

the analyses. Also, the heat-affected zone was ignored. Several elastic-plastic analyses were conducted to determine the appropriate monotonic loading; then, several creep analyses were performed to determine the appropriate duration of the constant-moment hold period. Results led us to choose the strain gage locations previously discussed and the phase 1 histogram shown in Fig. 2.14.

Current plans call for test initiation for welded-beam B18 (WB-1) early in CY 1979. Additional testing of this specimen is expected to follow phase 1; however, such test plans have not yet been finalized. Under consideration is a plan that calls for creep-fatigue-type cycles leading to specimen failure.

2.2.4 2 1/4 Cr–1 Mo steel circular plate test CP8 (Last reported in ORNL-5433, pp. 120-125)

This test, the only circular plate test on 2 1/4 Cr–1 Mo steel, was initiated in December 1977 and ended in April 1978. The bulk of progress reporting for this activity appeared in the last progress report. During the present period, data reduction and preliminary graphical display of all test results were completed. Preparations for including test results in forthcoming documents are being made; however, efforts to complete an elastic-plastic-creep analysis of the whole test have been postponed until the next report period.

2.2.5 Type 316 stainless steel circular plate test CP9 (Last reported in ORNL-5433, p. 125)

This test, the second type 316 stainless steel plate test, was initiated in July 1978 and was completed in December after more than 20 weeks of testing. The test essentially mirrored circular plate test CP8 of 2 1/4 Cr–1 Mo steel (see Sect. 2.2.4). The purpose for testing CP9 was to provide supplementary information to help confirm the adequacy of methods for creep-plasticity interactions for type 316 stainless steel.

The histogram for CP9 is shown in Fig. 2.15. The test was conducted under center deflection control and involved a series of 12 cycles with one- to two-week hold periods, each preceded by a short-term load excursion. Most of the excursions were simple load renewals (the load was

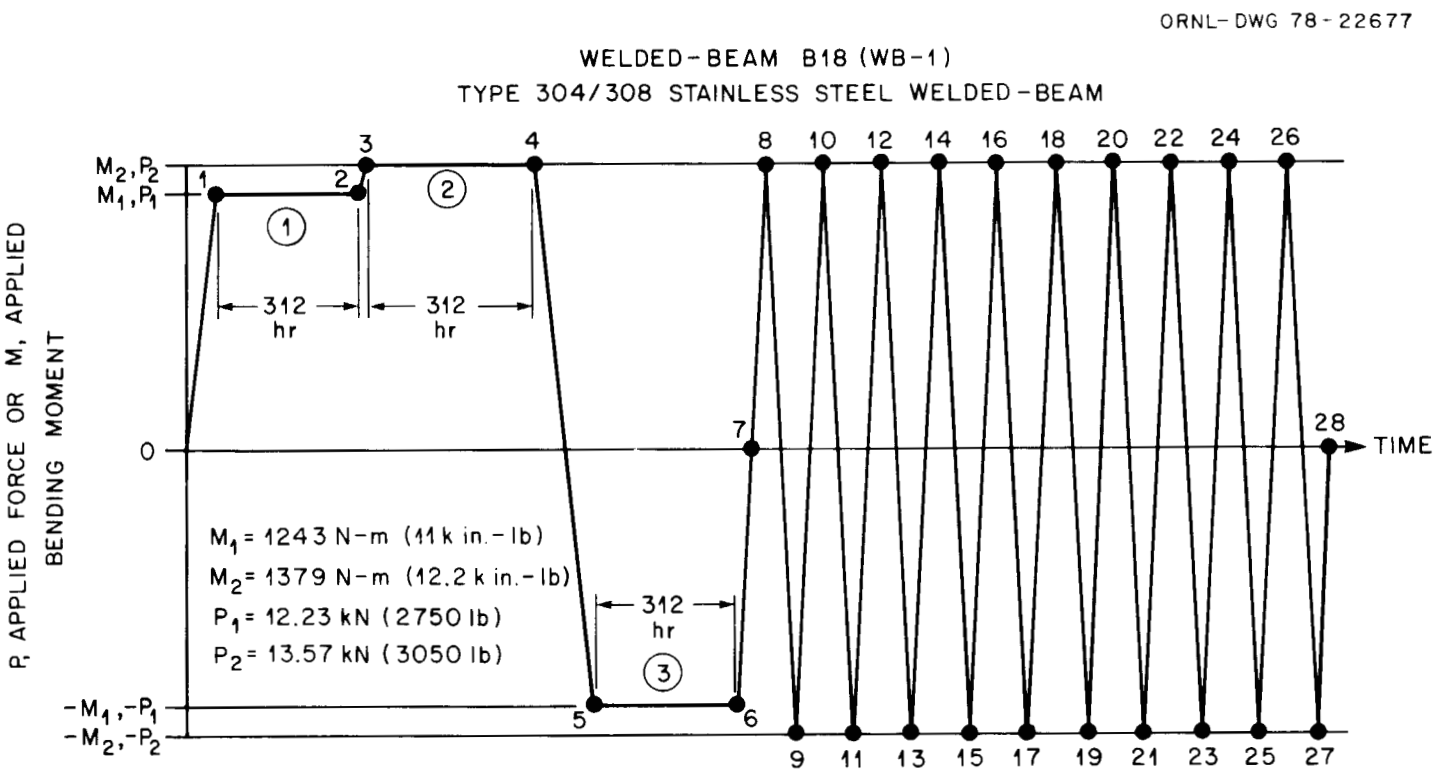

Fig. 2.14. Preliminary phase 1 histogram for testing welded-beam B18 (WB-1).

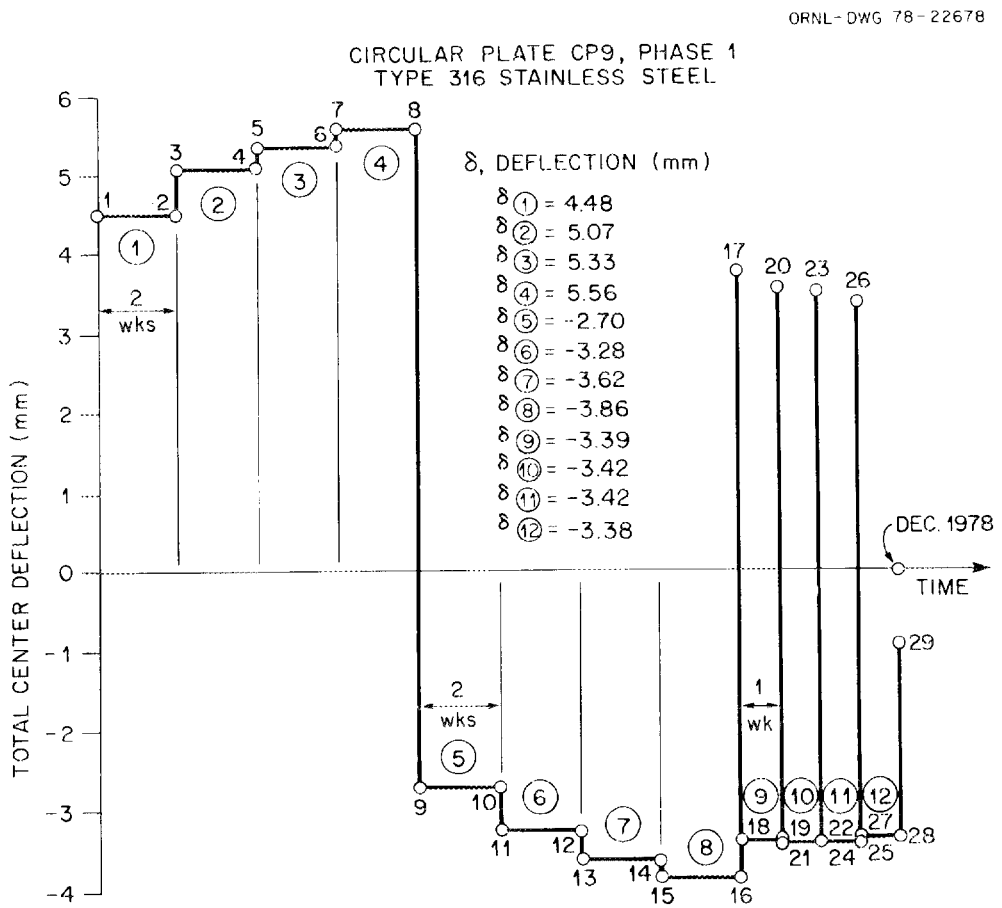

Fig. 2.15. Histogram of the center deflection for circular plate test CP9 of type 316 stainless steel. Test duration was slightly more than 20 weeks, and it was completed in December 1978.

returned to the initial magnitude) after relaxation periods; however, the excursion that preceded period 5 was a complete load reversal producing conditions for reversed creep, and the excursions preceding periods 9 through 12 were load renewals that followed short-term load reversals. Thus, this test covers a range of conditions that are especially important to further confirmation of the analytical model for this material.

In the following period, we will process the test data, graphically display the results, and prepare the test data for inclusion in reports. We will also conduct an analysis using RDT Standard F9-5T procedures, compare test and analytical results, and extract from this total exercise evidence of the validity of the overall analysis method.

2.3 Analysis of the Capped Cylindrical Shell Test CC2

W. K. Sartory

(Last reported in ORNL-5433, p. 125)

The test of the second capped cylinder specimen (CC2) involved two loading phases: the first phase was basically a deformation test, and the second was undertaken to produce creep rupture of the specimen. The test conditions, geometry, gage locations, and experimental results were reported earlier.[2] The load histogram is presented in Figs. 2.16 and 2.17. A finite-element grid of the specimen was developed in the previous report

ORNL-DWG 78-2308

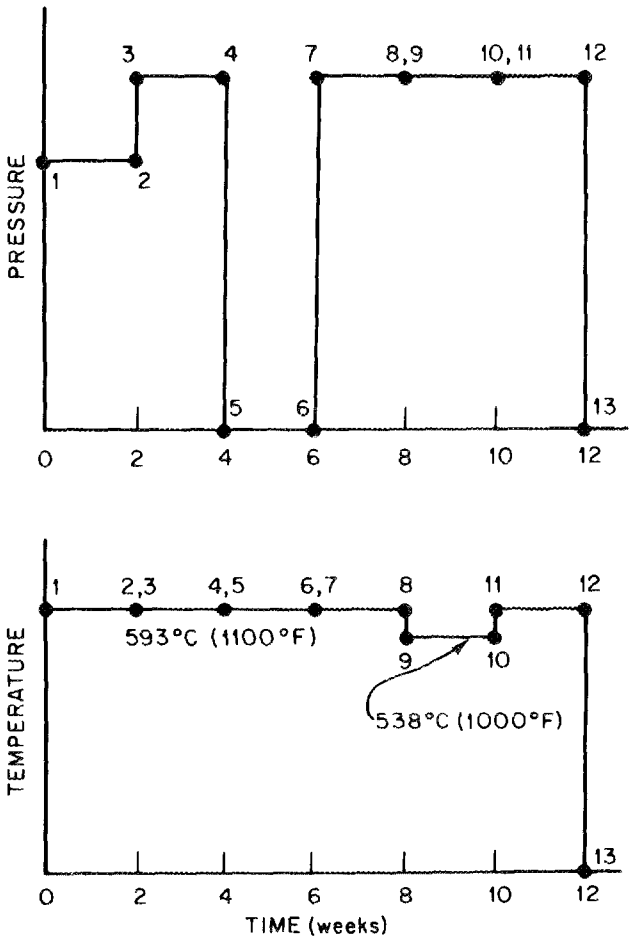

POINT	TIME (hr)	PRESSURE [MPa(psi)]
1	0.01	2.07(300)
2	335.53	2.08(301)
3	335.54	2.75(399)
4	671.49	2.76(400)
5	671.50	0.04 (6)
6	1009.05	0.01 (1.2)
7	1009.06	2.76(401)
8	1343.4	2.75(399)
9	1345.7	2.76(400)
10	1678.5	2.76(400)
11	1685.00	2.76(401)
12	2016.09	2.76(400)
13	2016.10	0.05 (7.8)

Fig. 2.16. Loading histogram for CC2 (phase 1) test.

ORNL-DWG 78-2309

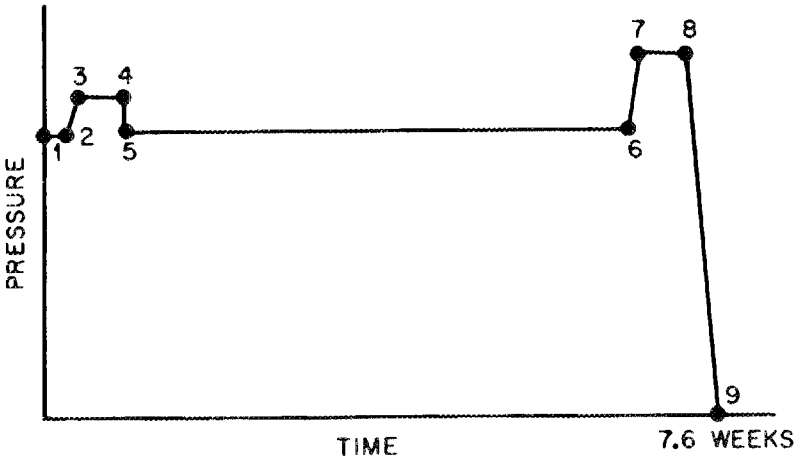

POINT	TIME (hr)	PRESSURE (MPa(psi))
1	0.02	6.92(1004)
2	2.10	6.98(1012)
3	4.36	7.49(1086)
4	20.92	7.57(1098)
5	21.16	6.78 (984)
6	1272.49	6.90(1001)
7	1272.54	8.14(1181)
8	1280.70	8.18(1187)
9	1284.70	0.08(11.8)

Fig. 2.17. Loading histogram for CC2 (phase 2) test.

period.[3] During the present period, an inelastic structural analysis and creep damage evaluation of the test was completed.

The analysis used the finite-element program PLACRE.[4] The plastic properties used are for the reference heat (9T2796) of type 304 stainless steel and are those discussed in Ref. 5. The creep equation developed by Clinard[6] was used at 593°C (1100°F), and the rational polynomial creep equation of Swindeman (see Sect. 1.3.2) was used at 538°C (1000°F). A creep damage evaluation according to Code Case 1592 (Ref. 7) was carried out. For the inelastic damage, the creep-rupture data used at both hold temperatures have been discussed by Swindeman:[8]

$$t_r = \left(\frac{49.9}{S}\right)^{8.819} \text{ at } 593°C\ (1100°F)$$

$$t_r = \left(\frac{70.6}{S}\right)^{8.864} \text{ at } 538°C\ (1000°F),$$

where S is the stress in ksi (1 ksi = 6.895 MPa) and t_r is the rupture time in hours.

The finite-element grid, which used 924 triangular elements, is shown in Fig. 2.18. The length of the cylindrical portion of the grid is less than the full length of the specimen but is in excess of $6\sqrt{rt}$ and, based on simple elastic shell theory, is sufficient to eliminate over 99% of the discontinuity stresses.

ORNL-DWG 78-22075

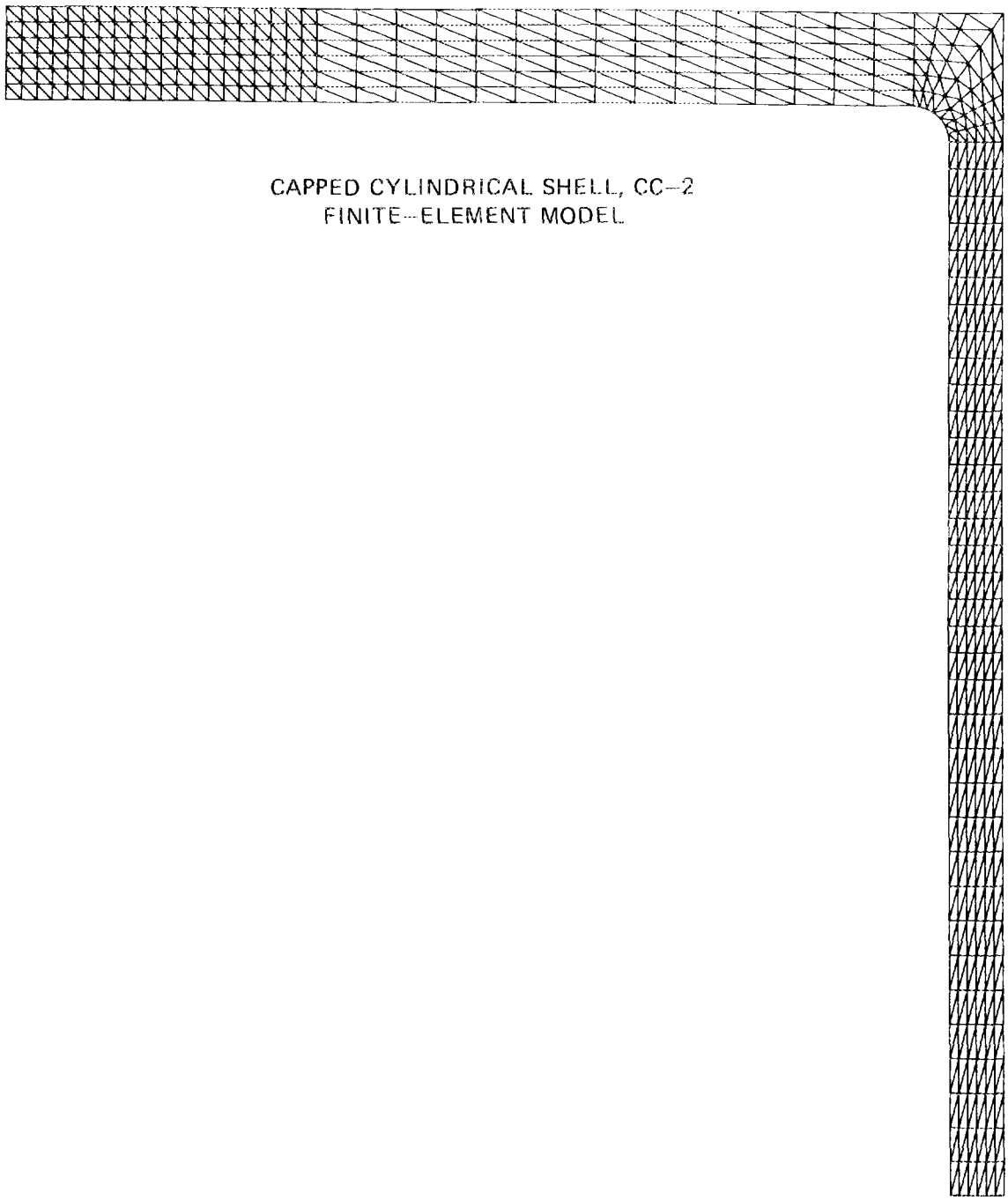

Fig. 2.18. Finite-element grid of the CC2 specimen. Thicker section is in cap.

For the first phase of the test, comparisons of the calculated strains with the experimental results for strain gages C3, C4, C5, and C6 are shown in Figs. 2.19 through 2.22. (Strain gages C1 and C2 failed early in the test and produced no useful results. The locations of the four surviving gages are given in Table 2.2.) Gages C3 and C4 were installed on the membrane region of the cylindrical shell and generally indicate less

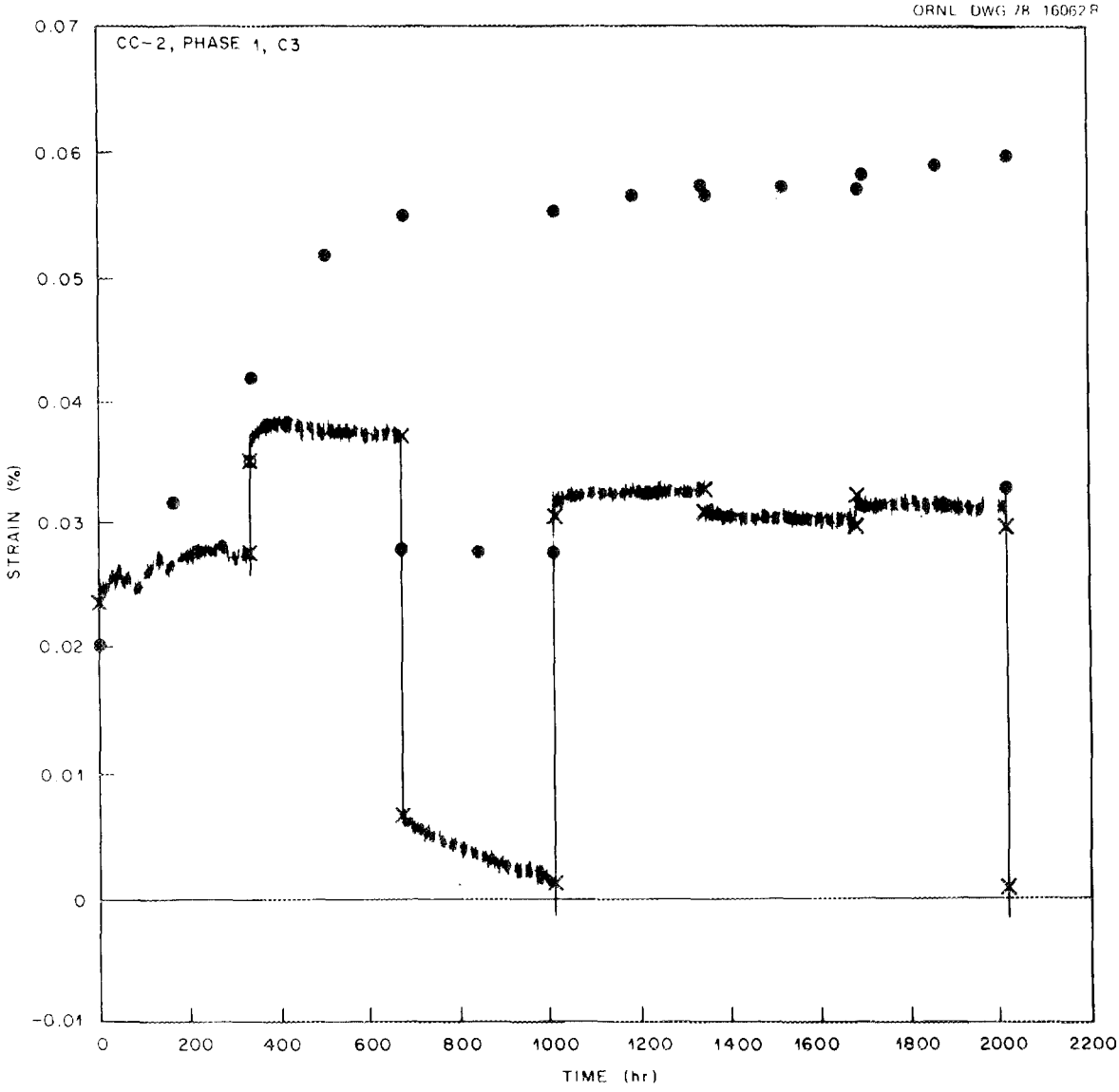

Fig. 2.19. Comparison of the measured and calculated strain at gage C3 during phase 1 of test CC2. Solid circles are calculated points. See Table 2.2 for gage location.

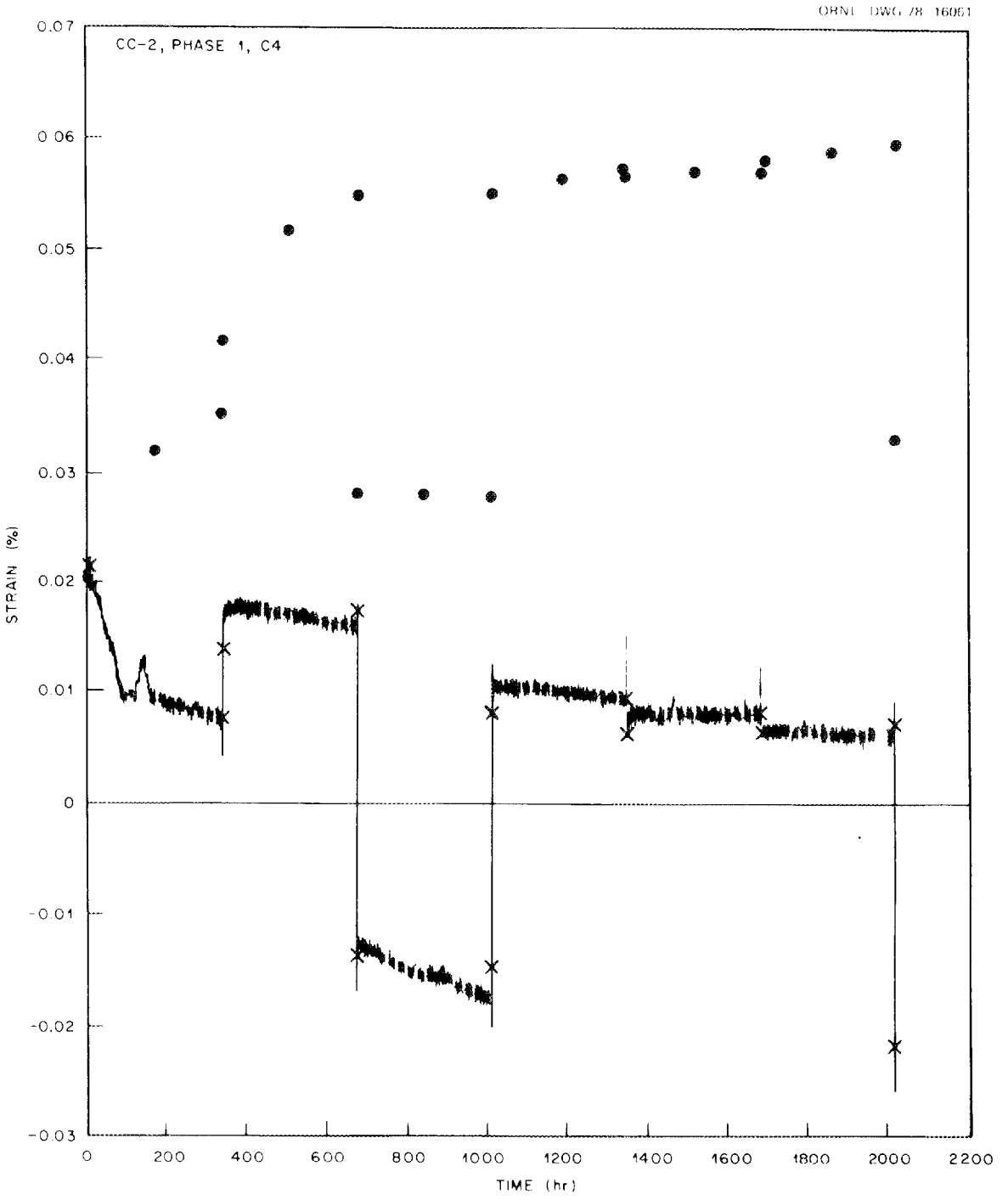

Fig. 2.20. Comparison of the measured and calculated strain at gage C4 during phase 1 of test CC2. Solid circles are calculated points. See Table 2.2 for gage location.

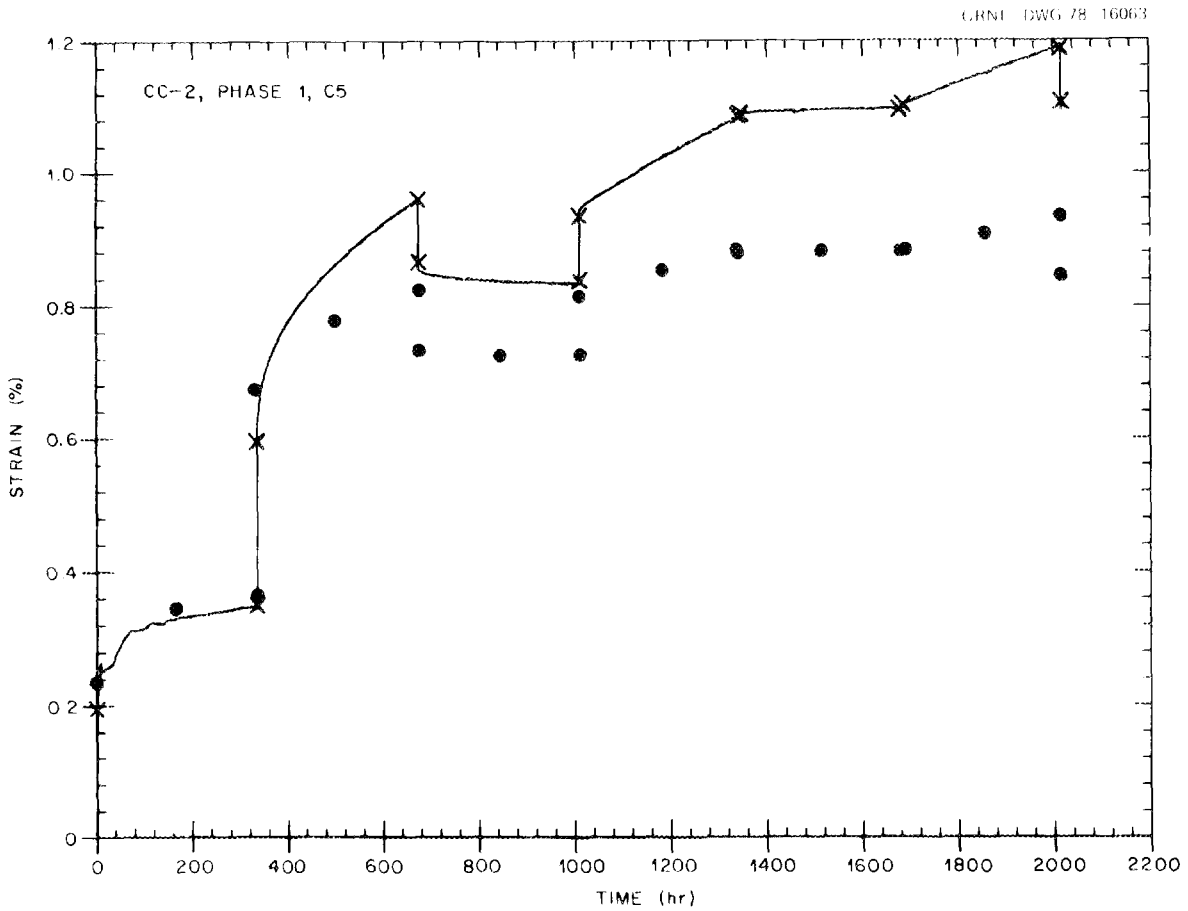

Fig. 2.21. Comparison of the measured and calculated strain at gage C5 during phase 1 of test CC2. Solid circles are calculated points. See Table 2.2 for gage location.

Table 2.2. Gage locations and orientations for test CC2

Designation[a]	Location			Orientation
	r^b [mm (in.)]	Z^b [mm (in.)]	θ^b (deg)	
C3	53.3 (2.1)	76.2 (3)	0	Circumferential
C4	53.3 (2.1)	76.2 (3)	90	Circumferential
C5	12.7 (0.5)	0	0	Circumferential
C6	9.5 (0.375)	0	180	Radial

[a]In Ref. 2, these same gages were referred to as gages H3 through H7. The present designation is intended to indicate capacitive gages.

[b]The origin of the coordinates is at the top center of the cap with the Z axis positive down the cylinder.

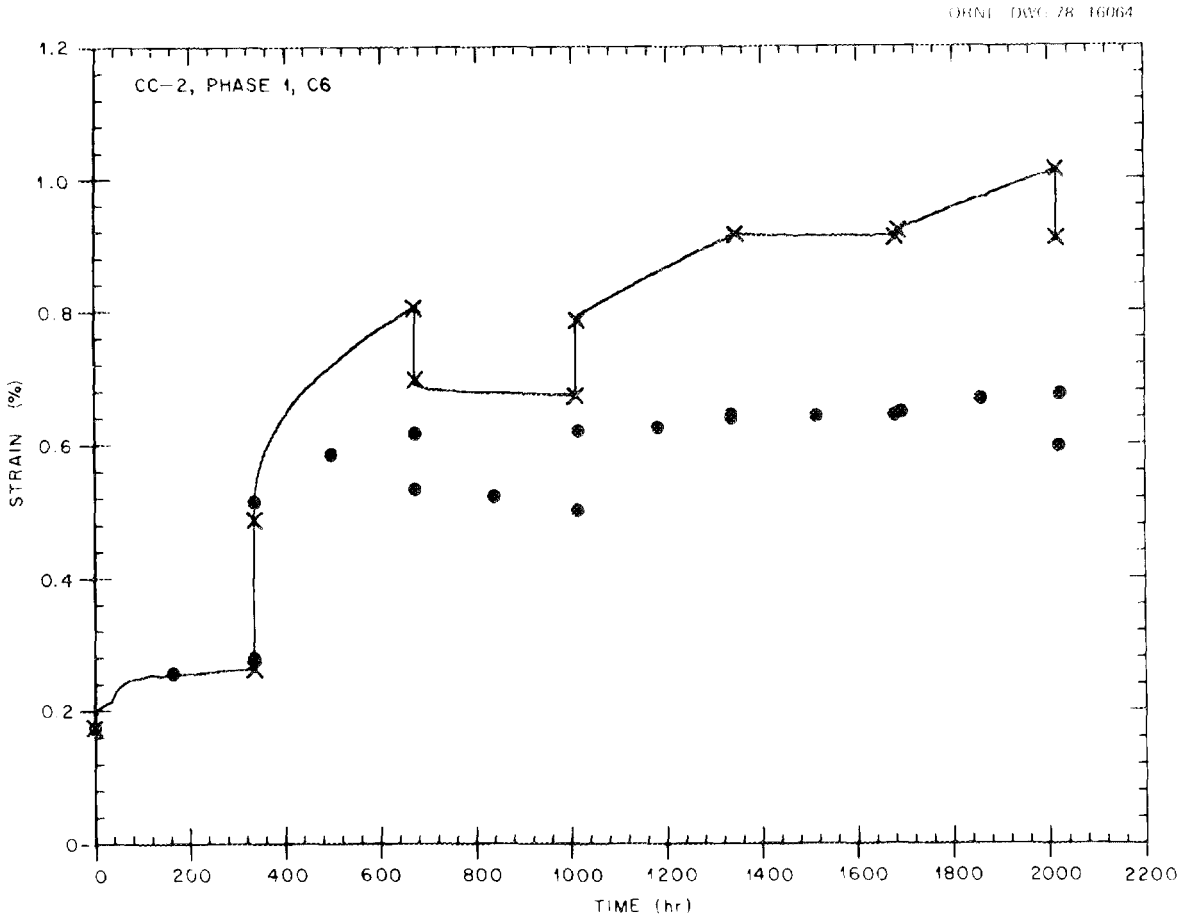

Fig. 2.22. Comparison of the measured and calculated strain at gage C6 during phase 1 of test CC2. Solid circles are calculated points. See Table 2.2 for gage location.

than the calculated strain; however, gages C5 and C6 were mounted on the cap and indicate somewhat more than the calculated strain.

Experimental results for gage C4 show a significant decrease in indicated strain during the first week or two of the first hold period. This change appears to be a result of drift of the gage. Such an apparent drift during the first few weeks of a test has been observed occasionally in earlier tests. If the experimental results from gage C4 were corrected to agree with those of C3 at the end of the first hold period, then the agreement between the experimental results of gages C3 and C4 would be significantly improved for the remainder of the test, and the agreement between the measured and calculated results for gage C4 would also be somewhat better.

Although an attempt was also made to analyze phase 2 of the test, computational difficulties developed that prevented completion of the analysis. The first load step of phase 2 consisted of pressurizing the specimen to about 6.9 MPa (1 ksi). The no-creep option of PLACRE was used for this load step. Although the initial load step of phase 2 was analyzed to completion, very large stresses [in excess of 690 MPa (100 ksi)] were predicted at the center of the cap. When the first creep-hold period of phase 2 was analyzed, the creep rate was so high and the stress redistribution so slow that no significant fraction of the structure hold time could be analyzed in an acceptable computer time. (Analysis of 10^{-10} hr of structure hold time required 0.55 hr of computer time.) The conclusion was reached that completing the analysis of phase 2 was not feasible.

Computational difficulties are attributed to the assumption of geometric linearity that is made in the program PLACRE. Because the deflections are assumed to be infinitesimal, the entire pressure loading on the flat cap must be supported by the bending moment that develops in the cap. In the actual specimen, we believe the cap deflection in phase 2 is so large that the membrane stresses in the deformed cap carry most of the pressure load. Thus, a more advanced computer program would be needed to analyze phase 2.

The inelastically calculated creep damage during phase 1 of the test is shown in Fig. 2.23 for two locations of greatest damage (the inside surface at the center of the cap and the fillet region between the cap and cylinder). The calculated creep damage is an order of magnitude greater at the center of the cap, where it reaches a damage fraction of about 0.63 at the end of the first phase of the test. Actual specimen failure, on the other hand, occurred in the fillet region. This difference between the predicted and observed failure location again could be caused by the assumption of geometric linearity in the analysis (as discussed above) or it could be caused by a sharp step that was known to be left in the fillet region during preparation of the specimen (due to machining limitations) but that could not be sufficiently well defined to be included in the finite-element grid of the fillet. Such a step would be expected to cause premature failure at the fillet.

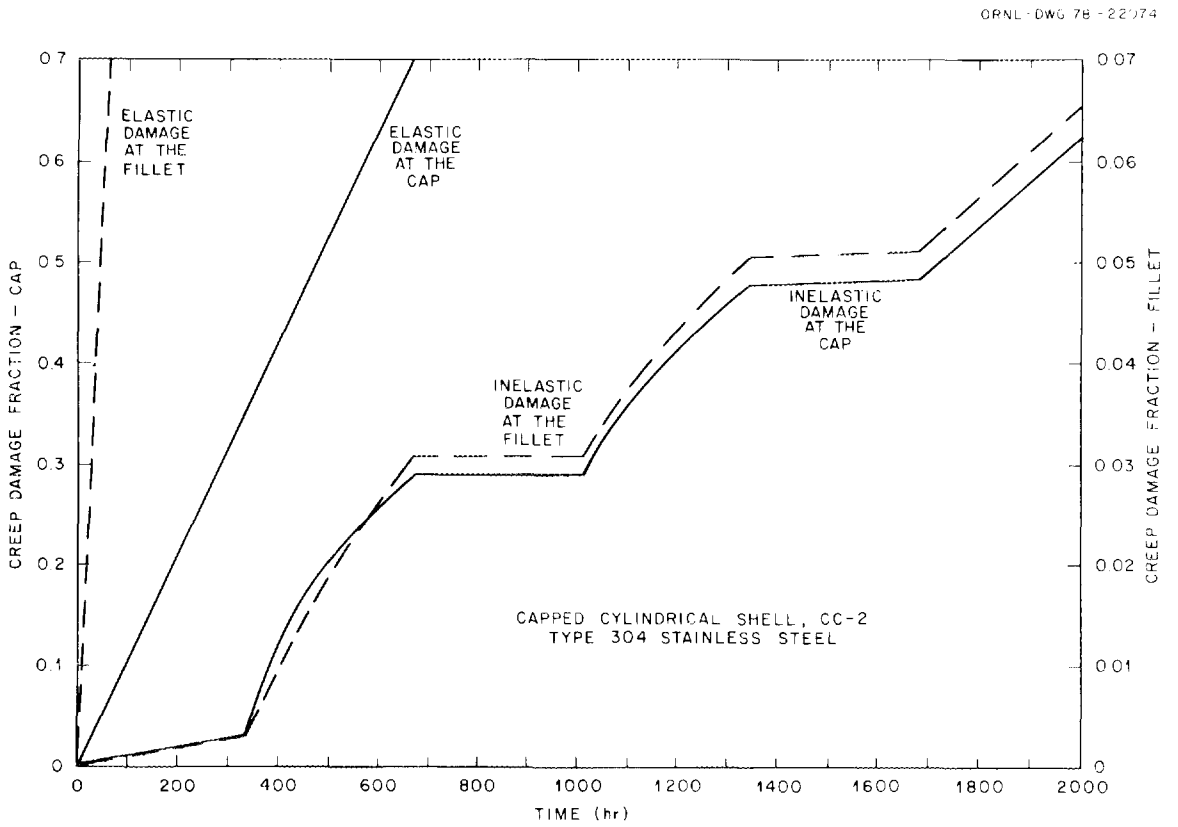

Fig. 2.23. Calculated creep damage at cap center and fillet during phase 1 of test CC2.

Creep damage was also evaluated according to the elastic procedures and using the material properties and creep rupture data of Code Case 1592 (Ref. 7). Results are also shown in Fig. 2.23. Because the calculated elastic stress exceeded 1.25 S_y at both the cap center and the fillet, the calculated rate of damage accumulation is the same at both locations, and failure is predicted to occur during phase 1.

In summary, the inelastic structural analysis of test CC2 gave fair agreement with the strain gage measurements during phase 1 of the loading and during the initial pressurization of phase 2. Analysis of phase 2 could not be completed due to limitations of the structural analysis program. Inelastic creep damage evaluations for phase 1 seem quite conservative because they extrapolate to failure in about 880 additional hours under the mild conditions of phase 1; the specimen actually withstood

over 1200 hr of additional testing under the much more severe load conditions of phase 2. The elastic damage predictions are even more conservative than the inelastic predictions.

We believe that the computational difficulties discussed above could be overcome by the use of a more sophisticated finite-element computer program, but we have no present plans to pursue the analysis further because it is not essential to our program.

2.4 Nozzle-to-Sphere Tests and Analyses

R. C. Gwaltney M. Richardson
R. L. Battiste

(Last reported in ORNL-5433, pp. 126-131)

2.4.1 High-temperature deformation phase of test of NS-2

The first high-temperature inelastic test of a nozzle-to-spherical-shell attachment has been completed. The model (NS-2) was instrumented with eight Boeing-HITEC capacitive strain gages — four 6.35-mm (1/4-in.) gages and four 25.4-mm (1-in.) gages. The gages were arranged along two lines running in the meridional direction and marked north (N) and south (S) in Fig. 2.24. There are four gages on the outside surface. The gages at location 2 are in the axial direction, but all the other gages are in the circumferential direction. The location number, type, and direction of the gages are listed in Table 2.3. The coordinate position of each gage is given by an insert in Fig. 2.24.

The test was run at 593°C (1100°F), and fused-carbonate salt was used for the pressurization medium. The test histogram is shown in Fig. 2.25, and the specimen is of type 304 stainless steel (heat 9T2796). After the pressure-only test was completed, the moment-only test was performed. The original plan was to also have a combined pressure-moment test, but this was dropped in favor of an earlier initiation of a subsequent failure test phase.

The CREEP-PLAST II program was used to analyze the pressure-only phase of the deformation test. A total of 984 three-node triangular elements and 581 nodes were used in the analytical model. Elastic-plastic

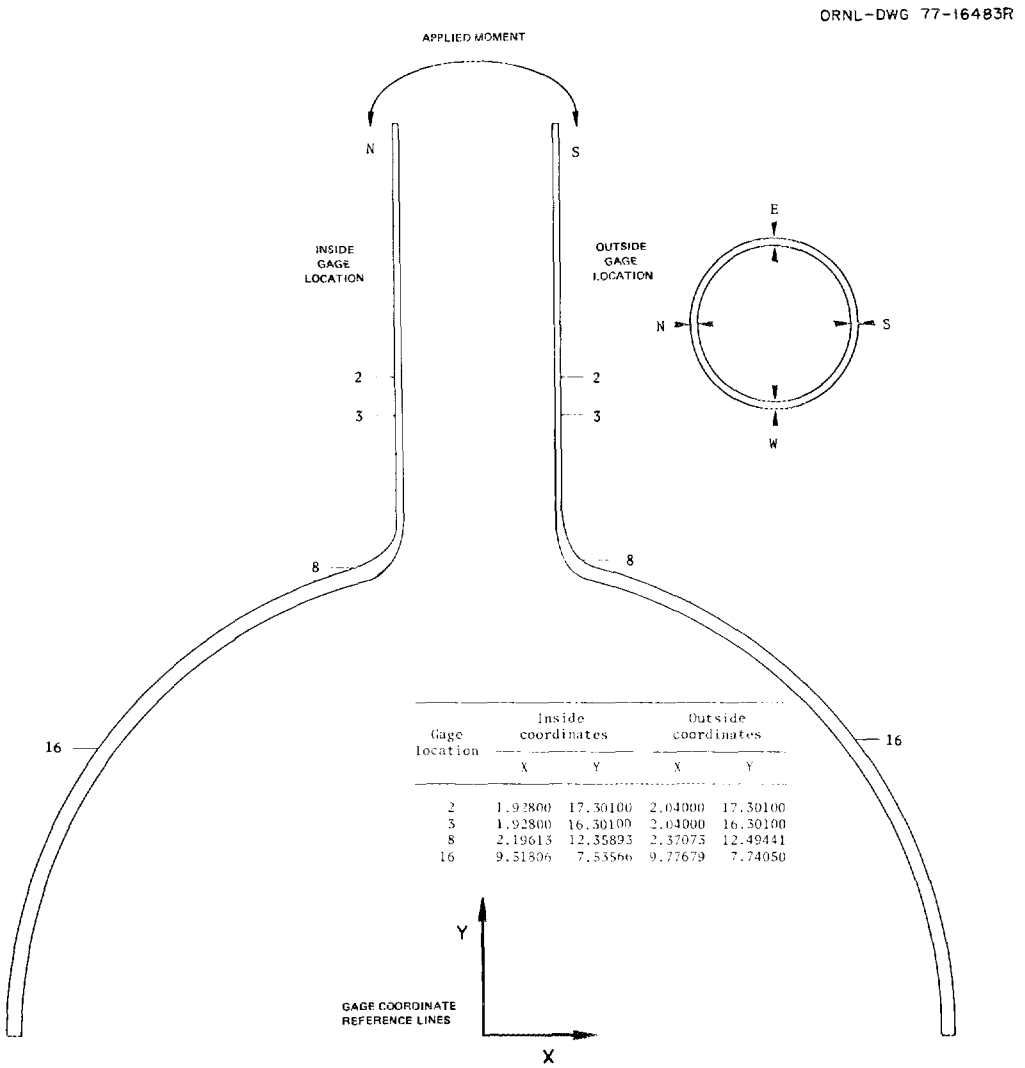

Gage location	Inside coordinates		Outside coordinates	
	X	Y	X	Y
2	1.92800	17.30100	2.04000	17.30100
3	1.92800	16.30100	2.04000	16.30100
8	2.19613	12.35893	2.37073	12.49441
16	9.51806	7.53566	9.77679	7.74050

Fig. 2.24. Gage location diagram for nozzle-to-sphere test NS-2.

properties used in the analysis were from the reference heat (9T2796) of type 304 stainless steel and are discussed in Refs. 5 and 9. Inelastic analysis predictions of strains in the junction region agree reasonably well with the experimental values. Figure 2.26 shows the predicted results calculated by the CREEP-PLAST II program compared with the experimental data taken by gage S8.

The computer program PLANS/HEX is being developed by Grumman Aerospace Corporation, and it will be used to analyze the moment-only phase of the deformation test. Experimental results for the moment loading are being reduced.

Table 2.3. Description of gages

Location	Boeing size	Direction
2 south	25.4 mm (1 in.)	Axial
3 south	6.35 mm (1/4 in.)	Circumferential
8 south	6.35 mm (1/4 in.)	Circumferential
16 south	25.4 mm (1 in.)	Circumferential
2 north	25.4 mm (1 in.)	Axial
3 north	6.35 mm (1/4 in.)	Circumferential
8 north	6.35 mm (1/4 in.)	Circumferential
16 north	25.4 mm (1 in.)	Circumferential

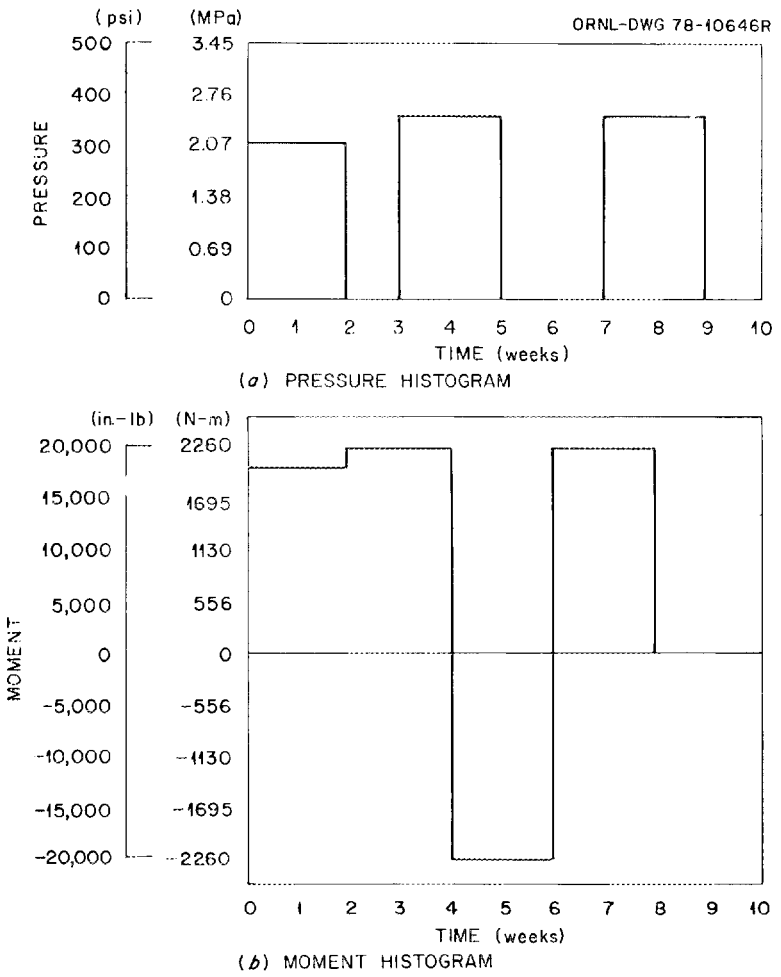

Fig. 2.25. Pressure and moment histograms for test NS-2.

ORNL-DWG 78-19003R

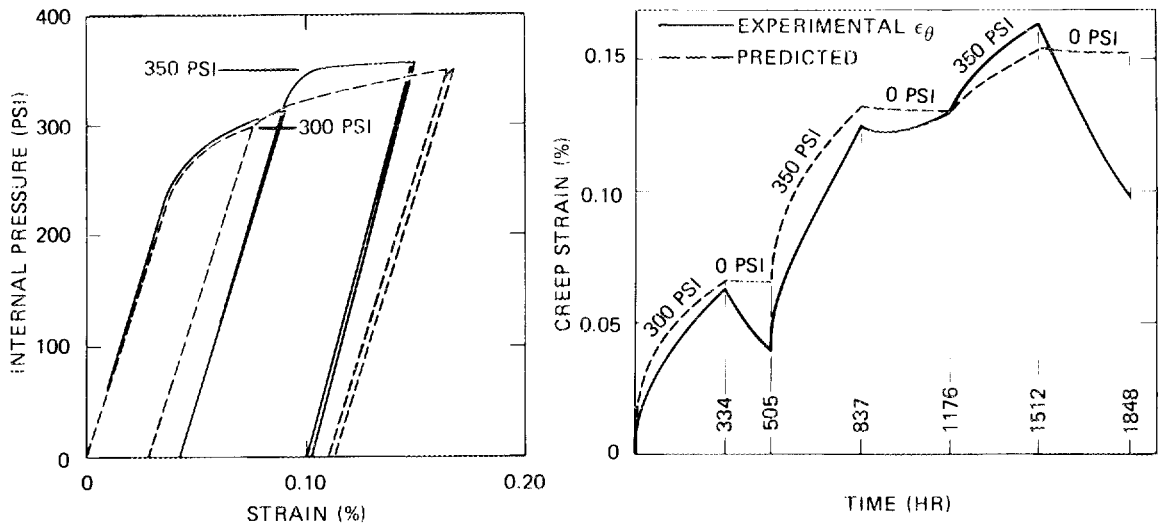

Fig. 2.26. Comparisons between predicted and experimental circumferential strains in the junction regions of specimen NS-2.

2.4.2 Test plan for failure phase of NS-2 (J. A. Clinard, R. C. Gwaltney) (Not previously reported)

A plan was developed for the phase of the test leading to failure of specimen NS-2. Test initiation is planned for early in CY 1979. The activities are reported here to illustrate the role that high-temperature design methods play in the planning phase of structural testing.

Two important questions were addressed in the planning of the NS-2 failure phase:

1. What is an appropriate failure target?
2. What loading histories will produce failure at that target?

2.4.2.1 Selecting the target. The first question was answered (without the aid of actual stress analysis) by employing the biaxial creep-rupture correlation (see Sect. 3.9) and scatter factors associated with the rupture correlation and the stress-strain analysis. This selection process was governed by considerations that included

1. test temperature of 593°C (1100°F) — mandated by availability of materials data and other design considerations,
2. a minimum desired test duration of one day,

3. a maximum desired test duration of two years,
4. a desire for simplicity in the loading histogram with a constant pressure loading being the most desirable selection.

Scatter factors such as the relative creep-rupture strength (R) of the specimen and analysis error (S) in stress predictions heavily influenced planning. The R factor was determined statistically (see Sect. 3.9); the S factor was postulated based on our analysis experience. The factors R and S may be explicitly included in the creep-rupture equation as follows:

$$t_r = RS(48.5453/\sigma)^{8.5551} ,$$

where t_r is time to rupture (hr) and σ is the calculated effective stress ($\sigma = \sqrt{3/2\ \sigma'_{ij}\ \sigma'_{ij}}$) in ksi. R varies from 0.1226 (weak specimen) to 8.156 (strong specimen); R has a range of 66.6. S varies (according to postulation) from 0.249 [due to a 15% underprediction of stress, $S = (0.85)^{8.5551}$] to 9.436 [due to a 30% overprediction of stress, $S = (1.3)^{8.5551}$]; the postulated range on S is 37.9. The range on combinations of R and S is 2524; the magnitude of the range indicates the difficulty in designing this failure test.

In the test design against maximum duration, the controlling factors are the strong specimen (R = 8.158) and the stress overprediction (S = 9.436); against minimum duration, the weak specimen (R = 0.1226) and the stress underprediction (S = 0.249). Test design to incorporate these RS factors is illustrated below:

<u>Design against maximum duration of N hr</u>

1. Expected target = $N/(8.158 \times 9.436) = N/76.98$ hr
2. Minimum test duration = $N/2524$ hr

<u>Design against minimum duration of L hr</u>

1. Expected target = $L/(0.1226 \times 0.249) = 32.8 \times L$ hr
2. Maximum test duration = $2524 \times L$ hr

Thus, we were unable (with a single pressure loading) to confidently select a histogram that met both the one-day and the two-year test limits because this range, two year/one day = 730, was far less than the RS range

of 2524. If we designed to preclude a test duration of more than two years, the possibility of a minimum test duration of (2 × 24 × 265)/2524 = 6.9 hr existed. If we designed to preclude a test duration of less than one day, the possibility of a maximum test duration of 24 × 2524 = 60,576 hr = 6.9 years existed.

Another important consideration was brought into focus so that the question concerning failure target could be answered: at test initiation, it seemed appropriate to emphasize guarding against violation of the minimum test duration. To accomplish this, we placed the short-test limit at *three* days for added safety. This put the "expected" failure target at (3 × 24 × 32.8) = 2362 hr, or about 14 weeks. Note also that this process placed the maximum test duration at 20.7 years. Thus, we decided that if (at constant pressure) the specimen survived for 6-1/2 months, we would then increase the pressure as necessary for compliance with the two-year-long test limit.

2.4.2.2 Selecting the initial pressure. Assuming a target of 2362 hr, we were faced with a remaining question. What pressure will produce rupture (damage = 1) at this time? In answering this question, we conducted (using CREEP-PLAST II[1]) three stress analyses (elastic-plastic-creep) of the nozzle-to-sphere geometry at pressures of 3.792, 4.999, and 5.516 MPa (550, 725, and 800 psi). Each analysis was carried out to as long a time as practical. Table 2.4 shows the resulting analysis time, t_{end}, and the accumulated damages, D_{end} [based on time fractions and the creep-rupture correlation in Eq. (2.1) with RS = 1]. Table 2.5 gives additional analysis information concerning the effective membrane stress in the sphere, σ_{sphere}; the maximum effective stress at the start of creep, σ_{max} at t_o; and the maximum effective stress at the end of the analysis, σ_{max} at t_{end}. The stress histories at the maximum damage locations are depicted in Fig. 2.27. The damage histories are depicted in Fig. 2.28.

Using the calculated damage curves of Fig. 2.28, an explicit expression for damage as a function of time and pressure was developed. Using, in turn, this expression (and setting damage = 1), the estimated time to rupture was solved as a function of pressure, and the results are plotted as Fig. 2.29(*a*). In Fig. 2.29(*b*), the range of RS is illustrated.

Table 2.4. Analysis time and accumulated damage for the three constant-pressure stress/failure analyses of the nozzle-to-sphere geometry

Material is type 304 stainless steel at 593°C (1100°F)

Internal pressure, p [MPa (psi)]	Analysis time, t_{end} (hr)	Damage[a] at t_{end}, D_{end}
3.792 (550)	26,778	2.25
4.999 (725)	636	0.54
5.516 (800)	200	0.46

[a]This is the maximum damage in the structure. In each case, it was calculated to occur in the fillet.

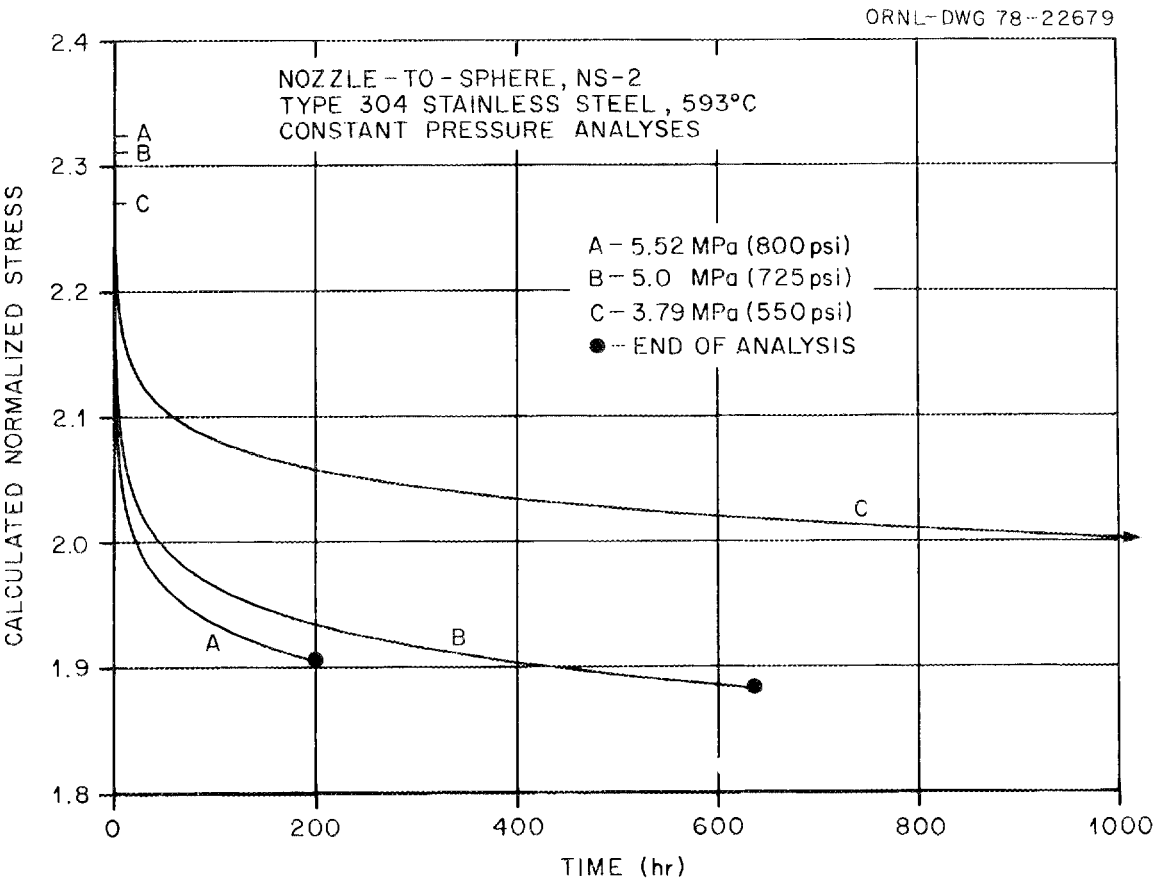

Fig. 2.27. Normalized stress (ratio of effective stress to stress in the sphere) vs time response at the location of maximum creep damage in the nozzle-to-sphere model NS-2. Three analyses were performed for different constant internal pressures. In each analysis, maximum stress (and, thus, maximum damage) occurred in the transition region between nozzle and sphere.

Table 2.5. Additional analysis information for NS-2

p [MPa (psi)]	σ_{sphere} [MPa (ksi)]	σ_{max} at t_o [MPa (ksi)]	σ_{max} at t_{end} [MPa (ksi)]	r^a at t_o	r^a at t_{end}
3.792 (550)	57.7 (8.375)	131.3 (19.05)	110.5 (16.03)	2.27	1.91
4.999 (725)	76.1 (11.04)	176.0 (25.52)	143.3 (20.78)	2.31	1.88
5.516 (800)	84.0 (12.18)	194.8 (28.25)	160.4 (23.26)	2.32	1.91

[a] r is the ratio of σ_{max} to σ_{sphere}.

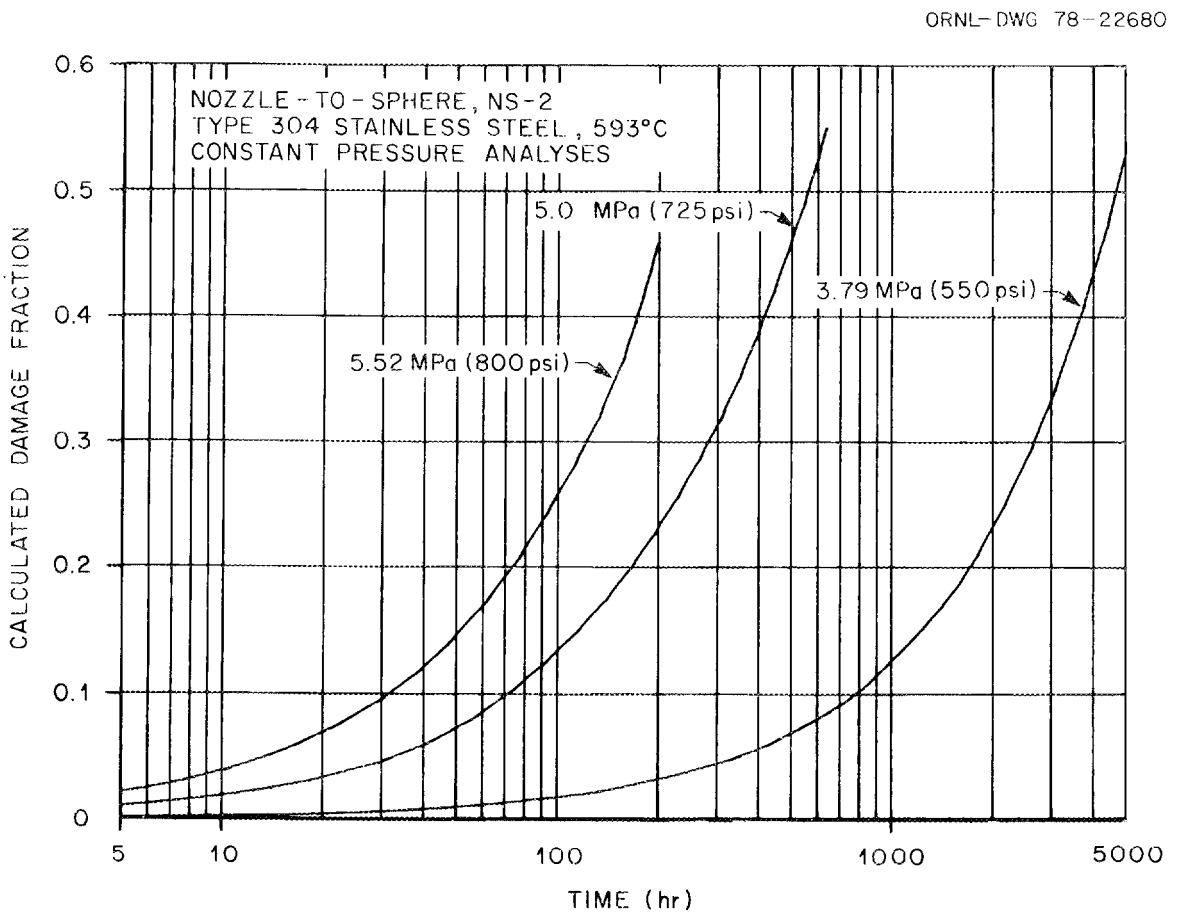

Fig. 2.28. Calculated damage vs time for NS-2. Stress responses depicted previously in Fig. 2.27 were employed as input (to a time-fraction damage model) for these computations of creep damage.

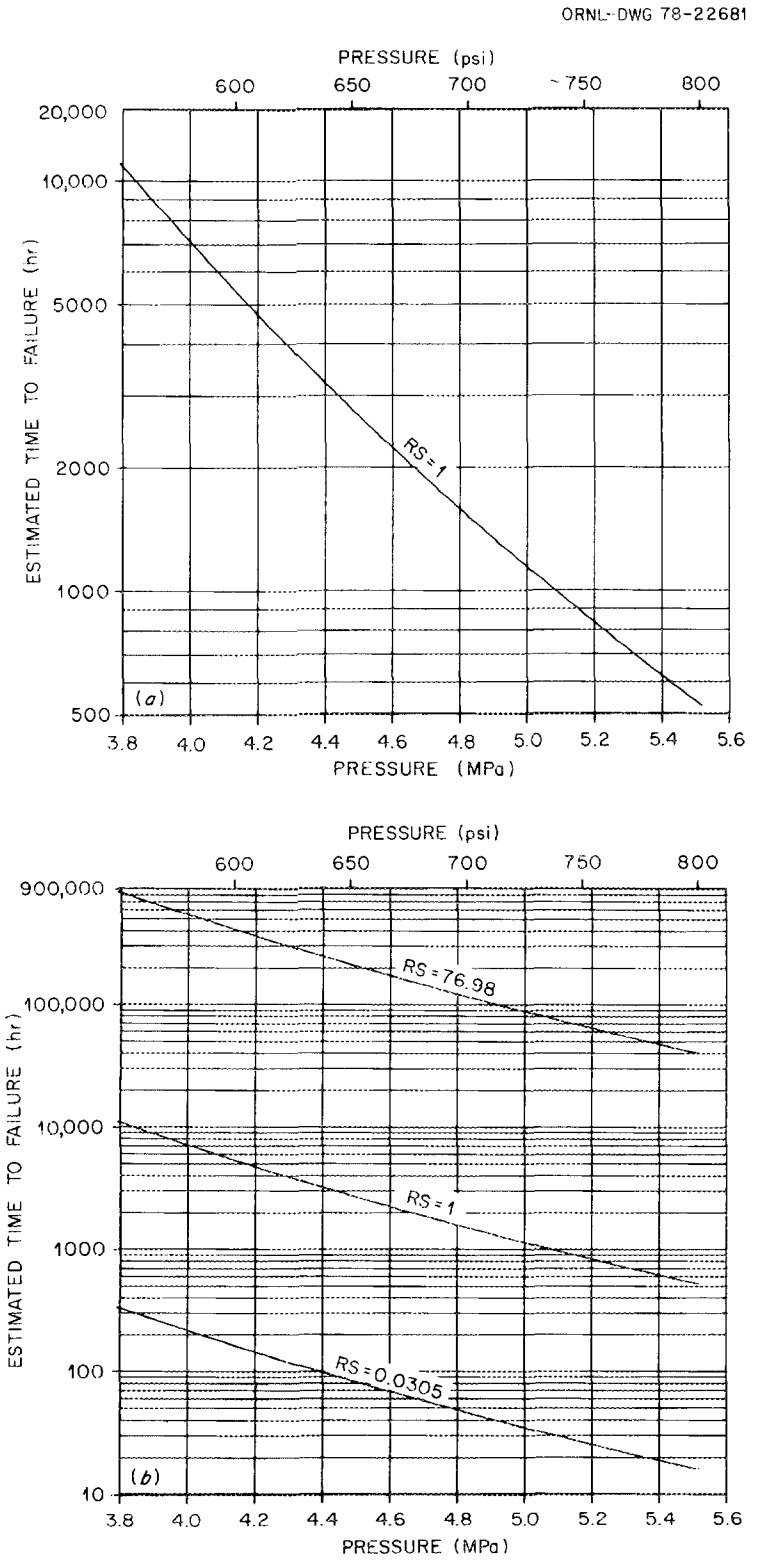

Fig. 2.29. Estimated time to rupture (damage = 1) as a function of applied internal pressure for NS-2. (*a*) Estimation based on *RS* scatter = 1, the "normal" condition. (*b*) Curves showing the effects of the postulated range of *RS* on the estimation of time to rupture.

For the estimated time-to-failure curve, Fig. 2.29 (*a*) is enlarged in Fig. 2.30 for pressures between 4.5 and 4.9 MPa. The answer to our question concerning pressure selection is also illustrated here. A pressure of 4.571 MPa (663 psi) was selected as that required for creep rupture at the failure target time of 2362 hr.

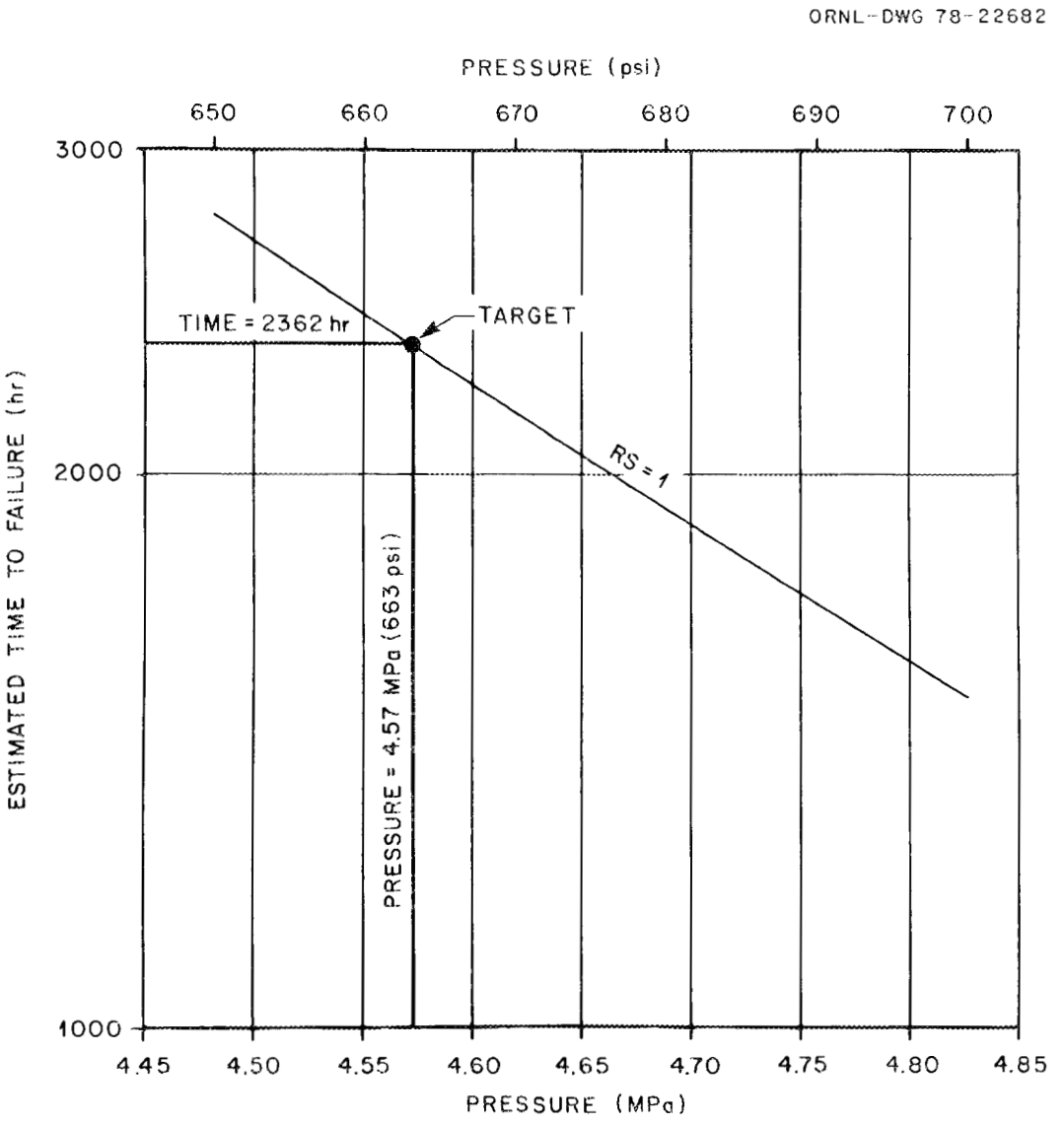

Fig. 2.30. Illustration of selection of the appropriate pressure to produce failure at the target. Note that the curve of time to rupture vs pressure is a simple enlargement of the curve plotted in previous Fig. 2.29(*a*).

In summary, the process of test definition was based, in part, on statistical observation and, in part, on postulations and analysis. In our estimation, there exists about a 50% chance that the specimen will fail by the target of 2362 hr (14 weeks). There is little chance that the specimen will fail in less than one day. Also, by using the 6-1/2-month "reevaluation" target, we will be able (if necessary) to adjust the pressure to meet the two-year-long test limit.

2.5 High-Temperature Strain Gage Development and Verification

J. E. Smith

(Last reported in ORNL-5433, pp. 131-133)

The systematic drift test (CMB-1) passed the 10,000-hr duration mark during this report period. This test is a continuing experiment being conducted with a constant-moment beam calibration apparatus (described in Ref. 10) and consists of two differential capacitance strain gages (Boeing-HITEC) and one CERL-Planer capacitive gage. Systematic drift of the gages was monitored while being held at a temperature of 593°C (1100°F). The gages used were as follows:

1. one Boeing-HITEC differential capacitance gage — 25.4-mm (1-in.) gage length,
2. one Boeing-HITEC differential capacitance gage — 6.4-mm (1/4-in.) gage length,
3. one CERL-Planer capacitive gage — 19-mm (3/4-in.) gage length Model C-5.

The test, originally targeted for 10,000 hr, was continued past that point to obtain maximum duration for the CERL-Planer gage, which was added to the beam after 2400 hr during a deactivation of the test.[11]

Average drift rates taken at different periods during the test are shown in Table 2.6. Also shown are the drift rates for 2400 hr that were measured for two Boeing gages during a similar test at Boeing Aerospace.[12]

This continuing test has verified and established the excellent stability of capacitive gages using air as the dielectric. It has also identified areas for further study as the development and verification

Table 2.6. Systematic drift for capacitive strain gages at 593°C (1100°F)

Gage	Average drift rate (με/hr) at various times		
	2400 hr	5000 hr	10,000 hr
Boeing-HITEC 6.4 mm (1/4 in.) length	0.028	0.016	0.0095
Boeing-HITEC 25.4 mm (1 in.) length	0.027	0.057	0.0495
CERL-Planer 19 mm (3/4 in.) length	0.018	0.014	0.013[a]
Boeing 25.4 mm (1 in.) length[b]	0.04		
Boeing 25.4 mm (1 in.) length[b]	0.04		

[a]Data for 9600 hr.
[b]Reference 12.

tests are continued. Of particular interest are

1. effects of power outages on gage stability,
2. effects of thermal cycling on the differential capacitance gages,
3. cause of short-term excursions seen in both structural tests and stability experiments.

Investigation of these areas will be emphasized in the future to further minimize uncertainties in strain measurements on high-temperature structural tests.

2.6 International Piping Benchmark Problem Effort

W. J. McAfee J. M. Corum

(Last reported in ORNL-5433, pp. 133-140)

A preferred format for presentation of solution to the International Atomic Energy Agency/International Working Group on Fast Reactors (IAEA/IWGFR) problems was prepared and distributed to the participants. This was intended primarily as a guideline, with latitude for individual author's

style and experience. The format was structured to make each presentation as complete and self-contained as possible and to make the different presentations consistent with one another. The recommended format is shown below.

FORMAT FOR REPORTING PIPING BENCHMARK PROBLEM SOLUTIONS

1. Computer Program
   a. Program name or identification.
   b. Brief description delineating the essential program features in conjunction with supporting references.*

2. Structural Model
   a. Describe the structural idealization used to model the test assembly. Such parameters as wall thickness, pipe diameter, elbow radius, attachment pipe lengths, etc., should be described if other than those of the actual test assembly.
   b. Describe the finite-element grid, type of element(s), etc. Inclusion of plots of the finite-element grid would provide additional visualization of the model.
   c. Describe the boundary conditions and any idealizations employed.

3. Constitutive Equations
   a. Describe implementation of plasticity model.
      i. Flow rule
      ii. Hardening law
   b. Describe implementation of creep model.
      i. Creep formulation (law)
      ii. Type of hardening and/or state parameters used

---

*References throughout this discussion are intended to mean documents that are readily available to the participants in this activity. If proprietary information/programs are involved, state this restriction but give as much information as is permitted.

4. Materials Properties
   a. The data in the form used by the computer program should be indicated.
   b. Where tabularized data were used, the type of interpolation should be specified.
   c. Correlations, tables, curves, etc., other than those supplied with each problem should be described in sufficient detail and referenced.

5. Results
   a. Tabular comparison of experiment and analyses (stress and/or strain/deflection as specified in the problem statement).
   b. Graphical presentation of above comparisons.
   c. Additional analytical results at the author's discretion of spatial distributions of stress or strain, or of strain/deflection time behavior of regions, or of points that exhibit characteristics of particular interest, for example, transition regions, stress concentration regions, etc.

6. Closure
   a. Comment on specific difficulties, or lack thereof, in setting up and solving the individual benchmark problem. Where applicable, assess the method(s) used to overcome the difficulties.
   b. Provide a general discussion and assessment of the comparison between experimental and analytical results. Consider factors that may have influenced the comparison such as the finite-element model chosen, the models for materials behavior used, the application of boundary conditions, etc.
   c. Discuss, if possible, the applicability, advantages, etc., of techniques used with respect to the problem solved. For example, if a simplified analysis was done, are the results adequate when cost and time savings are considered, or would a more detailed analysis be justified?

d. As an option, provide any comments on the benchmark problem such as better presentation, information lacking, suggestions for additional types of benchmark problems, etc.

A number of solutions were also received late in the report period. These are summarized in Table 2.7. It is expected that only a few more solutions will be received. When all the results are received, they will be organized and prepared in report form for publication.

Table 2.7. Summary of international piping benchmark problem solutions received

Author(s)	Problem No.		
	1	2	3
Hans-Peter Knapp and Jan Prij; Cooperative effort between Interatom and ECN		X	
A. K. Dhalla and S. Z. Newman; Westinghouse Advanced Reactors Division		X	
Osamu Watanabe and Hideomi Ohtsubo; Through Power Reactor and Nuclear Fuel Development Corporation, Japan	X		
K. Iwata, S. Asai, and H. Takeda; Through Power Reactor and Nuclear Fuel Development Corporation, Japan		X	
Akihiko Suzuki; Through Power Reactor and Nuclear Fuel Development Corporation, Japan		X	
Shinji Sakata, Tasuku Shimizu, and Masaharu Sumikawa; Through Power Reactor and Nuclear Fuel Development Corporation, Japan		X	
H. Bung, G. Clement, A. Hoffman, and H. Jakubowieg; Centre D'Etudes Nucleaires, De Saclay, France	X	X	X

References

1. J. A. Clinard, *CREEP-PLAST II User's Manual*, ORNL/TM-5868 (May 1978).

2. J. A. Clinard et al., "Capped Cylindrical Shell Test CC2," *High-Temperature Structural Design Program Prog. Rep. Dec. 31, 1977*, ORNL-5374, pp. 79-87.

3. W. K. Sartory, "Capped Cylindrical Shell Test CC2," *High-Temperature Structural Design Program Prog. Rep. June 30, 1978*, ORNL-5433, p. 125.

4. W. K. Sartory, *PLACRE User's Manual*, ORNL/TM-5626 (February 1977).

5. J. M. Corum, "Appendix: Material Property Data for Elastic-Plastic-Creep Analyses of Benchmark Problems," *Pressure Vessels and Piping: Verification and Qualification of Inelastic Analysis Computer Programs*, J. M. Corum and W. B. Wright, eds., American Society of Mechanical Engineers, G00088, New York, 1975.

6. J. A. Clinard, "Creep Equation," *High-Temperature Structural Design Program Prog. Rep. June 30, 1978*, ORNL-5433, pp. 137-40.

7. ASME Code Case 1592-13, *Class I Components in Elevated Temperature Service, Section III, Division 1, ASME Boiler and Pressure Vessel Code, Case Interpretations*, American Society of Mechanical Engineers, New York (September 1977).

8. R. W. Swindeman, "Creep-Rupture Correlations for Type 304 Stainless Steel Heat 9T2796," *Structural Materials for Service at Elevated Temperatures in Nuclear Power Generation, MPC-1*, A. O. Schaefer, ed., American Society of Mechanical Engineers, New York, 1975.

9. J. M. Corum, "Material Properties for Inelastic Structural Analysis," *High-Temperature Structural Design Methods for LMFBR Components Quart. Prog. Rep. March 31, 1974*, ORNL-4977, pp. 134-42.

10. J. E. Smith, "High-Temperature Strain Gage Development and Evaluation," *High-Temperature Structural Design Program Prog. Rep. June 30, 1975*, ORNL-5087, pp. 118-23.

11. J. E. Smith, "High-Temperature Strain Gage Development/Verification," *High-Temperature Structural Design Program Prog. Rep. Dec. 31, 1977*, ORNL-5374, pp. 90-92.

12. Daryl Harting, Boeing Aerospace, personal communication, 1975.

3. DESIGN CRITERIA AND RULES FOR TIME-DEPENDENT DEFORMATION AND FAILURE

R. L. Huddleston

The objective of this subtask is to assess and develop design rules and procedures aimed at precluding time-dependent failure through excessive deformation, cracking, and rupture and to support the development and evaluation of codes and standards in this area.

An understanding of factors leading to failure by excessive deformation, cracking, or rupture and the ability to conservatively model their effects is of primary importance to the development of a verified design technology for high-temperature reactor system components. These components will be subjected to histories of steady and fluctuating multiaxial loads and temperatures for which material response is both time and cycle dependent. The need to provide safe, cost-effective designs for these conditions has provided the motivation for detailed, systematic investigations of creep rupture, low-cycle fatigue, creep fatigue, and the associated mechanisms that lead to damage accumulation and failure at high temperature. These investigations have included the preparation of interpretive reports in 1972 and 1975[1,2] which summarize and place in perspective current knowledge on these subjects and suggest future courses of action leading to a better understanding of damage accumulation and improved methods for designing components for high-temperature service. The most recent report[2] was a comprehensive general assessment of time-dependent fatigue.

An overview of ORNL's failure-related activities was presented in the previous report in this series.[3] During this report period, failure activities included both uniaxial and multiaxial creep-rupture and time-dependent fatigue exploratory tests and assessments of failure criteria and design rules. Structural tests to failure, which are reported in Chapter 2, are also an integral part of the overall failure program.

3.1 Creep-Rupture Failure Under Uniaxial and Multiaxial Conditions

R. L. Huddleston C. C. Schultz
W. E. Leyda

(Last reported in ORNL-5433, p. 145)

This project was initiated in January 1972 and was completed during the current report period when the final biaxial tubular specimen BWTR-5 failed after 21,840 hr at 593°C (1100°F) and an effective stress level of 119.4 MPa (17.32 ksi). The study was conducted under subcontract by the Babcock & Wilcox Company. The objective of the study was to provide a better understanding of the accumulation of creep damage and the methods of evaluating and predicting creep failure under conditions of multiaxial and time-dependent loadings. Test specimens were made of type 304 stainless steel (reference heat 9T2796) and tested at 593°C (1100°F). Testing primarily consisted of constant-load uniaxial tests, constant-load multiaxial tests, and uniaxial step-load tests. A final report[4] covering the constant-load uniaxial and multiaxial tests was prepared and distributed during this period. Assessments of the uniaxial and multiaxial constant-load data have been reported by Blass.[5,6] The step-load tests were covered in earlier reports.[7,8] A summary of the specimen designs and data generated follows.

3.1.1 Constant-load uniaxial tests

Nineteen constant-load uniaxial creep-rupture tests were performed using the two smooth, solid-bar specimen designs shown in Figs. 3.1 and 3.2. Specimens were fabricated from 16-mm (5/8-in.) bar stock and subsequently annealed at 1093°C (2000°F) for 30 min. Test results are summarized in Table 3.1, with log-log plots of stress vs time to rupture and stress vs minimum creep rate in Figs. 3.3 and 3.4, respectively.

3.1.2 Constant-load multiaxial tests

Eleven constant-load multiaxial tests were conducted using the tubular specimen design shown in Fig. 3.5. Specimens were fabricated from nominal 48-mm-diam (1-7/8-in.) bar. The nominal 38-mm-diam (1.5-in.),

ORNL–DWG 78–22057

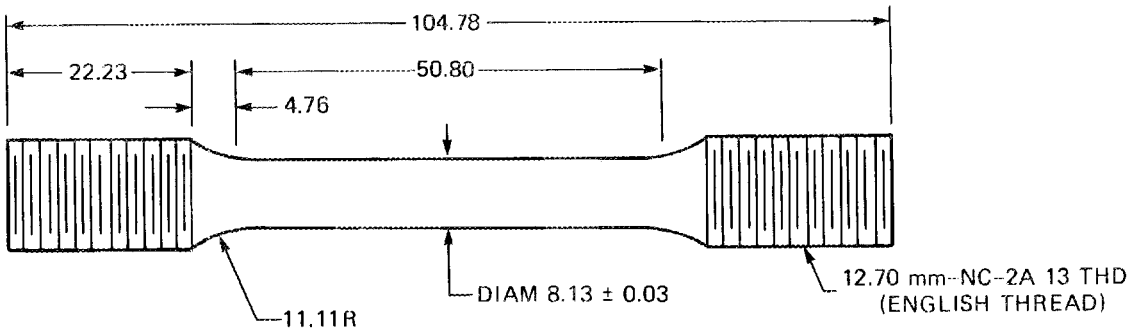

Fig. 3.1. Threaded uniaxial specimen for BWR and BWI tests [dimensions in millimeters (1 in. = 25.4 mm)].

ORNL–DWG 78–22058

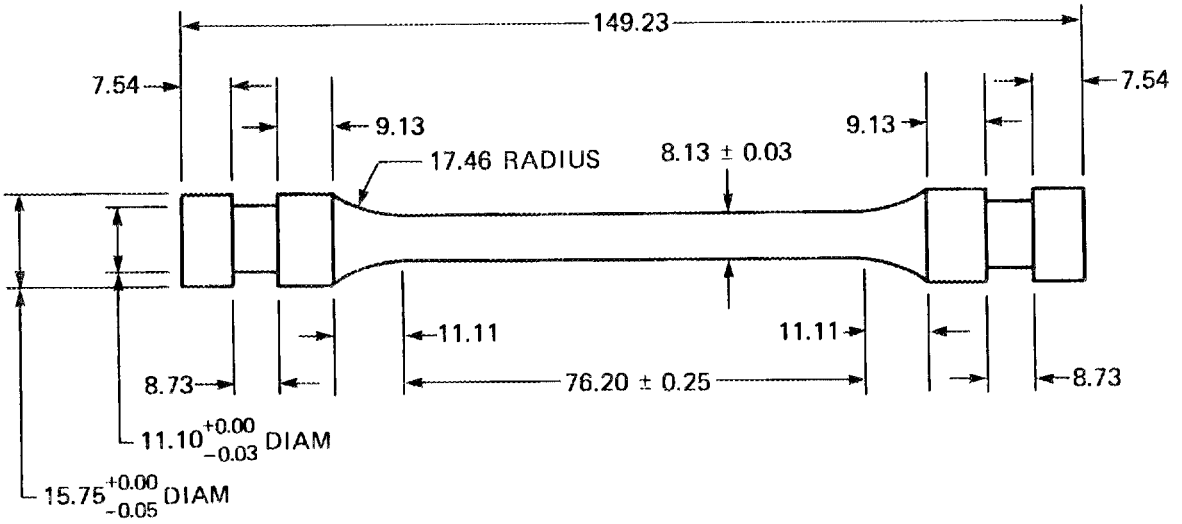

Fig. 3.2. Buttonhead uniaxial specimen for BWC and BWLF tests [dimensions in millimeters (1 in. = 25.4 mm)].

Table 3.1. Summary of constant-load, uniaxial creep-rupture tests at 593°C (1100°F) in air for 16-mm-diam (5/8-in.) type 304 stainless steel bar (heat 9T2796) reannealed 30 min at 1093°C (2000°F)

Test No.	Stress [MPa (ksi)]	Total strain on loading[a] (%)	Time to secondary creep (hr)	Minimum creep rate (%/hr)	Time to tertiary creep[b] (hr)	Intercept creep strain[c] (%)	Rupture time[d] (hr)	Fracture elongation[e] (%)	Reduction in area (%)
BWC-1	30 (207)	5.0					187 R	19.0	30.5
BWR-1	30 (207)	7.80					138 R	21.5	32.9
BWC-2	28 (193)	6.35	40	0.016	195	0.50	227 R	13.0	20.4
BWR-2	28 (193)	5.75	40	0.022	230	0.65	368 R	16.5	18.3
BWR-13	28 (193)	6.57	60	0.023	215	0.88	276 R	16.5	18.3
BWC-9	28 (193)	4.25	85	0.021	335	1.16	415 R	18.3	25.2
BWC-3[f]	25 (172)	4.20	80	0.0065	500	0.45	667 R	12.7	12.0
BWR-3	25 (172)	3.90	100	0.0079	585	0.71	948 R	17.0	23.2
BWC-4	22 (152)	4.00	175	0.0014	1,400	0.60	2,130 R	10.7	13.7
BWR-4	22 (152)	3.30	160	0.0030	1,170	0.72	2,026 R	12.5	16.6
BWC-5B	20 (138)	1.83	5,000	0.000165	8,700	1.84	9,584 R	10.5	12.0
BWR-14	20 (138)	2.02	3,200	0.00044	5,800	1.88	6,868 R	8.5	13.1
BWC-10	20 (138)	1.58	4,000	0.00021	8,000	2.30	9,450 R	9.3	14.3
BWI-1	19.5 (134)	0.9	5,600	0.00008	13,000	3.3	D		
BWI-2	19.5 (134)	1.07	5,400	0.00010	13,000	3.2	16,891 R	13.0	11.5
BWI-3	19.5 (134)	1.50	4,800	0.00019	9,000	3.2	11,608 R	11.0	13.3
BWI-4	19.5 (134)	0.98	7,000	0.00005	NA[g]	3.5	D		
BWI-5	19.5 (134)	1.65	3,800	0.00026	8,300	2.7	D		
BWI-6	19.5 (134)	1.30	3,800	0.00023	7,500	2.8	D		
BWR-6	19 (131)	1.48	6,000	0.000073	13,500	2.90	17,547 R	9.5	12.6
BWR-9	18 (124)	1.15	7,500	0.000036	18,000	2.40	24,495 R	8.5	13.8
BWR-11	17 (117)	1.35	6,000	0.000033	20,000	1.60	25,942 R	7.5	13.2
BWR-7	16 (110)	0.60	6,000	0.000009	32,000	1.15	44,296 R	6.0	13.1

[a]All specimens step loaded at 1.87 ksi increments, except test BWC-5B, which was step loaded at 1.49 ksi increments.

[b]Time to tertiary creep based on the 0.2% offset from the minimum rate line.

[c]Intercept creep strain does not include the elastic and initial plastic components.

[d]R = rupture, D = discontinued.

[e]Elongation over 3 in. in BWC series; over 2 in. in BWR and BWI series.

[f]Failure occurred near end of gage length.

[g]NA = not available.

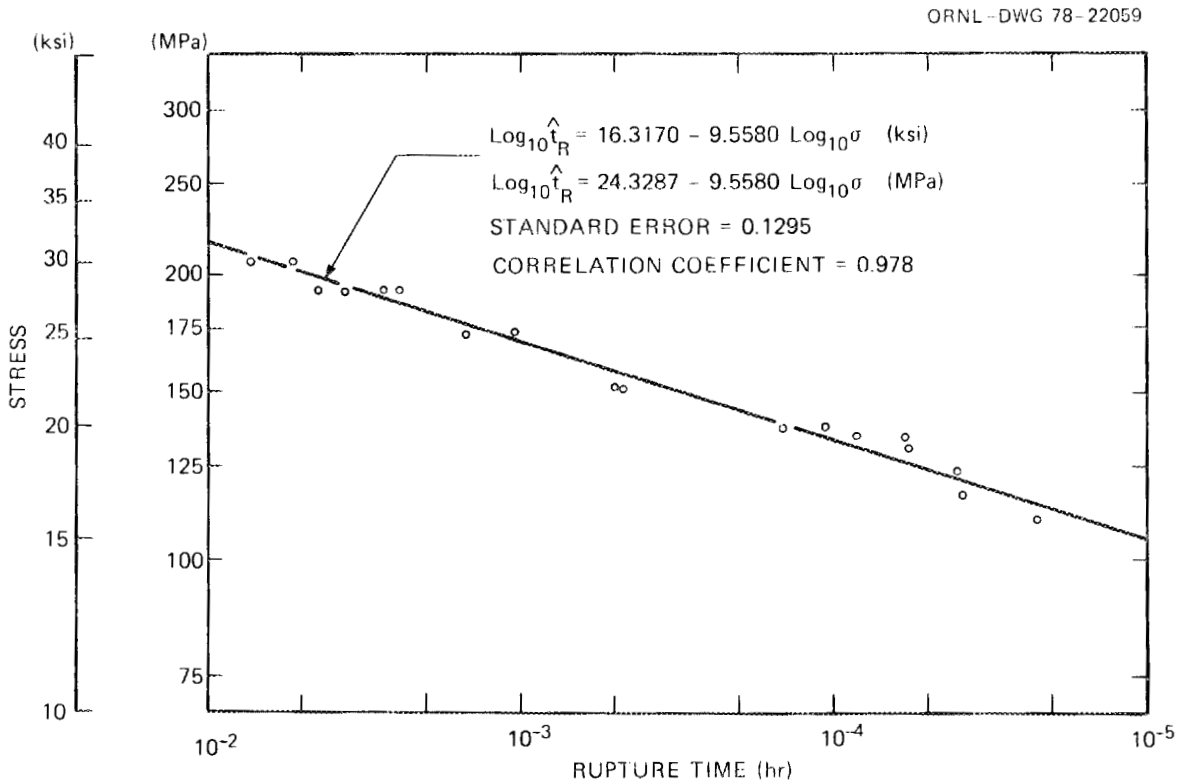

Fig. 3.3. Time to rupture from constant-load, uniaxial tests of 304 stainless steel (heat 9T2796) at 593°C (1100°F); 16-mm-diam (5/8-in.) bar reannealed at 1093°C (2000°F) for 30 min.

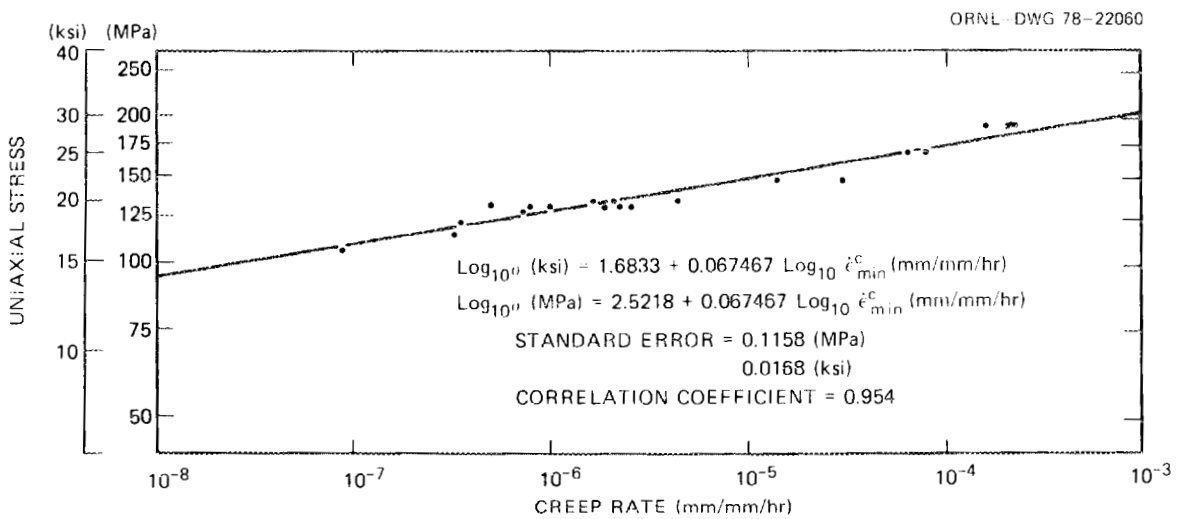

Fig. 3.4. Minimum creep rates from constant-load, uniaxial tests of 304 stainless steel (heat 9T2796) at 593°C (1100°F); 16-mm-diam (5/8-in.) bar reannealed at 1093°C (2000°F) for 30 min.

ORNL-DWG 78-22061

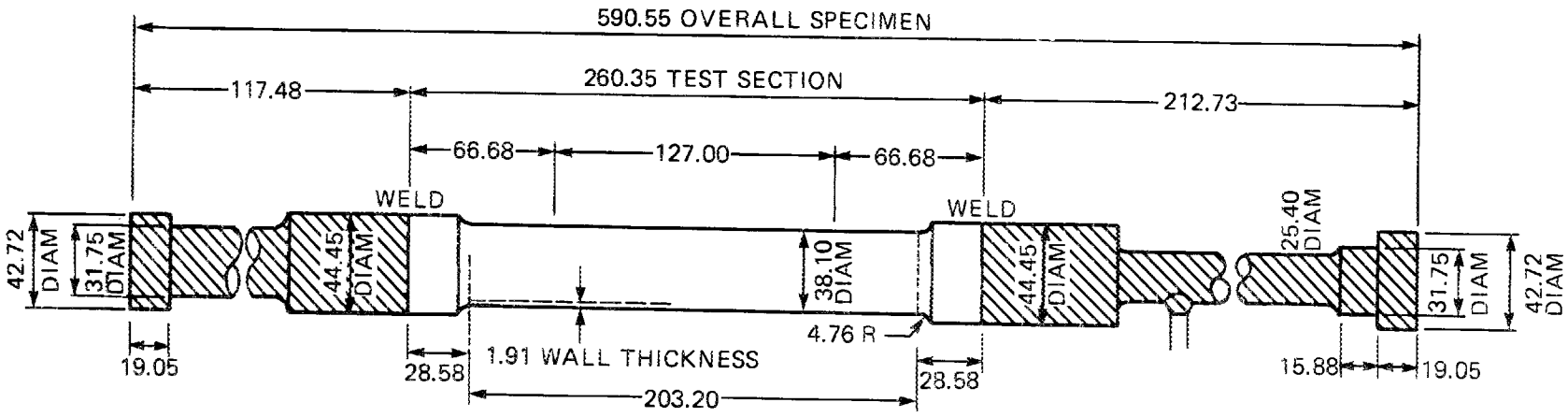

Fig. 3.5. Tubular specimen [dimensions in millimeters (1 in. = 25.4-mm)].

1.9-mm (0.075-in.) wall, 203-mm (8.0-in.) gage length specimens were loaded by internal pressure and axial tension. Tests were conducted with circumferential to axial stress ratios of 0 (uniaxial), 1/2, 1, and 2. Test conditions and numerical results are summarized in Table 3.2. Note that all specimens failed at a common axial location. The specimen temperature was determined to be 593°C (1100°F) at both the ends and center of the gage length. However, at the failure location, the temperature was somewhat higher. Additional tests to establish this temperature are to be conducted. Preliminary tests indicate that the peak temperature was in the 600 to 604°C (1112 to 1120°F) range.

The resulting creep-rupture data are plotted in Fig. 3.6, along with the least-squares line for the uniaxial solid-bar data taken from Fig. 3.3. No attempt was made to compensate for the "hot spot" at the rupture location. However, Schultz and Leyda[4] made what they felt was a conservative adjustment of 11°C (20°F) to the uniaxial line. This adjustment reduced the difference between the uniaxial and biaxial log t_R by about one-half.

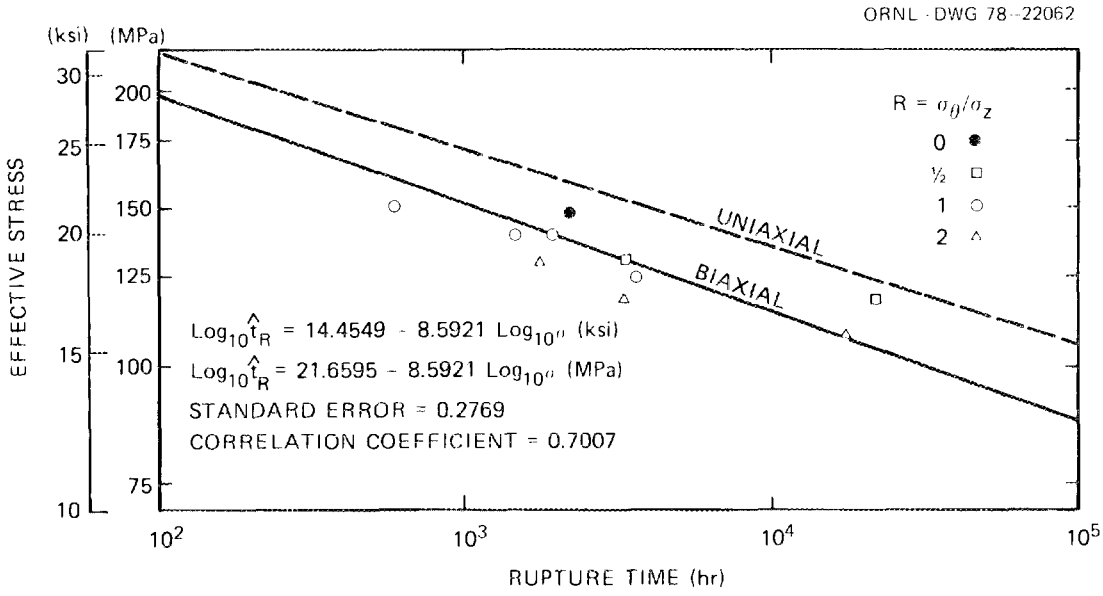

Fig. 3.6. Time to rupture as a function of Mises effective stress for multiaxial tubular specimens of 304 stainless steel (heat 9T2796) tested at 593°C (1100°F) with constant internal pressure and axial tension loadings.

Table 3.2. Summary of multiaxial creep-rupture test conditions and results for 304 stainless steel (heat 9T2796) tubular specimens tested in air at 593°C (1100°F) with internal pressure and axial tension loadings; material reannealed 30 min at 1093°C (2000°F)

Test No.	Internal pressure [MPa (psi)]	Additional axial load [N (lb)]	Average stress [MPa (psi)][a]			Rupture time (hr)	Measured minimum creep rates (in./in./hr)	
			Circumferential	Axial	Mises effective		Circumferential	Axial
BWTR-1	0 (0)	32,632 (7,336)	0 (0)	151 (21,850) 143 (20,730)	151 (21,850) 143 (20,730)	1,997		9.8×10^{-6}
BWTR-2	15.9 (2,300)		151 (21,850) 143 (20,700)	75 (10,925) 68 (9,800)	130 (18,920) 124 (17,940)	1,713		3.1×10^{-7}
BWTR-3	15.9 (2,300)	16,316 (3,668)	151 (21,850) 143 (20,700)	151 (21,850) 143 (20,730)	151 (21,850) 143 (20,710)	584	1.6×10^{-5}	3.2×10^{-5}
BWTR-4	7.9 (1,150)	24,465 (5,500)	75 (10,925) 71 (10,350)	151 (21,850) 147 (21,280)	130 (18,920) 127 (18,430)	3,336		8.2×10^{-6}
BWTR-5	7.3 (1,053)	22,401 (5,036)	69 (10,000) 65 (9,480)	138 (20,000) 134 (19,490)	119 (17,320) 116 (16,880)	21,840		4.9×10^{-7}
BWTR-6	14.5 (2,105)		138 (20,000) 131 (18,950)	69 (10,000) 62 (8,970)	119 (17,320) 113 (16,410)	3,272	3.4×10^{-6}	6.3×10^{-8}
BWTR-7	14.5 (2,105)	14,937 (3,358)	138 (20,000) 131 (18,950)	138 (20,000) 131 (18,980)	138 (20,000) 131 (18,960)	1,925	4.6×10^{-6}	5.8×10^{-6}
BWTR-11[b]	6.5 (948)	20,164 (4,533)	62 (9,000) 59 (8,530)	124 (18,000) 121 (17,540)	107 (15,590) 105 (15,190)	6,432		
BWTR-12	13.1 (1,895)		124 (18,000) 118 (17,060)	62 (9,000) 56 (8,080)	107 (15,590) 102 (14,780)	17,030	2.9×10^{-7}	4.0×10^{-8}
BWTR-13	13.1 (1,895)	13,443 (3,022)	124 (18,000) 118 (17,060)	124 (18,000) 118 (17,080)	124 (18,000) 118 (17,070)	3,595	1.7×10^{-6}	2.6×10^{-6}
BWTR-14	14.5 (2,105)	14,937 (3,358)	138 (20,000) 131 (18,950)	138 (20,000) 131 (18,980)	138 (20,000) 131 (18,960)	1,461		5.3×10^{-6}

[a]The first stresses shown are based on the mean diameter formula, and the second stresses shown are actual average stresses. The radial component of stress has been ignored in the determination of the effective stress. 3.8 cm (1.5 in.) outside diameter and 0.19 cm (0.075 in.) wall thickness.

[b]After 1825 hr, the loading conditions were changed to the conditions of test BWTR-13.

Also note that failure for the solid-bar specimens was taken as separation, but "failure" for the tubular specimens was taken as a loss of pressure. As a whole, without the 11°C (20°F) adjustment, the biaxial tubular data fall significantly below the uniaxial solid-bar data. On the average, failure time for a tubular specimen is ∿26% of the failure time for a corresponding uniaxial solid-bar specimen.

Measured creep rates for the biaxial specimens are also summarized in Table 3.2. Due to experimental difficulties, creep rates were not obtained for all specimens and, in several cases, were obtained only for the axial direction.

The creep flow rule in RDT Standard F9-5T [Levy-Mises-Reuss (L-M-R) flow rule] is used here to compare the measured biaxial minimum creep rates with the uniaxial data (see the equation in Fig. 3.4). The L-M-R equation is given by

$$\dot{\varepsilon}^{c}_{ij} = \frac{3}{2}\,\frac{\dot{\bar{\varepsilon}}(\bar{\sigma},T)}{\bar{\sigma}}\,\sigma'_{ij} \ , \tag{3.1}$$

where

$\dot{\varepsilon}^{c}_{ij}$ = creep strain rate component,
$\dot{\bar{\varepsilon}}$ = effective creep rate,
$\bar{\sigma}$ = effective stress,
T = temperature,
σ'_{ij} = deviatoric stress component.

$\dot{\bar{\varepsilon}}(\bar{\sigma},T)$ is determined from the equation shown in Fig. 3.4 to be

$$\dot{\varepsilon}^{c}_{min} = (1.12 \times 10^{-25})\bar{\sigma}^{14.82} \ . \tag{3.2}$$

Predicted and measured creep rates are compared in Fig. 3.7, with the measured rates being significantly greater than the predicted values based on the uniaxial data and the L-M-R equation.

For additional details of the test procedures, individual test descriptions, deformation data, and additional data correlations, the reader is referred to Ref. 4.

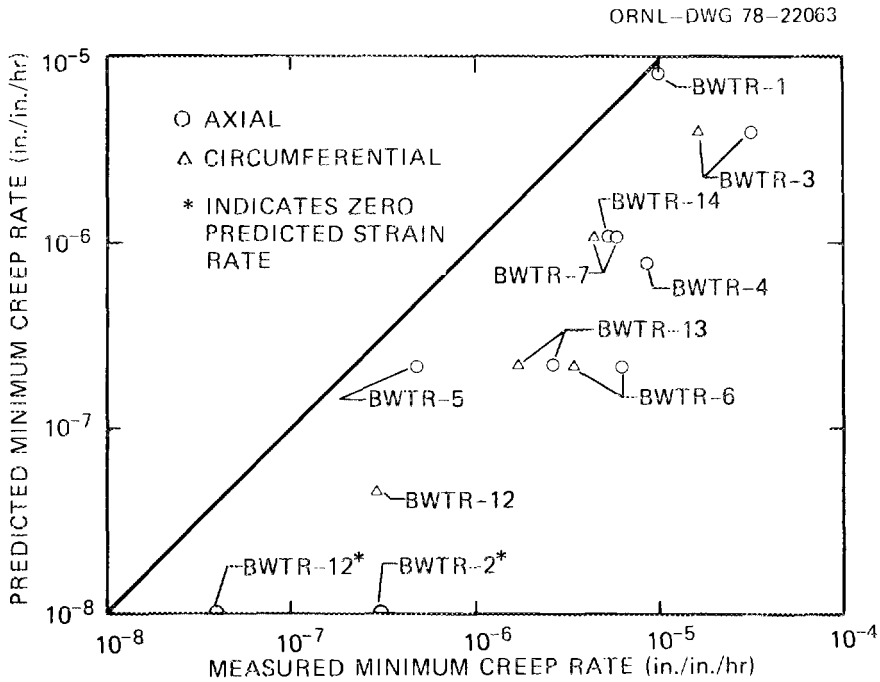

Fig. 3.7. Comparison of measured circumferential and axial minimum creep rates obtained in multiaxial tests of 304 stainless steel (heat 9T2796) tubular specimens with predicted rates based on uniaxial solid bar specimen data and the Levy-Mises-Reuss equation.

3.1.3 Uniaxial step-load tests

The objective of these tests was to define failure and assess cumulative damage rules for homogeneous variable stress conditions. Thirteen uniaxial step-load tests were run using the BWC and BWR (Babcock & Wilcox creep and rupture) specimen designs given in Figs. 3.1 and 3.2. A typical loading histogram included three constant-stress hold periods. The typical sequence was a constant-stress hold followed by a hold at a higher stress, with a final hold at a reduced stress level. Loading histories, failure times, and linear time fractions are summarized in Table 3.3. Strain histories are summarized in Ref. 7.

Summations of linear time fractions at failure ranged from 0.58 to 1.42, with a standard deviation from the average of the entire set being 0.27. Essentially duplicate loading histograms were applied to six sets of two specimens each (i.e., specimen sets A through F) with some pairs of tests such as sets, C, D, and F demonstrating reasonably good

Table 3.3. Uniaxial step-load rupture test results for type 304 stainless steel at 593°C (1100°F) (heat 9T2796)

Specimen set No.	Test No.	Stress [MPa (ksi)]	Total strain on loading (%)	Time at load (hr)	Life fraction (%)	Elongation (%)	Reduction in area (%)
A	BWC-6	110 (16)	0.42	3,871	6		
		172 (25)		136	15		
		138 (20)		9,251	121		
				13,258 R	142	9.0	16.0
A	BWR-10	110 (16)		3,871	6		
		172 (25)		136	15		
		138 (20)		5,655	74		
				9,662 R	95	11.5	17.8
B	BWC-7	117 (17)	0.76	3,699	10		
		172 (25)		136	15		
		138 (20)		5,066	67		
				8,901 R	92	12.0	20.6
B	BWR-8	117 (17)		3,703	10		
		172 (25)		136	15		
		138 (20)		8,901	117		
				12,740 R	142	11.0	13.8
C	BWC-8	124 (18)	1.78	5,071	24		
		172 (25)		136	15		
		138 (20)		5,420	71		
				10,627 R	110	8.0	15.5
C	BWR-12	124 (18)		4,897	24		
		172 (25)		136	15		
		138 (20)		3,996	53		
				9,029 R	92	11.5	17.2
D	BWLF-5B	145 (21)	2.62	500	10		
		172 (25)		200	22		
		145 (21)		1,236	26		
				1,936 R	58	10.3	15.9
D	BWLF-6	145 (21)	3.11	500	10		
		172 (25)		200	25		
		145 (21)		1,214	25		
				1,914 R	60	10.5	14.3
E	BWLF-7	145 (21)	2.25	750	16		
		172 (25)		136	15		
		145 (21)		2,003	42		
				2,889 R	73	12.3	20.5
E	BWLF-3	145 (21)		750	16		
		172 (25)		136	15		
		145 (21)		4,597	96		
				5,483 R	127		
F	BWLF-9	145 (21)	2.21	1,014	21		
		172 (25)		136	15		
		145 (21)		1,816	38		
				2,966 R	74	18.0	16.5
F	BWLF-10	145 (21)	2.47	1,006	21		
		172 (25)		136	15		
		145 (21)		2,286	48		
				3,428 R	84	16.0	18.2
G	BWLF-5	138 (20)	2.06	503	7		
		172 (25)		198	22		
		138 (20)		5,246	69		
				5,947 R	98	12.5	17.0

repeatability while others such as sets B and E demonstrated greater variability in damage at failure. The standard deviation depicting this within-set variation or inability to duplicate a test was 0.18. If the variability seen in damage at failure is due to material and testing variability, as opposed to representing inaccuracy in the linear time-fraction approach to modeling the actual damage behavior, then, given a large enough set of test data, the average damage at failure should approach 1.0. In fact, if one averages the damage at failure for all the tests in Table 3.3, the result is 0.96. The variability in cumulative damage at failure within the duplicate sets and within the uniaxial constant-load data base makes it difficult to assess the linear time fraction approach for predicting failure for a given test. A conservative failure estimate (95% confidence limit) could be made for all the tests summarized in Table 3.3 by adding a safety factor of 1.52 to the time fraction prediction or a safety factor of 1.045 to the stress for which one selects the estimated rupture time.

The range of damage fractions obtained at failure in the step-load tests can be projected knowing the variability in the baseline uniaxial constant-load data. Linear time-fraction damage is represented by

$$D = \sum_{i=1}^{n} \frac{t_i}{(t_R)_i} , \tag{3.3}$$

where (t_R) is the uniaxial constant-stress rupture time for a given stress level i, and t_i is the hold time at level i. Knowing the standard error for the uniaxial data base from which $(t_R)_i$ is estimated, 95% confidence limits on $(t_R)_i$ are approximated by

$$\log\ (\hat{t}_R)_i \pm 2S_E , \tag{3.4}$$

where $(t_R)_i$ is the mean or least-squares fitted value of rupture time and S_E is the standard error. In an analogous manner, approximate 95% confidence limits on damage may be taken as

$$\frac{1}{\text{antilog}\ (2S_E)} \sum_{i=1}^{n} \frac{t_i}{(t_R)_i} \le D \le \text{antilog}\ (2S_E) \sum_{i=1}^{n} \frac{t_i}{(t_R)_i} . \tag{3.5}$$

The standard error, S_E, for the uniaxial data base summarized in Table 3.1 was 0.1295 with antilog $2S_E$ being 1.82. Making this substitution into Eq. (3.3) results in ratios ranging from 0.55 to 1.82. Thus, even if linear time fractions damage were an *exact* cumulative damage theory

$$\sum_{i=1}^{n} \frac{t_i}{(t_R)_i} = 1 \text{ at rupture ,}$$

one would expect material and testing variability to cause sufficient deviation from a damage of 1.0 to produce a range in test data of $\sim 0.55 < D < 1.82$ in step-load tests. All tests conducted by Babcock & Wilcox fell within this range. For a given specimen, the primary means to narrow this expected range is by (1) selecting test materials with minimum variability (which may not represent prototype materials) or (2) improving load and temperature control.

3.2 Investigation of Cumulative Creep-Rupture Damage Under Variable Load and Temperature (VLT) Conditions

R. L. Huddleston

(Last reported in ORNL-5433, p. 145)

Plans for uniaxial and multiaxial VLT tests were described in a previous report.[3] The purpose of the uniaxial tests is to provide exploratory, low-variability cumulative damage data on the reference heat of type 304 stainless steel for assessing failure criteria under relatively homogeneous states of step-varying stress and temperature and also to assess differences in the creep-rupture behavior when different deformation mechanisms are operative. Six tests are to be performed at each uniaxial condition to develop a data set in which creep-rupture and cumulative damage behavior can be statistically separated from the material and testing variability. Biaxial tests will duplicate the effective stress-time history of selected uniaxial tests.

3.2.1 Uniaxial VLT tests

A subcontract was initiated with the Joliet Metallurgical Laboratory, Joliet, Illinois, during this report period to perform the uniaxial VLT

creep-rupture tests. The standard 6.40-mm-diam (0.252-in.), 51-mm (2.0-in.) gage length specimen shown in Fig. 3.8 is being utilized. Specimens are being fabricated from 48-mm-diam (1-7/8-in.) bar stock. The large bar diameter permits four specimens to be obtained from each specimen-length segment of bar. The bar stock was annealed at 1093°C (2000°F) for 30 min and subsequently given a 1000-hr, 663°C (1225°F) microstructural stabilization treatment. Test specimens were prepared by wet-form grinding.

Seventeen tests were initiated during this report period and had accumulated times up to 803 hr through the end of November. Initial test results are summarized in Table 3.4.

Table 3.4. Uniaxial creep-rupture test results for type 304 stainless steel (heat 9T2796) (Joliet Metallurgical Laboratory)

Specimen No.	Matrix test No.	Test temperature [°C (°F)]	Stress [MPa (ksi)]	Plastic strain on loading (%)	Running time[a] (hr)	Accumulated creep deformation (%)
1	A1-1-1	566 (1050)	159 (23)		[b]	
2	-2	566 (1050)	159 (23)	2.8	728.3	1.598
3	-3	566 (1050)	159 (23)	3.0	724.5	1.500
4	-4	566 (1050)	159 (23)	2.8	724.4	1.295
5	-5	566 (1050)	159 (23)	2.4	691.5	1.177
6	-6	566 (1050)	159 (23)	2.6	728.4	1.247
		Mean		2.72	719.4	1.363
		Standard deviation		0.23		0.178
		Coefficient of variation		8.5		13.1
7	A1-2-1	593 (1100)	159 (23)	2.6	730.4	9.042
8	-2	593 (1100)	159 (23)	2.8	802.8	9.023
9	-3	593 (1100)	159 (23)	3.5	802.9	9.855
10	-4	593 (1100)	159 (23)	1.6	802.8	9.960
11	-5	593 (1100)	159 (23)	1.7	802.7	10.947
12	-6	593 (1100)	159 (23)	2.2	730.3	10.091
		Mean		2.40	778.7	9.820
		Standard deviation		0.72		0.722
		Coefficient of variation		30.0		7.35
13	A2-2-1	663 (1225)	89.6 (13)	0.6	803.0	15.645
14	-2	663 (1225)	89.6 (13)	0.5	802.9	15.038
15	-3	663 (1225)	89.6 (13)	0.5	803.0	14.306
16	-4	663 (1225)	89.6 (13)	0.6	802.9	15.278
17	-5	663 (1225)	89.6 (13)	0.5	802.8	14.660
18	-6	663 (1225)	89.6 (13)	0.5	802.9	16.147
		Mean		0.53	802.9	15.179
		Standard deviation		0.05		0.666
		Coefficient of variation		9.4		4.4

[a]As of November 22, 1978.

[b]Temperature overshoot on heatup. No test.

ORNL-DWG 78-22064

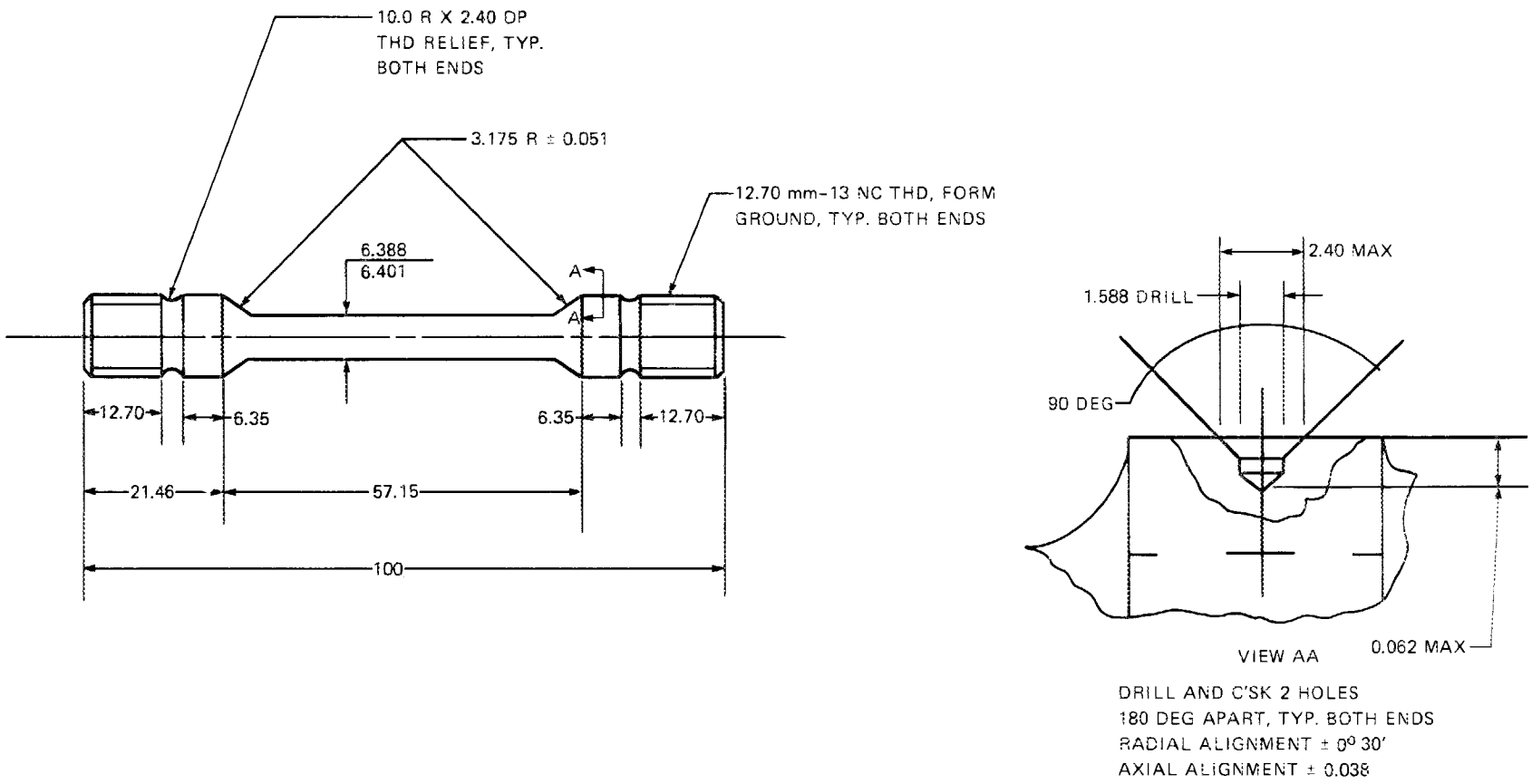

Fig. 3.8. Uniaxial VLT creep-rupture test specimen [dimensions in millimeters (1 in. = 25.4 mm)].

Grain sizes in the range American Society for Testing and Materials (ASTM) 1 through 5 were found in the bar stock after the annealing and stabilization heat treatment. Prior experience both at ORNL and at the Babcock & Wilcox Company has shown an influence of grain size variability on creep-rupture behavior.[7,8] Prior to initiation of testing at the Joliet Laboratory, serious consideration was given to changing to another product of the reference heat (9T2796) or to another heat of 304 stainless steel. The conclusion was, however, that the grain size problem is not peculiar to the reference heat nor to one product form. In addition, changing to another heat would uncouple data generated in this program from the large body of existing data for the reference heat. Thus, it was concluded that the program should use the 48-mm (1-7/8-in.) bar product form of the reference heat. Variability in strains and rupture times due to different grain sizes is, however, a continuing source of concern, and test results will be monitored closely early in the test program to establish the variability. Although no ruptures have occurred to date, early strain data are more variable than desired.

3.2.2 Multiaxial VLT tests (R. L. Huddleston, R. L. Battiste, M. Richardson, and J. A. Hawk)

Preliminary test plans, an experimental facility, and a nominal 31.8-mm-diam (1.25-in.), 1.0-mm (0.04-in.) wall, 152-mm (6-in.) gage length tubular specimen were described previously in Ref. 3 for some multiaxial VLT tests. These specific tests are to provide data on creep-rupture damage under step-varying internal pressure and temperature loadings (VPT). During this report period, one tubular specimen, VPT-2, was instrumented and tested to failure at 593°C (1100°F).

VPT-2 was fabricated from 48-mm-diam (1-7/8-in.) bar stock of heat 9T2796 of type 304 stainless steel. After final assembly, the specimen was annealed for 30 min at 1093°C (2000°F) and subsequently given a microstructural stabilization heat treatment [1000 hr at 664°C (1225°F)]. Instrumentation for VPT-2 included axial and circumferential Boeing-HITEC strain gages and Chromel-Alumel thermocouples at the center and each end of the gage length.

Photographs of the instrumented specimen and the specimen positioned in the test facility are shown in Figs. 3.9 and 3.10, respectively. The specimen was heated to 593 ± 1.7°C (1100 ± 3°F) and internally pressurized with argon to a Mises effective stress level of 159 MPa (23.0 ksi). Rupture occurred in 95 hr. The ruptured specimen is shown in Fig. 3.11. Expected failure time was 596 hr. The specimen is currently being examined to determine if the failure initiated at one of the small spot welds used for strain gage and lead wire attachment.

3.3 Effect of Biaxiality in Creep-Fatigue at Elevated Temperature

S. Y. Zamrik*

(Last reported in ORNL-5433, pp. 154-161)

An exploratory study of biaxial creep fatigue in type 304 stainless steel (heat 9T2796) at 538°C (1000°F) is being conducted by the Pennsylvania State University under a subcontract with ORNL. Test specimen configuration[9] and results have been given in previous progress reports.

Activities during the period of this report included the following: (1) a series of thermal and axial strain calibration tests at 538°C (1000°F) were conducted jointly with ORNL personnel and (2) six additional creep-fatigue tests were conducted. Calibration tests were initiated after poor correlation was obtained between the Pennsylvania State University experimental results and results computed from the ANL linear regression model (Diercks and Raske[10]) fitted to data from other sources (see Sect. 3.7).

Axial strain calibration tests were conducted using a standard 11.4-mm-diam (0.450-in.), 19.0-mm (3/4-in.) gage length, 1.5-mm (0.060-in.) wall tubular specimen instrumented with two high-temperature Boeing-HITEC capacitive strain gages. The instrumented test specimen is shown in Fig. 3.12. One of the specially prepared gages had a gage length of 3.2 mm (1/8 in.) and the other had a gage length of 19 mm (3/4 in.), which corresponded to the specimen gage length. The gages were located on

*Pennsylvania State University, University Park.

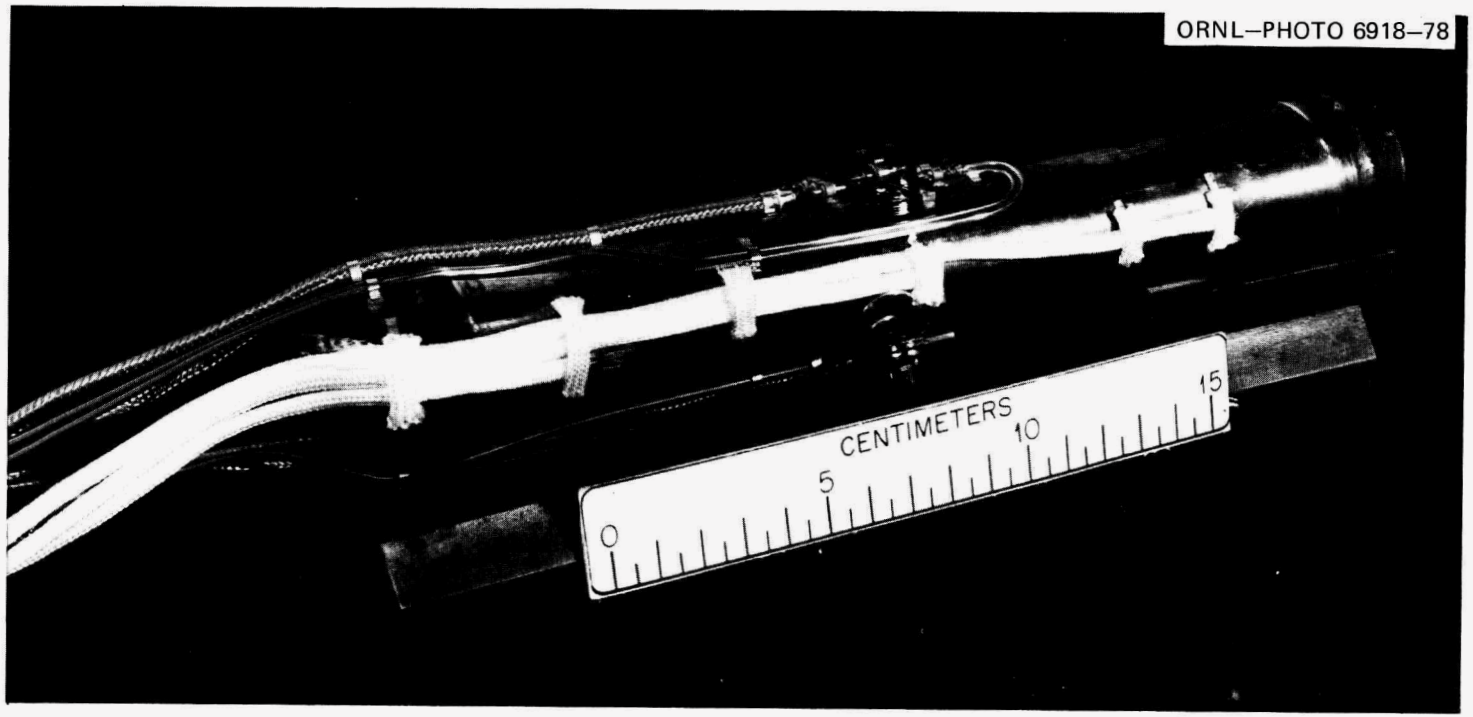

Fig. 3.9. VPT-2 instrumented specimen; type 304 stainless steel (heat 9T2796), nominal 32-mm diam (1.25 in.), 1-mm (0.040-in.) wall, 152-mm (6-in.) gage length.

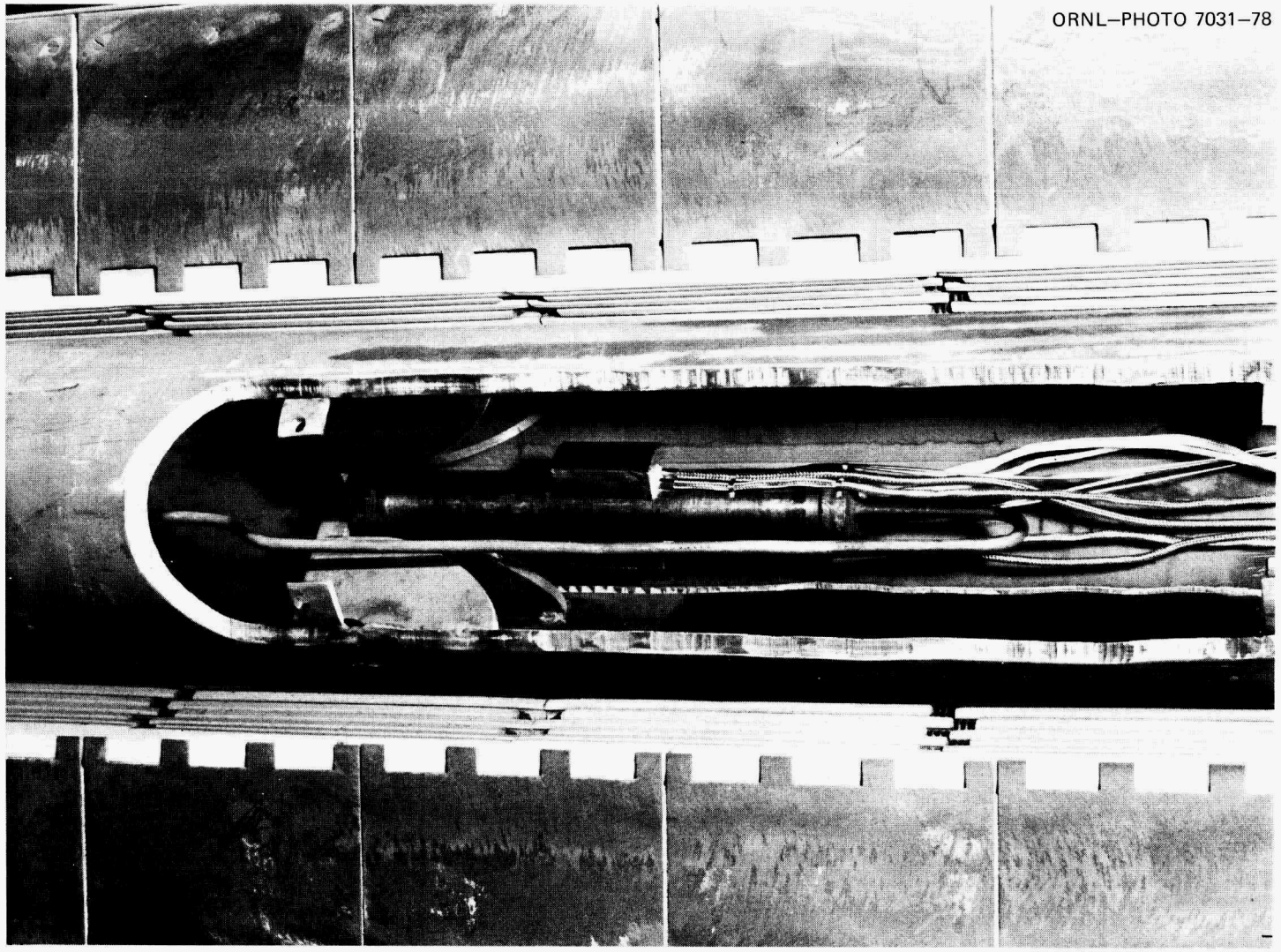

Fig. 3.10. VPT-2 specimen assembled in "clam-shell" furnace and surrounding safety container.

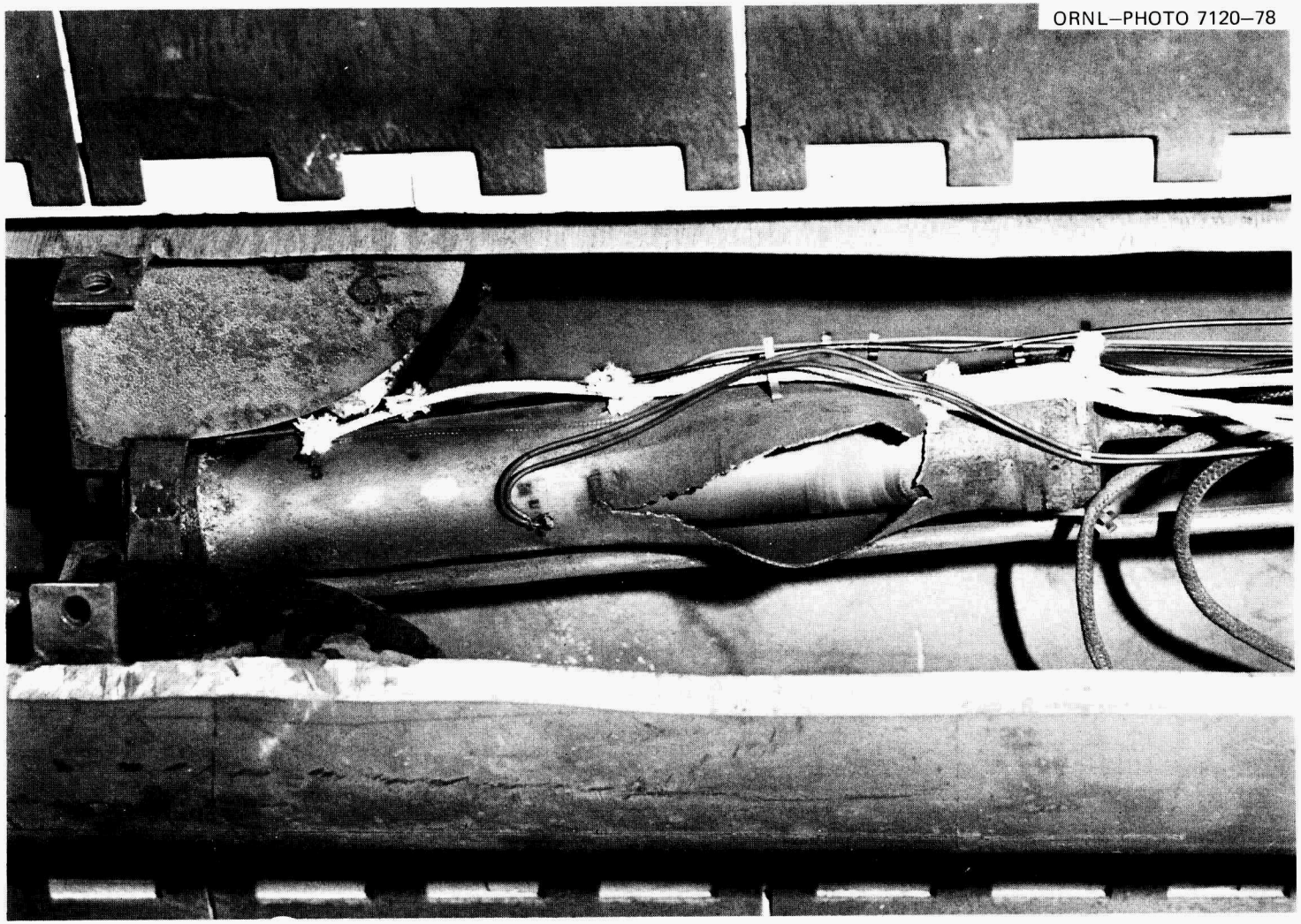

Fig. 3.11. VPT-2 specimen after rupture at 593°C (1100°F) and 159 MPa (23 ksi).

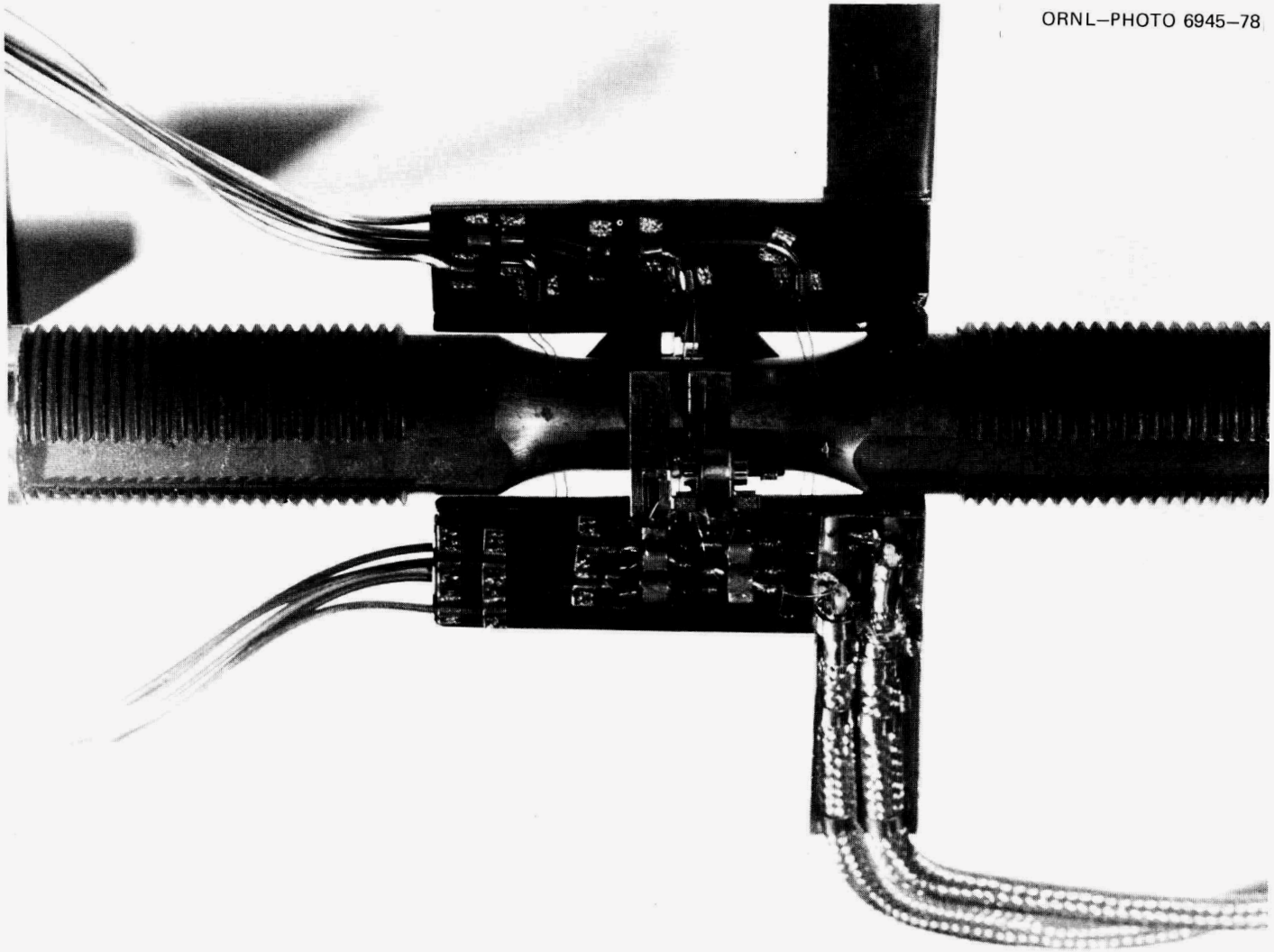

Fig. 3.12. Biaxial creep-fatigue specimen instrumented with two Boeing-HITEC strain gages and six Chromel-Alumel thermocouples in preparation for axial strain calibration tests.

opposite sides of the specimen at the midpoint of the specimen gage length. Cycling between fixed displacement limits resulted in a strain range approximately twice that previously reported for the same displacement range. A subsequent check of the strain calculation procedure revealed that an existing calibration curve relating cyclic axial displacement limits to axial strain amplitude had been misinterpreted as strain range. This resulted in axial strain range being reported as one-half its actual value for all cyclic data in which the linear ramp cycle has been utilized, as well as for a few of the tests involving 25-cpm sinusoidal cycling. Torsional strain range has been reported correctly. Corrected data sets and plots are given in Tables 3.5 and 3.6 and Figs. 3.13 through 3.15.

The preliminary thermal calibration experiments revealed undesirable thermal gradients within the specimen. Appropriate modifications are being made to the equipment to heat and insulate the specimen more uniformly. Test improvements are directed toward meeting targets of <5.6°C (10°F) difference between center and end, <1.7°C (3°F) between top and

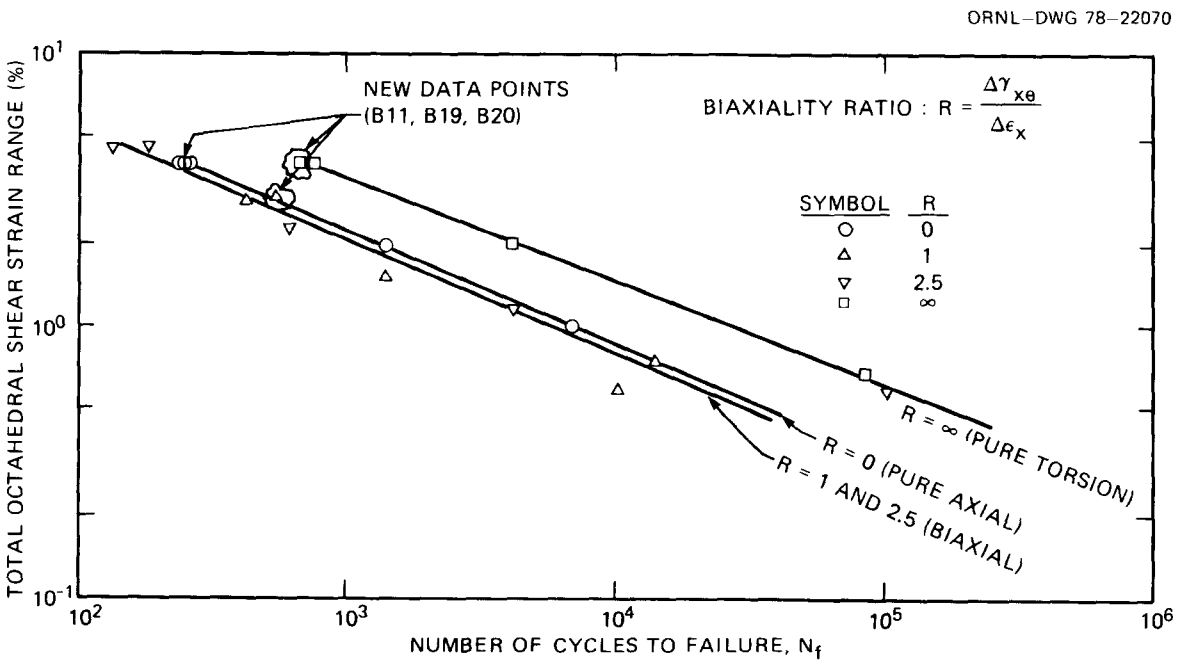

Fig. 3.13. Effect of biaxiality ratio, $R = \gamma_{\theta z}/\varepsilon_z$, on the low-cycle fatigue life of type 304 stainless steel (heat 9T2796) at 538°C (1000°F) for a 2-cpm triangular strain-time wave form.

Table 3.5. Results of biaxial creep-fatigue tests of type 304 stainless steel (heat 9T2796) at 538°C (1000°F) with triangular wave cycling (exclusive of hold time)

Specimen No.	Hold time (hr)	$\gamma_{\theta z}/\varepsilon_z$	Octahedral strain range $\Delta\gamma_{oct}$ (%)	Axial strain range $\Delta\varepsilon_z$ (%)	Torsional strain range $\Delta\gamma_{\theta z}$ (%)	Axial stress		Shear stress		Stress relaxation ($\Delta\sigma^{r}$)			Cycles to failure
						Maximum [MPa (ksi)]	Minimum [MPa (ksi)]	Maximum [MPa (ksi)]	Minimum [MPa (ksi)]	Axial [MPa (ksi)]	Shear [MPa (ksi)]	Cycle No. used	
						I. Zero hold tests							
A9	0	0	1.000	0.707	0	174.96 (25.375)	−174.96 (−25.375)	0	0	0	0	3,000	6,944
A8	0	0	2.000	1.414	0	229.25 (33.250)	−229.25 (−33.250)	0	0	0	0	800	1,400
A12	0	0	4.000	2.828	0	570.06 (82.680)	−570.06 (−82.680)	0	0	0	0	126	258
B11[a]	0	0	4.000	2.828	0	265.50 (38.50)	−265.50 (−38.50)	0	0	0	0	120	250
A7	0	0	4.000	2.828	0	541.42 (78.526)	−541.42 (−78.526)	0	0	0	0	115	240
A15	0	1	0.756	0.463	0.463	175.01 (25.383)	−175.01 (−25.383)	102.64 (14.887)	−102.64 (−14.887)	0	0	11,652	14,184
A13	0	1	1.512	0.926	0.926	189.70 (27.514)	−189.70 (−27.514)	115.54 (16.757)	−115.54 (−16.757)	0	0	700	1,392
B20[a]	0	1	3.024	1.852	1.852			100.5 (14.57)	−100.5 (−14.57)	0	0	350	560
A14	0	1	3.024	1.852	1.852	194.83 (28.258)	−194.83 (−28.258)	130.31 (18.900)	−130.31 (−18.900)	0	0	232	428
B6	0	2.5	0.575	0.232	0.579								103,180
B5	0	2.5	1.150	0.463	1.158	106.18 (15.400)	−106.18 (−15.400)	93.63 (13.580)	−93.63 (−13.580)	0	0	20	4,260
B4	0	2.5	2.300	0.926	2.315	146.65 (21.270)	−146.65 (−21.270)	171.22 (24.833)	−171.22 (−24.833)	0	0	120	618
B3	0	2.5	4.599	1.852	4.630	168.23 (24.400)	−168.23 (−24.400)	252.76 (36.660)	−252.76 (−36.660)	0	0	100	187
B2	0	2.5	4.599	1.852	4.630	192.71 (27.950)	−192.71 (−27.950)	213.12 (30.910)	−213.12 (−30.910)	0	0	122	135
A6	0	∞	0.670	0	0.820	0	0	81.57 (11.830)	−81.57 (−11.830)	0	0	20,000	85,088
A5	0	∞	2.000	0	2.450	0	0	181.33 (26.300)	−181.33 (−26.300)	0	0	2,000	4,092
A16	0	∞	4.000	0	4.899	0	0	216.08 (31.340)	−216.08 (−31.340)	0	0	538	754

Table 3.5 (continued)

Specimen No.	Hold time (hr)	$\gamma_{\theta z}/\varepsilon_z$	Octahedral strain range $\Delta\gamma_{oct}$ (%)	Axial strain range $\Delta\varepsilon_z$ (%)	Torsional strain range $\Delta\gamma_{\theta z}$ (%)	Axial stress		Shear stress		Stress relaxation ($\Delta\sigma^n$)			Cycles to failure
						Maximum [MPa (ksi)]	Minimum [MPa (ksi)]	Maximum [MPa (ksi)]	Minimum [MPa (ksi)]	Axial [MPa (ksi)]	Shear [MPa (ksi)]	Cycle No. used	
B19[a]	0	∞	4.000	0	4.899	0	0	207.9 (30.15)	−207.9 (−30.15)	0	0	94	668
						II. Symmetric hold tests							
B8[a]	0.1	1	1.512	0.926	0.926								590
B7[a]	0.1	1	3.024	1.852	1.852								189
N17	0.1	∞	1.0	0	1.225	0	0	117.21 (17.000)	−117.21 (−17.000)	0	7.308 (1.060)	600	6,240
B1	1.0	∞	2.0	0	2.449	0	0	175.50 (25.454)	−175.50 (−25.454)	0	50.82 (7.370)	158	360
						III. Positive hold tests							
M13	0.1	0	1.000	0.707	0	182.99 (26.540)	−182.99 (−26.540)	0	0	32.88 (4.769)	0	1,435	1,510
M10	0.1	0	2.000	1.414	0	253.04 (36.700)	−253.04 (−36.700)	0	0	33.04 (4.792)	0	260	397
M5	0.1	0	4.000	2.828	0	389.24 (56.455)	−296.56 (−43.013)	0	0	33.36 (4.838)	0	175	199
M19	0.1	1	0.756	0.463	0.463	163.41 (23.700)	−163.41 (−23.700)	58.05 (8.420)	−58.05 (−8.420)	27.56 (4.000)	6.69 (0.970)	1,500	1,672
M11	0.1	1	1.512	0.926	0.926	168.65 (24.460)	−168.65 (−24.460)	115.01 (16.680)	−115.01 (−16.680)	28.35 (4.112)	0	475	507
M7	0.1	1	3.024	1.852	1.852	234.90 (34.070)	−234.90 (−34.070)	185.47 (26.900) 161.88[b] (23.478)[b]	−185.47 (−26.900) −149.00[c] (−21.611)[c]	44.36 (6.434)	5.01 (0.726)	175	245
A19	0.1	2.5	2.300	0.926	2.315	97.62 (14.158)	−97.62 (−14.158)	163.57 (23.724)	−163.57 (−23.724)	9.96 (1.445)	9.94 (1.442)	150	159
N8	0.1	∞	1.000	0	1.225	0	0	131.00 (19.000)	−131.00 (−19.000)	0	7.72 (1.120)	5,000	5,060
M8	0.1	∞	2.000	0	2.449	0	0	153.99 (22.334)	−153.99 (−22.334)	0	10.50 (1.523)	1,370	1,416

Table 3.5 (continued)

Specimen No.	Hold time (hr)	$\gamma_{\theta z}/\varepsilon_z$	Octahedral strain range $\Delta\gamma_{oct}$ (%)	Axial strain range $\Delta\varepsilon_z$ (%)	Torsional strain range $\Delta\gamma_{\theta z}$ (%)	Axial stress		Shear stress		Stress relaxation ($\Delta\sigma^p$)			Cycles to failure
						Maximum [MPa (ksi)]	Minimum [MPa (ksi)]	Maximum [MPa (ksi)]	Minimum [MPa (ksi)]	Axial [MPa (ksi)]	Shear [MPa (ksi)]	Cycle No. used	
N7	0.1	∞	4.000	0	4.899	0	0	211.46 (30.670)	−211.46 (−30.670)	0	23.44 (3.400)	300	400
A11	1.0	0	1.000	0.707	0	198.67 (28.815)	−198.67 (−28.815)	0	0	80.61 (11.692)	0	50	105
N5	1.0	0	2.000	1.414	0	245.45 (35.600)	−245.45 (−35.600)	0	0	39.99 (5.800)	0	85	96
N1	1.0	0	4.000	2.828	0	266.63 (38.672)	−266.63 (−38.672)	0	0	45.51 (6.600)	0	35	38
N6	1.0	1	1.512	0.926	0.926	176.33 (25.575)	−176.33 (−25.575)	73.64 (10.680)	−73.64 (−10.680)	22.75 (3.300)	9.69 (1.405)	100	134
N2	1.0	1	3.024	1.852	1.852	238.74 (34.626)	−238.74 (−34.626)	128.55 (18.645) 110.171[b] (15.979)[b]	−128.55 (−18.645) −111.39[c] (−16.155)[c]	39.99 (5.800)	15.58 (2.260)	44	47
A20	1.0	2.5	2.300	0.926	2.315	128.99 (18.708)	−128.99 (−18.708)	193.21 (28.023)	−193.21 (−28.023)	33.56 (4.867)	37.70 (5.468)	51	74
A18	1.0	∞	1.000	0	1.225	0	0	106.23 (15.407)	−106.23 (−15.407)	0	9.19 (1.333)	100	243
N3	1.0	∞	2.000	0	2.449	0	0	171.68 (24.900)	−171.68 (−24.900)	0	23.44 (3.400)	100	396
N4	1.0	∞	4.000	0	4.899	0	0	209.43 (30.375)	−209.43 (−30.375)	0	31.03 (4.500)	100	130
N9	10.0	0	4.000	2.828	0	262.01 (38.000)	−262.01 (−38.000)	0	0	68.95 (10.000)	0	10	17
N10	10.0	1.0	3.024	1.852	1.852	241.33 (35.000)	−241.33 (−35.000)	107.56 (15.600) 103.42[b] (15.000)[b]	−107.56 (−15.600) −102.13[c] (−14.813)[c]	51.71 (7.500)	28.96 (4.200)	18	23
N16	10.0	∞	4.000	0	4.899	0	0	179.26 (26.000)	−179.26 (−26.000)	0	52.20 (7.571)	88	90
IV. Negative hold tests													
B14[a]	0.1	1	1.512	0.926	0.926								696
B13	1.0	1	3.024	1.852	1.852	276.20 (40.060)	−276.20 (−40.060)	113.01 (16.390)	−113.01 (−16.390)	151.41 (21.960)	29.17 (4.230)	124	189

[a]New data points generated during this report period.

[b]Maximum stress before hold time.

[c]Maximum stress before reversing load.

Table 3.6. Biaxial creep-fatigue test results for type 304 stainless steel (heat 9T2796) at 649°C (1200°F) with a sinusoidal strain-time wave form

Specimen No.	Hold time (hr)	$\gamma_{\theta z}/\varepsilon_z$	Octahedral shear strain range $\Delta\gamma_{oct}$ (%)	Axial strain range $\Delta\varepsilon_z$ (%)	Torsional shear strain range $\Delta\gamma_{\theta z}$ (%)	Axial stress		Shear stress		Stress relaxation			Cycles to failure
						Maximum [MPa (ksi)]	Minimum [MPa (ksi)]	Maximum [MPa (ksi)]	Minimum [MPa (ksi)]	Axial [MPa (ksi)]	Shear [MPa (ksi)]	Cycle No. used	
N20	0	0.25	3.45	2.40	0.60	252.51 (36.624)	−252.51 (−36.624)	355.77 (51.600)	−355.77 (−51.600)	0	0	200	405
N21	0	0.25	2.29	1.60	0.40	202.75 (29.407)	−202.75 (−29.407)	27.36 (3.968)	−27.36 (−3.968)	0	0	400	536
A2	0	0.50	2.12	1.44	0.72	131.54 (19.078)	−131.54 (−19.078)	422.06 (61.215)	−422.06 (−61.215)	0	0	110	407
A3	0	0.50	1.18	0.80	0.40	193.92 (28.125)	−193.92 (−28.125)	28.55 (4.141)	−28.55 (−4.141)	0	0	400	1,812
A4	0	2.5	2.98	1.20	3.00	48.86 (7.086)	−48.86 (−7.086)			0	0	60	246

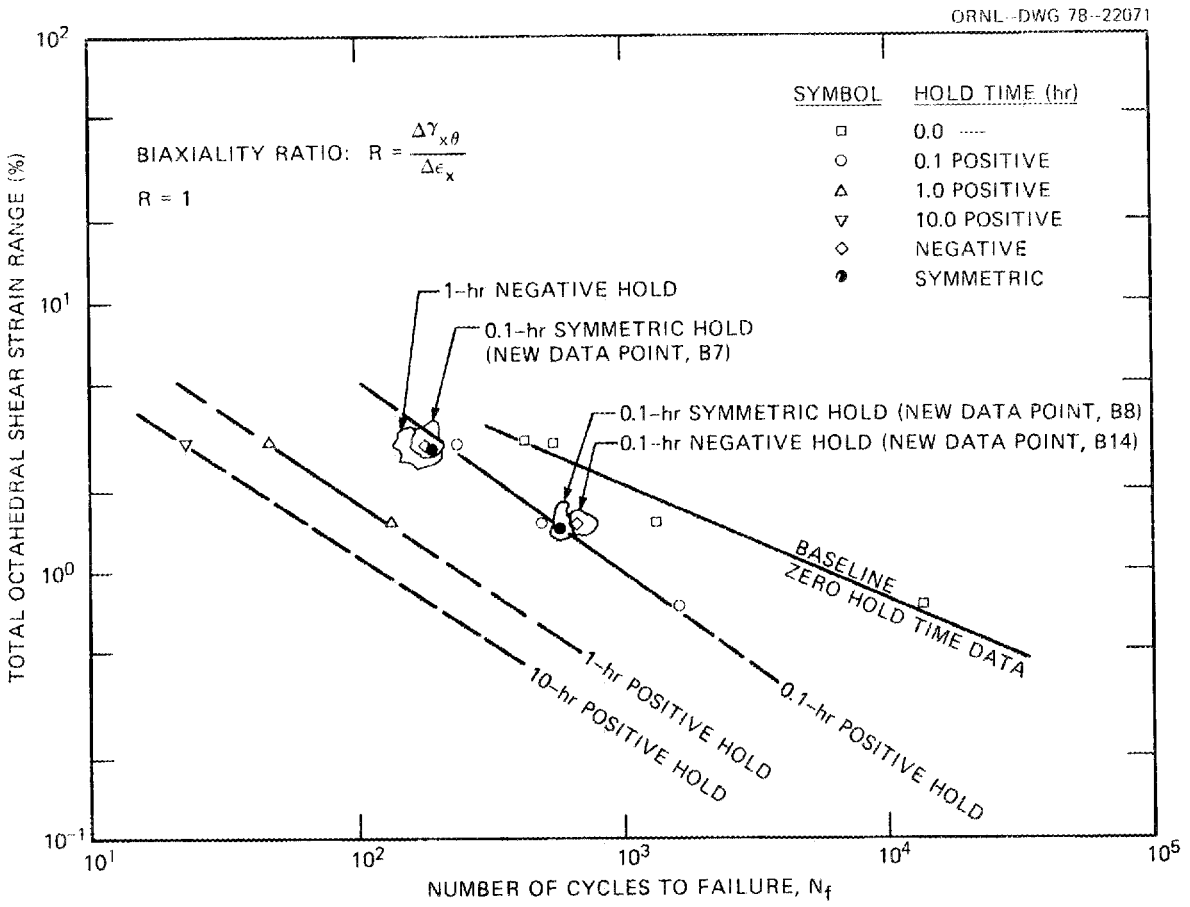

Fig. 3.14. Effect of hold time on the biaxial, low-cycle, creep-fatigue life of type 304 stainless steel (heat 9T2796) at 538°C (1000°F) and a biaxial ratio R = 1 for a 2-cpm triangular strain-time wave form (exclusive of hold time).

bottom (the specimen is tested in a horizontal position), and <1.7°C (3°F) thermal drift in a 10-hr period. Additional high-temperature axial and torsional strain calibration tests are planned after achieving these target levels and prior to initiation of additional biaxial fatigue tests.

A total of six additional biaxial creep-fatigue tests were completed at 538°C (1000°F). Two tests with a shear-to-axial-strain ration (ρ) of 1 and a symmetric hold time (t_h) of 0.1 hr were completed. In the first, specimen B7 failed after 189 cycles at a $\Delta\gamma_{oct}$ of 3.024%; in the second, specimen B8 failed after 590 cycles at a $\Delta\gamma_{oct}$ of 1.512%. One was completed with ρ = 1 and t_h = 0.1 hr at negative strain. In this test, specimen B14 failed after 696 cycles at a $\Delta\gamma_{oct}$ of 1.512%. Three additional

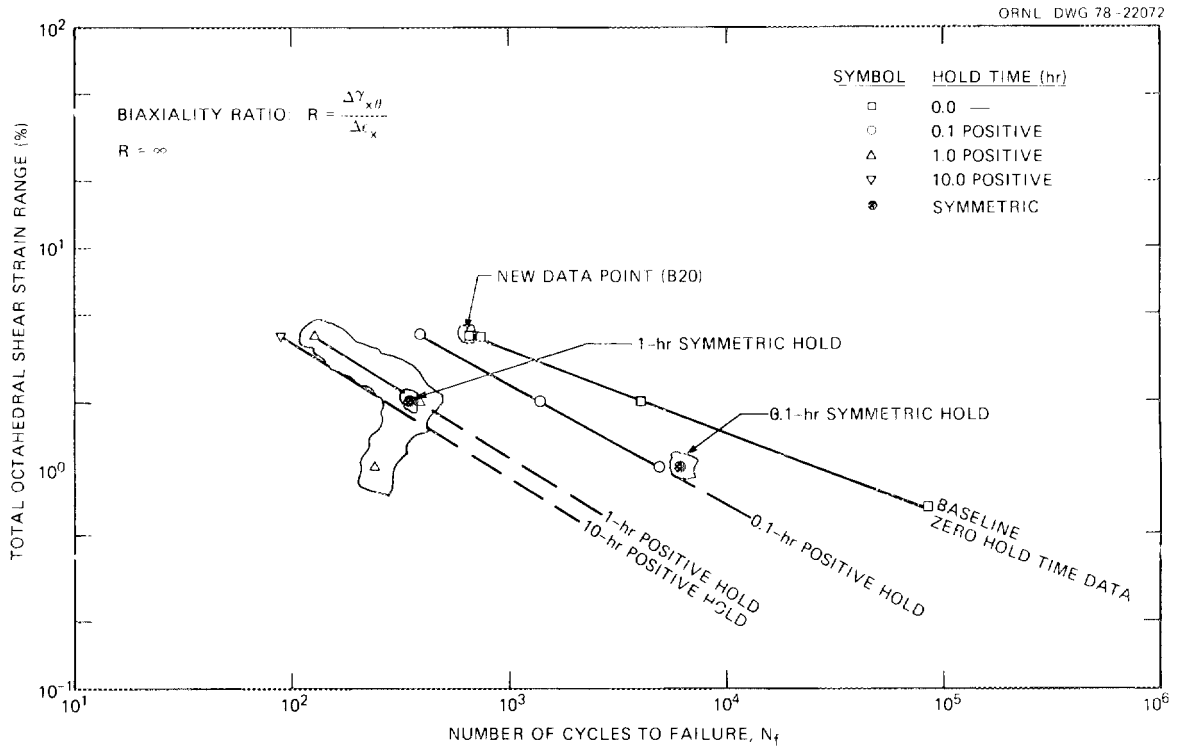

Fig. 3.15. Effect of hold time on the biaxial, low-cycle, creep-fatigue life of type 304 stainless steel (heat 9T2796) at 538°C (1000°F) and a biaxial ratio $R = \infty$ for a 2-cpm triangular strain-time wave form (exclusive of hold time).

tests (B11, B19, and B20) were run without hold time. These tests were duplicates of previous ones and were run during the course of conducting the calibration experiments. Specimens B11 ($\rho = 0$) and B19 ($\rho = \infty$) failed after 250 and 668 cycles, respectively, with $\Delta\gamma_{oct} = 4.0\%$. Specimen B20 ($\rho = 1$) failed after 560 cycles with $\Delta\gamma_{oct} = 3.024\%$. These new data are included in Table 3.5 and Figs. 3.13 through 3.15.

3.4 Failure Under Cyclic, Relaxing Residual Stresses: Restrained-Cylinder Tests

W. J. McAfee R. L. Battiste
T. J. Delph M. Richardson

(Last reported in ORNL-5433, pp. 161-166)

A series of exploratory tests (called restrained-cylinder tests) was implemented at ORNL. The objective of these tests is to study failure

under relaxing residual stresses such as those experienced by a restrained system or component undergoing thermal cycling at creep temperatures. The test specimen consists of a thin-walled tube of 304 stainless steel restrained by a stiff core bar of Inconel X750 rigidly attached to the ends of the tube. The test specimen, a tentative testing cycle, and the test equipment were described in previous progress reports.[11,12]

3.4.1 Base metal tests

A test specimen designated restrained-cylinder specimen 2 (RCS-2) was mounted in the furnace, and a series of shakedown tests was run at 649°C (1200°F) to evaluate different specimen and test parameters. Parameters that were adjusted or measured included air cooling rate, cooling time, specimen thermal response, and specimen-core temperature differential. Once the air cooling rate had been established, tests were run with cooling times ranging from 15 sec to 2 min. Based on a preliminary evaluation of these results, a test histogram that involved cooling for 30 sec followed by holding for 12 hr at 649°C (1200°F) was selected. The thermal response of the specimen and core for a 30-sec cooling time is shown in Fig. 3.16.

The transient drop in core temperature was slightly greater than had been calculated. This, together with the faster response of the specimen, can result in the specimen temperature overtaking the core temperature during reheating, as shown in Fig. 3.16. If the specimen temperature exceeds the core temperature by too large a margin, the specimen can unload, wiping out the desired compressive stresses. This indicated the need for a more detailed analysis of the specimen assembly in an effort to optimize the thermal cycle. In the interim, the test was initiated using the 30-sec-cool, 12-hr-hold cycle.

The computer code PLACRE[13] was used to analyze the specimen assembly, which was treated as a two-bar linkage. Two axisymmetric elements, one representing the specimen and the other the core, were used, and only radial variations in temperature, stress, and strain were considered. Material properties, constitutive equations, etc., were either for the ORNL reference heat of type 304 stainless steel or were taken from the

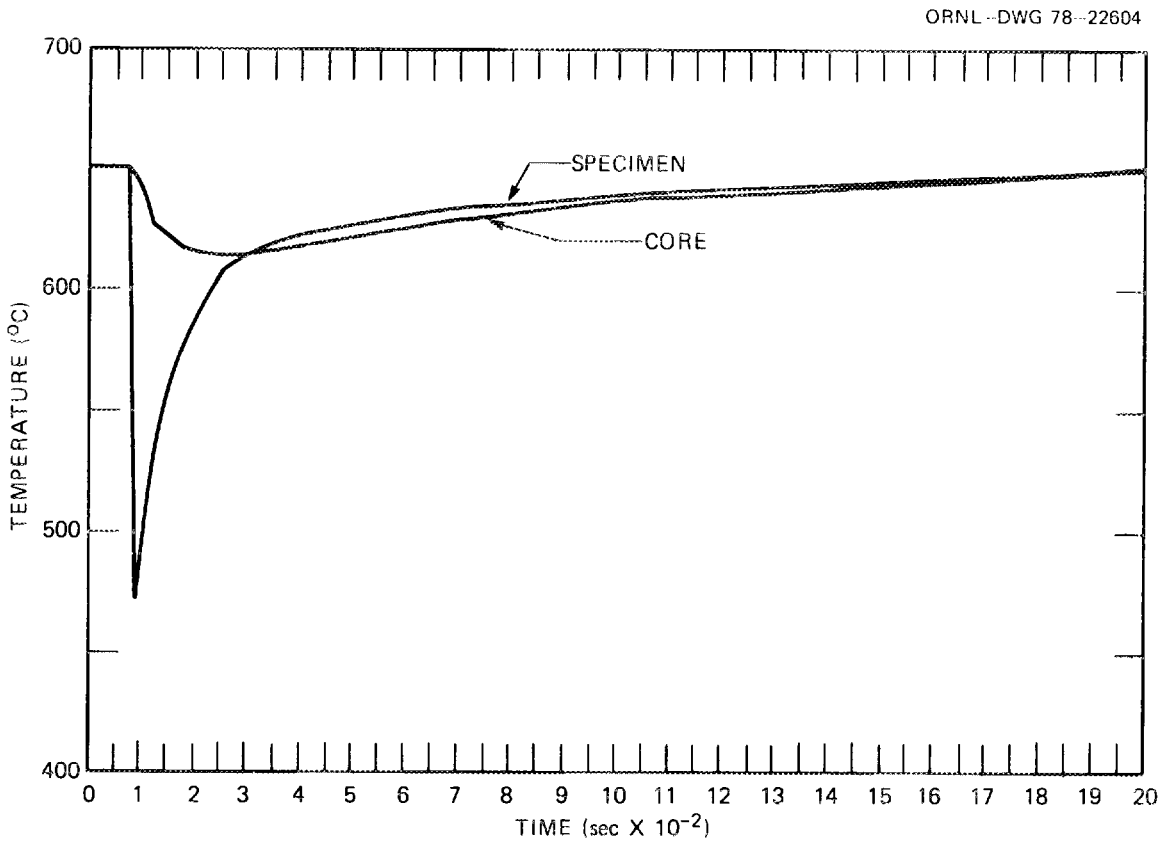

Fig. 3.16. Measured thermal response at assembly midheight of specimen and core of RCS-2 for 30-sec cooling.

Nuclear Systems Materials Handbook.[14] The temperature histograms were the actual temperatures measured in the test.

Damage accumulation was assessed using the procedures built into PLACRE which are based on American Society of Mechanical Engineers (ASME) Code rules.[15] For conservatism, these rules assume that compressive stresses are as damaging as tensile stresses. Ten cycles of the kind discussed above were analyzed. The increment of damage accumulated during the tenth cycle was taken as the limiting value, that is, the damage per cycle was assumed to be constant for cycles beyond the tenth. A specimen lifetime was then predicted on this basis.

Two sets of calculations were performed. The first set was for 30 sec of cooling followed by hold times of 6, 8, 12, and 16 hr. The second was for 45 sec of cooling and the same hold times as above. Figure 3.17 shows a typical specimen stress-temperature history for ten cycles (45-sec cool,

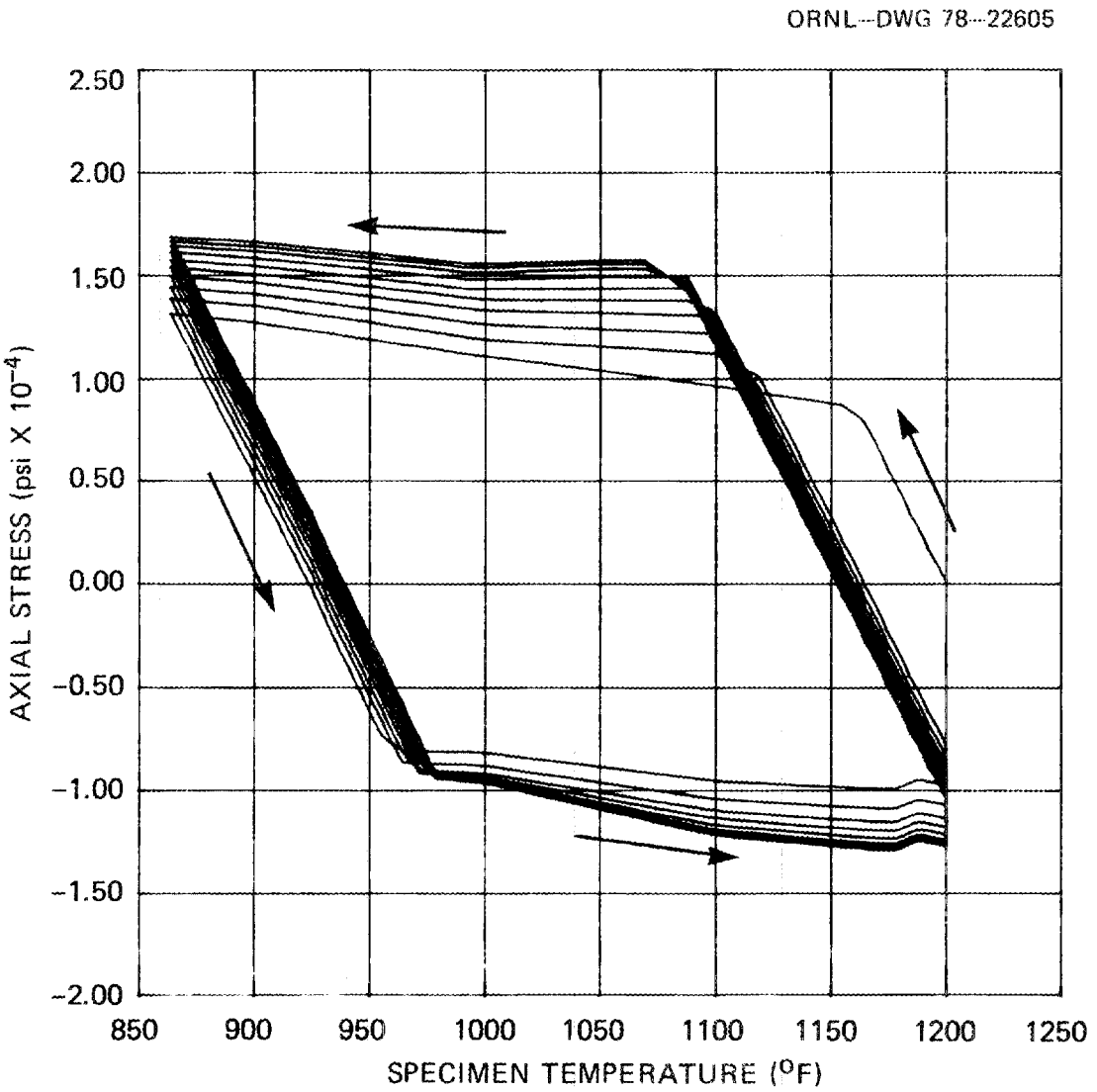

Fig. 3.17. Restrained cylinder specimen stress-temperature histogram for ten cycles using a 45-sec cool, 6-hr hold (1 ksi = 6.895 MPa).

6-hr hold). Note the complicated interaction between the specimen and core during the last stages of reheating shown in the lower right of Fig. 3.17 where the specimen starts to unload slightly. The resulting stress-strain behavior is shown in Fig. 3.18, and the stress relaxation behavior is shown in Fig. 3.19.

The results of the calculations are summarized in Table 3.7. The combination of 45 sec of cooling followed by a 6-hr hold time at 649°C (1200°F) gave the greatest amount of damage. Shorter hold times were

Table 3.7. Summary of damage calculations ($\times 10^3$) using inelastic analysis results for 30- and 45-sec cooling

Hold time (hr)	Damage source	Cycle 1	2	3	4	5	6	7	8	9	10	Damage = 1 at Cycle	Days
						30-sec cooling							
6	Creep	0.24014	0.65346	1.2379	1.9778	2.8847	3.9461	5.1351	6.4606	7.8267	9.2014	710	177
	Fatigue	0.05295	0.0966	0.13917	0.18078	0.22166	0.26188	0.301481	0.34056	0.37921	0.41753		
	Total	0.29308	0.75008	1.3771	2.1586	3.1064	4.2079	5.4366	6.8011	8.2059	9.6199		
	Change	0.29308	0.45700	0.62697	0.78152	0.94778	1.1016	1.2286	1.3646	1.4048	1.414		
8	Creep	0.27206	0.73994	1.4045	2.2463	3.2869	4.5167	5.9000	7.4537	9.0846	10.7485	581	193
	Fatigue	0.052945	0.096992	0.13989	0.18179	0.22291	0.26332	0.30305	0.34221	0.3809	0.41928		
	Total	0.32500	0.83693	1.5444	2.4281	3.5098	4.7800	6.2031	7.7959	9.4656	11.1678		
	Change	0.32500	0.51193	0.70748	0.8837	1.0817	1.2702	1.4230	1.5929	1.6696	1.7022		
12	Creep	0.31336	0.85397	1.6315	2.6309	3.8851	5.3991	7.1426	9.1303	11.2600	13.4824	446	223
	Fatigue	0.05295	0.09753	0.14089	0.18313	0.22450	0.26509	0.30493	0.34416	0.38291	0.42124		
	Total	0.36631	0.95150	1.7724	2.8140	4.1096	5.6642	7.4475	9.4745	11.6429	13.9036		
	Change	0.36631	0.58519	0.82090	1.0416	1.2956	1.5546	1.7833	2.0270	2.1684	2.2607		
16	Creep	0.33913	0.92976	1.7978	2.9455	4.4128	6.2109	8.3110	10.7441	13.3942	16.2043	355	230
	Fatigue	0.05295	0.09791	0.14155	0.18402	0.22554	0.26623	0.30612	0.34537	0.38411	0.42243		
	Total	0.39207	1.0277	1.9394	3.1295	4.6383	6.4772	8.6171	11.0895	13.7783	16.6267		
	Change	0.39207	0.63559	0.91171	1.1902	1.5088	1.8389	2.1400	2.4724	2.6888	2.8484		
						45-sec cooling							
6	Creep	0.3274	0.91187	1.7596	2.8535	4.1420	5.5092	6.8964	8.3014	9.7238	11.1627	644	161
	Fatigue	0.13464	0.25773	0.37939	0.50003	0.61977	0.73890	0.85761	0.97600	1.0941	1.2120		
	Total	0.46207	1.1676	2.1390	3.3535	4.7618	6.2481	7.7540	9.2774	10.8178	12.3747		
	Change	0.46207	0.70754	0.76942	1.2145	1.4083	1.4863	1.5059	1.5235	1.5404	1.5569		
8	Creep	0.36683	1.0190	1.9684	3.2047	4.6728	6.2529	7.8877	9.5711	11.2956	13.0654	532	177
	Fatigue	0.13464	0.25823	0.38033	0.50133	0.62135	0.74067	0.85950	0.97795	1.0761	1.2139		
	Total	0.50146	1.2773	2.3487	3.7060	5.2941	6.9936	8.7472	10.5491	12.3917	14.2793		
	Change	0.50146	0.77579	1.0715	1.3573	1.5881	1.6994	1.7536	1.8019	1.8426	1.8876		
12	Creep	0.41674	1.1652	2.2610	3.7104	5.4824	7.4425	9.5313	11.7386	14.0538	16.4708	398	199
	Fatigue	0.13464	0.25897	0.38159	0.50295	0.62324	0.74271	0.86161	0.98006	1.0981	1.2159		
	Total	0.55137	1.4242	2.6425	4.2134	6.1056	8.1852	10.3929	12.7186	15.1519	17.6867		
	Change	0.55137	0.87278	1.2184	1.5708	1.8923	2.0796	2.2077	2.3257	2.4333	2.5348		
16	Creep	0.44748	1.2565	2.4666	4.0995	6.13801	8.4355	10.9390	13.6393	16.5084	19.5327	322	214
	Fatigue	0.13464	0.25945	0.38244	0.50400	0.62439	0.74388	0.86275	0.78116	1.0992	1.2169		
	Total	0.58212	1.5160	2.8490	4.6035	6.7624	9.1793	11.8018	14.6205	17.6076	20.7496		
	Change	0.58212	0.93385	1.3330	1.7545	2.1598	2.4167	2.6225	2.8187	2.8871	3.142		

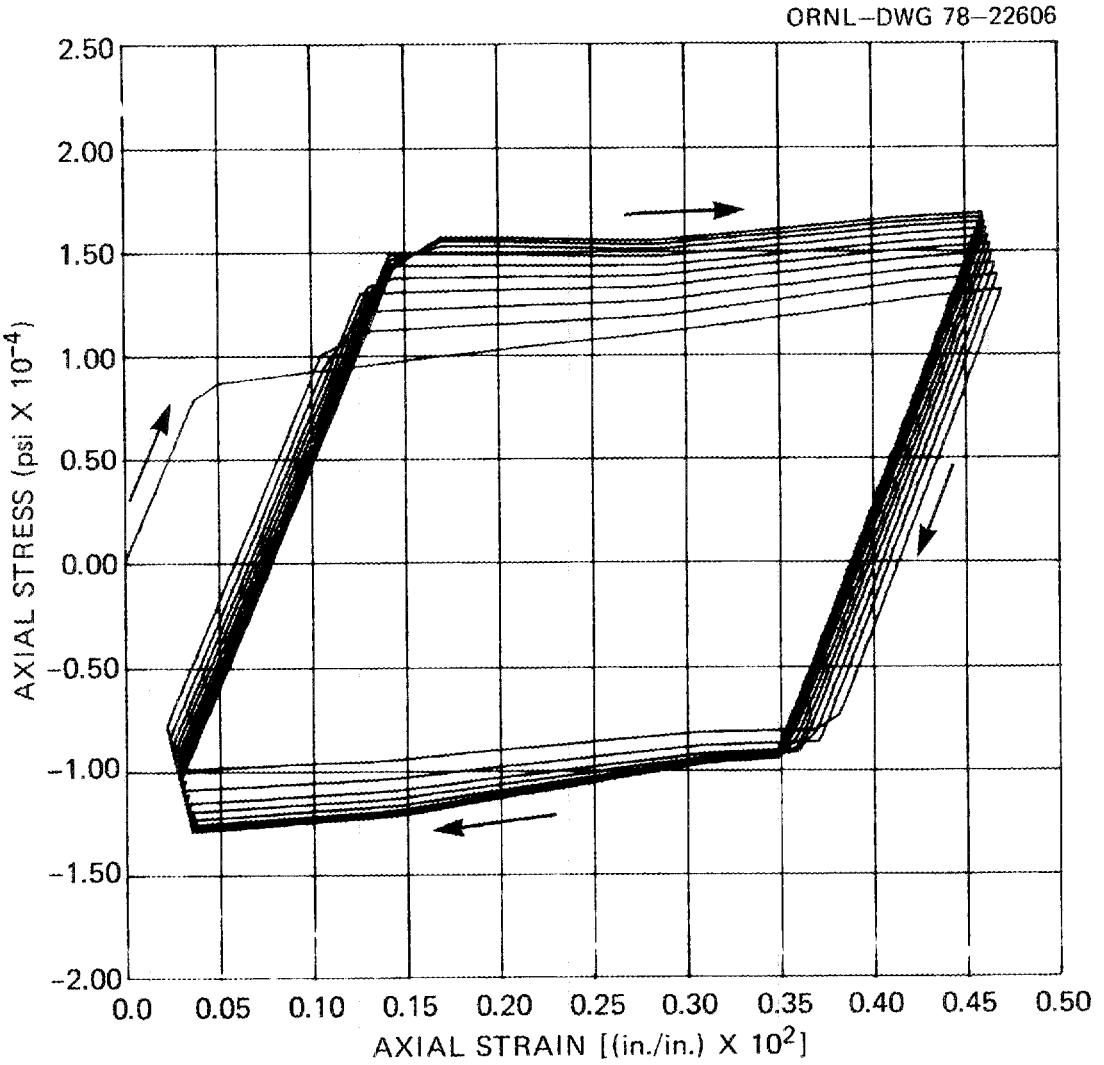

Fig. 3.18. Restrained cylinder specimen stress-strain histogram for ten cycles using a 45-sec cool, 6-hr hold (1 ksi = 6.895 MPa).

not desirable because fatigue was becoming a more significant part of total damage. Based on these calculations, the test program was changed to the most damaging cycle. At the end of this report period, the speciment will have been subjected to 474 cycles with a calculated total damage greater than 70%.

Also during this report period, plans were made for further testing of type 304 stainless steel specimens and to initiate testing of 2 1/4 Cr–1 Mo steel. Six specimens of each material are being fabricated. To test the 2 1/4 Cr–1 Mo specimens, a new external restraint fixture was

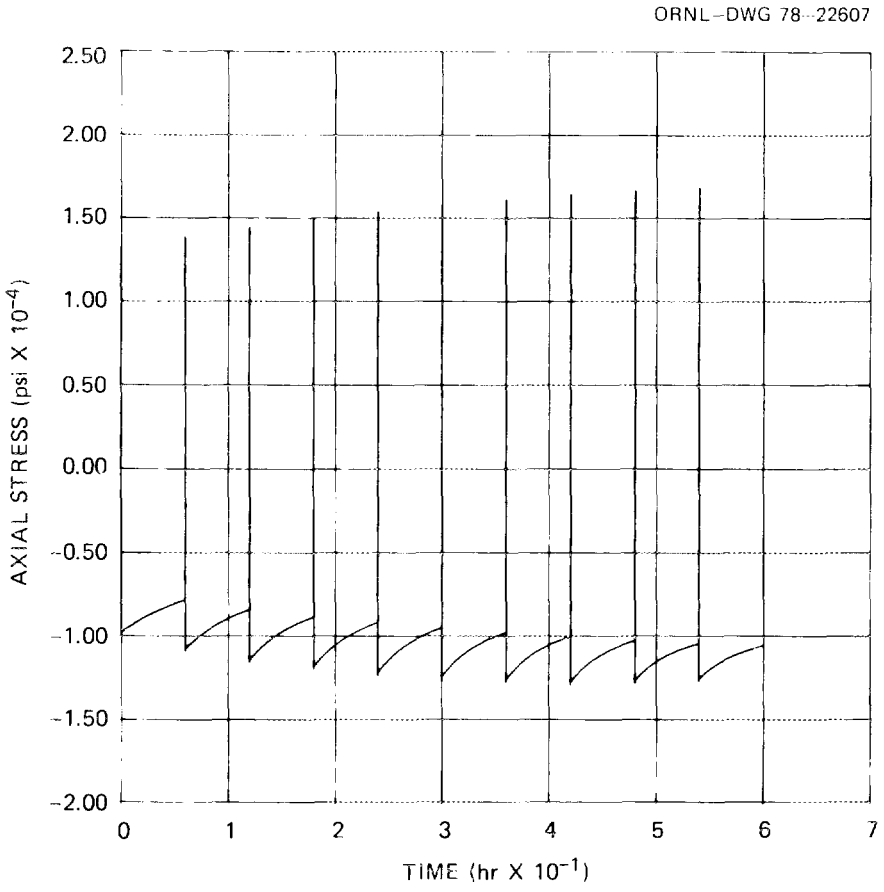

Fig. 3.19. Restrained cylinder specimen stress-time histogram for ten cycles using a 45-sec cool, 6-hr hold (1 ksi = 6.895 MPa).

designed to take the place of the internal core bar. The principal of operation is the same, and the supplied thermal cycle will be the same. Cooling air will be injected inside the specimen without removing it from the furnace. This arrangement is particularly well suited to testing of 2 1/4 Cr–1 Mo. Testing of these specimens will start early in 1979.

3.4.2 Weldment tests

Testing is also under way on a 304 stainless steel specimen containing a circumferential 308 CRE weld. The weld joint was of single-V geometry and was made by the gas-tungsten arc technique. After welding, the specimen was machined to slightly greater than finished dimensions, annealed, and then machined to finished dimensions. At the end of this

report period, this specimen will have accumulated 444 thermal cycles. In addition to this test of an annealed weldment, a test is planned of a weldment in the as-deposited condition.

3.5 Failure Studies and Notched-Bar Rupture Tests on Type 304 Stainless Steel

R. W. Swindeman

(Last reported in ORNL-5433, p. 166)

3.5.1 Failure studies on type 304 stainless steel

An updated study of the creep-rupture data produced on the reference heat of type 304 stainless steel was undertaken as a part of an effort to develop Ashby-type fracture maps.[16] We also examined the validity of the Monkman-Grant correlation[17] between rupture life and creep rate. Most of this information was assembled into a report,[18] and the following statements represent our conclusions.

1. At temperatures above 650°C (∿1200°F), the stress and temperature dependencies of the secondary creep rate ($\dot{e}_s$) and rupture life (t_R) are similar. The product $\dot{e}_s t_R$ is relatively constant, and the exponent in the Monkman-Grant relation is close to −1.0. These observations apply for times to at least 4×10^6 sec (1100 hr).

2. At temperatures below 650°C (∿1200°F), the stress and temperature dependencies of $\dot{e}_s$ and t_R are often different. The product $\dot{e}_s t_R$ decreases with decreasing stress and decreasing temperature. The exponent in the Monkman-Grant relation changes from −1.0 toward zero as temperature and $\dot{e}_s$ decreases. These observations apply for times in the range 10^4 to 10^8 sec (3 to 3×10^4 hr).

3. The fact that $\dot{e}_s$–t_R correlations are stress and temperature sensitive below 650°C (∿1200°F) is primarily due to changes in the $\dot{e}_s$ behavior rather than changes in the rupture mechanism. Changes in the $\dot{e}_s$ behavior could be attributed to either a high internal stress, σ_i, produced by the development of a precipitation-stabilized dislocation network or to a somewhat complex solute hardening mechanism.

4. Although grain boundary carbide sizes and crack densities changed over the range of stress and temperature of concern, there was no evidence to indicate that these features of microstructure greatly influenced the stress and temperature dependence of the rupture life.

A modest rupture testing program will continue on type 304 stainless steel. In particular, we will continue some tensile tests at very low strain rates ($<10^6$/sec) in the temperature range 427 to 538°C (800 to 1000°F) and some long-time (>10,000-hr) rupture tests at temperatures in the range 482 to 621°C (900 to 1150°F). Both the slow tensile and long-term rupture tests are needed to examine the validity of parametric methods and assumed damage mechanisms.

Several years ago we made attempts to develop parametric relationships for type 304 stainless steel.[19] Data produced subsequent to these developments are being used to assess the predictability of parametric approaches.

3.5.2 Notch-bar rupture tests on type 304 stainless steel

The results of short-time rupture tests on circumferentially notched bars were reported previously.[20] Two tests are still under way — one at 482°C (900°F) and the other at 593°C (1100°F). The status of these tests are listed in Table 3.8. We find notch strengthening at all stress and

Table 3.8. Status of long-time notch-bar stress-rupture tests on type 304 stainless steel (heat 9T2796)

Specimen No.	Temperature [°C (°F)]	Stress[a] [MPa (ksi)]	Rupture life[b] (hr)	Smooth-bar rupture life (hr)
191	482 (900)	276 (40)	9100 I	8000
187	538 (1000)	207 (30)	6626 R	2200
192	593 (1100)	138 (20)	8200 I	5000

[a]Net stress at root of notch $K_t = 1.32$.

[b]I = in test; R = rupture.

temperature levels. Preliminary data suggest that notch strengthening does not occur when the stress is cycled. We plan to do more testing on this subject.

3.6 Analysis of a Notched-Bar Specimen

W. K. Sartory

(Not previously reported)

To provide analytical support for the notched-bar tests, an elastic analysis and creep-fatigue damage evaluation of a typical notched-bar specimen are now being undertaken. The specimens are essentially 6.4-mm-diam (0.25-in.) cylindrical rods of type 304 stainless steel with a circumferential groove at the center. At both ends of the specimen, the diameter increases to 13 mm (0.5 in.) for attachment to the test machine. The initial tests by Swindeman[20] concentrate on a rather shallow notch with a stress concentration factor of $K_t \sim 1.5$. This notch, which has a radius of 1.8 mm (0.072 in.) and a depth of 0.19 mm (0.0073 in.) is being adopted for the present analysis.

The structural analysis is being performed using the finite-element program PLACRE.[13] An initial finite-element grid using 550 triangular elements was developed and tested, but preliminary elastic analyses indicated that the grid was too coarse in the vicinity of the notch. A second grid using 976 elements was then developed, with most of the additional elements concentrated near the notch. The second grid, which seems satisfactory based on elastic analysis, is illustrated in Fig. 3.20.

The loading conditions planned for the analyses consist of a fully reversed cyclic load of ±4.37 kN (1980 lb) leading to a stress of ±138 MPa (±20 ksi) in the 6.4-mm-diam (0.25-in.) section far from the notch. A creep-hold period of 0.1 hr will be included at each maximum tensile loading. These load conditions were chosen as a compromise between the conflicting requirements for feasibility of an analysis of several cycles and of testing to failure.

By comparing the predicted and measured failure times, we hope to contribute to an assessment of the conservatism of the creep-fatigue

ORNL-DWG 78-22065

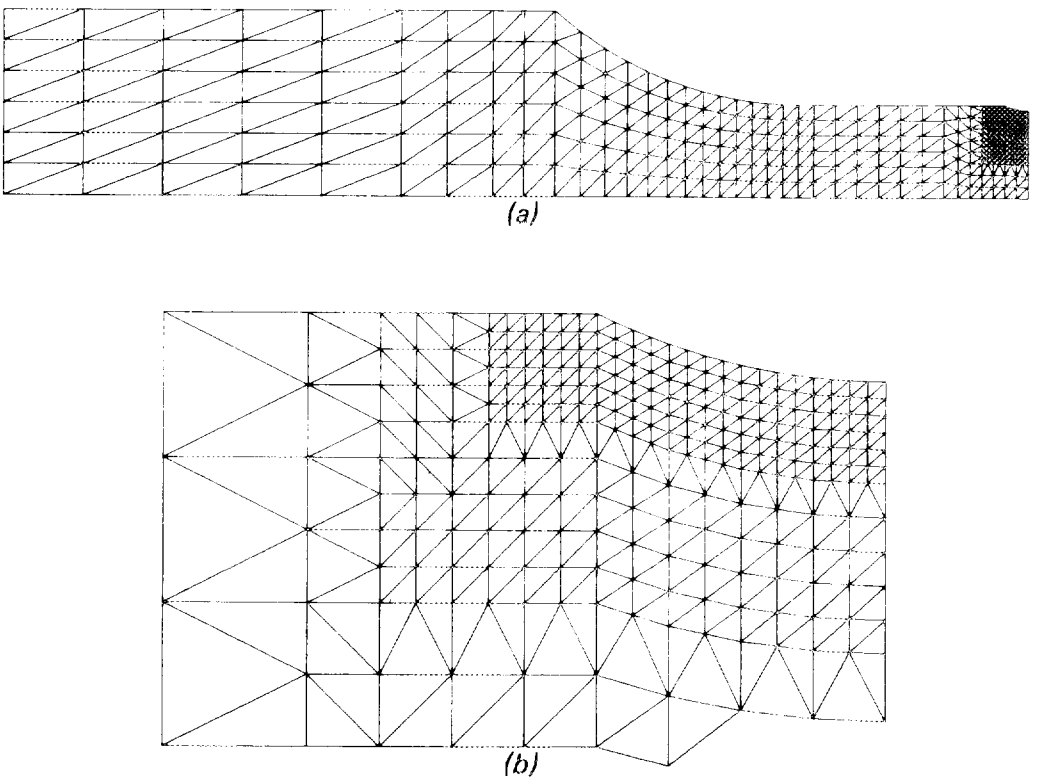

Fig. 3.20. Finite-element grid of a notched-bar specimen. (*a*) Complete grid of one quadrant of the specimen. (*b*) Closeup of the notch region.

failure analysis of ASME Code Case N-47 (Ref. 15) for a structure involving a complex inhomogeneous stress distribution.

3.7 Assessment of Multiaxial Fatigue Criteria for Type 304 Stainless Steel

J. J. Blass

(Last reported in ORNL-5374, pp. 117-126)

In a previous progress report on this subject,[21] the strain analog of Gough's Ellipse Quadrant was used to correlate the results of combined axial and torsional strain cycling tests of type 304 stainless steel at room temperature, 538°C (1000°F), and 649°C (1200°F).

In terms of inelastic strain ranges, this relationship may be written

$$\left(\frac{\Delta\varepsilon_z^{in}}{\Delta\varepsilon_o^{in}}\right)^2 + \left(\frac{\Delta\gamma_{\theta z}^{in}}{\Delta\gamma_o^{in}}\right)^2 = 1 \ , \tag{3.6}$$

where ε_o is the axial strain in uniaxial stress and γ_o is the engineering shear strain in pure torsion. If the appropriate strain range vs life relationships are known for the denominators of Eq. (3.6), this equation may be solved numerically for the cyclic life in the case of combined axial and torsional straining. As shown in Ref. 21, Eq. (3.6) is an example of a multiaxial fatigue failure criterion based on the theory of Brown and Miller[22] involving the shear and normal strains acting on the planes of maximum shear strain. They make a distinction between two types of loading based on the orientation of the maximum shear planes relative to the surface of the specimen. In what they refer to as case A loading, the planes of maximum shear strain are normal to the surface of the specimen, and cracks tend to propagate along the surface. In case B, the planes intersect the surface at an angle of 45°, and cracks propagate inward from the surface. For the same strain ranges, case B leads to shorter fatigue lives. Combined axial and torsional cycling is case A, with uniaxial stress marking the transition from case A to case B.

The data used in the previous study came from the series of tests[23] by S. Y. Zamrik and coworkers conducted at Pennsylvania State University using continuous strain cycling with a sinusoidal wave form. In the latest series of tests at Pennsylvania State,[24] the effect of hold time at maximum strain on combined axial and torsional fatigue of annealed type 304 stainless steel (heat 9T2796) at 538°C (1000°F) was investigated. Tests have been conducted with hold times (t_h) of 0, 0.1, 1, and 10 hr; ratios of engineering shear to axial strain ($\rho = \gamma_{\theta z}/\varepsilon_z$) of 0, 1, 2.5,*

---

*Readers familiar with the content of previous progress reports will notice that the intermediate value of ρ given here is one-half the values previously reported. As described in Sect. 3.3, it was subsequently determined that the axial strain components originally reported by Pennsylvania State were underestimated by a factor of 2.

and ∞; and nominal* equivalent strain ranges ($\Delta\varepsilon_{eq}$) lying between 0.41 and 3.3%. The material, tubular specimens, and test methods were the same as those of Ref. 23 except that extension and twist were simultaneously varied linearly rather than sinusoidally with time between equal positive and negative limits. The cyclic period in each test was equal to 30 sec plus hold time. During the hold or dwell periods, total strains were kept constant at their positive limiting values and stresses were permitted to relax with time (positive hold).†

In a recently prepared topical report,[25] methods of accounting for the interaction of creep and fatigue damage processes were briefly reviewed and the latest Pennsylvania State data were analyzed by the method of linear summation of creep and fatigue damage. The results of that analysis and, in particular, the aspects that are related to multiaxial fatigue failure criteria are summarized in the remainder of this section.

Figures 3.21 through 3.24 show the Pennsylvania State data (symbols) plotted on the basis of $\Delta\varepsilon_{eq}$ vs cycles to failure (N_f) with the shear-to-axial-strain ratio ρ as a parameter and for hold times t_h of 0, 0.1, 1, and 10 hr, respectively. Also shown for comparison in each figure is the corresponding uniaxial curve derived from an empirical model for cyclic life as a function of strain range, strain rate, temperature, and hold time. This model was developed by Diercks and Raske[10] to correlate data from 435 tests of type 304 stainless steel from a number of different heats. Their analysis indicated that material from heat 9T2796 exhibited much lower fatigue lives in tests with hold time than predicted by the model. This effect was associated with the lower creep strength of this heat. Agreement between the Pennsylvania State data with $\rho = 0$ and the Diercks and Raske model is quite good in Figs. 3.21 and 3.22, and the differences apparent in Figs. 3.23 and 3.24 can be explained by the lower creep strength of this heat of material.

---

*Assuming incompressible material behavior.

†A few tests have also been conducted with hold time at the negative strain limit (negative hold) and with equal hold times at both positive and negative strain limits (symmetric hold). More such tests are planned, and the results are expected to be the subject of future progress reports.

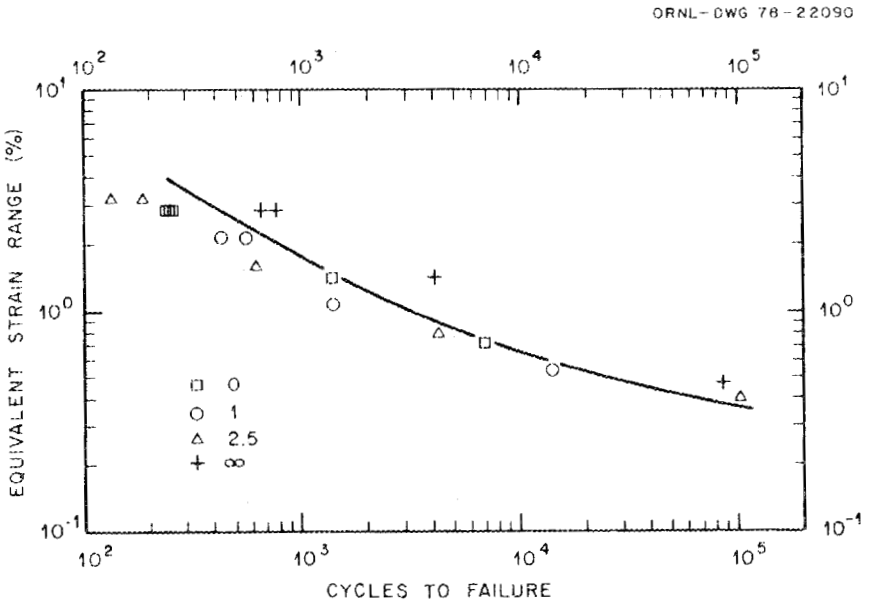

Fig. 3.21. Nominal equivalent strain range vs cycles to failure in multiaxial fatigue tests of annealed type 304 stainless steel (heat 9T2796) at 538°C (1000°F) without hold time and with ρ = 0, 1, 2.5, and ∞. Uniaxial curve based on an empirical model developed by Diercks and Raske[10] is shown for comparison.

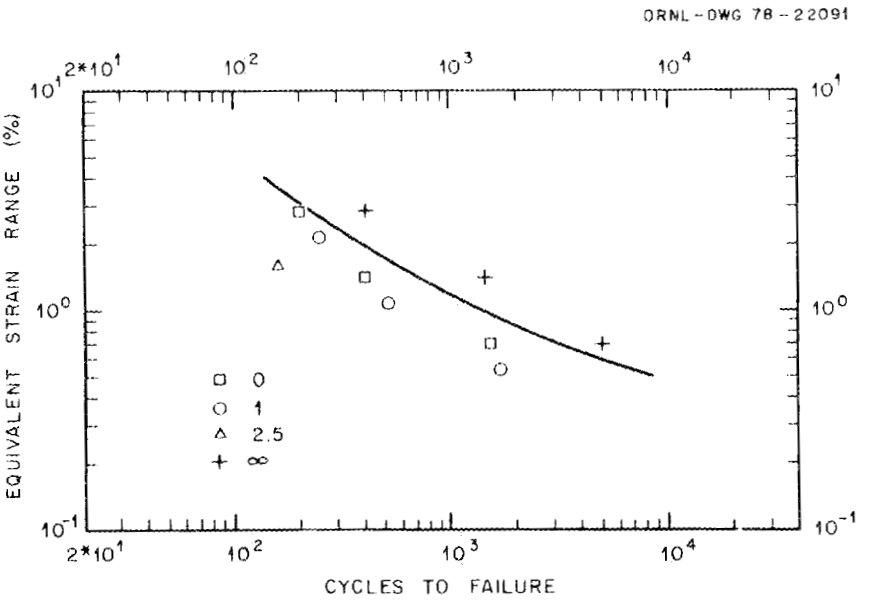

Fig. 3.22. Nominal equivalent strain range vs cycles to failure in multiaxial fatigue tests of annealed type 304 stainless steel (heat 9T2796) at 538°C (1000°F) with 0.1-hr hold time at maximum positive strain and with ρ = 0, 1, 2.5, and ∞. Uniaxial curve based on an empirical model developed by Diercks and Raske[10] is shown for comparison.

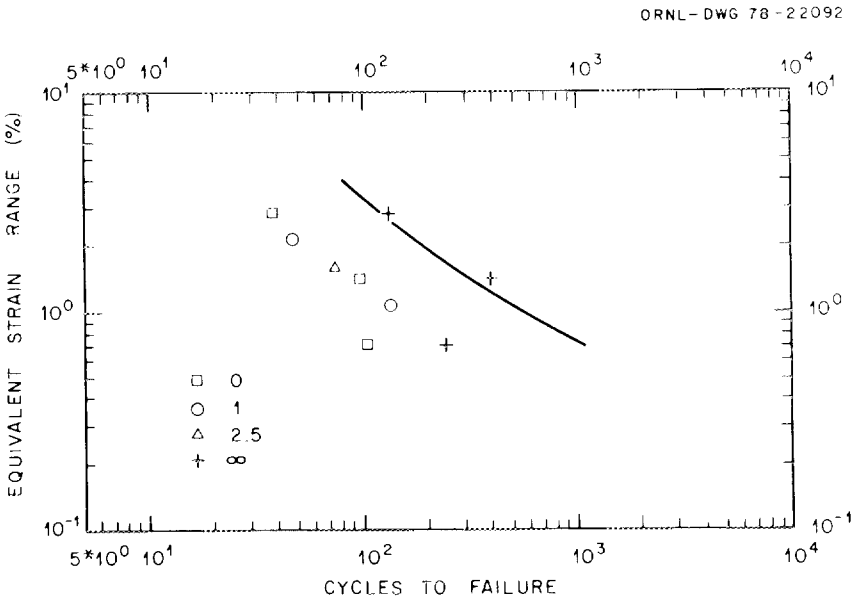

Fig. 3.23. Nominal equivalent strain range vs cycles to failure in multiaxial fatigue tests of annealed type 304 stainless steel (heat 9T2796) at 538°C (1000°F) with 1.0-hr hold time at maximum positive strain and with ρ = 0, 1, 2.5, and ∞. Uniaxial curve based on an empirical model developed by Diercks and Raske[10] is shown for comparison.

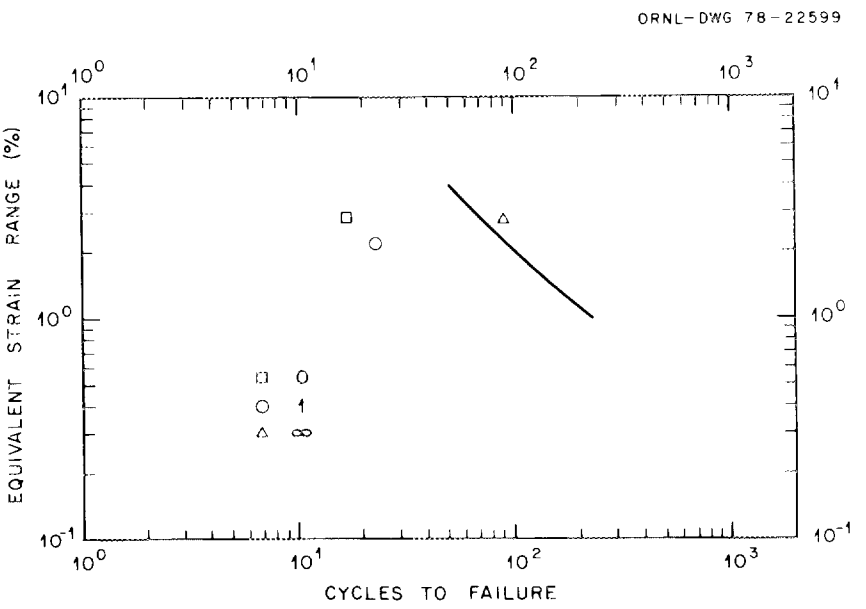

Fig. 3.24. Nominal equivalent strain range vs cycles to failure in multiaxial fatigue test of annealed type 304 stainless steel (heat 9T2796) at 538°C (1000°F) with 10.0-hr hold time at maximum positive strain and with ρ = 0, 1, and ∞. Uniaxial curve based on an empirical model developed by Diercks and Raske[10] is shown for comparison.

As the earlier continuous-cycling tests[23] showed, for the same equivalent strain range, a larger number of cycles is required to cause failure with purely torsional straining than with purely axial straining ($\rho = \infty$ vs $\rho = 0$ in Figs 3.21 through 3.24). This effect appears to increase with increasing hold time, as seen by comparing successive figures or by careful study of Fig. 3.25, which is, in effect, a composite of Figs. 3.21 through 3.24. These figures also show the marked reduction in cyclic life caused by the hold periods for the model and for each data set associated with a particular value of ρ. This effect increases as strain range decreases, that is, the curves and the data sets that parallel them get steeper as hold time increases.

Figure 3.26 shows more clearly the effect of ρ on the results of the tests without hold time. The data are plotted on the basis of equivalent

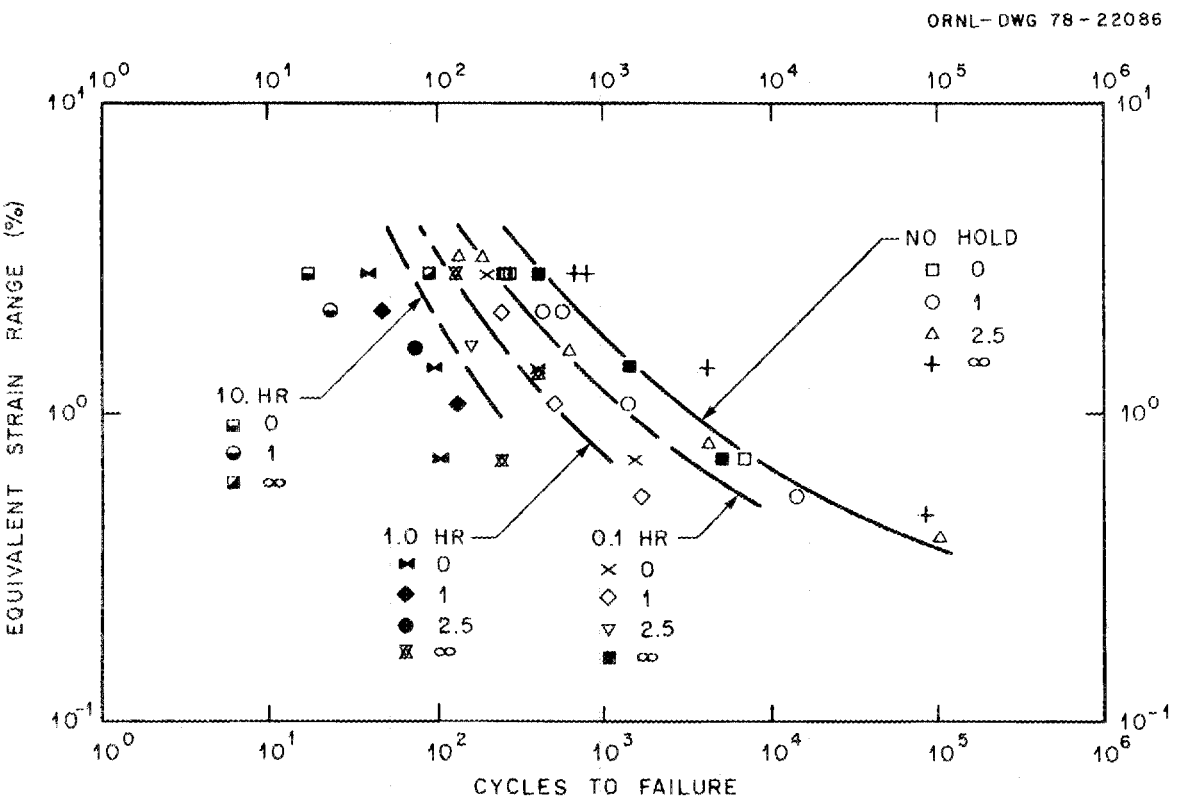

Fig. 3.25. Nominal equivalent strain range vs cycles to failure in multiaxial fatigue tests of annealed type 304 stainless steel (heat 9T2796) at 538°C (1000°F) with hold times t_h = 0, 0.1, 1.0, and 10 hr and ρ = 0, 1, 2.5, and ∞. Uniaxial curves based on empirical model developed by Diercks and Raske[10] is shown for comparison.

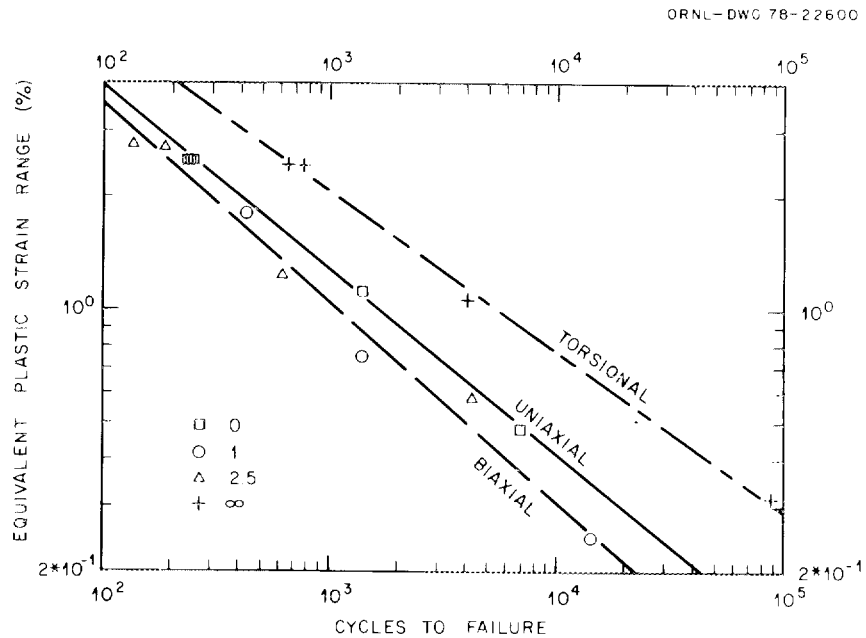

Fig. 3.26. Equivalent inelastic strain range vs cycles to failure in multiaxial fatigue tests of annealed type 304 stainless steel (heat 9T2796) at 538°C (1000°F) without hold time and with ρ = 0, 1, 2.5, and ∞. Uniaxial (ρ = 0), biaxial (ρ = 1 and 2.5), and torsional (ρ = 0) least-squares lines are also shown.

inelastic strain range ($\Delta\varepsilon_{eq}^{in}$) vs N_f. Three straight lines (generalizations of the well-known Coffin-Manson law) were fitted to the log N_f vs log $\Delta\varepsilon_{eq}^{in}$ data by the method of least squares. These are also shown in Fig. 3.26. The uniaxial line was fitted to the ρ = 0 data, the biaxial line to the combined data for ρ = 1 and 2.5, and the torsional line to the $\rho = \infty$ data. The lines have different slopes, indicating that multiplication by factors independent of strain range will not bring the biaxial and torsional data into coincidence with the uniaxial data, as was suggested by Manson and Halford in a discussion of Ref. 23. The ratio of torsional life varies from 2.4 at $\Delta\varepsilon_{eq}^{in}$ = 3% to 4.6 at $\Delta\varepsilon_{eq}^{in}$ = 0.3%. The difference between torsional and biaxial lines is even greater, with the corresponding life ratios being 3.0 and 8.6.

In Fig. 3.27, the number of cycles observed in each of the tests without hold time is compared with the number of cycles estimated in accordance with the rules of ASME Code Case N-47-13.[15] That is, the

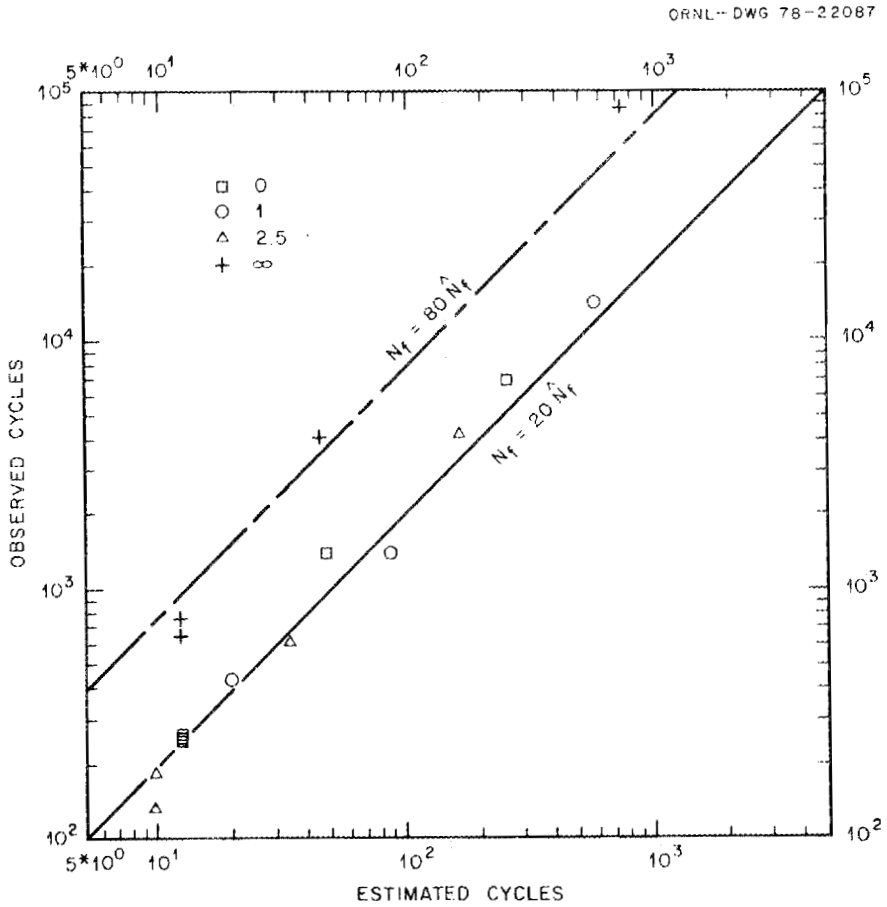

Fig. 3.27. Cycles to failure observed in multiaxial fatigue tests of annealed type 304 stainless steel (heat 9T2796) at 538°C (1000°F) without hold time and with ρ = 0, 1, 2.5, and ∞ vs cycles estimated on the basis of equivalent strain range and the fatigue design curve in ASME Code Case N-47-13.

estimates are based on $\Delta\varepsilon_{eq}$ and the Code's design curve of strain range vs number of cycles. The latter includes a safety factor of 20 on life[26] in the range of lives considered here. This factor is represented by the 45° line shown in Fig. 3.27. The uniaxial and biaxial observations are about 20 times greater than the Code estimates and the torsional observations about 80 times greater; thus, the Code approach appears to be overly conservative only for pure torsion.

For Fig. 3.28, the estimates are based on $\Delta\varepsilon_{eq}^{in}$ and a power-law fit to the data from the uniaxial tests, while, for Fig. 3.29, they are based on the inelastic strain analog of Gough's Ellipse Quadrant, Eq. (3.6),

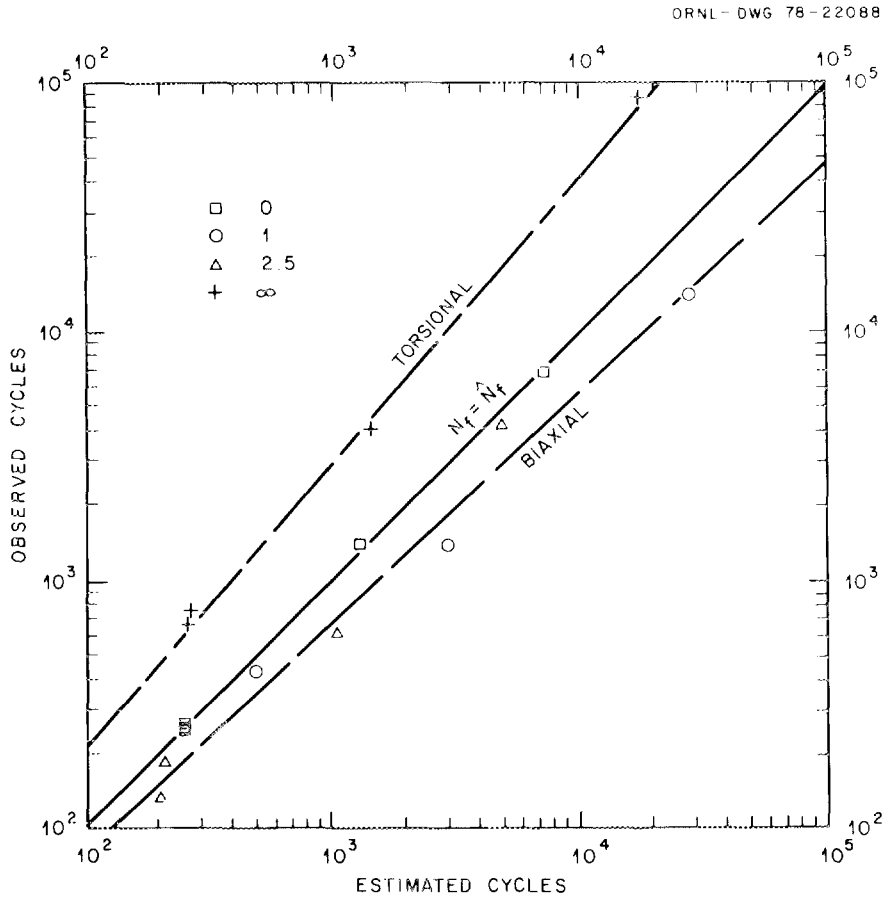

Fig. 3.28. Cycles to failure observed in multiaxial fatigue tests of annealed type 304 stainless steel (heat 9T2796) at 538°C (1000°F) without hold time and with ρ = 0, 1, 2.5, and ∞ vs cycles estimated on the basis of equivalent plastic strain range and a power-law fit to the data from uniaxial tests.

and power-law fits to the data from purely axial and purely torsional tests. Comparison of these two figures shows that Eq. (3.6) results in improved agreement between observed and estimated lives in torsion but decreased agreement for biaxial stresses. The excellent agreement shown in Fig. 3.28 of Ref. 21 was achieved by a global fit to all of the data, not just the data with ρ = 0 and ∞. The latter is a more severe test of the predictive capability of Eq. (3.6). Although Eq. (3.6) is a convenient analytical form, a different representation of the shape of constant life contours on Brown and Miller's Γ-plane apparently would be more effective.

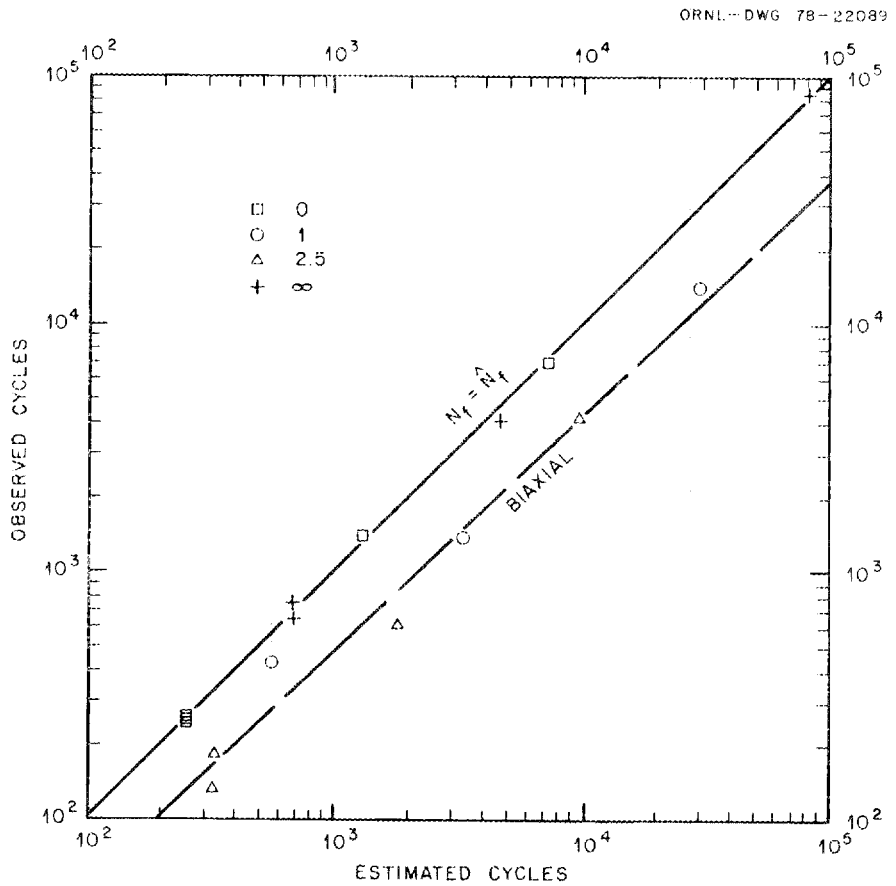

Fig. 3.29. Cycles to failure observed in multiaxial fatigue test of annealed type 304 stainless steel (heat 9T2796) at 538°C (1000°F) without hold time and with ρ = 0, 1, 2.5, and ∞ vs cycles estimated on the basis of the strain analog of Gough's Ellipse Quadrant and power-law fits to the data from purely axial and purely torsional tests.

Plots of creep damage fraction D_c vs fatigue damage fraction D_F for the Pennsylvania State tests with hold time are shown in Figs. 3.30 through 3.32. Only the stresses at the beginning and end of the hold period in each test were available, but these were sufficient to calculate[25] upper and lower bounds on D_c. These are plotted as pairs of symbols connected by vertical lines in Figs. 3.30 through 3.32. Also shown for reference in these figures is the ASME Code's bilinear creep-fatigue damage interaction rule for types 304 and 316 stainless steel. Because the results vary over such a wide range, logarithmic coordinates were used on which the Code's bilinear damage rule plots as a curve asymptotic to D_c = 1

ORNL-DWG 78-22601

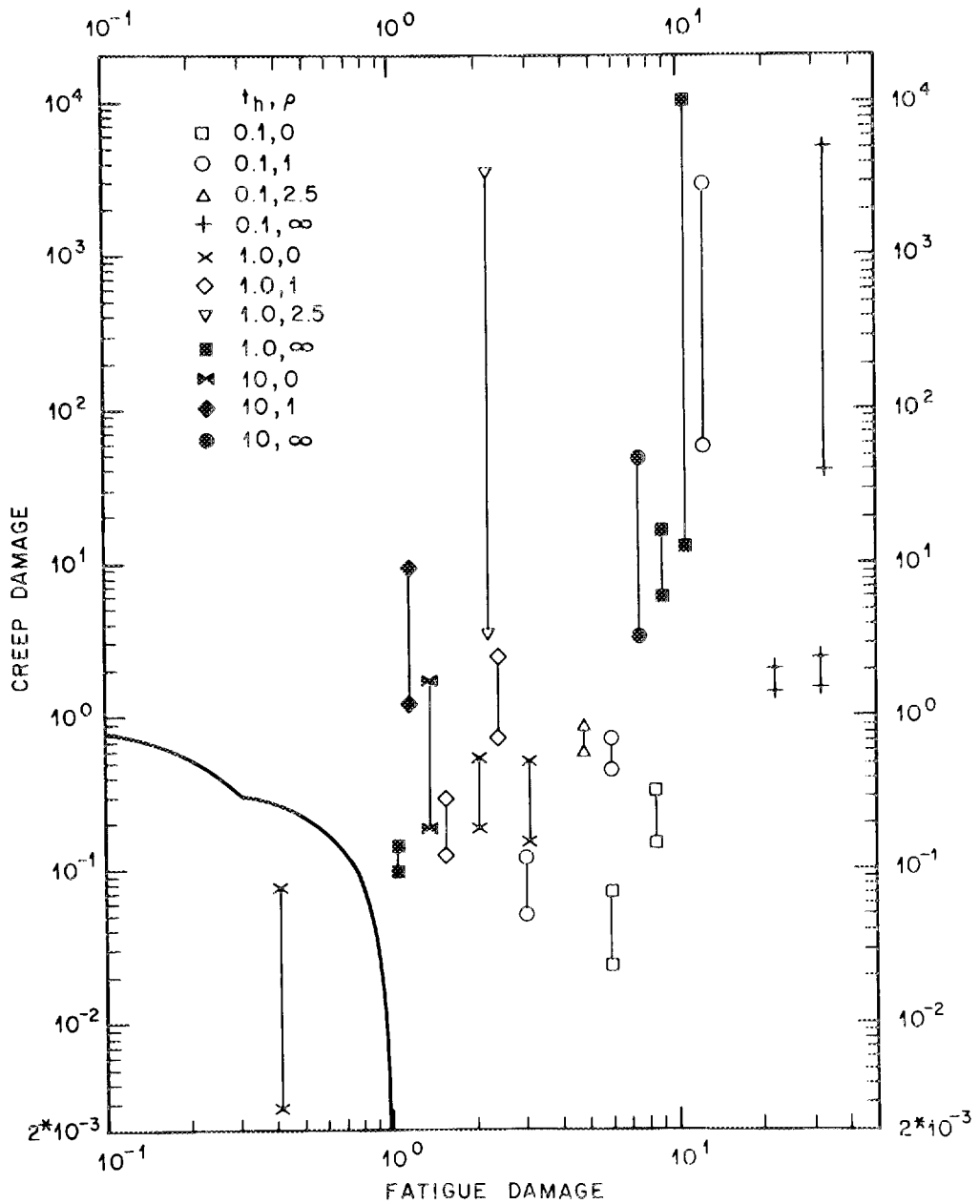

Fig. 3.30. Creep damage fraction vs fatigue damage fraction for multiaxial tests of annealed type 304 stainless steel (heat 9T2796) at 538°C (1000°F) with t_h = 0.1, 1.0, and 10 hr and ρ = 0, 1, 2.5, and ∞ based on ASME Code Case N-47-13 creep and fatigue design rules. ASME Code's creep-fatigue damage interaction curve is shown for comparison.

ORNL-DWG 78-22602

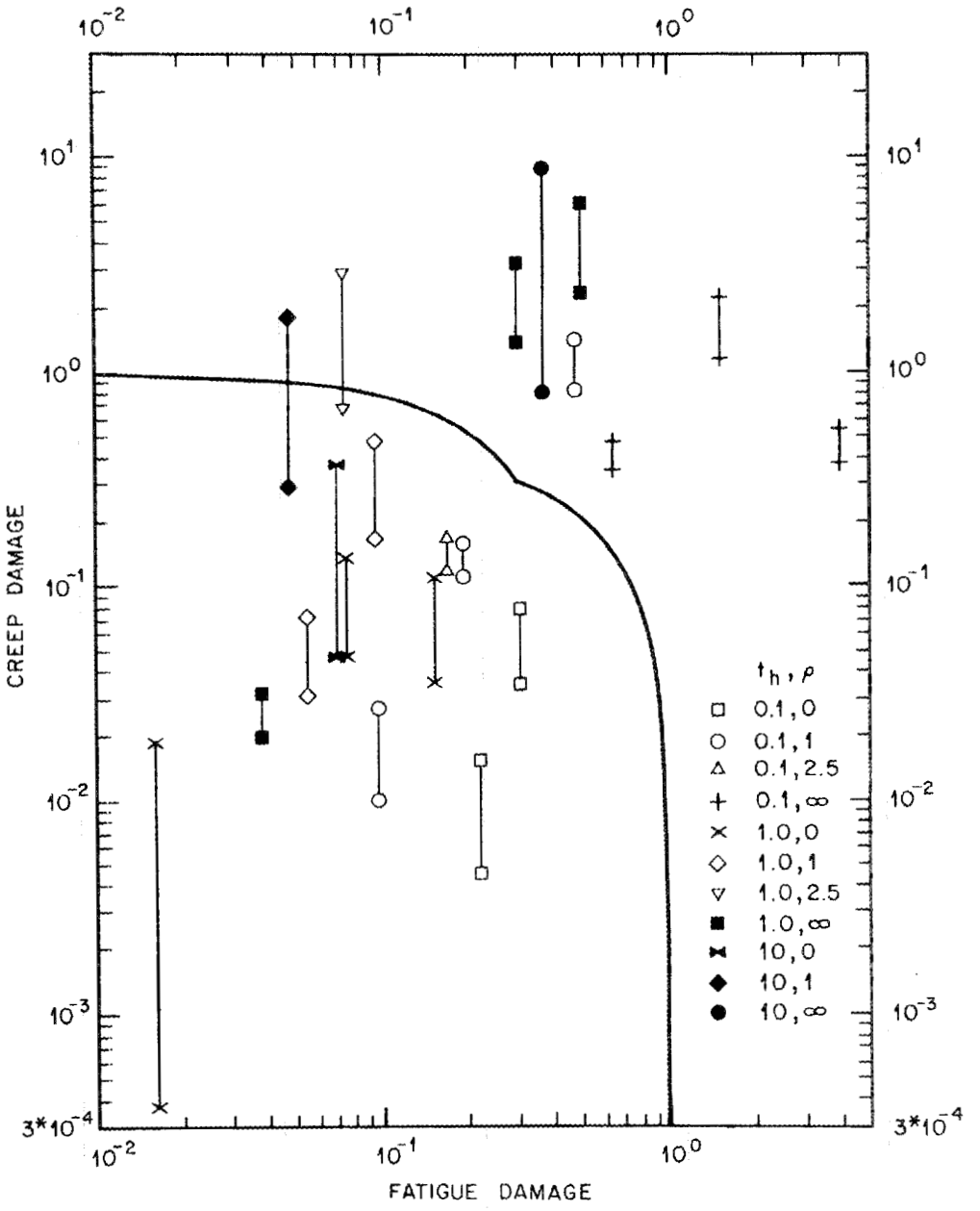

Fig. 3.31. Creep damage fraction vs fatigue damage fraction for multiaxial tests of annealed type 304 stainless steel (heat 9T2796) at 538°C (1000°F) with t_h = 0.1, 1.0, and 10 hr and ρ = 0, 1, 2.5, and ∞ based on equivalent stress, the ORNL stress-rupture law, equivalent inelastic strain range, and a power-law fit to the Pennsylvania State University uniaxial fatigue data. ASME Code's creep-fatigue damage interaction curve is shown for comparison.

ORNL-DWG 78-22603

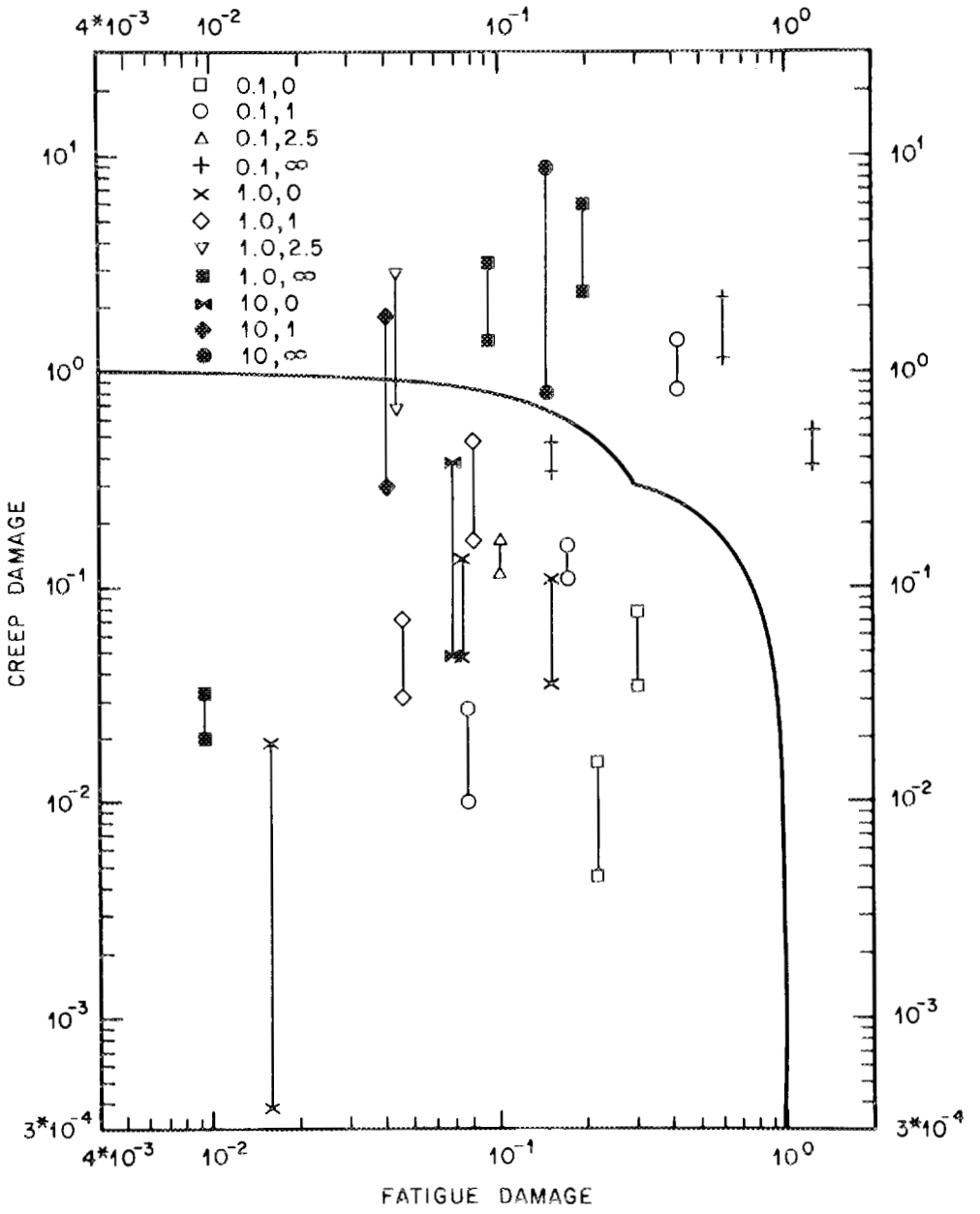

Fig. 3.32. Creep damage fraction vs fatigue damage fraction for multiaxial tests of annealed type 304 stainless steel (heat 9T2796) at 538°C (1000°F) with t_h = 0.1, 1.0, and 10 hr and ρ = 0, 1, 2.5, and ∞ based on equivalent stress, the ORNL stress-rupture law, the strain analog of Gough's Ellipse Quadrant, and fits to the Pennsylvania State University purely axial and purely torsional plastic-strain fatigue data. ASME Code's creep-fatigue damage interaction curve is shown for comparison.

and to $D_F = 1$ and with cups at (0.3, 0.3). For Fig. 3.30, equivalent stress σ_{eq}, $\Delta\varepsilon_{eq}$, and the ASME Code's design curves of stress vs rupture time and strain range vs cycles were used as bases for the creep and fatigue damage calculations. In spite of the large safety factors involved, the results of one test fell within the Code's damage envelope. This may be a faulty observation because, in this test, the amount of stress relaxation (which affects both upper and lower bounds on D_c) did not seem to follow the pattern of other tests.

For Fig. 3.31, σ_{eq}, $\Delta\varepsilon_{eq}^{in}$, a power-law fit to ORNL stress-rupture data for this heat, and a power-law fit to the data from the uniaxial tests at Pennsylvania State without hold time were used as bases for the creep and fatigue damage calculations. The degree of correlation of results achieved by this treatment of the data from multiaxial tests with $\rho = 0$, 1, 2.5, and ∞ (as evidenced by Fig. 3.31) is not very different from that achieved in previous investigations using data from uniaxial tests.[26,27]

In Fig. 3.32, the creep damage fractions are identical to those of Fig. 3.31; only the fatigue damage fractions are different. In this case, Eq. (3.6) and fits to the data from purely axial and purely torsional tests without hold time were used in the fatigue damage calculations. Comparison of Fig. 3.32 with Fig. 3.31 shows that the results of the six torsional tests that lay to the right of the interaction curve were moved closer to the curve, while the one to the left was moved farther away. The overall effect has been to moderately reduce the total variation about the curve for all the data. The use of a different multiaxial fatigue failure criterion based on the shear and normal strains on the planes of maximum shear strain might be expected to lead to a somewhat greater improvement in agreement between results of tests with different ratios of shear to axial strain, even with hold periods at constant strain.

These results tend to confirm the adequacy of current design methods while indicating that a more effective alternative to the usual equivalent strain approach can be developed. In addition to the effects described here, note that the *sign of the normal strain* on the maximum shear plane *has a potential for distinguishing* between multiaxial effects

analogous to the differences observed *between tensile and compressive hold* periods in uniaxial tests. This potential will be explored when sufficient data from multiaxial tests with hold periods at negative strains become available.

3.8 Sensitivity Study of Current Design Rules to Heat-to-Heat Material Property Variations

W. J. McAfee W. K. Sartory

(Last reported in ORNL-5433, p. 175)

A study has been implemented to determine the sensitivity of current high-temperature design methods to heat-to-heat variations in materials properties and to use this information in assessing the degree of conservatism built into currently recommended design rules. The study consists of two phases: (1) compilation of applicable 304 stainless steel material property data and analysis of their heat-to-heat variation and (2) use of these data in an inelastic ratchetting analysis of an infinite pipe to study the sensitivity to property variations and to compare the results with design limits.

3.8.1 Compilation and analysis of applicable data

In an effort to guide and simplify selection and treatment of the materials properties data, ground rules were established that were intended to reflect the specific needs and aims of the inelastic analyses. Also, definition of both the problem to be analyzed and of a tentative histogram aided in determining what data were needed, as well as the most useful format for data presentation. Of the properties generally used in analyses, the most influential and important are those associated with inelastic behavior and failure. These are:

1. bilinearized yield stress, (a) monotonic — κ_0 (T), (b) tenth cycle — κ_1 (T),
2. slope of plastic portion of stress-strain curve, or $E^p(T)$,
3. creep strain vs time at constant stress and temperature,
4. stress to rupture — $\sigma_r(T, t_r)$,
5. fatigue strain range — $\varepsilon_t(T, N_f)$.

These properties were given primary consideration in collecting and evaluating variable material properties data. Other properties considered included

6. Young's modulus — $E(T)$,
7. Poisson's ratio — $\nu(T)$,
8. instantaneous thermal expansion coefficient — $\alpha(T)$,
9. volumetric heat capacity — $\rho C_p(T)$,
10. thermal conductivity — $k(T)$.

In performing the data compilation, heats were generally included only if two or more of the required inelastic properties were available. This was done so that the resulting data sets would provide a valid basis for preparing any required cross correlations of different materials properties. We anticipated that cross correlations of some properties might be useful as a means of restricting the size of the total field representing the materials variability. The type of cross correlation one might expect is shown schematically in Fig. 3.33.

In an effort to further simplify the analysis of heat-to-heat variability, a particular property was assumed to follow the same basic trend for all heats. In other words, property curves for a number of heats

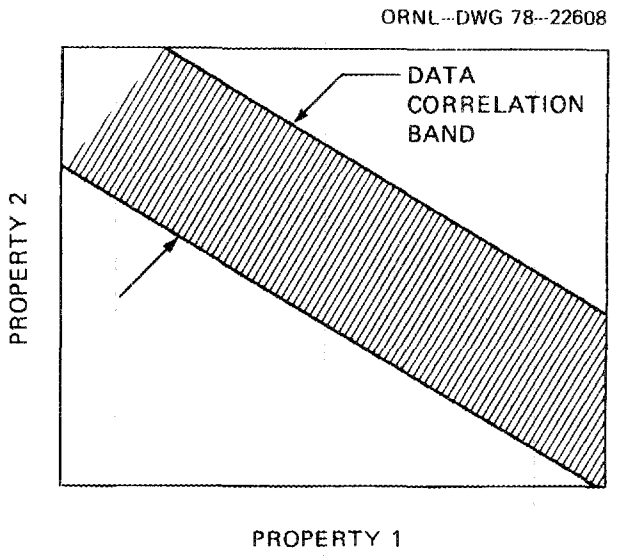

Fig. 3.33. Hypothetical correlation of two materials properties that permits restriction of variability consideration to band rather than entire data field.

were modeled as a family of parallel curves, with one curve for each heat. For example, the correlation for time to rupture (isothermal) was

$$\log (t_r)_{\text{all data}} = \log (a\sigma^b)_{\text{all data}} .$$

Rupture time for a given heat was then represented by

$$\log (t_r)_{\text{heat}} = \log (a\sigma^b)_{\text{all data}} + H_{\text{heat}} ,$$

where H_{heat} is a factor representing the displacement of the curve for that heat from the master curve for all heats. This procedure was confirmed as adequate for this study.

The inelastic analyses to be conducted are based on a ratchetting problem involving a period of isothermal creep followed by a plastic cycle with a strain range of ∿0.4%. Only cyclic stress-strain data for 0.4% strain range were thus required. The isothermal hold is at 593°C (1100°F), and the minimum temperature in the transient is ∿427°C (800°F). The range of data was thus restricted to 400 to 650°C (752 to 1202°F).

Existing data compilations and correlations were used wherever possible, with modifications to reflect the particular needs and/or limits of this study. Only data for material in the reannealed condition were utilized, primarily because this is essentially the only condition in which a complete set (tensile, creep, fatigue, etc.) of data is available. A brief discussion of the material properties data compilation and analysis is given below.

3.8.1.1 Tensile yield (0.2%) and ultimate strength. These tensile properties, though not required as direct input to the inelastic analysis, were utilized in some property models and are thus included here for completeness. Tensile data for the 20 heats of type 304 stainless steel used in this study are presented in Refs. 28 through 33. Table 3.9 lists the heats and manufacturers, and the chemical compositions of these heats are given in Ref. 31.

For yield strength (0.2%), 129 data points were used to establish a master curve of yield stress vs temperature over the range 400 to 650°C (752 to 1202°F). Regressions analysis indicated the adequacy of an

Table 3.9. Listing of heats used in variability study

Vendor[a]	Identification No.[b]	Heat No.[c]
Allegheny Ludlum	3	337187
	11	55697
	19	345866
	9	346544
	5	337330
	18	346845
	13	346779
Cameron	2	3121
Carlson	7	310390
	8	600414
	10	60551
	12	616737
	6	300380
	1	544086
Republic	17	8043813
United States Steel	14	9T2796
	16	X22807
	15	9T2797
	4	R23283
	20	R22926

[a]Allegheny Ludlum = Allegheny Ludlum Steel Corporation, Pittsburgh, Pa.; Cameron = Cameron Iron Works, Inc., Houston, Tex.; Carlson = Carlson Steel Company, Coatesville, Pa.; Republic = Republic Steel Corporation, Cleveland, Ohio; United States Steel = United States Steel Corporation, Pittsburgh, Pa.

[b]Identifying number used for this study.

[c]Manufacturer's heat number.

equation of the form

$$\bar{\sigma}_y = a_1 + a_2 T \ , \tag{3.7}$$

where $\bar{\sigma}_y$ is the mean value of yield stress [MPa (ksi)] for all heats, T is temperature (°C), and a_1, a_2 are fitted coefficients. The results of the

regression are contained in Table 3.10. The heat-to-heat variability of yield stress, as discussed previously, was modeled by

$$\begin{aligned} \sigma_{y_{heat}} &= \bar{\sigma}_y + H_{heat} \\ &= (a_1 + H_{heat}) + a_2 T \\ &= a_1' + a_2 T \quad . \end{aligned} \tag{3.8}$$

The tabulated results for each heat are contained in Table 3.11. In addition, a value of standard error of estimate (SEE) is shown for each heat. The fit to all data is shown in Fig. 3.34. The limits shown represent ±2SEE. One adjusted fit for heat number 14 (9T2796) is shown in Fig. 3.35 and is typical of the agreement found between data and curves for other heats.

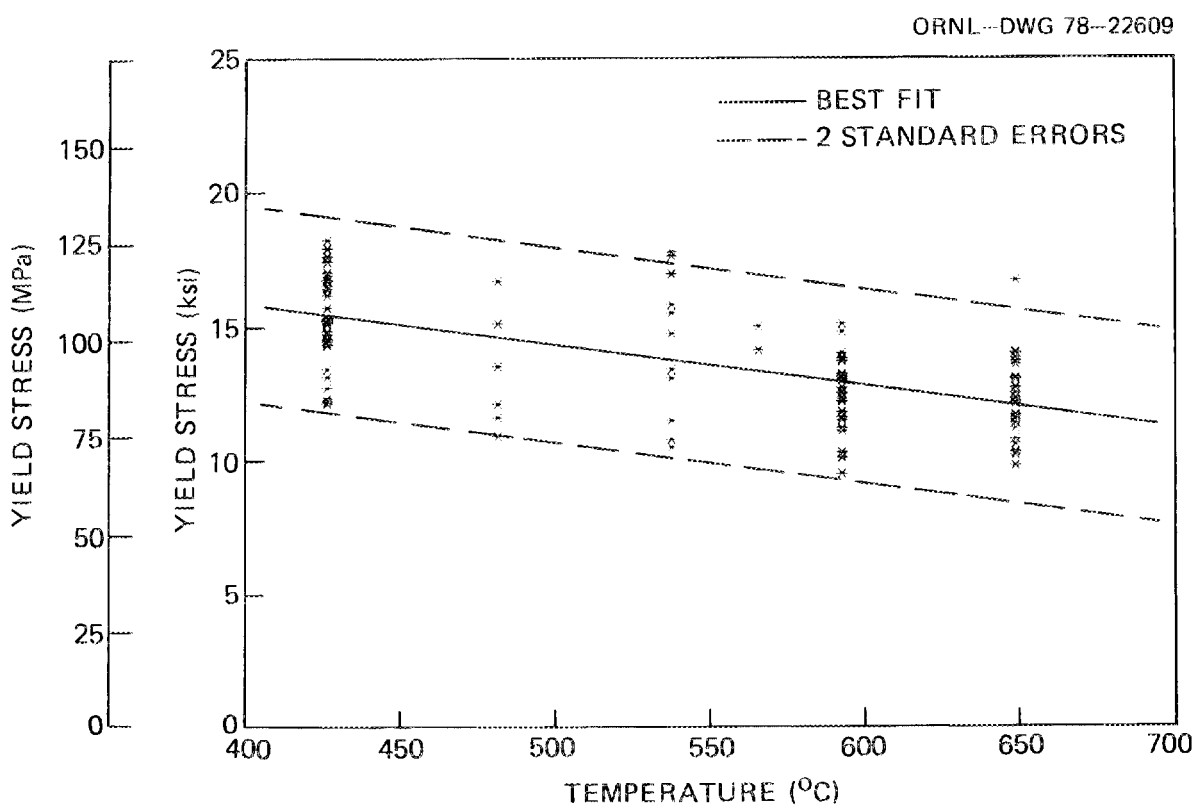

Fig. 3.34. Yield stress (0.2% vs temperature over the range 400 to 650°C (750 to 1200°F) for 20 heats of type 304 stainless steel (1 ksi = 6.895 MPa).

Table 3.10. Summary of results of least-squares fits to tensile yield and ultimate strength data [MPa (ksi)]

Property	Order of equation	a_1	a_2	a_3	R^2[a]	SEE[b]
Yield stress	1	151.80 (22.01597)	−0.10589 (−0.015358)		0.98284	12.5386 (1.8185)
Ultimate stress	2	117.54 (17.04717)	1.55265 (0.22533)	-1.98123×10^{-3} $(-2.87343 \times 10^{-4})$		20.4582 (2.9671)

[a] R = correlation coefficient.

[b] SEE = standard error of estimate.

Table 3.11. Heat-to-heat variability of yield stress (0.2%) and ultimate stress functions [MPa (ksi)]

Heat identification No.	Yield stress parameters			Ultimate stress parameters		
	a_1	H	SEE	a_1	F	SEE
1	153.1437 (22.2108)	1.3436 (0.1949)	1.5857 (0.2300)	126.3813 (18.3294)	8.8410 (1.2822)	11.6265 (1.6862)
2	150.6155 (21.8442)	−1.1846 (−0.1718)	2.2770 (0.3302)	87.7693 (12.7294)	−29.7710 (−4.3178)	13.7471 (1.9938)
3	141.8819 (20.5775)	−9.9182 (−1.4385)	3.1098 (0.4510)	101.7891 (14.7627)	−15.7511 (−2.2844)	13.3380 (1.9344)
4	145.3294 (21.0775)	−6.4707 (−0.9385)	3.0499 (0.4423)	125.4619 (18.1961)	7.9217 (1.1489)	6.1657 (0.8942)
5	165.0950 (23.9442)	13.2949 (1.9282)	1.0702 (0.1552)	126.6111 (18.3627)	9.0709 (1.3156)	21.7274 (3.1512)
6	165.0037 (23.9309)	13.2036 (1.9150)	2.6849 (0.3894)	133.9658 (19.4294)	16.4255 (2.3822)	13.0019 (1.8857)
7	151.6498 (21.9942)	−0.1503 (−0.0218)	1.9036 (0.2761)	141.2055 (20.4794)	23.6653 (3.4322)	5.2173 (0.7567)
8	159.3562 (23.1118)	7.5561 (1.0959)	5.5185 (0.8004)	138.0921 (20.0279)	20.5518 (2.9807)	16.3313 (2.3686)
9	160.9580 (23.3442)	9.1579 (1.3282)	5.8635 (0.8504)	130.7481 (18.9627)	13.2079 (1.9156)	13.4628 (1.9525)
10	155.3284 (22.5277)	3.5283 (0.5117)	8.7367 (1.2671)	103.5171 (15.0134)	−14.0231 (−2.0338)	53.6719 (7.7842)
11	161.5360 (23.4280)	9.7359 (1.4120)	12.8020 (1.8567)	112.0467 (16.2504)	−5.4935 (−0.7967)	20.3934 (2.9577)
12	152.3393 (22.0942)	0.5392 (0.0782)	5.3468 (0.7755)	141.2055 (20.4794)	23.6653 (3.4322)	6.6711 (0.9675)
13	164.4055 (23.8442)	12.6054 (1.8282)	4.1807 (0.6063)	129.1393 (18.7294)	11.5990 (1.6822)	12.6466 (1.8342)
14	136.5599 (19.8056)	−15.2402 (−2.2103)	8.7505 (1.2691)	105.8485 (15.3515)	−11.6917 (−1.6957)	14.2413 (2.0655)
15	139.8134 (20.2775)	−11.9867 (−1.7385)	3.6184 (0.5248)	122.7039 (17.7961)	5.1637 (0.7489)	0.8324 (0.1207)
16	148.6443 (21.5583)	−3.1558 (−0.4577)	3.9230 (0.5690)	90.7637 (13.1637)	−26.7765 (−3.8835)	11.7637 (1.7061)
17	150.5094 (21.8288)	−1.2907 (−0.1872)	4.1390 (0.6003)	134.6820 (19.5333)	17.1417 (2.4861)	15.9452 (2.3126)
18	157.5341 (22.8476)	5.7340 (0.8316)	9.5790 (1.3893)	130.9779 (18.9961)	13.4377 (1.9489)	28.6979 (4.1621)
19	152.8800 (22.1726)	1.0799 (0.1566)	13.2839 (1.9266)	113.5318 (16.4658)	−4.0084 (−0.5813)	15.9250 (2.3096)
20	153.3753 (22.2442)	1.5734 (0.2282)	2.9558 (0.4287)	118.3371 (17.1627)	0.7969 (0.1156)	6.6905 (0.9703)

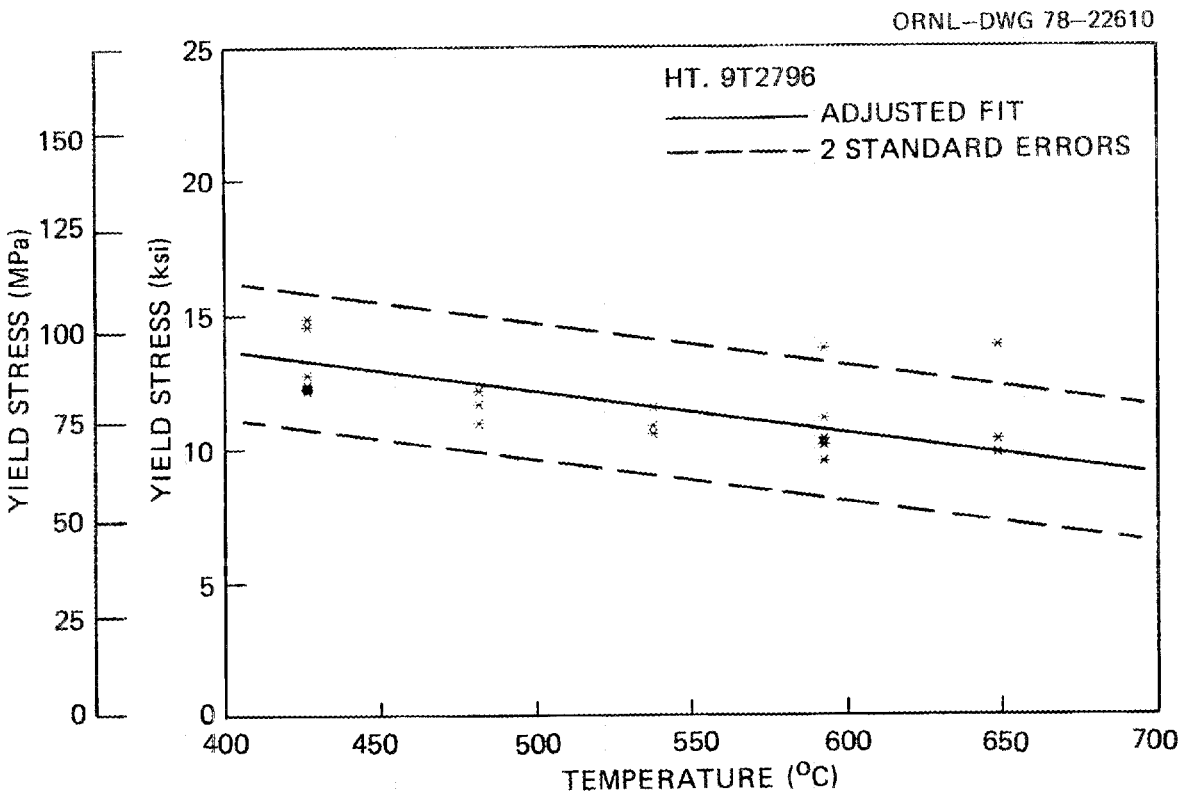

Fig. 3.35. Comparison of yield stress data and adjusted fit to heat 9T2796 over the range 400 to 650°C (750 to 1200°F) (1 ksi = 6.895 MPa).

Ultimate tensile strength data were treated in the same manner as the yield stress data. Regression analysis indicated that an adequate description of data over the temperature range 400 to 650°C (750 to 1200°F) is provided by an equation of the form

$$\bar{\sigma}_u = a_1 + a_2 T + a_3 T^2 \ , \tag{3.9}$$

where $\bar{\sigma}_u$ is the mean value of ultimate strength [MPa (ksi)] for all data, T is the temperature (°C), and a_1, a_2, a_3 are fitted coefficients. The results of the regression analysis are shown in Table 3.10, and the fit is shown in Fig. 3.36.

The heat-to-heat variability of $\bar{\sigma}_u$ was modeled by

$$\begin{aligned} \sigma_{u_{\text{heat}}} &= \bar{\sigma}_u + F_{\text{heat}} \\ &= (a_1 + F_{\text{heat}}) + a_2 T + a_3 T^2 \\ &= a_1' + a_2 T + a_3 T^2 \ . \end{aligned} \tag{3.10}$$

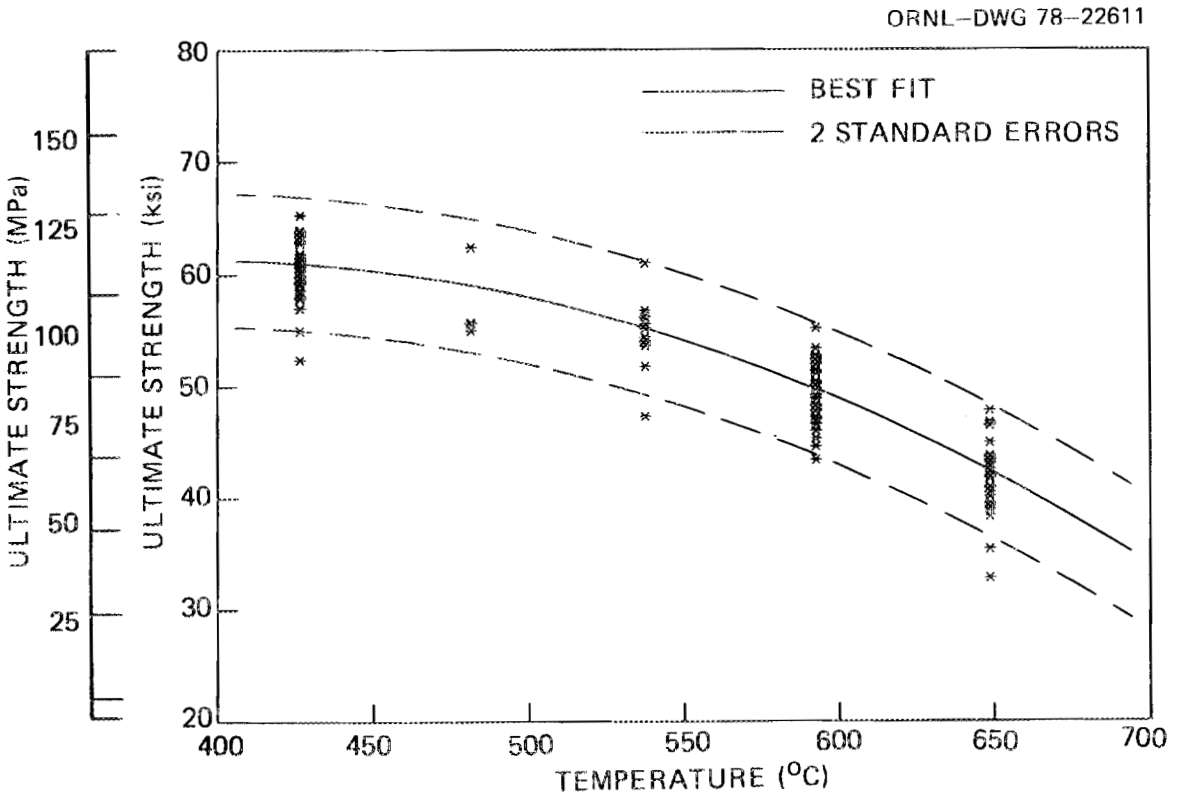

Fig. 3.36. Ultimate tensile strength vs temperature over the range 400 to 650°C (750 to 1200°F) for 20 heats of type 304 stainless steel (1 ksi = 6.895 MPa).

Figure 3.37 shows how well the adjusted fit agrees with the data for a particular heat (9T2796).

3.8.1.2 Bilinear yield stress and hardening parameters. There is only a limited amount of data available on the bilinear yield stress and hardening parameters for type 304 stainless steel.[33-36] Furthermore, these data are all for a single heat of material (9T2796). For the purpose of analyzing a specific structural member, we select here only the data that correspond to the strain range (0.4%) of interest.

In lieu of an adequate heat-to-heat variability data base, an effort was made to relate the bilinearized stress-strain curve to conventional stress-strain parameters. By assuming that the bilinear yield would have the same temperature dependency as 0.2% offset yield, a relationship was developed for its heat-to-heat variability with temperature. In particular, the yield stress data (0.2%) for the heat 9T2796 were represented by

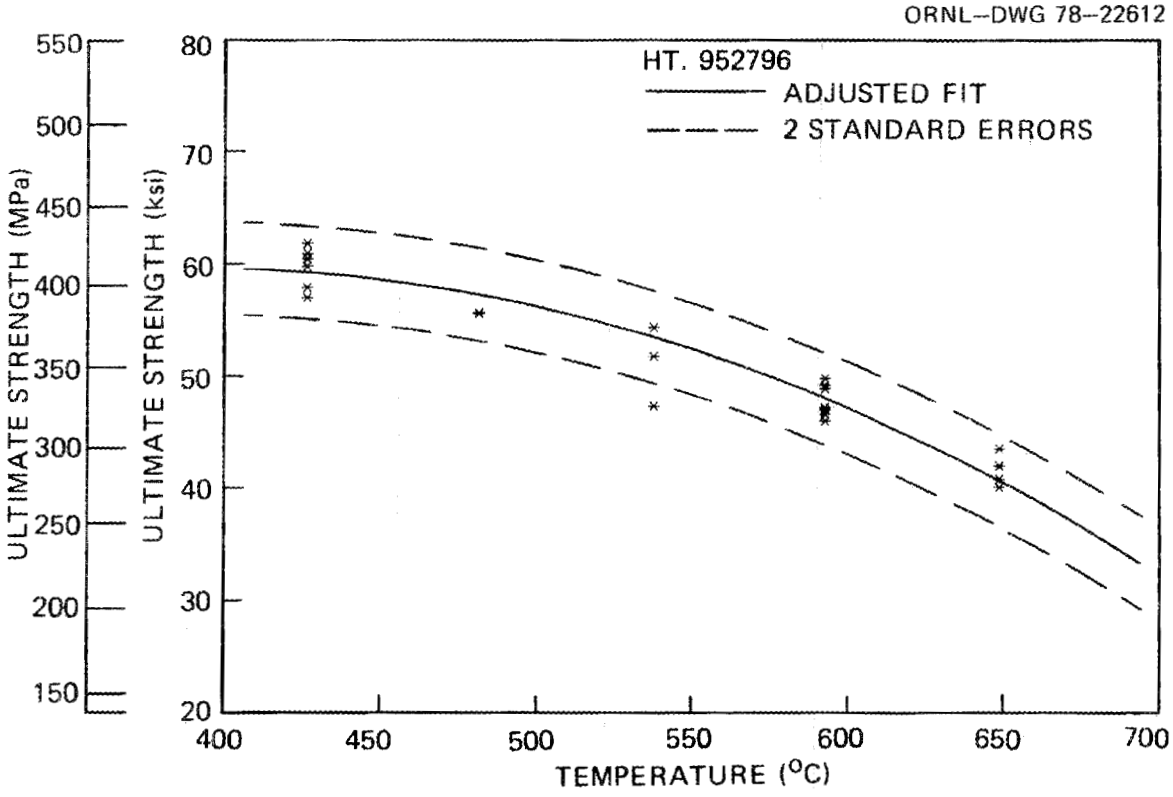

Fig. 3.37. Comparison of ultimate strength data and adjusted fit for heat 9T2796 over the range 400 to 650°C (750 to 1200°F) (1 ksi = 6.895 MPa).

the equation

$$\sigma_y = a_1 + a_2 T \ , \tag{3.11}$$

where σ_y is 0.2% offset yield stress (MPa), T is temperature (°C), and the regression coefficients are a_1 = 121.5 and a_2 = −0.07850. The equation,

$$\begin{aligned} \sigma_y)_o &= a_1' + a_2 T \\ &= b a_1 + a_2 T \ , \end{aligned} \tag{3.12}$$

where $\sigma_y)_o$ is the initial bilinear yield stress (MPa), which was fitted to the available bilinear yield stress data in Table 3.12 by the method of least squares, with a_1 and a_2 held constant. The results were a_1' = 107.6 or b = 0.886. The fit is shown in Fig. 3.38.

Table 3.12. Summary of bilinear yield stress and hardening parameters

Temperature [°C (°F)]	$(\sigma_y)_0$[a] [MPa (ksi)]	$(\sigma_y)_1$[b] [MPa (ksi)]
427 (800)	76.26 (11.06)[c]	89.36 (12.96)[c]
	69.80 (10.12)[d]	79.90 (11.59)[d]
482 (900)	69.16 (10.03)[c]	91.36 (13.25)[c]
538 (1000)	68.74 (9.97)[c]	89.91 (13.04)[c]
	76.96 (11.16)[d]	82.43 (11.96)[d]
593 (1100)	62.06 (9.00)[c]	99.63 (14.45)[c]
	48.81 (7.08)[d]	94.11 (13.65)[d]

[a] $(\sigma_y)_0$ = initial bilinear yield stress.
[b] $(\sigma_y)_1$ = tenth cycle bilinear yield stress.
[c] ORNL data, Ref. 34.
[d] ANL data, Ref. 33.

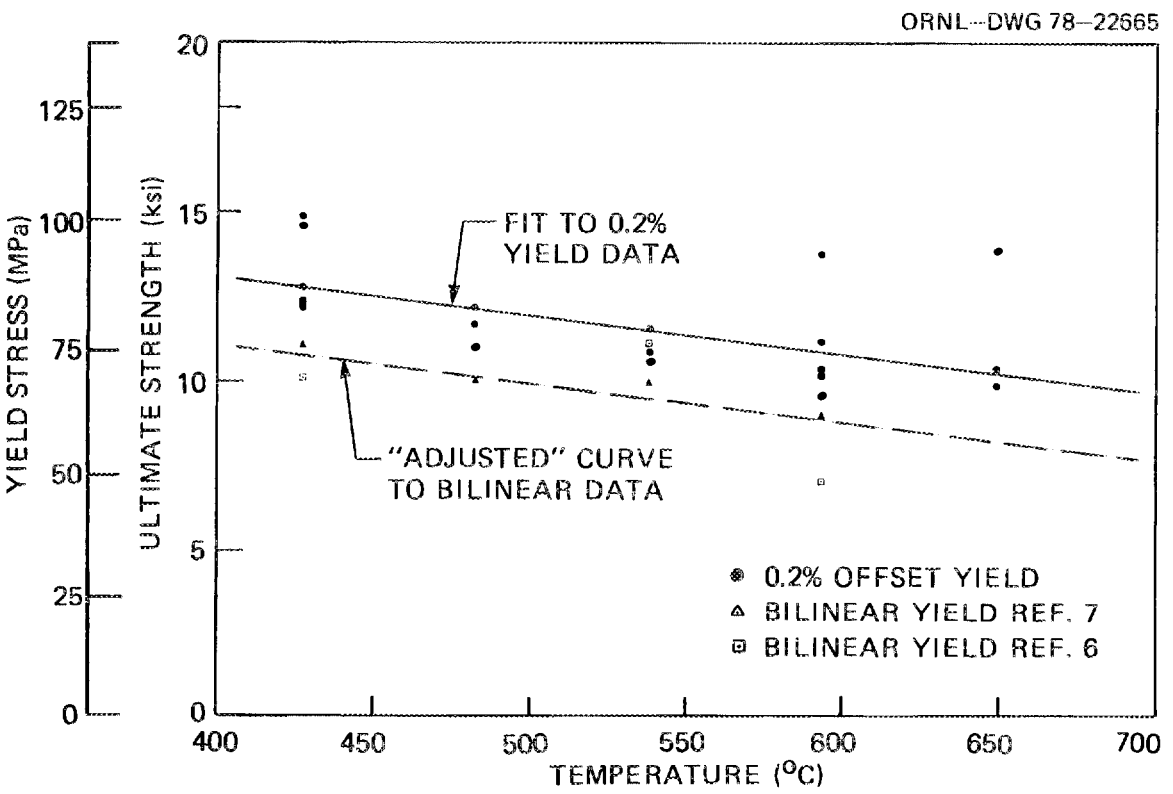

Fig. 3.38. Initial bilinear yield stress vs temperature for type 304 stainless steel, heat 9T2796 (1 ksi = 6.895 MPa).

The factor b in Eq. (3.12) was taken to be constant for all heats. Thus, the bilinear yield stress for any heat is obtained by multiplying the constant a_1 in Eq. (3.8) by 0.886. This was done, and the resulting heat-to-heat variability is summarized in Table 3.13.

Efforts to relate tenth-cycle yield and the slope of the elastic-plastic curve (C and E^p) to conventional stress-strain parameters were unsuccessful. The parameters C or E^p could be calculated from a parametric representation of the initial loading true stress-strain curve such as is contained in the *NSM Handbook*.[14] Heat-to-heat variability would

Table 3.13. Summary of heat-to-heat variability of coefficients[a] for initial bilinearized yield stress [MPa (ksi)]

Heat identification No.	a_1	a_1'
1	153.1437 (22.2108)	135.6853 (19.6788)
2	150.6155 (21.8442)	133.4454 (19.3539)
3	141.8819 (20.5775)	125.7073 (18.2317)
4	145.3294 (21.0775)	128.7618 (18.6747)
5	165.0950 (23.9442)	146.2742 (21.2145)
6	165.0037 (23.9309)	146.1933 (21.2028)
7	151.6498 (21.9942)	134.3617 (19.4868)
8	159.3562 (23.1118)	141.1896 (20.4771)
9	160.9580 (23.3442)	142.6088 (20.6829)
10	155.3284 (22.5277)	137.7210 (19.9595)
11	161.5360 (23.4280)	143.1209 (20.7572)
12	152.3393 (22.0942)	134.9726 (19.5754)
13	164.4055 (23.8442)	145.6633 (21.1259)
14	136.5599 (19.8056)	120.9921 (17.5478)
15	139.8134 (20.2775)	123.8746 (17.9659)
16	148.6443 (21.5583)	131.6989 (19.1006)
17	150.5094 (21.8288)	133.3513 (19.3403)
18	157.5341 (22.8476)	139.5753 (20.2430)
19	152.8800 (22.1726)	135.4517 (19.6449)
20	153.3735 (22.2442)	135.8890 (19.7083)

[a] $\sigma_y)_0 = a_1' - 0.10589T$, when stress is in MPa and T is in °C; $\sigma_y)_0 = (a_1') - 0.015358T$, when stress is in ksi and T is in °C. $a_1' = 0.886\ a_1$.

then be introduced through the yield stress. This approach was not pursued here. For interim recommendations, it is suggested that *NSM Handbook* values be used for bilinear stress-strain parameters other than initial yield.

3.8.1.3 Stress-rupture properties. Time to rupture as well as secondary creep rate were addressed in this study, and the extensive work contained in Refs. 37 and 38 was utilized. Data from Refs. 7, 19, 28, 29, and 39 were also used. Primary consideration was given to data at 593°C (1100°F) because in the proposed analysis, all time-dependent deformation will occur at this temperature.

For time to rupture, 229 data points from 19 heats of material were available to establish a "master" creep-rupture curve. Consideration was given to several potential functions to use in the representations. Based on the previous work in Refs. 37 and 38, we decided (at least for interim use) to fit the data with a power-law formulation, that is,

$$\bar{t}_r = a_1 \sigma^{a_2} , \tag{3.13}$$

where $\bar{t}_r$ is mean time to rupture for all heats, σ is stress [MPa], and a_1, a_2 are regression coefficients. The results of the fit to all data are given in Table 3.14. The data and fit are compared in Fig. 3.39.

Table 3.14. Summary of results of least-squares fits[a] to time-to-rupture and minimum creep rate data

Property	Coefficients [MPa (ksi)]			
	a_1	a_2	R^2[b]	*SEE*[c]
Time to rupture	7.24031×10^{-19} (3.34556×10^{-13})	−7.55519	0.96883	0.44118
Minimum creep rate	1.06345×10^{-24} (1.45649×10^{-16})	9.70335	0.90771	0.56634

[a]Fits were done to $\log_{10}$ form of power law.

[b]R = correlation coefficient.

[c]*SEE* = standard error of estimate.

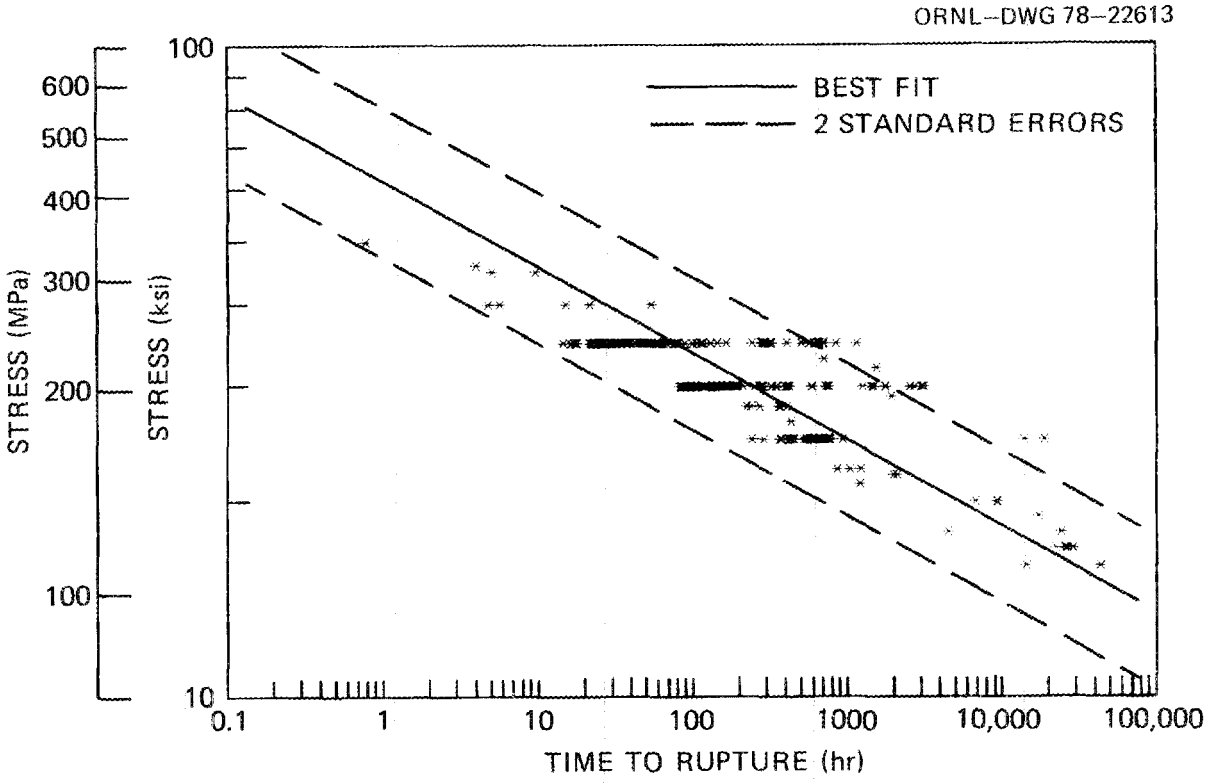

Fig. 3.39. Time to rupture vs stress for 19 heats of type 304 stainless steel at 593°C (1100°F) (1 ksi = 6.895 MPa).

The heat-to-heat variability was computed based on the equation

$$\log (t_r)_{\text{heat}} = \log \bar{t}_r + \log B_{\text{heat}}$$

$$= \log (a_1 B_{\text{heat}}) + a_2 \log \sigma$$

$$= \log a_1' + a_2 \log \sigma \ . \tag{3.14}$$

The variability results are summarized in Table 3.15. For comparison, Fig. 3.40 shows the data for heat 9T2796 and the adjusted fits.

The minimum creep rate data were handled in much the same manner. Several formulations have been advanced for correlating minimum creep rate with applied stress, but, for interim use in this study, a power law was utilized, that is,

$$\bar{\dot{\varepsilon}}_m = a_1 \sigma^{a_2} \ , \tag{3.15}$$

where $\bar{\dot{\varepsilon}}_m$ is mean minimum creep rate for all heats (percent per hour) and

Table 3.15. Heat-to-heat variability of time-to-rupture and minimum creep rate functions per type 304 stainless steel at 593°C (1100°F)

Heat identification No.	Time-to-rupture parameters			Minimum creep rate parameters		
	a_1' [MPa (ksi)]	B	SEE	a_1' [MPa (ksi)]	E	SEE
1	2.7654×10^{14} (4.0107×10^{13})	1.19879	0.17706	8.3518×10^{-16} (1.2113×10^{-16})	0.83164	0.21290
3	1.2144×10^{14} (1.7613×10^{13})	0.52646	0.25924	1.8445×10^{-15} (2.6751×10^{-16})	1.83666	0.23888
4	2.5322×10^{14} (3.6725×10^{13})	1.09771	0.10852	1.3773×10^{-15} (1.9975×10^{-16})	1.37144	0.08776
5	2.5201×10^{14} (3.6550×10^{13})	1.09250	0.20015	7.9076×10^{-16} (1.1469×10^{-16})	0.78742	0.20161
6	6.2713×10^{14} (9.0954×10^{13})	2.71863	0.18858	1.3922×10^{-16} (2.0191×10^{-17})	0.13863	0.24565
7	9.2089×10^{14} (1.3356×10^{14})	3.99209	0.00917	9.4520×10^{-17} (1.3708×10^{-17})	0.09412	*a*
8	1.2704×10^{15} (1.8424×10^{14})	5.50711	0.25386	8.1758×10^{-17} (1.1858×10^{-17})	0.08141	0.17640
9	2.9651×10^{14} (4.3003×10^{13})	1.28536	0.15437	7.3987×10^{-16} (1.0717×10^{-16})	0.73585	0.24299
10	1.8670×10^{15} (2.7078×10^{14})	8.09370	0.29418	1.2606×10^{-16} (1.8283×10^{-17})	0.12553	0.39129
11	1.5592×10^{14} (2.2613×10^{13})	0.67592	0.23927	1.6184×10^{-15} (2.3471×10^{-16})	1.61151	0.16488
12	3.1855×10^{15} (4.6200×10^{14})	13.80919	0.09407	4.0187×10^{-17} (5.8284×10^{-18})	0.04002	0.09957
13	3.2517×10^{14} (4.7161×10^{13})	1.40964	0.17858	5.7298×10^{-16} (8.3101×10^{-17})	0.57056	0.17112
14	1.5029×10^{14} (2.1797×10^{13})	0.65152	0.25195	1.6001×10^{-15} (2.3206×10^{-16})	1.59329	0.30595
15	1.5283×10^{14} (2.2165×10^{13})	0.66253	0.25706	1.1696×10^{-15} (1.6964×10^{-16})	1.16470	0.23212
16	8.0555×10^{13} (1.1683×10^{13})	0.34921	0.20320	1.9236×10^{-14} (2.7898×10^{-15})	19.15453	0.95311
17	1.2312×10^{15} (1.7857×10^{14})	5.33740	0.39793	1.6834×10^{-16} (2.4415×10^{-17})	0.16763	0.50301
18	1.3581×10^{15} (1.9697×10^{14})	5.88743	0.25330	1.0264×10^{-16} (1.4886×10^{-17})	0.10221	0.46285
19	1.1003×10^{14} (1.5958×10^{13})	0.47697	0.11603	5.1034×10^{-15} (7.4015×10^{-16})	5.08178	0.05322
20	2.0733×10^{15} (3.0070×10^{14})	8.98796	0.15981	1.0042×10^{-16} (1.4565×10^{-17})	0.10000	0.23285

[a]Not enough data for statistical significance.

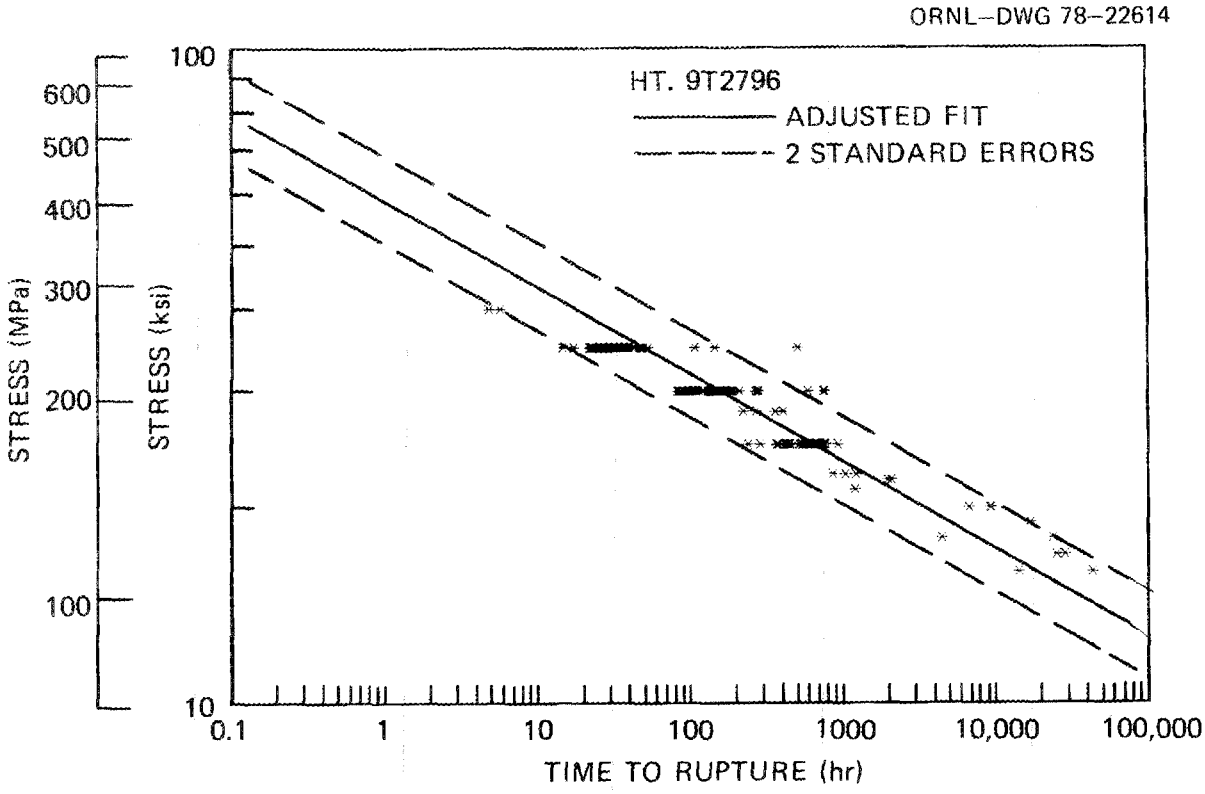

Fig. 3.40. Comparison of time to rupture data to adjusted fit for heat 9T2796 at 593°C (1100°F) (1 ksi = 6.895 MPa).

α_1, α_2 are regression coefficients. At 593°C, 232 data points on 19 heats of material were analyzed, yielding the results in Table 3.14 and shown graphically in Fig. 3.41.

The heat-to-heat variability was treated like that for time to rupture. Thus,

$$\begin{aligned} \log (\varepsilon)_{heat} &= \log \bar{\dot{\varepsilon}} + \log E_{heat} \\ &= \log (\alpha_1 E_{heat}) + \alpha_2 \log \sigma \\ &= \log \alpha_1' + \alpha_2 \log \sigma \ . \end{aligned} \tag{3.16}$$

These results are summarized in Table 3.15, and Fig. 3.42 shows a comparison between data and adjusted fit for heat 9T2796.

3.8.1.4 Fatigue properties. In considering fatigue properties, it was concluded that reliance on previous work was essential due to problem complexity. Diercks and Raske[10] performed a thorough statistical

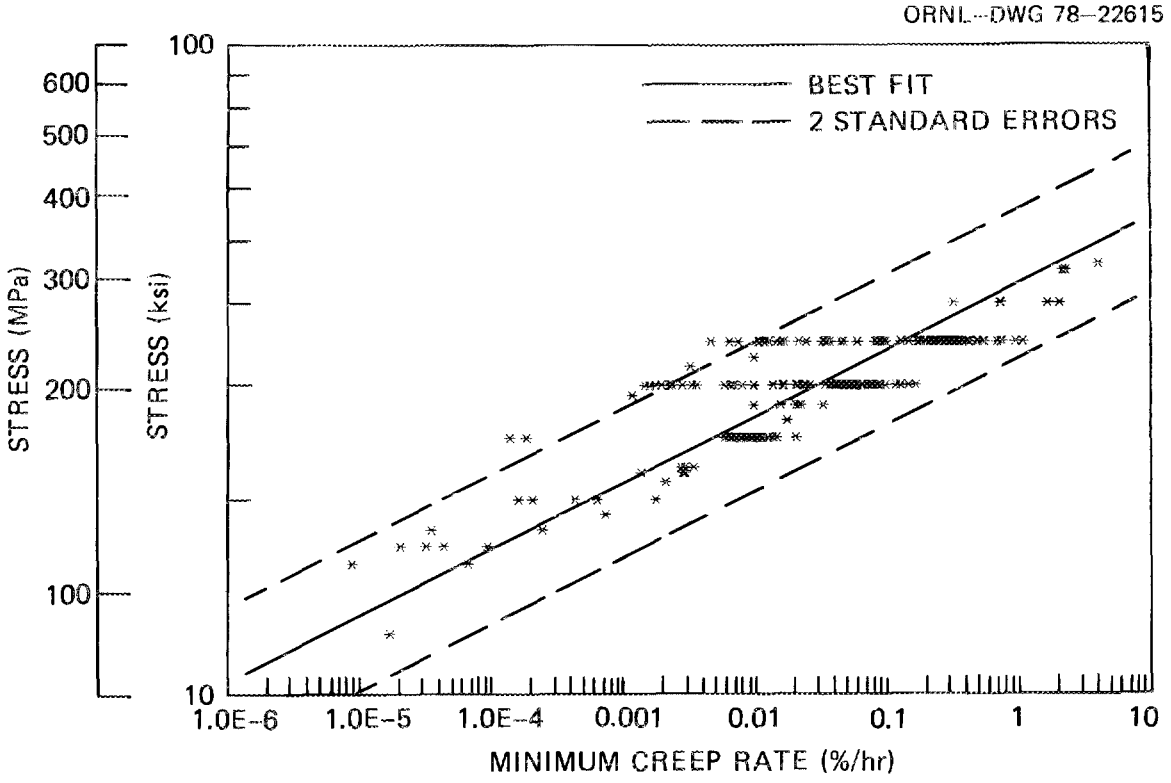

Fig. 3.41. Minimum creep rate vs stress for 19 heats of type 304 stainless steel at 593°C (1100°F) (1 ksi = 6.895 MPa).

analysis of the then-available data on type 304 stainless steel. With respect to heat-to-heat variability, they concluded that, for continuous cycling, there were no statistically significant differences in the data from the different heats.

For zero hold-time conditions, that is, those to be used in the structural analyses, the formulation proposed in Ref. 10 reduces to

$$(\log_{10} N_f)^{-1/2} = 1.2055 + 0.6600S + 0.1804S^2 - 0.008143S^4$$

$$+ (2.53 \times 10^{-4})RS^4 + (2.18 \times 10^{-4})TS^4 - (5.466 \times 10^{-4})RT^2 \ . \quad (3.17)$$

Here

$S = \log_{10} (\Delta\varepsilon_t/100)$,

$R = \log_{10} (\dot{\varepsilon})$,

$T = T_c/100$,

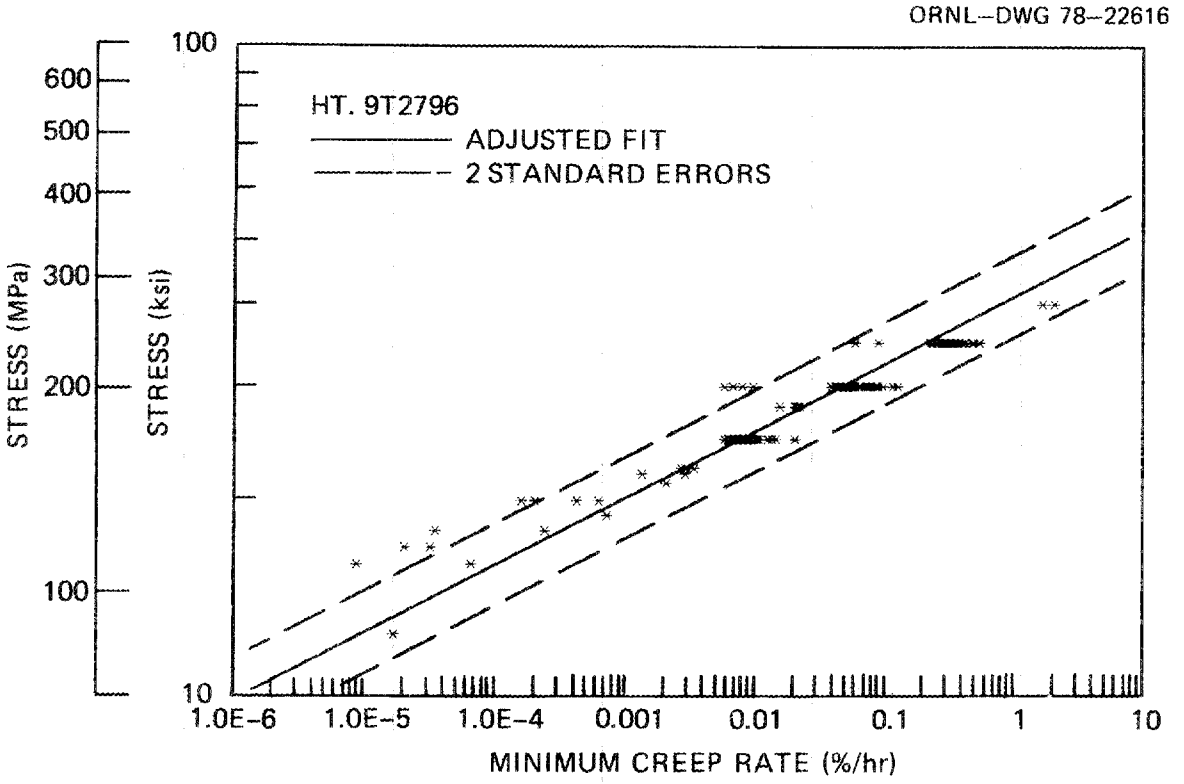

Fig. 3.42. Comparison of minimum creep rate data to adjusted fit for heat 9T2796 at 593°C (1100°F) (1 ksi = 6.895 MPa).

where

N_f = cycles to failure,

$\Delta\varepsilon_t$ = total strain range (%),

$\dot{\varepsilon}$ = strain rate (sec^{-1}),

T_c = temperature (°C).

Utilizing this equation and the approach adopted for the variability study, analyses were performed using the available data and

$$(\log N_f)^{-1/2}_{\text{heat}} = (\log \overline{N}_f)^{-1/2} + N_{\text{heat}} \; ; \tag{3.18}$$

little discernable difference between heats could be detected. Thus, we recommend that no fatigue heat-to-heat variability be considered in the structural analyses.

3.8.1.5 Creep deformation properties. The scope of this effort was not to develop new creep equations but to evaluate heat-to-heat variability

using existing materials properties formulations wherever possible. A brief review of potential equations depicting creep behavior[14,40,41] indicated that the rational polynomial[41] was the most amenable for use in the heat-to-heat variability studies. The exponential formulation[14,40] has received wider exposure and verification, but the rational polynomial as used by Booker[41] offers a way of modeling material variability in creep without extensive fitting of creep curves. This, of course, assumes that the governing equations accurately capture the distribution, as well as the mean creep behavior.

Following the development in Ref. 41, the rational polynomial equations can be summarized as

$$\varepsilon_c = \frac{Cpt}{1 + pt} + \dot{\varepsilon}_m t \ , \tag{3.19}$$

$$C = 0.685 \ (1.11 \ \dot{\varepsilon}_m^{\ 0.974} - \dot{\varepsilon}_m) t_r^{\ 0.968} \ , \tag{3.20}$$

$$p = \frac{1}{C}(3.43 \ \dot{\varepsilon}_m^{\ 0.974} - \dot{\varepsilon}_m) \ , \tag{3.21}$$

where ε_c is creep strain (percent), $\dot{\varepsilon}_m$ is minimum creep rate (percent per hour), t_r is time to rupture (hour), and t is time (hour). The stress dependency of creep parameters C and p enters through the stress dependency of $\dot{\varepsilon}_m$ and t_r.

In evaluating the limits on creep, it would at first seem that all combinations of maxima and minima for $\dot{\varepsilon}_m$ and t_r would need to be considered. However, there is a strong correlation between $\dot{\varepsilon}_m$ and t_r for the various heats. That is, heats that have lower minimum creep rates also have longer rupture lives. This is demonstrated in Fig. 3.43, where the heat-to-heat adjustment factors T and E are plotted against one another. Thus, realistic limits can be established for creep deformation of type 304 stainless steel from Eq. (3.19) by calculating C and p using only the combinations $[\dot{\varepsilon}_m)_{max}, \ t_r)_{min}]$ and $[\dot{\varepsilon}_m)_{min}, \ t_r)_{max}]$. Using these limits on C and p, that is, the mean value ±2SEE, the variation in creep strain is quite large, as is shown in Fig. 3.44 for a stress of 138 MPa (20 ksi).

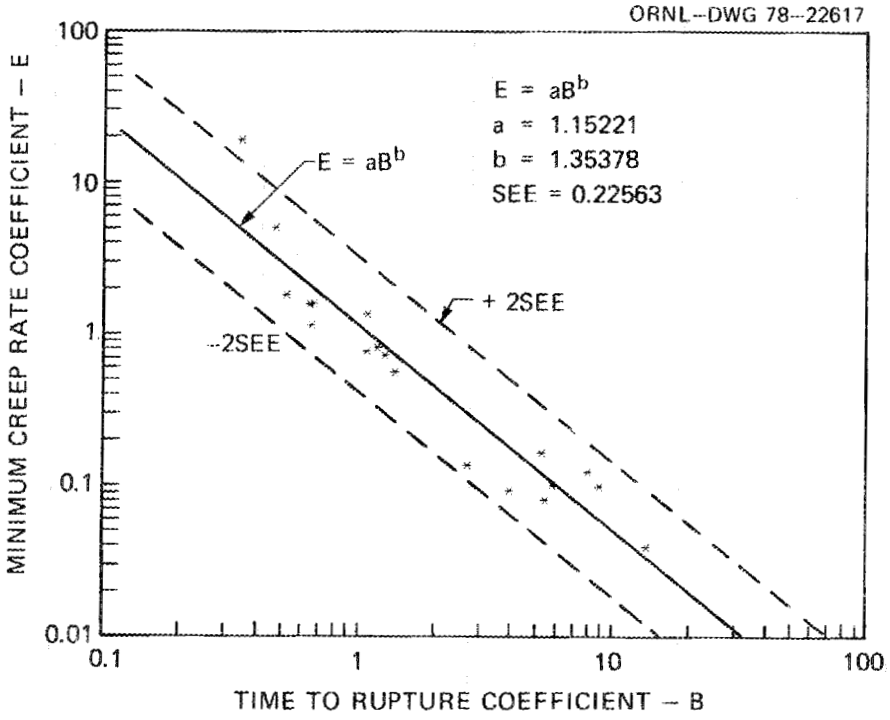

Fig. 3.43. Demonstrated heat-to-heat relationship between minimum creep rate and time to rupture for 19 heats of type 304 stainless steel at 593°C (1100°F) (1 ksi = 6.895 MPa).

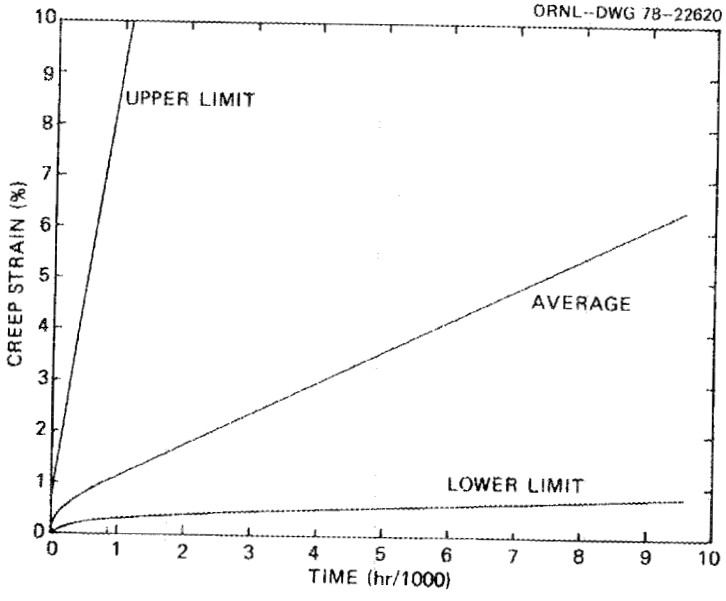

Fig. 3.44. Predicted mean and limit creep lines for 137.9 MPa (20 ksi) using the rational polynomial equation and calculated values of C and p for type 304 stainless steel at 593°C (1100°F) [stress = 137.9 MPa (20 ksi)].

Values of C and p for each heat are listed in Table 3.16 and plotted in Fig. 3.45. They are based on values of $\dot{\varepsilon}_m$ and t_r adjusted for each heat from the fit to all data. The heat variation in creep deformation behavior is shown in Fig. 3.46 for a stress of 138 MPa (20 ksi). Observe that the behavior of the extreme heats, 12 and 19, compares well to the limits shown in Fig. 3.44.

Table 3.16. Heat and stress dependency of the creep equation parameter C and parameter p for type 304 stainless steel at 593°C (1000°F)

Heat No.	Various stress values (ksi)[a]							
	5	10	15	20	25	30	35	40
				Parameter C				
1	0.052492	0.182896	0.358323	0.552763	0.744037	0.912508	1.040384	1.111291
3	0.050044	0.172327	0.333502	0.507317	0.671431	0.806081	0.893378	0.916870
4	0.077346	0.267528	0.520166	0.795531	1.059790	1.283006	1.438067	1.500038
5	0.045567	0.158893	0.311547	0.481038	0.648186	0.796006	0.909110	0.973337
6	0.021257	0.075829	0.152122	0.240858	0.334094	0.424775	0.506499	0.573364
7	0.021355	0.076530	0.154219	0.245354	0.342160	0.437730	0.525791	0.600561
8	0.025409	0.091213	0.184108	0.293415	0.409972	0.525638	0.633020	0.725300
9	0.050019	0.174584	0.342652	0.529651	0.714628	0.879024	1.006023	1.080148
10	0.055623	0.198659	0.398998	0.632537	0.878627	1.118930	1.336798	1.516893
11	0.056331	0.194366	0.376950	0.574809	0.763025	0.919552	1.024429	1.059300
12	0.031523	0.114064	0.231999	0.372721	0.525394	0.680378	0.828910	0.962907
13	0.042996	0.150605	0.296662	0.460427	0.624201	0.772302	0.890517	0.965765
14	0.053782	0.185604	0.360022	0.549111	0.729097	0.878950	0.979627	1.013614
15	0.040654	0.140959	0.274767	0.421442	0.563401	0.685083	0.772394	0.812368
16	0.306413	1.012698	1.873240	2.697061	3.322441	3.606772	3.421226	2.647525
17	0.048902	0.174045	0.348358	0.550213	0.761097	0.964576	1.145736	1.290837
18	0.033635	0.120421	0.242438	0.385320	0.536753	0.685797	0.822521	0.937769
19	0.118823	0.402444	0.765121	1.139731	1.469279	1.705418	1.796617	1.707032
20	0.049622	0.177705	0.357855	0.568909	0.792728	1.013196	1.215680	1.386692
				Parameter p				
1	0.000003	0.000197	0.002296	0.013493	0.054567	0.174694	0.478076	1.174583
3	0.000006	0.000393	0.004620	0.027385	0.111829	0.362270	1.007204	2.533248
4	0.000003	0.000201	0.002351	0.013888	0.056502	0.182194	0.503354	1.253867
5	0.000004	0.000217	0.002529	0.014853	0.060029	0.192039	0.525044	1.288256
6	0.000002	0.000114	0.001305	0.007538	0.029942	0.093922	0.250732	0.596278
7	0.000001	0.000083	0.000946	0.005448	0.021565	0.067404	0.179203	0.424067
8	0.000001	0.000062	0.000706	0.004061	0.016059	0.050127	0.133077	0.314371
9	0.000003	0.000187	0.002179	0.012789	0.051648	0.165077	0.450808	1.104320
10	0.000001	0.000040	0.000460	0.002654	0.010531	0.033004	0.088011	0.209027
11	0.000005	0.000314	0.003686	0.021814	0.088927	0.287471	0.796921	1.995401
12	0.000000	0.000028	0.000319	0.001821	0.007161	0.022222	0.058607	0.137398
13	0.000003	0.000177	0.002057	0.012043	0.048498	0.154503	0.420191	1.023468
14	0.000005	0.000326	0.003824	0.022632	0.092250	0.298160	0.826349	2.068308
15	0.000005	0.000335	0.003910	0.023060	0.093628	0.301171	0.829341	2.055929
16	0.000007	0.000432	0.005223	0.031981	0.135927	0.465965	1.422890	4.339828
17	0.000001	0.000058	0.000663	0.003834	0.015257	0.047946	0.128270	0.305849
18	0.000001	0.000056	0.000643	0.003703	0.014668	0.045879	0.122080	0.289183
19	0.000006	0.000379	0.004500	0.027011	0.111950	0.369739	1.057632	2.791034
20	0.000001	0.000038	0.000428	0.002465	0.009763	0.030531	0.081221	0.192344

[a] 1 ksi = 6.895 MPa.

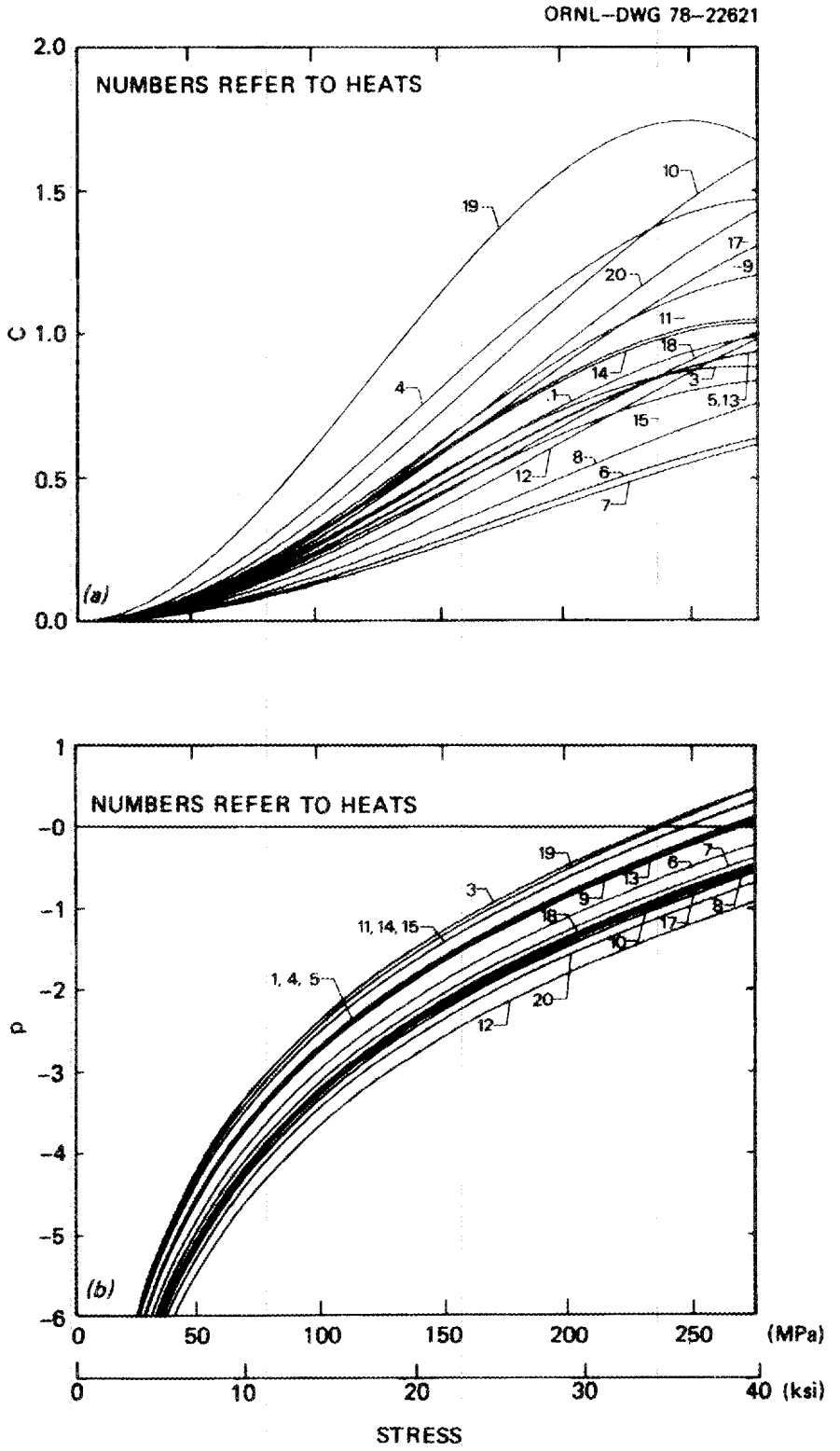

Fig. 3.45. Heat-to-heat variability of creep equation parameters C and p for type 304 stainless steel at a stress of 137.9 MPa (20 ksi) and temperature of 593°C (1100°F) (1 ksi = 6.895 MPa).

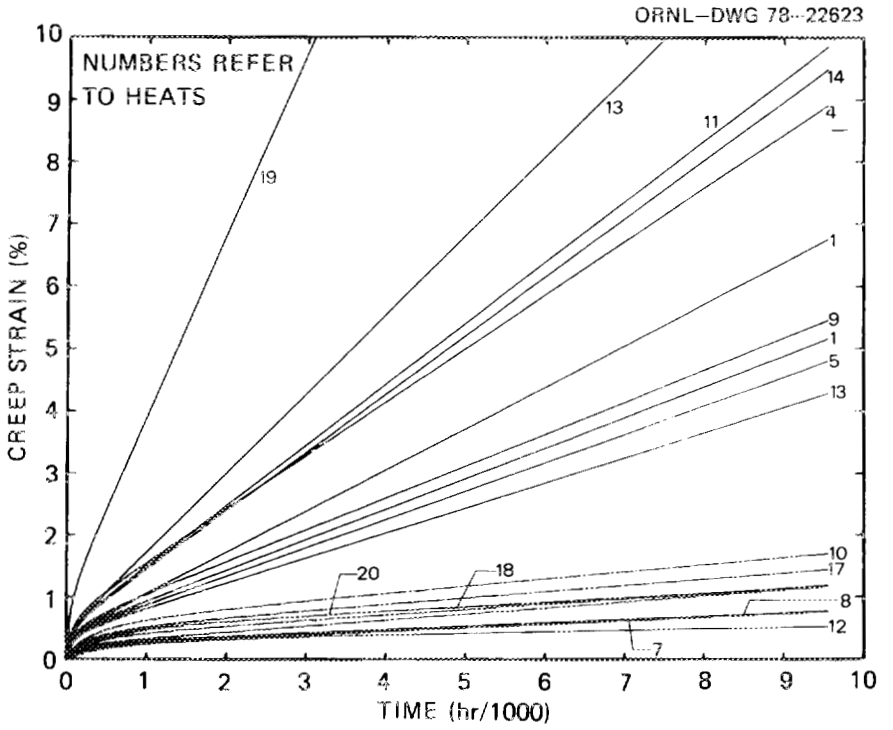

Fig. 3.46. Predicted heat variability of creep strain using the rational polynomial equation and individual heat values of C and p for type 304 stainless steel at a stress of 137.9 MPa (20 ksi) and temperature of 593°C (1100°F) (1 ksi = 6.895 MPa).

3.8.2 Inelastic ratchetting analyses

The effort in this activity was restricted while awaiting the results of the first phase of the study. Setup and solution of the selected ratchetting problem will begin early in the next report period.

3.9 Fatigue and Creep-Rupture Curves for Use in Projecting Failure in ORNL Laboratory Structural Tests

R. L. Huddleston J. J. Blass

(Not previously reported)

This activity was undertaken to provide guidance to our overall program on common procedures and data correlations for estimating creep rupture and fatigue (crack initiation) life. One major application is in

predicting failure of structural specimens of annealed type 304 stainless steel (heat 9T2796) and tested at 593°C (1100°F). Presently, procedures analogous to those of ASME Code Case N-47 (Ref. 15) are being followed, with the fatigue and creep-rupture curves for the ORNL reference heat being utilized. The life-reduction factors normally incorporated in the Code are not employed here. A fatigue curve and two creep-rupture curves (one uniaxial and one biaxial) have been generated to replace the curves in ASME Code Case N-47. The uniaxial creep-rupture curve is designed for projection of failures in our uniaxial tests and the biaxial curve for multiaxial phenomenological and structural tests.

The curves generated represent fits to selected data sets and have no built-in safety margin. One of the first applications of these curves and procedures will be to establish load levels for the rupture phase of the nozzle-to-sphere specimen (see Sect. 2.4.2). The procedures hopefully will avoid premature failure during or near initial loading and define test conditions to induce failure in a reasonable period of time. In this regard, the curves are to be used more for interpolation than for extrapolation because the range of data on stresses, cycles, time, and strain range exceeds that for which this laboratory test is designed. These curves are not intended for general use in extrapolation to longer lives.

3.9.1 Fatigue curve for annealed type 304 stinless steel (heat 9T2796) at 593°C (1100°F) (J. J. Blass) (Not previously reported)

The fatigue design curve in Fig. T-1420-1A of ASME Code Case N-47-13 is based on data from a number of heats of material and includes safety factors of 2 on strain or 20 on life, whichever has the greater effect.[26] To estimate the crack initiation life of model structures, it would be better to use a curve based on available data for the material, heat, and temperature of interest without a built-in safety margin. Accordingly, a relationship was developed for this purpose on the basis of a two-term power law or Basquin/Coffin-Manson law given by

$$\Delta\varepsilon_t = 1.393\, N_f^{-0.1782} + 42.92\, N_f^{-0.5010} , \qquad (3.22)$$

where $\Delta\varepsilon_t$ is the total strain range in percent and N_f is the number of

cycles to failure (or crack initiation in the case of a structure). The first term in Eq. (3.22) was obtained from a least-squares fit of the expression,

$$\log N_f = \log a_1 + a_2 \log \Delta\varepsilon_e \ , \tag{3.23}$$

to the available data for the ORNL reference heat of type 304 stainless steel in the annealed condition, where $\Delta\varepsilon_e$ is the elastic component of the strain range. The second term in Eq. (3.22) was obtained from a least-squares fit of

$$\log N_f = \log a_3 + a_4 \log \Delta\varepsilon_p \tag{3.24}$$

to the same data, where $\Delta\varepsilon_p$ is the plastic component of the strain range. The data are from tests conducted at Argonne National Laboratory (ANL) on the 16-mm (5/8-in.) HR bar product form. These data are reproduced in Table 3.17 in part because previously published tabulations[10,42] contained some inconsistencies.*

*D. T. Raske of ANL resolved these inconsistencies by consulting the original data sheets.

Table 3.17. Argonne National Laboratory fatigue data for 16-mm (5/8-in.) hot-rolled bar of annealed type 304 stainless steel (heat 9T2796) at 593°C (1100°F)

Specimen No.	Total strain range (%)	Elastic strain range (%)	Plastic strain range (%)	Total strain rate ($s^{-1} \times 10^3$)	Cycles to failure
AA-2	2.02	0.41	1.61	4.0	737
T-17	2.02	0.43	1.59	4.0	753
T-14	2.01	0.41	1.60	4.2	1,020
T-23	1.02	0.35	0.67	4.1	2,853
AA-24	1.00	0.35	0.65	4.0	2,651
AA-11	0.76	0.29	0.47	4.1	4,853
T-16	0.51	0.24	0.27	4.0	16,439
AA-9	0.51	0.22	0.29	4.0	25,925
AA-6	0.50	0.21	0.29	4.0	20,834
T-15	0.50	0.22	0.28	4.0	98,181
AA-12	0.36	0.20	0.16	4.1	52,343

Table 3.18 contains selected $\Delta\varepsilon_t$ vs N_f values calculated by means of Eq. (3.22), and Fig. 3.47 shows a comparison of Eq. (3.22) plotted as a solid line with the ANL data. The dashed lines in Fig. 3.47 were obtained by multiplying and dividing N_f for a given $\Delta\varepsilon_t$ by a factor of 3. This factor was chosen so that the dashed lines would correspond roughly

Table 3.18. Selected values of total strain range vs cycles to failure calculated by means of Eq. (3.22)

Cycles to failure N_f	Total strain range $\Delta\varepsilon_t$ (%)	Cycles to failure N_f	Total strain range $\Delta\varepsilon_t$ (%)
200	3.561	10,000	0.695
500	2.368	20,000	0.539
1000	1.755	50,000	0.392
2000	1.312	100,000	0.313
5000	0.907	500,000	0.194

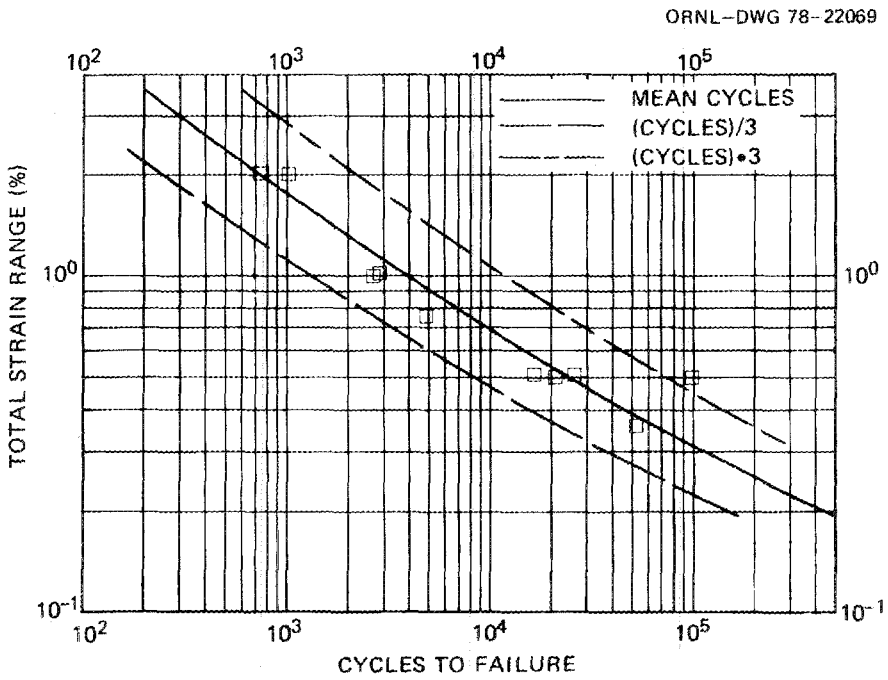

Fig. 3.47. Total strain range vs cycles to failure for annealed type 304 stainless steel (heat 9T2796) at 593°C (1100°F). Comparison of Eq. (3.22) (solid line) with ANL data (symbols). Dashed lines correspond roughly to 95% confidence limits.

(at least near the middle of the range of the data) to 95% confidence limits on the mean or expected life.

3.9.2 Uniaxial and biaxial 593°C (1100°F) creep-rupture curves for annealed type 304 stainless steel (heat 9T2796) (R. L. Huddleston) (Not previously reported)

A uniaxial curve and a biaxial creep-rupture curve, the associated equations, and 95% confidence limits were generated for the reference heat of type 304 stainless steel using the data summarized in Tables 3.19 and 3.20. The bulk of the uniaxial data were taken from the product form characterization test data,[29] with two additional data points for 25-mm (1-in.) plate[19] and results for 19-mm (5/8-in.) bar taken from the recently completed Babcock & Wilcox uniaxial and multiaxial creep-rupture study.[4] Biaxial data were also taken from the Babcock & Wilcox study. The total uniaxial data set encompasses 14 product forms of the reference heat, with a combined total of 87 data points. Biaxial data are from only one product form (48-mm bar) and a total of ten data points.

Prior to incorporation of the biaxial data into the analyses, an 11°C (20°F) correction was applied to the data, as described in Sect. 3.1. The biaxial data correction factor was generated from the thermal sensitivity of the creep-rupture constants a_0 and a_1 for the 25-mm (1-in.) plate data for the reference heat. These data are reported by Swindeman in ASME MPC-1.[19] The resulting values of a_0 and a_1 as a function of temperature are plotted in Fig. 3.48. A data correction factor was applied as follows:

$$\left[\log t_R\right]_{B,1100F} = \left[\log t_R\right]_{B,1120F} \times \left[\frac{(\log t_R)_{1100F}}{(\log t_R)_{1120F}}\right]_U , \qquad (3.25)$$

$$\left[\log t_R\right]_{B,1100F} = \left[\log t_R\right]_{B,1120F} \times \left[\frac{14.9841 - 8.8114 \log \sigma}{14.3500 - 8.4300 \log \sigma}\right] , \qquad (3.26)$$

where B denotes biaxial and U denotes the uniaxial 25-mm (1-in.) plate

Table 3.19. Uniaxial creep-rupture data[a] for type 304 stainless steel (heat 9T2796) at 593°C (1100°F)

σ [MPa (ksi)]	t_R (hr)
9.5-mm (3/8-in.) plate	
241 (35)	14.9
207 (30)	150.7
172 (25)	527.3
12.7-mm (1/2-in.) plate	
241 (35)	47.6
207 (30)	158.2
172 (25)	759.0
241 (35)	29.9
241 (35)	50.9
207 (30)	117.0
19-mm (3/4-in.) plate	
241 (35)	26.0
207 (30)	123.9
172 (25)	769.6
241 (35)	28.0
241 (35)	23.5
207 (30)	107.0
25-mm (1-in.) plate	
241 (35)	27.3
207 (30)	104.4
172 (25)	612.0
276 (40)	4.9[b]
276 (40)	5.8[b]
241 (35)	25.1[b]
241 (35)	29.6[b]
207 (30)	110.8[b]
207 (30)	98.5[b]
172 (25)	440.1[b]
172 (25)	619.2[b]
172 (25)	552.9[b]
155 (22.5)	878.1[b]
155 (22.5)	1,247[b]
155 (22.5)	1,063[b]
147 (21.25)	1,230[b]
51-mm (2-in.) plate	
241 (35)	22.5
207 (30)	89.7
172 (25)	382
124 (18)	4,547[c]
110 (16)	14,647[c]
64-mm (2-1/2-in.) CD pipe	
241 (35)	38.5
207 (30)	177
172 (25)	758
102-mm (4-in.) pipe	
241 (35)	36
207 (30)	161
172 (25)	786
203-mm (8-in.) pipe	
241 (35)	32
207 (30)	164
172 (25)	695
16-mm (5/8-in.) bar	
241 (35)	23
207 (30)	101
172 (25)	430
172 (25)	376
241 (35)	43.7
207 (30)	169
207 (30)	187[d]
207 (30)	138[d]
193 (28)	227[d]
193 (28)	368[d]
193 (28)	276[d]
193 (28)	415[d]
172 (25)	667[d]
172 (25)	948[d]
152 (22)	2,130[d]
152 (22)	2,026[d]
138 (20)	9,584[d]
138 (20)	9,450[d]
138 (20)	6,868[d]
134 (19.5)	16,891[d]
134 (19.5)	11,608[d]
131 (19)	17,547[d]
124 (18)	24,495[d]
117 (17)	25,942[d]
110 (16)	44,296[d]
25-mm (1-in.) bar	
241 (35)	26.3
207 (30)	135
172 (25)	581
44-mm (1-3/4-in.) bar	
241 (35)	34
207 (30)	143
172 (25)	601
48-mm (1-7/8-in.) bar	
241 (35)	32.5
207 (30)	169
172 (25)	614
114-mm (4-1/2-in.) bar	
241 (35)	40.2
207 (30)	169
172 (25)	766
207 (30)	179
172 (25)	458
64-mm (2-1/2-in.) gun-drilled bar	
241 (35)	23.3
207 (30)	141
172 (25)	691

[a] All data from ORNL-5222, unless otherwise noted.

[b] Data from ORNL-5103, p. 242, or MPC-1, p. 30.

[c] Data from ORNL-5326, p. 77.

[d] Data from ORNL/Sub-3654-4, p. 18.

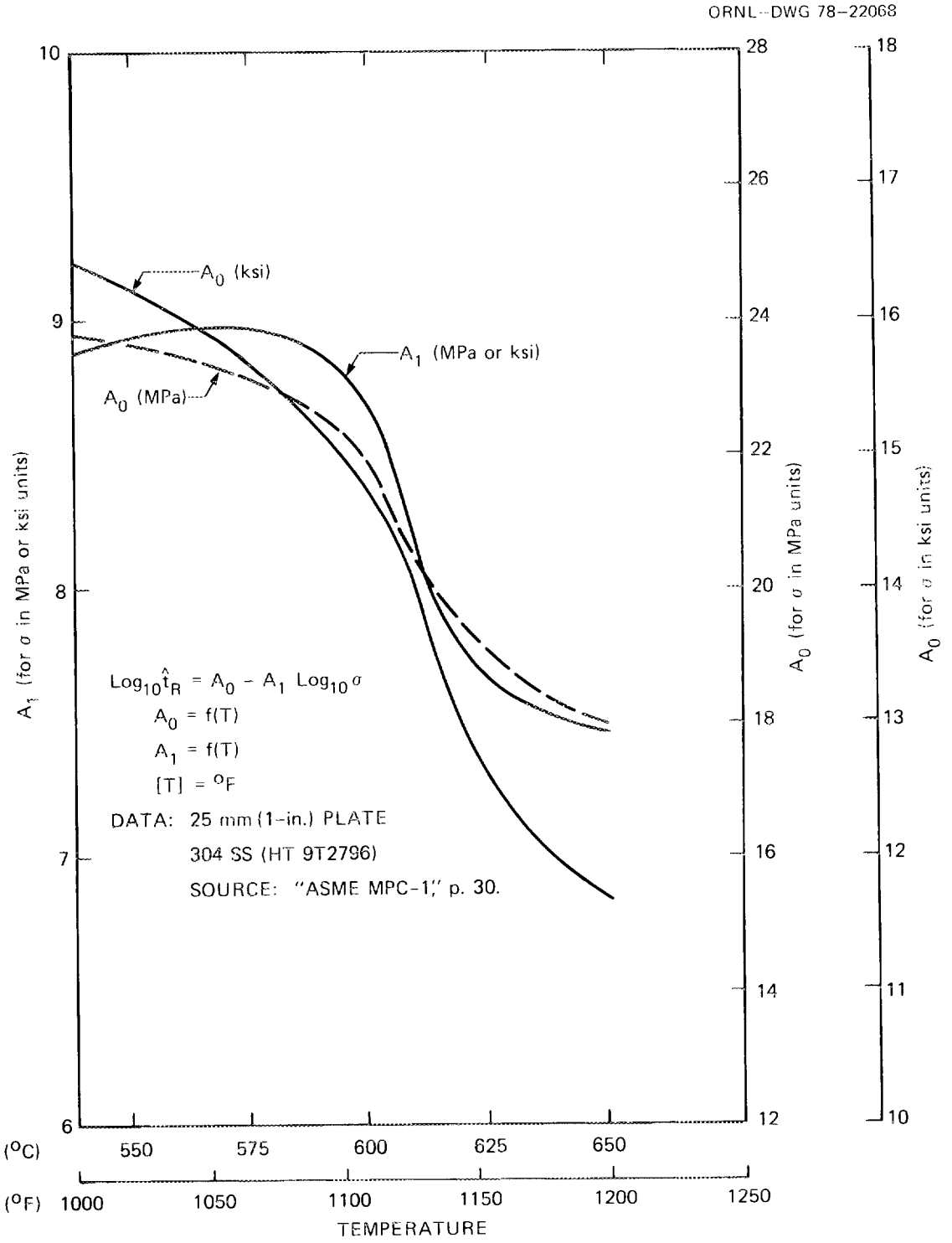

Fig. 3.48. Temperature dependency of creep-rupture slope and intercept constants for 304 stainless steel [heat 9T2796, 25-mm (1-in.) plate].

Table 3.20. Biaxial creep-rupture data for type 304 stainless steel (heat 9T2796) at 604°C (1120°F), tubular specimens from 48-mm (1-7/8-in.) bar

σ_θ/σ_z	σ_{eq} [MPa (ksi)]	T_R (hr)	t_R[a] (hr)
0.0	150.65 (21.85)	1,997	2,077
0.5	130.45 (18.92)	3,336	3,473
0.5	119.42 (17.32)	21,840	22,744
1.0	150.65 (21.85)	584	608
1.0	137.90 (20.00)	1,925	2,003
1.0	124.11 (18.00)	3,595	3,743
1.0	137.90 (20.00)	1,461	1,521
2.0	130.45 (18.92)	1,713	1,783
2.0	119.42 (17.32)	3,272	3,407
2.0	107.49 (15.59)	17,030	17,740

[a]Estimated rupture time corrected to 593°C (1100°F).

parameter. Both the original and corrected biaxial data are given in Table 3.20.

A standard log-log creep-rupture model was fitted to the selected data with mean time to rupture $\hat{t}_R$ for a given stress level σ given by

$$\log_{10} \hat{t}_R = a_0 - a_1 \log_{10} \sigma \ . \tag{3.27}$$

The statistical 95% confidence limits on log t_R for another single observation are given by

$$L = \log_{10} \hat{t}_R \pm d_o \ ,$$
$$d_o = t_{0.025,\nu} \, S_{ee} \sqrt{1 + (1/n) + \frac{(x - \bar{x})^2}{S_{xx}}} \ , \tag{3.28}$$

where L is estimated 95% confidence limit on rupture time (hour), $\hat{t}_R$ is

expected rupture time (hour), a_1, a_0 are slope and intercept constants, $t_{0.025,\nu}$ is student's t statistic for 95% (two-tail) confidence limit with $\nu = n - 1$ degress of freedom, S_{ee} is standard error of estimate of log t_R on log σ, n is number of data points, x is log σ, $\bar{x}$ is mean x, and S_{xx} is given by

$$S_{xx} = \sum_{i=1}^{n} x_i^2 - \frac{1}{n}\left(\sum_{i=1}^{n} x_i\right)^2 \quad . \tag{3.29}$$

If one has a data set that spans a relatively large range of x, S_{xx} becomes large, and the third term in the equation for d_o becomes negligible with respect to $1 + (1/n)$. The resulting confidence limits are then independent of log σ and are straight lines parallel to the log $\hat{t}_R$ vs log σ line. The uniaxial data span was sufficient to make this simplification (i.e., $16 \leq \sigma \leq 40$ ksi) while maintaining an accuracy of better than 10% on the confidence limits over the entire range $1 \leq \sigma \leq 10^5$ hr. The biaxial data range is much tighter (i.e., $15.59 \leq \sigma \leq 21.85$); thus, S_{xx} is small. If the biaxial set is considered by itself, the resulting confidence limits are dependent on log σ and are diverging hyperbolic-shaped curves about the least-squares lines. From a technical viewpoint, it is reasonable to lump the uniaxial and biaxial data sets together to establish S_{xx}. The two sets were thus lumped, the result being an S_{xx} large enough to make the third term in Eq. (3.28) negligible. Both the uniaxial and biaxial confidence limits were then approximated by

$$d_o = t_{0.025,\nu}\, S_{ee}\sqrt{1 + (1/n)} \quad . \tag{3.30}$$

The following summary describes the balance of the methodology used in preparation of the two curves. The resulting curves and associated equations are given in Figs. 3.49 and 3.50.

- The combined uniaxial and corrected biaxial data sets were utilized to generate a common slope constant, the result being $a_1 = -8.5551$.
- A least-squares intercept constant was determined for the combined uniaxial data set (14 product forms), with the result being $a_0 =$ 21.9351 MPa (14.7615 ksi). The standard error of the estimate of

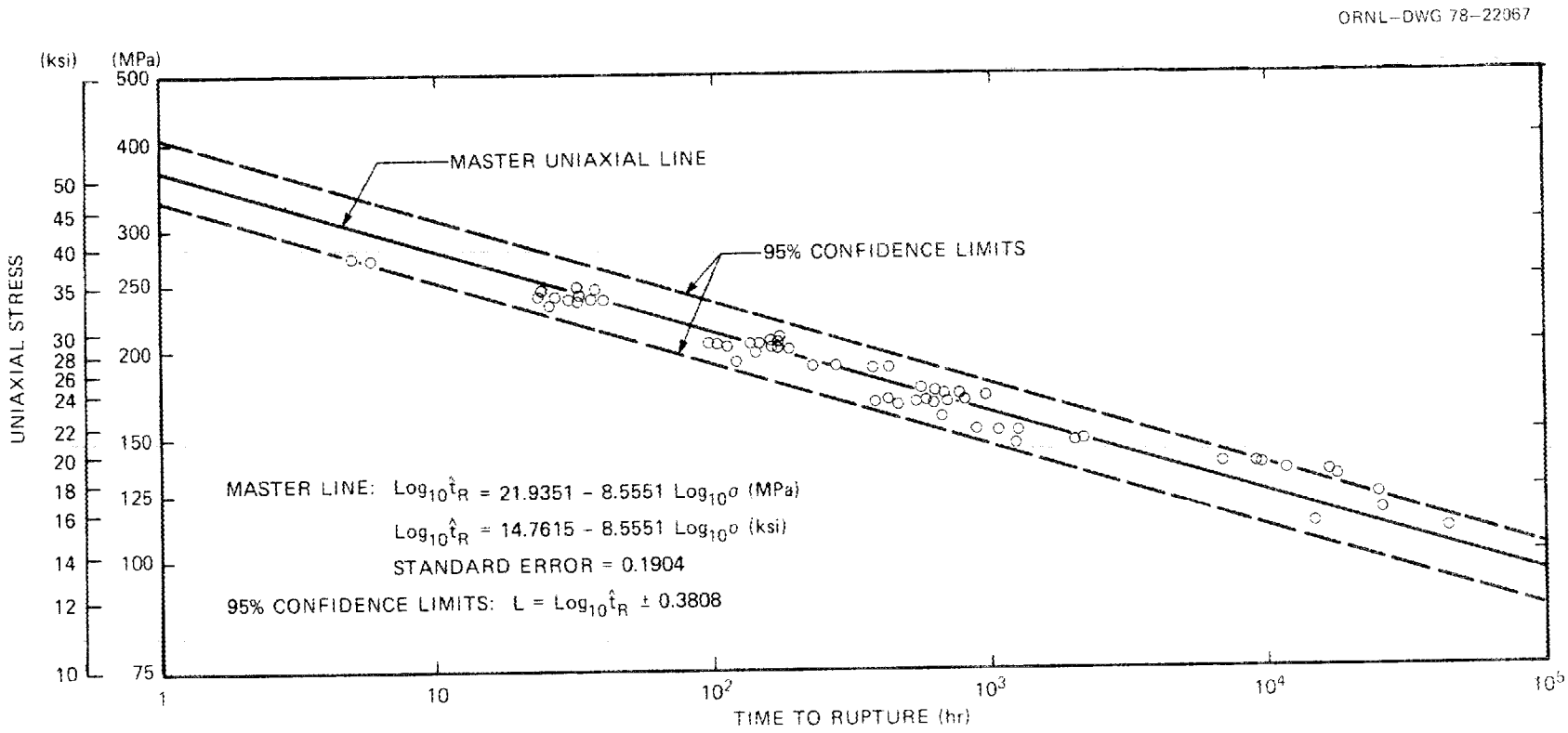

Fig. 3.49. Uniaxial stress vs rupture time for annealed type 304 stainless steel (heat 9T2796) at 593°C (1100°F).

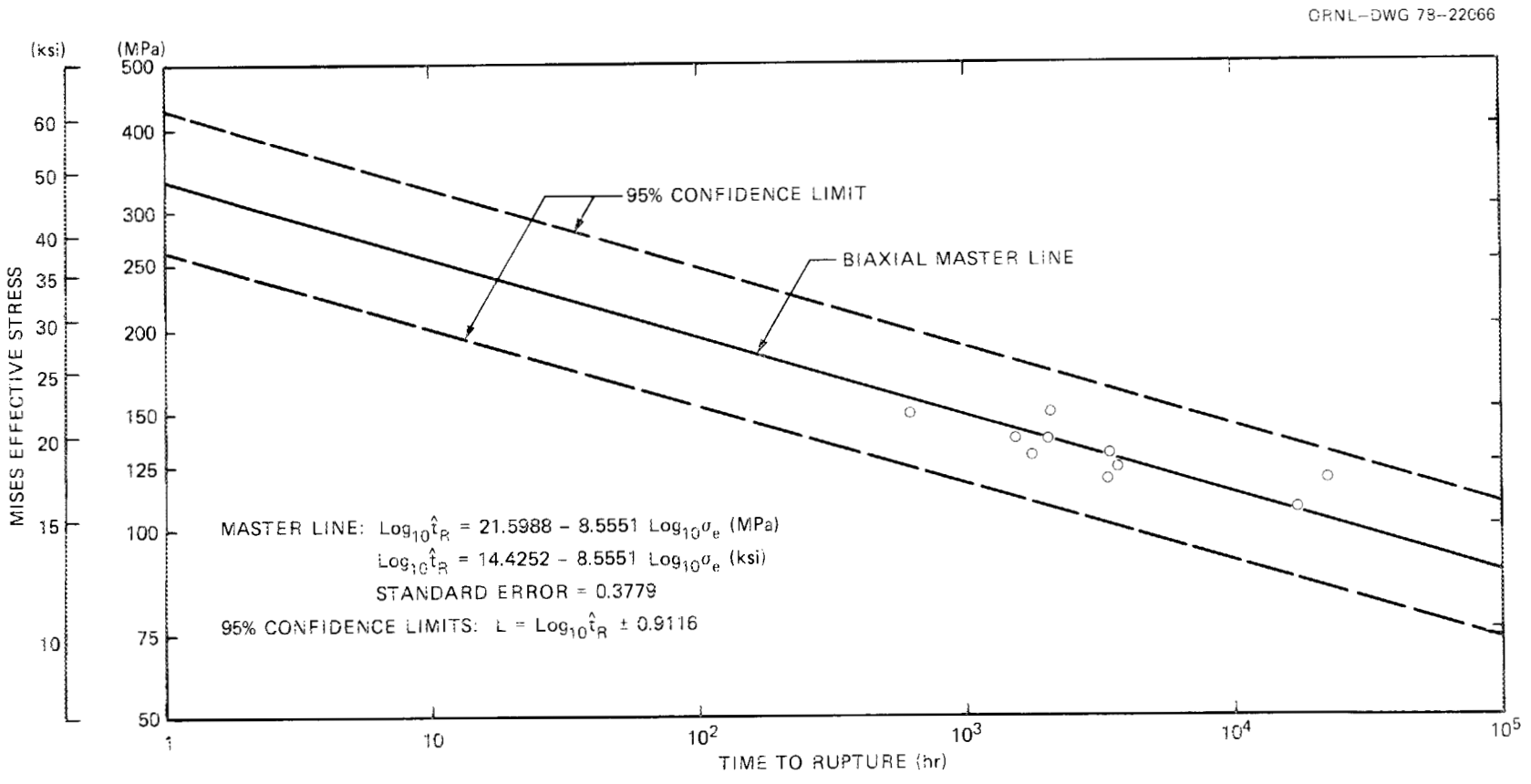

Fig. 3.50. Mises equivalent stress vs rupture time for annealed type 304 stainless steel (heat 9T2796) representing multiaxial behavior at 593°C (1100°F).

$\log_{10} \hat{t}_R$ on log σ for the combined uniaxial data set was 0.1904. The common slope constant a_1 and a separate least-square intercept constant a_0 for each of the 14 product forms represented in Table 3.19 resulted in a standard error of log $\hat{t}_R$ on log σ of 0.1395, which is representative of an average for one product form. The ratio of the variability for the combined uniaxial data set to that for one product form is thus 1.3649.

- A biaxial least-squares intercept was determined for the corrected biaxial data set and the previously determined slope. This represents only the one product form. The resulting intercept was a_0 = 21.5988 MPa (14.4252 ksi). The standard error was 0.2769. Because no biaxial data were available to establish the variability for all 14 product forms about the biaxial line, it was assumed that the ratio of variability for all 14 product forms to that for the one available was the same as the equivalent uniaxial ratio. The resulting standard error representing the 14 product forms was thus taken as 0.2769 × 1.3649 = 0.3779.

3.10 Development of Matrix of Tests for Evaluation of Creep-Fatigue Methods

G. T. Yahr

(Not previously reported)

The ASME Boiler and Pressure Vessel Code's Task Force on Strain Limits and Creep Fatigue is trying to determine whether an improved method for evaluating creep-fatigue damage should be included in Code Case N-47 (1592).[15] There are several candidate methods, including strain-range partitioning,[43] frequency separation,[44] and damage rate,[45] that have been proposed to replace the linear damage rules currently in Code Case N-47. Each of the methods have been shown to do an adequate job of fitting most available data. However, there can be considerable differences in the predictions of the different methods for conditions of long hold times and low strain range. Tests are now under way at ANL to produce

test results for such conditions;[46] these results will be useful for determining which of the methods are most accurate under conditions that more nearly approximate design conditions. However, a considerable amount of time will be needed to generate these data because of the very nature of the tests. Therefore, it was proposed at the September 1978 meeting of the Task Force that some effort should be given to developing a matrix of short-time tests that can provide additional data to aid in the determination of which of the various candidate creep-fatigue methods should be used as the basis for elevated-temperature design.

The decision was that the test matrix should not include cumulative damage or multiaxiality. After considerable discussion with several people active in the area, after discussion at the October 1978 meeting of the Task Force, and after a special meeting at Lewis Research Center on November 21, 1978, that was called by the Chairman of the Task Force, it became clear that the desired objective would be difficult to achieve using short-term tests. The most promising short-term tests identified were those with a creep or relaxation hold period at some intermediate stress during loading or reloading such as proposed by D. N. Robinson[47] some time ago. General Electric[48] has proposed that the most damaging loading sequence would be one with a hold at zero stress after the compressive strain. A. E. Carden[49] has conjectured that a hold time at zero stress would lower the cycles to failure for certain tests. S. S. Manson[50] has expressed great doubt that a hold period at zero stress would have much effect on the number of cycles to failure unless a metallurgical change occurs.

Thermomechanical tests are recognized to be a potentially useful type of test for differentiating between the various creep-fatigue methods. However, specific tests of this type have not been identified.

If the candidate methods do not give predicted lives that differ by a factor of 2 or more, the inherent material variability will probably mask any differences in the methods.

Additional work will be required to develop the proposed matrix of tests.

References

1. E. P. Esztergar, *Creep-Fatigue Interaction and Cumulative Damage Evaluations for Type 304 Stainless Steel; Hold-Time Fatigue Test Program and Review of Multiaxial Fatigue*, ORNL-4657 (June 1972).

2. L. F. Coffin et al., *Time-Dependent Fatigue of Structural Alloys, A General Assessment (1975)*, ORNL-5073 (January 1977).

3. R. L. Huddleston, "Design Criteria and Rules for Time-Dependent Deformation and Failure," *High-Temperature Structural Design Program Prog. Rep. June 30, 1978*, ORNL-5433, pp. 143-75.

4. C. C. Schultz and W. E. Leyda, *Creep Failure Under Uniaxial and Multiaxial Stress Conditions*, Babcock & Wilcox Company, ORNL/Sub-3654-4 (August 1978).

5. J. J. Blass, "Assessment of Multiaxial Creep-Rupture Criteria for Type 304 Stainless Steel," *High-Temperature Structural Design Program Prog. Rep. June 30, 1978*, ORNL-5433, pp. 168-74.

6. J. J. Blass, "Investigation of Creep Failure Under Uniaxial and Multiaxial Conditions," *High-Temperature Structural Design Program Prog. Rep. Dec. 31, 1977*, ORNL-5374, pp. 109-14.

7. C. C. Schultz and W. E. Leyda, *Variability in Creep and Rupture Tests Results in a Single Heat of Type 304 Stainless Steel*, Babcock & Wilcox Company, ORNL/Sub-3654-3 (September 1975).

8. J. J. Blass, "Influence of Grain Size Variability on Creep Rupture of Type 304 Stainless Steel," *High-Temperature Structural Design Program Prog. Rep. June 30, 1975*, ORNL-5087, pp. 81-90.

9. S. Y. Zamrik, "Study of the Effect of Biaxiality in Creep-Fatigue at Elevated Temperatures," *High-Temperature Structural Design Methods for LMFBR Components Prog. Rep. June 30, 1972*, ORNL/TM-3917, pp. 106-18.

10. D. R. Diercks and D. T. Raske, *Elevated-Temperature, Strain-Controlled Fatigue Data on Type 304 Stainless Steel: A Compilation, Multiple Linear Regression Model and Statistical Analysis*, ANL-76-95, Argonne National Laboratory (December 1976).

11. W. F. McAfee, "Rupture Tests of Simple Structures," *High-Temperature Structural Design Program Prog. Rep. June 30, 1977*, ORNL-5339, pp. 170-73.

12. W. J. McAfee, R. L. Battiste, and M. Richardson, "Failure Under Cyclic Relaxing Residual Stresses — Restrained Cylinder Tests," *High-Temperature Structural Design Program Prog. Rep. June 30, 1978*, ORNL-5433, pp. 161-66.

13. W. K. Sartory, *PLACRE User's Manual*, ORNL/TM-5626 (February 1977).

14. *Nuclear Systems Materials Handbook, Vol. 1, Design Data*, TID-26666, Handford Engineering Development Laboratory.

15. ASME Code Case N-47 (1592), *Class I, Components in Elevated Temperature Service, Section III, Division 2, ASME Boiler and Pressure Vessel Code, Case Interpretations*, American Society of Mechanical Engineers, New York (September 1977).

16. M. F. Ashby, R. J. Fields, and T. Weerasooriya, *Fracture-Mechanism in Two Austenitic and One Ferritic Steel*, CUED/C/MATA/TR.47, Cambridge University.

17. F. C. Monkman and N. J. Grant, "An Empirical Relationship Between Rupture Life and Minimum Creep Rate in Creep-Rupture Tests," *Proc. ASTM* 56, 593-605 (1956).

18. R. W. Swindeman, *Creep Rupture Correlations for Type 304 Stainless Steel Heat 9T2796* (in preparation).

19. R. W. Swindeman, "Creep Rupture Correlations for Type 304 Stainless Steel (Heat 9T2796)," pp. 1-30 in *Structural Materials for Service at Elevated Temperatures in Nuclear Power Generation*, MPC-1, A. O. Schaefer, ed., American Society of Mechanical Engineers, New York, 1975.

20. R. W. Swindeman, "Notched-Bar Rupture Testing of Type 304 Stainless Steel," *High-Temperature Structural Design Program Prog. Rep. June 30, 1977*, ORNL-5433, pp. 166-68.

21. J. J. Blass, "Assessment of Multiaxial Fatigue Criteria," *High-Temperature Structural Design Program Prog. Rep. Dec. 31, 1977*, ORNL-5374, pp. 116-26.

22. M. W. Brown and K. J. Miller, "A Theory for Fatigue Failure Under Multiaxial Stress-Strain Conditions," *Proceedings, Institution of Mechanical Engineers* 187, 745-55 (1973). (Discussion, pp. D229-D243.)

23. J. J. Blass and S. Y. Zamrik, "Multiaxial Low-Cycle Fatigue of Type 304 Stainless Steel," *1976 ASME-MPC Symposium on Creep-Fatigue Interaction*, American Society of Mechanical Engineers, MPC-3, 1976, pp. 129-59. (Discussion, *J. Eng. Mater. Technol.*, pp. 283-86, July 1977.)

24. S. Y. Zamrik, *The Effect of Biaxiality in Creep-Fatigue at Elevated Temperatures*, Pennsylvania State University, ORNL/Sub-3649-5 (April 1979).

25. J. J. Blass, *Multiaxial Creep and Fatigue Damage Summation for Type 304 Stainless Steel*, ORNL/TM-6438 (March 1979).

26. *Criteria for Design of Elevated Temperature Class I Components in Section III, Division 1, of the ASME Boiler and Pressure Vessel Code*, American Society of Mechanical Engineers (May 1976).

27. R. D. Campbell, "Creep/Fatigue Interaction Correlation for 304 Stainless Steel Subjected to Strain-Controlled Cycling with Hold Times at Peak Strain," *Trans. ASME Sec. B, J. Eng. Industry* 93(4), 887-92 (1971).

28. H. E. McCoy, *Tensile and Creep Properties of Several Heats of Type 304 Stainless Steel*, ORNL/TM-4709 (November 1974).

29. R. W. Swindeman et al., *Product Form Characterization of Type 304 Stainless Steel (Heat 9T2796)*, ORNL-5222 (February 1977).

30. J. M. Steichen, *High Strain Rate Mechanical Properties of Types 304 and 316 Stainless Steel (RM-17)*, HEDL-TME 71-164 (November 1971).

31. V. K. Sikka et al., *Tensile Properties of Type 304 Stainless Steel*, ORNL-5325 (February 1978).

32. V. K. Sikka et al., *Influence of Laboratory Annealing on Tensile Properties of Time-Independent Design Stress Intensity Limits for Type 304 Stainless Steel*, ORNL-5175 (December 1976).

33. P. S. Maiya, *Bilinear Cyclic Stress-Strain Parameters for Type 304 and 316 Stainless Steel*, ANL-78-57 (July 1978).

34. J. M. Corum, M. Richardson, and J. A. Clinard, *Elevated-Temperature Benchmark Tests of Simply Supported Beams and Circular Plates Subjected to Time-Varying Loadings*, ORNL-5301 (September 1977).

35. C. F. Cheng and C. Y. Cheng, *Bilinear Representations of the Cyclic Stress-Strain-Behavior of Types 304 and 316 Stainless Steel from 800 to 1200°F*, ANL-8002 (February 1974).

36. C. F. Cheng and C. Y. Cheng, *Bilinear Representations of Stress-Strain-Behavior of Types 304 and 316 Stainless Steel Cyclically Deformed at 800 to 1200°F*, Paper L 3/7, Second International Conference on Structural Mechanics in Reactor Technology, Berlin, Federal Republic of Germany (September 1973).

37. M. Keith Booker, *Mathematical Analysis of the Elevated-Temperature Creep Behavior of Type 304 Stainless Steel*, ORNL/TM-6110 (December 1977).

38. V. K. Sikka, M. K. Booker, and C. R. Brinkman, *Use of Ultimate Tensile Strength to Correlate and Estimate Creep and Creep-Rupture Behavior of Types 304 and 316 Stainless Steel*, ORNL-5286 (October 1977).

39. C. E. Pugh, "Creep Law Development for the ORNL Reference Heat of Type 304 Stainless Steel at 1100°F," *High-Temperature Structural Design Methods for LMFBR Components Prog. Rep. Sept. 30, 1972*, ORNL/TM-4058, pp. 31-43.

40. L. D. Blackburn, "Isochronous Stress-Strain-Curves for Austenitic Stainless Steels," in *The Generation of Isochronous Stress-Strain Curves*, American Society of Mechanical Engineers Publication for Winter Annual Meeting, November 26-30, 1972, pp. 15-48.

41. M. K. Booker and V. K. Sikka, *Analysis of the Creep Strain-Time Behavior of Type 304 Stainless Steel*, ORNL-5190 (October 1976).

42. R. W. Weeks, D. R. Diercks, and C. F. Cheng, *ANL Low-Cycle Fatigue Studies Program, Results, and Analysis*, ANL-8009, Argonne National Laboratory (November 1973).

43. S. S. Manson, "Observations and Correlations Emphasizing Wave Shape and Other Salient Features," pp. 155-322 in *Time-Dependent Fatigue of Structural Alloys, A General Assessment (1975)*, ORNL-5073 (January 1977).

44. L. F. Coffin, Jr., "Observations and Correlations Emphasizing Frequency and Environmental Effects," pp. 37-153 in *Time-Dependent Fatigue of Structural Alloys, A General Assessment (1975)*, ORNL-5073 (January 1977).

45. S. Majumdar and P. S. Maiya, "Wave-Shape Effects in Elevated Temperature Low Cycle Fatigue of Type 304 Stainless Steel," in *Inelastic Behavior of Pressure Vessel and Piping Components*, T. Y. Chang and E. Krempl, eds., American Society of Mechanical Engineers, G00136, 1978.

46. C. E. Pugh and R. W. Swindeman, "Update of Revisions to Recommend Base Creep-Fatigue Test Program for Type 304 Stainless Steel," *High-Temperature Structural Design Program Prog. Rep. Dec. 31, 1977*, ORNL-5374, pp. 103-09.

47. D. N. Robinson, ORNL, "Experiments in the Time-Dependent Failure of Metals," unpublished internal document.

48. Letter, C. N. Spalaris (General Electric Company) to P. Patriarca (ORNL), "Creep Fatigue Testing of 2 1/4 Cr-1 Mo" (Nov. 10, 1978).

49. Letter, A. E. Carden (University of Alabama) to J. J. Blass (ORNL) (Nov. 15, 1978).

50. S. S. Manson, Case Western Reserve University, private communication (Nov. 21, 1978).

4. SIMPLIFIED DESIGN METHODS

G. T. Yahr

Inelastic analyses are generally required to satisfy the ASME Code Case 1592 deformation and strain limits and creep-fatigue criteria. However, inelastic analyses are costly and time-consuming, and the Code Case states that elastic and simplified inelastic methods of analysis may sometimes be justified and used. The objective of this subtask is to provide such simplified elastic and inelastic methods and to carefully verify their range of applicability.

Some simplified methods are provided in Code Case N-47 (1592) and RDT Standards F9-4T and F9-5T. However, their range of applicability is severely limited (generally to axisymmetric structures subjected to axisymmetric loadings and away from local structural discontinuities), and the designer generally has had to devise some justification to use them. Before some of these methods were adopted, analytical parameter studies were undertaken under this subtask to demonstrate their conservatism over their limited range of applicability. Scores of inelastic analyses were carried out on simple cylinders and on a nozzle-to-sphere geometry to provide the basis for this demonstration. After adoption of these simplified methods, a much larger two-phased effort was undertaken to extend the range of their applicability.

The phase 1 study consisted of performing a number of detailed inelastic analyses on geometries ranging from axisymmetric cylinders to nozzle-to-sphere and nozzle-to-cylinder configurations; the results of these analyses were used as a basis for assessing the applicability of simplified methods. With a few minor exceptions, the existing ratchetting and creep-fatigue evaluation procedures based on elastic analyses were found to be conservative compared with detailed inelastic analysis predictions for this set of problems. Thus, the designer now has some justification for applying these elastic procedures to a broader range of applications than was previously permitted. Conversely, although one-dimensional problems gave insight into the behavior, a method was not found for ensuring reasonably conservative predictions.

Phase 2 studies are now in progress and include further detailed inelastic analyses of axisymmetric nozzle-to-sphere geometries and an investigation of the applicability of simplified methods to less severe loadings than were considered in phase 1. Additional temperatures are being investigated, and the O'Donnell-Porowski method is being improved to include temperature-dependent yield strength, loading into the plastic ratchetting regimes, primary bending, and biaxiality. Bounds will be derived for the strain range (for elastic fatigue evaluations) during plastic cycling in the presence of creep, and their validity will be tested by comparisons with detailed inelastic analysis results. A sizable effort will be devoted to developing guidance for the designer on how simplified inelastic analyses can best be used for screening analyses and when they can be used for final design assessments. The use of time-dependent isochronous stress-strain analyses is being evaluated as a method of decreasing the cost of inelastic analyses.

Simplified methods are especially needed for high-temperature piping systems. The simplified piping system structural analysis program PACE was obtained from United Kingdom Atomic Energy Authority, and it was used to analyze the Battelle-Columbus elbow inelastic test.[1] Comparisons were made with other analyses done by both PIRAX2 (Ref. 2) and MARC (Ref. 3) and with experimental data from the elbow test. We found that the PIRAX2 analysis fitted the experimental data better than the other analyses. However, note that none of the simplified analyses were as accurate as the detailed inelastic analysis of the elbow.

4.1 Analyses of Axisymmetric Cylindrical Shells

G. T. Yahr

(Last reported in ORNL-5433, p. 180)

A series of detailed inelastic analyses of type 304 stainless steel cylindrical shells is being performed to evaluate the applicability of simplified methods to more realistic stresses and lower temperatures than were covered in the phase 1 studies.[4] Twenty analyses of one-dimensional infinite cylinders, two analyses of notched circular cylindrical shells, one analysis of a circular cylindrical shell with a step change in wall

thickness, and two analyses of built-in circular cylindrical shells were performed. Ratchetting and creep-fatigue damage determined by using the detailed inelastic analyses will be used as the basis of comparison for evaluating the applicability of the current elastic rules for ratchetting in Code Case N-47 (Ref. 5) and RDT Standard F9-5T (Ref. 6).

4.1.1 One-dimensional infinite cylinders

Bree-type diagrams, which allow an estimation of the amount of ratchetting strain from the elastically calculated primary and secondary stresses in a component, were developed earlier[7] for type 304 stainless steel with 200-hr hold periods at 593°C (1100°F). Similar diagrams have now been developed for 200-hr hold periods at 482 and 538°C (900 and 1000°F).

The special pipe-wall ratchetting element of the PLACRE finite-element computer program[8] was used in a series of 20 detailed inelastic analyses of one-dimensional infinite cylinders, each using the temperature and pressure histogram shown in Fig. 4.1. The thermal down transient for

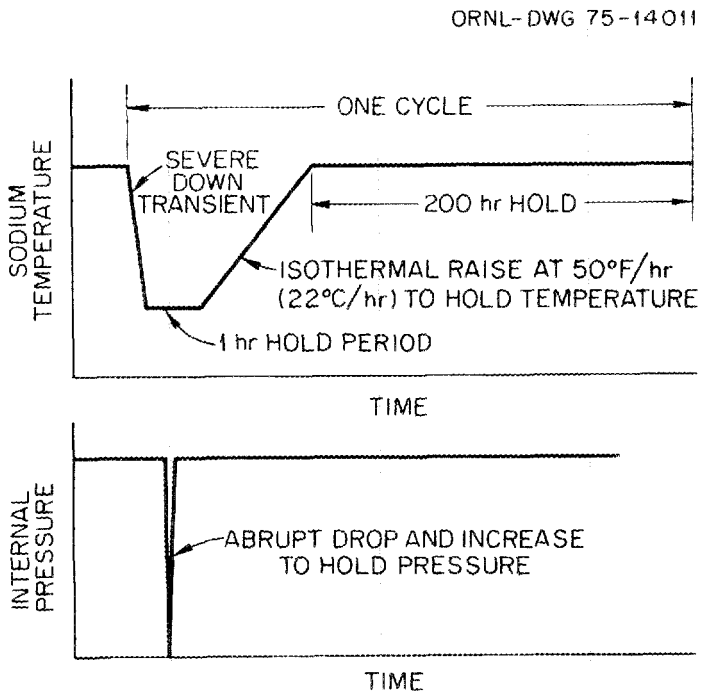

Fig. 4.1. Schematic of internal pressure and sodium temperature cycle used in one-dimensional infinite cylinder analyses.

one set of these analyses was from 482 to 316°C (900 to 600°F), and for the other, it was from 538 to 371°C (1000 to 700°F). The transient rate was varied to produce different secondary thermal stresses in the cylinders. Incremental circumferential strains between the fourth and fifth cycles and between the ninth and tenth cycles are given in Table 4.1. Bree-type design curves, developed from the data in Table 4.1, are given in Figs. 4.2 and 4.3. The yield stress σ_y was used to normalize the elastically calculated secondary stress σ_T produced by the thermal downshock and the elastically calculated primary stress σ_p produced by the internal pressure. Constant incremental strain contours are drawn so that the incremental strain can be estimated from elastically calculated values of primary stress. Of course, these diagrams are only applicable to type 304 stainless steel at 482 and 538°C (900 and 1000°F) with a 200-hr hold time during each cycle.

Table 4.1. Results of one-dimensional analyses of infinite cylinders of type 304 stainless steel exposed to −167°C (−300°F) thermal transients

Run No.	Temperature during creep hold [°C (°F)]	Thermal downshock rate [°C/sec (°F/sec)]	Internal pressure [MPa (psi)]	Incremental ratchet strain (%)	
				Fifth cycle	Tenth cycle
200	482 (900)	4.44 (8)	1.05 (152)	0.00000	0.00000
201	482 (900)	4.44 (8)	2.09 (304)	0.00000	0.00000
202	482 (900)	4.44 (8)	3.14 (456)	0.00005	0.00005
203	482 (900)	4.44 (8)	4.19 (608)	0.00040	0.00040
204	482 (900)	11.11 (20)	1.05 (152)	0.00000	0.00000
205	482 (900)	11.11 (20)	2.09 (304)	0.00005	0.00000
206	482 (900)	11.11 (20)	3.14 (456)	0.00040	0.00040
207	482 (900)	33.33 (60)	1.05 (152)	0.00000	0.00000
208	482 (900)	33.33 (60)	1.57 (227)	0.00005	0.00001
209	482 (900)	33.33 (60)	2.09 (304)	0.00020	0.00020
210	538 (1000)	4.44 (8)	1.01 (146)	0.00000	0.00000
211	538 (1000)	4.44 (8)	2.02 (293)	0.00000	0.00000
212	538 (1000)	4.44 (8)	3.03 (439)	0.00320	0.00250
213	538 (1000)	4.44 (8)	4.03 (585)	0.01430	0.00750
214	538 (1000)	11.11 (20)	1.01 (146)	0.00005	0.00005
215	538 (1000)	11.11 (20)	2.02 (293)	0.00280	0.00200
216	538 (1000)	11.11 (20)	3.03 (439)	0.01180	0.00600
217	538 (1000)	33.33 (60)	1.01 (146)	0.00080	0.00050
218	538 (1000)	33.33 (60)	1.51 (219)	0.00380	0.00240
219	538 (1000)	33.33 (60)	2.02 (293)	0.00850	0.00440

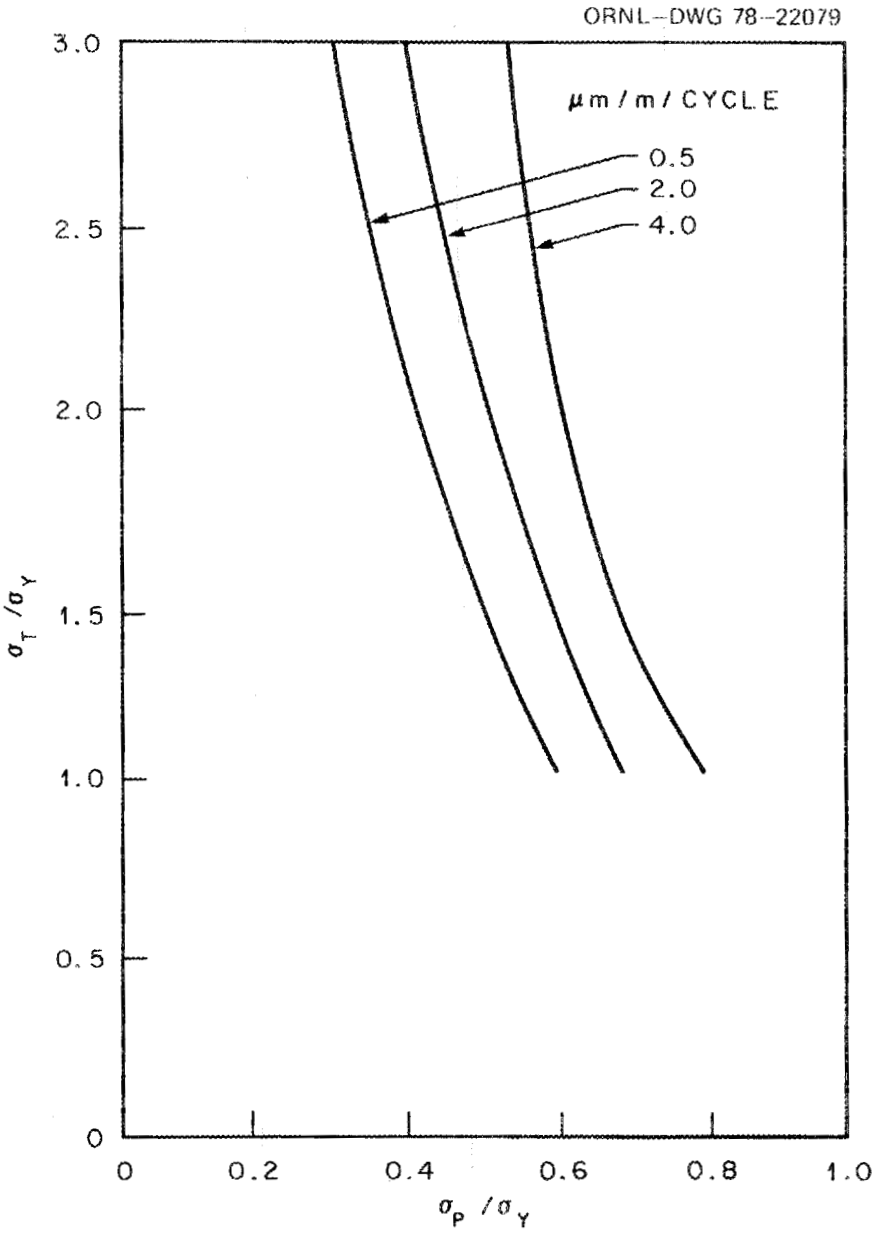

Fig. 4.2. Incremental strain between fourth and fifth cycles with 200-hr hold at 482°C (900°F).

4.1.2 Two-dimensional circular cylindrical shell analyses

Five cases of two-dimensional circular cylindrical shells were analyzed. Two of the cases had circumferential notches, one case had a step change in the wall thickness, and the remaining two cases were built-in

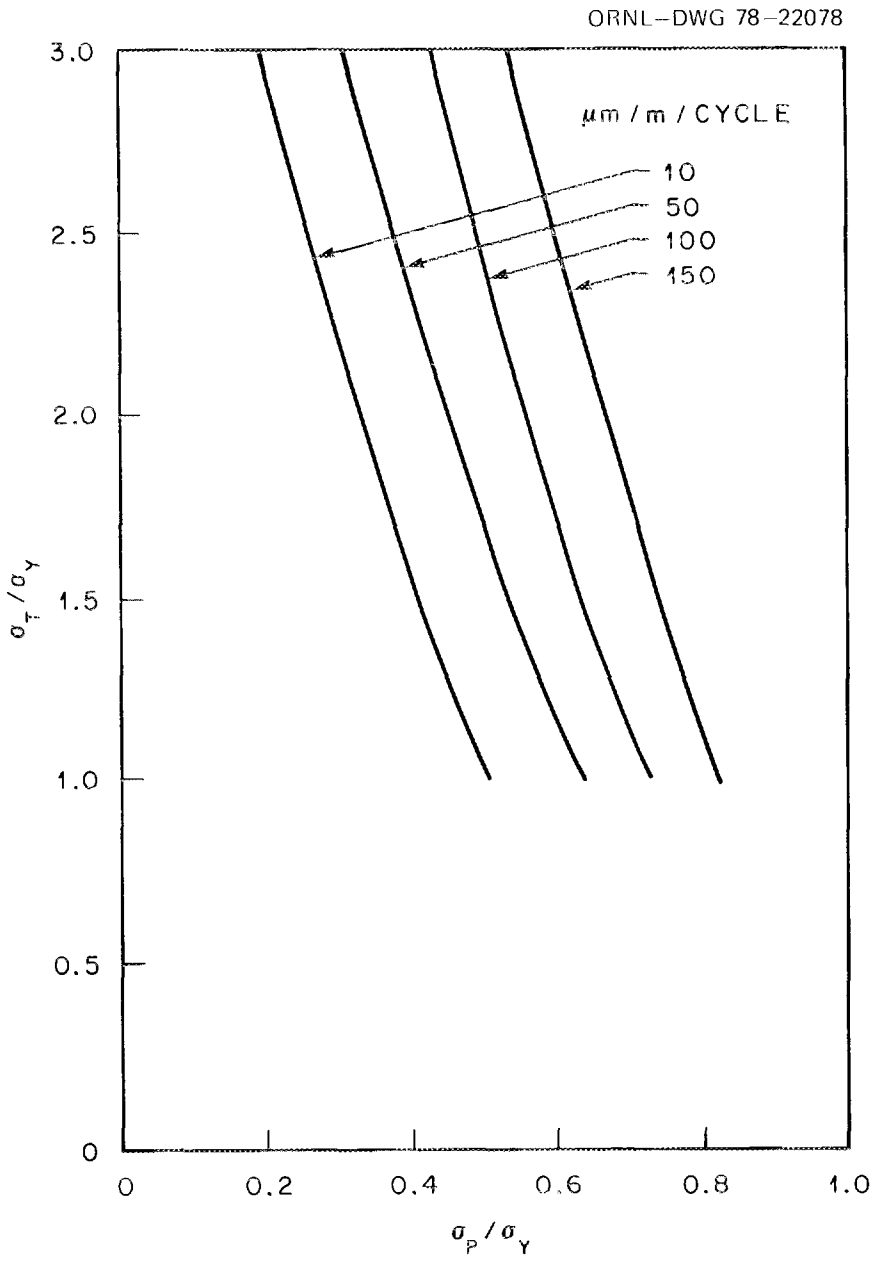

Fig. 4.3. Incremental strain between fourth and fifth cycles with 200-hr hold at 538°C (1000°F).

cylinders. The loading for all five cases included a thermal downshock on the inner surface and internal pressure. Temperature and pressure histograms are the same as for the one-dimensional infinite cylinder analyses shown in Fig. 4.1. An axial load was applied to the notched cylinders in addition to the pressure load.

A ten-cycle inelastic analysis and a one-cycle elastic analysis have now been completed for all five cases using the finite-element program PLACRE.[8] Results will be postprocessed during the next report period to determine accumulated inelastic strains and creep-fatigue damage.

4.2 Detailed Inelastic Analysis of Nozzle-to-Spherical-Shell Attachment

R. C. Gwaltney

(Last reported in ORNL-5433, p. 183)

The axisymmetric analysis of a nozzle-to-spherical-shell attachment is continuing. The analysis duplicates the nonaxisymmetric analysis of a nozzle-to-spherical-shell attachment done at Atomics International as part of the phase 1 investigation, except that a moment is not applied to the nozzle. The moment is simulated by an axial force.

The inelastic analysis has been completed for five full cycles. The histogram for each of the five cycles is shown in Fig. 4.4. Note that temperature, pressure, and axial force change during each cycle. Major points of interest in the first cycle are marked by large capital letters and are listed in Table 4.2.

For the model, calculation of the creep-fatigue damage is being performed in accordance with ASME Code Case N-47 (Ref. 5). A specially

Table 4.2. Segments of histogram for nozzle-to-sphere analyses

Load change	Path
Thermal downshock on inside surface	A-B
Transient to steady-state temperature	B-C
Depressurization cycle and addition of axial force	C
Heatup	C-D
Creep-hold period	D-E

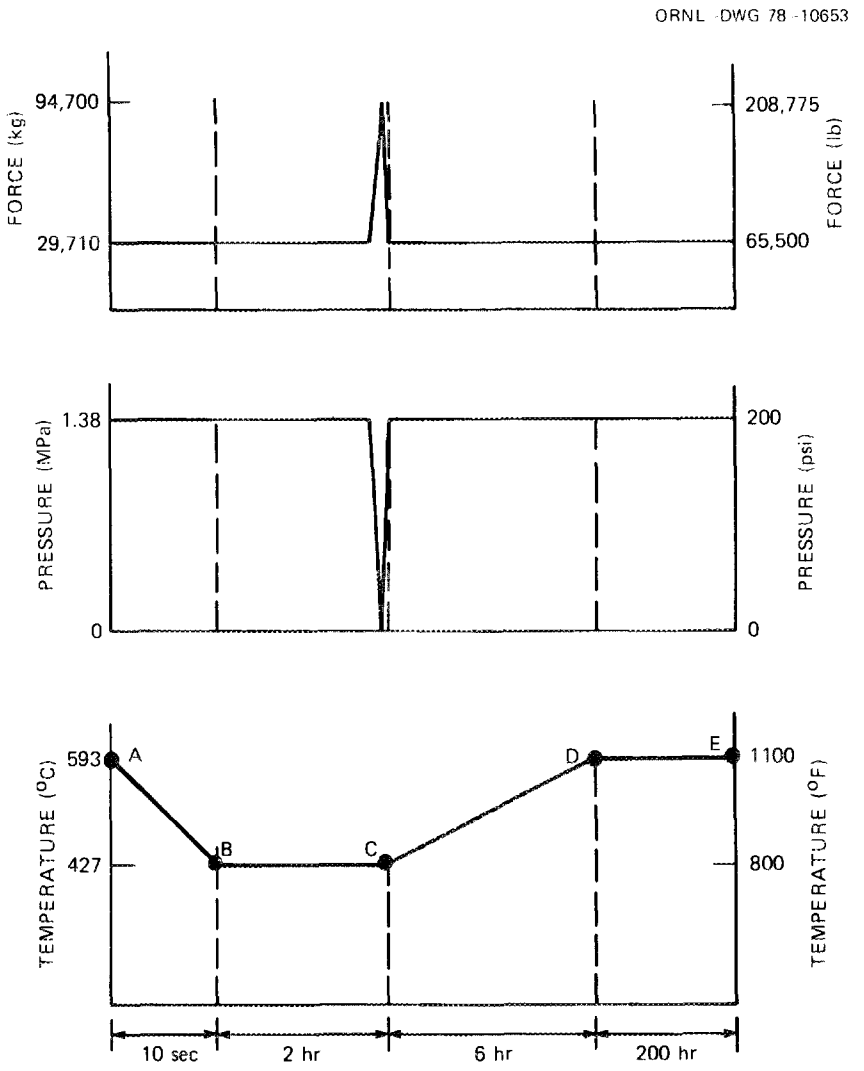

Fig. 4.4. Histogram for each of the five cycles analyzed for the nozzle-to-spherical-shell attachment. Letters A through E indicate major points of interest in the cycle.

developed postprocessor computer program is being used in these evaluations. Ten critical sections or lines through the wall have been chosen, and the postprocessing is being done along these lines. The ten sections are shown in Fig. 4.5. The creep-fatigue damage is being calculated at the inner and outer surfaces of each section. Damage calculations based on the inelastic analysis will be compared with simplified methods damage calculations. The stress-strain response curves predicted for the inner and outer surfaces of section 7A for the five cycles are shown in Figs. 4.6 and 4.7.

ORNL-DWG 78-10644

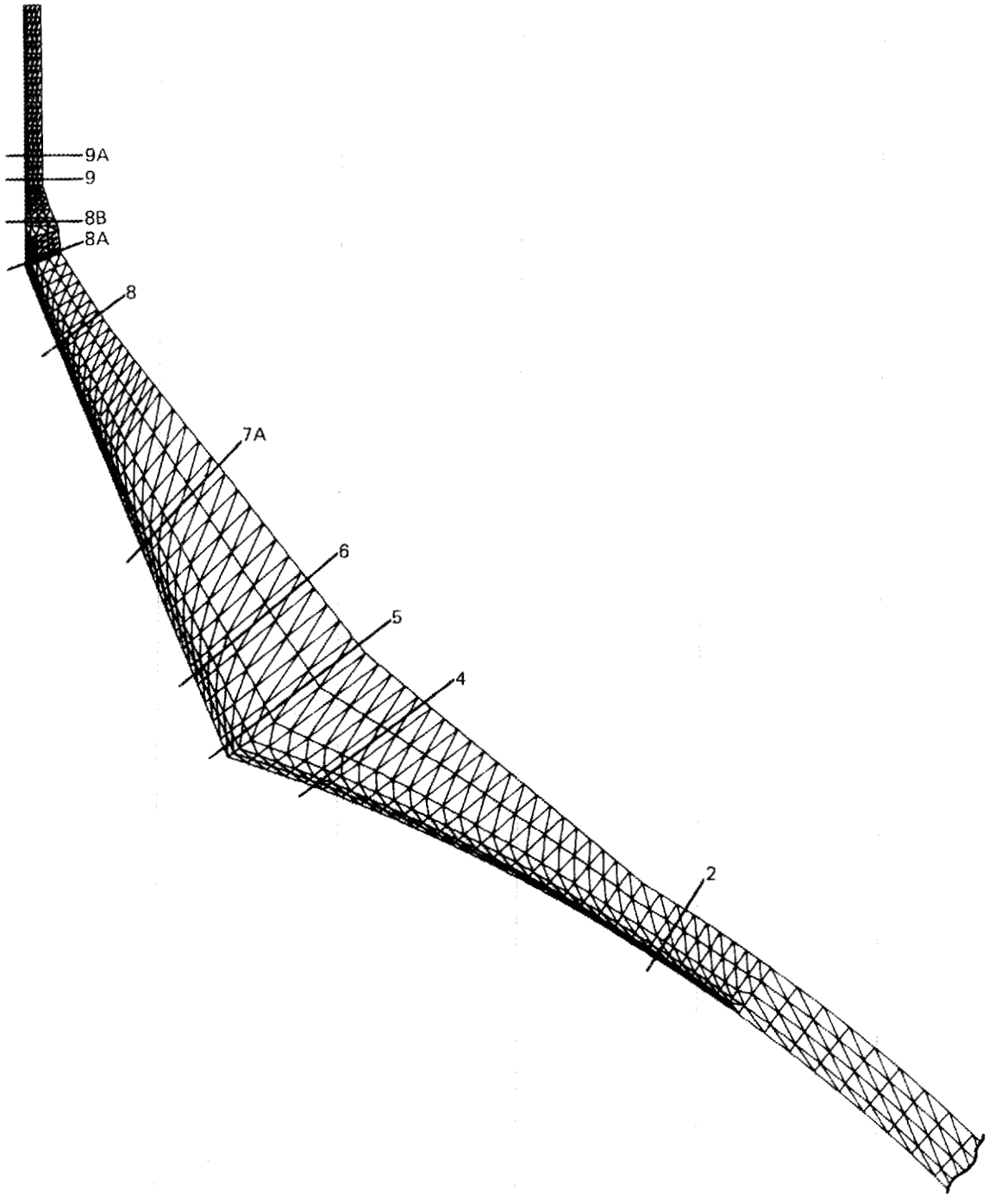

Fig. 4.5. Critical sections of nozzle-to-spherical-shell attachment.

ORNL-DWG 78-22076

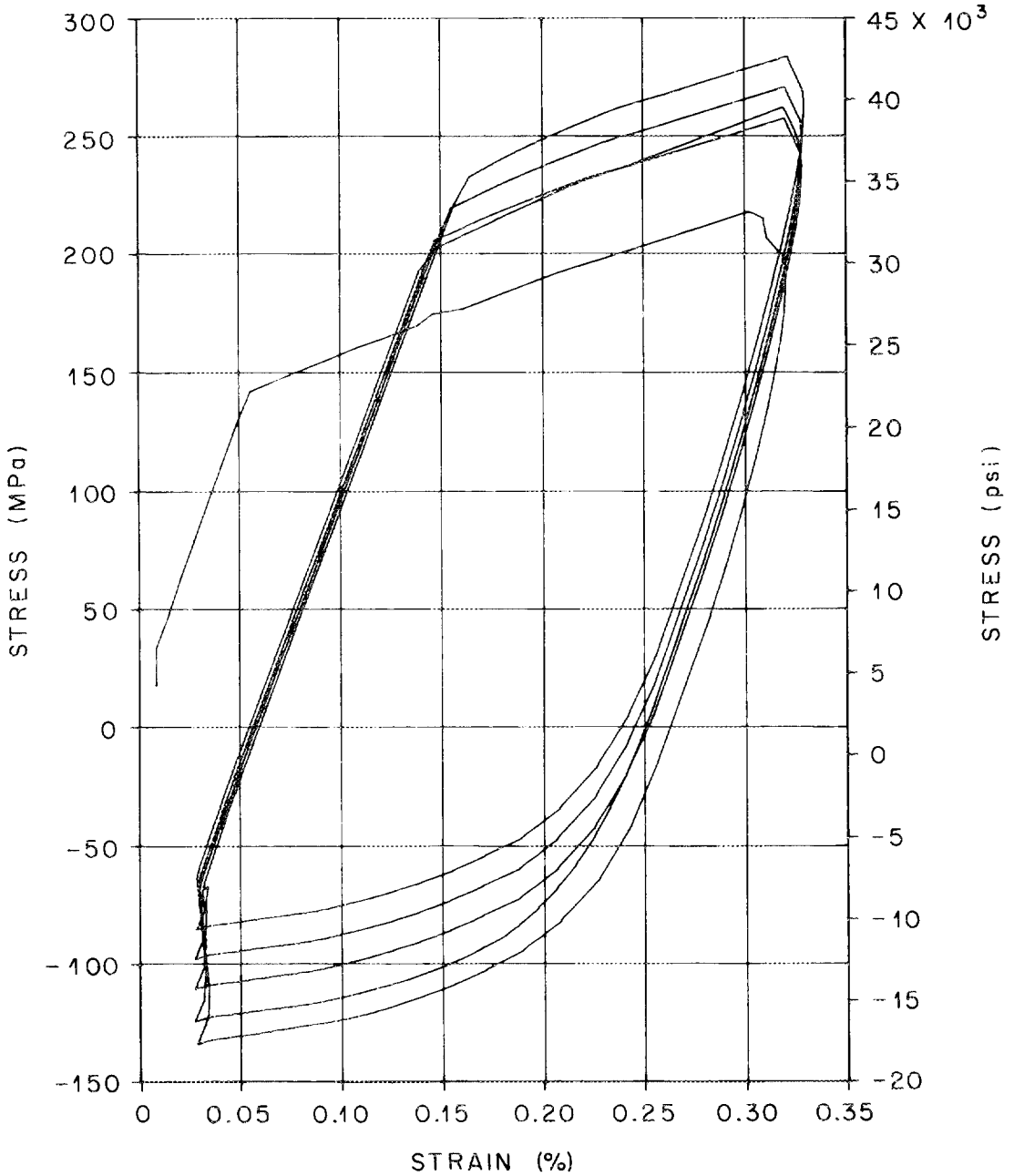

Fig. 4.6. Stress-strain response at inner surface of section 7A.

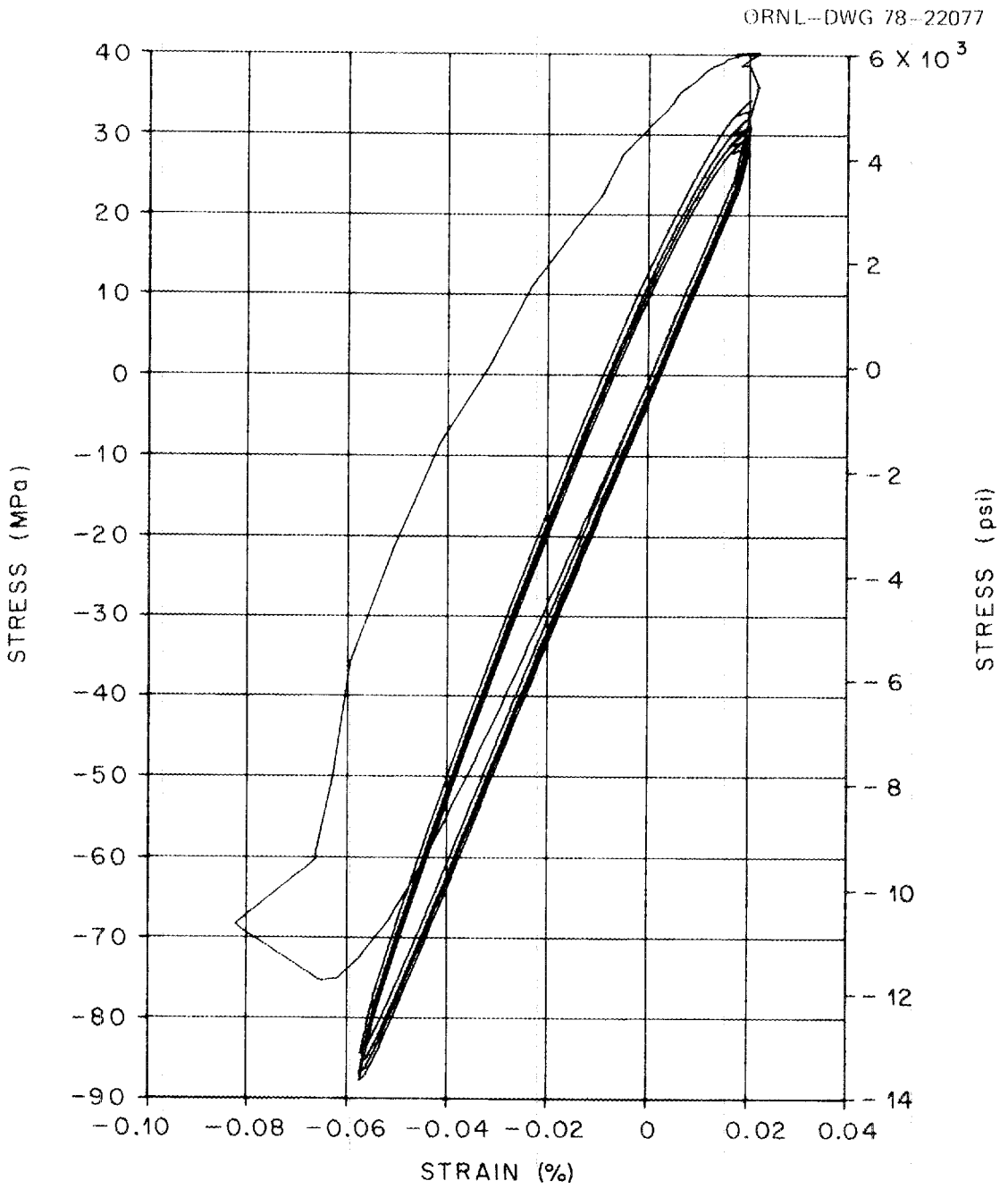

Fig. 4.7. Stress-strain response at outer surface of section 7A.

This analysis is also being prepared as a benchmark problem for submission to the Elevated Temperature Design Subcommittee of the Pressure Vessel Research Committee. The description of the problem has already been submitted.

4.3 Improved Elastic Ratchetting and Creep-Fatigue Damage Evaluation Procedures

W. J. O'Donnell* J. S. Porowski*

(Last reported in ORNL-5433, pp. 185-196)

Bounds on creep ratchetting for load histograms, which include severe cycles into the plastic ratchetting regimes, were obtained. The maximum energy available for dissipation within a cycle was used to bound the inelastic strain increment that is caused by relaxation and redistribution of stresses. The concept of partial relaxation of the elastic core stress was introduced, and the solution was obtained for strain-hardening materials with temperature-dependent yield strengths. The bounds are presented in a topical report that was prepared during this report period.[9] A brief review of the resulting design rules and equations is given here.

The total inelastic strain accumulated within the given cyclic load history is given by

$$\Sigma\varepsilon_{(n)} = \Sigma v_{(n)} + \Sigma\delta_{(n)} + \Sigma\delta_{(n+1)} + \Sigma\eta_{(n)} , \tag{4.1}$$

where $\Sigma v_{(n)}$ is the strain accumulated at constant stresses $\sigma_{c_{(n)}}$ or $\sigma_{\ell_{(n)}}$ obtained from isochronous curves for the lifetime of the component, $\Sigma\delta_{(n)}$ and $\Sigma\delta_{(n+1)}$ are the sums of the strain increments due to relaxation and enhanced creep, and $\Sigma\eta_{(n)}$ is the sum of the plastic-strain increments. The partial relaxation stress σ_ℓ can be arbitrarily selected between the elastic core stress $\sigma_c \geq S_{y_H}$ and the primary stress σ_p. This selection can be optimized to obtain the most efficient bounds. The corresponding

*O'Donnell and Associates, Inc., Pittsburgh, Pennsylvania.

strain increment is bounded by

$$\delta_{(n)} = \frac{1}{E} \frac{\sigma^2_{c_{(n)}} - \sigma^2_{\ell_{(n)}}}{\sigma_{\ell_{(n)}}} , \tag{4.2}$$

where E is the elastic modulus averaged between the low- and the high-temperature extremes of the thermal cycle.

In case the stress $\sigma_{\ell_{(n)}}$ of the preceding cycle is higher than the core stress $\sigma_{\ell_{(n+1)}}$ of the subsequent cycle, the relaxation strain increment for $(n+1)$ cycle must be increased by

$$\delta_{(n+1)} = \frac{1}{E} \frac{\sigma^2_{\ell_{(n)}} - \sigma^2_{c_{(n+1)}}}{\sigma_{c_{(n)}}} . \tag{4.3}$$

Plastic straining does not occur if

$$\sigma_{c_L} \leq S_{y_H} . \tag{4.4}$$

If inequality (4.4) is not satisfied, the plastic increment occurs at one or both ends of the cycle and is given by

$$\eta_{(n)} = \frac{1}{E} \left[\left(A - S_{y_L} \right) + \left(\{\sigma_c\}_H - S_{y_H} \right) \right] , \tag{4.5}$$

where $A = \sigma_{c_L}$ if $Z_L \leq 1.0$ or $A = \left\{ \sigma_{c_L} \right\} = Z_L > 1.0$. The S_{y_L} and S_{y_H} are the yield strengths at cold and hot ends of the cycle, respectively.

A sample core stress history is shown in Fig. 4.8. The dimensionless core stress parameter Z is determined for each end of the cycle using dimensionless primary $X = \sigma'_p$ and secondary $Y = \sigma'_t$ stress components in Fig. 4.9. The stresses are normalized using the relations

$$X = \sigma'_p = \frac{2\sigma_p - \left(S_{y_T} - S_{y_C} \right)}{S_{y_T} + S_{y_C}} , \tag{4.6}$$

ORNL–DWG 78–22646

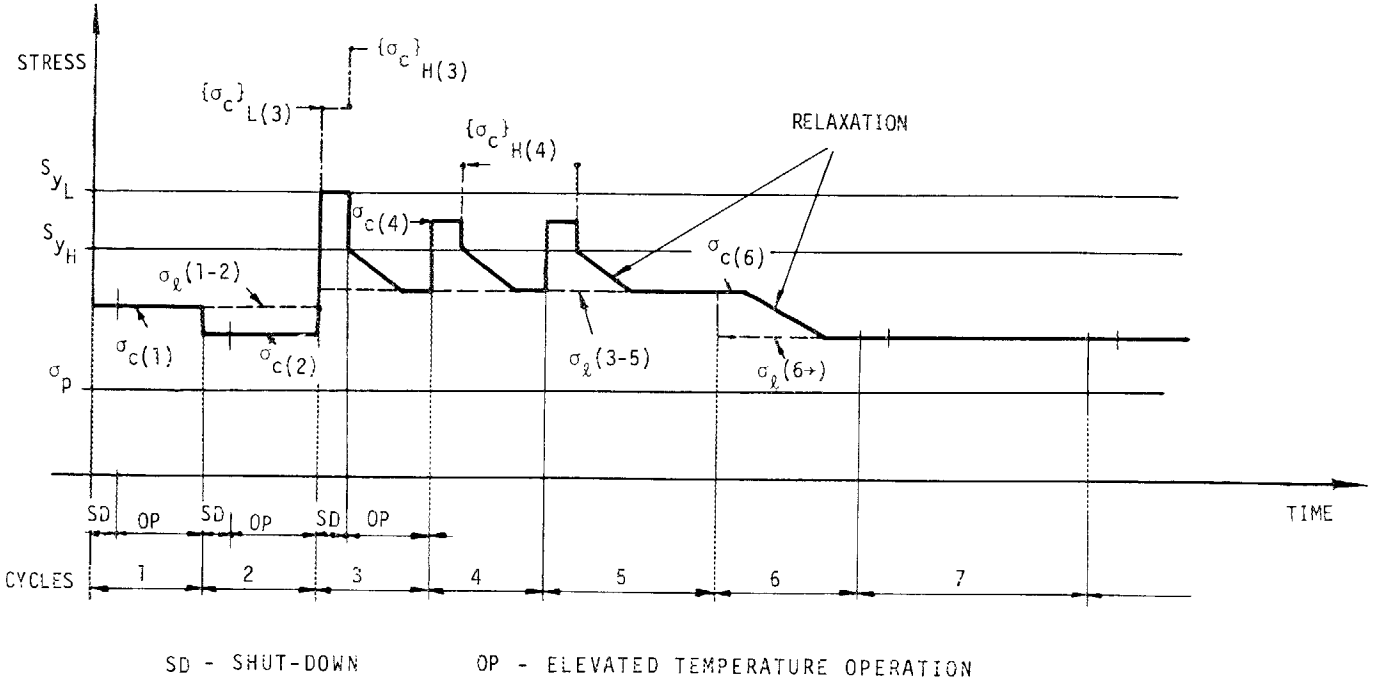

SD - SHUT-DOWN OP - ELEVATED TEMPERATURE OPERATION

Fig. 4.8. Diagram of middle plane stress histogram.

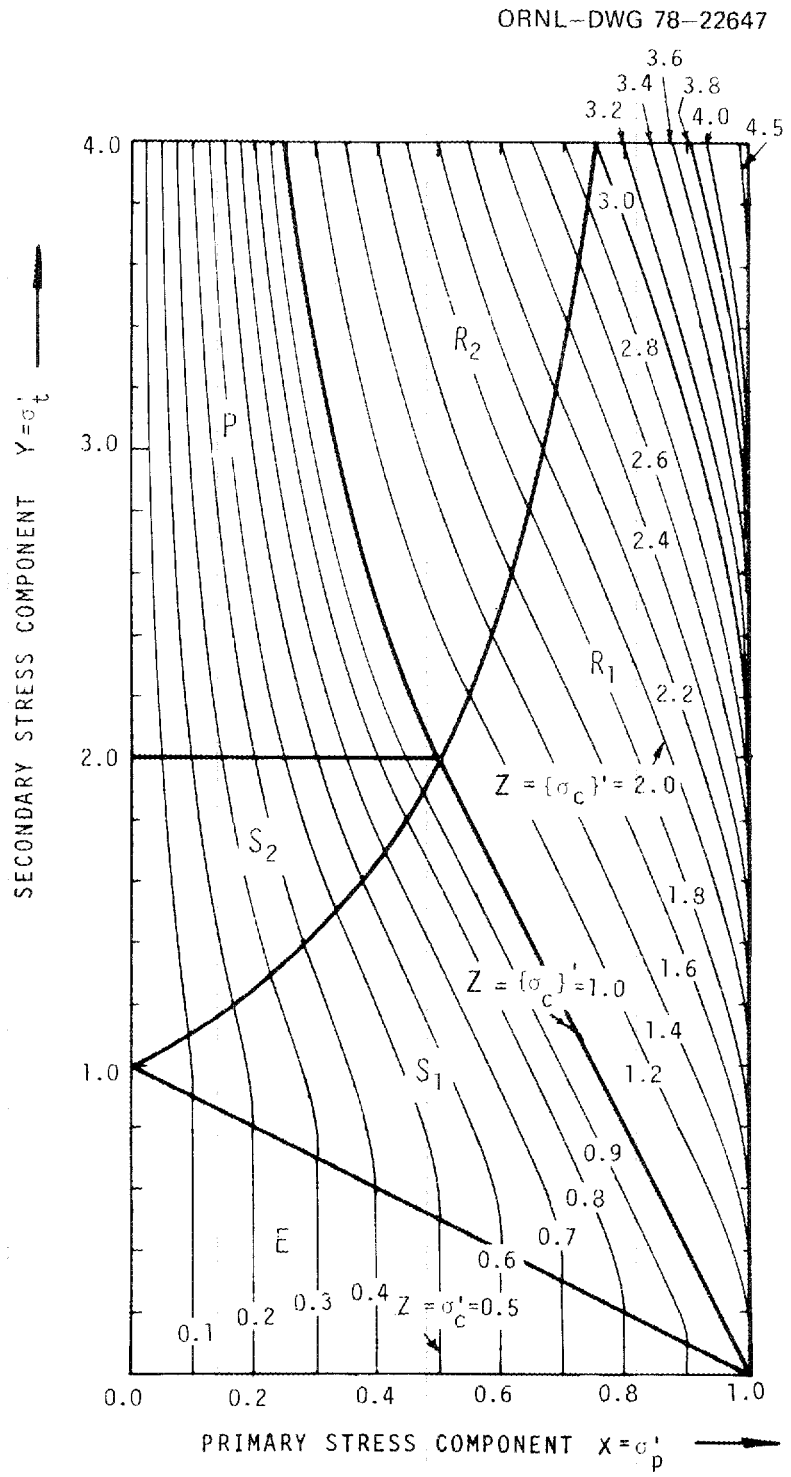

Fig. 4.9. Generalized core stress graph.

and

$$Y = \sigma_t' = \frac{2\sigma_t}{S_{y_T} + S_{y_C}} , \tag{4.7}$$

where S_{y_T} and S_{y_C} are the yield strengths of hardening material in tension and compression for each considered cycle, respectively. The core stress is obtained from the relation

$$\sigma_c = (1/2)\left[Z\left(S_{y_T} + S_{y_C}\right) + \left(S_{y_T} - S_{y_C}\right)\right] . \tag{4.8}$$

For the kinematically hardening material, the relations (4.6) through (4.8) simplify to

$$X = \sigma_p' = (\sigma_p - B)/S_{y_o} , \tag{4.6a}$$

$$Y = \sigma_t' = \sigma_t/S_{y_o} , \tag{4.7a}$$

and

$$\sigma_c = ZS_{y_o} + B , \tag{4.8a}$$

where $B = (1/2)(S_{y_T} - S_{y_C})$ defines the current position of the yield surface origin. For the uniaxial case, $B = E_p \Sigma n_{(n)}$, where E_p is a plastic modulus for linearly strain-hardening material.

4.4 Examination of Simplified Inelastic Analysis Procedures

J. M. Chern* S. A. Kamal*

(Last reported in ORNL-5433, pp. 196-209)

The main objectives of this effort are to (1) investigate the applicability of special-purpose efficient computer codes in the assessment of

---

*Foster-Wheeler Energy Corporation, Livingston, New Jersey.

inelastic structural response of actual components and (2) recommend guidelines for the use of simplified methods in engineering analysis.

The simplified analyses are being performed for the Clinch River Breeder Reactor Plant—Intermediate Heat Exchanger (CRBRP-IHX) primary inlet nozzle and Z-forging. Detailed inelastic analyses on these two components were done to verify the design and are available for comparison with the simplified analysis results. Results have been obtained for the primary inlet nozzle, as reported here.

4.4.1 Summary of CRBRP-IHX primary inlet nozzle inelastic analysis results

The primary inlet nozzle serves as an inlet to the CRBRP-IHX for the primary sodium coming from the reactor via a piping system. The dimensions of the nozzle and loading conditions were discussed in the last progress report.[10] Loadings include internal pressure and predominantly radial thermal gradients. The inelastic analysis was based on an axisymmetric model in which the shell was modeled as a sphere with twice the radius of the actual cylindrical shell to reproduce the maximum pressure stresses; the detailed results are given in Ref. 11.

A procedure for simplified inelastic analysis using one-dimensional generalized plane-strain models to evaluate the stress-strain conditions at critical sections in an axisymmetric structure was developed and applied at two sections in the CRBRP-IHX primary inlet nozzle.[11] Simplified analysis results were compared with the available detailed analysis results on the basis of ASME Code Case N-47 design rules[5] for the evaluation of inelastic strains and creep and fatigue damage.

In the simplified analysis, the assumption is that the thermal and elastic stress analyses for the full structural model have been performed so that the most critical sections can be identified. Should further inelastic analysis be necessary, these may be simulated by simplified structural models subjected to appropriately derived loadings.

In the case of the CRBRP-IHX primary inlet nozzle, the loading of the axisymmetric structural model[11] consists of (1) nozzle load F_z induced by the deadweight and thermal expansion of the attached piping system, (2) primary sodium pressure p_i, and (3) thermally induced stresses during the

fast transient events. Loading in the simplified analysis consists of (1) an equivalent internal pressure p_i^*, (2) equivalent temperature distribution through the wall $T^*(r)$, and (3) axial force with equivalent mean stress Q. For each load step in the loading histogram, the values of p_i^*, $T^*(r)$, and Q are obtained from the elastic stresses and temperature distributions at the critical section of the axisymmetric model being simulated. To satisfy the Code Case N-47 design rules, two separate simplified analyses corresponding to surface and average conditions have to be performed. The methods of load simulation in the two analyses are the results of several attempts to systematically approach the detailed inelastic analysis results.

The method of load simulation for evaluating the inelastic strain accumulations corresponding to the 1 and 2% strain limits which also correspond to average conditions were given in the last progress report[11] and are not repeated here.

To evaluate creep-fatigue damage and the 5% strain limit corresponding to surface conditions, the primary stress and the secondary stress range are determined at both the inner and outer surface of the critical section from the elastic analysis of the structural model. The values at the surface where the secondary stress range is the higher are used to determine primary and secondary stresses in the simplified analysis to evaluate creep and fatigue damage and peak strain accumulation.

Internal pressure for the simplified analysis p_i^* is selected so that the primary stress in the circumferential direction is equal to the elastically calculated primary stress in the structural model. The radial temperature distribution $T^*(r)$ in the simplified analysis is determined as follows:

$$T^*(r) = T(r) + (\Delta T_\theta - \Delta T_r)(r - \bar{r})/t \text{ if } \Delta T_\theta > \Delta T_r ,$$

or

$$T^*(r) = T(r) \text{ if } \Delta T_\theta \leq \Delta T_r ,$$

where $T(r)$ is the temperature distribution through the wall of the structural model, ΔT_r is equivalent linear temperature gradient in the structural model, and ΔT_θ is the linear temperature gradient that will produce

a thermal bending stress in the simplified analysis model equal to the elastically calculated thermal bending stress in the structural model. An axial stress is applied to the simplified analysis model which will cause the total axial stress at the surface of interest to be equal to the total linearized meridional stress in the structural model.

Both methods of analysis obviously involve a number of assumptions and approximations. The two following points, however, are emphasized for their relatively large influence on the accuracy of the results.

1. The material properties (elastic, plastic, and creep), if temperature dependent, have to be evaluated at the actual temperature distribution through the wall $T(r)$ rather than at the fictitious distribution $T^*(r)$.
2. The smaller the difference between the thermally induced bending stresses in the hoop and meridian directions, the better the simulation will be in the simplified analyses.

Using the present methods, simplified inelastic analyses were performed at two critical sections A and B in the primary inlet nozzle, as shown in Fig. 4.10.

The simplified analyses were performed for six unit cycles of the histogram described in Ref. 10, using the FW-1045 computer code.[12] Results of the simplified analyses are compared with those of the detailed analysis of the axisymmetric model in Tables 4.3 through 4.5 for section A and in Tables 4.6 through 4.8 for section B.

The creep damage evaluation presented in Tables 4.3 and 4.6 for sections A and B, respectively, show excellent agreement between the simplified and detailed analyses during the sixth unit cycle. Similar trends have been found in the results of the preceding unit cycles.

The fatigue damage evaluations at sections A and B are shown in Tables 4.4 and 4.7, respectively. The relatively large difference in the values of $(1/N_d)$, despite the excellent agreement in the strain range, is due to the extremely small slope of the fatigue curve at small strain range values. Insignificant fatigue damages, however, are associated with small strain ranges. Tables 4.5 and 4.8 show for sections A and B, respectively, the accumulation and growth of the inelastic strains for the six

ORNL-DWG 78-22648

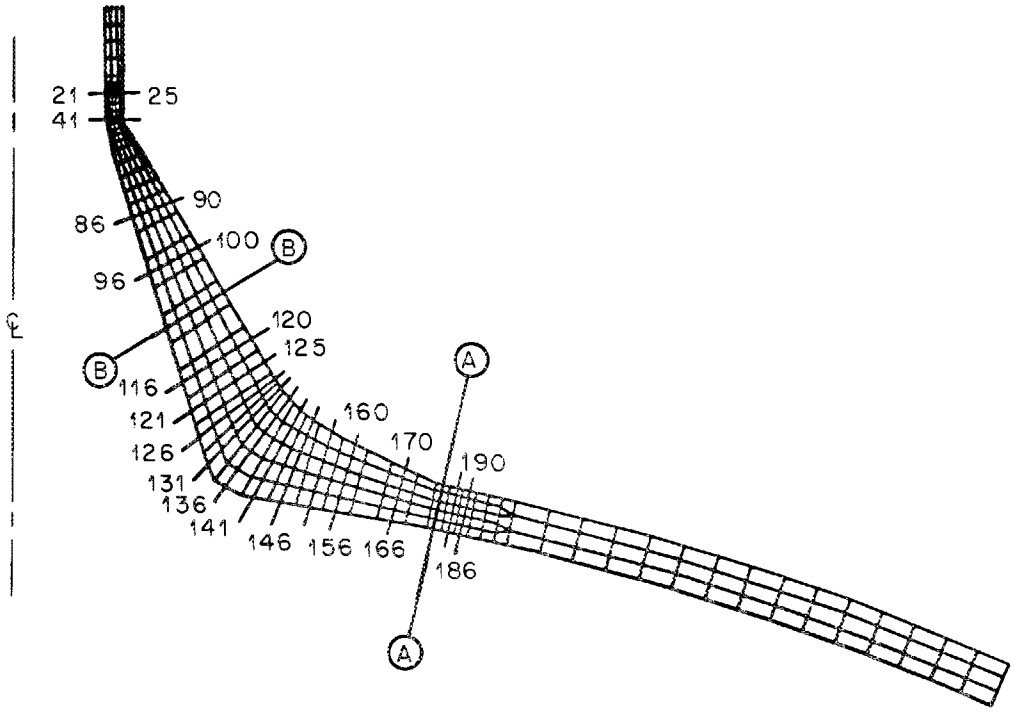

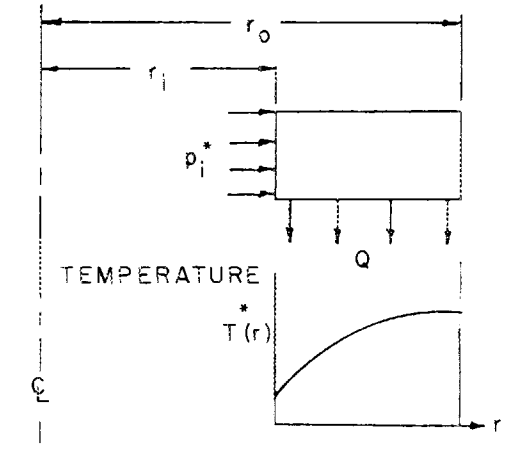

LOADING OF SIMPLIFIED ANALYSIS

Fig. 4.10. Sections A and B of primary inlet nozzle selected for simplified inelastic analysis.

Table 4.3. Comparison of creep damage evaluation at section A

Transient	σ_e [MPa (ksi)]		$(t/T_d) \times 10^3$	
	Detailed	Simplified	Detailed	Simplified
1U	97 (14.1)	105 (15.3)	0.573	0.931
2U	108 (15.7)	105 (15.3)	1.160	0.973
NC	104 (15.1)	102 (14.8)	0.892	0.782
1U	103 (14.9)	105 (15.3)	0.817	0.973
NC	99 (14.4)	101 (14.7)	0.655	0.749
Σ (t/T_d) for sixth unit cycle			4.097	4.408

Table 4.4. Comparison of fatigue damage evaluation at section A

Transient	$\Delta\varepsilon_{eq}$ $(\times 10^3)$		$(1/N_d) \times 10^5$	
	Detailed	Simplified	Detailed	Simplified
2U	1.909	1.926	3.72	3.89
NC	0.237	0.241	0.00	0.00
1U	1.486	1.602	0.86	1.37
NC	0.239	0.241	0.00	0.00
1U	1.486	1.602	0.86	1.37
Σ $(1/N_d)$ for sixth unit cycle			5.44	6.63

unit cycles. Extrapolated values at the end of life are based on the growth of the sixth unit cycle for both the simplified and detailed analyses. Agreement between the two analyses was less satisfactory for the accumulated inelastic strains. Better agreement, however, was found when the accumulated plastic and creep strains were considered individually, as shown in Table 4.9.

Table 4.5. Comparison of inelastic strains (10^{-3} in./in.) at section A

Cycle	Peak at $r = r_i$		Linearized at $r = r_i$		Average		Linearized at $r = r_o$	
	ε^i	$\Delta\varepsilon^i$	ε^i	$\Delta\varepsilon^i$	ε^i	$\Delta\varepsilon^i$	ε^i	$\Delta\varepsilon^i$
				Detailed analysis				
1	0.563	0.000	0.318	0.000	0.106	0.000	0.143	0.000
2	0.601	0.038	0.341	0.023	0.133	0.027	0.188	0.045
3	0.622	0.021	0.359	0.013	0.155	0.022	0.268	0.080
4	0.639	0.017	0.379	0.020	0.174	0.019	0.331	0.063
5	0.652	0.013	0.398	0.019	0.192	0.018	0.384	0.053
6	0.664	0.012	0.418	0.020	0.208	0.016	0.431	0.047
174	2.680		3.778		2.896		8.327	
				Simplified analysis				
1	0.677	0.000	0.558	0.000	0.195	0.000	−0.160	0.000
2	0.695	0.018	0.599	0.041	0.239	0.044	−0.113	0.047
3	0.712	0.017	0.639	0.040	0.281	0.042	−0.069	0.044
4	0.729	0.017	0.676	0.037	0.321	0.040	−0.027	0.042
5	0.747	0.018	0.712	0.036	0.358	0.037	0.012	0.039
6	0.765	0.018	0.745	0.033	0.394	0.036	0.048	0.037
174	3.789		6.289		6.442		6.264	

Table 4.6. Comparison of creep damage evaluation at section B

Transient	σ_e [MPa (ksi)]		$(t/T_d) \times 10^3$	
	Detailed	Simplified	Detailed	Simplified
1U	99 (14.3)	105 (15.2)	0.627	0.931
2U	105 (15.3)	106 (15.4)	0.973	1.016
NC	101 (14.6)	101 (14.7)	0.716	0.749
1U	101 (14.7)	104 (15.1)	0.749	0.892
NC	98 (14.2)	101 (14.6)	0.599	0.716
Σ (t/T_d) for sixth unit cycle			3.664	4.304

Table 4.7. Comparison of fatigue damage evaluation at section B

Transient	$\Delta\varepsilon_{eq}$ $(\times 10^3)$		$(1/N_d) \times 10^5$	
	Detailed	Simplified	Detailed	Simplified
2U	1.660	1.951	1.47	4.17
NC	0.149	0.119	0.00	0.00
1U	1.390	1.650	0.55	1.64
NC	0.162	0.117	0.00	0.00
1U	1.390	1.650	0.55	1.64
Σ $(1/N_d)$ for sixth unit cycle			2.57	7.45

In summary, a simplified inelastic analysis using a one-dimensional generalized plane-strain model can be used to evaluate, with reasonable accuracy, the creep and fatigue damage and peak inelastic strain accumulation at a critical section in an axisymmetric structural model. Based on the inelastic analysis of six unit cycles, the simplified analysis results were conservative compared with the detailed analysis. Accuracy of the simplified analysis varies from one section to another, depending on the

Table 4.8. Comparison of inelastic strains (10^{-3} in./in.) at section B

Cycle	Peak at $r = r_i$		Linearized at $r = r_i$		Average		Linearized at $r = r_o$	
	ε^i	$\Delta\varepsilon^i$	ε^i	$\Delta\varepsilon^i$	ε^i	$\Delta\varepsilon^i$	ε^i	$\Delta\varepsilon^i$
				Detailed analysis				
1	0.738	0.000	0.422	0.000	0.104	0.000	0.278	0.000
2	0.746	0.008	0.429	0.007	0.108	0.004	0.284	0.006
3	0.755	0.009	0.437	0.006	0.112	0.006	0.288	0.004
4	0.765	0.010	0.445	0.009	0.117	0.005	0.291	0.003
5	0.775	0.010	0.454	0.009	0.121	0.006	0.294	0.003
6	0.786	0.011	0.463	0.009	0.126	0.007	0.297	0.003
174	2.634		1.975		1.302		0.801	
				Simplified analysis				
1	1.350	0.000	0.460	0.000	0.139	0.000	−0.182	0.000
2	1.480	0.130	0.465	0.005	0.145	0.006	−0.176	0.006
3	1.550	0.070	0.469	0.004	0.150	0.005	−0.170	0.005
4	1.610	0.060	0.474	0.005	0.155	0.005	−0.165	0.005
5	1.670	0.060	0.479	0.005	0.160	0.005	−0.160	0.005
6	1.710	0.040	0.484	0.005	0.165	0.005	−0.155	0.005
174	8.430		1.324		1.005		0.685	

Table 4.9. Comparison of creep and plastic strains at section B

Cycle	Creep strain (10^{-3})				Plastic strain (10^{-3})			
	Detailed[a]		Simplified[b]		Detailed[a]		Simplified[b]	
	ε_θ^c	$\Delta\varepsilon_\theta^c$	ε_θ^c	$\Delta\varepsilon_\theta^c$	ε_θ^p	$\Delta\varepsilon_\theta^p$	ε_θ^p	$\Delta\varepsilon_\theta^p$
1	−0.118	0.000	−0.159	0.000	0.88	0.00	1.51	0.00
2	−0.244	−0.126	−0.334	−0.175	1.02	0.14	1.81	0.30
3	−0.357	−0.113	−0.477	−0.143	1.14	0.12	2.03	0.22
4	−0.458	−0.101	−0.596	−0.119	1.25	0.11	2.21	0.18
5	−0.549	−0.091	−0.695	−0.099	1.35	0.10	2.36	0.15
6	−0.633	−0.084	−0.780	−0.085	1.44	0.09	2.49	0.13

[a]At $r = r_i + 0.028\ (r_o - r_i)$.
[b]At $r = r_i$.

capability of simulating the elastically calculated stresses of the full structural model. Results of the simplified analysis at section A differed from the detailed analysis by 8% in the combined creep and fatigue damage and by 41% in the peak strain. At section B, the differences were 19 and 220%, respectively.

The inelastic strain accumulation corresponding to 1 and 2% limits which reflect the average section behavior can be evaluated by a separate simplified inelastic analysis. Although the results of this simplified analysis did not consistently lie on the conservative side, the inelastic strains showed relatively small differences from the corresponding detailed inelastic analysis: −25 to +122% at section A and −33 to −14% at section B.

4.5 Analytical Investigation of the Applicability of the Isochronous Method for Predicting Deformations in Simple Beam and Plate Structures

J. A. Clinard

(Not previously reported)

A limited analytical investigation of the applicability of an isochronous method for predicting deformations in simple beam and plate structures was conducted, and a report[13] was written.

The two specific problems included in the study were selected from benchmark experimental tests conducted at ORNL. Both were type 304 stainless steel structures tested under isothermal conditions at 593°C (1100°F) and for loads producing significant plastic and creep deformations. The first structure was a simply supported, centrally loaded beam of uniform rectangular cross section; the second, a simply supported circular plate axisymmetrically loaded over the center portion. Both tests were conducted under load control. For both problems, the portion of the loading considered in this study consisted of a short-term monotonic loading followed by a constant-load hold period of nearly two weeks.

To assess the predictive capability of the isochronous method, both problems were analyzed using detailed elastic-plastic-creep methods and using an isochronous elastic-plastic method which approximately incorporated the effects of creep.

Solutions were compared with experimental results and with each other. The detailed inelastic prediction of peak deflection differed from the measured deflection by 5% (underprediction) in the case of the beam and by 6% (overprediction) in the case of the plate. The isochronous

prediction of peak deflection differed from the measured deflection by 21% (underprediction) in the case of the beam and by 28% (underprediction) in the case of the plate.

Whole-field stress and strain predictions by the two methods were compared with each other. Isochronous predictions of stresses were (as expected) in good agreement with detailed predictions. Peak stresses differed at most by only 3% in the case of the beam and by 16% in the case of the plate. In general, isochronous predictions of deflections and strains were in relatively poor agreement with detailed predictions. Peak deflections differed by 17% in the case of the beam and by 32% in the case of the plate; peak strains, by 6% in the case of the beam and by as much as 45% in the case of the plate. For all quoted comparisons (between solutions by the two methods), the isochronous method predicted the lesser value.

Conclusions drawn from the study are (1) isochronous solutions are appreciably cheaper (about 60%) than detailed solutions; (2) isochronous predictions, though they include the gross effects of creep in a qualitatively correct fashion, may vary considerably with data and with detailed solutions; and (3) the level of agreement is problem dependent.

Concerning the third conclusion, for the case of the beam, the agreement was marginal; for the plate, poor. The poor agreement for the plate problem is probably attributable to the complexity of the stress state and to the extreme inhomogeneity of the deformations (stresses and strains were concentrated to a somewhat discontinuous region of the structure). This agreement is supported by results for the beam where the stress state was nearly uniaxial, structure uniform, and agreement considerably better.

The report[13] was written to expand the documented analysis experience with the isochronous method which, at present, is scant. In summary, the isochronous method appears to show promise as a simplified method to be used in elevated temperature design; however, questions as to a specific role for this method remain largely unanswered.

References

1. W. I. Griffith and E. C. Rodabaugh, *Report on Tests of Two 4-Inch Sch. 10 Elbow Assemblies*, Battelle Columbus Laboratories, ORNL/Sub-3651-2 (December 1974).

2. G. H. Workman and E. C. Rodabaugh, *User's Manual for PIRAX2, Inelastic Analysis of 3-Dimensional Piping Systems*, Battelle Columbus Laboratories, ORNL/Sub-3651-3 (December 1974).

3. MARC-CDC, developed by MARC Analysis Research Corporation, Providence, R.I.

4. G. T. Yahr, *Simplified Analysis Methods for High-Temperature Structural Design — Summary of Phase 1 Study*, ORNL-5289 (October 1977).

5. ASME Code Case N-47-13 (1592-13), *Class I Components in Elevated Temperature Service, Section III, Division 1, ASME Boiler and Pressure Vessel Code, Case Interpretations*, American Society of Mechanical Engineers, New York (September 1977).

6. Energy Research and Development Administration, *Guidelines and Procedures for Design of Nuclear System Components at Elevated Temperatures*, RDT Standard F9-5T (September 1974).

7. Y. M. Yoo and G. T. Yahr, "Infinite Cylinder Analyses," *High-Temperature Structural Design Program Prog. Rep. Dec. 31, 1975*, ORNL-5136, pp. 94-96.

8. W. K. Sartory, *PLACRE User's Manual*, ORNL/TM-5626 (February 1977).

9. J. S. Porowski and W. J. O'Donnell, *More Efficient Creep Ratchetting Bounds*, O'Donnell and Associates, Inc., ORNL/Sub-7322-1 (October 1978).

10. J. M. Chern and S. A. Kamal, "Examination of Simplified Inelastic Analysis Procedures," *High-Temperature Structural Design Program Prog. Rep. June 30, 1978*, ORNL-5433, pp. 196-209.

11. Foster-Wheeler Energy Corporation, *Manufacturer's Stress Report, CRBRP-IHX*, FWEC Document No. ND/77/45, Section 7, 1977.

12. J. M. Chern, *User's Manual of Computer Code R-1045: Cyclic Elastic-Plastic-Creep Analysis of an Infinitely Long Thick-Walled Cylinder*, FWR-35 (April 1973).

13. J. A. Clinard, *Analytical Investigation of the Applicability of the Isochronous Method for Predicting Deformations in Simple Beam and Plate Structures*, ORNL/TM-6673 (to be published).

5. THERMAL RATCHETTING TESTS

W. K. Sartory

The ORNL thermal ratchetting tests are being conducted to provide carefully obtained ratchetting test data and creep-fatigue failure data under ratchetting conditions for evaluating basic design analysis methods and failure criteria and for verification and qualification of inelastic analysis computer codes by benchmark problem calculations. Structural geometries include cylindrical shells without structural discontinuities, dissimilar metal welds, seam-welded and seamless pipe, a step change in wall thickness, and a notched shell geometry. The structures are loaded by internal pressure or axial load and are subjected to repeated thermal downshocks. Materials considered are types 304 and 316 stainless steel, 2 1/4 Cr–1 Mo steel, and Alloy 800, with type 308 stainless steel, Inconel 82, and 16-8-2 stainless steel weldment filler metals.

We are presently phasing out our work in this area. Activity will resume if approval to proceed with two proposed future tests (TTT-5 and TT-6) to creep-fatigue failure is obtained.

5.1 Analysis of the Weldment Region of Specimen TTT-3

W. K. Sartory

(Last reported in ORNL-5433, pp. 211-217)

Specimen TTT-3 is a 2 1/4 Cr–1 Mo steel to type 316 stainless steel pipe specimen (with an Inconel 82 weldment) that was subjected to ratchetting loading conditions. A report describing the final test results and one-dimensional analyses was published in October 1977.[1] A two-dimensional axisymmetric inelastic analysis of the weldment region of the specimen has now been completed through all 19 cycles of the test.

The analysis was performed using the finite-element program PLACRE.[2] The finite-element grid, material properties, and other inputs to the analysis were described in the previous progress report.[3] To aid in the presentation of the results of the analysis, a computer program was written that accepts a postprocessor tape prepared by PLACRE and produces contour

plots of temperature, strain, etc. A typical contour plot showing the effective creep-strain distribution at the end of the test is presented in Fig. 5.1. Note that the maximum creep strain in the 2 1/4 Cr–1 Mo steel section is slightly over 0.25% and occurs in the outer portion of the wall in the region far from the weldment. A comparison of the calculated circumferential ratchetting strain with two strain gage measurements at the outer surface at the center plane of the weldment is illustrated in Fig. 5.2. The agreement shown is considered very satisfactory because it is much better than was obtained earlier[1] for the type 316 stainless steel section far from the weldment and is comparable to the agreement obtained for the 2 1/4 Cr–1 Mo steel section far from the weldment.

The inelastic damage evaluation for the analysis was limited to creep damage for the 2 1/4 Cr–1 Mo steel section of the specimen. (We anticipated that creep damage would be much larger than fatigue damage for this test and that the 2 1/4 Cr–1 Mo steel section would be the weakest part of the specimen with respect to creep rupture.) The Larson-Miller correlation of Jaske and Mindlin[4] was used to provide creep-rupture data. Damage results, when extrapolated linearly from the 18th and 19th cycles to a creep damage fraction of 1.0, indicate that the specimen could withstand 1845 cycles of the maximum severity used in this test [593°C (1100°F) creep-hold temperature with a two-week hold time, 16.7°C/sec (30°F/sec) downshock rate for 10 sec, and 4.83 MPa (700 psi) internal pressure]. It is also of interest that the greatest creep damage was predicted to occur far from the weldment. However, the heat-affected zone (HAZ) of the 2 1/4 Cr–1 Mo steel was not accounted for in the analysis.

After completion of the analysis, a report on the work was written, reviewed, and revised and is now awaiting final approval before being edited.

In summary, the results of this investigation suggest that it is possible to analyze a weldment region and obtain agreement with measured ratchetting strain that is comparable to that achievable for simple pipes without structural discontinuities.

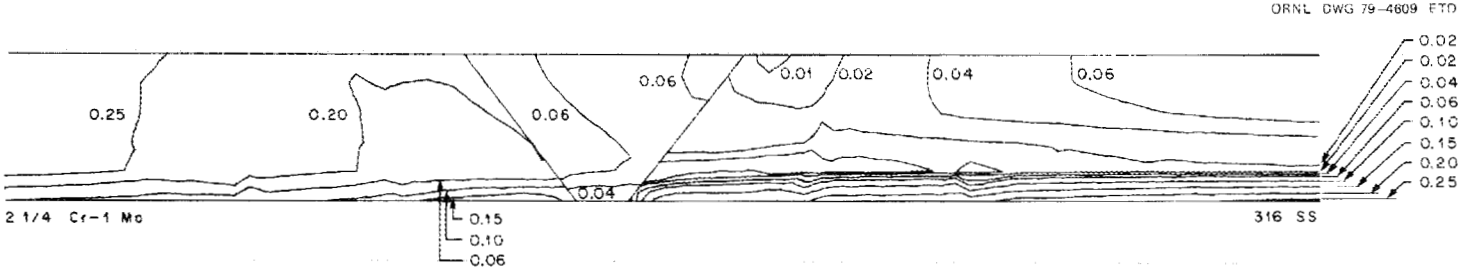

Fig. 5.1. Calculated effective creep strain distribution at the end of the 19th creep-hold period in the weldment region of specimen TTT-3. Strains are in percent.

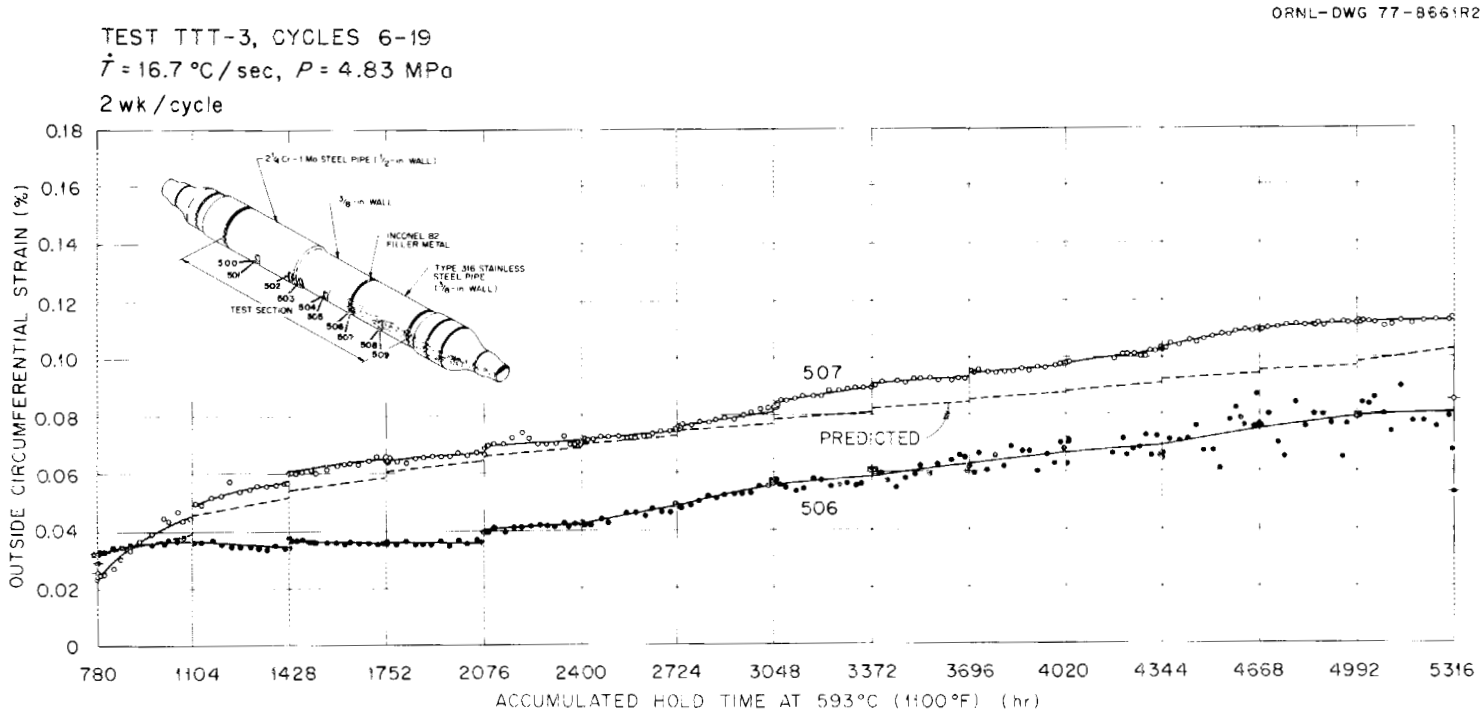

Fig. 5.2. Outside surface circumferential strain at center plane of the weldment of specimen TTT-3 during the creep-hold periods of cycles 6 to 19.

5.2 Type 316 Stainless Steel Seamless to Seam-Welded Pipe Specimen TTT-4

(Last reported in ORNL-5433, pp. 217-219)

Test TTT-4 involved a length of seam-welded type 316 stainless steel pipe welded to a length of seamless type 316 stainless steel pipe. The purpose of this test was to demonstrate the adequacy of welded pipe under the more severe CRBRP transients and also to obtain basic ratchetting data on type 316 stainless steel seamless and welded pipe. The final report on this test was published in September.[5] Test results indicated that welded pipe was just as resistant to ratchetting as seamless pipe.

5.3 Test TT-6 of a Type 304 Stainless Steel Pipe to Creep-Fatigue Failure

W. K. Sartory

(Last reported in ORNL-5433, pp. 224-225)

TT-6 is a proposed test in which creep-fatigue failure is to be induced for a type 304 stainless steel pipe without structural discontinuities. The specimen is being designed at ORNL, but it is proposed that the testing be performed at the Energy Technology Engineering Center (ETEC). During the present report period, preliminary discussions were conducted with ETEC personnel, and a request for approval-in-principle (AIP) was prepared and sent to the Director, Reactor Research and Technology.[6] The response from ETEC indicated that the test could be carried out in their Thermal Transient Facility but that it would be much simpler to perform if it were not necessary to hold the specimen internal pressure constant during the test, as originally proposed. A calculated, readily attainable pressure-time history was received from ETEC. A few revised ratchetting analyses [which also incorporated recently developed creep-plasticity interaction rules (Sect. 1.1), creep damage correlations (Sect. 3.9.2), and fatigue-damage correlations (Sect. 3.9.1)] were carried out using the ETEC pressure history. The analyses indicate that no major revision in the test condition is required to accommodate the new pressure history. When the final test request is written, however, we will select

a series of axial load levels of gradually increasing severity to compensate for the wide variability in creep rupture strength that has been calculated.

References

1. W. K. Sartory et al., *Thermal Ratchetting Test of 2 1/4 Cr–1 Mo Steel to Type 316 Stainless Steel Pipe: Test TTT-3*, ORNL-5330 (October 1977).

2. W. K. Sartory, *PLACRE User's Manual*, ORNL/TM-5626 (February 1977).

3. W. K. Sartory, "Analysis of the Weldment Region of Specimen TTT-3," *High-Temperature Structural Design Program Prog. Rep. June 30, 1978*, ORNL-5433, pp. 211-17.

4. C. E. Jaske and H. Mindlin, "Elevated-Temperature Low-Cycle Fatigue Behavior of 2 1/4 Cr–1 Mo and 1 Cr–1 Mo–1/4 V Steels," pp. 237-210 in *2 1/4 Chrome–1 Molybdenum Steel in Pressure Vessels and Piping*, A. O. Schafer, American Society of Mechanical Engineers, New York, 1971.

5. W. K. Sartory et al., *Thermal Ratchetting Test of Type 316 Stainless Steel Seamless to Seam-Welded Pipe: Specimen TTT-4*, ORNL-5430 (September 1978).

6. Letter, P. Patriarca (ORNL) to Director (Reactor Research and Technology), "Request for Approval-In-Principle for a Pipe Thermal Ratchetting Test to Failure at the Energy Technology Engineering Center" (July 19, 1978).

6. STRUCTURAL DESIGN METHODS FOR WELDMENTS

T. J. Delph

The objectives of this subtask are to investigate the high-temperature deformation and failure behavior of weldments, to evaluate approximate methods for obtaining the stress and deformation distributions in weld regions, and to develop appropriate failure criteria. Weldment-related studies are also being undertaken as part of the thermal ratchetting test series (reported in Chapter 5) and the restrained cylinder test series (reported in Chapter 3).

6.1 Plate-Weldment Tests

6.1.1 Room-temperature tests

We have completed reduction of experimental data from a series of room-temperature plate-weldment tests, along with concurrent elastic-plastic finite-element analyses. The specimens for this test series were fabricated from the reference heat (9T2796) of 304 stainless steel and contained a 308 stainless steel controlled residual element (CRE) weld located on the transverse centerline of the specimen. The specimens were approximately 46 cm (18.1 in.) long, 7.62 cm (3 in.) wide, and 0.63 cm (0.25 in.) thick and were loaded in tension along the longitudinal axis. The weld joint was of double-V geometry, tapering uniformly from about 0.75 cm (0.3 in.) wide at the surface to about 0.25 cm (0.1 in.) at the root. The purpose of these initial tests was to obtain accurate deformation data for comparison with analysis.

The specimens for the first two tests, designated W-1 and W-2, were welded by the shielded metal arc method using stick electrodes. After welding, both specimens were given our reference solution anneal. Specimen W-3 was welded using the gas-tungsten arc procedure. Both halves of this specimen were given the reference solution anneal prior to welding, but the weld was left in the unannealed, as-deposited condition.

All specimens were loaded monotonically in tension until an average tensile stress of ∿250 MPa (36.3 ksi) was reached, with pauses in the

loading process for data acquisition. Strain data were acquired by conventional foil strain gages, as well as by the moire technique in tests W-2 and W-3. Figure 6.1 shows a specimen installed in the loading frame prior to testing.

Results from the first two tests and comparisons with finite-element analyses were presented in two previous progress reports.[1,2] Detailed results from all three tests will be given in a forthcoming topical report.[3] Some of the results from the W-3 test are summarized here.

Figure 6.2 shows the strain gage locations for the W-3 test specimen. A moire grid containing 1000 lines/in. was applied to one side of the specimen, and those strain gage locations not masked by the grid were repeated on this side. Moire data were acquired in the brief pauses during the loading process by means of a Photolastic, Inc., moire analyzer.

An analysis of the W-3 test was conducted concurrently utilizing the CREEP-PLAST finite-element program and a bilinear, elastic-plastic stress-strain relationship. The values of Young's modulus, the bilinear yield stress, and the tangent modulus for the weld metal were taken from a series of room-temperature constant-strain-rate tests[4] on 308 CRE weld metal. These values were $E = 2.14 \times 10^5$ MPa (3.11×10^7 psi), $\sigma_y = 340$ MPa (49,300 psi), and $E_T = 71{,}700$ MPa (1.04×10^7 psi). The bilinear yield stress and tangent modulus were based on a strain range of 0.3%. The value of Poisson's ratio for the weld metal was taken as $\nu = 0.24$, as in the analyses of the W-1 and W-2 tests. Corresponding values for the 304 stainless steel base metal were derived from strain gage data taken from location J (Fig. 6.2). These values were $E = 1.9 \times 10^5$ MPa (2.8×10^7 psi), $\nu = 0.29$, $\sigma_y = 155$ MPa (22,500 psi), and $E_T = 9{,}300$ MPa (1.35×10^6 psi) and were based on a strain range of 0.4%. They compare favorably with previously reported values.[5] The finite-element grid for the analysis was identical to that used previously for the analysis of the W-1 and W-2 tests.[1]

Figure 6.3 shows the longitudinal strain values at location B (Fig. 6.2) as obtained from strain gage data and as predicted by analysis vs the average longitudinal stress. The agreement between experiment and analysis is quite good at this point, both indicating little yielding.

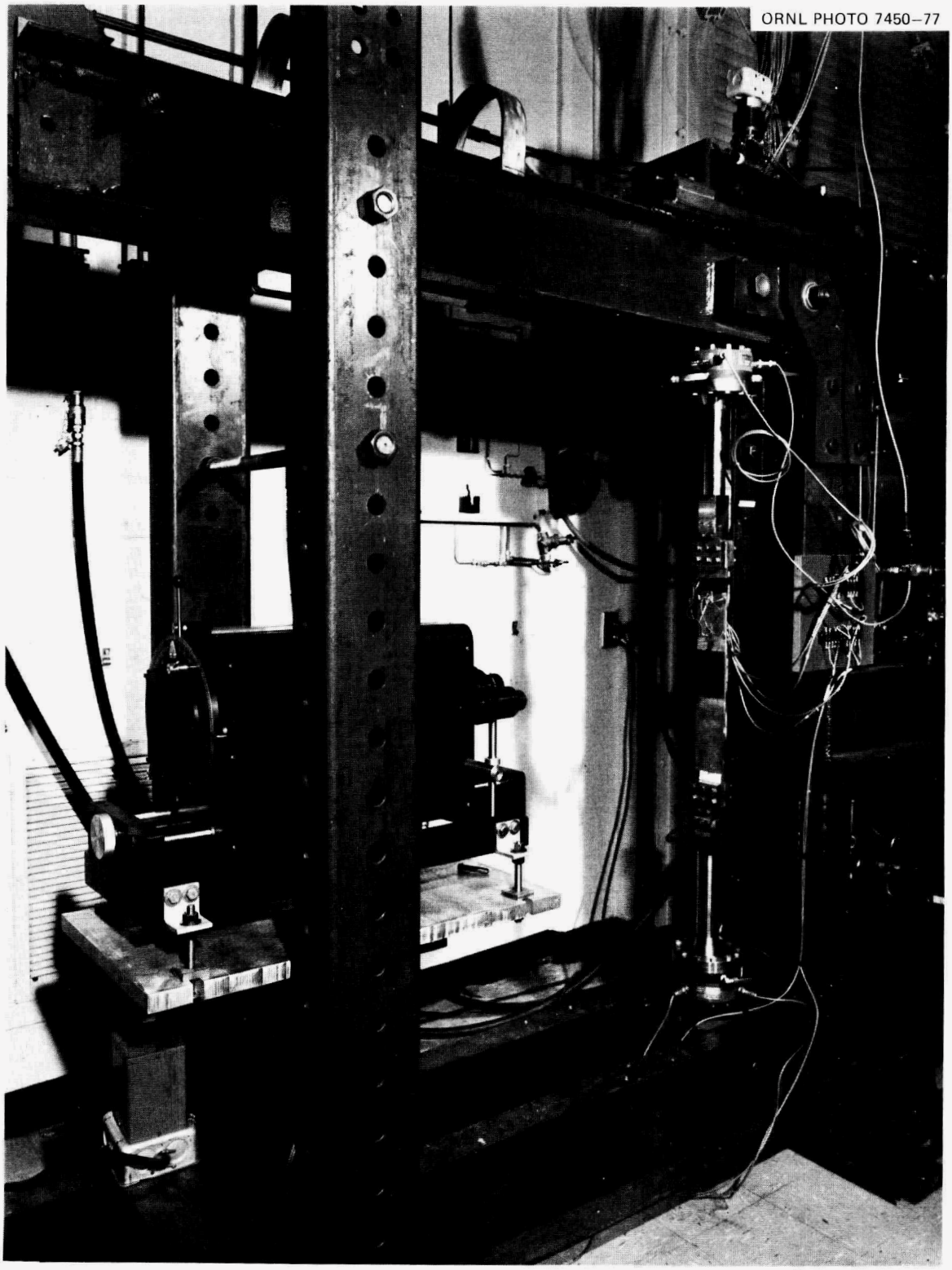

Fig. 6.1. Plate-weldment specimen installed in loading frame.

ORNL-DWG 78-12950

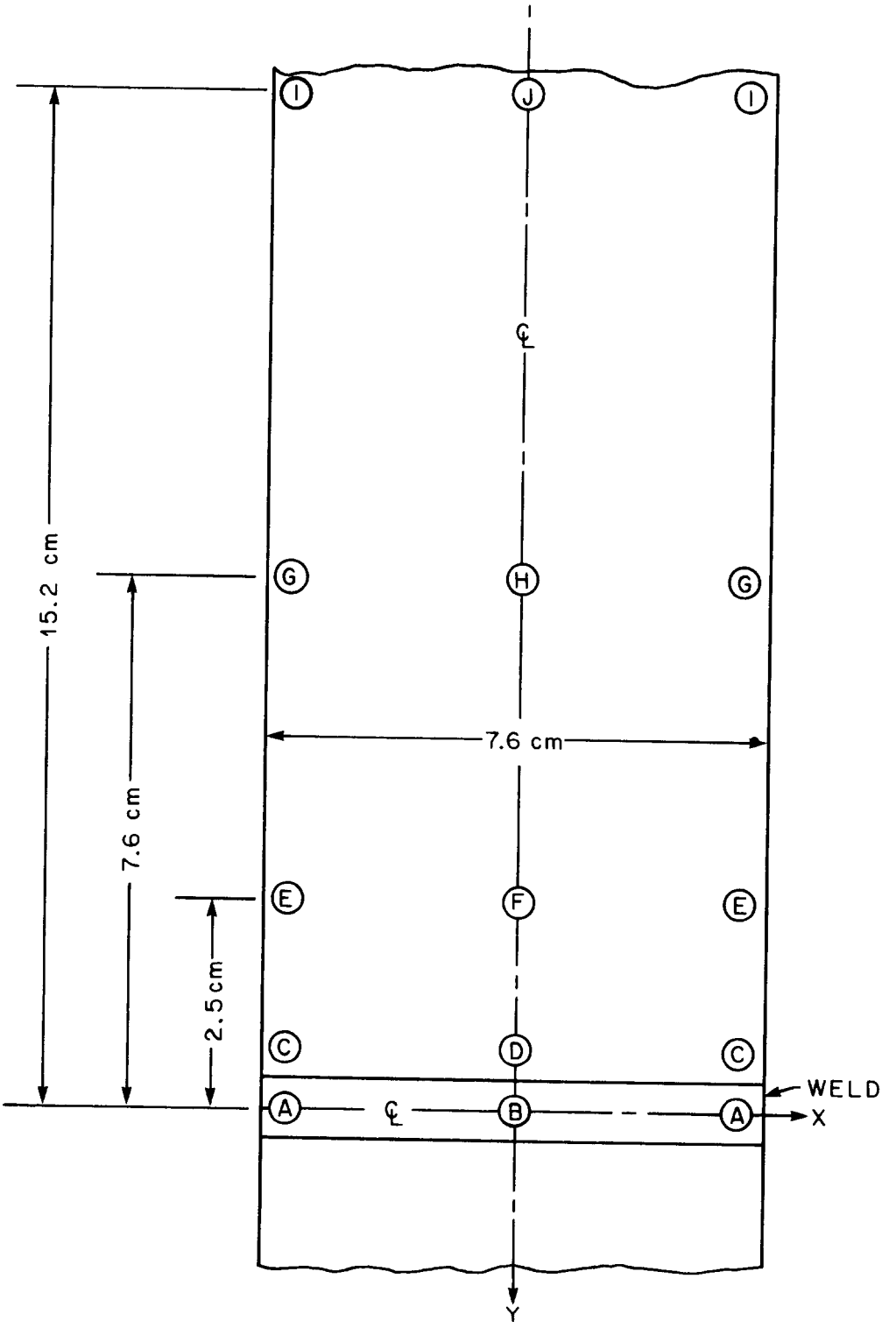

Fig. 6.2. Strain gage locations, specimen W-3 (dimensions in centimeters).

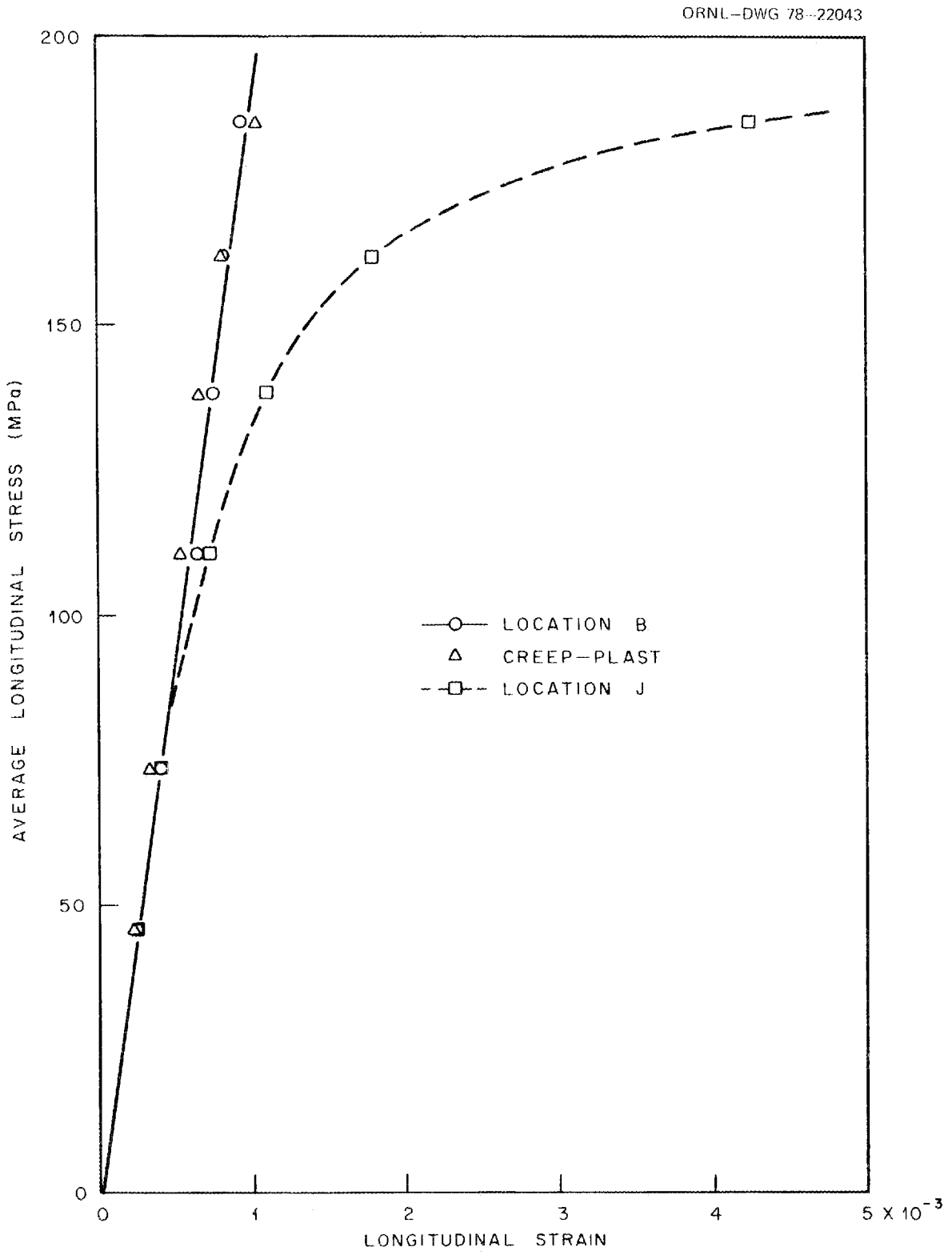

Fig. 6.3. Measured (strain gage) and predicted values of longitudinal strain vs net section stress at location B (see Fig. 6.2).

Longitudinal strain gage data taken from location J is also included for comparison, showing substantial plastic deformation in the base metal at higher load levels for points well removed from the weld. Figure 6.4 shows the transverse strain values at the same location, again compared with experimental data taken from location J. Agreement between experiment and analysis is reasonably good here as well. The departure from linear elastic behavior at higher stress levels seems to be because of the nonlinear behavior of the surrounding base metal which loads the weld metal nonproportionally with increasing specimen load. Although this makes it impossible to determine from the experimental data whether or not the weld metal has yielded, the analysis indicates that the weld metal remains in an unyielded condition at the highest load level considered.

Figures 6.5 and 6.6, respectively, show the measured and predicted longitudinal and transverse strains at location D, which spans the heat-affected zone (HAZ). At this location, the analysis tends to overpredict the experimental strain data to a considerable extent. A similar disagreement between analysis and experiment is also present at location C. Reasons for this lack of agreement are not presently known. However, possible explanations are differing material properties in the HAZ and the effects of a high residual stress field in the as-welded specimen. Presently, we are trying to measure the residual stress field in a similar specimen in hopes of quantifying the effects of the residual stresses on the deformation behavior of the specimen. This effect is discussed more fully in Sect. 6.2.

At locations further removed from the weld than locations C and D, agreement between strain gage data and analysis was generally favorable. Thus, the only location where significant disagreement between experiment and analysis was noted was in the neighborhood of the HAZ.

As noted earlier, we also acquired whole-field strain data over the central portion of the weldment by means of the moire technique. Details of the experimental apparatus and the data reduction procedure are being presented at some length in a topical report;[3] we will only mention here some of the problems encountered and show some representative results.

Our initial use of the moire technique was in conjunction with the W-2 test. The results obtained here were reasonably encouraging but were

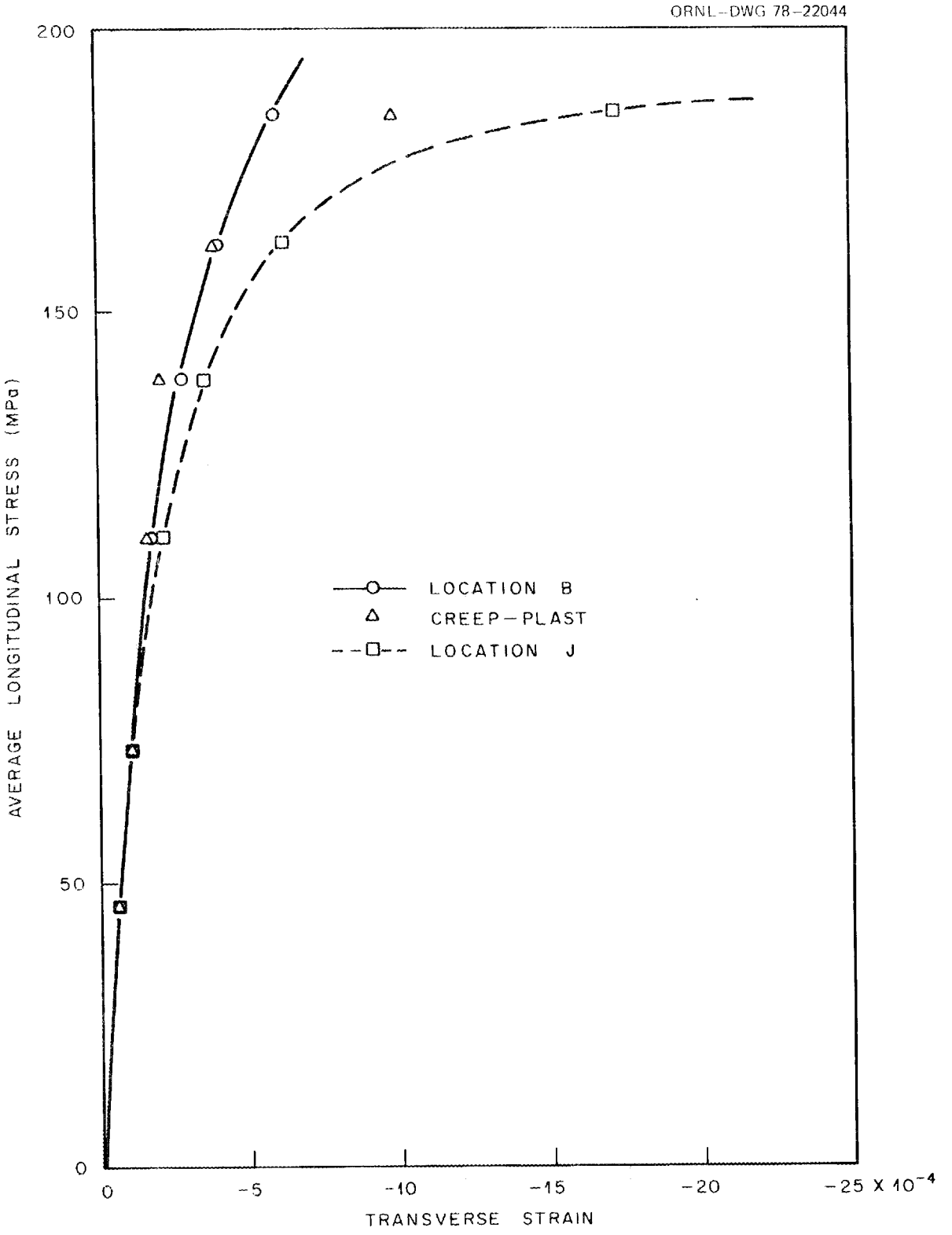

Fig. 6.4. Measured (strain gage) and predicted values of transverse strain vs net section stress at location B (see Fig. 6.2).

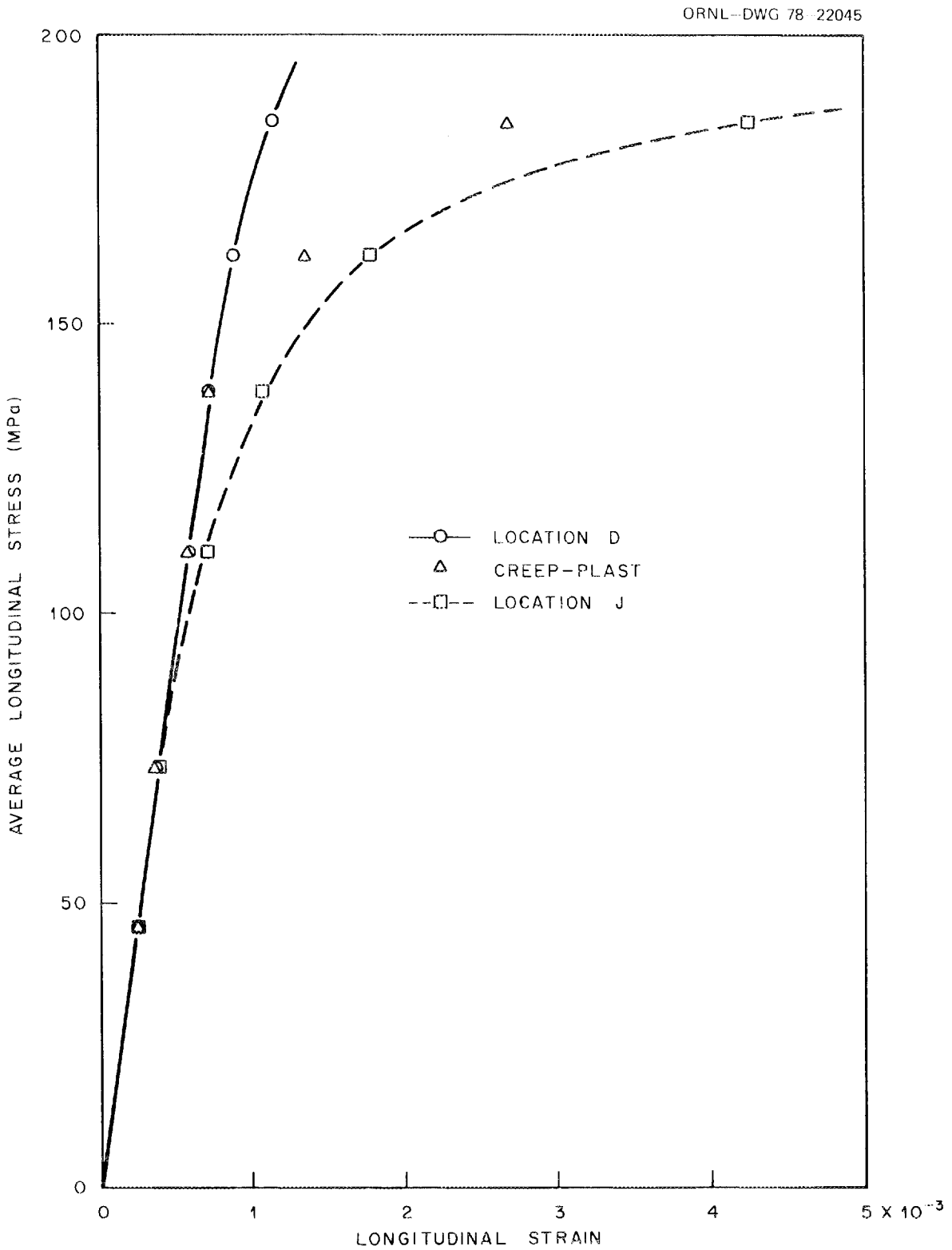

Fig. 6.5. Measured (strain gage) and predicted values of longitudinal strain vs net section stress at location D (see Fig. 6.2).

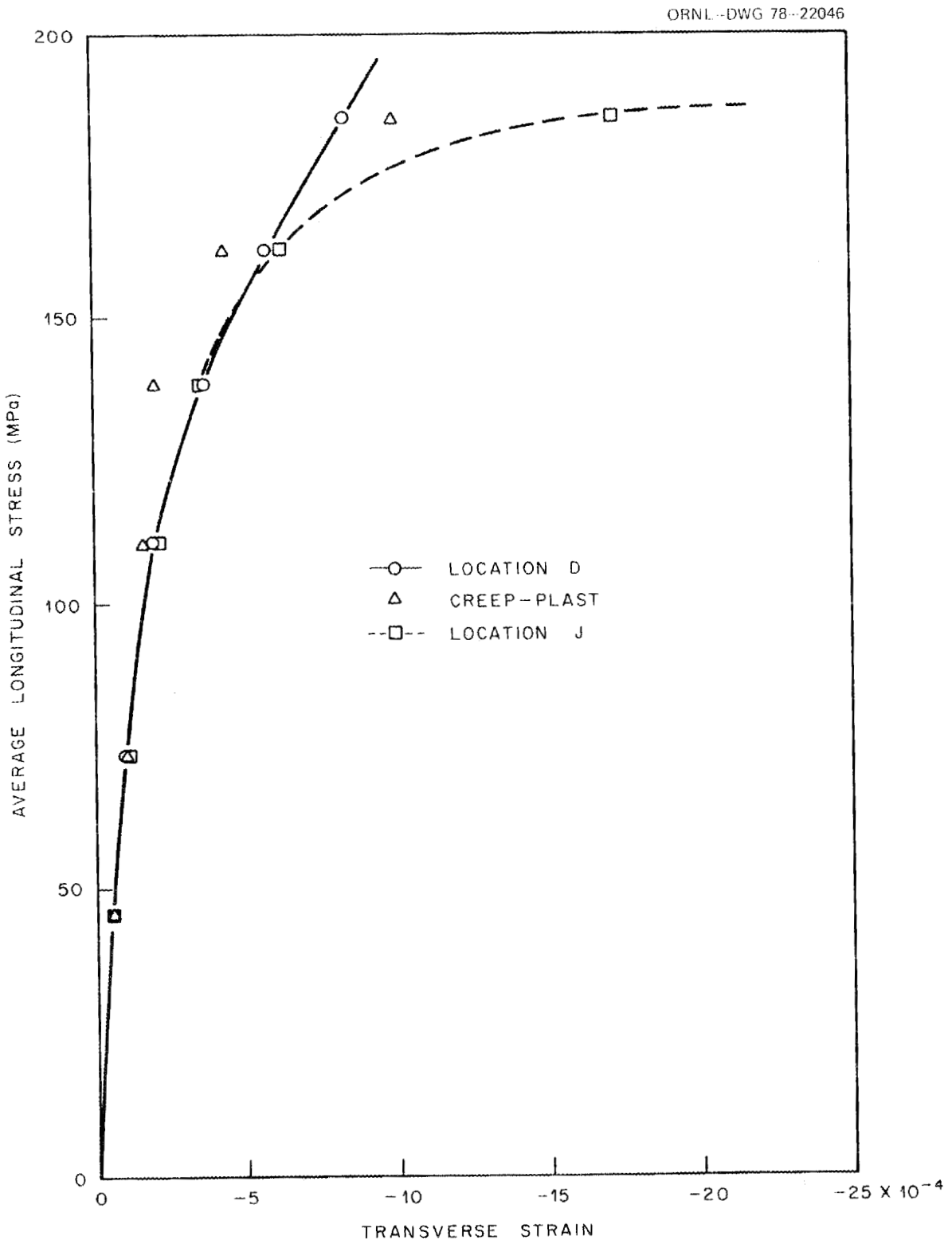

Fig. 6.6. Measured (strain gage) and predicted values of transverse strain vs net section stress at location D (see Fig. 6.2).

marred by poor fringe contrast caused by a specimen grid of low quality. This difficulty was corrected in the W-3 test through the assistance of Professor Gary Cloud of Michigan State University, who applied a high-quality specimen grid to the W-3 specimen by a photo-resist technique. Some problems were still encountered with the W-3 test, however, due to small out-of-plane specimen motions occasioned by a slight specimen warpage and by the design of the loading frame. The moire technique is sensitive to out-of-plane motion because this induces some amount of fictitious strain into the results. Thus, the strains measured by the moire technique generally did not yield as good agreement with analytical predictions as did the strain gage data.

Figure 6.7 shows the longitudinal strains as measured by the moire techniques along the line $x = 0$ at an average longitudinal stress of 185 MPa (26.8 ksi). Analytical predictions and strain gage data are also shown for comparison. The moire strain data are derived from a curve-fitting procedure, which, by its nature, cannot reproduce the discontinuity in longitudinal strain across the weld fusion line. This fact is apparent in the figure. The moire strains agree reasonably well with analytical predictions in the neighborhood of the weldment in and around the HAZ but are considerably in excess of analytically predicted values and strain gage data elsewhere. The previously mentioned disagreement between the strain gage data and analysis in the HAZ is evident here as well.

As noted earlier, discrepancies in the moire strain data are felt to result from small out-of-plane specimen motions. In future tests of this type, this problem will be corrected by experimentally measuring the out-of-plane motion by means of extensometers or dial gages and applying appropriate analytical correction factors to the moire data.

The purpose of this series of room-temperature plate-weldment tests was to investigate the deformation behavior of a simple structural member containing a weldment and to determine whether or not this behavior could be predicted by a finite-element analysis based on two different material property zones, one for the base metal and one for the weld metal. For the case of specimens containing an annealed weld, it was found that the

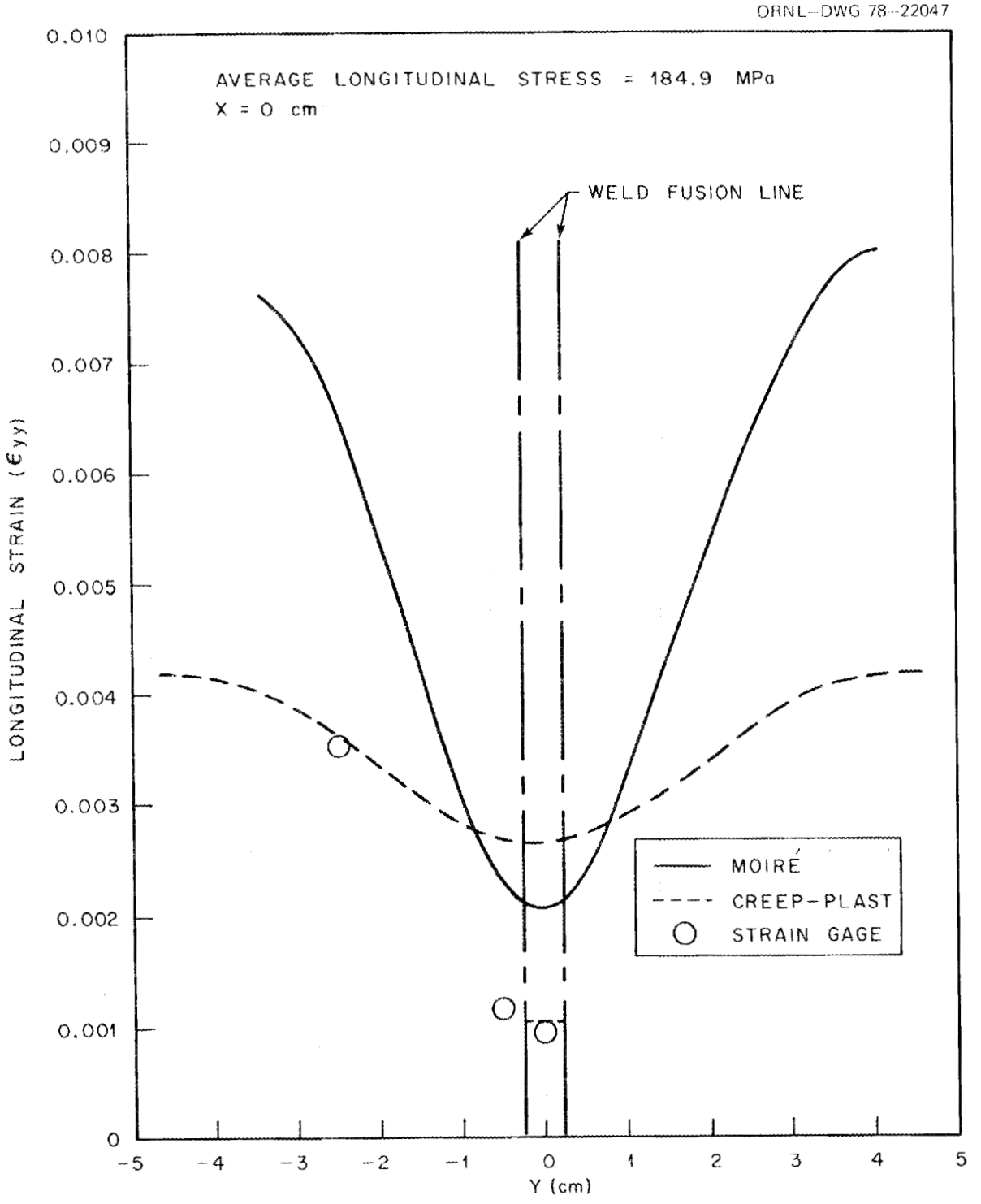

Fig. 6.7. Measured and predicted values of longitudinal strain along the line x = 0.

presence of the weld did not greatly affect the deformation behavior and that finite-element predictions gave reasonably good agreement with experimental results. In the case of the W-3 test, which contained an as-deposited weld, good agreement between experiment and analysis was also noted, except in the area of the HAZ. This implies that the two-property zone approach may not be adequate in the case of as-deposited weldments or that residual stresses may have a substantial effect on the deformation behavior. We are now investigating the latter possibility by attempting to measure the residual stress field in a specimen similar to that used in the W-3 test. This effort is described in more detail in Sect. 6.2.2.

6.1.2 Elevated-temperature tests

Our first elevated-temperature plate-weldment test was initiated during this report period. The purpose of the test, designated WPCT-4, is to investigate the deformation and failure behavior of a simple structure containing a weldment under creep conditions at high temperature. The specimen for this test bears some similarity to those used in the room-temperature test series. It is fabricated of 304 stainless steel with a 308 stainless steel weld laid down by the gas-tungsten arc method. The weld was left in the as-deposited condition, with no postweld heat treatment applied. The specimen is ∿46 cm (18 in.) long, 7.6 cm (3.0 in.) wide, and 0.63 cm (0.25 in.) thick. The weld joint is of double-V geometry, tapering uniformly from about 0.75 cm (0.3 in.) wide at the surface to about 0.25 cm (0.1 in.) at the root.

The principal difference between the specimens used in the room-temperature series and the WPCT-4 specimen is that the weldment in the latter is located on the longitudinal axis of the specimen, instead of on the transverse axis. This configuration was chosen because the longitudinal strain in such a specimen should be very nearly constant across the specimen width, as well as along most of the length. Thus, generalized plane-strain conditions should prevail in the specimen but with differing values of longitudinal stress in weld and base metal.

In order to measure the specimen longitudinal strain, two high-temperature capacitive strain gages were attached to the specimen. These

gages were mounted, directly opposed to one another and along the longitudinal axis, on the two faces of the specimen. Figure 6.8 shows the instrumented specimen.

The first portion of the test is a constant-load creep phase at 593°C (1100°F). The specimen was loaded at a constant strain rate of 0.0005/min until a specimen load of 32 kN (7200 lb) was achieved, corresponding to an average longitudinal stress of 66 MPa (9.6 ksi). The load was then held constant at this value. On completion of the first phase of the test at ∿1000 to 2000 hr after initiation, we plan to increase the specimen load and allow the test to proceed to failure.

Figure 6.9 shows the experimentally measured total longitudinal strain together with analytical predictions for the first 620 hr of the test. The experimental value represents the averaged values of the two back-to-back strain gages. The analytical predictions were obtained from the two-bar analysis used earlier[6] to analyze the weldment transition joint specimen being tested by the ORNL Metals and Ceramics Division. That transition joint specimen has a geometry similar to the WPCT-4 specimen. The creep law used for the 304 stainless steel base metal was a three-term exponential equation developed for the reference heat.[7] A one-term rational polynomial model[8] derived from a limited number of uniaxial tests was used to describe the creep law for the 308 stainless steel weld metal.

Neither experiment nor analysis indicated any yielding on initial loading, and Fig. 6.9 shows that the initial experimental and analytically predicted strains agree quite well. However, there is an increasing divergence between the two with increasing time, and, at the end of 620 hr, the analysis overpredicts the measured strains in the weld by roughly a factor of 2. Reasons for this lack of agreement are not presently known. However, two possible explanations are a deficiency in the 308 stainless steel weld metal creep equation and residual stress effects. We are currently obtaining additional 308 stainless steel uniaxial creep data, which will be used to improve the creep law. The improved creep law, when available, will be incorporated into the analysis. Additionally, we plan to carry out residual stress measurements on a specimen

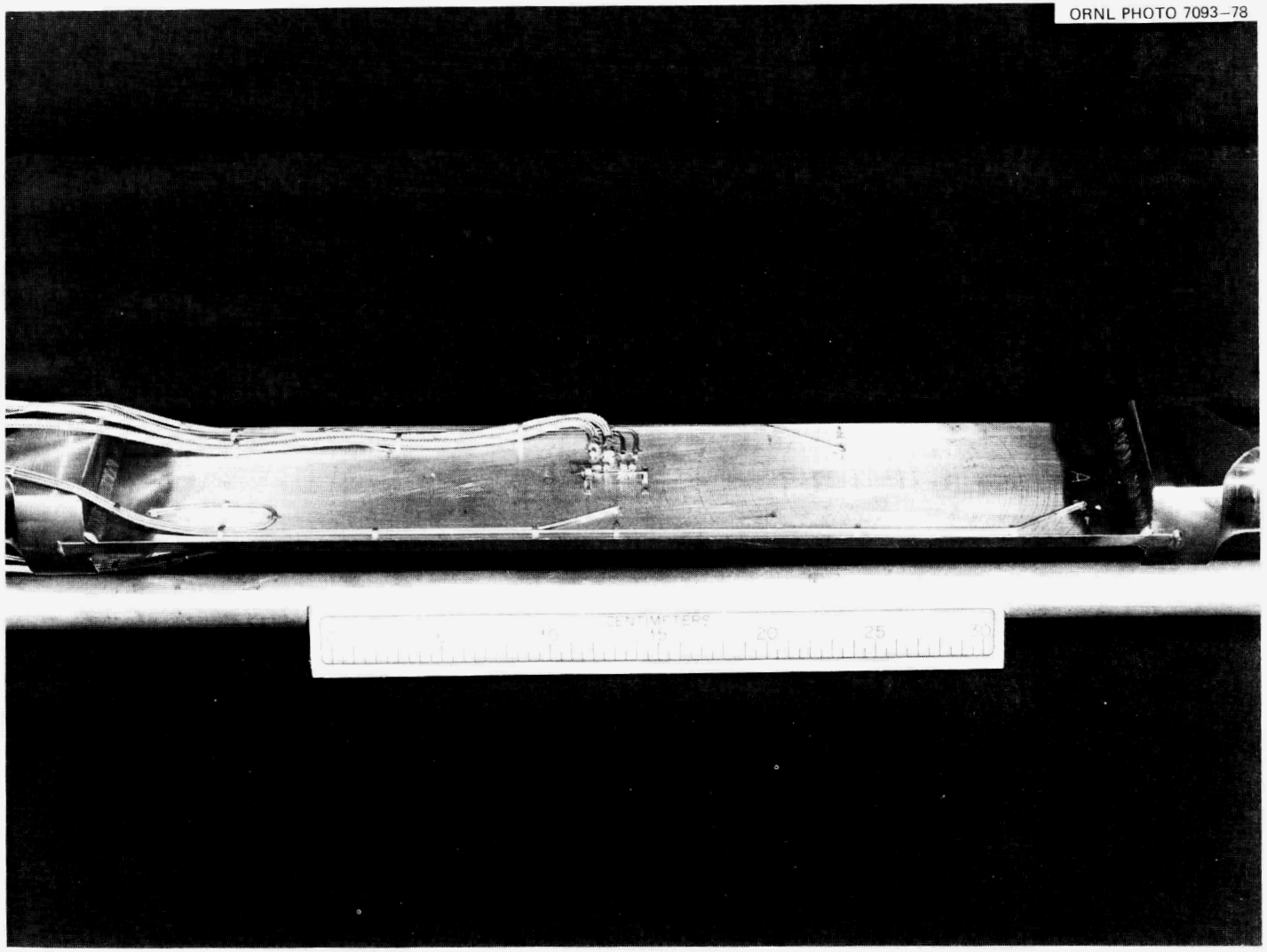

Fig. 6.8. Instrumented test specimen for test WPCT-4.

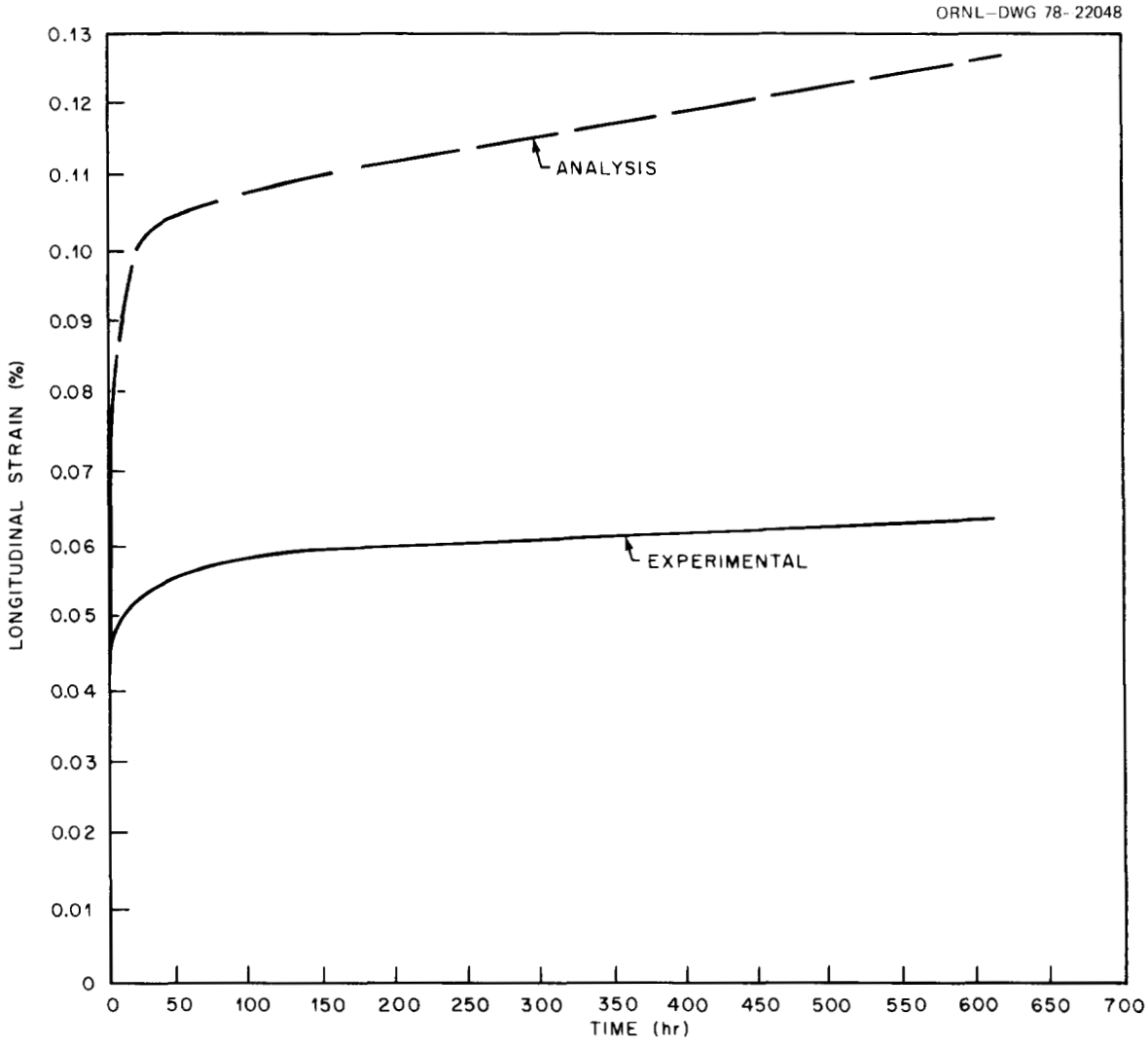

Fig. 6.9. Measured and predicted longitudinal strains for test WPCT-4.

similar to the WPCT-4 specimen and incorporate the measured residual stresses into the analysis.

6.2 Residual Stress Effects

It is well known that the high temperatures associated with the welding process can induce a residual stress field in the vicinity of the weldment, often of a magnitude on the order of the yield stress. The purpose of this investigation is to assess the effects of residual stresses

on the deformation and failure of welded structural components and to determine whether or not a knowledge of the residual stress field is necessary to predict component behavior.

6.2.1 Simulation of residual stress in a thermal ratchetting problem (T. J. Delph and W. K. Sartory)

As a preliminary investigation into the effects of residual stresses at high temperatures, we performed an analytical study of a pipe thermal ratchetting problem in the presence of an assumed residual stress field. The particular problem considered was the analytical model of the TTT-1 test,[9] which simulated the behavior of a section of 304 stainless steel pipe subjected to cyclic thermal and internal pressure loadings.

The analysis was carried out using the PLACRE finite-element code with 16 pipe wall elements. Material properties were identical to those used in the TTT-1 analysis. The loading histogram was also identical to that used in the TTT-1 analysis, consisting of 13 thermal/pressure loading cycles. The residual stress field was simulated by assuming a bending angle to be applied to the pipe wall section sufficient to produce $\sim$0.2% plastic strain at the pipe wall surface. We know that the welding process leads to substantial "drawdown" near a pipe weldment, resulting in residual bending stresses of rather large magnitude. The simulated residual stress field was chosen to model these bending stresses.

Some of the results of the analysis are shown in Figs. 6.10 and 6.11, which show, respectively, circumferential (hoop) stress vs circumferential strain at the outer surface in the presence and absence of the assumed residual stress field. After 13 cycles, little difference between the 2 is evident.

A similar trend is apparent in the variation of axial stresses with time, which differ by only about 7 MPa (1 ksi) after 13 cycles, but which differed by about 83 MPa (12 ksi) at the start of cycling. Thus, the residual stress field apparently may not play an important role in the long-term response of pipe weldment areas subjected to thermal ratchetting conditions.

The effect of residual stresses on component behavior of high temperatures is still, however, an area where little is known. The residual

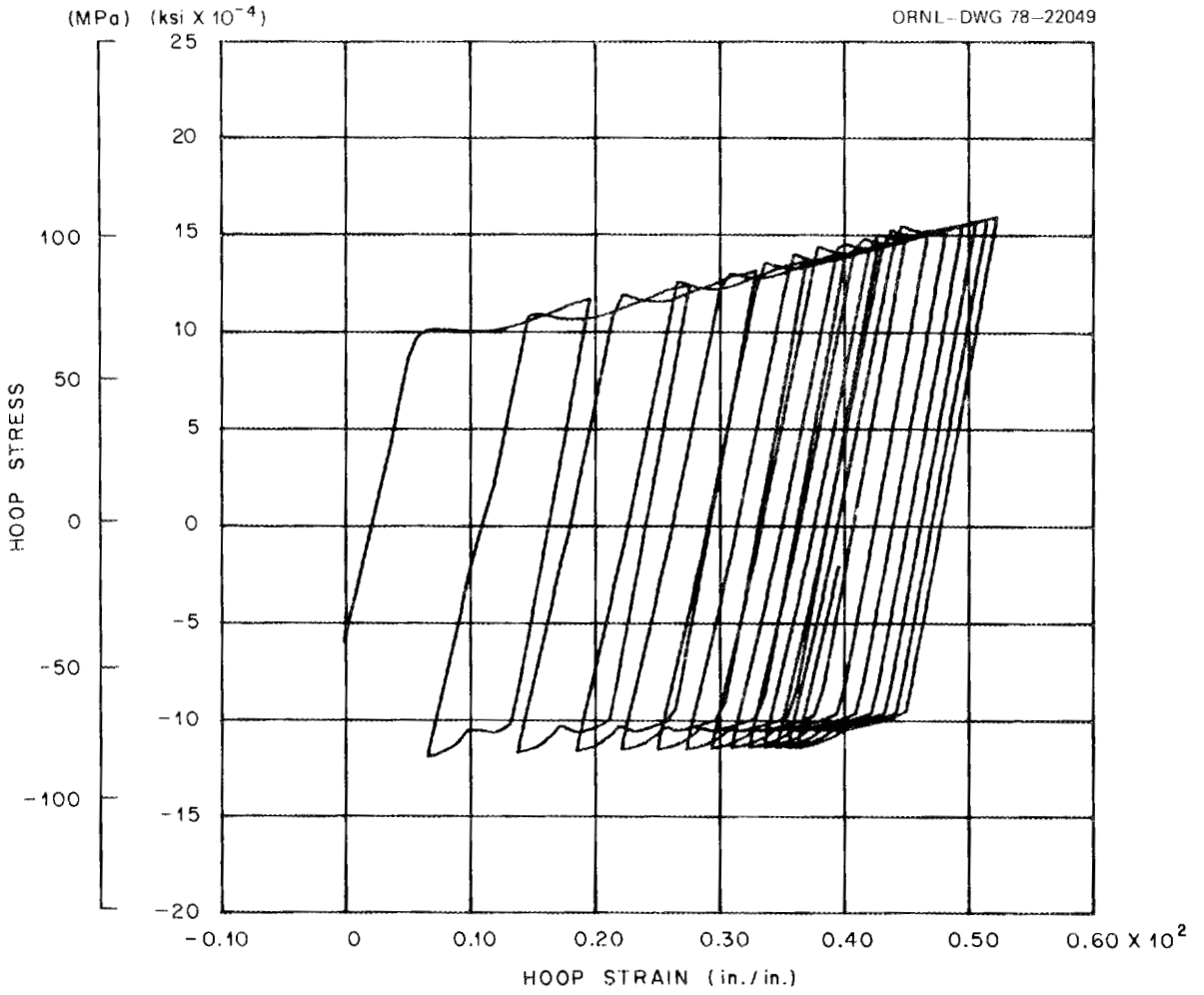

Fig. 6.10. Circumferential (hoop) stress vs circumferential strain at outer surface with residual stresses.

stresses will relax somewhat at high temperatures, but they may still significantly affect the component deformation and failure responses. We plan to investigate this question further in connection with high-temperature tests of plates and beams containing weldments.

6.2.2 Measurement of residual stresses by the hole-drilling technique (T. J. Delph)

To determine the effect of the residual stress field on the deformation field in our plate-weldment specimens, it was necessary to experimentally measure the residual stresses in the neighborhood of the weldment. For this purpose, we selected two plate-weldment specimens similar

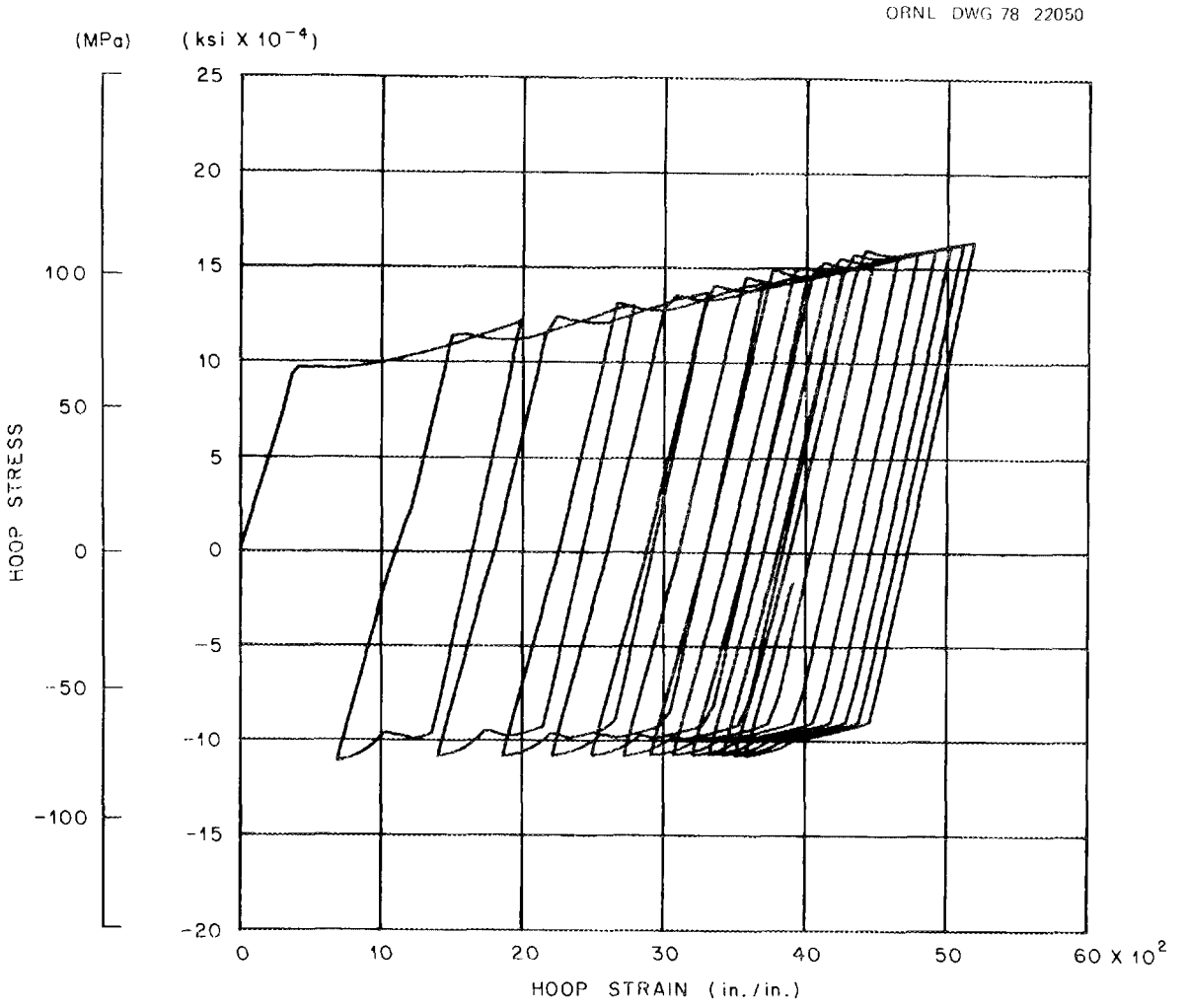

Fig. 6.11. Circumferential (hoop) stress vs circumferential strain at outer surface without residual stresses.

to those used in the room-temperature test series, one containing an annealed weldment and the other a weldment in the as-deposited condition.

The specimens were initially sent to the Development Division of the Oak Ridge Y-12 Plant, where they hoped to make residual stress measurements by the x-ray diffraction technique. This technique was particularly attractive because of its nondestructive nature. Unfortunately, the grain size of the 304 stainless steel base metal/308 stainless steel weld metal combination proved too large to allow accurate measurements to be made. We next turned to the hole-drilling technique, a semidestructive technique

which had previously been used with some success in the Heavy-Section Steel Technology Program at ORNL.[10]

This technique utilizes special rosette strain gages, with the three legs of the rosette oriented radially with respect to the center of the gage. A small-diameter hole is drilled into the center of the gage, and the difference is measured between the gage readings before and after the hole is drilled. These strain measurements are then used in conjunction with the theory of elasticity solution for a hole in an infinite sheet under in-plane loading to obtain the residual stresses at the strain gage location.

In practice, several precautions must be observed. First, the depth of the hole must be sufficiently great that no change in the measured strains occurs with increasing hole depth. A hole depth greater than or equal to the hole diameter is considered adequate for this purpose.[11,12] Second, it has been noted[11] that the hole-drilling process may itself introduce residual stresses into the specimen under investigation, especially if a rotating cutter is used. To avoid this problem, several investigators[11,12] have employed air-abrasive machining as a drilling method. In this technique, fine particles of abrasive material are entrained in an air jet and are directed against the specimen surface. The particles erode away the metal surface immediately under the jet nozzle at a controlled rate, allowing holes of repeatable depth and diameter to be drilled. Spurious residual stresses introduced into the specimen by this method have been shown to be negligible.[11,12] In our investigations, we utilized an Airbrasive Model K air-abrasive drilling device manufactured by S. S. White Co.

To gain confidence in the hole-drilling technique, a number of uniaxial tension specimens were instrumented with Micro-Measurements EA-06-062RE-120 rosette strain gages. These gages are especially designed for use with the hole-drilling technique. Holes were drilled in the center of each rosette, and the specimens were then loaded uniaxially in a testing machine to see how well the hole-drilling technique could measure the known stress field. Results of this initial series of tests were quite encouraging because we found that the stress values determined by the hole-drilling technique were generally within 10% of the known values.

Additionally, we found that the use of a table of calibration factors given by Beaney[12] for the hole-drilling technique seemed to give slightly better results than those obtained by making use of the theory of elasticity solution to obtain the stress values. Accordingly, Beaney's calibration factors were used in subsequent work.

The next step was to instrument one of the two plate-weldment specimens to be used for residual stress measurements with rosette strain gages. The specimen containing the annealed weldment was selected for the first series of measurements. Figure 6.12 shows the drilling in progress on this specimen.

Because the specimen had been used previously in the unsuccessful x-ray defraction experiments, a portion of the surface in the neighborhood and on either side of the weldment had been chemically etched away to a depth of 0.050 to 0.127 mm (0.002 to 0.005 in.). Outside the etched area, compressive residual stresses on the order of 97 MPa (14 ksi) were measured, while inside the etched area, the magnitude of the measured stresses did not exceed 28 MPa (4 ksi).

The conclusion was that the large stresses measured outside the etched area had been introduced by the light machining of the specimen received after annealing. Subsequently, we discovered that other investigators utilizing the hole-drilling technique have found that residual stresses induced by surface machining are usually confined to a thin surface layer.[13] The effects of these surface stresses may be removed by chemically etching away the surface to a depth of 0.02 to 0.03 mm.

An effort was made to correct for the effect of machining stresses outside the etched area by subtracting an average stress value measured at a location remote from the weld from the calculated stress values. This procedure did not prove successful, however, because it led to inconsistent results. Thus, data taken at strain gage locations outside the etched area were ignored. In subsequent residual stress experiments, strain gage locations will be chemically etched to avoid the effects of machining stresses.

Figure 6.13 shows the results of the residual stress measurements made inside the etched area of the specimen. Back-to-back gage locations are drawn so that they occupy similar positions in the figure. The normal

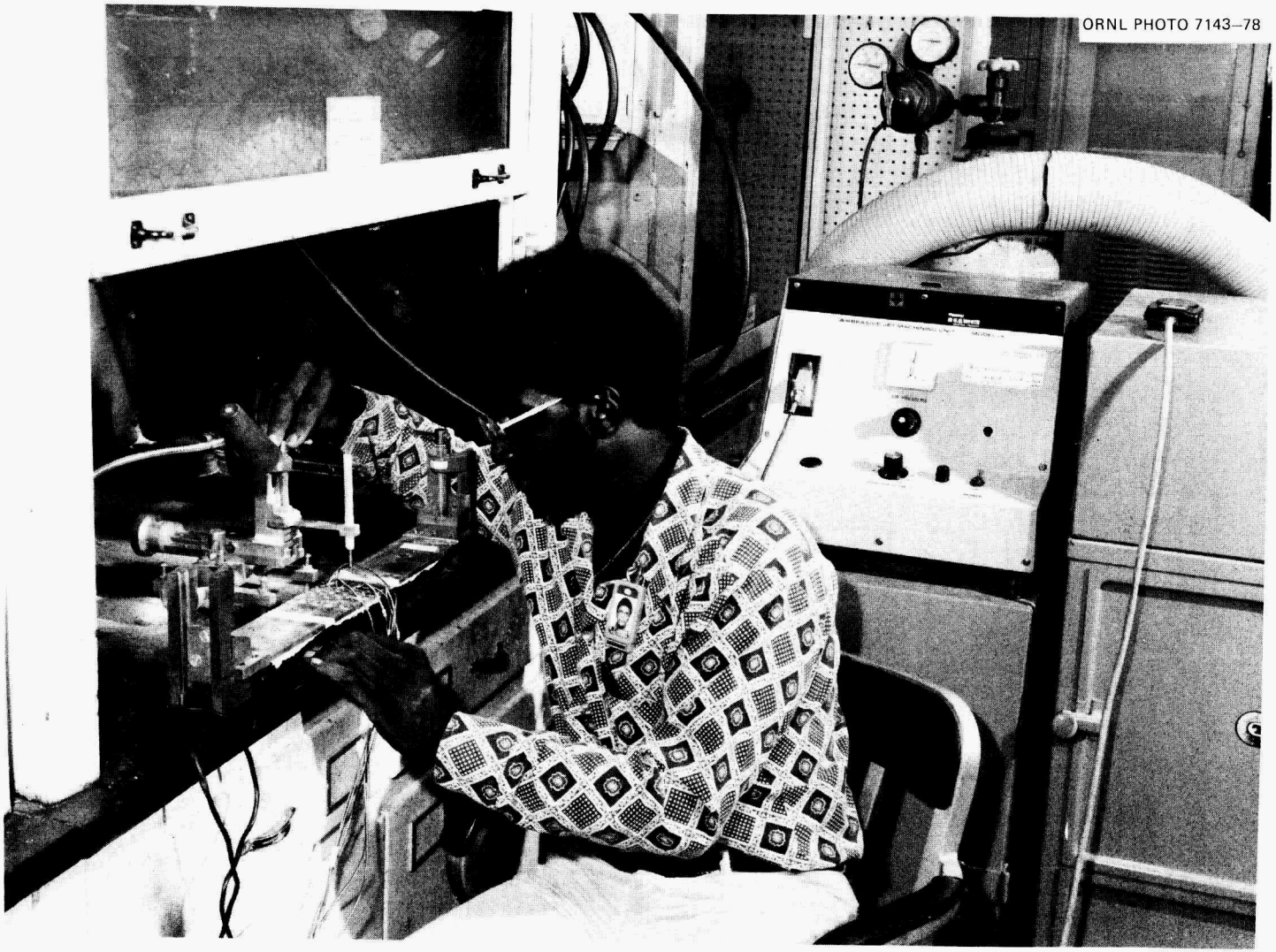

Fig. 6.12. Residual stress measurements being made on plate-weldment specimen.

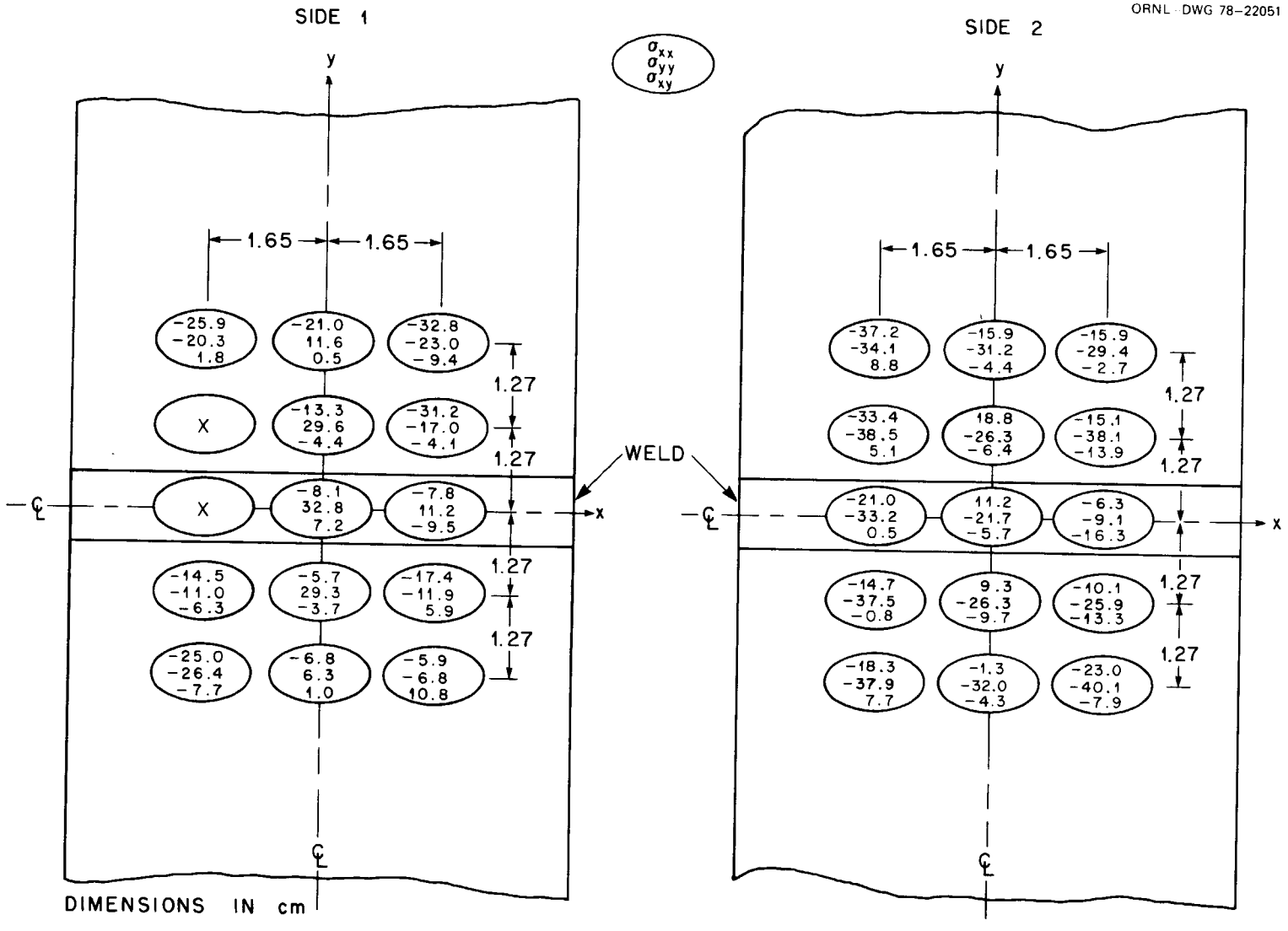

Fig. 6.13. Measured residual stresses on both sides of annealed plate-weldment specimen (stresses in MPa, dimensions in cm).

stresses seem to form a fairly consistent pattern. Oddly enough, some of the largest stress magnitudes were measured at the gage locations most remote from the weldment centerline. The magnitude of the measured shear stresses are usually, though not always, about 30% or less of the normal stress magnitudes measured at that location. These values show considerable scatter and do not seem to fit into a consistent pattern, a fact that may be related to their generally small magnitude.

We are now in the process of making residual stress measurements on a similar specimen containing a weldment in the as-deposited condition. We expect that the residual stress field for this specimen will be considerably larger in magnitude than that in the annealed specimen reported here.

6.2.3 Analysis of plate-weldment deformation field in the presence of residual stresses (T. J. Delph, J. A. Clinard)

As noted previously, the purpose of the plate-weldment residual stress measurements is to enable us to determine whether or not the residual stress field has a significant influence on specimen deformation characteristics. To this end, an idealization of the measured residual stress pattern discussed in the previous section was constructed to serve as an input to a finite-element analysis. The finite-element model used to analyze the plate-weldment specimens was devised by assuming that both the specimen and the applied loading were symmetric about the longitudinal and transverse centerlines, thus making it necessary to model only a quarter of the specimen. To produce a residual stress field with the same symmetries, residual normal stresses measured at symmetric locations with respect to the transverse and longitudinal centerlines were averaged, as well as normal stress values measured at back-to-back locations. Due to their low magnitude and inconsistent variation, the shear stresses were neglected. The resulting idealized residual stress field is shown in Fig. 6.14.

The stress pattern shown in Fig. 6.14 contains two additional assumptions that were made necessary by the limited extent of the etched area over which we were able to obtain reliable data. First, we assumed that the σ_{yy} values at points along the longitudinal edge of the specimen were the same as those measured at the nearest interior point. The σ_{xx} values

ORNL DWG 78-22052

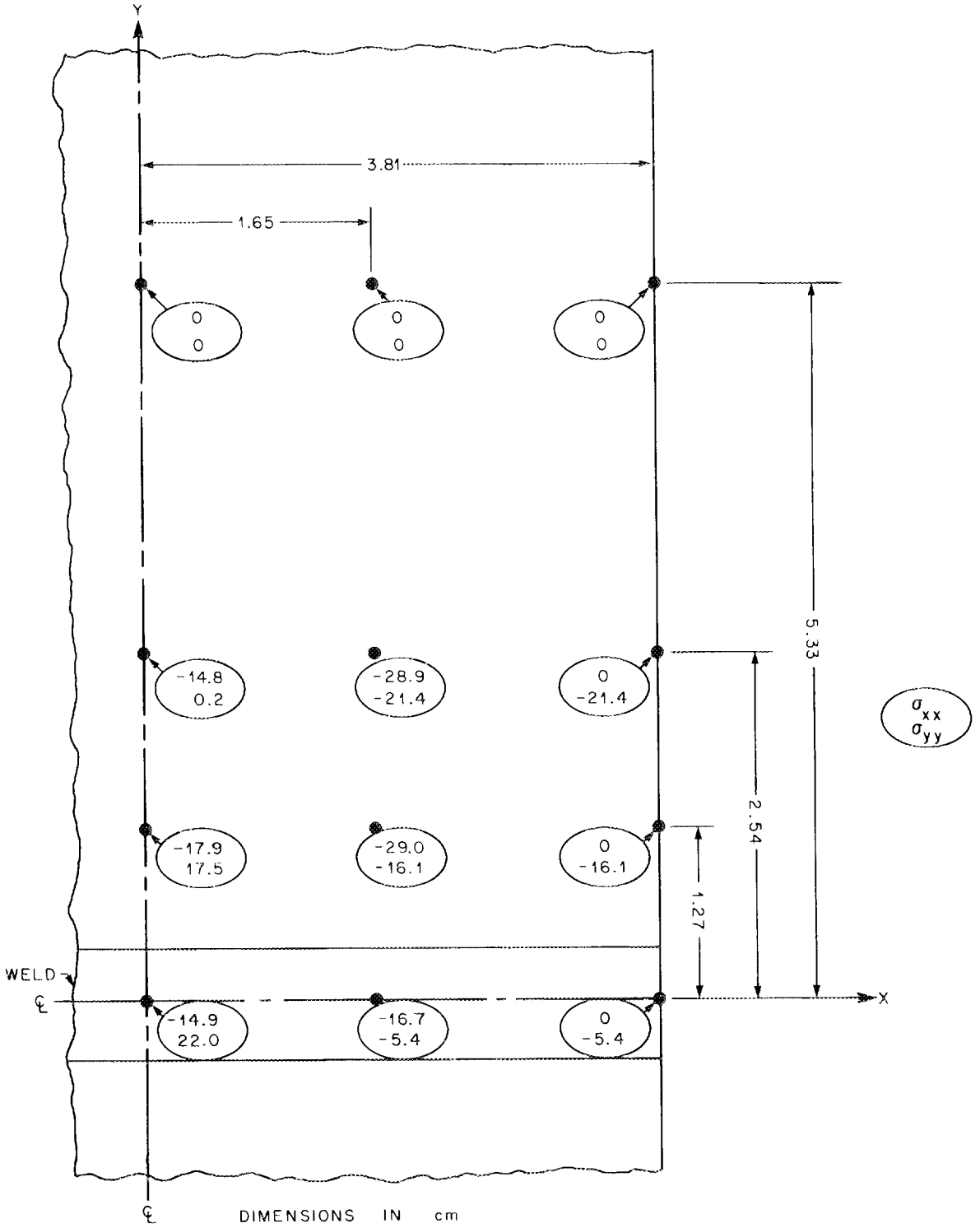

Fig. 6.14. Idealization of measured residual stress field for input to finite-element analysis (stresses in MPa, dimensions in cm).

at these points must, of course, vanish to satisfy the boundary conditions. Second, the arbitrary assumption was made that the residual stress field decays to negligible magnitude along a line 5.33 cm (2.10 in.) from the transverse centerline.

Residual stress values at the centroid of each element were obtained by linearly interpolating between the data shown in Fig. 6.14 and assuming that the residual stresses vanished for values of u greater than y = 5.33 cm. The centroidal residual stress values were then used as input to the CREEP-PLAST II finite-element program, where they were used to define an initial stress state for an elastic-plastic analysis. The initial strains were taken to vanish. We assumed that the annealing process had returned the material to a nearly virgin state, so that shifts in the yield surface due to plastic flow in the welding process could be neglected.

The analysis was carried out by taking the stresses at any point during the loading process to be the sum of the residual stress components plus those due to the loading. Thus, each stress increment was in overall equilibrium with the loading increment, but the total stresses were not.

Material properties used in the analyses were identical to those used in the W-2 test[2] so that a comparison could be drawn between the predictions of the analysis with and without residual stresses included and the experimental strain data taken from the W-2 test. Results of the comparison showed that the inclusion of residual stresses into the analysis, while not affecting the predicted strain values too greatly, generally worsened the degree of agreement between analysis and experiment. Figures 6.15 and 6.16 show some representative results for predicted and measured (strain gage) longitudinal and transverse strain values at a location on the longitudinal centerline immediately adjacent to the weld fusion line (location B). Note that, for both the longitudinal and transverse strain components, the analysis without the incorporation of residual stresses overpredicts the measured strain values at the higher load levels, and the inclusion of residual stresses into the analysis leads to even greater overprediction.

Why the inclusion of the residual stress field into the analysis serves to degrade the agreement between analysis and experiment is not immediately apparent. However, one possibility is that the assumption

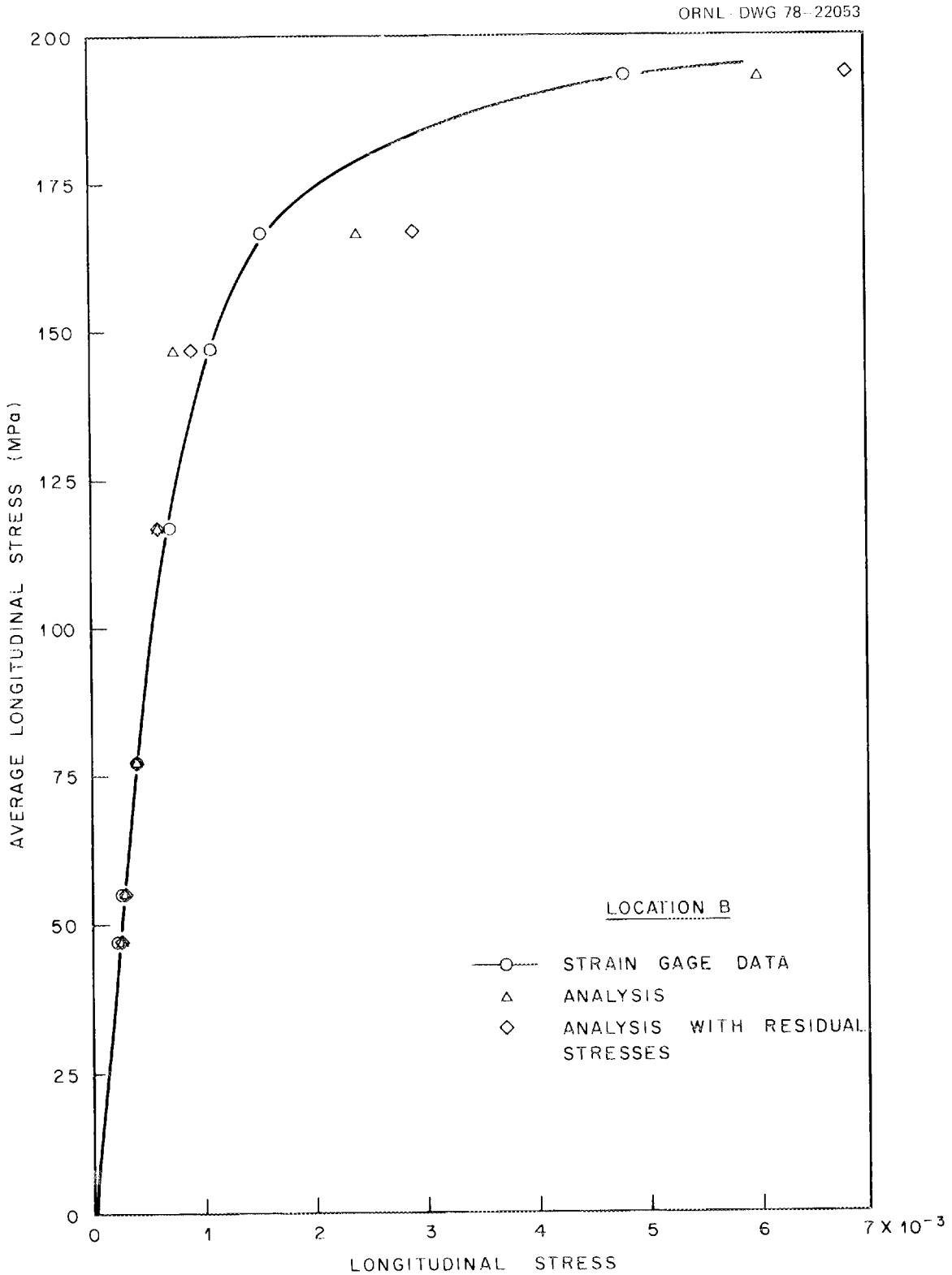

Fig. 6.15. Predicted and measured longitudinal strains at location B, test W-2.

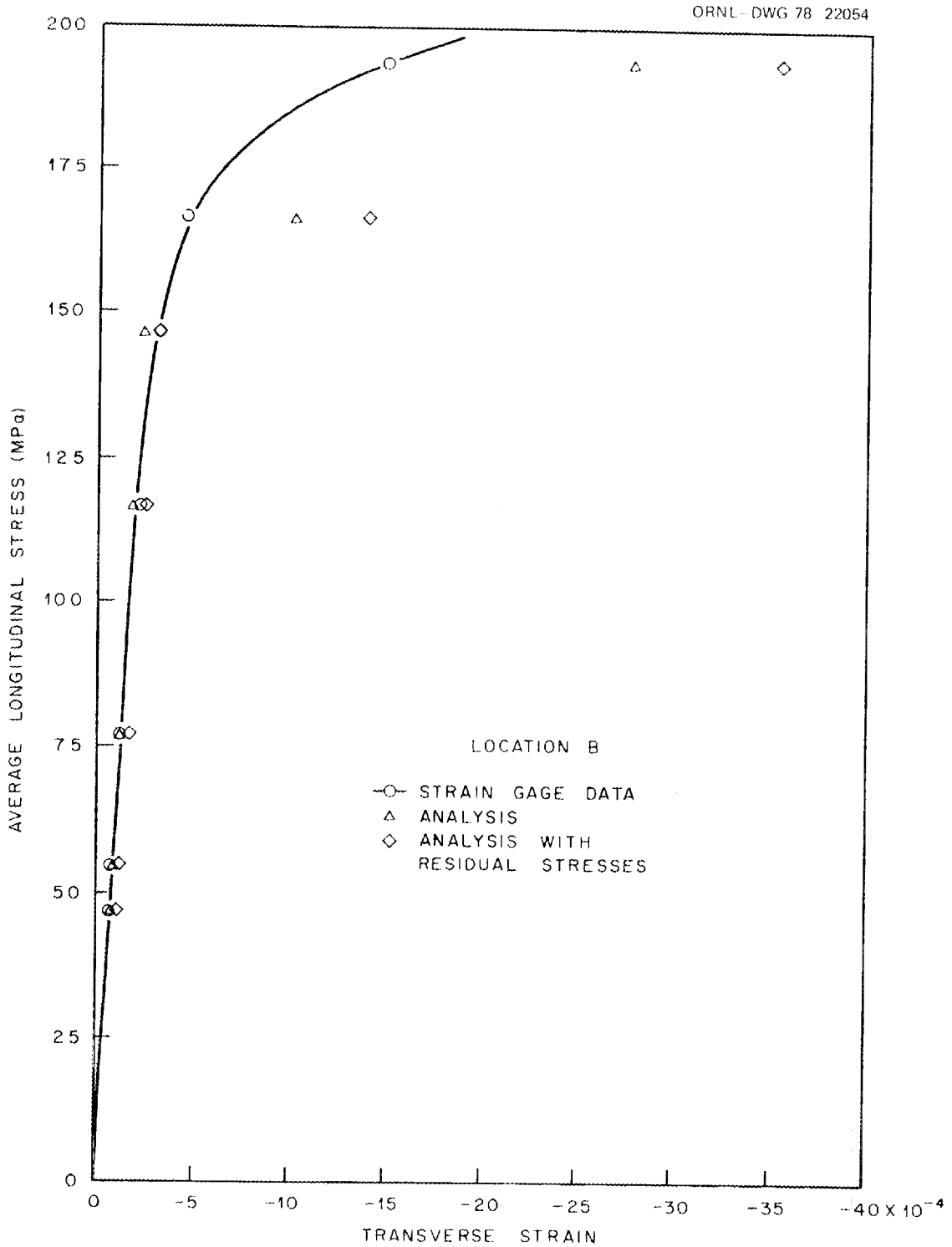

Fig. 6.16. Predicted and measured transverse strains at location B, test W-2.

that the yield surface was not shifted by prior plastic deformations may be invalid. We are now performing residual stress measurements on a plate-weldment specimen containing an as-deposited weldment. We then plan to reanalyze the W-3 test, incorporating the residual stress field measured on this specimen, to see if a similar trend in the analytical predictions is noted.

6.3 Uniaxial Tests of Type 308 Stainless Steel Weld Metal

T. J. Delph

To provide data for constitutive equation development and analysis for type 308 stainless steel weld metal, we have continued the subcontract with Battelle-Columbus Laboratories (BCL) for providing limited uniaxial testing on this material. Some of the early results of this effort, consisting of cyclic stress-strain and constant-load creep data, were given in the previous report in this series.[8] Since that time, the testing program has been extended to include an additional six cyclic stress-strain tests at total strain ranges of 0.4 to 1.0%, an additional five constant-load creep tests at stress levels from 86.2 MPa (12.5 ksi) to 155 MPa (22.5 ksi), and three composite cyclic-creep tests in which periods of creep are interspersed with periods of constant strain-rate cycling. The purpose of the composite tests is to investigate possible creep-plasticity interactions. All tests to date have been performed at 593°C (1100°F) and have utilized specimens of as-deposited 308 CRE stainless steel weld laid down by the gas-tungsten arc process from a single heat of weld metal.

The results of the cyclic and cyclic-creep composite tests have been received at ORNL and are currently being analyzed. These will be reported in the next report in this series. We have also received the remainder of the data from the first series of creep tests. This series consisted of three tests where the load was held constant at different stress levels for ∿2400 hr. Thereafter, various step changes in load were imposed, and the tests were continued to ∿3500 hr.

Results of the uninterrupted constant-load portions of the tests (prior to 2400 hr) were used to construct a creep equation[8] in the form of a one-term rational polynomial. Figures 6.17 and 6.18 show the results of two of the creep tests (tests C-1 and C-3, respectively), along with the predictions of the creep equation made using the strain-hardening hypothesis. The initial stress in test C-1 was 96.2 MPa (12.5 ksi), which was held until ∿2400 hr. The stress level was then raised to 138 MPa (20 ksi), dropped to 103 MPa (15 ksi) at ∿2660 hr, and raised again to 138 MPa (15.5 ksi). Lack of agreement between experimental data and the creep equation is primarily due to a large apparent anelastic strain recovery on unloading. The existence of this anelastic strain component, however, is somewhat suspect because of inconsistencies in the loading and unloading strains measured in the test. Also, note that no anelastic strain recovery was observed in the stress-drop portion of test C-1. We plan to investigate this matter further in subsequent tests.

Considerable creep recovery is noted on reloading from the zero-load portion of test C-3, as evidenced by the reappearance of a primary-creep phase. The strain-hardening hypothesis, by its nature, is incapable of predicting such recovery behavior.

6.4 Notch Effects in Uniaxial Tension Specimens

T. J. Delph

To provide background information for projected ORNL work concerning the effects of notches on the failure of weldments, a survey of the literature on notch effects in uniaxial tension specimens was completed.[14] Particular regard was paid to the effects of notches in specimens containing weldments. Notch effects are particularly interesting because, under certain circumstances, notched specimens possess the paradoxical property of having longer constant-load rupture lives than equivalent unnotched specimens having the same nominal stress. Here, nominal stress is taken to be the load divided by the minimum cross-sectional area. This phenomenon is known as notch strengthening, while the converse behavior is known as notch weakening. Notched specimen tests are widely used in

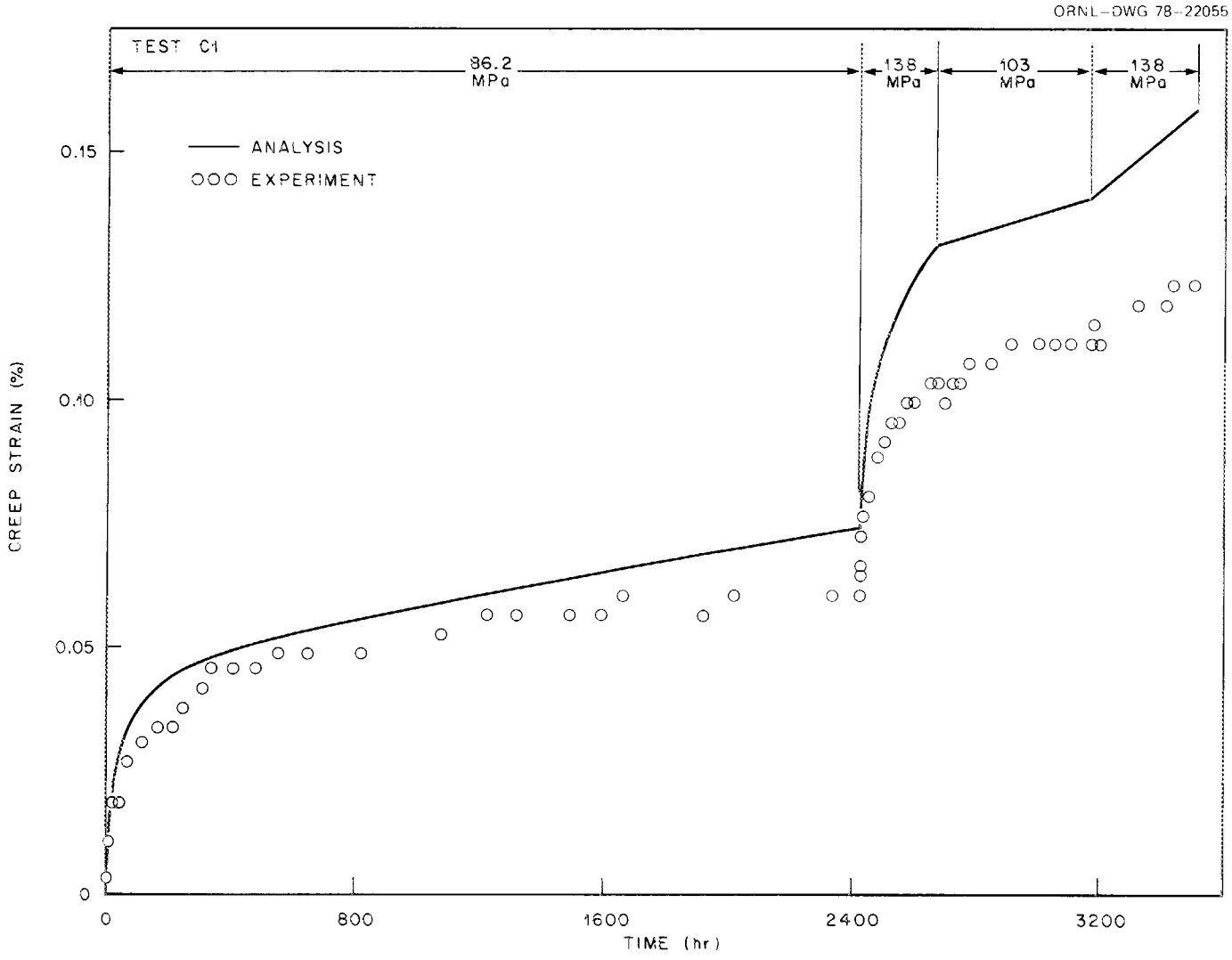

Fig. 6.17. Experimental and predicted creep strains, test C-1.

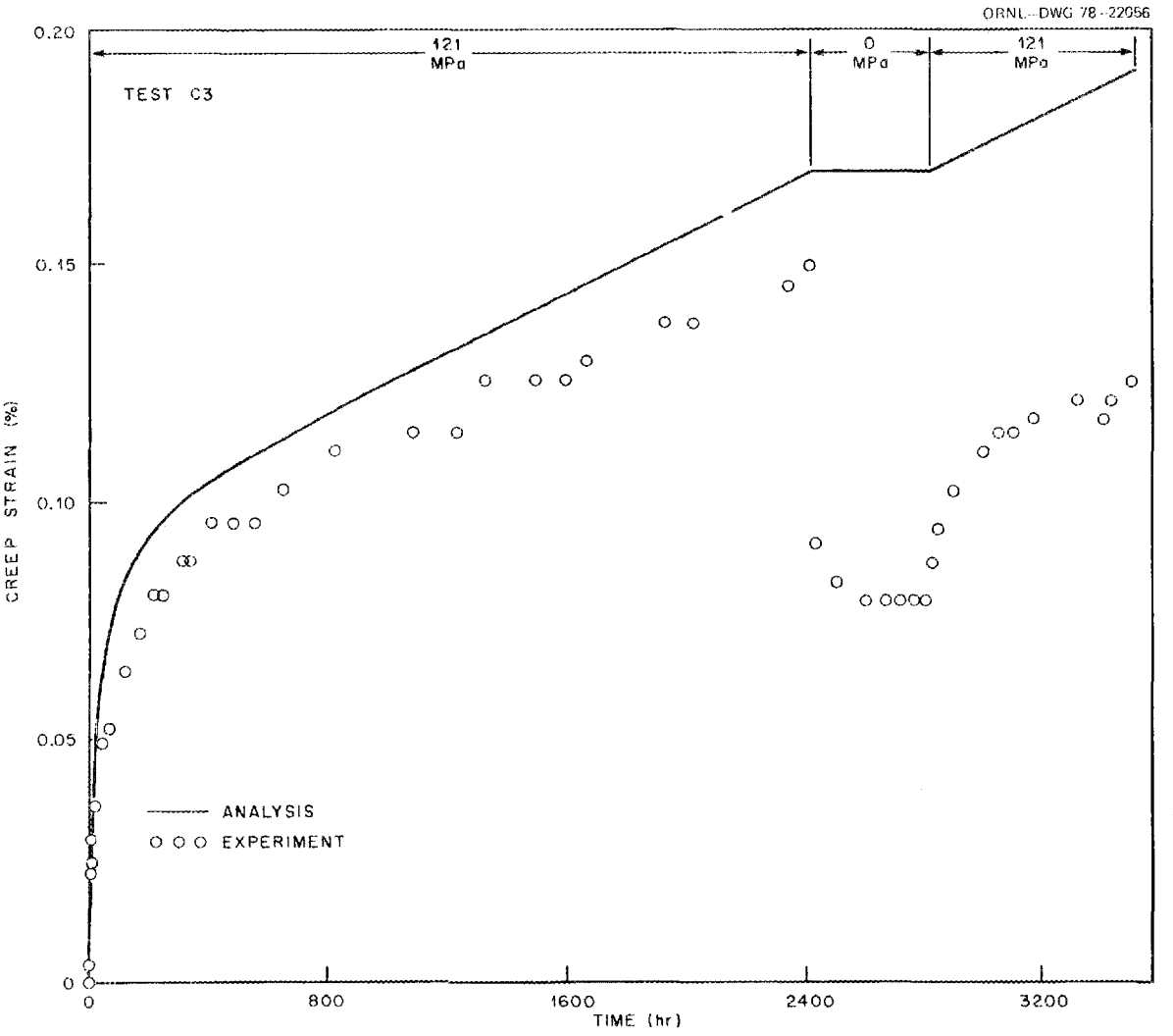

Fig. 6.18. Experimental and predicted creep strains, test C-3.

industrial applications, where they are used to measure in a qualitative fashion the sensitivity of a particular material to stress concentrations.

Early workers in this area believed notch strengthening or weakening to be more or less an intrinsic material property related to the ductility of the material. However, subsequent investigations have revealed the phenomenon to be much more complex than this, depending not only on the material but possibly on notch geometry, prior heat treatment, load level, temperature, and specimen size as well. The same material may exhibit notch strengthening under one set of conditions and notch weakening under another.

Many qualitative explanations of the notch effect phenomenon have been put forward, but not a great deal of quantitative work has been performed. A careful inelastic analysis, coupled with current failure criteria, might provide a deeper understanding than is presently available. Such an analysis is currently under way at ORNL.

6.5 Development of High-Temperature Moire Technology

G. L. Cloud* T. J. Delph

Our experiences with the moire strain measurement technique in room-temperature applications were described in Sect. 6.1. We are also developing the capability of making moire strain measurements at elevated temperatures, principally through the consulting efforts of Professor G. L. Cloud at Michigan State University. An earlier effort in this direction,[15] performed under ORNL subcontract, met with only limited success but was sufficiently promising to warrant further investigation.

Two of the principal difficulties associated with high-temperature moire measurements are the presence of "optical noise" due to convection currents in the furnace and degradation of the specimen grid caused by prolonged exposure to elevated temperatures. The first of these problem areas appears to have been successfully resolved in experiments performed at Michigan State University. Utilizing a high-resolution lens, stroboscopic flash lighting, high-resolution holographic film, and Fourier optical processing of the resulting photographs, moire fringe patterns of excellent quality have been obtained from specimens at elevated temperatures.

The second area of difficulty, that of developing a suitable high-temperature moire specimen grid, is still the subject of development work, although the results to date have been quite encouraging. Three methods of producing high-temperature grids are under active consideration at Michigan State: a metal film deposition technique, a direct grating deposition technique, and the electroetching process. In the metal film deposition technique, a fine grid of some precious metal (e.g., platinum or gold) is deposited on the metal surface by a vacuum deposition unit. A

---

*Consultant, Michigan State University.

platinum grating of high quality has been formed on a type 304 stainless steel specimen by this method. Unfortunately, it was destroyed during high-temperature testing by contamination due to outgasing from the furnace. This problem has now been corrected, and efforts along this line are continuing.

Alternatively, a direct grating deposition technique has been used to deposit a grating of Pyromark high-temperature paint on the metal surface. This method is quite simple to apply and yields an excellent, high-contrast grating which has produced moire fringe photographs of good quality at 593°C (1100°F). Grids produced by this method, however, may be susceptible to flaking caused by specimen straining, a possibility we intend to investigate.

The third method for forming high-temperature grids, the electroetching technique, involves chemically etching the grid outline into the bare metal surface. This method was used in the earlier ORNL study[15] but proved tricky to apply and yielded grids of uneven quality. Some experiments with this technique are planned, however.

We expect that one of these three methods, with minor modifications, will produce a usable moire specimen grid that will be able to withstand prolonged periods of exposure to high temperature. When this is accomplished, we will be well on our way toward achieving a whole-field strain measurement technique applicable at elevated temperatures.

References

1. T. J. Delph et al., "Plate-Weldment Test," *High-Temperature Structural Design Program Prog. Rep. Dec. 31, 1977*, ORNL-5374, pp. 193-99.

2. T. J. Delph et al., "Plate-Weldment Tests," *High-Temperature Structural Design Program Prog. Rep. June 30, 1978*, ORNL-5433, pp. 227-38.

3. T. J. Delph et al., *Room-Temperature Elastic-Plastic Tests of Plate-Weldment Specimens*, ORNL/TM-6669 (to be published).

4. R. T. King, Metals and Ceramics Division, Oak Ridge National Laboratory, unpublished data.

5. J. A. Clinard and R. W. Swindeman, "Room-Temperature Properties for 1-in. Plate of Heat 9T2796 of Type 304 Stainless Steel," *High-Temperature Structural Design Program Prog. Rep. June 30, 1977*, ORNL-5339, p. 153.

6. T. J. Delph, "Analysis of Composite Transition Joint Specimen," *High-Temperature Structural Design Program Prog. Rep. June 30, 1978*, ORNL-5433, pp. 244-47.

7. J. A. Clinard, "Creep Equation," *High-Temperature Structural Design Program Prog. Rep. Dec. 31, 1977*, ORNL-5433, pp. 137-40.

8. T. J. Delph, Uniaxial Tests of 308 Stainless Steel Weld Metal," *High-Temperature Structural Design Program Prog. Rep. June 30, 1978*, ORNL-5433, pp. 238-44.

9. J. M. Corum et al., *Thermal Ratchetting Tests of Type 304 Stainless Steel Pipe: Specimens TTT-1 and TTT-2*, ORNL-5386 (June 1978).

10. G. C. Smith and P. P. Holz, *Repair Weld Induced Residual Stresses Thick-Walled Steel Pressure Vessels*, ORNL/NUREG/TM-153 (June 1978).

11. A. J. Bush and F. J. Kromer, "Simplification of the Hole-Drilling Method of Residual Stress Measurement," *ISA Transactions* 12, 249 (1973).

12. E. M. Beaney, *Accurate Measurement of Residual Stress on Any Steel Using the Center Hole Method*, Report No. RD/B/N3568, Berkeley Nuclear Laboratory, Central Electricity Generating Board (December 1975).

13. J. A. Williams, Marchwood Engineering Laboratories, Central Electricity Generating Board, private communication.

14. T. J. Delph, *Notch Effects in Uniaxial Tension Specimens*, ORNL/TM-6716 (to be published).

15. A. J. Durelli and J. Buitrago, *Experimental Determination of Strains at High Temperatures*, prepared for Oak Ridge National Laboratory under P. O. Contract 11Y-92204V, Catholic University of America (October 1975).

ORNL-5540
Dist. Category UC-79,
-79h, -79k

Internal Distribution

1. R. L. Battiste
2. J. J. Blass
3. C. R. Brinkman
4. J. P. Callahan
5. J. A. Clinard
6. C. W. Collins
7-16. J. M. Corum
17. J. R. Ellis
18. W. L. Greenstreet
19. R. C. Gwaltney
20. W. O. Harms
21. J. F. Harvey
22. R. F. Hibbs
23. R. L. Huddleston
24. P. R. Kasten
25. R. T. King
26. R. L. Klueh
27. Milton Levenson
28. K. C. Liu
29. B. S. Maskewitz
30. W. J. McAfee
31. H. E. McCoy
32. H. C. McCurdy
33. J. G. Merkle
34. S. E. Moore
35. E. T. Onat (consultant)
36. P. Patriarca
37. H. Postma
38-42. C. E. Pugh
43-44. J. L. Rich
45. M. Richardson
46. D. N. Robinson
47. W. K. Sartory
48. V. K. Sikka
49. G. M. Slaughter
50. J. E. Smith
51. J. P. Strizak
52. R. W. Swindeman
53. H. E. Trammell
54. D. B. Trauger
55. J. R. Weir
56. G. D. Whitman
57. G. T. Yahr
58. Patent Office
59-61. Central Research Library
62. Y-12 Document Reference Section
63-69. Laboratory Records Department
70. Laboratory Records (RC)

Subcontractors

71. J. M. Chern, Foster-Wheeler Energy Corporation, 110 S. Orange Avenue, Livingston, NJ 07039
72. C. E. Jaske, Battelle-Columbus Laboratories, 505 King Avenue, Columbus, OH 43201
73. F. A. Leckie, University of Illinois, Urbana, IL 61801
74. A. Levy, Grumman Aerospace Corporation, Bethpage, NY 11714
75. W. J. O'Donnell, O'Donnell and Associates, 5100 Centre Avenue, Pittsburgh, PA 15236
76. C. C. Schultz, Babcock & Wilcox Company, P. O. Box 835, Alliance, OH 44601
77. S. Y. Zamrik, Pennsylvania State University, University Park, PA 16802

External Distribution

78-79. Director, Division of Reactor Research and Technology, Department of Energy, Washington, DC 20545
80. Office of Assistant Manager, Energy Research and Development, DOE, ORO
81. Director, Nuclear Research and Development Division, DOE, ORO
82-268. Given distribution as shown in TID-4500 under categories UC-79, -79h, -79k

☆ U. S. GOVERNMENT PRINTING OFFICE: 1980-640-245-256